EKSPLOATACJA I NIEZAWODNOŚĆ
MAINTENANCE AND RELIABILITY

Science and Technology

GUZOWSKI S, MICHNEJ M. **Influence of technological methods increasing surface layer durability on axles fretting wear in railway wheel sets**. Eksploatacja i Niezawodnosc – Maintenance and Reliability 2016; 18 (1): 1–9, http://dx.doi.org/10.17531/ein.2016.1.1.

The article presents studies whose aim is to use such technologies of improving surface layer of a wheel seat that would eliminate fretting wear. The studies were carried out on a simplified physical model of an actual connection between the wheel and the axle of a wheel set with a self-acting wheel track change. The results of carried out wear studies show that fretting wear development can be successfully limited when metallic coating in the form of molybdenizing is used. Carried out studies indicate that such a solution can be fully used in actual exploitation.

YANG Y-J, PENG W, ZHU S-P, HUANG H-Z. **A bayesian approach for sealing failure analysis considering the non-competing relationship of multiple degradation processes**. Eksploatacja i Niezawodnosc – Maintenance and Reliability 2016; 18 (1): 10–15, http://dx.doi.org/10.17531/ein.2016.1.2.

Abstract: Degradation analysis is an effective method for reliability analysis when failure time data is rare or hard to observe. Multiple degradation analysis with competing risk model is often used to implement the degradation analysis. However, in reality, the failure of a system is often a result of a combination of multiple degradation processes, such as the sum of multiple degradations. To handle this non-competing relationship of multiple degradation processes, this paper presents a new reliability model for multiple degradation processes analysis. The proposed model is demonstrated through a case-study of a spool valve. In this paper, the gamma process is adopted to construct the reliability model. The Bayesian method is used to obtain the estimations of model parameters and reliability indexes by taking account of uncertainty. The results can then be further used as valuable information for further degradation analysis and decision-making considering uncertainty.

KOPECKI T, MAZUREK P, LIS T, CHODOROWSKA D. **Post-buckling deformation states of semi-monocoque cylindrical structures with large cut-outs under operating load conditions. Numerical analysis and experimental tests**. Eksploatacja i Niezawodnosc – Maintenance and Reliability 2016; 18 (1): 16–24, http://dx.doi.org/10.17531/ein.2016.1.3.

The paper is a presentation of experimental model studies on thin-walled cylindrical structures containing large cut-outs subject to torsional deflection. The effect of rigidity of the frame reinforcing a cut-out on form and magnitude of post-buckling deformations occurring in operation conditions is analysed. A methodology based on numerical tools is proposed for determining alternative solutions in the design of structure skeleton leading to improvement of operation stability.

LIU T, CHENG L, PAN Z, SUN Q. **Cycle life prediction of Lithium-ion cells under complex temperature profiles**. Eksploatacja i Niezawodnosc – Maintenance and Reliability 2016; 18 (1): 25–31, http://dx.doi.org/10.17531/ein.2016.1.4.

Nowadays, the extensive use of Lithium-ion cells requires an accurate life prediction model. Failure of Lithium-ion cells usually results from a gradual and irreversible capacity fading process. Experimental results show that this process is strongly affected by temperature. In engineering applications, researchers often use the regression-based approach to model the capacity fading process over cycles and then perform the cycle life prediction. However, because of neglecting temperature influences, this classic method may lead to significant prediction errors, especially when cells are subject to complex temperature profiles. In this paper, we extend the classic regression-based model by incorporating cell temperature as a predictor. Two effects of temperature on cell capacity are considered. One is the positive effect that high temperature lets a cell discharge more capacity in a cycle; The other is the negative effect that high temperature accelerates cell capacity fading. A cycle life test with six cells are conducted to valid the effectiveness of our method. Results show that the improved model is more suitable to capture the dynamics of cell capacity fading path under complex temperature profiles.

GŁADYSIEWICZ L, KAWALEC W, KRÓL R. **Selection of carry idlers spacing of belt conveyor taking into account random stream of transported bulk material**. Eksploatacja i Niezawodnosc – Maintenance and Reliability 2016; 18 (1): 32–37, http://dx.doi.org/10.17531/ein.2016.1.5.

The study on the design optimisation of belt conveyors used in the mining industry – the proper selection of carry idlers - aiming to decrease the specific energy consumption of transportation with regard to different operational conditions is presented. High capacity overburden belt conveyors from a surface lignite mine as well as copper ore ones from underground ines are analysed. Calculations are

GUZOWSKI S, MICHNEJ M. **Wpływ technologicznych metod podwyższenia trwałości warstwy wierzchniej na zużycie frettingowe osi kolejowych zestawów kołowych**. Eksploatacja i Niezawodnosc – Maintenance and Reliability 2016; 18 (1): 1–9, http://dx.doi.org/10.17531/ein.2016.1.1.

W niniejszym artykule przedstawiono badania mające na celu zastosowanie takich technologii ulepszania warstwy wierzchniej podpiaścia zestawu kołowego, które eliminowałoby zużycie frettingowe. Badania zostały przeprowadzone na uproszczonym modelu fizycznym rzeczywistego połączenia koła i osi zestawu kołowego z samoczynną zmianą rozstawu kół. Wyniki przeprowadzonych badań zużyciowych wskazują, że obróbką skutecznie ograniczająca rozwój zużycia frettingowego może być zastosowanie powłoki metalicznej w postaci molibdenowania. Przeprowadzone badania wskazują na pełną możliwość zastosowania tego rozwiązania w rzeczywistej eksploatacji.

YANG Y-J, PENG W, ZHU S-P, HUANG H-Z. **Zastosowanie metody Bayesa do analizy uszkodzeń uszczelnień z uwzględnieniem współwystępujących procesów degradacji o charakterze niekonkurującym**. Eksploatacja i Niezawodnosc – Maintenance and Reliability 2016; 18 (1): 10–15, http://dx.doi.org/10.17531/ein.2016.1.2.

Analiza degradacji jest skuteczną metodą analizy niezawodnościowej w przypadkach gdy dane są skąpe lub trudne do zaobserwowania. W badaniach często wykorzystuje się analizę współwystępujących degradacji z zastosowaniem modelu zagrożeń konkurujących. Jednak w rzeczywistości, awaria systemu często jest wynikiem wystąpienia degradacji niekonkurujących, t.j. wynikiem sumy lub kombinacji współwystępujących procesów degradacji. Aby uwzględnić tę relację między niekonkurującymi procesami degradacji, w artykule przedstawiono nowy model niezawodności służący do analizy współwystępujących procesów degradacji. Proponowany model zilustrowano za pomocą studium przypadku rozdzielnika suwakowego. Przedstawiony w pracy model niezawodności skonstruowano w oparciu o proces gamma. Do oszacowania parametrów modelu oraz indeksów niezawodności zastosowano metodę Bayesa z uwzględnieniem niepewności. Uzyskane wyniki można wykorzystać w przyszłości jako cenne dane do dalszej analizy degradacji i podejmowania decyzji z uwzględnieniem niepewności.

KOPECKI T, MAZUREK P, LIS T, CHODOROWSKA D. **Stany zakrytycznych deformacji półskorupowych konstrukcji walcowych z dużymi wykrojami w warunkach obciążeń eksploatacyjnych. Analiza numeryczna i badania eksperymentalne**. Eksploatacja i Niezawodnosc – Maintenance and Reliability 2016; 18 (1): 16–24, http://dx.doi.org/10.17531/ein.2016.1.3.

W pracy zaprezentowano wyniki modelowych badań eksperymentalnych cienkościennych, skręcanych struktur walcowych zawierających duże wykroje. Przeanalizowano wpływ sztywności ramy wzmacniającej wykrój na postać i wielkość deformacji zakrytycznych, występujących w warunkach eksploatacji. Zaproponowano metodykę określania alternatywnych rozwiązań konstrukcyjnych szkieletu struktury, zapewniające poprawę trwałości eksploatacyjnej, w oparciu o narzędzia numeryczne.

LIU T, CHENG L, PAN Z, SUN Q. **Prognozowanie cyklu życia ogniw litowo-jonowych przy złożonych profilach temperaturowych**. Eksploatacja i Niezawodnosc – Maintenance and Reliability 2016; 18 (1): 25–31, http://dx.doi.org/10.17531/ein.2016.1.4.

Obecne szerokie zastosowanie ogniw litowo-jonowych wymaga stworzenia trafnego modelu prognozowania ich trwałości. Uszkodzenia ogniw litowo-jonowych zazwyczaj wynikają ze stopniowego i nieodwracalnego procesu utraty pojemności. Wyniki doświadczeń pokazują, że na ten proces silny wpływ wywiera temperatura. W zastosowaniach inżynieryjnych, naukowcy często wykorzystują podejście oparte na regresji do modelowania procesu utraty pojemności w poszczególnych cyklach by następnie dokonać prognozy trwałości w danym cyklu pracy. Jednakże, ta klasyczna metoda nie bierze po uwagę wpływu temperatury, co może prowadzić do znacznych błędów predykcji, w szczególności, gdy ogniwa pozostają pod wpływem złożonych profili temperaturowych. W prezentowanym artykule, rozszerzono klasyczny model oparty na regresji poprzez włączenie temperatury ogniwa jako czynnika prognostycznego. Przeanalizowano dwa rodzaje wpływu temperatury na pojemność ogniw. Z jednej strony, wysoka temperatura oddziałuje pozytywnie pozwalając ogniwu na uzyskanie większej pojemności w danym cyklu; z drugiej strony jest to wpływ negatywny, ponieważ wysoka temperatura przyspiesza utratę pojemności ogniwa. Przy użyciu sześciu ogniw, przeprowadzono badanie trwałości w danym cyklu pracy w celu potwierdzenia skuteczności naszej metody. Wyniki pokazują, że udoskonalony model pozwala lepiej uchwycić dynamikę ścieżki utraty pojemności ogniwa w warunkach złożonych profili temperaturowych.

GŁADYSIEWICZ L, KAWALEC W, KRÓL R. **Dobór rozstawu krążników górnych przenośnika taśmowego z uwzględnieniem losowo zmiennej strugi urobku**. Eksploatacja i Niezawodnosc – Maintenance and Reliability 2016; 18 (1): 32–37, http://dx.doi.org/10.17531/ein.2016.1.5.

Przedstawiono studium optymalizacji konstrukcyjnej – właściwego doboru rozstawu krążników górnych - górniczych przenośników taśmowych, pod kątem zmniejszenia zużycia jednostkowej energii transportu z uwzględnieniem zróżnicowanych warunków eksploatacyjnych. Analizowano przenośniki nadkładowe dużej wydajności z kopalni odkrywkowej węgla brunatnego i podziemne z kopalni rud

performed in the specialised engineering software with the use of characteristics of idlers' rotational resistance as a function of radial loading that were obtained in the laboratory and identified distribution of actual capacity of main haulage and division belt conveyors. The purposefulness of the individual treatment to the carry idler spacing, depending on the conveyor's location within the haulage system and its operational loadings – bigger for the main haulage and smaller for the division conveyors is found. The presented results of calculations are evidences for further economic analysis, which take into account – apart of energy costs – also costs of installation and replacements of idlers.

BABEŁ M, SZKODA M. **Diesel locomotive efficiency and reliability improvement as a result of power unit load control system modernisation**. Eksploatacja i Niezawodnosc – Maintenance and Reliability 2016; 18 (1): 38–49, http://dx.doi.org/10.17531/ein.2016.1.6.

The article presents an idea of modernisation of a diesel locomotive power unit load control using SM31 locomotive. In the proposed solution an electronic rotations and power governor of a8C22W diesel engine is applied, developed in cooperation with Lokel (the Czech Republic) and Newag S.A. (Poland), in which a new optimal operational characteristic is realized in the locomotive. This characteristic was selected following optimization calculations using a mathematical model mapping the real conditions of the motor-generator work in a diesel engine. Test stand experimental investigations together with an over three-year supervised observation of the locomotive equipped with the electronic governor have proved its correct and reliable operation. Based on the data collected in supervised observation the efficiency of the proposed solution has been assessed, supported by an LCC (Life Cycle Cost) analysis.

ŁABĘDA-GRUDZIAK ZM. **Diagnostic technique based on additive models in the tasks of the ongoing exploitation of gas network**. Eksploatacja i Niezawodnosc – Maintenance and Reliability 2016; 18 (1): 50–56, http://dx.doi.org/10.17531/ein.2016.1.7.

The article presents a method of estimating the pressure value at given nodes of natural gas transmission network for the purposes of predicting changes of the process state during its exploitation. For this purpose additive regression model was applied together with non-parametric estimation techniques, which was used for monitoring the operation of gas networks, as well as designing the system of fault detection, and then – the assessment of sensitivity for particular faults. Research was conducted on the basis of data from the analytical model of network simulator, which is adjusted to the actual gas transmission network.

ZIEJA M, WAŻNY M, STĘPIEŃ S. **Distribution determination of time of exceeding permissible condition as used to determine lifetimes of selected aeronautical devices/systems**. Eksploatacja i Niezawodnosc – Maintenance and Reliability 2016; 18 (1): 57–64, http://dx.doi.org/10.17531/ein.2016.1.8.

The paper refers to the modelling of changes in ever-growing deviations from diagnostic parameters that describe health/maintenance status of one from among numerous aircraft systems, i.e. of a sighting system. Any sighting system has been intended, first and foremost, to find a sighting angle and a lead angle, both of them essential and indispensable to fight hostile targets. Destructive factors such as, e.g. ageing processes, that keep affecting the aircraft as a whole throughout its operation, make these angles change: actual values thereof differ from the calculated ones. Such being the case, a considerable error may be introduced in the process of aiming the weapons to, in turn, result in the reduction of values that describe the quality of the sighting process. That is why any sighting system requires specific checks possibly (if need be) followed with some adjustments (based on the findings of these checks) to remove negative effects of any ageing processes that might have affected this system. Determination of the density function of the deviation using difference equations and the Fokker-Planck equation is a basic element of the presented method, which enables next analyses. Innovative elements of the paper are as follows:– determination of distributions of time of exceeding the permissible (boundary) condition using the density function of the deviation, – application of distributions of time of exceeding the permissible (boundary) condition for modification of operation/maintenance systems of selected aeronautical devices.The paper has been concluded with a numerical example that proves the application-oriented nature of the issues in question, represented by the earlier conducted assessment of lifetimes of the systems intended to find the sighting and lead angles (ε and β). The in the paper discussed method to assess the lifetime may as well be applied to another systems/devices. It shows a versatile nature and makes a valuable contribution to the methods of maintaining any engineered systems in good condition (i.e. of providing maintenance to any engineered systems).

MIERZEJEWSKA ŻA, KUPTEL P, SIDUN J. **Analysis of the surface condition of removed bone implants**. Eksploatacja i Niezawodnosc – Maintenance and Reliability 2016; 18 (1): 65–72, http://dx.doi.org/10.17531/ein.2016.1.9.

miedzi. Obliczenia wykonano w środowisku specjalistycznego oprogramowania inżynierskiego wykorzystując wyznaczone laboratoryjnie charakterystyki oporu obracania krążników w funkcji obciążenia oraz zidentyfikowane rozkłady strugi urobku w odstawie głównej i oddziałowej. Stwierdzono celowo zróżnicowania rozstawu zestawów krążników górnych w zależności od rzeczywistego obciążenia strugą urobku – większego dla przenośników odstawy głównej (zbiorczych) i mniejszego dla przenośników oddziałowych. Przedstawione wyniki obliczeń są przesłankami do analiz ekonomicznych, uwzględniających - oprócz kosztu energii – również koszt zabudowy i wymian krążników.

BABEŁ M, SZKODA M. **Poprawa efektywności i niezawodności lokomotyw spalinowych w wyniku modernizacji układu sterowania obciążeniem zespołu napędowego**. Eksploatacja i Niezawodnosc – Maintenance and Reliability 2016; 18 (1): 38–49, http://dx.doi.org/10.17531/ein.2016.1.6.

W artykule przedstawiono koncepcję modernizacji układu sterowania obciążeniem zespołu napędowego lokomotywy spalinowej na przykładzie lokomotywy serii SM31. Proponowane rozwiązanie polega na zastosowaniu elektronicznego regulatora obrotów i mocy silnika wysokoprężnego a8C22W, opracowanego w wyniku wspólnych prac autorów z firmą Lokel (Czechy) i Newag S.A. (Polska), realizującego na lokomotywie nową, optymalną charakterystykę eksploatacyjną. Charakterystyka ta została wybrana w wyniku obliczeń optymalizacyjnych z wykorzystaniem opracowanego modelu matematycznego odwzorowującego rzeczywiste warunki pracy zespołu silnik-prądnica na lokomotywie spalinowej. Badania stanowiskowe oraz ponad trzyletnia eksploatacja obserwowana lokomotywy z zamontowanym regulatorem elektronicznym wykazały poprawne i niezawodne jego działanie. Bazując na danych zgromadzonych podczas eksploatacji obserwowanej, przeprowadzono ocenę efektywności proponowanego rozwiązania w oparciu o analizę LCC (Life Cycle Cost).

ŁABĘDA-GRUDZIAK ZM. **Technika diagnostyki oparta na addytywnych modelach regresyjnych w zadaniach bieżącej eksploatacji sieci gazowej**. Eksploatacja i Niezawodnosc – Maintenance and Reliability 2016; 18 (1): 50–56, http://dx.doi.org/10.17531/ein.2016.1.7.

W artykule przedstawiono metodę oszacowania wartości ciśnienia w określonych punktach węzłowych sieci przesyłowej gazu ziemnego dla potrzeb przewidywania zmiany stanu procesu w trakcie jego eksploatacji. W tym celu wykorzystano addytywny model regresji wraz z nieparametrycznymi technikami estymacji, który posłużył zarówno do monitorowania pracy sieci gazowej, jak i do konstrukcji układu detekcji uszkodzeń, a następnie do oceny wrażliwości na występowanie poszczególnych uszkodzeń. Badania przeprowadzono na podstawie danych z modelu analitycznego symulatora sieci, który dostrojony jest do rzeczywistej sieci przesyłowej gazu.

ZIEJA M, WAŻNY M, STĘPIEŃ S. **Wyznaczenie rozkładu czasu przekraczania stanu granicznego i jego zastosowanie do określania trwałości wybranych urządzeń lotniczych**. Eksploatacja i Niezawodnosc – Maintenance and Reliability 2016; 18 (1): 57–64, http://dx.doi.org/10.17531/ein.2016.1.8.

Praca dotyczy modelowania zmian narastających odchyłek parametrów diagnostycznych charakteryzujących stan techniczny jednego z systemów statku powietrznego, tj. systemu celowniczego. Jednym z głównych zadań systemu celowniczego jest wyznaczenie kątów celowania i wyprzedzenia niezbędnych do zwalczania celów przeciwnika. Oddziaływanie w czasie eksploatacji statku powietrznego czynników destrukcyjnych m.in. procesów starzeniowych, powoduje, że kąty te ulegają zmianie i ich rzeczywiste wartości różnią się od wartości kątów obliczeniowych. Wystąpienie takiej sytuacji powoduje wprowadzenie dość istotnego błędu do procesu celowania i obniża wartość wskaźników charakteryzujących jakość jego przebiegu. Z tego też względu system celowniczy wymaga określonej kontroli i w oparciu o uzyskane wyniki, potencjalnej regulacji mającej na celu usunięcie ujemnych skutków procesów starzeniowych celownika. Podstawowym elementem pracy umożliwiającym dalsze analizy było wyznaczenie funkcji gęstości odchyłki z wykorzystaniem równań różnicowych oraz równania Fokkera-Plancka. Do nowatorskich elementów pracy należy zaliczyć: – wyznaczenie rozkładu czasu przekroczenia stanu dopuszczalnego (granicznego) z wykorzystaniem funkcji gęstości odchyłki, – zastosowanie rozkładu czasu osiągania stanu granicznego do modyfikacji systemów eksploatacji urządzeń lotniczych. Praca podsumowana jest przykładem obliczeniowym przedstawiającym aplikacyjny charakter poruszanej tematyki, odwzorowanej na przykładzie oceny trwałości układów określających kąt celowania i wyprzedzenia (ε i β). Przedstawiona metoda oceny trwałości w niniejszym artykule może być zastosowania do innych urządzeń. Ma ona ogólny charakter i stanowi wkład do metod utrzymania systemów technicznych.

MIERZEJEWSKA ŻA, KUPTEL P, SIDUN J. **Analiza stanu powierzchni usuniętych implantów kostnych**. Eksploatacja i Niezawodnosc – Maintenance and Reliability 2016; 18 (1): 65–72, http://dx.doi.org/10.17531/ein.2016.1.9.

The requirements that must be met by implant materials are rigorous and diverse. These materials are tasked with supporting or replacing sick or damaged parts of the musculoskeletal system, where loads and a heterogeneous stress state frequently occur. Thus, they must have the appropriate strength properties and resistance to many types of corrosion, which is related to biotolerance, or neutrality of the material to the human body during use. This article presents the results of studies of three implant groups: set for stabilization of long bones made of 316L austenitic steel, set for intramedullary nail insertion in grafts of femur bones made of Ti6Al4V titanium alloy, and a straighty reconstruction plate made of Ti6Al4V titanium alloy coated with an oxide layer. These implants were implanted into the human body and then removed at the end of the treatment process or due to implant failure during its operation. Next, implants were studied in order to determine the level of wear. Investigations were carried out using an Hitachi S-3000N scanning microscope. Their results indicate a series of changes that took place on implant surfaces and confirm the existence of typical implant wear mechanisms presented in reports in the literature. Traces of corrosion, fatigue cracks, tribological wear, and traces of fretting were found on examined implant surfaces. The study of implant wear cases, determination of their character, and evaluation of the intensity of destructive processes may contribute to the improvement of both the mechanical properties of these implants and their shape, so that modern bone implants perform their roles without the risk of failure during their operation.

GZIUT O, KUCZMASZEWSKI J, ZAGÓRSKI I. **Analysis of chip fragmentation in AZ91HP alloy milling with respect to reducing the risk of chip ignition**. Eksploatacja i Niezawodnosc – Maintenance and Reliability 2016; 18 (1): 73–79, http://dx.doi.org/10.17531/ein.2016.1.10.

Magnesium alloys are used as advanced structural materials for producing machine components for the aircraft or automotive industry. The machining of these components involves the risk of uncontrolled ignition during machining operations and production of fine-grained chip fractions causing the wear of kinematic pairs in technological machines. Given the operation of machine tools, the determination of a method for assessing risk based on determining a safe milling range and suitable operational parameters seems justified. The paper presents the results of investigations on chip fragmentation, chip mass and dimensions. Based on these parameters, we determine effective and safe regions with respect to operation of machine tools. The experiments are performed on magnesium alloy AZ91HP, one of the most widely used casting alloys.

QIN J, NIU Y, LI Z. **A combined method for reliability analysis of multi-state system of minor-repairable components**. Eksploatacja i Niezawodnosc – Maintenance and Reliability 2016; 18 (1): 80–88, http://dx.doi.org/10.17531/ein.2016.1.11.

This paper discusses the multi-state system (MSS) consisted of multi-state components with minor failure and minor repair. In order to obtain the reliability indices of MSS, a new combined method is suggested. This method is based on the Markov stochastic process and the universal generating function (UGF) technology. The traditional idea of modeling the MSS is to use straightforward Markov process. That is not effective enough for the MSS because the model of the system is complicated usually and the state space often arouses "dimension curse" - huge numbers of the states. We suggest it should model the multi-state components and the UGF of multi-state components can be obtained firstly. Then the MSS can be decomposed into several subsystems which only contain simple series-parallel structure. According to the physical nature of the subsystems, the UGF of those subsystems can be employed recursively. Furthermore the UGF of the entire MSS will be obtained. Therefore, the reliability indices of the MSS can be evaluated easily. The suggested method simplifies greatly the complexity of calculation and is well formulized. Two numerical examples illustrate this method.

WENDEKER M, CZYŻ Z. **Analysis of the bearing nodes loads of turbine engine at an unmanned helicopter during a jump up and jump down maneuver**. Eksploatacja i Niezawodnosc – Maintenance and Reliability 2016; 18 (1): 89–97, http://dx.doi.org/10.17531/ein.2016.1.12.

The article is part of the work, which was made to systematize the operating conditions of bearing loads in the rotor assembly of FSTC-1 turbine engine, which is designed in the Department of Thermodynamics, Fluid Mechanics and Aviation Propulsion Systems at Lublin University of Technology. This engine assumes the use of the gas bearing in compressor drive unit to improve the operating characteristics. This is justified by difficult working conditions associated with high speeds, high temperatures and difficult access, as in the case of gas bearings is not a major problem. A mathematical model of possible states of load bearing nodes in compressor drive unit was also presented. Load analysis was carried out for maneuver jump up and jump down based on the time course of geometric altitude from the radio altimeter based on real

Wymagania stawiane materiałom na implanty są wysokie i bardzo zróżnicowane. Mają one wspomagać lub zastępować chore lub uszkodzone części układu kostno-mięśniowego, gdzie często pojawiają się obciążenia i różnorodny stan naprężeń. Muszą zatem charakteryzować się odpowiednimi własnościami wytrzymałościowymi i odpornością na różne rodzaje korozji, powiązaną z biotolerancją oznaczającą neutralność materiału wobec organizmu podczas użytkowania. W pracy przedstawiono wyniki badań trzech grup implantów: zestawu do stabilizacji kości długich, wykonanego ze stali austenitycznej 316L, zestawu do gwoździowania śródszpikowego do zespoleń złamań kości udowej, wykonanego ze stopu tytanu Ti6Al4V oraz płytki rekonstrukcyjnej prostej, wykonanej ze stopu tytanu Ti6Al4V pokrytego warstwą tlenków. Implanty te wszczepione były do organizmu ludzkiego, a następnie usunięte, wraz z zakończeniem procesu leczenia lub wskutek uszkodzenia implantu podczas jego eksploatacji. Następnie poddano je badaniom w celu określenia stopnia zużycia. Badania realizowano z wykorzystaniem mikroskopu skaningowego Hitachi S-3000N. Wyniki badań wskazują na szereg zmian, które zaszły na powierzchni implantów i potwierdziły istnienie typowych mechanizmów zużycia implantów prezentowanych w doniesieniach literaturowych. Na powierzchni badanych implantów zauważono ślady korozji, pęknięcia zmęczeniowe, zużycie tribologiczne oraz ślady frettingu. Badania zużycia implantów, określenie ich charakteru oraz ocena intensywności zachodzenia procesów niszczenia mogą w przyszłości znacznie wpłynąć na poprawę zarówno właściwości mechanicznych tych implantów, jak również na próbę zmiany ich kształtu tak, by nowoczesne implanty kostne spełniały swoją rolę bez ryzyka zniszczenia w trakcie ich eksploatacji.

GZIUT O, KUCZMASZEWSKI J, ZAGÓRSKI I. **Analiza fragmentacji wiórów podczas frezowania stopu AZ91HP w aspekcie zmniejszenia ryzyka zapłonu**. Eksploatacja i Niezawodnosc – Maintenance and Reliability 2016; 18 (1): 73–79, http://dx.doi.org/10.17531/ein.2016.1.10.

Stopy magnezu są wykorzystywane jako nowoczesne materiały konstrukcyjne na elementy maszyn wytwarzane m.in. na potrzeby przemysłu lotniczego czy motoryzacyjnego. Obróbka skrawaniem tych elementów wiąże się z ryzykiem niekontrolowanego zapłonu podczas wykonywania operacji obróbkowych oraz powstawaniem drobnoziarnistych frakcji wiórów powodujących przyspieszone zużycie węzłów kinematycznych maszyn technologicznych. Zaproponowanie oceny ryzyka związanego z wyborem zakresu, uznawanego za bezpieczny, parametrów technologicznych frezowania, wydaje się celowe ze względów eksploatacyjnych maszyn obróbkowych. W artykule przedstawiono wyniki badań fragmentacji wiórów, ich masy oraz wymiarów charakterystycznych wiórów. Istotnym wydaje się określenie (na podstawie wymienionych wskaźników) obszarów uznawanych ze efektywne a zarazem bezpieczne z punktu widzenia eksploatacji maszyn obróbkowych. Do badań wytypowano często stosowany stop magnezu, z grupy odlewniczych, AZ91HP.

QIN J, NIU Y, LI Z. **Łączona metoda analizy niezawodności systemu wielostanowego składającego się z elementów podlegających drobnej naprawie**. Eksploatacja i Niezawodnosc – Maintenance and Reliability 2016; 18 (1): 80–88, http://dx.doi.org/10.17531/ein.2016.1.11.

W artykule omówiono system wielostanowy (multi-state system, MSS) składający się z elementów wielostanowych, które mogą ulegać drobnym uszkodzeniom i podlegają drobnym naprawom. Zaproponowano nową metodę łączoną, która pozwala wyznaczać wskaźniki niezawodności MSS. Metoda ta opiera się na procesie stochastycznym Markowa oraz technologii uniwersalnej funkcji tworzącej (universal generating function, UGF). Tradycyjnie do modelowania MSS wykorzystuje się sam proces Markowa. Metoda ta nie jest jednak wystarczająco skuteczna w przypadku MSS, ponieważ modele tego typu systemów są zazwyczaj skomplikowane, a przestrzeń stanów często prowadzi do tzw. "przekleństwa wielowymiarowości" – konieczności uwzględnienia ogromnej liczby stanów. Nasza metoda polega na modelowaniu elementów wielostanowych, dla których, w pierwszej kolejności wyznacza się UGF. Następnie MSS można rozłożyć na kilka podsystemów, które mają prostą strukturę szeregowo-równoległą. Charakter fizyczny tych podsystemów, pozwala na rekurencyjne stosowanie UGF dla tych podsystemów. Ponadto metoda umożliwia wyznaczenie UGF dla całego MSS, co pozwala na łatwą ocenę wskaźników niezawodności MSS. Proponowana metoda znacznie upraszcza obliczenia i jest dobrze sformalizowana. W pracy przedstawiono dwa przykłady numeryczne, które ilustrują omawianą metodę.

WENDEKER M, CZYŻ Z. **Analiza obciążeń węzłów łożyskowych silnika turbinowego w bezzałogowym śmigłowcu podczas manewru skok w górę i skok w dół**. Eksploatacja i Niezawodnosc – Maintenance and Reliability 2016; 18 (1): 89–97, http://dx.doi.org/10.17531/ein.2016.1.12.

Artykuł stanowi część prac, w których dokonano usystematyzowania eksploatacyjnych stanów obciążeń łożysk zespołu wirnikowego silnika turbinowego FSTC-1, który projektowany jest w Katedrze Termodynamiki, Mechaniki Płynów i Napędów Lotniczych na Politechnice Lubelskiej. Silnik ten zakłada zastosowanie w zespole wytwornicowym łożysk gazowych w celu poprawy właściwości eksploatacyjnych. Jest to uzasadnione trudnymi warunkami pracy związanymi z dużymi prędkościami obrotowymi, wysokimi temperaturami oraz trudnym dostępem, co w przypadku łożysk gazowych nie stanowi większego problemu. Przedstawiono również matematyczny model możliwych do wystąpienia stanów obciążeń węzłów łożyskowych zespołu wytwornicowego. Analizę obciążeń przeprowadzono dla manewru skok w górę i skok w dół na podstawie przebiegu

tests of a manned PZL W3-Sokol helicopter. The dependence of the altitude changing during the time was approximated by the least squares method and then the velocity and acceleration changes were determined. On this basis, the forces acting on the bearing in compressor drive unit under static and dynamic conditions were calculated. These values will be confronted with the values obtained during other maneuvers, and will be used as input assumptions to project of the gas bearings.

czasowego wysokości geometrycznej z radiowysokościomierza w oparciu o rzeczywiste badania załogowego śmigłowca PZL W3-Sokół. Zależność zmiany wysokości w czasie aproksymowano metodą najmniejszych kwadratów a następnie wyznaczono dla niej zmiany prędkości oraz przyspieszeń. Na tej podstawie wyznaczono wartości sił działających na łożyska zespołu wytwornicowego w warunkach statycznych jak i dynamicznych. Wartości te zostaną skonfrontowane z wartościami uzyskanymi podczas innych manewrów oraz posłużą, jako założenia wejściowe do projektu łożysk gazowych.

Considering the degradation and catastrophic failure modes simultaneously, a general reliability analysis model was presented for the competing failure processes with unbalanced data. For the degradation process with highly unbalanced data, we developed a linear random-effects degradation model. The model parameters can be estimated based on a simple least square method. Furthermore, to fully utilize the degradation information, we considered the last measured times of the degradation units that had only one or two measured time points as zero-failure data or right-censored data of the catastrophic failure mode. Then the incomplete data set was composed of zero-failure data and catastrophic failure data. To analyze the incomplete data, the definition of the interval statistics was firstly given. The best linear unbiased parameter estimators of catastrophic failure were obtained based on the Gauss-Markov theorem. Then, the reliability function of the competing failure processes was given. The corresponding two-sided confidence intervals of the reliability were obtained based on a bootstrap procedure. Finally, a practical application case was examined by applying the proposed method and the results demonstrated its validity and reasonability.

W pracy przedstawiono ogólny model analizy niezawodności procesów związanych z powstawaniem uszkodzeń konkurujących, który pozwala na wykorzystanie danych niezbilansowanych oraz umożliwia jednoczesne uwzględnienie uszkodzeń wynikających z obniżenia charakterystyk i uszkodzeń katastroficznych. Opracowano liniowy model efektów losowych dla procesu degradacji o wysoce niezbilansowanych danych. Parametry tego modelu można określić na podstawie prostej metody najmniejszych kwadratów. Ponadto, aby w pełni wykorzystać informacje dotyczące obniżenia charakterystyk, dane pochodzące z ostatniego pomiaru jednostek podlegających degradacji, dla których przeprowadzono tylko jeden lub dwa pomiary, rozpatrywano jako dane o zerowym uszkodzeniu lub jako ucięte prawostronnie dane dotyczące uszkodzenia katastroficznego. W ten sposób otrzymano zbiór niepełnych danych składający się z danych o uszkodzeniach zerowych oraz danych o uszkodzeniach katastroficznych. Aby móc przeanalizować uzyskane niepełne dane, podano definicję statystyki przedziałowej. Najefektywniejszy nieobciążony estymator liniowy (BLUE) parametrów uszkodzeń katastroficznych uzyskano na podstawie twierdzenia Gaussa-Markowa. Następnie, podano wzór funkcji niezawodności procesów związanych z powstawaniem uszkodzeń konkurujących. Odpowiednie dwustronne przedziały ufności dla oszacowanej niezawodności uzyskano metodą bootstrapową. Na koniec, przedstawiono przypadek praktycznego zastosowania proponowanej metody, którego wyniki wykazały jej trafność i zasadność.

The Design of experiment (DOE) method was used in this paper to rubber conveyor belt tension testing. Using DOE method were from experimentally obtained data established effects of factors and interactions that affect the value of the measured strength and also were determined regression models, which apply input and output variables to the relation. The regression model presents the complete multifactor experiment that contains main factors and interactions.

Metoda planowania eksperymentu (DOE) w artykule użyta do testowania napięcia taśm przenośnikowych tkaninowo – gumowych. Korzystanie z metody DOE były ustalonych poszczególnych czynników oraz ich interakcji ze danych uzyskanych w sposób doświadczalny. Czynniki i interakcje wpływające na wartość zmierzonej wytrzymałości, a także określono modele regresji, wykazującego związki pomiędzy zmiennymi wejściowymi i wyjściowymi. Model regresyjny przedstawia kompletny wieloczynnikowy eksperyment obejmujący podstawowe zmienne oraz ich interakcje.

A novel methodology is presented for condensation in power generation plants; this section is the main intersection of heat loss, typically 40% thermal efficiency of a plant. Condensate section is interfaced with the generating section to enhance the active contribution of the system. Both the cooling section and the condensate section are integrated and interfaced through the low-pressure and high-pressure cycles to attain the improved electrical efficiency, which affects the heat transfer capability of the power generation plants. This paper proposess a Cooling-cum-Condensate-Extraction System (CCES), to dedicate a 36-MW- captive power plant. The paper is dedicated for the design and development of an effective CCES, analyzing its impact over the systems in terms of system reliability optimization, and the role of real-time optimization. The designed model also contributes in discharging lesser amount of flu gases as against existing technologies with its improved active operation hours.

W artykule przedstawiono nowatorską metodologię procesu skraplania do zastosowania w części kondensacyjnej elektrowni, gdzie dochodzi do największych strat ciepła – przeważnie aż 40% wydajności termicznej elektrowni. W proponowanym rozwiązaniu instalację kondensacyjną sprzężono z częścią prądotwórczą aby zwiększyć aktywny wkład systemu. Część chłodzącą zintegrowano i sprzężono z częścią kondensacyjną poprzez cykle nisko- i wysokociśnieniowe, uzyskując w ten sposób lepszą wydajność elektryczną, co ma wpływ na zdolność wymiany ciepła w elektrowni. W artykule przedstawiono układ chłodzenia z systemem odprowadzania skroplin (CCES) przeznaczony dla elektrowni potrzeb własnych o mocy 36 MW. Pracę poświęcono projektowaniu i konstrukcji efektywnego CCES, analizując jego wpływ na systemy elektrowni w zakresie optymalizacji niezawodności systemów oraz roli optymalizacji w czasie rzeczywistym. Zaprojektowany przez nas model, w porównaniu z istniejącymi technologiami, przyczynia się również do zmniejszenia emisji gazów odlotowych dzięki zoptymalizowanemu czasowi pracy.

In the paper the method of determining the mathematical relationship for calculating the flank wear VBc of the most worn hob tooth is discussed. The relationship, in the form of a multiple regression function, was determined based on the acceptance and rejection method. The data for the calculations was obtained from experiments carried out for hobbing of carbon steel C45 with the use of a cutting fluid supplied in flood mode (WM) and with a minimum quantity lubrication mode (MQL). Based on the developed equations the impact of the selected machining parameters the course of the hob wear was assessed. In the final part of the paper, the obtained mathematical relationships were analysed and verified.

W artykule omówiono metodę wyznaczania zależności matematycznej do obliczania wielkości starcia VBc najbardziej zużytego ostrza frezu ślimakowego. Zależność w postaci funkcji regresji wielorakiej wyznaczono metodą dołączania i odrzucania. Dane do obliczeń uzyskano przeprowadzając badania eksperymentalne frezowania stali węglowej C45 z udziałem cieczy obróbkowej podawanej w trybie obfitym oraz z minimalnym wydatkiem (MQL). W oparciu o wyznaczone równania dokonano oceny wpływu wybranych warunków obróbki na przebieg zużycia frezów ślimakowych. W końcowej części artykułu dokonano analizy uzyskanych zależności matematycznych oraz przeprowadzono ich weryfikację.

KUMAR R, CHATTOPADHYAYA S, HLOCH S, KROLCZYK G, LEGUTKO S. **Wear characteristics and defects analysis of friction stir welded joint of aluminium alloy 6061-t6**. Eksploatacja i Niezawodnosc – Maintenance and Reliability 2016; 18 (1): 128–135, http://dx.doi.org/10.17531/ein.2016.1.17.
This paper deals with the wear characteristics and defects developed during friction stir welding at different process parameter of aluminium alloy (AA) 6061-T6 having thickness 6 mm. Four welded samples are prepared with rotational speed 500 rpm, 710 rpm, 1000 rpm and with welding speed of 25 mm/min & 40 mm/min. Welded samples and base material are put in wear condition under grinding machine for 120 s. Material removal is measure by taking the difference of weight before and after wear. Different types of defects and fracture are observed on the wear surface. These defects and fractures are analysed under field emission scanning electron microscope (FESEM). It is concluded that material removal from welded sample is less compared to base metal, hence wear resistance increases after friction stir welding.

BARTNIK G, PIENIAK D, NIEWCZAS AM, MARCINIAK A. **Probabilistic model for flexural strength of dental composites used in modeling reliability of the "tooth-dental composite" system**. Eksploatacja i Niezawodnosc – Maintenance and Reliability 2016; 18 (1): 136–141, http://dx.doi.org/10.17531/ein.2016.1.18.
In the article the application of Bayesian probabilistic modeling was presented as a way to standardize development of measurement results, which completes the operational and procedural standardization of determining the strength of dental composites. The traditional way of conducting studies of strength performed as services and calculations, and which do not refer to previous studies, was changed into an adaptation process of knowledge accumulation in a form of an increasing precise models. Probabilistic flexural strength models were used to create a reliability ranking of studied dental composites. Conceptualization of reliability of a biotechnological system, such as a "tooth-dental composite" required the expansion of the notion of "failure" with random events involving the occurrence of compatibility failure.

DJURIĆ R, MILISAVLJEVIĆ V. **Investigation of the relationship between reliability of track mechanism and mineral dust content in rocks of lignite open pits**. Eksploatacja i Niezawodnosc – Maintenance and Reliability 2016; 18 (1): 142–150, http://dx.doi.org/10.17531/ein.2016.1.19.
This paper describes a mathematical relation which is developed to estimate the occurrence of track mechanism failure in function on the mineral dust (SiO2) content, i.e. wear intensity. This relation is based on actual data of track-type machine (bulldozers) failures, the properties of rocks and measurements of wear intensity on the upper rollers of track mechanism. Failures of bulldozers were recorded during the period of 12 months on six open pits in Serbia, together with their location which is correlated rock type and SiO2 content. This enabled establishment of the reliability indicators using two-parameter Weibull distribution. Further on, correlation is interpreted based on the linearization model using the method of least square. This research has impact on proper management of track-type machines operating on lignite open pits, in the sense of predicting time to failures and cost of maintenance of these machines. This approach provided guidelines for the establishment of reliability centered maintenance model.

SKRUCANY T, SARKAN B, GNAP J. **Influence of aerodynamic trailer devices on drag reduction measured in a wind tunnel**. Eksploatacja i Niezawodnosc – Maintenance and Reliability 2016; 18 (1): 151–154, http://dx.doi.org/10.17531/ein.2016.1.20.
The value of aerodynamic drag is the largest, when a vehicle is moving with higher velocity. It seems that drag reduction is the most important step for reducing the fuel consumption of haulage trailer sets. Using aerodynamic trailer devices is one of many ways for reduction of fuel consumption. This paper deals with experimental measuring of the truck set model in a wind tunnel. The scale of the model was 1/24. Resultant values of the drag reduction for chosen aerodynamic devices are discussed at the end of the paper.

KUMAR R, CHATTOPADHYAYA S, HLOCH S, KROLCZYK G, LEGUTKO S. **Charakterystyka zużycia i analiza uszkodzeń złącza ze stopu aluminium 6061-T6 zgrzewanego tarciowo z przemieszaniem**. Eksploatacja i Niezawodnosc – Maintenance and Reliability 2016; 18 (1): 128–135, http://dx.doi.org/10.17531/ein.2016.1.17.
Praca dotyczy charakterystyki zużycia i uszkodzeń podczas zgrzewania tarciowego z przemieszaniem stopu aluminium (AA) 6061-T6 o grubości 6 mm dla zmiennych parametrów. Cztery zgrzewane próbki były wykonane z prędkością obrotową 500 obr/min, 710 obr/min, 1000 obr/min dla prędkości zgrzewania 25 mm/min i 40 mm/min. Zgrzewane próbki i materiał bazowy były poddawane zużywaniu za pomocą szlifierki w czasie 120 s. Ubytek materiału mierzono jako różnicę wagi przed i po zużywaniu. Różne rodzaje wad i pęknięć zaobserwowano na zużytej powierzchni. Wady i pęknięcia analizowano za pomocą mikroskopu polowego (FESEM). Stwierdzono, że ubytek materiału ze zgrzewanych próbek jest mniejszy w porównaniu z ubytkiem dotyczącym materiału bazowego. Zwiększa się więc odporność na zużycie po zgrzewaniu tarciowym z przemieszaniem.

BARTNIK G, PIENIAK D, NIEWCZAS AM, MARCINIAK A. **Probabilistyczny model wytrzymałości na zginanie kompozytów stomatologicznych w zastosowaniu do modelowania niezawodności układów „ząb – kompozyt stomatologiczny"**. Eksploatacja i Niezawodnosc – Maintenance and Reliability 2016; 18 (1): 136–141, http://dx.doi.org/10.17531/ein.2016.1.18.
W pracy przedstawiono zastosowanie bayesowskiego modelowania probabilistycznego jako sposobu standaryzacji opracowania wyników pomiarów, uzupełniającego standaryzację operatorowo – proceduralną wyznaczania wytrzymałości kompozytów stomatologicznych. Tradycyjny sposób prowadzenia badań wytrzymałościowych, wykonywanych usługowo i obliczeniowo nienawiązujących do badań poprzednich, zmieniono w adaptacyjny proces kumulacji wiedzy w postaci coraz dokładniejszych modeli. Probabilistyczne modele wytrzymałości na zginanie wykorzystano do utworzenia rankingu niezawodnościowego badanych kompozytów stomatologicznych. Konceptualizacja niezawodności układów biotechnologicznych takich jak „ząb – wypełnienie stomatologiczne" wymagała rozszerzenia zakresu pojęcia uszkodzenie o losowe zdarzenia polegające na zaistnieniu niezgodności pomiędzy komponentami układu biotechnologicznego (compability failure).

DJURIĆ R, MILISAVLJEVIĆ V. **Badanie związku między niezawodnością podwozia gąsienicowego a zawartością pyłów mineralnych w skałach kopalni odkrywkowych węgla brunatnego**. Eksploatacja i Niezawodnosc – Maintenance and Reliability 2016; 18 (1): 142–150, http://dx.doi.org/10.17531/ein.2016.1.19.
Artykuł opisuje relację matematyczną, która pozwala oszacować czas do wystąpienia uszkodzenia podwozia gąsienicowego w funkcji zawartości pyłu mineralnego (SiO2), czyli intensywności zużycia. Relacja ta została oparta na rzeczywistych danych o uszkodzeniach maszyn gąsienicowych (spycharek) i właściwościach skał oraz na pomiarach intensywności zużycia rolek podtrzymujących (górnych) podwozia gąsienicowego. Uszkodzenia koparek rejestrowano przez okres 12 miesięcy w sześciu kopalniach odkrywkowych w Serbii. Obserwacje prowadzono w kopalniach o lokalizacji podobnej pod względem występujących typów skał z zawartości SiO2. Pozwoliło to na wyznaczenie wskaźników niezawodności przy pomocy dwuparametrycznego rozkładu Weibulla. Omawianą korelację interpretowano na podstawie modelu liniowego z zastosowaniem metody najmniejszych kwadratów. Przedstawione badania mają znaczenie dla właściwego zarządzania maszynami gąsienicowymi pracującymi w kopalniach odkrywkowych węgla brunatnego, jako że pozwalają na przewidywanie czasu do uszkodzenia oraz kosztów utrzymania tych maszyn. Prezentowana metoda zawiera wytyczne do opracowania niezawodnościowego modelu utrzymania ruchu.

SKRUCANY T, SARKAN B, GNAP J. **Wpływ wyposażenia aerodynamicznego naczep na zmniejszenie oporu powietrza mierzonego w tunelu aerodynamicznym**. Eksploatacja i Niezawodnosc – Maintenance and Reliability 2016; 18 (1): 151–154, http://dx.doi.org/10.17531/ein.2016.1.20.
Wartość oporu aerodynamicznego jest największa gdy pojazd porusza się z większą prędkością. Wydaje się, że redukcja oporu jest najważniejszym krokiem do zmniejszenia zużycia paliwa zestawów transportowych zawierających naczepy. Zastosowanie wyposażenia aerodynamicznego naczep jest jednym z wielu sposobów na zmniejszenie zużycia paliwa. Niniejszy artykuł poświęcony jest eksperymentalnym pomiarom modelu zestawu ciągnika z naczepą w tunelu aerodynamicznym. Skala modelu wynosiła 1:24. Uzyskane wartości zmniejszenia oporu powietrza dla wybranych elementów wyposażenia aerodynamicznego omówiono w końcowej części pracy.

SCIENCE AND TECHNOLOGY

Stanisław GUZOWSKI
Maciej MICHNEJ

INFLUENCE OF TECHNOLOGICAL METHODS INCREASING SURFACE LAYER DURABILITY ON AXLES FRETTING WEAR IN RAILWAY WHEEL SETS

WPŁYW TECHNOLOGICZNYCH METOD PODWYŻSZENIA TRWAŁOŚCI WARSTWY WIERZCHNIEJ NA ZUŻYCIE FRETTINGOWE OSI KOLEJOWYCH ZESTAWÓW KOŁOWYCH*

The article presents studies whose aim is to use such technologies of improving surface layer of a wheel seat that would eliminate fretting wear. The studies were carried out on a simplified physical model of an actual connection between the wheel and the axle of a wheel set with a self-acting wheel track change. The results of carried out wear studies show that fretting wear development can be successfully limited when metallic coating in the form of molybdenizing is used. Carried out studies indicate that such a solution can be fully used in actual exploitation.

***Keywords**: wheel set, surface layer, fretting wear.*

W niniejszym artykule przedstawiono badania mające na celu zastosowanie takich technologii ulepszania warstwy wierzchniej podpiaścia zestawu kołowego, które eliminowałoby zużycie frettingowe. Badania zostały przeprowadzone na uproszczonym modelu fizycznym rzeczywistego połączenia koła i osi zestawu kołowego z samoczynną zmianą rozstawu kół. Wyniki przeprowadzonych badań zużyciowych wskazują, że obróbką skutecznie ograniczającą rozwój zużycia frettingowego może być zastosowanie powłoki metalicznej w postaci molibdenowania. Przeprowadzone badania wskazują na pełną możliwość zastosowania tego rozwiązania w rzeczywistej eksploatacji.

***Słowa kluczowe**: zestaw kołowy, warstwa wierzchnia, zużycie frettingowe.*

1. Introduction

A wheel set is one of the most important subassemblies of a rail vehicle, whose durability and reliability decides about the safety of railway traffic. Its proper functional quality decides both about the safety of railway traffic and about the costs connected with the exploitation of a rail vehicle.

A wheel set of rail vehicles, due to the specific work conditions, is especially exposed to fatigue wear development. Because of the role it plays in driving the vehicle on the track, its failures are inadmissible. Results of exploitation studies of the wheel sets show that occurring wears have a significant influence on lowering the fatigue strength or may be a focal point of fatigue cracks, mainly of a set axle which is its basic element. Observations of a wheel seat surface after the wheel set has been disassembled many times revealed, among others, fretting failures in the area of axle wheel seat contact with a wheel hub.

The results achieved by the authors of this article show that fretting wear may significantly influence development of fatigue wear, especially in a forced-in connection of wheel – axle of a wheel set [2].

A similar problem appears in the case of a wheel set with a self-acting wheel track change in which, because of construction reasons, dimensions of the wheel-axle connection surface fulfill the running fit conditions.

Complex physical-chemical phenomena taking place on the contact surface of the associated surfaces and the influence of many factors cause that the mechanism of fretting wear development is difficult to be described and in literature there is no unique definition. What is common for different scholarly publications is only a statement that fretting wear development is conditioned by the occurrence of surface thrusts in the association and oscillatory slides of very low amplitude not exceeding 150 μm [2, 17, 18, 19]. Fretting wear image can be illustrated by corrosion traces on the surface of elements, increase in the surface roughness, micro-cracks in the surface layer, pits. Fretting is a phenomenon of a very complex wear mechanism, in which overlap or follow in succession: adhesive wear, surface fatigue, exfoliation, oxidation, abrasion of surface irregularities by tops and loose wear products. Fretting wear studies were first of all carried out for associations of concentrated or flat contact and also referred to the proposed wear models [7, 10, 16].

It follows from the review of fretting wear study results that wear development is closely connected with actual contact of associated surface elements and with presence in the contact area of the so called third body, while the form of this wear depends mainly on the conditions of slide oscillation and amplitude [9, 10, 11]. Straight majority of authors, enumerating examples of elements or connections in which fretting wear occurs, most often indicate forced-in connections [9, 10, 11, 12, 16]. However, studies on such connections were occasionally carried out [16, 17].

Quoted in work [2] statistical data referring to wear failures of the axle in exploitation conditions show that the place of wear cracks development coincides with fretting wear area development. The above is also proved by the results of wear studies carried out by L. Stasiak [12] on actual wheel sets in laboratory conditions. This shows that there is a probable link of wear failures occurrence of the wheel set axle with fretting wear development.

In the light of the above facts an essential element of providing reliability and safety of the exploited rail vehicle is to eliminate or significantly limit fretting wear development in the wheel – wheel set axle connection. The article presents the results of model studies carried out by the authors, the influence of chosen technological methods of increasing durability of the surface layer on fretting wear of railway wheel sets with an automatic wheel track change.

2. Research object

A classic wheel set of rail vehicles consists of an axle and two wheels which are connected with the axle by forcing-in. Such a stable connection ensures correct and safe rolling of the vehicle along the track. Apart from this basic rail set construction in rail vehicles there are also special solutions, allowing, for example, rolling of the wheel on the axle wheel seat.

In the 90s of the previous century in the Central Construction Office of PKP (Polish Railways) in Poznań a wheel set SUW2000 was designed and made, which allowed automatic, self-acting passing from a track of one width to another one of a different width, performed on a track shift stand.
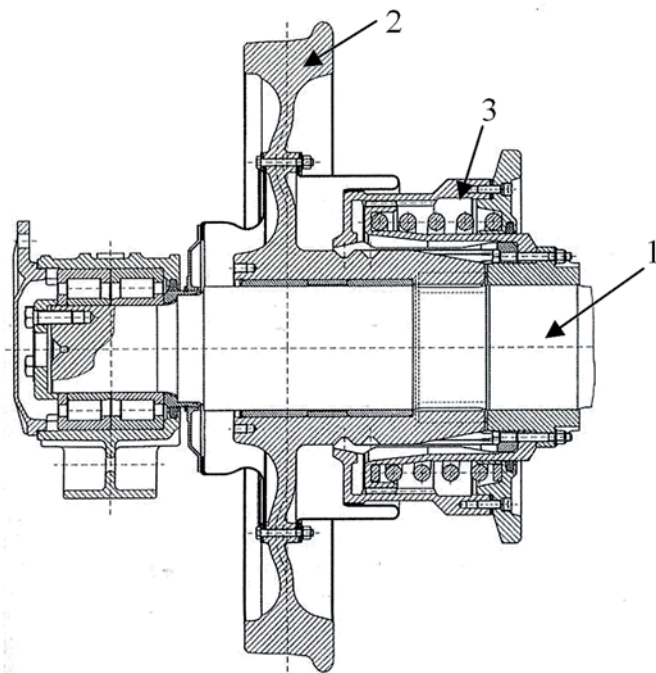
Fig. 1. *Cross section of a wheel set with automatic change of wheel track SUW2000 [13];1 – wheel set axle, 2 – wheels rolling on the set axle, 3 – lockup mechanism*

A fragment of a cross section of the designed set is presented in Fig. 1. A significant element of the presented construction is the connection of a wheel with an axle. In contrast to the classic wheel set, where the wheels are permanently connected with the axle in result of forcing-in, in this construction the connection is a running fit. Such a solution enables the axial movement of the wheel when changing the gauge at the next lockup of the wheel in relation to the axle when driving. In the prototype set both the wheel and the axle were made from materials in accordance with UIC standards. The wheel from R7E steel and the axle from A1N steel. Chemical composition of those steels is shown in Table 2.

Initial exploitation of the set showed that after not a very long run (about 1.5000 km) there occur big problems during the change of the wheel track [13, 14]. The force necessary to shift the wheels on the axle was increasing significantly, thus leading even to failures in the shift stand. Observations of the axle wheel seat after having disassembled the wheel set showed, among others, fretting failures at the contact area with a wheel hub, as well as significant processes of lubricant ageing. These factors caused lockup of wheels on the axle during its wheel track change. The characteristic feature of fretting wear occurring on the axle of the wheel set with an automatic wheel track change (running fit) is that the place of occurrence and the image of wear is very much like in the case of an axle of a classic wheel set (forced-in connection). Fig. 2 presents a fragment of an axle of both types of a wheel set with fretting wear on their surfaces.

Wear, whose characteristic image is shown in Fig. 2, comprises an area from the front of the hub into the depth of the connection of 30mm in width. Wear occurs on the whole perimeter of the wheel
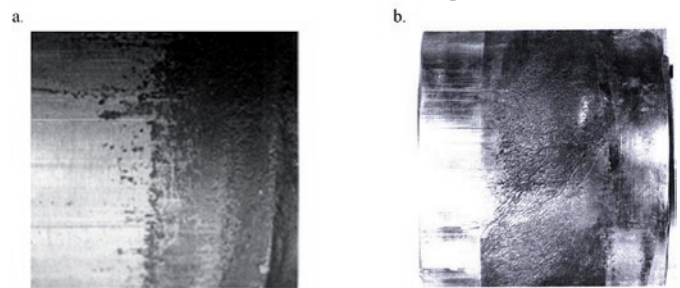
Fig. 2. *Fretting wear at the edge of axle wheel seat: a) traditional wheel set [2], b) wheel set with automatic wheel track change [13]*

seat surface in the form of a characteristic ring. Failures observed in this surface area are mainly pits and build-ups. The area is also of a characteristic dark brown – black colour, what proves its oxidation. The only difference in wear on both the axles is the place in which it occurs. In the case of traditional connection it occurs mainly in the central part of the axle, while in a running connection it occurs on both sides of the wheel set axle.

2.1. Work conditions of a wheel set

Work conditions of the analysed connection of the running fit a wheel – an axle of the wheel set with an automatic wheel track change may be with a great approximation referred to the forced-in connection a wheel – an axle of a traditional wheel set. The basic difference is only in the initial stress state caused in the top layer of the connected elements. In the forced-in connection, in result of forcing-in the wheel on the axle on the whole contact area there originates an initial state of compressive stresses. It is also accompanied by deformation state in the surface layer of the connected elements. In the case, however, of the running connection a wheel – an axle of a wheel set with an automatic wheel track change, only a non - conformal

contact occurs and the stresses result from axial force coming from the set loading.

For studies the scheme of a rail set load presented in Fig. 3 is most often accepted. According to the accepted scheme, a complex system of a wheel set load when the rail vehicle is in motion, is as follows:

- vertical concentrated load P_1 and P_2 acts on the pivots
- lateral force H_1, dependent on the wheel position in relation to the rail head, acts on the edge of rolling wheels.

In the wheel set axle there occurs a bending moment which is the result of loads acting on it (Fig. 3). The maximum value of this mo-
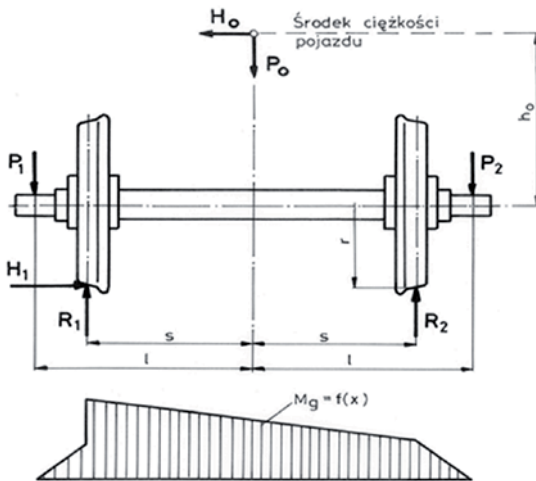
Fig. 3. Load scheme of a wheel set and corresponding to it bending moment distribution when the set is moved to the left [2]

ment occurs on the axle wheel seat in the plane of R_1 and R_2 reaction (the point of wheel and rail contact), in the area of connection with a wheel hub. The axle, therefore, works in the conditions of rotary bending. The effects of the above, during the set rolling, may be oscillations between an axle and a wheel hub at the edge of connection. The authors of work [1] explain the occurrence of relative microdisplacements in forced-in connection of the axle wheel seat with the wheel hub in the following way: under the influence of external loads (Fig. 3), the axle of the wheel set experiences strains shown in Fig. 4. In the upper axle layers the strains are tensile, while in the lower layers they are compressive ones. This kind of axle strain would not have significant meaning if the wheel hub had similar strains. To have a simultaneous strain of the axle wheel seat and the wheel hub, unitary friction forces p_T at the contact point should be greater or at least equal to the normal strains σ_n in the axle wheel seat. Fretting wear image stated by the authors proves that in this area relative wheel slides occur, what is in agreement with Mindlin's model:

$$p_T = p_{sr} \cdot \mu \leq \sigma_n \qquad (1)$$

Such a state of loads and strains distribution can also be referred to a wheel set with an automatic wheel track change. In the wheel set between the sliding sleeve and the axle appears running fit, thus, because there are no surface assembling pressures, there is a considerably greater probability of oscillation occurrence between the associated surfaces of the elements, what together with an unfavourable influence of the external forces can lead to wear and failure of the axle, especially in the place of a wheel and an axle connection.

It is difficult to measure the actual sliding amplitude between the contact surface of the sleeve and the shaft in rotary-flexural wear studies. As the results achieved by different authors show, fretting wear development is closely connected with oscillation occurrence. Therefore, it is essential whether in the studied connection oscillations may occur, whose visible effect should be an image of failures
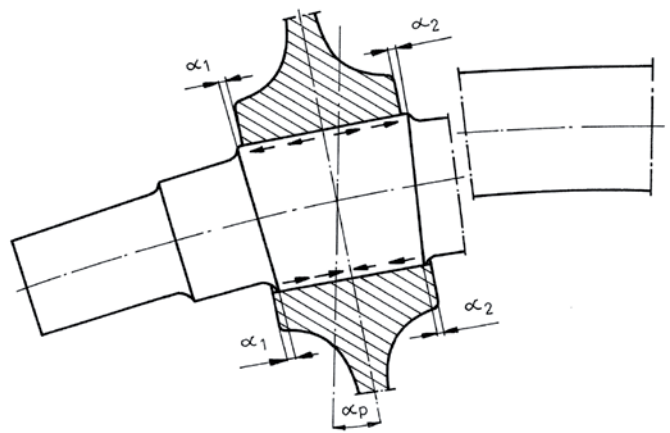
Fig. 4. Wheel set deformation under the influence of external load [1]

on the connection surface. In the work a very simple, approximate evaluation of the sliding amplitude value was proposed, which will be the result of shaft deflection under the influence of acting force Q and P. Fig. 5 presents a scheme of slide occurrence between connected elements of running fit. Fig. 5a shows associated elements without bending moment load but with force P only. Due to this the sleeve is pressed to the upper surface of the shaft, while in the lower surface maximum clearance appears, what is the result of running fit. Points A_1–A_2 are connected with the shaft surface and determine the contact place of the shaft surface and the sleeve head. In result of shaft deflection under the action of the bending moment (Fig. 5b) also the plane coming through points A_1–A_2 will rotate. It will take the position determined by points A_1'–A_2' covering the radius of the shaft deflection curvature. Concave surface of the shaft (compressed) will shorten and the convex (tensioned) one will elongate. In result of this, point A_1 will relocate on the compressed surface under the sleeve, taking position A_1', and on the tensioned surface point A_2 will move outside the sleeve head, taking position A_2'. Displacement quantity of point A_1 in relation to the sleeve head was marked α'.

Point A_2 on the tensioned surface due to the clearance caused by running fit will not have contact with the shaft surface. A direct
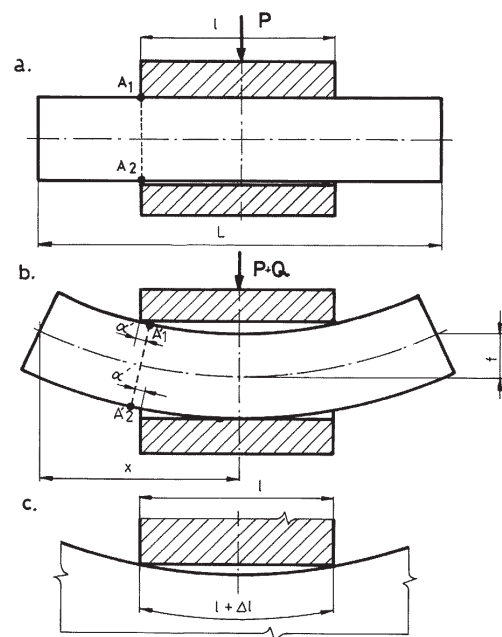
Fig. 5. A scheme of determining slide amplitude between the sleeve head and the surface of the shaft seat: a) a sample in a free state loaded only by force P, b) a sample loaded by bending moment, c) a scheme of sleeve association with the shaft to determine oscillation amplitude

slide between the associated surfaces will take place only on the compressed surface of the shaft. Maximum oscillation amplitude will occur at the sleeve edge and will be equal to α′, while in the symmetry connection axis it reaches zero value.

To determine estimated slide amplitude in the studied connection a model presented in Fig. 5c was used. Loading of the sample by bending moment will cause deflection of the shaft and its result will be elongation of its surface on the length of contact with the sleeve by Δ*l*. value. If we assume that the shaft deflection is a small one and strains are elastic, then to determine Δ*l* elongation Hooke's law can be used, according to which relative linear elongation ε may be determined by formulas:

$$\varepsilon = \frac{\sigma_n}{E} \quad \text{and} \quad \varepsilon = \frac{\Delta l}{l},$$

hence:

$$\Delta l = \frac{\sigma_n \cdot l}{E} \tag{2}$$

Total relative displacement (slide amplitude) of the shaft surface in relation to the sleeve head will therefore be equal to $\alpha = \Delta l/2$. Table 1 presents calculated acc. to formula (2), estimated slide amplitude value between the sleeve head and the shaft surface for accepted model study parameters (column 2)

Table 1. *Estimated α slide amplitude value and the vector value of deflection f_0, f_{rz} of the sample*

1	2	3	4
(P + Q) [N]	α [mm]	f_o [mm]	f_{rz} [mm]
350	0,0046	0,51	0,75

According to formula (2) oscillation amplitude depends on normal stresses, and hence on the value of applied bending moment, which in turn will decide about the bending value of the sample. Therefore there will be a close connection between the shaft deflection and the oscillation amplitude. The above was made use of to verify the calculated estimated oscillation amplitude value in comparison to the actual amplitude. The vector value of shaft deflection f_o was analytically calculated and compared with the actual measured value of sample deflection f_{rz}. To calculate shaft deflection value a scheme of sample loading as in Fig. 7 was used. The analytically calculated deflection vector f_o was placed in Table 1 in column 3. The actual value of deflection vector f_{rz} determined during static measurements of the sample deflection was placed in table 1 in column 4. Comparison of those two values shows that actual deflection is greater than the analytically calculated value. Hence it may be judged that actual slide amplitude may also be greater than the analytically calculated one. It is necessary here to underline that in analytical calculations of the slide amplitude simplifications were accepted. First of all friction forces on the contact of connected surfaces were not taken into consideration.

3. Research methodology

Because of the wheel sets dimensions the studies on an actual object are expensive and time consuming, as it is necessary to use a specialist test stand and also adequately long study time. Due to this, wear tests were carried out on samples modelling the connection sleeve – axle

making use of a fatigue machine of the MUJ type. Fatigue tests of the sample in rotary bending conditions ensure simulation of actual loads of the wheel set in exploitation conditions.

Experimental tests referred to:
- determination of the actual surface layer state in the area of sleeve connection with the shaft after wear tests for singled out technological processes
- determination of the influence of chosen technological processes on fretting wear development

What was important when choosing a sample modelling slide sleeve – axle of the wheel set was dimensional similarity behaviour in the connection area. For this, proportions of connection length and axle diameter as well as fitting were kept

The sleeve was fixed in relation to the shaft by means of a headless screw with a socket, what prevented axle and perimeter shifts and ensured the sleeve movement in relation to the shaft in the radial direction during rotation.
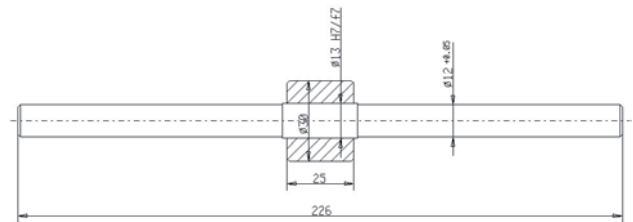
Fig. 6. Sample dimensions for model tests [6]

For initial tests the shaft was made from steel 45 and the sleeve from steel 36HNM, through machining with no additional strengthening of the surface layer. The choice of materials provided close properties to the materials from which the actual object was made in the prototype version (Table 2). Such a model was to be a reference point for different variants of the sleeve – axle association, which should limit or eliminate wear, at the same time providing the least shift force in the axial direction.

On the basis of literature analysis, referring to the mechanism of fretting wear development in forced-in connections of the wheel and axle such technological processes were proposed that should limit fretting wear initiation on the shaft surface and would allow to obtain a suitable state of a wheel seat which would ensure minimum, stable force necessary to move the sleeve along a wheel seat before and after the wear tests. Table 3 presents chosen variants of a sleeve slide axle friction pair model.

For wear tests a fatigue machine of the MUJ type was used, which allowed to achieve parameters simulating actual exploitation condi-

Table 2. *Chemical composition of steels used to produce axle and wheel of the wheel set with an automatic wheel track change and of the sleeve and shaft modelling the studied connection*

Material symbol	Chemical composition [%]					Mechanical properties [MPa]	
	C	Mn	Si	P max	S max	R_e	R_m
ER7	0,52	0,80	0,40	0,020	0,015	≥ 520	820-940
A1N	0,40	1,20	0,50	0,020	0,020	≥ 320	550-650
45	0,42- 0,50	0,50- 0,80	0,10- 0,40	0,040	0,040	340	600-700
36HNM	0,32-040	0,50- 0,80	0,17-0,37	0,035	0,035	750-800	850-1000

tions of a wheel set. Construction of the machine allows to obtain periodically changing load with a simultaneous bending of the rotating sample. In fretting wear tests it was important to achieve such a distribution of the bending moment on the axle wheel seat that would result in its deflection, what is the condition of oscillatory contact shifts between the surfaces in contact.

Table 3. Chosen association models singled out for wear tests

No.	Sample type	Shaft seat surface	Sleeve material
1	basic	steel	steel
3	modified	molybdenum	steel
8	modified	Hardened steel	steel
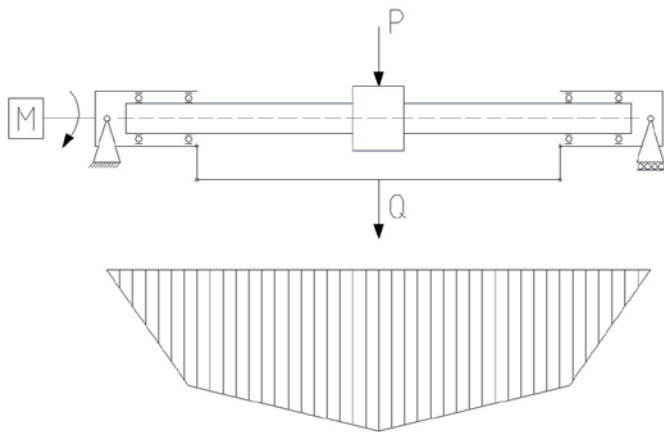
Fig. 7. Scheme of sample loading on a testing machine of MUJ type and corresponding to it bending moment distribution

Fig. 7 presents a scheme of sample loading on a testing machine of MUJ type. The scheme corresponds to the wheel set loading in which it was assumed that the wheel set rolls along straight rail without running onto the rail head.

Sample parameters tested on a testing machine were as follows:
- revolutions   n=1360 rev/min
- sample loading   Q= 300 N
- sample loading   P= 50 N
- number of cycles   r > 6x10^6

Assumed rotational speed of the sample corresponds to the speed of 75km/h of a railway car.

In wear tests of the sample modelling the connection slide sleeve – wheel set axle the value of loads was assumed for which the stress value on the shaft seat surface was higher than the stresses in an actual axle. The stresses in the sample were calculated by finite elements method in ANSYS programme. The values of forces Q=300 N and P=50 N were assumed.

Distribution of normal stresses on the shaft surface for the set load values did not cause plastic strains (deflection vector 0.27 mm). The maximum strain value for assumed load conditions was 61 MPa. The value exceeds local strain values in an actual axle, which are 40-50 MPa.

4. Experimental tests

4.1. Base sample

The aim of testing a base sample was to verify the model choice by achieving a similar wear image as in an actual object and as a reference to the proposed changes. Macrographic observations of the steel shaft seat surface in a base sample show that surface failures occur on both sides of the shaft seat (Fig. 8) A big contact area of cooperating elements of tribological nodes creates conditions for adhesive tacking formation on the connection edge, which cause surface layer destruction and in consequence formation of distinct fretting wear traces.

In macroscopic photographs of the shaft surface presented in Fig. 9 brown colour was observed in the area of fretting wear occurrence, typical of atmospheric iron corrosion. The most probable reason of this phenomenon is the contact of the damaged area with oxygen because of the fissure being formed between the surfaces of the shaft and the sleeve in result of sample deflection.
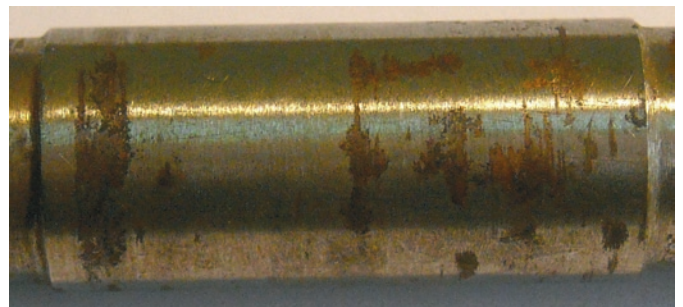
Fig. 8. Base shaft surface after fatigue tests - distinct traces of fretting wear on the shaft edges of lower intensity into the connection centre, magnified. about 3x [6]
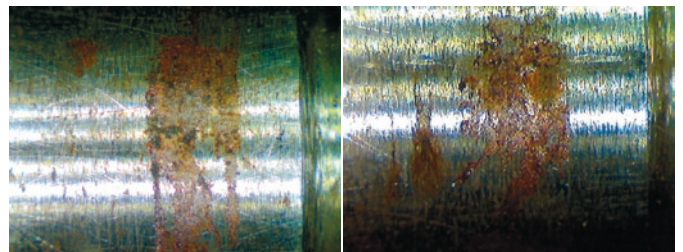
Fig. 9. Base sample after fretting wear, magnified about 15x. Lack of machining strengthening the surfaces. Visible traces of fretting wear [6]

In the images of spatial roughness profile (Fig. 10) and in the scanning images (Fig. 11) of the base shaft seat characteristic material growths may be noticed, which undergo plastic deformation and oxidation. Observations of the surface showed local abrasions and micro-pits. Surface failures in the form of micro-growths and micro-
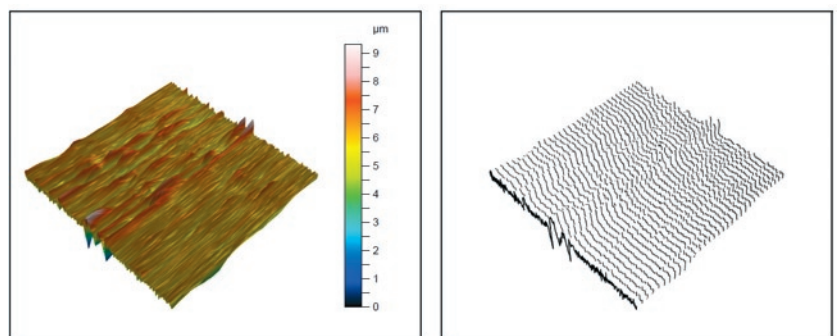
Fig. 10. Spatial image of shaft surface roughness profile in the area of fretting wear
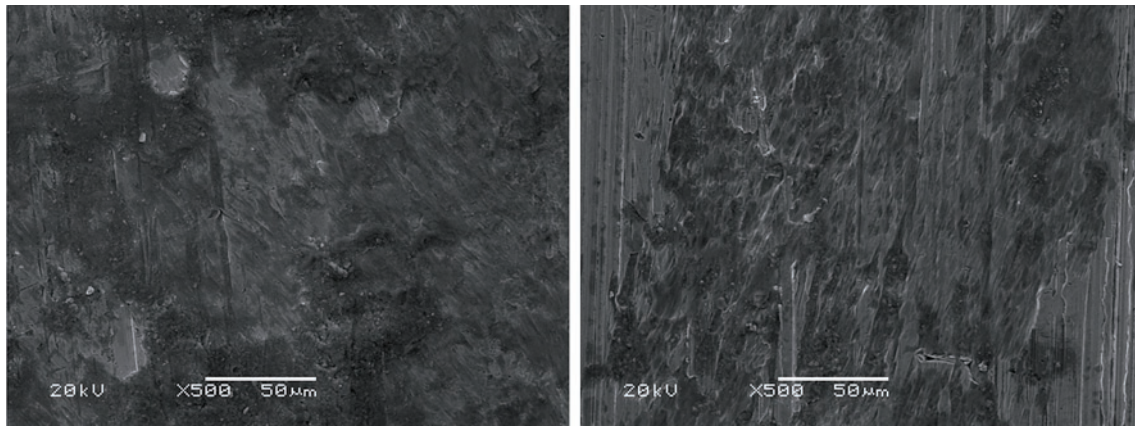
Fig. 11. Base shaft surface wear images, magnified 500x

pits have their origin in adhesion phenomena being an element of fretting wear development mechanism. This mechanism in the discussed case is also connected with the occurrence of relative contact shifts between the surfaces of connected elements. The assumed load generates maximum oscillation amplitude between the shaft and surface at the connection edge.

Obtained wear image proves that the assumed model is correct and reflects work conditions and connected with them failure image of an actual association wheel – axle.

4.2. Molybdenized sample

High molybdenizing costs, in spite of good tribological properties, limit its usage only to traction units axle and the cars of high speed trains. Molybdenum coating was put onto a sample by means of a metal spraying method after having completed the peening process of the shaft seat surface layer, what influences adherence of the coating to the base. Thickness of the coating was about 37.5 μm, that is about 0.58% of the shaft diameter. In the case of actual axle it was about 0.54%. Fig 12 presents the image of molybdenized shaft seat surface, associated in a running fit connection with a steel sleeve, after fatigue tests. Molybdenized surface hardness was 460 HV, while that of the steel shaft 210 HV. It is visible that fretting wear was completely eliminated.

Carried out tests prove the theses in works [2, 7, 9], that molybdenizing, as a modification method of the surface layer used in contact nodes exposed to fretting, limits the tendency for adhesive associations, causes diminishing of the frictional force, increases resistance to mechanical impact and increases the corrosion resistance.

The images of molybdenized surface presented in Fig. 15 show lack of characteristic for fretting wear failures in the form of micro-

Fig. 13. Molibdenized sample after wear test, magnified about 15x.
No traces of fretting wear [6]
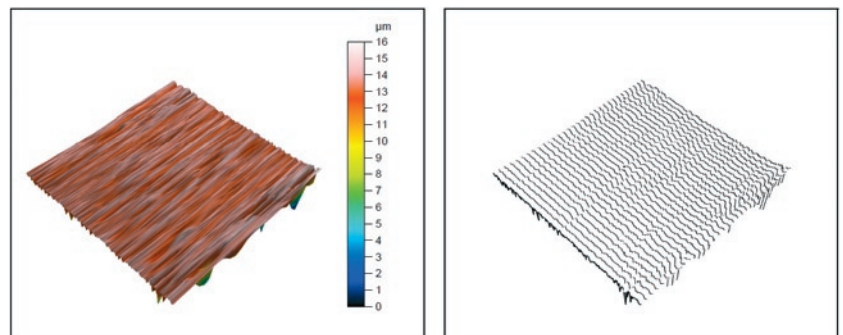
Fig. 14. Spatial roughness profile image of molybdenized shaft surface in the theoretical area of fretting wear

pits or growths with their subsequent oxidation. Large surface hardness of the molybdenum coating, and surface roughness of 1.1 μm cause that at the tested number of cycles 6.57 x 106 fretting wear on the seat does not occur.

In spite of the lack of fretting wear traces on the shaft surface, wear products gathering in the micro-gaps (the effect of shot peening) as a result of fretting wear on the inner surface of the sleeve will cause an increase of frictional properties of the connection.

4.3. Surface hardened sample

One of the methods of surface after- machining of the axle of wheel sets, having influence on increasing the fatigue strength, is hardening. For model tests a sample was used, subjected to surface hardening by induction, which is the most popular method and has good technological properties. The process of sample hardening con-

Fig. 12. Molyibdenized shaft surface after fatigue tests – no fretting wear, magnified about 3x
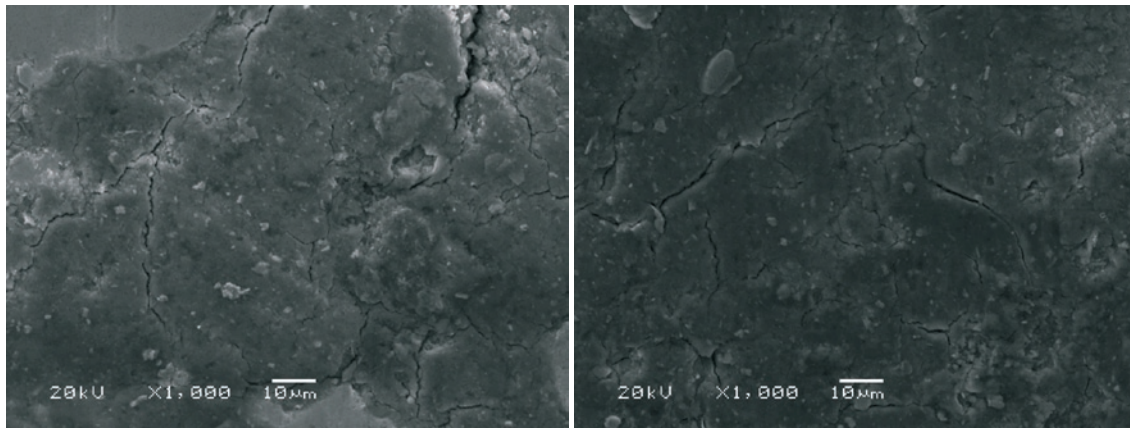
Fig. 15. Images of molybdenized sample surface, magnified 1000x
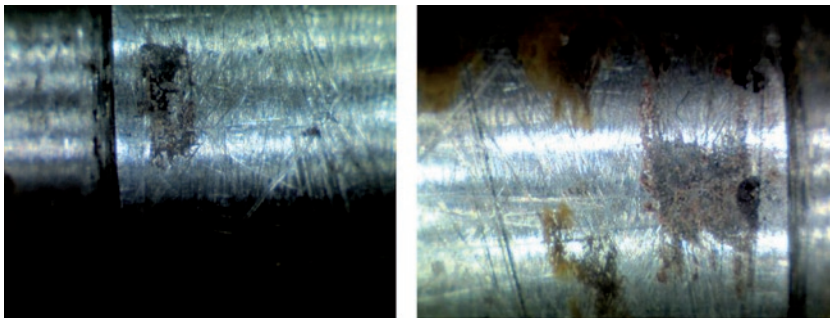
*Fig. 16. Surface hardened sample after wear test, magnified 15x.
Visible large areas of fretting wear*
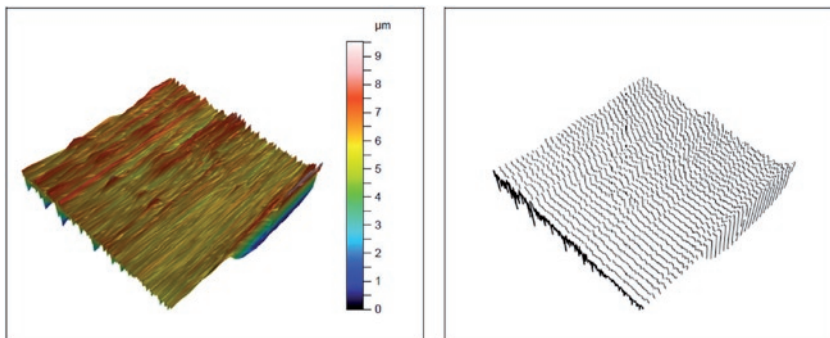
Fig. 17. Spatial roughness profile image of the hardened shaft surface in the fretting wear area

sisted of heating the surface layer to a hardening temperature, then rapid cooling followed. The samples were heated for about 1.5 minutes by means of the current induced in the magnetic field. After the induction hardening process the sample was subjected to tempering for one hour in a PEH -2 furnace at a temperature of about 380°.

The images of presented in Fig. 16 wear on the surface hardened shaft show that despite the high gradient of the surface layer hardness of the two associated elements there are numerous failures on the surface layer (fretting mainly), which led to the sleeve blocking and prevented its sliding on the shaft.

During macro- and microscopic tests material growths susceptible to plastic deformations and oxidation were identified. The growths, due to their properties and local physical and mechanical conditions, have a strong tendency for cracking and breaking off. As there were numerous wear products in the form of worn away material particles and a large range of deformations, the sleeve on the shaft was blocked. The above results disqualify the possibility of applying the tested set of friction pair elements in an actual wheel set.

4. Conclusions

The image of fretting wear in the studied connection of base sample (Fig. 8) is similar to the wear in forced-in shaft-sleeve connection subjected to analogous load conditions [2]. In a forced-in connection of
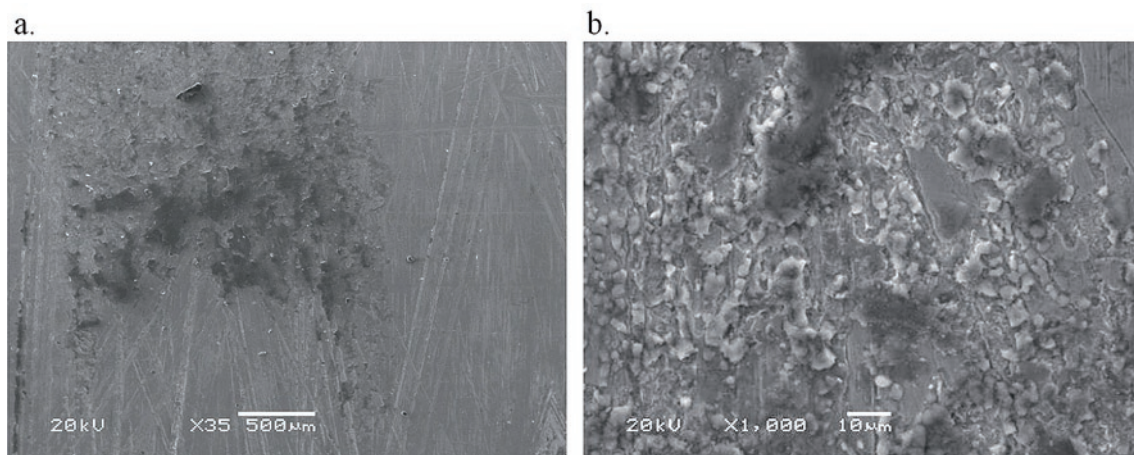
Fig. 18 Images of wear on the hardened shaft surface, a) magnified 500x, b) magnified 100x

Table 4.   Results of measurements

No	Sample	Shaft – sleeve association	Force indispensable to slide the sleeve down [N]		Shaft hardness [HV]	Sleeve hardness [HV]	Shaft surface state after test
			Before tests	After tests			
1	base	Steel - stel	1,4	24,3	210	189	Distinct fretting wear
2	modified	molybdenum - steel	8,1	43,2	460	190	Lack of fretting wear
3	modified	hardened steel – steel	1,7	>50	549	192	Traces of fretting wear

fretting wear development the adhesion phenomenon plays a domineering function in wear initiation. Formation and breaking off of the adhesive tacking [2]. The condition for adhesive tacking development is forming actual areas of the first bodies contact in result of forcing-in of one element into another one (micro-irregularities, plastic deformation of the surface layer and oxides layer removal). In the case of running fit connection, because of the connection character, forming of the actual contact areas of the first bodies will take place only in the course of rotary bending of a sample. In result of relative displacements of the sleeve and shaft surface, whose amplitude is the highest at the edge of connection, there occurs frictional wear of the associated surfaces. It is the result of micro-machining of the surface micro-projections. Wear products are removed from the contact connection in the course of a sample half rotation. The actual contact surface formed in this way (after having removed the oxide layer and the so called third body) will be susceptible to form adhesive tacking and initiate fretting wear. Therefore, analogously to the fretting wear development mechanism in a forced-in connection, a similar mechanism of running fit can be proposed as a few stages process whose most important elements are:

- forming areas of actual contact of the first bodies in the course of generating relative displacements of very low amplitude on the elements contact surface as a result of bending.
- forming adhesive tacking in the areas of actual contact, especially at the connection edge (the highest amplitude of relative slides), which then undergo disruption, forming gaps and growths on the contact surfaces,
- oxidation of the earlier damaged area,
- micro-machining by oxidized tops of the growths on the opposite surface.

Adhesion processes will be an indispensable condition in the proposed mechanism of fretting wear development in a connection of running fit. Formation and disruption of adhesive tacking. According to M. Hebda [3] a special tendency to form adhesive tacking will be displayed in the case of associating material of the same kind and of similar mechanical properties. This explains, among others, such an intensive fretting wear image on the base sample (steel – steel).

However, according to [3] an increase in adhesive wear resistance can be achieved, among others, by high mechanical properties (hardness, yield point).

Limiting fretting wear development is, first of all, connected with not allowing adhesion phenomenon to occur. Limiting oscillation, because of the association work conditions, is practically impossible.

In the studies two ways were accepted to increase the hardness of the shaft surface – by coating with molybdenum and by surface hardening. Table 4 presents the results of hardness measurements on the surface of associated elements, the force necessary to move the sleeve axially on the shaft and the identified wear image.

Quoted measurement results and observations indicate that the influence of a high hardness gradient of the associated surfaces on the fretting wear limitation is a complex one. While in the case of the same kind of materials and similar surface hardness (steel – steel) fretting wear development is a very intensive one, in the case of molybdenum coated and hardened surface the situation is different. In spite of the fact that the hardness gradient of the shaft surface with molybdenized coating in relation to the sleeve is about 20% lower than the shaft with hardened surface, fretting wear for this association has been fully eliminated. Whereas on the hardened shaft surface distinct traces of fretting wear appear. The above may indicate that as well as the high hardness of the surface, the chemical composition of the material and crystallographic structure of the surface layer of the associated materials will limit fretting wear.

It must be stressed that the main aim of the article was to present the research results on limiting fretting wear on the shaft surface by means of available technological processes. The main focus was on the shaft surface as in an actual connection wheel – axle of the wheel set with an automatic wheel track change, the axle is just an element which determines durability of the whole wheel set.

The examples of the shaft surface states after fatigue tests show that among the tested technological processes aiming at increasing the fatigue durability of the connection only molybdenizing favourably influences fretting wear elimination. Whereas surface hardened surfaces are susceptible to fretting wear development, and what is more, they do not allow for a free movement of the sleeve on the shaft.

References

1. Gąsowski W, Stasiak L. Badania wytrzymałości zmęczeniowej wagonowych osi zestawów kołowych w ośrodku korozyjnym. Korozja stykowa. Zeszyty Naukowe Politechniki Śląskiej, Transport, z. 14, Gliwice, 1989, 103-121.
2. Guzowski S. Analiza zużycia frettingowego w połączeniach wciskowych na przykładzie osi zestawów kołowych pojazdów szynowych. Monografia 284, Politechnika Krakowska, Kraków, 2003.
3. Hebda M. Procesy tarcia, smarowania i zużywania maszyn. Wyd. ITeE-PIB, Warszawa, 2007.
4. Kaczmarek J, Hanzel-Powierża Z. Aktualny stan i perspektywy diagnostyki technologicznej warstwy wierzchniej, IMJON -79, Warszawa, 1979.
5. Kula P. Inżynieria warstwy powierzchniowej, Monografie, Wydawnictwo Politechniki Łódzkiej, Łódź, 2000.
6. Michnej M. Proces zużycia w połączeniu obrotowym na przykładzie modelu zestawu kołowego z samoczynną zmianą rozstawu kół. Rozprawa doktorska, Kraków 2012.

7. Miller K. How to Reduce Fretting Corrosion - Influence of Lubricants. Tribology International, 8.2, (1975): 57-64.
8. Młynarczyk A, Jakubowski J, Obróbka powierzchniowa i powłoki ochronne. Wydawnictwa Politechniki Poznańskiej, Poznań, 1998.
9. Neyman A. Fretting w elementach maszyn. Wydawnictwo Politechniki Gdańskiej, Gdańsk, 2003.
10. Nosal S. Tribologiczne aspekty zacierania się węzłów ślizgowych. Politechnika Poznańska, Rozprawy, Poznań, nr 328, 1998.
11. Pytko S, Szczerek M. Fretting – forma niszczenia elementów maszyn. Tribologia nr 6, 1994, 673-693.
12. Stasiak L. Doświadczalna determinacja charakterystyk wytrzymałości zmęczeniowej osi zestawów kołowych pojazdów szynowych. Politechnika Poznańska, Rozprawy, Nr.173, Poznań, 1986.
13. Suwalski R.M. System samoczynnej zmiany rozstawu kół pojazdów szynowych. Monografia AGH, Kraków, 2006.
14. Szkoda M. Assessment of Reliability, Availability and Ma intainability of Rail Gauge Change Systems. Eksploatacja i Niezawodnosc - Maintenance and Reliability 2014; 16 (3): 422-432.
15. Szulc S, Stefko A. Obróbka powierzchniowa części maszyn – podstawy fizyczne i wpływ na własności użytkowe. Warszawa WNT 1976.
16. Volchok A, Halperin G, Etsion I. The effect of surface regular microtopography on fretting fatigue life. Wear 253 (2002): 509-515, http://dx.doi.org/10.1016/S0043-1648(02)00148-5 .
17. Waterhouse R.B. Fretting corrosion. Pergamon Press Ltd, Oxford, 1972.
18. Waterhouse R.B. Fretting fatigue. Applied Science Publishers Ltd., London, 1981.
19. Waterhouse RB. Fretting Wear, ASM Handbook, vol.18, Friction, Lubrication and Wear technology. Cleveland, OH: ASM International, 992: 233-256.

Stanisław GUZOWSKI
Maciej MICHNEJ
Cracow University of Technology
Faculty of Mechanical Engineering
Institute of Rail Vehicles
al. Jana Pawła II 37, 31-864 Krakow, Poland
E-mail: wojtek@mech.pk.edu.pl, maciej.michnej@mech.pk.edu.pl

Yuan-Jian YANG
Weiwen PENG
Shun-Peng ZHU
Hong-Zhong HUANG

A BAYESIAN APPROACH FOR SEALING FAILURE ANALYSIS CONSIDERING THE NON-COMPETING RELATIONSHIP OF MULTIPLE DEGRADATION PROCESSES

ZASTOSOWANIE METODY BAYESA DO ANALIZY USZKODZEŃ USZCZELNIEŃ Z UWZGLĘDNIENIEM WSPÓŁWYSTĘPUJĄCYCH PROCESÓW DEGRADACJI O CHARAKTERZE NIEKONKURUJĄCYM

Abstract: Degradation analysis is an effective method for reliability analysis when failure time data is rare or hard to observe. Multiple degradation analysis with competing risk model is often used to implement the degradation analysis. However, in reality, the failure of a system is often a result of a combination of multiple degradation processes, such as the sum of multiple degradations. To handle this non-competing relationship of multiple degradation processes, this paper presents a new reliability model for multiple degradation processes analysis. The proposed model is demonstrated through a case-study of a spool valve. In this paper, the gamma process is adopted to construct the reliability model. The Bayesian method is used to obtain the estimations of model parameters and reliability indexes by taking account of uncertainty. The results can then be further used as valuable information for further degradation analysis and decision-making considering uncertainty.

Keywords*: Bayesian method, reliability analysis, degradation process, sealing.*

Analiza degradacji jest skuteczną metodą analizy niezawodnościowej w przypadkach gdy dane są skąpe lub trudne do zaobserwowania. W badaniach często wykorzystuje się analizę współwystępujących degradacji z zastosowaniem modelu zagrożeń konkurujących. Jednak w rzeczywistości, awaria systemu często jest wynikiem wystąpienia degradacji niekonkurujących, t.j. wynikiem sumy lub kombinacji współwystępujących procesów degradacji. Aby uwzględnić tę relacje między niekonkurującymi procesami degradacji, w artykule przedstawiono nowy model niezawodności służący do analizy współwystępujących procesów degradacji. Proponowany model zilustrowano za pomocą studium przypadku rozdzielnika suwakowego. Przedstawiony w pracy model niezawodności skonstruowano w oparciu o proces gamma. Do oszacowania parametrów modelu oraz indeksów niezawodności zastosowano metodę Bayesa z uwzględnieniem niepewności. Uzyskane wyniki można wykorzystać w przyszłości jako cenne dane do dalszej analizy degradacji i podejmowania decyzji z uwzględnieniem niepewności.

Słowa kluczowe*: metoda Bayesa, analiza niezawodności, proces degradacji, uszczelnienie.*

1. Introduction

Degradation is generally considered as one type of damage to a device. It accumulates over time or task, and finally results in a failure once the accumulated damage reaches a predefined threshold. Degradation models have been widely used in reliability engineering, and have been well reviewed recently by Gorjian [6] and Elsayed [3]. In reality, the degradation of a system may consist of multiple degradation processes. There are some studies [15, 20-22] focusing on the multiple degradation processes, and they are all based on the competing model of multiple degradation processes. In competing model, the system fails when any of the multiple degradation processes reaches its corresponding failure threshold. However, it may not be suitable for some mechanical devices, because the relationship of different degradation processes is not always competing. According to this issue, this paper presents a modified multiple degradation model to describe some degradation processes which are common in mechanical systems. A spool valve is taken as the object of this study to investigate the non-competing relationship of degradation processes. Spool valves are basic parts in hydraulic systems, and their reliability performance has a direct impact on the reliability of the entire hydraulic system. In spool valves, the spool slides in and out of position within the sleeve, alternately blocking and opening the fluid intake and outtake ports. The high frequency and numerous sliding operations results in the wearing of spool and sleeve, making the sealing deteriorated, and eventually leading to the sealing failure. The leakage, usually caused by the wear degradation of spools and sleeves, is the main failure mode of this device, and has been investigated by many studies [2, 4, 5, 19]. However, the detailed analysis of this wear degradation process has not been well studied. A further investigation of the failure mechanism and reliability assessment of

sealing are carried out in this paper. A modified multiple degradation process model is introduced and the detailed analysis is implemented using Bayesian method. Normally, Bayesian method is flexible for incorporating various types of information to improve the reliability estimation and analysis. To achieve this point, multiple sources of information should be available. However, in this study, there is no other information available other than the degradation observations. This paper attempts to highlight another significant aspect of Bayesian method. It is the ability for incorporating the uncertainty within the estimation results, which are normally given as posterior distributions of model parameters. These posterior distributions are of critical importance for further analysis of newly-observed data, which can be further used as the prior information for the Bayesian analysis of these newly-observed data. These posteriors are also critical for the optimal decision-making for the system operation and management, for which uncertainty should be incorporated. Because the degradation observations are the only available information for this research, non-informative prior distribution based Bayesian method is used. This is due to the fact that uniform distribution is a simple distribution that can express no prior information in Bayesian calculation. It is also can facilitate the Markov chain Monte Carlo simulation for the calculation of posterior distribution. For more information about derivation of non-informative priors, please refer to the works by O'Hagan and Forster [13]. Based on these considerations, the Bayesian method is used to aggregate quantitative prior information for further degradation analysis and for uncertainty-related decision making.

The remaining segments of this paper are organized as follows. Section 2 introduces the structure and working principle of a spool valve, and analyses the root causes of failure and mechanisms of the sealing. In Section 3, a multiple degradation model with no competing relationship is established based on the gamma process. Section 4 uses an example to illustrate the proposed model and parameter estimation. Section 5 presents the conclusion of this paper and discusses the future work.

2. The sealing failure analysis of a spool valve

When a spool valve is used to control the flow directions of the oil of a hydraulic system, this spool valve is called a directional valve. A 3-position directional valve, with two working positions and one normal position, is taken as an example to illustrate the working principle of such type of spool valve. A spool valve consists of a cylindrical spool and a sleeve. When the spool slides towards right forming the normal position, as shown in left of Fig. 1, the hydraulic oil flows through the valve from port P to port B, and form A to port T. On the contrary, when the spool slides towards left forming the normal position, the hydraulic oil flows through the valve from port P to port A, and form B to port T. When the spool is in the normal position, all ports are closed. In this study, the movement of a spool moving from the normal position to the right or left position and then return to the normal position is called one stroke.

As shown in Fig 1, the clearance is formed between the spool and the sleeve. The quantity of internal leakage fluid passing through
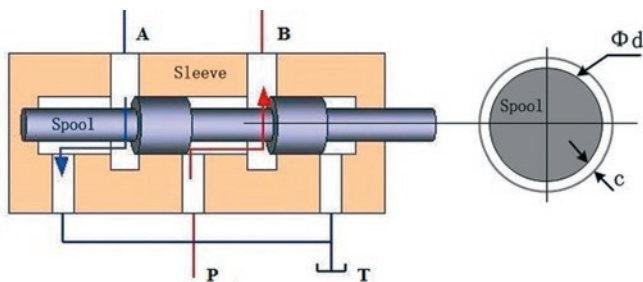
an assembled valve, of which the spool is in the normal position, is called null leakage. The null leakage is controlled in a certain range. The upper limit of this range depends on the valve sealing class and the valve size, which is given by some standards, such as the ANSI/FCI 70-2-2006, GB/T 17213.4-2005, and IEC 60534-4-2006 3.0. The flow in the narrow circular clearance of a spool valve can be viewed as laminar, and is governed by the following equation [7, 10],

$$Q = \Delta P \frac{\pi d c^3}{12 \mu L} \qquad (1)$$

where Q denotes the flow of leakage due to the clearance. ΔP is the pressure difference between both sides of the clearance, π is the circumference ratio, d denotes the valve spool diameter, c is the radial clearance height, L is the clearance length, and μ is the dynamic viscosity of hydraulic oil.

The movement of the spool restricts or permits the flow, thus it controls the amount of oil flow. At the same time, the high frequency back-and-forth movements of sliding cause the wear of spools and sleeves. It finally causes the increase of clearance and null leakage. The degradation of sealing of a spool valve can be represented by the increasing value of clearance, which is due to the wear degradation of the spool and sleeve. When the null leakage increases to the maximum level, the sealing of the spool valve is failed. When the maximum allowable null leakage is determined by the corresponding standard, the maximum allowable clearance can be estimated approximately by Eq. (1) or calculated precisely by CFD (Computational Fluid Dynamics) Methods [8, 17].

3. The multiple degradation models

The Wiener process and Gamma process are common stochastic processes for modelling degradation processes. The increments of the Wiener process may be negative, but always positive for the Gamma process. For mechanical devices, degradations, such as wear, erosion, fatigue, is always irreversible. Hence there is a nonnegative characteristic of the degradation values. In this paper, the Gamma process, which involves independent nonnegative increments, is adopted to characterize the wear-out degradation of the spool valve.

A non-negative valued process $\{X(t), t > 0\}$ is considered. $X(t)$ represents the measured degradation for an individual unit at time t. A gamma process has the following properties [18]:

- $X(0) = 0$;
- The increments $\Delta X(t)$ are independent;
- $\Delta X(t)$ follows a gamma distribution $Ga(\Delta \alpha(t), \lambda)$, where $\alpha(t)$ is a given monotone increasing function with $\alpha(0) = 0$, and the probability density function (PDF) $g(x)$ is defined by:

$$g(x|\alpha(t), \lambda) = \frac{\lambda^{\alpha(t)}}{\Gamma(\alpha(t))} x^{\alpha(t)-1} e^{-\lambda x} \qquad (2)$$

A system is considered failed when the degradation value reach the threshold, the cumulative distribution function of the time-to-failure can be written as:

$$F(t) = \Pr\{X(t) \geq C\} = \int_{x=C}^{\infty} g(x)dx = \frac{\Gamma(\alpha(t), C\lambda)}{\Gamma(\alpha(t))} \qquad (3)$$

Fig. 1. Schema of a spool valve and clearance

where $\Gamma(a,b)=\int_{z=b}^{\infty}z^{a-1}e^{-z}dz$ is the upper incomplete gamma function with $a>0$ and $b\geq 0$.

The reliability of a system at time t can be calculated by:

$$R(t)=1-F(t) \tag{4}$$

In reality, a product may consist of multiple degrading components or a component may have multiple degradation processes. In such case, it is necessary to use the multiple degradation processes models. Zhao and Elsayed [23] investigated a reliability modelling method with both catastrophic and degradation failures under accelerated stress conditions. Wang and Coit [20] presented a general modelling framework for multiple degradation measures. Pan and Balakrishna [15] introduced a reliability estimation method for a system with bivariate degradations that involve two or more performance characteristics. Wang and Pham [22] developed a model of the dependent competing risks with multiple degradation processes and random shock using time-varying copulas. In all these studies, the multiple degradations processes are treated as mutually competing. In fact, the relationship is not always competing in certain mechanical devices. This section firstly presents the competing model with multiple degradation processes according to the previous studies [15, 20, 22, 23].

In the competing model with multiple degradation processes, assuming that m is the number of the degradation processes, $D_i(t)$ is the degradation measure of the ith degradation process at time t, C_i is the failure threshold of the ith degradation process. A component or a system is considered as failed, when any of its degradation processes reaches the corresponding failure threshold. The component or system reliability at time t can be written as:

$$R(t)=\Pr\{D_1(t)<C_1,D_2(t)<C_2,\ldots,D_i(t)<C_i\},i=1,\ldots,m \tag{5}$$

As discussed above, each degradation process may reach a corresponding failure threshold at different time. For some mechanical devices, different degradation processes may lead to one failure, and Eq. (5) may not be able to capture the relationship between the reliability and the multiple degradation processes.

More generally, a system with m degradation processes, which lead to one failure mode, C is the failure threshold, the reliability at time t can be defined as:

$$R(t)=\Pr\{D_1(t)+D_2(t)+\ldots+D_i(t)<C\},i=1,\ldots,m \tag{6}$$

At the same time, if X_i follows a Gamma distribution with shape parameter k_i and scale parameter θ for $i=1,2,\ldots,N$, the following relationship can be obtained as:

$$\sum_{i=1}^{N}X_i\sim Gamma(\sum_{i=1}^{N}k_i,\theta) \tag{7}$$

Based on the properties of gamma process, Eq. (6) and Eq. (7), a new general setting of multiple degradation processes model is obtained, which is applicable when the relationship is not competing. A system with m degradation processes leading to one failure mode together, and the ith degradation process follow the gamma process with the parameter $k_i\Delta t$ and θ for $i=1,2,\ldots,m$, where C is the failure threshold. According to Eq. (3), Eq. (4) and Eq. (6) the reliability of the system at time t can be expressed as,

$$R(t)=1-\frac{\Gamma(\sum_{i=1}^{m}k_i\,t,C\theta)}{\Gamma(\sum_{i=1}^{m}k_i\,t)} \tag{8}$$

4. Illustrative example and Parameter estimation

As discussed in Section 2, the radial clearance height is the crucial factor for the reliability of sealing. When the total wear of spool and sleeve is bigger than the maximum allowable clearance height, the null leakage increases to the maximum level, and the sealing of the spool valve is failed. When the clearance between the spool and the sleeve reaches the maximum allowable value, the sealing fails. The increased clearance is caused by the wear degradation of the spool and the sleeve. $D_{sp}(n)$ is the wear volume of a spool after n strokes, with $D_{sp}(n)=0$. $D_{sl}(n)$ is the wear volume of a sleeve after n strokes, with $D_{sl}(n)=0$. D_M is the maxima allowable wear value that represents the failure threshold of the sealing, which can be calculated by subtracting the initial fit clearance from the maximum allowable clearance value. The initial fit clearance is a basic parameter for a spool valve. The calculation of the maximum allowable clearance is presented in Section 2. After n strokes, the reliability of a spool valve sealing can be estimated by:

$$R_s(n)=\Pr\left(D_{sp}(n)+D_{sl}(n)<D_M\right) \tag{9}$$

Assuming that the wear of a spool occurs randomly in every stroke and it can be described by a gamma process $D_{sp}(n)$ with $\Delta D_{sp}(n)\sim Ga(\alpha_1\Delta n,\lambda)$, where $\Delta D_{sp}(n)=D_{sp}(n+\Delta n)-D_{sp}(n)$, and $Ga(\alpha_1\Delta n,\lambda)$ is a gamma distribution with a shape parameter $\alpha_1\Delta n$ and a scale parameter λ. In this paper, the wear degradation of a sleeve is described by another gamma process $D_{sl}(n)$ with $\Delta D_{sl}(n)\sim Ga(\alpha_2\Delta n,\lambda)$, where $\Delta D_{sl}(n)=D_{sl}(n+\Delta n)-D_{sl}(n)$, and $Ga(\alpha_2\Delta n,\lambda)$ is a gamma distribution with a shape parameter $\alpha_2\Delta n$ and a scale parameter λ, which is the same as $D_{sp}(n)$.

Therefore, we have $\Delta D_{sp}(n)+\Delta D_{sl}(n)\sim Ga((\alpha_1+\alpha_2)\Delta n,\lambda)$. According the properties of the gamma process, $\{D_{sp}(n)+D_{sl}(n)\}$ can be described by a new gamma process. In addition, $\Delta(D_{sp}(n)+D_{sl}(n))=\Delta D_{sp}(n)+\Delta D_{sl}(n)\sim Ga((\alpha_1+\alpha_2)\Delta n,\lambda)$. According to Eq. (8), the reliability of a spool valve sealing can be obtained as follows:

$$R_s(n)=1-\frac{\Gamma(\alpha_1 n+\alpha_2 n,D_m\lambda)}{\Gamma(\alpha_1 n+\alpha_2 n)} \tag{10}$$

Note that the reliability evaluation of sealing is the probability as shown in Eq. (6). The proposed model and parameter estimation is illustrated in this section.

In this paper, simulated data, as shown in Table 1, are generated to demonstrate the applicability of the proposed multiple degradation models and parameter estimation. The number of samples is six, and the wear volumes are observed per 50,000 strokes. The threshold is set to 120. Then, the wear degradation path of spool valves can be depicted in Fig. 2.

Table 1 Simulated wear volumes of spool valves (unit: micron)

Unit		Number of strokes (10 thousand)																			
		5	10	15	20	25	30	35	40	45	50	55	60	65	70	75	80	85	90	95	`100
Sample 1	spool	7	9	19	22	28	34	37	39	45	46	50	54	58	64	69	74	76	81	83	86
	sleeve	4	6	8	13	14	18	19	21	22	24	27	30	32	34	37	39	46	49	52	55
Sample 2	spool	6	9	13	16	17	20	24	27	30	35	38	39	43	48	51	53	58	60	66	68
	sleeve	3	4	12	12	14	15	17	18	19	21	23	24	26	28	30	32	34	36	38	45
Sample 3	spool	4	8	12	16	20	25	28	31	35	37	41	44	47	50	56	59	63	65	66	70
	sleeve	1	2	5	8	10	14	16	20	23	26	27	32	33	35	37	40	41	43	47	49
Sample 4	spool	1	5	9	13	15	17	21	25	28	32	34	37	41	41	45	49	54	55	60	63
	sleeve	5	7	9	10	11	13	17	18	21	25	29	33	33	36	39	43	45	46	47	50
Sample 5	spool	2	4	8	9	12	17	19	22	25	29	32	34	37	46	48	50	52	54	57	60
	sleeve	1	2	9	11	13	16	22	24	29	31	32	35	35	37	41	43	44	46	47	51
Sample 6	spool	6	8	11	13	18	24	29	30	35	37	40	42	44	47	48	53	58	60	63	68
	sleeve	4	7	8	11	16	19	20	24	26	28	30	32	33	35	36	38	41	43	45	47
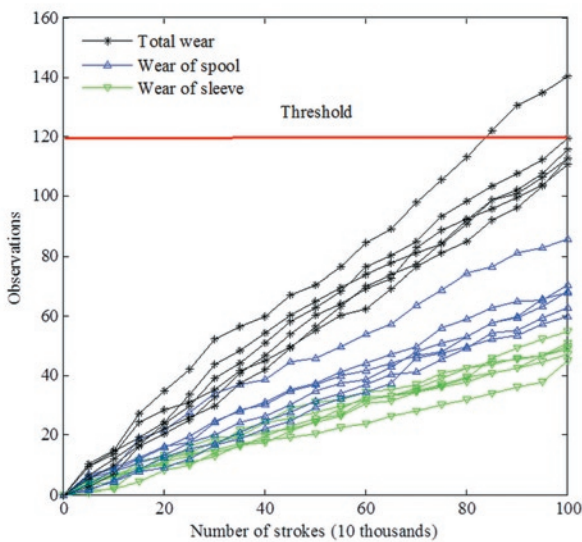
Fig. 2. Wear degradation paths of spools

Let $D_{sp}(n_{ij})$ with $j = 1,2,\ldots,20$ and $i = 1,2,\ldots,6$ be the jth spool wear observation of sample i. Let $d_{ij} = D_{sp}(n_{ij}) - D_{sp}(n_{i,j-1})$, be the wear increment of unit i. Following the degradation model introduced above, the wear increments d_{ij} obtained from the simulated data are independent and follow a gamma distribution $Ga(\alpha_1 \Delta n_{ij}, \lambda)$ with $\Delta n_{ij} = n_{ij} - n_{i,j-1}$. At the same time, let $D_{sl}(n_{ij})$ with $j = 1,2,\ldots,20$ and $i = 1,2,\ldots,6$ be the jth sleeve wear observation of sample i. Let $d'_{ij} = D_{sl}(n_{ij}) - D_{sl}(n_{i,j-1})$ denote the wear increment of unit i, and d'_{ij} follow another gamma distribution $Ga(\alpha_2 \Delta n_{ij}, \lambda)$ with $\Delta n_{ij} = n_{ij} - n_{i,j-1}$. When the wear observations of the valves are obtained as D with $\mathbf{v} = (\alpha_1, \alpha_2, \lambda)$ being the parameter vector, the information contained in this simulated data is presented as the likelihood function,

$$L(D, \mathbf{v} \mid \alpha_1, \alpha_2, \lambda) = \prod_{i=1}^{6} \prod_{j=2}^{20} g\left(\Delta d_{ij} \mid \alpha_1, \lambda\right) g\left(\Delta d'_{ij} \mid \alpha_2, \lambda\right) \quad (11)$$

where $g(\bullet)$ is the probability density function of a gamma distribution as shown in Eq. (2), $g\left(\Delta d_{ij} \mid \alpha_1 \Delta n_{ij}, \lambda\right)$ stands for the probability that the observed value is Δd_{ij}, where the parameter vector is $(\alpha_1 \Delta n_{ij}, \lambda)$,

$$\begin{aligned} L(D, \mathbf{v} \mid \alpha_1, \alpha_2, \lambda) &= \prod_{i=1}^{6} \prod_{j=2}^{20} g\left(\Delta d_{ij} \mid \alpha_1, \lambda\right) g\left(\Delta d'_{ij} \mid \alpha_2, \lambda\right) \\ &= \prod_{i=1}^{6} \prod_{j=2}^{20} \frac{\lambda^{\alpha_1 \Delta n_{ij}}}{\Gamma(\alpha_1 \Delta n_{ij})} \Delta d_{ij}^{\alpha_1 \Delta n_{ij} - 1} e^{-\lambda \Delta d_{ij}} \frac{\lambda^{\alpha_2 \Delta n_{ij}}}{\Gamma(\alpha_2 \Delta n_{ij})} \Delta d_{ij}'^{\alpha_2 \Delta n_{ij} - 1} e^{-\lambda \Delta d'_{ijij}} \end{aligned}$$

$$(12)$$

Suppose prior information for the wear of the spool valves can be obtained and quantified as joint prior distribution for the model parameters as $\pi(\boldsymbol{\theta}) = \pi(\alpha_1, \alpha_2, \lambda)$. Bayesian method has widely been used in reliability research [9, 11, 14, 16, 24]. More details about Bayesian theory can be referred to O'Hagan et al. [1, 11, 12]. Following the Bayesian theory, the joint posterior distribution of model parameters is obtained as:

$$\begin{aligned} p(\alpha_1, \alpha_2, \lambda, \mathbf{v}) &\propto \pi(\boldsymbol{\theta}) L(D, \mathbf{v} \mid \boldsymbol{\theta}) = \pi(\alpha_1, \alpha_2, \lambda) L(D, \mathbf{v} \mid \alpha_1, \alpha_2, \lambda) \\ &= \pi(\alpha_1, \alpha_2, \lambda) \prod_{i=1}^{6} \prod_{j=2}^{20} \frac{\lambda^{\alpha_1 \Delta n_{ij}}}{\Gamma(\alpha_1 \Delta n_{ij})} \Delta d_{ij}^{\alpha_1 \Delta n_{ij} - 1} e^{-\lambda \Delta d_{ij}} \frac{\lambda^{\alpha_2 \Delta n_{ij}}}{\Gamma(\alpha_2 \Delta n_{ij})} \Delta d_{ij}'^{\alpha_2 \Delta n_{ij} - 1} e^{-\lambda \Delta d'_{ijij}} \end{aligned}$$

$$(13)$$

where $p(\alpha_1, \alpha_2, \lambda, \mathbf{v})$ is the joint posterior distribution for model parameters. It is a description of the combination of prior information and the information contained in the observed degradation data. The reliability assessment of the valve spool sealing after n strokes, is calculated based on the joint posterior distribution of model parameters as:

$$R_s(n \mid D) = \int_{\alpha_1, \alpha_2, \lambda > 0} p(\alpha_1, \alpha_2, \lambda \mid D) \frac{\Gamma(\alpha_1 n + \alpha_2 n, D_m \lambda)}{\Gamma(\alpha_1 n + \alpha_2 n)} d\alpha_1 d\alpha_2 d\lambda$$

$$(14)$$

Based on the historical data, prior distributions for these parameters are given as:

$$\alpha_1 \sim U(0,100), \alpha_2 \sim U(0,100), \lambda \sim U(0,100)$$

where $U(0,100)$ is the uniform distribution with an interval of $(0,100)$. In this paper, these non-informative priors are given in the form of uniform distributions with relevant large intervals. A uniform distribution with large interval is sufficient to be chosen as a non-informative prior.

The MCMC method is used to generate posterior samples of model parameters. The WinBUGS is adopted to facilitate the implementation of MCMC for the Bayesian degradation analysis of the wear degradation data. 20,000 posterior samples are generated using WinBUGS with 10,000 samples for burn-in. Estimations of model parameters are presented in Table 2.

These posterior distributions are kernel distributions of posterior samples generated using MCMC simulation. By obtaining these posterior distributions, information conveyed by degradation observations presented in Table 1 are quantified and translated into probability

Fig. 3. Posterior distributions of model parameters

Fig. 4. Reliability of the spool valve sealing

Table 2. Estimations of model parameters

	Mean	Standard Deviation	Confidence interval	
			2.5%	97.5%
α_1	0.938	0.08679	0.7745	1.113
α_2	0.663	0.06116	0.5477	0.7878
λ	1.351	0.1258	1.113	1.606

The estimation results presented in Table 2 are summarized from the generated posterior samples. Posterior distributions of model parameters α_1, α_2 and λ are shown in Fig. 3. The mean of α_1 is 0.938 with a standard deviation 0.08679, the mean of α_2 is 0.663 with a standard deviation 0.06116, and the mean of λ is 1.351 with a standard deviation 0.1258. The estimation confidence intervals of these parameters are obtained as [0.7745, 1.113] for α_1, [0.5477, 0,7878] for α_2, and [1.113, 1.606] for λ.

As discussed above, the wear of a spool is described by a gamma process $\{D_{sp}(n); n \geq 0\}$, of which the shape parameter is a function of n (times of operation), written as $0.938n$, the scale parameter is 1.351. For the other gamma process $\{D_{sl}(n); n \geq 0\}$ used to describe the wear degradation of a sleeve, the shape parameter is $0.663n$, and the scale parameter is 1.351. Based the estimations of parameters presented above, we have

$$\Delta(D_{sp}(n) + D_{sl}(n)) \sim Ga((\alpha_1 + \alpha_2)\Delta n, \lambda) = Ga(1.601\Delta n, 1.351).$$ As discussed in Section 3, according to the new gamma process, the shape parameter is a function of time (times of operation) $1.601\Delta n$, and the scale parameter is 1.351. It describes the wear degradation of a spool valve and quantify the change of clearance height between the sleeve and the spool of a valve. When the failure threshold is set as 120, the reliability of the spool valve sealing can be obtained using Eq. (9), as presented in Fig. 4. The reliability assessment of sealing is close to engineering experience. It indicates that the proposed multiple degradation processes model and parameter estimation method are applicable for this case study of spool valves.

distributions of model parameters. These distributions can be further used for reliability analysis of similar valves based on newly observed degradation observations, which can be implemented through the proposed degradation model and Bayesian method in this paper.

5. Conclusion and future work

This paper presents a new multiple degradation model based gamma process to characterize the reliability of spool valve sealing subject to multiple degradation processes. The reliability analysis of sealing is investigated based on the valve structure and its working principle. The joint wear degradation of the spool and sleeve lead to the sealing failure. The maximum allowable clearance is used to indicate the failure threshold of sealing, and its calculation method is also presented in this paper. Moreover, a non-competing multi-degradation processes model is proposed based on the sealing failure analysis of a spool valve. This model is suitable for the situation where multiple degradation processes lead to one failure mode, which is quite common for mechanic devices. A numerical example is further provided to verify the model and illustrate the proposed method.

As future efforts, this paper leaves some open questions. First, the dependence of the multiple degradation processes is not considered. Second, the assumption that the wear degradation process of spool and sleeve has the same scale parameter can be eliminated. Third, the reliability data, which are used to illustrate the model, are simulated, and it is desirable to test the model in real-world cases. These are the interesting topics that deserve further investigation.

References

1. Bernardo JM, Smith AF. Bayesian theory vol. 405: John Wiley & Sons, 2009
2. Ellman A. Leakage behaviour of four-way servovalve. Proceedings of ASME International Mechanical Engineering Congress and Exposition 1998; 163-167.
3. Elsayed EA. Overview of reliability testing. IEEE Transactions on Reliability 2012; 61(2): 282-291, http://dx.doi.org/10.1109/TR.2012.2194190.
4. Eryilmaz B, Wilson BH. Combining leakage and orifice flows in a hydraulic servovalve model. Journal of dynamic systems, measurement, and control 2000; 122(3): 576-579, http://dx.doi.org/10.1115/1.1286335.
5. Gordić D, Babić M, Milovanović D, Savić S. Spool valve leakage behaviour. Archives of Civil and Mechanical Engineering 2011; 11(4): 859-866, http://dx.doi.org/10.1016/S1644-9665(12)60082-X.
6. Gorjian N, Ma L, Mittinty M, Yarlagadda P, Sun Y. A review on degradation models in reliability analysis. London: Springer, 2010, http://dx.doi.org/10.1007/978-0-85729-320-6_42.
7. Han SS, Liu X, Chao Z, Meng A. Evaluation Model Study of Hydraulic Components Leakage for In Situ Testing. Machine tool & Hydraulics 2009; 37(3): 119-121.
8. Jiang J, Guo Y, Zeng Lc, Zhan CC, Fu SG. Simulation and Analysis of Leakage for Clearance Seal of Hydraulic Cylinder. Lubrication Engineering 2013; 38(7): 75-79.
9. Li YF, Mi J, Huang HZ, Xiao NC, Zhu SP. System reliability modeling and assessment for solar array drive assembly based on Bayesian networks. Eksploatacja i Niezawodnosc - Maintenance and Reliability 2013; 15: 117-122.
10. Li Y. Research to the Wear and Geometric Error Relations of Electro hydraulic Servo Valve. Procedia Engineering 2011; 15: 891-896, http://dx.doi.org/10.1016/j.proeng.2011.08.165.
11. Mi J, Li YF, Huang HZ, Liu Y, Zhang X. Reliability analysis of multi-state systems with common cause failure based on Bayesian Networks. Proceedings of International Conference on Quality, Reliability, Risk, Maintenance, and Safety Engineering 2012; 1117-1121, http://dx.doi.org/10.1109/icqr2mse.2012.6246417.
12. O'Hagan A, Buck CE, Daneshkhah A, Eiser JR, Garthwaite PH, Jenkinson DJ, Oakley JE, Rakow T. Uncertain judgements: eliciting experts' probabilities. John Wiley & Sons, 2006, http://dx.doi.org/10.1002/0470033312.
13. O'Hagan A, Forster JJ. Kendall's advanced theory of statistics, volume 2B: Bayesian inference vol. 2: Arnold, 2004.
14. Pan R. A Bayes approach to reliability prediction utilizing data from accelerated life tests and field failure observations. Quality and Reliability Engineering International 2009; 25(2): 229-240, http://dx.doi.org/10.1002/qre.964.
15. Pan Z, Balakrishnan N. Reliability modeling of degradation of products with multiple performance characteristics based on gamma processes. Reliability Engineering & System Safety 2011; 96(8): 949-957, http://dx.doi.org/10.1016/j.ress.2011.03.014.
16. Peng W, Huang HZ, Xie M, Yang Y, Liu Y. A Bayesian Approach for System Reliability Analysis With Multilevel Pass-Fail, Lifetime and Degradation Data Sets. IEEE Transactions on Reliability 2013; 63(3): 689-699, http://dx.doi.org/10.1109/TR.2013.2270424.
17. Tallman J, Lakshminarayana B. Numerical simulation of tip leakage flows in axial flow turbines, with emphasis on flow physics: Part I: Effect of tip clearance height. Journal of turbomachinery 2001; 123(2): 314-323, http://dx.doi.org/10.1115/1.1368881.
18. Van Noortwijk J. A survey of the application of gamma processes in maintenance. Reliability Engineering & System Safety 2009; 94(1): 2-21, http://dx.doi.org/10.1016/j.ress.2007.03.019.
19. Vaughan N, Pomeroy P, Tilley D. The contribution of erosive wear to the performance degradation of sliding spool servovalves. Proceedings of the Institution of Mechanical Engineers, Part J: Journal of Engineering Tribology 1998; 212(6): 437-451, http://dx.doi.org/10.1243/1350650981542245.
20. Wang P, Coit DW. Reliability prediction based on degradation modeling for systems with multiple degradation measures. Proceedings of The Annual Reliability and Maintainability Symposium 2004; 302-307, http://dx.doi.org/10.1109/rams.2004.1285465.
21. Wang Y, Pham H. Dependent competing-risk degradation systems. London: Springer, 2011, http://dx.doi.org/10.1007/978-0-85729-470-8_7.
22. Wang Y, Pham H. Modeling the dependent competing risks with multiple degradation processes and random shock using time-varying copulas. IEEE Transactions on Reliability 2012; 61(1): 13-22, http://dx.doi.org/10.1109/TR.2011.2170253.
23. Zhao W, Elsayed E. An accelerated life testing model involving performance degradation. Proceedings of The Annual Reliability and Maintainability Symposium 2004; 324-329.
24. Zhu SP, Huang HZ, Smith R, Ontiveros V, He LP, Modarres M. Bayesian framework for probabilistic low cycle fatigue life prediction and uncertainty modeling of aircraft turbine disk alloys. Probabilistic Engineering Mechanics 2013; 34: 114-122, http://dx.doi.org/10.1016/j.probengmech.2013.08.004.

Yuan-Jian YANG
Weiwen PENG
Shun-Peng ZHU
Hong-Zhong HUANG

Institute of Reliability Engineering
University of Electronic Science and Technology of China
No. 2006, Xiyuan Avenue, West Hi-Tech Zone
Chengdu, Sichuan, 611731, P. R. China

E-mail: hzhuang@uestc.edu.cn, yuanjyang@hotmail.com, zspeng2007@uestc.edu.cn, weiwenpeng@hotmail.com

Tomasz KOPECKI
Przemysław MAZUREK
Tomasz LIS
Dorota CHODOROWSKA

POST-BUCKLING DEFORMATION STATES OF SEMI-MONOCOQUE CYLINDRICAL STRUCTURES WITH LARGE CUT-OUTS UNDER OPERATING LOAD CONDITIONS. NUMERICAL ANALYSIS AND EXPERIMENTAL TESTS

STANY ZAKRYTYCZNYCH DEFORMACJI PÓŁSKORUPOWYCH KONSTRUKCJI WALCOWYCH Z DUŻYMI WYKROJAMI W WARUNKACH OBCIĄŻEŃ EKSPLOATACYJNYCH. ANALIZA NUMERYCZNA I BADANIA EKSPERYMENTALNE*

The paper is a presentation of experimental model studies on thin-walled cylindrical structures containing large cut-outs subject to torsional deflection. The effect of rigidity of the frame reinforcing a cut-out on form and magnitude of post-buckling deformations occurring in operation conditions is analysed. A methodology based on numerical tools is proposed for determining alternative solutions in the design of structure skeleton leading to improvement of operation stability.

Keywords: *operating loads, loss of stability, thin-walled structures, aircraft load-bearing structures, torsional deflection, finite element method, nonlinear numerical analyses, operating stability.*

W pracy zaprezentowano wyniki modelowych badań eksperymentalnych cienkościennych, skręcanych struktur walcowych zawierających duże wykroje. Przeanalizowano wpływ sztywności ramy wzmacniającej wykrój na postać i wielkość deformacji zakrytycznych, występujących w warunkach eksploatacji. Zaproponowano metodykę określania alternatywnych rozwiązań konstrukcyjnych szkieletu struktury, zapewniające poprawę trwałości eksploatacyjnej, w oparciu o narzędzia numeryczne.

Słowa kluczowe: *obciążenia eksploatacyjne, utrata stateczności, ustroje cienkościenne, lotnicze struktury nośne, skręcanie, metoda elementów skończonych, nieliniowe analizy numeryczne, trwałość eksploatacyjna.*

1. Introduction

The dynamic evolution of solutions used by designers of aircraft load-bearing structures, initiated in the 1920s, resulted in establishment of aircraft operation standards based on assumptions which would be unacceptable for any other type of engineering structures. One of such assumptions is the admissibility of post-buckling deformations of semi-monocoque skin structures provided that the loss of stability is of local and linear-elastic nature [1, 2]. The rule applies mainly to skins made of isotropic materials, because in case of glass, carbon, and aramid composites which are used in the aircraft industry for a relatively short period of time, destruction processes occurring in the course of their prolonged operation in post-buckling deformation conditions are still the subject of numerous studies [6–8, 10, 13, 19].

Although composites become more and more popular in the aircraft technology, aluminium alloys still remain the materials most universally used by the industry for their well-known mechanical properties and high reliability. Application of these materials for aircraft skins was initially connected with some distrust as designers traditionally strove after elimination of post-buckling deformations in the first place. In such cases, the need to increase skin thickness emerged resulting in inevitable increase of the overall mass of the structure. For some time, the problem had been solved by using corru-

gated sheet metal for fuselage skins. This technology was commonly applied only in the beginning of 1930s, e.g. in designs of such aeroplane manufacturers as Ford and Junkers. With improvement of aircraft performance parameters, such structures became more and more troublesome because of the related aerodynamic problems, as a result of which it became necessary to coma back to smooth skin materials and admit the possibility of occurrence of local post-buckling deformations [11, 14].

While in case of skin fragments without geometrical singularities, the above-mentioned phenomenon does not result in any decrease of their operating durability stability, presence of cut-outs of any type becomes a source of problems. Aircraft structures, by virtue of for what they are intended and in what conditions are to be operated, are characterised with existence of a large number of cut-outs with various dimensions. Such discontinuities may occur within segments of skin of a semi-monocoque structure limited by skeleton components (e.g. passenger cabin windows or small inspection openings). They can also represent major discontinuities of the structure with larger dimensions, e.g. doors, cargo loading hatches, or large access openings (Fig. 1), which make segmentation of stringers necessary.

From the point of view of strength properties and operating durability of a structure, presence of cut-outs is a very unfavourable circumstance. They reduce overall rigidity of the structure and force

---
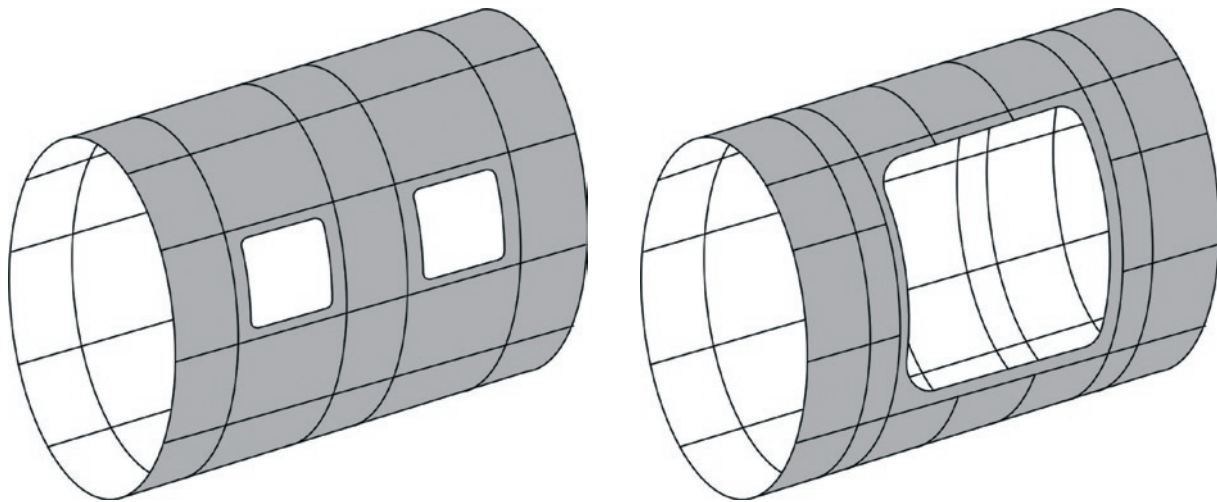
Fig. 1. Examples of cut-outs in aircraft structure skins

the designers to use additional structural elements in the form of sufficiently rigid frames, which in turn contributes to an increase of the aircraft mass. Moreover, cut-outs represent those zones of any structure which are most susceptible to fatigue-induced damage zone capable to end up with a very serious failure or even destruction of the whole object [1, 12, 16, 18, 20].

In the course of research on aircraft structures, design teams have worked out a number of design canons securing the safety margin required by applicable norms to be maintained in operating conditions. It should be however emphasised that many of these commonly adopted standards were established at the technology development level when numerical tools still had not been available and each of the new solutions had to be verified in the course of costly experimental tests.

Nowadays, it is possible to carry out virtual experiments with the use of sophisticated engineering tools, including software packages based on the finite element method. Moreover, recent progress in the materials engineering has broadened significantly the range of options available when relatively inexpensive experiments with the use of model materials are planned. It seems to be therefore appropriate to undertake attempts aimed at finding alternative design solutions focused on securing as high reliability of the structure as possible, with its mass reduced to a minimum at the same time [12].

This paper presents a number of results obtained from experiments and numerical analyses concerning a representative fragment of semi-monocoque aircraft load-bearing structure weakened by presence of a cut-out.

2. Purpose and scope of the study

The subject of the study was a typical fragment of aircraft load-bearing structure weakened by presence of a cut-out (Fig. 2), corresponding to e.g. a helicopter tail boom with an inspection opening providing access to the tail rotor drive shaft or a separated aeroplane fuselage fragment with a window.

In similar cases, the most commonly adopted design canon provides for situating the cut-out between neighbouring elements of the skeleton, with cut-off wedges situated as close as possible to joints between the skeleton and the skin. In practice, implementation of this imperative runs up against a number of limitations. The most fundamental of them is the necessity to reinforce the cut-out with an appropriate frame the role of which consists not only in providing sufficient rigid-

ity to the skinless segment of the structure but also allowing to mount the glass pane in an aeroplane window or the cover to an inspection opening.

If, moreover, a design provides for cut-out edge with too small round-off radii, there is a high risk of deterioration of the overall operating durability caused by nucleation of fatigue cracks.

Another rule adopted commonly in the design processes is aspiring to minimise post-buckling deformations by means of reinforcing the skeleton through introducing many additional components to its structure. The final result is usually the increased mass of the structure accompanied by overall overdimensioning in many cases.

The purpose of the study was to determine the effect of rigidity of the frame reinforcing a cut-out on the nature of post-buckling deformations of the skin and identify design solutions allowing to increase critical load levels and thus also the service life of the structure, with as little skeleton components as possible.

The study's point of departure was an experiment with a model tested on a dedicated research set-up. Skin deformations were observed by means of an optical scanner. High optical sensitivity of the material from which the model was made allowed to carry out qualitative assessments of stress distribution patterns by means of optical
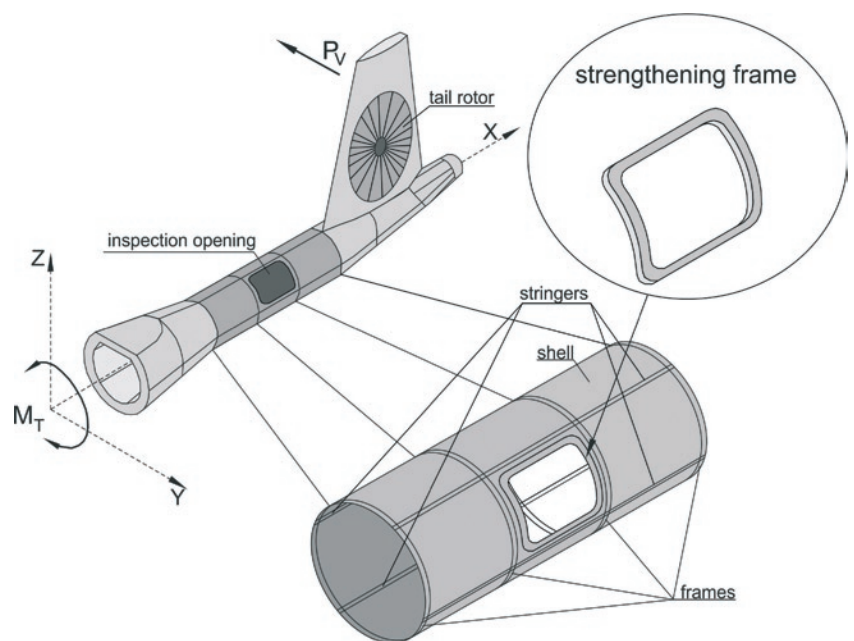
Fig. 2. An example of location of the examined object in the aircraft structure

polarimetry methods. The experimental data were used as a base on which results obtained from nonlinear analyses carried out by means of the finite elements method were verified. Development of an appropriate numerical model allowed to identify structural design solutions meeting assumed mass- and stiffness-related criteria.

3. The experiment

The subject of the model experiment was a thin-walled cylindrical structure reinforced by means of four stringers and four frames (Fig. 3). The outermost closing frames were solid elements, while frames in the area of the cut-out had a fragmentary form.
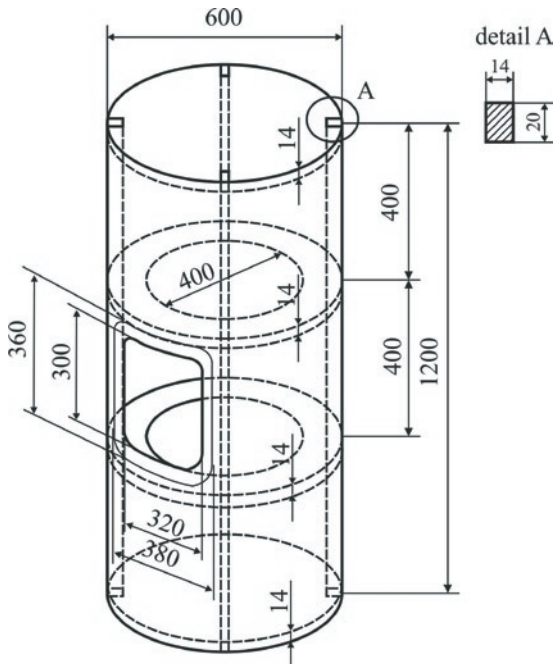
Fig. 3. Schematic view of the structure

Models of all variants of the structure were made out of polycarbonate marketed under trade name of Makrolon for which the tensile strength test was carried out and the following material constants determined: the Young's modulus $E = 3000$ MPa and the Poisson ratio $v = 0.36$.

The characteristic of the material corresponding to one-dimensional tensile stress was also determined (Fig. 4). Clearly distinguishable elastic and inelastic deformation zones suggest the possibility to approximate the actual material characteristic by the ideal elastic-plastic model. However, due to the fact that only a local elastic loss of
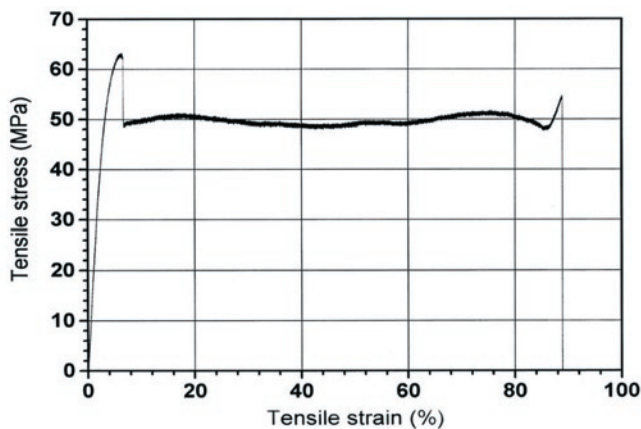
Fig. 4. The tensile stress plot for the polycarbonate specimen

Fig. 5. The research set-up with the model subject to the experiment
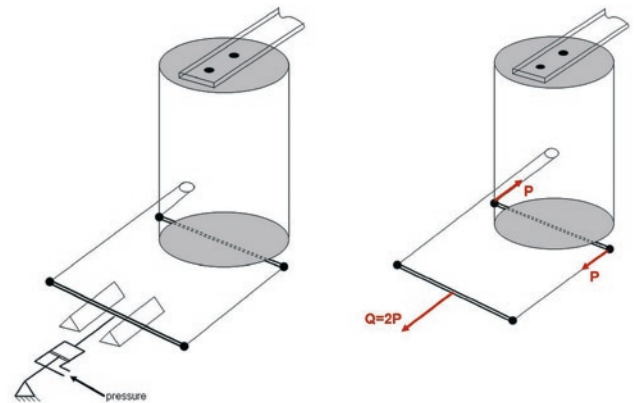
Fig. 6. Schematic sketch of model mounting and the load application system

stability of the structure is acceptable, the elastic nature of the material was assumed in all numerical models. Moreover, because of its low elasticity modulus value (by two orders of magnitude less than this of steel) it was possible to carry out experiments using low values of the applied external loads.

Inner surfaces of the skin have been coated with a reflexive substance which allowed to apply optical polarimetry methods for qualitative determination of stress distribution patterns.

Experiments were carried out with the use of dedicates research set-up (Fig. 5). The model was fixed and loaded according to the schematic drawing shown in Fig. 6. The load was applied by means of the displacement method with the use of a hydraulic servo coupled with a dynamometer.

Two variants of the structure were examined, differing with thickness of the cut-out reinforcing frame (3 mm in the first and 6 mm in the second version). In both cases, skin displacement measurements were taken by means of ATOS optical scanner (Fig. 7). Distribution patterns of optical effects occurring in skins were observed with the use of a reflected light polariscope (Fig. 8). In the course of load application, the relationship between the torque moment value and the structure's total torsion angle was determined which has been assumed to be the quantity representative for the skin state (Fig. 9).

It follows from the obtained results that differences between displacement distribution patterns observed in advances post-buckling states of the examined model versions are small. Making the reinforcing frame twice as thick resulted in little less depths of folds occurring in the area close to the cut-out corner, contributing on the other hand

a)   b)
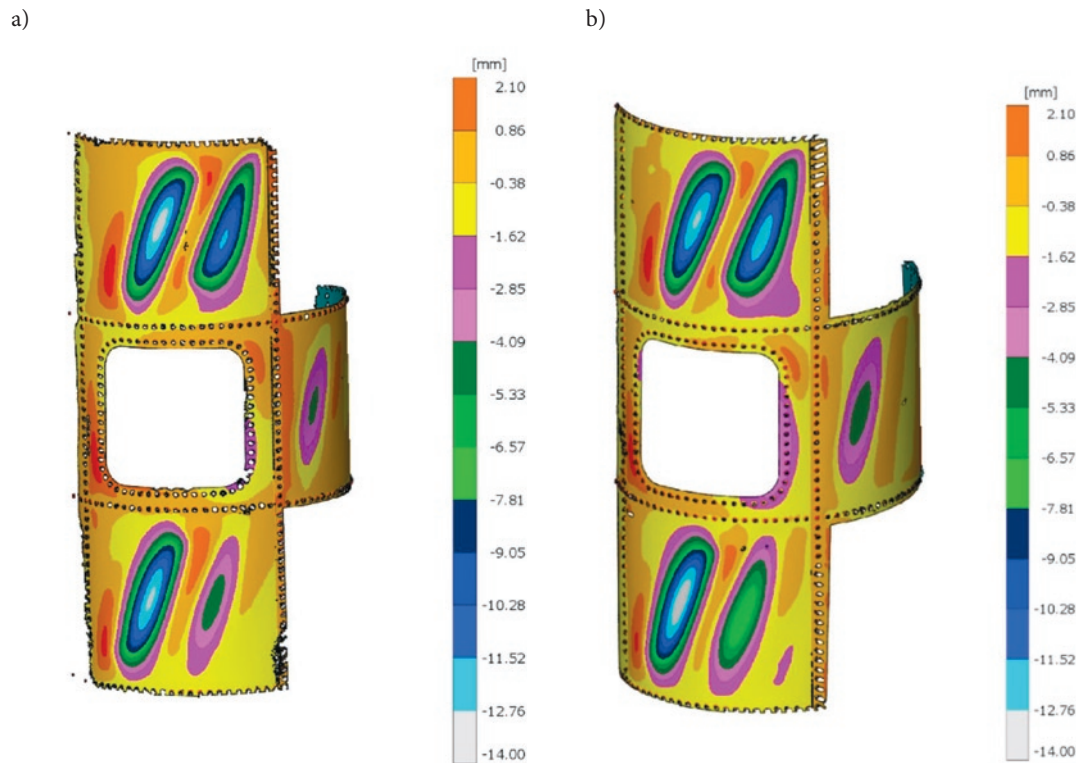
Fig. 7. Skin displacement distribution patterns determined as a result of scanning: (a) model with 3-mm thick frame; (b) model with a 6-mm thick frame
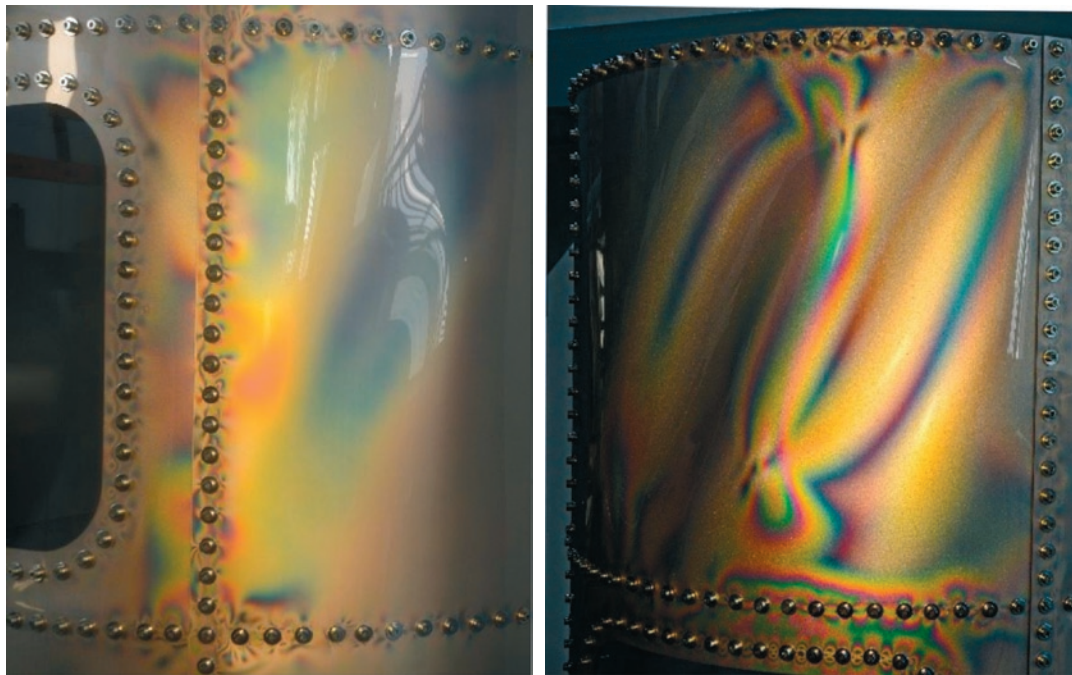
Fig. 8. Distribution patterns of optical effects: (a) in the cut-out area; (b) in the skin segment above the cut-out

to deepening deformations in skin fragments bordering to the cut-out segment (Fig. 7).

Comparison of representative equilibrium paths proves that in the sub-critical range, torsional rigidities of the two structures were virtually identical. Making the frame thicker resulted in the critical load value being increased by about ten percent. Taking into account relatively small increase of the mass structure following from the applied change, the modification may be considered cost-effective from the point of view of the examined object's durability. In fact, an increase of the load value which triggers occurrence of larger deformations re-

sults in a decrease of the number of cycles leading to bifurcations and post-buckling deformations which, although admissible, contribute to reduction of the structure's overall service life.

It should be borne in mind that while application of a thicker cut-out frame in case of an isolated inspection opening does not affect significantly the overall mass of the structure, introduction of similar modification in case of many cut-outs (e.g. a row of cabin windows) can result in major deterioration of its operating merits. In such cases, it is recommended to undertake more detailed analysis of deficiencies and advantages of the considered design solution change.
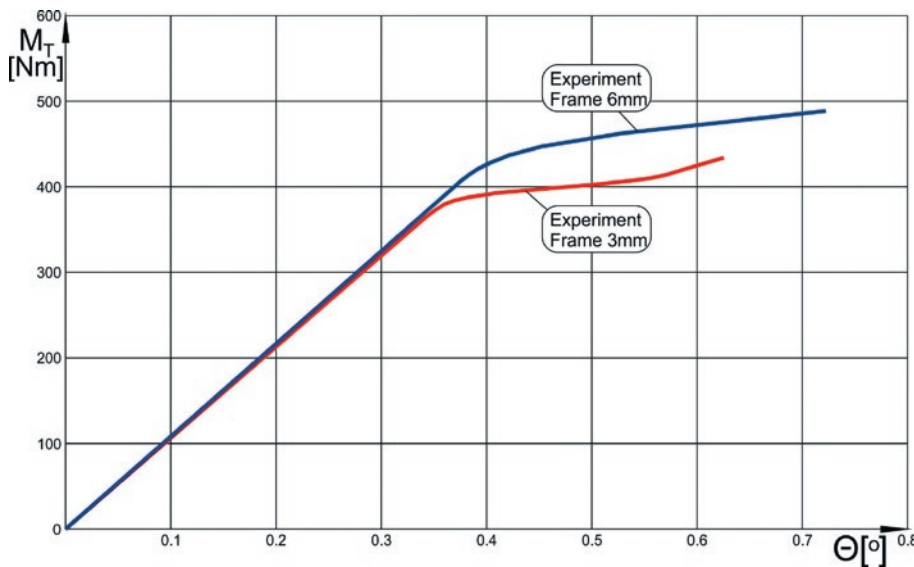
Fig. 9. Representative equilibrium paths — results of the experiment

A singularity in the form of a segment with a cut-out results in situation where post-buckling deformations occur in skin segments bordering on the opening whereas the other segments remain in the pre-buckling state. This is the origin of an important design recommendation according to which adding successive skin stiffening elements to the structure skeleton requires taking into account the uneven nature of post-buckling deformations.

The experiment has revealed that post-buckling deformations of the examined skin, in view of their magnitude and rather violent course of the phenomenon, despite their local and elastic nature can significantly reduce the overall service life of the structure. It seems therefore to be necessary to introduce additional stiffening elements to its crucial zones.

The research cycle described here was based on assumption that determination of the effect of design changes on the nature of post-buckling deformations and the critical load value can be a subject of numerical simulations. However, satisfactory conformity of physical properties represented by numerical and laboratory test models remains the fundamental criterion of credibility of the obtained results. The assessment of appropriateness of initial models was therefore based on comparison of deformation patterns and courses of representative equilibrium paths observed in structures subject to test and their numerical models implemented by means of the finite elements method.

3. Numerical analyses

Numerical models of the examined structures were implemented with the use of MSC PATRAN/MSC MARC software. In view of the necessity to reflect the phenomena related to the loss of stability in numerical models, nonlinear procedures were used in the analyses which allowed to take into account large deformations and the resulting changes in orientation of active force vectors [3, 5].

The fundamental link in an nonlinear problem determining the relationship between the state of a structure and the load in the finite elements method is the so-called equilibrium path of the system, representing in general as a hypersurface in the hyperspace of states [4, 5]. The relationship represents fulfilment of the equation of residual forces in a matrix form [9, 15]:

$$\mathbf{r}(\mathbf{u}, \mathbf{\Lambda}) = \mathbf{0}, \qquad (1)$$

where $\mathbf{u}$ is the state vector containing displacement components of nodes of the structure corresponding to its current geometrical configuration, $\mathbf{\Lambda}$ is a matrix composed of control parameters corresponding to the current load level, and $\mathbf{r}$ is the residual vector composed of uncompensated force components related to the current system deformation state. The set of control parameters can be represented by a single parameter λ being a function of the load. Equation (1) takes then the form:

$$\mathbf{r}(\mathbf{u}, \lambda) = \mathbf{0}, \qquad (2)$$

called the single-parameter equation of residual forces.

The prediction-correction methods of determining consecutive points of the equilibrium path used in modern software routines contain also a correction phase based on the requirement that the system satisfies an additional equation called the increment control equation or the equation of constraints [9, 17]:

$$c(\Delta \mathbf{u}_n, \Delta \lambda_n) = 0, \qquad (3)$$

where the increments:

$$\Delta \mathbf{u}_n = \mathbf{u}_{n+1} - \mathbf{u}_n, \quad \text{and} \quad \Delta \lambda_n = \lambda_{n+1} - \lambda_n$$

correspond to transition from state n to state $n + 1$.

In view of lack of possibility to represent equilibrium paths for systems with more than 2 degrees of freedom in a form of 2D plots, in practice, for the purpose of comparison, the so-called representative equilibrium paths are used that represent a functional relationship between a selected parameter characterising deformation of the system and a single control parameter related to the applied load. Reliability of results obtained from FEM-based nonlinear numerical analyses is usually accepted when a satisfactory convergence is found between two representative equilibrium paths, namely the actual one determined in the course of an experiment and this obtained numerically. It is also necessary to obtain convergence between the forms of deformations following from the calculations [9] with results of the corresponding experiment. On the grounds of the rule of uniqueness of solutions, according to which one and only one distribution of the reduced stress corresponds to each deformation state, the obtained reduced stress distributions in the deformed skin can be therefore also considered reliable [11].

As the nonlinear numerical analysis is an iterative process aimed at finding successive equilibrium states, its correctness is, to a large degree, determined by correct choice of the prognostic method, the correction strategy, and a number of control parameters. In the case described here, the Newton-Raphson method was used in combination with the control parameter correction strategy (the so-called state control). Usually, when carrying out numerical analyses of post-buckling deformations, it is necessary to employ more advances correction strategies from the group of the so-called arc-length control methods which include e.g. the Riks-Ramm strategy [17] and the Crisfield strategy [4]. However, computational practice reveals that with respect to shells with relatively large curvatures, including cylindrical ones, proper selection of the set of parameters controlling nonlinear analysis in combination with basic correction strategies allows to obtain correct solutions with significantly reduced computation time.

Numerical models of the examined structure variants were based on the same overall geometrical layout (Fig. 10).
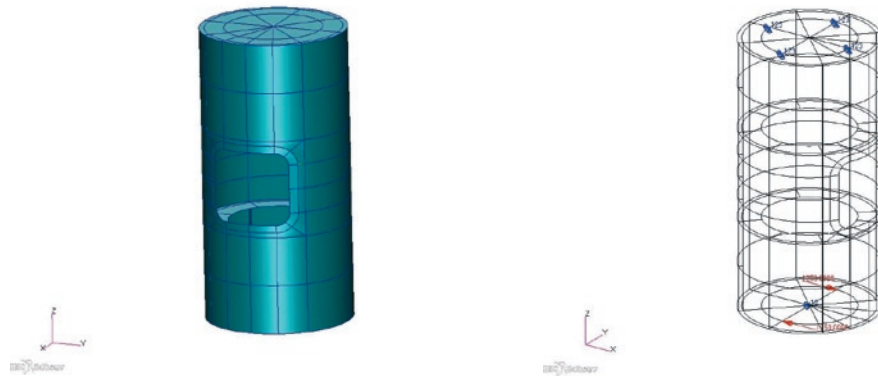
Fig. 10. Geometrical model of the structure with schematic view of its mounting and the load application system

a)

b)
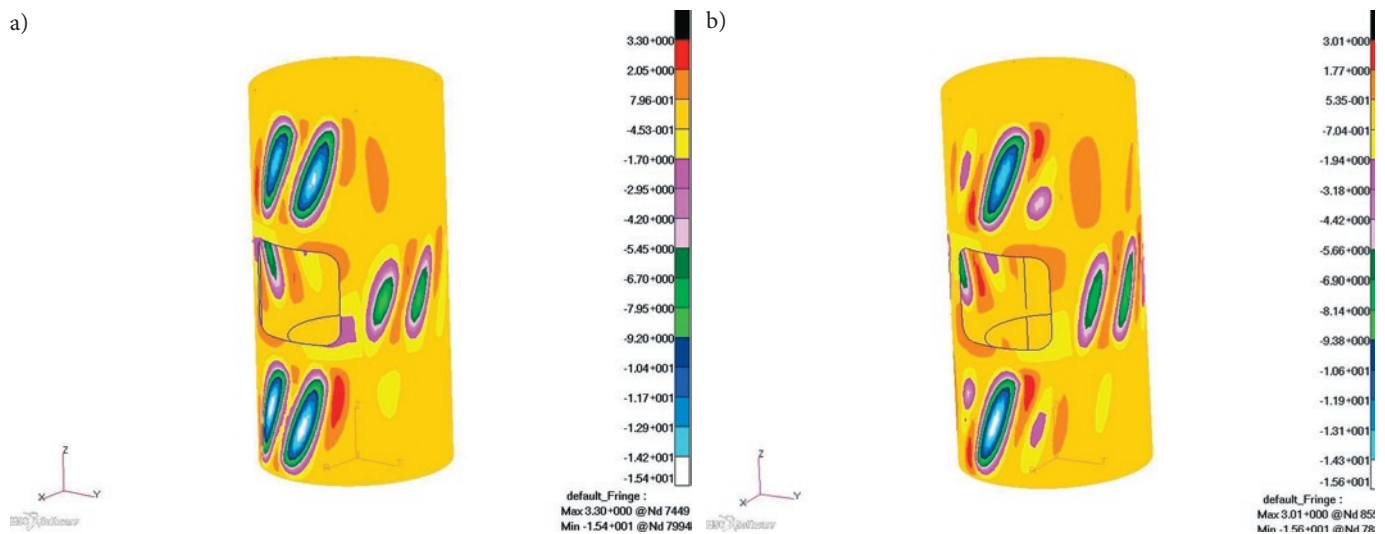
Fig. 11. Resultant displacement distribution patterns (in mm): (a) model with 3-mm thick frame; (b) model with 6-mm thick frame

Numerical models were based on surface-type structures, with the use of thin-shell elements, thick-shell elements (to represent frames and stringers), and four-node shell elements with bilinear shape functions. With the assumed mesh density, about 10,400 nodes and about 10,500 elements were used in total.

Fig. 12. Comparison of representative equilibrium paths

Resultant displacement distribution patterns obtained for the examined models from nonlinear numerical analysis are presented in Fig. 11.

The obtained deformation distribution patterns conformed to experimental test results both qualitatively and quantitatively. Based on result of numerical analyses, representative equilibrium paths were determined representing relationships between the overall angle of torsion of the structure and the torque moment value. The characteristics obtained from experiments and those calculated on the grounds of numerical analyses are juxtaposed in Fig. 12.

It should be emphasised that the presented characteristics were drawn with the use of data obtained from measurements carried out for steady-state conditions. In the course of origination and further development of post-buckling deformations, a number of local bifurcations arise as a result of which some subsets of state parameters are subject to changes. Such changes may result in occurrence of abrupt offsets in representative characteristics; however, from the point of view of durability and reliability of the structure, its seems to be unnecessary to reproduce them in detail.

Consistence of the two model versions should be acknowledged satisfactory. In the linear regime, the similarity can be considered

a)

b)

complete, while in the post-buckling range, discrepancies between calculated control parameters and those obtained from the experiment, for determined states of the structure, do not exceed 9% (7% in case of 6-mm thick frame).

It can be therefore stated that that the adopted numerical models are appropriate and show properties satisfactorily consistent with those of actual objects.

As it has been already mentioned above, deformation patterns and magnitude of the displacements connected with them seem to be unfavourable from the point of view of the structure reliability. It seems therefore to be justified to undertake an attempt to introduce additional skeleton elements the purpose of which would be to stiffen crucial areas of the skin at the structure mass increase kept as small as possible.

The verified numerical models were used to determine properties of the modified structure variants. Successive modifications were limited to providing the structure's skeleton with additional components aimed at local improvement of rigidity and inducing a change in post-buckling deformation

Fig. 13. Modified models of the examined structures: (a) version with fragmentary frames, (b) version with fragmentary frames and stringers

a)

b)
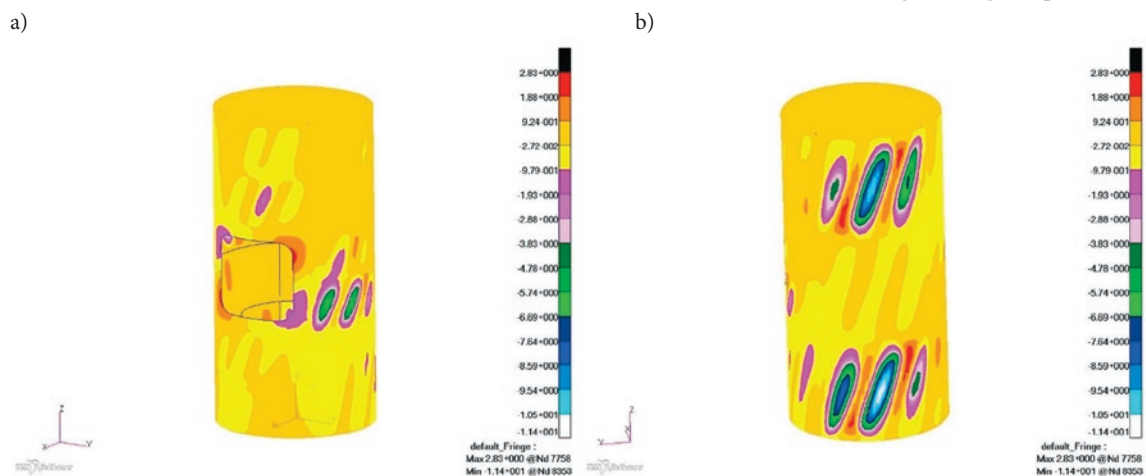
Fig. 14. (a) Displacement distribution (in mm) in the model with fragmentary frames; (b) a fragment of the rear portion of the structure

a)

b)
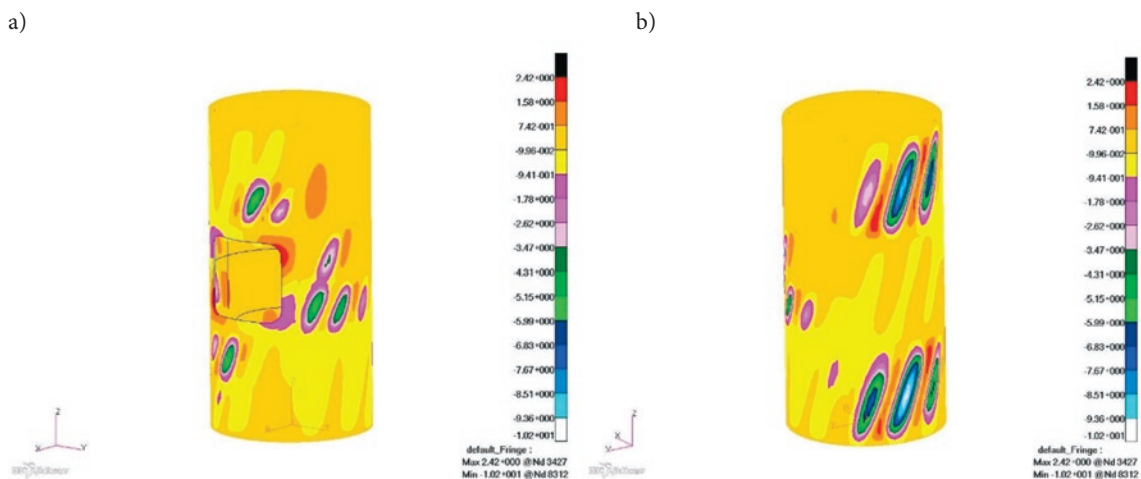
Fig. 15. (a) Displacement distribution (in mm) in the model with fragmentary frames and stringers; (b) a fragment of the rear portion of the structure

patterns. The process was aimed at determining a solution as favourable as possible from the point of view of durability and reliability of the structure, with the increase of its mass limited to a minimum at the same time.

The first of the alternative solutions consisted in providing the skin segments bordering to the cut-out with additional skeleton components in the form of fragmentary frames. In another version of the structure, fragmentary stringers have been also added (Fig. 13).

Numerical calculations were carried out in both cases by means of the set of procedures the same as this used in earlier models. The sizes of new tasks did not change significantly.

Post-buckling displacement distribution patterns obtained from the analyses were characterised with forms significantly differing from those observed in case of initial structures (Figs. 14 and 15).

In both cases, presence of additional skeleton components resulted in significantly increased rigidity of skin segments bordering to the cut-out, forcing at the same time occurrence of post-buckling deformations in the structure's rear segments (opposite with respect to the opening). It can be therefore claimed that the adjustment to the design solution resulted in more even reaction of the structure and reduction of maximum post-buckling displacement values. As far as the quantitative comparison is concerned, the solution employing fragmentary stringers seems to be more favourable, as in this case the maximum displacements are smaller by about 10% compared to the structure in which only fragmentary frames were used as stiffening components. It should be however emphasised that the presented results correspond to maximum load values applied in the course of the experiment. In operating conditions, deformations of this magnitude are in general inadmissible which follows from the necessity to maintain stiffness of the whole structure.

When developing a numerical model to be verified experimentally it is appropriate to compare magnitude and nature of deformations within a wide range of load values as this allows to assess appropriately the properties of the virtual structure and their conformity with properties of its actual counterpart. It is assumed that in real-life operating conditions, there are post-buckling deformations corresponding to relatively small increases of representative structure state parameters with respect to their values occurring at critical loads.

Under such assumption, a ten-percent difference between maximum displacement values observed in the above-presented structures does not seem to be significant. An important factor allowing to assess reliably the properties of the proposed solutions is the juxtaposition of representative equilibrium paths and comparing them with the characteristic corresponding to the initial version (Fig. 16).

It follows from the presented characteristics that the proposed modifications result in an increase of the critical load in the range of about 20–30% which, at expected small increase of the mass, seems to be a satisfactory figure. Although introduction of fragmentary stringers results in increased stiffness of the structure and higher critical load value, it seems to be advisable to precede selection of the target solution with detailed analysis of mass increase for the complete structure including the proposed modifications. For the model material used in the course of experimental tests, the estimated mass increase with respect to the initial structure mass was about 0.5% for the solution employing fragmentary frames and about 1% for the version with fragmentary frames and stringers. If therefore the considered structure corresponds to a fragment of aircraft fuselage with a single inspection
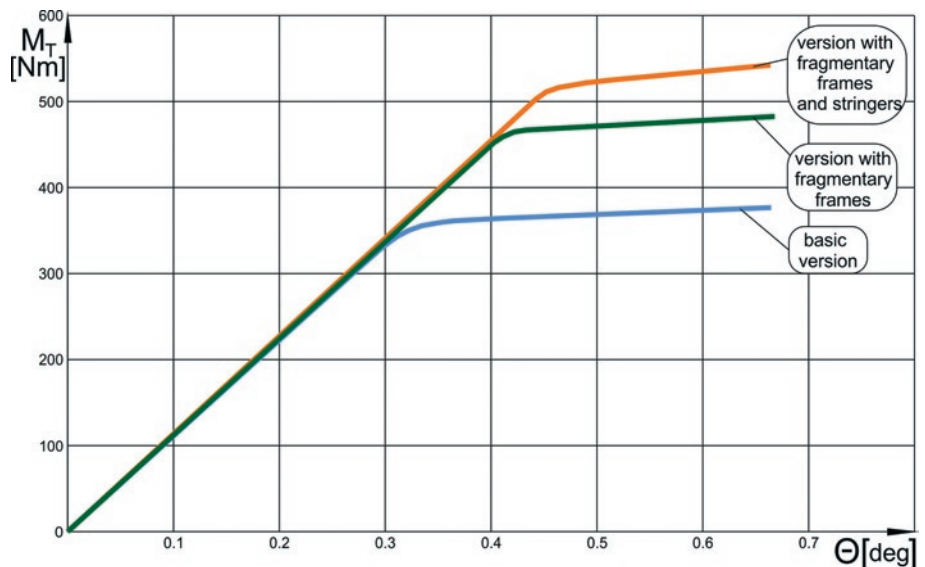
Fig. 16. Comparison of representative equilibrium paths for numerical models with a 3-mm thick frame reinforcing the cut-out

opening, application of fragmentary stringers must be acknowledged as a viable solution.

4. Summary and conclusions

On the grounds of experimental test it has been proven that by increasing rigidity of a frame reinforcing the cut-out edge, only relatively small increase of rigidity of the analysed structure is obtained. Usefulness of application of modifications of that type depends of location and quantity of cut-outs in actual aircraft structure. In case when the analysed cut-off is a repeatable fuselage feature, e.g. a passenger cabin window edge, the effect of increased mass of the reinforcing frame an the structure as a whole on its operating durability and reliability should be a subject of separate detailed analyses.

The purpose of the presented considerations was also to point out a potential for prospecting for alternative design solutions allowing to increase the service life of the structure. The proposed methodology consist in using results of a dedicated experiment for developing an appropriate initial numerical model implemented within the framework of the finite elements method and elaborating it be means of gradual modifications.

In the light of the above-presented results, the methodology seems to be effective. It allows to eliminate, in a relatively easy way, the design errors reducing potentially the service life of the structure by means of a number of numerical tests, reducing thus to a minimum the number of necessary experiment and minimising the related costs.

Experimental tests carried out on initial design solutions allow to elaborate appropriate numerical models characterised with high consistence of their rigidity-related properties with those of actual structures which allows to assume that results obtained from nonlinear numerical analyses of models in which modifications were introduced are reliable.

It should be however emphasised that the search for new and more effective versions of a structure by introducing successive modifications to numerical models means continuously increasing departure from the verified initial solution and thus decreasing reliability of the obtained results. It seems therefore to be necessary to verify experimentally the structure in its target form recognised as the satisfactory one from the point of view of the adopted criteria.

The presented solutions alternative with respect to the initial design are only some examples of modifications aimed at increasing

operating stability of the structure. It seems to be appropriate to carry out a number of another numerical tests allowing to identify flaws and merits of a sequence of design solutions. For instance, it would be advisable to determine the effect of presence of additional fragmentary skeleton components in rear skin segments which, in case of stiffening applied to areas bordering to an opening, are subject to large post-buckling deformations.

It is planned that the solutions assessed as the most promising will be tested experimentally and final versions of the numerical models possible elaborated.

References

1. Arborcz J. Post-buckling behavior of structures. Numerical techniques for more complicated structures. Lecture Notes In Physics 1985; 288: 83-142.
2. Aborcz J., Hol J.M.A. Recent development in shell stability analysis, Report LR-633 Faculty of Aerospace Engineering. Delft: University of Technology, 1990.
3. Bathe K. J. Finite element procedures. Prentice Hall, 1996.
4. Crisfield M. A Non-linear finite element analysis of solid and structures. J. Wiley & Sons, 1997.
5. Doyle J.F. Nonlinear analysis of thin-walled structures. Springer-Verlag, 2001, http://dx.doi.org/10.1007/978-1-4757-3546-8.
6. Dębski H., Kubiak T., Teter A. Numerical and experimental studies of compressed composite columns with complex open cross-sections. Composite Structures, 2014; 118: 28-36, http://dx.doi.org/10.1016/j.compstruct.2014.07.033.
7. Dębski H., Kubiak T., Teter A. Experimental investigation of channel-section composite profiles' behavior with various sequences of plies subjected to static compression. Thin-Walled Structures, 2013; 71: 147-154, http://dx.doi.org/10.1016/j.tws.2013.07.008.
8. Dębski H. Experimental investigation of post-buckling behavior of composite column with top-hat cross-section. Eksploatacja i Niezawodnosc – Maintenance and Reliability, 2013; 16 (2): 1056-109.
9. Felippa C. A., Crivelli L. A., Haugen B. A survey of the core-congruential formulation for nonlinear finite element. Archive of Computer Methods in Engineering, 1994, http://dx.doi.org/10.1007/BF02736179.
10. Kolakowski Z., Mania R. Semi-analytical method versus the FEM for analysis of the local post-buckling of thin-walled composite structures Composite Structures, 2012; 97: 99-106, http://dx.doi.org/10.1016/j.compstruct.2012.10.035.
11. Kopecki T., Mazurek P. Problems of numerical bifurcation reproducing in post-critical deformation states of aircraft structures. Journal of Theoretical and Applied Mechanics, 2013; 51(4): 969-977.
12. Kopecki T., Mazurek P. Numerical representation of post-critical deformations in the processes of determining stress distributions in closed multi-segment thin-walled aircraft load-bearing structures. Eksploatacja i Niezawodnosc – Maintenance and Reliability, 2014; 16(1):164-169.
13. Li C., Wu Z. Buckling of 120° stiffened composite cylindrical shell under axial compression - Experiment and simulation. Composite Structures, 2015; 128: 199-206, http://dx.doi.org/10.1016/j.compstruct.2015.03.056.
14. Lynch C. A. Finite element study of the post buckling behavior of a typical aircraft fuselage panel. PhD Thesis, Queen's University Belfast, 2000.
15. Rakowski G., Kacprzyk Z. The finite elements method in mechanics of structures. Oficyna Wydawnicza Politechniki Warszawskiej, 1993.
16. Rudawska A., Dębski H. Experimental and numerical analysis of adhesively bonded aluminium alloy sheets joints, Eksploatacja i Niezawodnosc – Maintenance and Reliability, 2011; 49(1): 4-10.
17. Riks E. An incremental approach to the solution of snapping and buckling problems. International Journal of Solid and Structures, 1979; 15: 529-551, http://dx.doi.org/10.1016/0020-7683(79)90081-7.
18. Sonat C., Topkaya C., Rotter J.M. Buckling of cylindrical metal shells on discretely supported ring beams. Thin-walled Structures, 2015; 93: 22-35, http://dx.doi.org/10.1016/j.tws.2015.03.003.
19. Teter A., Kołakowski Z. Coupled dynamic buckling of thin-walled composite columns with open cross-sections. Composite Structures, 2013; 95(1): 28-34, http://dx.doi.org/10.1016/j.compstruct.2012.08.006.
20. Yeh M., Lin M., Wu W. Bending buckling of an elastoplastic cylindrical shell with a cutout Engineering Structures, 1999; 21(11): 996-1005.

Tomasz KOPECKI
Przemysław MAZUREK
Tomasz LIS
Department of Mechanical Engineering and Aviation
Rzeszów University of Technology
al. Powstańców Warszawy 12, 35-959 Rzeszów, Poland

Dorota CHODOROWSKA
State Higher Vocational School in Krosno
ul. Wyspiańskiego 20, 38-400 Krosno, Poland

E-mail: tkopecki@prz.edu.pl, pmazurek@prz.edu.pl
dorota.chodorowska@pwsz.krosno.pl

Tianyu LIU
Long CHENG
Zhengqiang PAN
Quan SUN

CYCLE LIFE PREDICTION OF LITHIUM-ION CELLS UNDER COMPLEX TEMPERATURE PROFILES

PROGNOZOWANIE CYKLU ŻYCIA OGNIW LITOWO-JONOWYCH PRZY ZŁOŻONYCH PROFILACH TEMPERATUROWYCH

Nowadays, the extensive use of Lithium-ion cells requires an accurate life prediction model. Failure of Lithium-ion cells usually results from a gradual and irreversible capacity fading process. Experimental results show that this process is strongly affected by temperature. In engineering applications, researchers often use the regression-based approach to model the capacity fading process over cycles and then perform the cycle life prediction. However, because of neglecting temperature influences, this classic method may lead to significant prediction errors, especially when cells are subject to complex temperature profiles. In this paper, we extend the classic regression-based model by incorporating cell temperature as a predictor. Two effects of temperature on cell capacity are considered. One is the positive effect that high temperature lets a cell discharge more capacity in a cycle; The other is the negative effect that high temperature accelerates cell capacity fading. A cycle life test with six cells are conducted to valid the effectiveness of our method. Results show that the improved model is more suitable to capture the dynamics of cell capacity fading path under complex temperature profiles.

Keywords: *Lithium-ion cells, capacity fade, complex temperature profiles, life prediction, reliability assessment.*

Obecne szerokie zastosowanie ogniw litowo-jonowych wymaga stworzenia trafnego modelu prognozowania ich trwałości. Uszkodzenia ogniw litowo-jonowych zazwyczaj wynikają ze stopniowego i nieodwracalnego procesu utraty pojemności. Wyniki doświadczeń pokazują, że na ten proces silny wpływ wywiera temperatura. W zastosowaniach inżynieryjnych, naukowcy często wykorzystują podejście oparte na regresji do modelowania procesu utraty pojemności w poszczególnych cyklach by następnie dokonać prognozy trwałości w danym cyklu pracy. Jednakże, ta klasyczna metoda nie bierze po uwagę wpływu temperatury, co może prowadzić do znacznych błędów predykcji, w szczególności, gdy ogniwa pozostają pod wpływem złożonych profili temperaturowych. W prezentowanym artykule, rozszerzono klasyczny model oparty na regresji poprzez włączenie temperatury ogniwa jako czynnika prognostycznego. Przeanalizowano dwa rodzaje wpływu temperatury na pojemność ogniw. Z jednej strony, wysoka temperatura oddziałuje pozytywnie pozwalając ogniwu na uzyskanie większej pojemności w danym cyklu; z drugiej strony jest to wpływ negatywny, ponieważ wysoka temperatura przyspiesza utratę pojemności ogniwa. Przy użyciu sześciu ogniw, przeprowadzono badanie trwałości w danym cyklu pracy w celu potwierdzenia skuteczności naszej metody. Wyniki pokazują, że udoskonalony model pozwala lepiej uchwycić dynamikę ścieżki utraty pojemności ogniwa w warunkach złożonych profili temperaturowych.

Słowa kluczowe: *Ogniwa litowo-jonowe, utrata pojemności, złożone profile temperaturowe, prognozowanie trwałości, ocena niezawodności.*

1. Introduction

Lithium-ion cells have been widely applied to many portable consumer electronics, such as cell phones, laptops, digital cameras and so on [8]. Compared with other secondary batteries, Lithium-ion cells perform a large number of advantages, for example, no memorability, high nominal voltage, long cycle life, low self-discharge rate, high energy density and low pollution, etc., all of which make it one of the most ideal power sources in the 21th century. The recent trend shows that Lithium-ion cells also have a brilliant future in the application of electric vehicles, defense industry and power storage for renewable energy sources. Cycle life is one of the most significant indices by which the performance of Lithium-ion cells can be measured. Therefore, how to accurately predict cycle life becomes crucially necessary for the popularization of Lithium-ion cells, especially for the Lithium-

ion cells of special uses (such as the spacecraft power system), where imprecise prediction of cycle life can lead to consequences ranging from operation impairment to even catastrophic failures [9].

In many cases, an underlying degradation process can be traced to product failure [14]. Capacity is often treated as a key indicator measuring the performance degradation of Lithium-ion cells [3]. Many studies have focused on the cycle life prediction of Lithium-ion cells based on the capacity fading models. Meng et al. [13] studied the capacity fading curves of Lithium-ion power cells at a certain constant temperature, and then used the Weibull distribution to conduct the cycle life prediction. Wang et al. [18] investigated the cycling-induced capacity fading mechanisms in Lithium-ion cells and proposed a linear regression model to quantify the capacity loss over cycles. After studying the accelerated degradation test of numerous LiFePO$_4$ cells, Lam and

Bauer [10] proposed an empirical linear model describing the capacity fade, and the Arrhenius function was used to describe the fading rates under different temperatures. Besides the linear model, there are some studies centering on capacity fading models for different Lithium-ion type cells, such as the radical and linear model [19] and the quadratic and linear model [15].

These studies mentioned above, however, are mainly conducted based on the cycle life tests under one or more deterministic temperature levels, in which the high-precision temperature chamber and rigid data acquisition methods are required. Unlike the laboratory testing condition, cells in the field-use condition are usually run under complex temperature profiles. Previous researches indicate that the capacity fading process of Lithium-ion cells is significantly influenced by temperature [5, 7, 10]. In [10], capacity fading of Lithium-ion cells can be divided into true capacity fading and temporary capacity loss. True capacity fading leads to permanent capacity loss as a result of lithium ion and active material consuming, where high temperatures will accelerate the fading rate. On the other hand, temporary capacity loss is due to the temperature drop in a certain cycle, which is somewhat recoverable if the temperature goes back. A more accurate capacity fading model can be obtained by considering these temperature effects, especially for the cells operating under field-use conditions.

However, because of the difficulty in modeling the complicated temperature effects, the existing papers regarding capacity fading modeling or cycle life prediction under complex temperature profiles are very rare. In most of them, the classic regression-based approach [6] is adopted, which assumes that field conditions are deterministic or to simply use the mean value of temperatures while ignore their variability. This approach may result in significant prediction errors. For predicting the cycle life of Lithium-ion cells without the temperature chamber, this paper proposes a cycle life prediction method considering complex temperature profiles, including a cycle life test plan and an improved capacity fading model.

In our test, cells experience ambient temperature that continuously varies at all times. It will lead to the variance of cell capacity. The variance contains abundant information about cycle life and the relationship between cycle life and temperature. If we can effectively mine the information from the immense performance data using data modeling methods, the cycle life of Lithium-ion cells can be predicted accurately.

In this paper, firstly, the cycle life test plan for Lithium-ion cells under complex temperature profiles is introduced. Then, the classic regression-based life prediction method which ignores temperature effects is reviewed. Based on the classic method, we establish a more accurate capacity fading model, by taking into account the effects of temperature on both the actual capacity fading and the temporal capacity loss. Using the data acquired from the cycle life test, the parameters of the model are estimated. At last, the cycle life of this type of Lithium-ion cells is predicted.

2. Experimental

2.1. Testing procedures

In the cycle life test, 6 LiFePO$_4$ 18650 cells, which are indexed as Cell #1, Cell #2, $\cdots$, Cell #6 respectively, are used to charge and discharge repetitively. The parameters setup of these cells is listed in Table 1.

Fig. 1(a) and Fig. 1(b) show the scheme and photograph of our Lithium-ion cell cycle life test system, respectively. The system main-

Table 1. Parameters setup for LiFePO$_4$ 18650 cell

Parameter	Value	Unit
Rated capacity	2000	mAh
Nominal voltage	3.7	V
End of charge voltage	4.2	V
End of discharge voltage	2.75	V

ly consists of a personal computer, an ACCEXP battery test system and a temperature acquisition instrument 18B20 with some thermocouples. The PC communicates with the ACCEXP battery test system that monitors the parameters of our interest, including current, voltage and capacity. The temperature measurement of each cell is performed by the thermocouples. And the temperature data are acquired and sent to the PC by the temperature acquisition instrument 18B20. Through the PC, we can set the charge/discharge algorithm for the ACCEXP battery test system.

According to the constant current/voltage charge and constant current discharge regime, cells are simultaneously tested as the following steps. (1) Charge with the constant current of 1C until the voltage reaches the end of charge voltage, then with the constant voltage
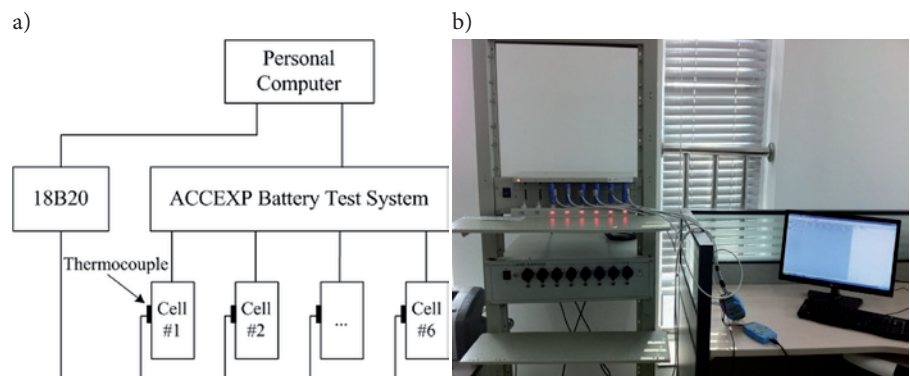
Fig. 1. Lithium-ion cells cycle life test platform
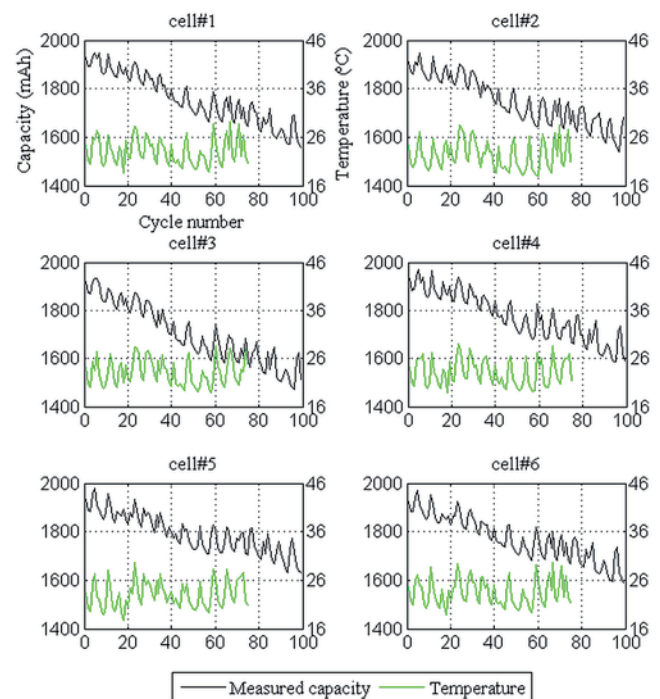
Fig. 2. Capacity fade and temperature variation versus cycle

of until the current declines to C/100; (2) Stand by for 30 minutes; (3) Discharge the constant current of 1C until the voltage declines to the end of discharge voltage; (4) Stand by for 30 minutes; (5) Repeat the steps from (1) to (4) until the cycle number reaches 100.

For a 2000 mAh cell, the 1C corresponds to a current of 2000mA. During the test, the temperature of each cell is measured every 10 seconds. Then, we can get the average Celsius temperature of each cell in each cycle. Because these cells are exposed to the ambient temperature, cell temperature varies irregularly with the ambient conditions over time, which is defined as complex temperature profiles in this paper.

The test results are illustrated in Fig. 2, it is clear that cell capacity fades gradually over cycles and correlates strongly with temperature. It is noted that the temperature signals after 75th cycle are unavailable due to failure of the temperature acquisition instrument.

2.2. Failure mechanism analysis

Capacity fading is one of the main failure modes for secondary cells. Ideally, in addition to the reaction of the Lithium ion shuttling between two electrodes, there are no side reactions inside the cell. Thus the total amount of Lithium ion remains unchanged and cell capacity will not fade. However, during calendar storage or charge/discharge cycles, cell capacity fades gradually due to some unexpected side reactions, such as oxidation of anode materials, lithium corrosion on cathode, electrolyte decomposition and solid electrolyte interface (SEI) formation, among which the SEI formation usually dominates. During cycle life tests, the charge/discharge current produces diffusion induced stress and triggers cracks on the graphite particle. Consequently, it will lead to the SEI formation on the cracked surfaces, which will consume the active Lithium-ion. This diffusion-induced-stresses failure mechanism usually makes capacity fade linearly over cycles [1, 10, 18].

3. Classic cycle life prediction method

3.1. Capacity fading model ignoring temperature effect

As cell temperature varies in a narrow range in the test, classic cycle life prediction methods often assume that temperature has no effect on the capacity fading process. In this case, we can regard the capacity fading data in Fig. 2 as a case of constant stress degradation tests, and the regression-based model is often used to handle this type of degradation data [6]. In the previous literature [1, 10, 18], capacity fading of Lithium-ion cells is generally assumed to follow a linear trend with cycles, namely:

$$c(n) = a - b \cdot n, \tag{1}$$

where the intercept a and slope b are unknown parameters, $c(n)$ is the cell capacity at nth cycle.

The estimators of model parameters for each cell can be obtained with the linear regression techniques. The end of life (EOL) for Lithium-ion cell is often defined as the number of charge/discharge cycles before cell capacity falls below 80% of its rated capacity [13]. Thus the failure threshold is set to be 2000×80% = 1600mAh. Then we can calculate the cycle life T of each cell, respectively. Because T is an
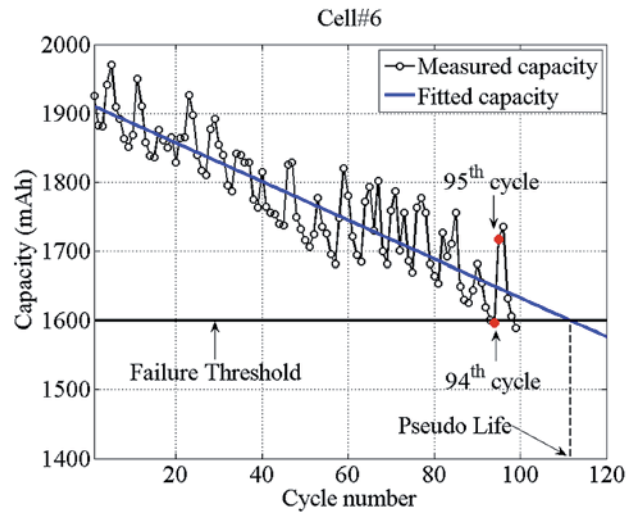
Fig. 3. Capacity fade plotted as a linear function of cycles

extrapolated life rather than the actual value, we call it pseudo life. The results of parameter estimation and pseudo life for each cell in the test are shown in Table 2. Take Cell #6 as an example, the cycle life extrapolation method is illustrated in Fig. 3.

3.2. Life prediction ignoring temperature effect

Reliability is an important tool in lifetime prediction for components especially in the electronic industry [16]. Evaluating the reliability indices such as the MTTF (mean time to failure) and percentile of the cycle life distribution, is an essential task in cycle life prediction for Lithium-ion cells. What distribution the cycle life follows should be known before conduct the prediction. The Kolmogorov-Smirnov (K-S) goodness-of-fit test is used to test the goodness of some typical lifetime distributions [12]. Take a sample $x_1, \cdots x_n$, from a certain type of distribution F and consider the two hypotheses:

$$\begin{cases} H_0 : F(x) = F_0(x) \\ H_1 : F(x) = F_1(x) \end{cases}, \tag{2}$$

where F is the empirical cumulative distribution function of the sample and $F_0(x)$ is a given cumulative distribution function.

The K-S statistic is:

$$D_n = \sup | F_0(x_i) - F(x_i) | = \max \left\{ | F_0(x_i) - \frac{i-1}{n} |, | F_0(x_i) - \frac{i}{n} | \right\} .$$

Then we compare D_n with D_n^α, which is the cutoff value for determining whether D_n is significant, where α is the significance level. If $D_n < D_n^\alpha$, we accept the null hypothesis H_0. Otherwise, we accept the alternative hypothesis H_1. The adequacy of the pseudo life distribution is judged by comparing D_n calculated for the Weibull, Normal, Log-normal, Exponential and Gamma distribution. The K-S statistic for the five distributions are 0.182, 0.204, 0.232, 0.519, 0.212 respectively, and the cutoff value $D_n^\alpha = 0.52$ for n=6 and α=0.05. Results show that the Weibull has the minimum D_n, indicating that Weibull is better than the other four distributions for fitting these pseudo lives. Fig. 4 depicts the process of classic regression-based cycle life prediction method.

The probability density function $f(t)$, cumulative distribution function $F(t)$ and reliability function $R(t)$ of the Weibull distribution are given as follows:

Table 2. Parameter estimation and pseudo life (classic)

	Cell#1	Cell#2	Cell#3	Cell#4	Cell#5	Cell#6
a	1918.7	1894.3	1893.7	1920.8	1908.0	1906.5
b	3.3	3.0	3.9	3.0	2.3	2.7
T	97.8	98.8	75.9	107.6	131.1	111.7
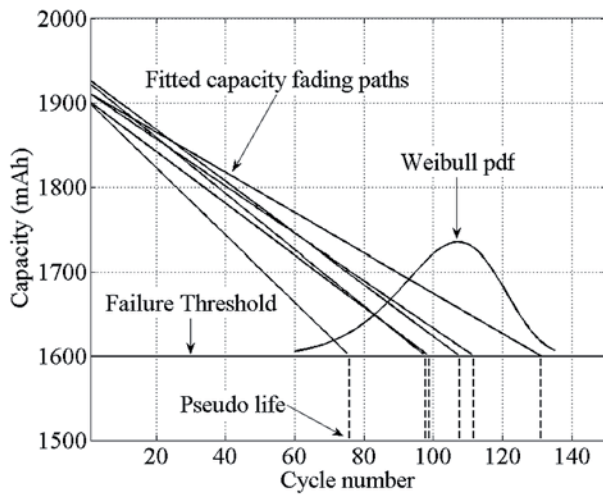
Fig. 4. Pseudo life distribution based on the Weibull distribution

$$\begin{cases} f(t) = \dfrac{m}{\eta}\left(\dfrac{t}{\eta}\right)^{m-1} exp\left\{-\left(\dfrac{t}{\eta}\right)^{m}\right\} \\[2mm] F(t) = 1 - exp\left\{-\left(\dfrac{t}{\eta}\right)^{m}\right\} \\[2mm] R(t) = 1 - F(t) \end{cases}, \qquad (3)$$

where η is the scale parameter and m is the shape parameter.

The Maximum Likelihood Estimate (MLE) of the Weibull parameters are: $\hat{\eta} = 110.91$ and $\hat{m} = 6.95$. Some indices of interest like *MTTF* (Mean time to failure) and T_q (the $100q$th percentile of lifetime distribution) can be obtained through (4). Because the sample in the test is small, we utilize the Parametric Bootstrap method to perform the interval estimate of these indices. For more information about Parametric Bootstrap method, see reference [4]. The point estimation and interval estimation with 80% confidence of *MTTF* and T_q are shown in Table 3.

$$\begin{cases} MTTF = \displaystyle\int_{0}^{\infty} f(t)\,\mathrm{d}t \\[3mm] T_q = R^{-1}(q) \end{cases} \qquad (4)$$

Table 3. *Cycle life prediction results (Classic)*

MTBF	$T_{0.9}$	$T_{0.8}$	$T_{0.5}$
103.2	80.2	89.4	105.2
[94.3,112.4]	[69.1,97.2]	[79.6,103.4]	[96.0,114.4]

However, the classic cycle life prediction method has some drawbacks because it ignores the temperature effects on Lithium-ion cells. From Fig. 2, we can see that the temperature cycles and capacity cycles are correlated. In Fig. 3, although the cell's capacity dropped below 1600mAh in the 94th cycle, it went back above 1700mAh in the next cycle due to temperature rising. Thus, besides cycle number, temperature is another factor that strongly affects capacity variation. In reality, the ambient environment and the battery's charge/discharge work together to cause its temperature fluctuation. Meanwhile, the varying temperature can in turn affect the reactions in the charge/discharge process and lead to the capacity fluctuation.

To study the correlation between temperature and cell capacity directly, we let the measured capacity in each cycle plus the degradation term $b \cdot n$ for compensating the cycle caused capacity variation. Then, the Pearson correlation test is conducted between the capacity after compensation and the temperature measured in the test. The correlation coefficients for the six cells are 0.94, 0.96, 0.92, 0.94, 0.85 and 0.95, respectively. Results indicate that the linear correlation between cell capacity and temperature is significant. To improve the accuracy of prediction, an improved cycle life prediction method is proposed by adding the temperature effects into the capacity fading model in Section 4.

4. Improved cycle life prediction method

4.1. Capacity fading model considering temperature effects

Numerous researches indicate that the capacity fading process of Lithium-ion cells is strongly affected by temperature. According to [11] and [15], the effect of temperature on the performance of lithium-ion cells, on the one hand, is positive. High temperature enhances the activities of lithium ions and decreases internal resistance, which makes a cell release more capacity in a certain cycle. On the other hand, the effect is negative. It means that high temperature causes faster side reactions which bring permanent damage to cells. Meanwhile it accelerates capacity fade and shortens cell life. In the following parts, both of the two effects are considered in the improve regression model.

Firstly, we focus on the positive temperature effect. Based on the analysis in section 3.2, if we ignore the cycle caused capacity fade, the linear correlation between cell capacity and temperature is significant. Thus, the relationship between cell capacity and temperature can be modeled by a linear function:

$$C(temp) = \alpha + \beta \cdot temp \qquad (5)$$

where $C(temp)$ is the capacity a cell can discharge at temperature *temp*, α and β are unknown parameters. The slope β in (5) is positive, indicating that enhancing temperature will make a cell discharge more capacity in a cycle.

In practice, the actual capacity of a new cell fades linearly over charge/discharge numbers. As a result, the relationship between cell capacity and cycle number should be introduced into (5). Here we assume that the intercept term α accounts for the cycle caused capacity loss. Let $\Delta\alpha_i$ be the degradation increment between the ith cycle and the $(i-1)$[th] cycle, namely,

$$\Delta\alpha_i = \alpha_i - \alpha_{i-1}, i = 1, 2, \cdots, \qquad (6)$$

where α_0 is the initial value of α for a totally new cell.

Now, the negative effect of temperature can be taken into account. As high temperature accelerates cell capacity fade, it is reasonable to use an Arrhenius function to model the relationship between temperature and capacity fading rate. Then, $\Delta\alpha_i$ can be expressed as,

$$\Delta\alpha_i = -exp\left\{\varphi + \frac{\eta}{temp_i + 273.15}\right\}, \qquad (7)$$

where *A* is unknown parameter, $temp_i$ is the average Celsius temperature in the ith cycle, φ and η are unknown parameters.

According to the cumulative exposure theory, the cumulative degradation value of can be obtained approximately by summing the

degradation increment. Then, the remaining value of α after n charge/discharge cycles can be expressed as:

$$\alpha_n = \alpha_0 + \sum_{i=0}^{n}\Delta\alpha_i , \qquad (8)$$

Then, a new capacity fade model under complex temperature profiles can be expressed as:

$$C_n = \alpha_n + \beta \cdot temp_n . \qquad (9)$$

Substituting (7) and (8) into (9), we can obtain:

$$C_n = \alpha_0 - \sum_{i=0}^{n}\exp\left\{\varphi + \frac{\eta}{temp_i + 273.15}\right\} + \beta \cdot temp_n , \qquad (10)$$

where C_n is the capacity a cell discharge in the nth cycle, $temp_n$ is the temperature in the nth cycle, and $\{temp_1, temp_2, temp_n\}$ denotes the complex temperature profiles the cell experiences from the 1st cycle to the nth cycle.

The nonlinear least square method is used to estimate the parameters in (10) for the six 6 cells respectively, and the results are shown in Table 4.

Table 4.   Parameter estimation of the improved capacity fade model

	Cell#1	Cell#2	Cell#3	Cell#4	Cell#5	Cell#6
a_0	1580.6	1642.4	1578.4	1670.8	1647.4	1554.1
φ	8.9	10.2	11.2	10.9	10.9	11.0
η	−2255.9	−2653.9	−2892.4	−2938.3	−2907.1	−2952.2
β	14.9	11.8	14.1	10.5	12.0	15.3
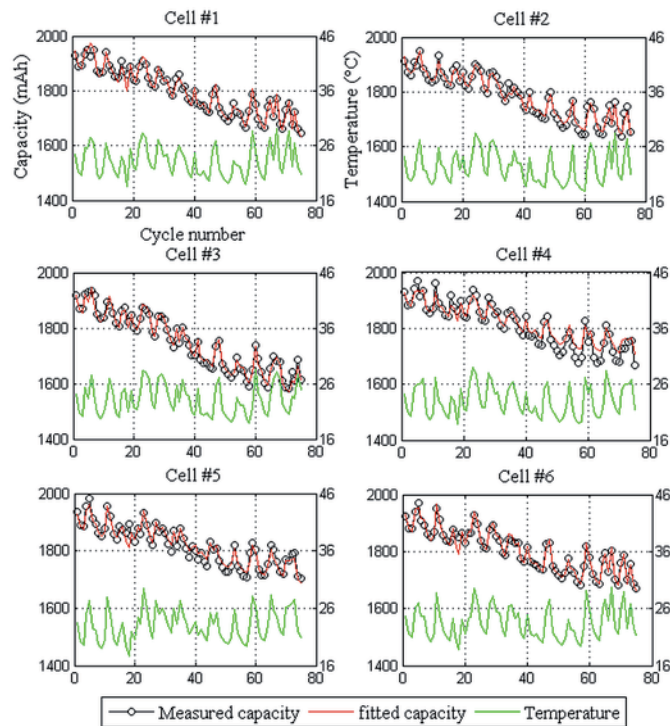
Substituting these estimators and the corresponding temperature profiles $\{temp_1, temp_2, temp_{75}\}$ (as only temperatures before the 75th cycle are available) into (10), we can predict the capacity fading curves under complex temperature profiles. Fig. 5 compares the measured capacities and the predicted values for the six cells. It is clear that the measured capacities are consistent with the predicted value quite well. From the criteria aim to minimize the sum of the squares of the errors, the improved model is a more accurate parametric model than the classic one.

4.2.   Model cross-validation

To further demonstrate the superiority of the improve capacity fading model over the classic one, the cross-validation method would be conducted in this section. In the cross-validation, we used 5 cells' data to build the model, and then validate it using the remaining one cell. The main steps are as follows: (1) Estimate the 5 cells' model parameters, respectively; (2) Calculate the mean values of the parameter estimators in (1); (3) Substitute the mean parameter estimators into the corresponding capacity fading model, and compare the results with the measured capacity of the remaining one cell. The results of cross-validation for the two models are illustrated in Fig. 6, respectively.

It is observed that for most of these cells (expect Cell #3), the improved model is more suitable to capture the dynamics of cell capacity fading path under complex temperature profiles. Notice that, for Cell #3, both the classic model and the improved one underestimate its capacity fading rate. This may be due to the fact that, capacity of Cell #3 fades apparently faster than others, while the predicted model in cross-validation reflects the mean performance of the other five cells. To directly test the reasonability of the proposed model, the mean absolute error between the actual capacity and the predictions for each cell is calculated. The obtained results are summarized in Table 5. From Table 5, we can find that the improved model is more accurate than the classic regression model (except Cell #3), which is consistent with Fig. 5.

Fig. 5. Capacity fade plotted using the improve model considering temperature effect
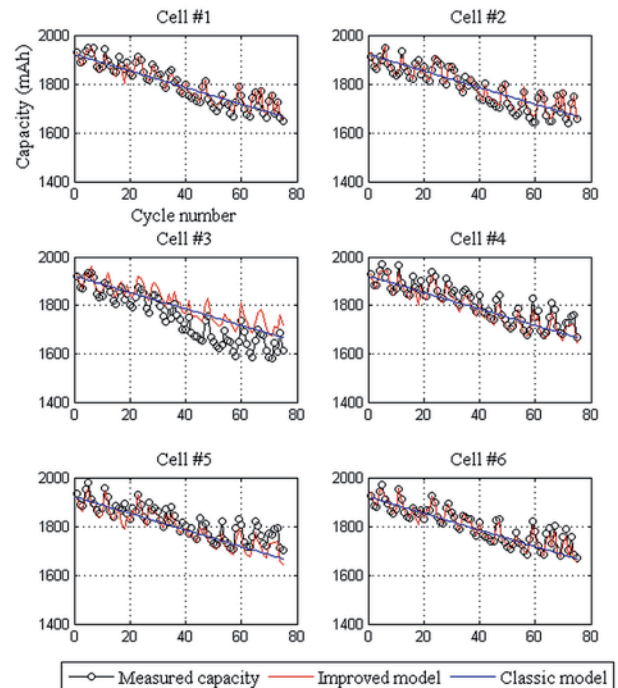
Fig. 6. Cross-validation results

Table 5. Mean predicted error of each cell (unit: mAh)

	Cell#1	Cell#2	Cell#3	Cell#4	Cell#5	Cell#6	Total
Improved	9.86	9.70	59.68	20.09	26.26	9.40	135.00
Classic	30.63	36.59	51.26	35.77	38.07	33.59	225.90

4.3. Life prediction considering temperature effect

Using (10) we can predict the cell capacity fading path under a given complex temperature profile . Now we set the temperature to be deterministic, namely $temp_1 = temp_0$, for $i=1,2,\cdots$. Then, at the deterministic temperature $temp_0$, the theoretical measured capacity of a cell after n charge/discharge cycles can be predicted as:

$$C(n, temp_0) = \alpha_0 - \exp\left\{\varphi + \frac{\eta}{temp_0 + 273.15}\right\} \cdot n + \beta \cdot temp_0. \quad (11)$$

Generally, the rated capacity of Lithium-ion type cells refers to the capacity a new cell can discharge at room temperature, say $temp_1 = 25°C$. Thus, an accurate definition of EOL (end of life) is the number of cycles when the capacity a cell can discharge at 25°C crosses the threshold value $D_f = 0.8 C_{rated}$. However, $C(n, temp_0)$ in (11) refers to the capacity a cell can discharge at temperature $temp_0$ after n cycles. In order to determine whether the cell really fails, we should firstly convert $C(n, temp_0)$ to the equivalent capacity at room temperature, which is defined as room-temperature-capacity and denoted as $C^r(n, temp_0)$.

According to (5), the difference between a cell's capacity at $temp_r$ and $temp_0$ is:

$$\Delta C(temp_r, temp_0) = \beta \cdot (temp_r - temp_0) \quad (12)$$

The equivalent room-temperature-capacity for (11) can be expressed as:

$$C^r(n, temp_0) = C(n, temp_0) + \beta \cdot (temp_r - temp_0), \quad (13)$$

where $C(n, temp_0)$ is defined in (11) to denote the theoretical measured capacity of a cell after n cycles at deterministic temperature $temp_0$.

Using the new definition of EOL and (13), we can predict a Lithium-ion cell's cycle life under any specified temperature. The cycle life of a cell subject to deterministic temperature $temp_0$ can be calculated by:

$$T_{temp_0} = \left\{ n \mid C^r(n, temp_0) = D_f \right\}. \quad (14)$$

Note that our objective is to predict the life of these Lithium-ion cells under complex temperature profiles. Here, we use the mean value of the temperatures in the cycle life test to represent the complex temperature profiles. The mean temperature in our test is 23°C, namely let $temp_0 = 23°C$. Under this temperature, the pseudo life of the six cells is predicted using (14) respectively. The results are shown in Table 6. We can use these pseudo lives to represent the cells' cycle life under complex temperature profiles approximately.

We still use the Weibull, Normal, Log-normal, Exponential and Gamma distribution as the given distributions to conduct the K-S

Table 6. Pseudo life under complex temperature profiles

	Cell#1	Cell#2	Cell#3	Cell#4	Cell#5	Cell#6
$T_{23°C}$	103.2	102.2	79.4	132.6	123.7	117.5

goodness-of-fit test. The K-S statistic D_n are 0.186, 0.178, 0.209, 0.515, 0.186, respectively. This time, we see that the Normal distribution has the smallest D_n rather than the Weibull distribution. The probability density function $f(t)$, cumulative distribution function $F(t)$ and reliability function $R(t)$ of the Normal distribution are given as follows:

$$\begin{cases} f(t) = \frac{1}{\sqrt{2\pi}\sigma} exp\left\{-\left(\frac{t-\mu}{\sigma}\right)^2\right\} \\ F(t) = \Phi\left(\frac{t-\mu}{\sigma}\right) \\ R(t) = 1 - F(t) \end{cases} , \quad (15)$$

where μ is the mean, σ is standard deviation and $\Phi(\cdot)$ is the cumulative distribution function of a standard normal distribution.

Using the technique of MLE, we can obtain the estimators of the Normal parameters: $\hat{\eta} = 109.75$ and $\hat{\sigma} = 109.75$. The corresponding indices MTTF and T_q can be calculated by (4), too. The Parametric Bootstrap method is also used to obtain the confidence intervals of these indices. Table 7 gives the results of point estimation and 80% confidence intervals for MTTF and T_q using the improved cycle life prediction methods.

Table 7. Cycle life prediction results (Improved)

MTBF	$T_{0.9}$	$T_{0.8}$	$T_{0.5}$
109.3	85.5	93.8	109.7
[99.5,118.9]	[72.7,99.1]	[83.1,105.5]	[100.0,119.4]
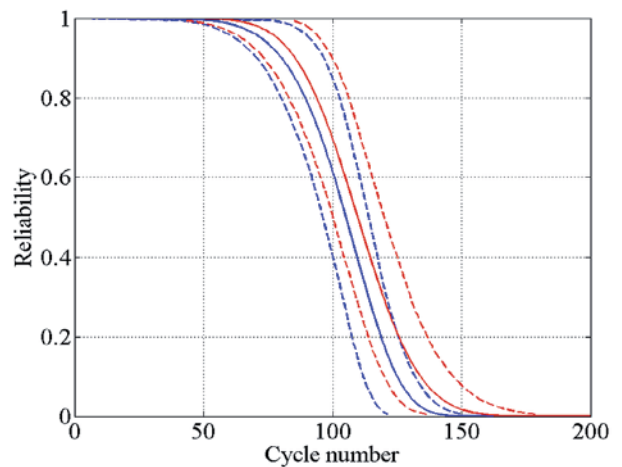
Fig. 7. Comparison of Lithium cell's reliability between classic method (blue) and improved method (red).

Fig. 7 compares the reliability plots of Lithium cells using classic method (blue) and the improve one (red). The 80% confidence intervals are obtained using the Parametric Bootstrap method and plotted in dotted lines. Compared with the improved method, the classic method underestimates the cell's reliability. The distribution type of cycle life also changes after considering temperature effects. In practical conditions, the amplitudes of temperature fluctuation may be more drastic than that in our test. In this case, ignoring temperature effects will lead to more significant prediction errors.

5. Conclusion

Many papers have been published on Lithium-ion cell life prediction, but they mainly focus on the laboratory settings where cells experience deterministic temperatures. In some field conditions, cells are tested without temperature controllers. In this case, cell capacity

fades over time and is strongly affected by the temperature variations. In this paper, we extend the classis cycle life prediction method based on a regression model by considering the temperature effects. Comparisons are conducted between the classic and improved method, results show that the improved capacity fading model is more suitable to capture the characteristics of cell capacity fading paths under complex temperature profiles. With the advantages of low cost and easy popularization, the method of testing and analyzing cycle life in this paper can be conducted in field conditions and does not need to control the temperature accurately. In addition, the temperature of Lithium-ion cells in operation is always time-varying, so the model also provides a fundamental theory for the remaining useful life (RUL) prediction of Lithium-ion cells. The method proposed in this paper is a general method that can be applied to other batteries.

In the future work, two possible issues should be studied:

(1) Charge/discharge rates is another key parameter that affects Lithium-ion cell capacity fading processes. The model will be more complicated if both current rate and temperature are in complex profiles.

(2) Since the temperature in our test varies in a narrow range, the accelerated effect of high temperature on capacity fade is not significant enough. To verify the accelerated effect of high temperature, an accelerated degradation test under several temperature levels should be conducted.

References

1. Arora P, White R E, Doyle M. Capacity fade mechanisms and side reactions in Lithium-ion batteries. Journal of Electrochemical Society 1998; 145(10): 3467-3667, http://dx.doi.org/10.1149/1.1838857.
2. Bloom I, Cole B W, Sohn J J, Jones S A, Polzin E G, Battaglia V S, Henriksen G L, Motloch C, Richardson R, Unkelhaeuser T, Ingersoll D, Case H L. An accelerated calendar and cycle life study of Li-ion cells. Journal of Power Sources 2001; 101: 238-247, http://dx.doi.org/10.1016/S0378-7753(01)00783-2.
3. Dubarry M, Svoboda V, Hwu R, Liaw B. Capacity and power fade mechanism identification from a commercial cell evaluation. Journal of Power Sources 2007; 165: 566-572, http://dx.doi.org/10.1016/j.jpowsour.2006.10.046.
4. Efron B. Bootstrap Confidence intervals for a class of parametric problems. Biometrika, 1985; 72: 45-58, http://dx.doi.org/10.1093/biomet/72.1.45.
5. Fellner J P, Loeber G J, Sandhu S S. Testing of lithium-ion 18650 cells and characterizing/ predicting cell performance. Journal of Power Sources 1999; 81: 867-871, http://dx.doi.org/10.1016/S0378-7753(98)00238-9.
6. Freitas M A, Maria G T, Toledo M L G, Colosimo E A, Pires M C. Using degradation data to assess reliability: a case study on train wheel degradation. Quality and Reliability Engineering International 2009; 25:607-629, http://dx.doi.org/10.1002/qre.995.
7. Gui C Q. Influence of temperature on LiFePO4 Lithium-ion power battery. Battery Bimonthly 2011; 41(2): 88-91.
8. Inaba M, Ogumi Z. Up-to-date development of Lithium-ion batteries in Japan. Electrical Insulation Magazine 2001; 17(6): 6-20, http://dx.doi.org/10.1109/57.969941.
9. Kim S Y, Caster J C, Saleh J H. Spacecraft electrical power subsystem: failure behaviour, reliability, and multi-state failure analyses. Reliability Engineering and System Safety 2012; 98: 55-65, http://dx.doi.org/10.1016/j.ress.2011.10.005.
10. Lam L and Bauer P. Practical capacity fading model for Li-Ion battery cells in electric vehicles. IEEE transactions on power electronics 2013; 28(12):5910-5918, http://dx.doi.org/10.1109/TPEL.2012.2235083.
11. Li Z, Han X B, Lu L G, Ouyang M G. Temperature characteristics of power LiFePO4 batteries. Journal of Mechanical Engineering 2011; 18: 115-120, http://dx.doi.org/10.3901/JME.2011.18.115.
12. Massey F. The Kolmogorov-Smirnov test for goodness of fit. Journal of the American Statistical Association 1951; 46: 68-78. http://dx.doi.org/10.1080/01621459.1951.10500769.
13. Meng X F, Sun F C, Lin C, Wang Z P. Cycle life prediction of power battery. Chinese Journal of Power Sources 2009; 33(11): 955-969.
14. Nechval K N, Nechval N A, Berzins G, Purgailis M. Probabilistic assessment of the fatigue reliability. Eksploatacja i Niezawodnosc-Maintenance and Reliability 2007; 3(35): 3-6.
15. Ramadass P, Haran B, White R, Popov BN. Mathematical modeling of the capacity fade of Li-ion cells. Journal of Power Sources 2003; 123(2): 230-240, http://dx.doi.org/10.1016/S0378-7753(03)00531-7.
16. Salvinder S K, Shahrum A, Nik A N. Reliability analysis and prediction for time to failure distribution of an automobile crankshaft. Eksploatacja i Niezawodnosc - Maintenance and Reliability 2015; 17(3): 408-415, http://dx.doi.org/10.17531/ein.2015.3.11.
17. Tang Z Y, Ruan Y L. Progress in Capacity Fade Mechanism of Lithium-ion Battery. Progress In Chemistry 2005; 1: 1-7.
18. Wang J, Purewal J, Liu P, Hicks-Garner J, Soukazian S, Sherman E, Sorenson A, Vu L, Tataria H, Verbrugge M W. Degradation of lithium ion batteries employing graphite negatives and nickel-cobalt-manganese oxide +spinel manganese oxide positives: Part 1, aging mechanisms and life estimation. Journal of Power Sources 2014; 269: 937-948, http://dx.doi.org/10.1016/j.jpowsour.2014.07.030.
19. Zhang Y C, Wang C Y. Cycle-life characterization of automotive lithium-ion batteries with LiNiO2 cathode. Journal of Electrochemical Society 2009;156(7): 527-535, http://dx.doi.org/10.1149/1.3126385.

Tianyu LIU
Long CHENG
Zhengqiang PAN
Quan SUN
College of Information System and Management
National University of Defense Technology
Sanyi Avenue, Changsha, China
E-mail: 815487375@qq.com, sunquan@nudt.edu.cn

Lech GŁADYSIEWICZ
Witold KAWALEC
Robert KRÓL

SELECTION OF CARRY IDLERS SPACING OF BELT CONVEYOR TAKING INTO ACCOUNT RANDOM STREAM OF TRANSPORTED BULK MATERIAL

DOBÓR ROZSTAWU KRĄŻNIKÓW GÓRNYCH PRZENOŚNIKA TAŚMOWEGO Z UWZGLĘDNIENIEM LOSOWO ZMIENNEJ STRUGI UROBKU*

The study on the design optimisation of belt conveyors used in the mining industry – the proper selection of carry idlers - aiming to decrease the specific energy consumption of transportation with regard to different operational conditions is presented. High capacity overburden belt conveyors from a surface lignite mine as well as copper ore ones from underground ines are analysed. Calculations are performed in the specialised engineering software with the use of characteristics of idlers' rotational resistance as a function of radial loading that were obtained in the laboratory and identified distribution of actual capacity of main haulage and division belt conveyors. The purposefulness of the individual treatment to the carry idler spacing, depending on the conveyor's location within the haulage system and its operational loadings – bigger for the main haulage and smaller for the division conveyors is found. The presented results of calculations are evidences for further economic analysis, which take into account – apart of energy costs – also costs of installation and replacements of idlers.

Keywords: belt conveyor, idlers spacing, working loadings, energy consumption.

Przedstawiono studium optymalizacji konstrukcyjnej – właściwego doboru rozstawu krążników górnych - górniczych przenośników taśmowych, pod kątem zmniejszenia zużycia jednostkowej energii transportu z uwzględnieniem zróżnicowanych warunków eksploatacyjnych. Analizowano przenośniki nadkładowe dużej wydajności z kopalni odkrywkowej węgla brunatnego i podziemne z kopalni rud miedzi. Obliczenia wykonano w środowisku specjalistycznego oprogramowania inżynierskiego wykorzystując wyznaczone laboratoryjnie charakterystyki oporu obracania krążników w funkcji obciążenia oraz zidentyfikowane rozkłady strugi urobku w odstawie głównej i oddziałowej. Stwierdzono celowość zróżnicowania rozstawu zestawów krążników górnych w zależności od rzeczywistego obciążenia strugą urobku – większego dla przenośników odstawy głównej (zbiorczych) i mniejszego dla przenośników oddziałowych. Przedstawione wyniki obliczeń są przesłankami do analiz ekonomicznych, uwzględniających - oprócz kosztu energii – również koszt zabudowy i wymian krążników.

Słowa kluczowe: przenośnik taśmowy, rozstaw krążników, obciążenia robocze, badania, zużycie energii.

1. Introduction

In carry belt on a conveyors is usually supported with three-roller idlers, installed at a fixed spacing distance of 0.8 to 2.5 meters along the whole conveyor route. Idlers are therefore the most numerous element of a conveyor that is crucial for its reliability and energy efficiency. In the mines with belt conveyor transport, users and constructors attention is focused on main elements deciding of the costs: conveyor belt and idlers. The savings may be sought, as in case of the other means of transport, in the precise selection of conveyor equipment considering the properly identified transport requirements.

Well-known method of cutting the energy consumption and reducing the capital or operational costs is enlarging the idler sets spacing. In some version of long range conveyors, the idler sets located ever more than 3.0 m from each other, are installed. These are, however, specific construction use under stable loading from transported material, ensuring the predictable load of idlers [9]. In mine haulage systems the variability of actual capacity is much bigger, what, for a long period of mine, was the reason for common usage of oversized conveyor constructions. But, the compilation of tests results of high capacity conveyor idlers in Rhineland Basin [1] with operation data has enabled to verify the concept óf upper idlers spacing [5].

The experiences were used to analyze the selection of upper idler sets of conveyors, use also in Polish mining [6], taking also into consideration, experimentally determined characteristics of idlers rotating resistance in the function of temporary yield [14] and calculated, expected life-time of idlers in the real operational conditions [3, 11, 12, 18]. The analysis of the optimal carry idlers spacing is based on the identified total resistances to motion [4, 21] and on idlers rotational resistance with regard to the distribution of transported bulk material [2, 10,13]. The criteria used for optimal selection of idlers spacing are: the specific energy consumption i.e. energy per unit of route length and unit of capacity [5] as well as predicted number of annual idler sets replacement. The second criterion is defined as a quotient of total number of installed sets and calculating the lifetime of idlers set, estimated basing on minimal life of roller in the idler [3].

The basic tool used for the optimisation analysis is the in-house computer system QNK-TT [16], supported with advanced computing algorithms for calculating primary resistances to motion of a belt conveyor with regard to belt parameters, characteristics of transported material as well as construction and operational parameters of conveyor [4]. The concept of adjusting the distance between upper idler sets to the real operational loads requires exact calculations of movement resistance generated on the idler set [4, 21] and identification of the

distribution of transported bulk material stream [2, 13]. This identification is more and more reliable due to implementation of IT systems, collecting complex data (technical, operational, diagnostic) about the transport system of the mine [7, 8, 19, 22]. Automated data processing gives the credible evaluation of conveyor elements condition [17], and additionally, supported by results of simulatory calculations [16], allows to reduce, the assumed so far, construction margin, without prejudice for safety and reliability of belt conveyors utilization.

Summary of the to date attempts of the selection of upper idler set spacing in the mine belt conveyors, typical for the biggest belt transport systems i.e. haulage of overburden in lignite open-pit mine and haulage of copper ore in KGHM Polska Miedź SA mine, was made in the paper. For the both systems, typical conveyors were chosen, used alternatively for diversified transport task, representing the work with full load (main transport – conveying the collective stream of the output from several mine district) and with partial load (local transport – conveying the output from one mining division, with typical, numerous operation periods without load). These conveyors were equipped alternatively with standard idler sets as well as with modified ones, having reduced rotation resistance. For those route configurations and conveyor positions within the transport system, variants of upper idler sets spacing, for which changes of construction would not be necessary, were checked.

2. Simulation tests for belt conveyors used in open-pit mines

The presented considerations concerning the optimal support of carry belt strand, concerned the biggest conveyors, used for output haulage, where the belt width is 2.25 m, and in carry belt strand, idlers having Ø of 194 mm and casing length of 800 mm, are used. Two types of idlers were taken into consideration – standard and modernized ones, for which characteristics of rotating resistance as square function of radial load, were determines [11, 14] (fig.1). They were used as virtual methods for calculating the movement resistance in simulating calculations cycle.

In optimization analyzes, identification of operational capacity in the given transport system is necessary [10]. For selected locations of conveyors in the transport system of open-pit mine:
- major haulage (combined) – conveyor hauling the overburden from several mining levels,
- division haulage – conveyor taking the material from one level (from single excavator)
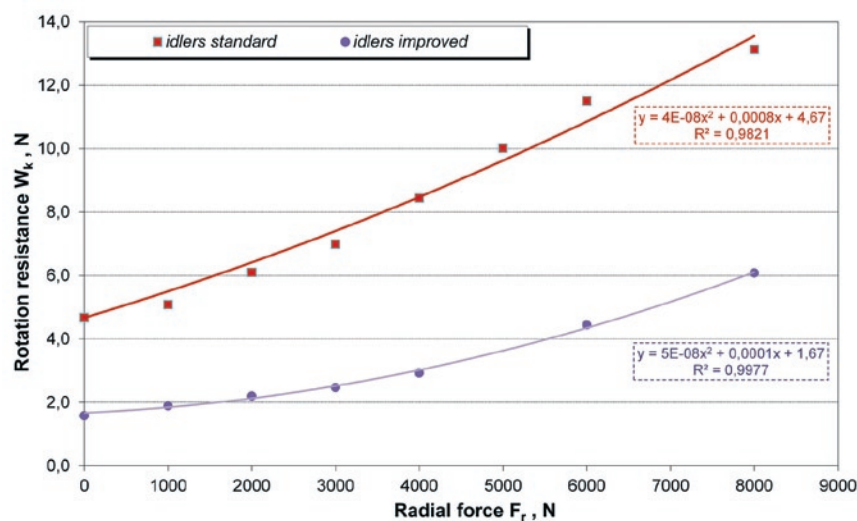
Fig. 1. Average resistance of Ø194×670mm idlers rotation Wk in function of radial force - Fr obtained (calculated) for standard and modernized idler.
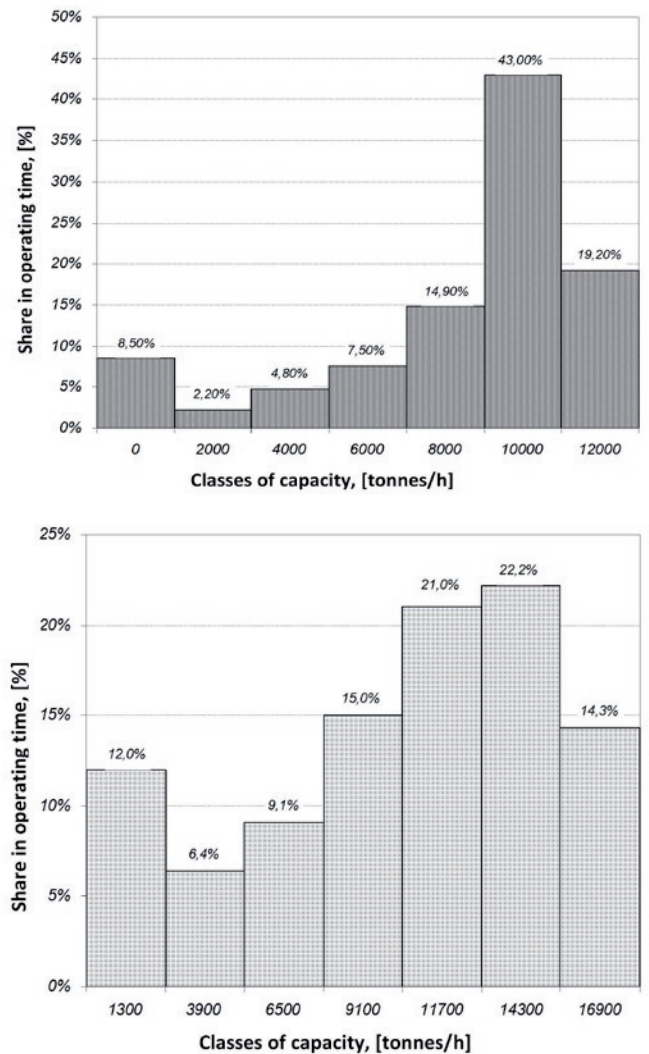
Fig. 2. Histograms of recorded temporary capacities of overburden: a) from a single excavator, b) on a main haulage conveyor

the histograms of instantaneous capacity of the transported overburden stream, representing real distribution of output load on the idler sets in carry belt strand of conveyor, were made (fig.2).

In spite of random nature of output stream, the analyses considered the seasonal impact of ambient temperature on resistances to motion of conveyor. Thus, the calculations were made for three distinguished season temperatures, taking into consideration average monthly 24 hours temperatures on Polish Lowland. The results were presented as weighted mean for calculative temperature of conveyor operation (tab.1).

Figure 3 present calculated specific energy consumption (SEC) index in carry belt strand of overburden conveyor, depending on temporary value of capacity, equal the radial load of idlers. In the case of standard idlers, within the whole range of load, the SEC value for 1.45 m distance is slightly lower that for the most often used in Polish lignite mines, distance of 1.2 m. In the case of modernized idlers, having lower rotation resistances (fig.1), these char-

Table 1. Major calculating parameters of high capacity belt conveyor

Parameter	Open-pit conveyor
Transported output, density, kg/m³	Overburden, 1700
Calculating work temperature, ℃	0 (45%), 11 (25%), 19 (30%)
Length, m; gradient	1205; levels
Belt width, mm	2250
Belt; cover plates, mm	St3150; 14+7
Belt speed, m/s	5.98
Spacing of upper idles sets, m	Variants: 1.2; 1.45
Rotation resistance of upper idler, N	According to quoted characteristics
Calculating capacity, t/h	100-18000
Note	Belt tension settled for maximum load

Table 2. Expected number of idlers replaced per year (per 1 km of a conveyor route)

Carry belt idlers spacing, m	main haulage	single BWE loading
1,2	104	52
1,45	172	86
2,0	250	167

From the perspective of using the specific transport system, more vital are the average values of specific energy consumption, complying with typical, for the facility, load of transported material stream, described by capacity distribution (fig. 2). The result of average specific energy consumption in top belt strand, distinguishing the alternative spacing of carry idler sets for the conveyor of major haulage (combined) and for the division haulage conveyor (taking the output from one chain and bucket excavator) are presented on figure 4.

Division conveyor (taking the output from one excavator) works under much lower average load, but has a significant part of idle running (fig.2), thus, the clearly higher values of specific energy consumption than in case of main haulage conveyor, are not surprising. It can be concluded, from diagram no. 4, that the increase of carry idlers spacing (from the standard 1.2m to 1.45m) should give the savings in energy consumption for division conveyors and, in fact, will not affect the energy consumption of main haulage conveyors. The spacing of 2.0m increases the SEC of the main haulage conveyor while in the case of division conveyors the SEC depends on the type of idlers. The considered increase of carry idlers spacing reduces their total number which, due to the increase of radial loading (different for main haulage and division conveyors) affects the estimated increase of number of idler sets replaced every year (tab.2).

The economic analyze of calculation results concerning specific energy consumption and number of idlers replacement is not presented, since it depends on operation costs of the mine and can be made only having such data.

Fig. 3. Specific energy consumption (SEC) in top belt as a function of actual capacity of a belt conveyor (conveyor parameters in tab.1)

Fig. 4. Averaged specific energy consumption (ASEC) in top belt of a main and secondary transportation overburden belt conveyor with regard to carry idlers spacing

acteristics are almost the same, what is caused by lower contribution of this constituent in total movement resistance.

3. Simulation tests for conveyors used in underground mine

The necessity of reducing the mining costs, increasing distance of underground transportation routes in copper ore mines as well as more frequent usage of long belt conveyors form main coal haulage in hard coal mines together with the observed improvement of technical culture of conveyors operation [8, 22] give grounds for investigating the possibility of upper idlers sets optimization, on those conveyors. One should remember, that conveyors in underground mines have bigger construction reserves, which are used to prevent the failures caused by objective operational difficulties in tight mine workings.

Published results of detailed tests of rotation resistance of carry idlers in conveyors designed for underground mines [14, 15] in connection with analyzes of variable transported material streams in those mines (fig. 6) [13], enable to carry out the study of carry idler selection for underground copper ore haulage. The tests results confirmed the dependence between idler rotation resistance and the radial force. As a result of laboratory tests, the individual characteristics of carry idlers as a square function were calculated (fig.5), which were used then in the module for calculation the conveyor movement resistance – method of primary resistances QNK-TT software.

As demonstrated the long-term measurements of temporary capacity, made in the underground copper mine [13], division and main

Fig. 5. Average rolling resistance of idler Ø133×370mm depending of radial force for standard and modernized rollers

For the analyses, variant values of upper idler sets spacing, were taken, i.e. from 0.83 to 1.66 m, which application does not require the construction changes. Other parameters of conveyor are standard ones (tab. 3).

Underground conveyors operate, in fact, in constant, high temperature, which is favorable to obtain the low value of idlers rotation resistance (fig. 5). On both below diagrams (fig. 7) the calculated index of specific energy consumption – SEC, in upper belt strand of underground conveyor, is presented, depending on temporary capacity, equal the radial load of standard idlers (fig. 7a) and modernized, with reduced energy consumption (fig. 7b). Characteristic is the intersection of the specific energy consumption curves. For the small load by output stream, the more favorable is bigger spacing of upper idles, while for bigger load – the smaller one. Therefore, there is no possibility to give the general answer, which spacing of upper sets will reduce the energy consumption costs. Calculating the average

Table 3. Selected parameters of tested underground conveyors

Parameter	Underground conveyor
Transported output, density, kg/m^3	Copper ore, 1700
Calculating work temperature , ^{o}C	25
Length, m; gradient	1500; horizontal
Belt width, mm	1000
Belt; covers thickness, mm	Slow-burning, EP2000/4 6+3;
Belt speed, m/s	2,8
Spacing of carry idlers, m	Variants: 0.83; 1.25; 1.66
Rotation resistance of upper idler , N	According to quoted characteristics
Calculating capacity, t/h	200-1400
Note	Belt tension settled for maximum load

Fig. 6. Example histograms of mass capacity of conveyors used in KGHM PM.S.A underground copper mine: a) division haulage conveyor, b) main haulage conveyor
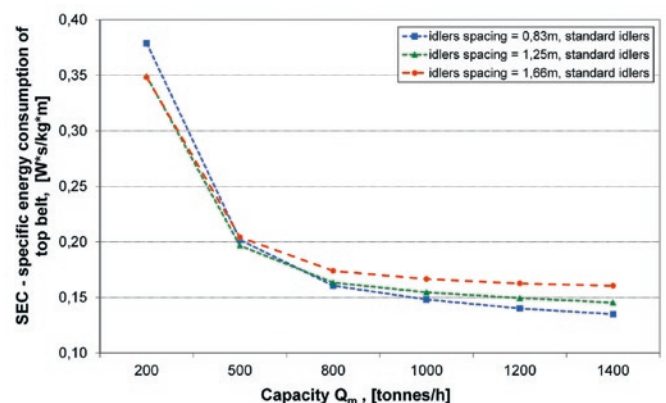
Fig. 7a. Specific energy consumption (SEC) in top belt as a function of actual capacity of an uderground belt conveyor for copper ore transportation (conveyor parameters in tab.3): a) standard idlers

conveyors have different characteristics of the stream of output being hauled (fig. 6).

Using the division ore bunkers makes possible to differentiate the operating time of the division and main haulage conveyors. It is estimated that main haulage conveyors work ca. 6 thousand hour per year, while the division ones – ca. 4 thousand hours. This difference has the impact on evaluating the lifetime of upper idler sets.

specific energy consumption, in accordance with identified load of main and division conveyors, suggests maintaining rather the standard spacing (0.83 m) for the main ones and possible increase of spacing (up to 1.25 cm) for the less loaded, division ones (fig. 8).

Fig. 7b. *Specific energy consumption (SEC) in top belt as a function of actual capacity of an uderground belt conveyor for copper ore transportation (conveyor parameters in tab.3): b) modernized idlers*

Fig. 8. *Averaged specific energy consumption (ASEC) in top belt of a main and secondary transportation underground belt conveyor with regard to top belt idlers spacing*

Fig. 9. *Examples of premature wear of idlers [10]*

Table 4. *Number of idlers replaced per year (per 1 km of conveyor route)*

Idlers spacing	main transport	secondary transport
0.83	21	10
1.25	47	23
1.66	86	40

Similarly, as in the case of open-pit conveyors, the extension of distance between idler sets causes the increase in radial load (different for main and division haulage conveyors), what has the impact on the estimated growth of number of idler sets replaced every year (tab. 4). It should be emphasized that in the underground mine, the corrosion seizing of bearings or coating erasure are the reasons of premature wear of idlers (fig. 9) [10] and thus they do not reach the assumed lifetime resulting from the operational loads [3].

4. Conclusions

The results of considerations about typical conveyors, operating in the open-pit lignite mine and in the underground copper mine, show that some 2-3% of energy savings are possible due to the optimized carry idlers spacing. Seeking the optimal solutions for the criteria of specific energy consumption and the expected number of idlers replacements requires taking into account both the identified resistances to motion and the knowledge about the random stream of transported bulk material.

Non-linear characteristics of idlers rotation resistance and identified, different stream of material, transported on main haulage and division conveyors, indicate that the individual treatment to the idler spacing in carry belt strand, depending on the conveyors location within the haulage system and on accessibility of components – sets of standard or modernized idlers, is necessary.

The calculation results evidence that for the overburden conveyor, with 2.25 wide belt, it is advisable, especially in case of conveyors taking the output from one excavator – enlarging the standard spacing from 1.2 to 1.45 or even up to 2.0 meters both for standard and for modernized idlers (with reduced rotation resistance).

In underground conveyors, with 1.0 m wide belt, designed for copper ore transport, it is also possible to enlarge the standard idler sets spacing from 0.83 m to 1.25 m. In the case of main haulage it gives the savings only in reduction of the number of installed idlers, but for less loaded division conveyors, in addition the energy savings may be expected.

References

1. Bukowski J., Gładysiewicz L., Król R. Tests of belt conveyor resistance to motion. Eksploatacja i Niezawodnosc - Maintenance and Reliability 2011; 3: 17-25.
2. Dworczyńska M., Gładysiewicz L, Król R. Model transportowanego urobku dla szacowania trwałości krążników. Transport Przemysłowy i Maszyny Robocze 2013; 1(19):22-26.
3. Geesmann F.O. Experimentale und Theoretische Untersuchungen der Bewegungswiderstände von Gurtfördenanlege. Praca doktorska. Universität Hannover 2001; (niepublikowana).
4. Gładysiewicz L., Hardygóra M., Kawalec W. Determining belt resistance. Bulk Handling Today 2009; 5: 23-28.
5. Gładysiewicz L., Kawalec W. Carrying idler spacing with regard to the distribution of conveyed stream. Bulk Solids Europe 2010: International Conference on Storing, Handling and Transporting Bulk, Glasgow, Scotland, September 9-10, 2010 / Vogel Business Media, Institution of Mechanical Engineers.

6. Gładysiewicz L., Kawalec W. Dobór rozstawów krążników górnych nowej generacji w przenośnikach nadkładowych dużej wydajności. Transport Przemysłowy Maszyny Robocze 2011; 3(13):7-10.
7. Hardygóra M. et al. Comprehensive studies on the multi-criterial effectiveness of large belt conveyor transportation system. Proceedings of the Twentieth International Symposium on Mine Planning and Equipment Selection, MPES 2011, Almaty, October 12-14, 2011:881-895.
8. Kacprzak M., Kulinowski P., Wędrychowicz D. Computerized information system used for management of mining belt conveyors operation. Eksploatacja I Niezawodnosc - Maintenance and Reliability 2011; 2(50): 81-93.
9. Kawalec W. Przenośniki taśmowe dalekiego zasięgu. Transport Przemysłowy 2003; 1(11):13-20.
10. Król R. Metody badań i doboru elementów przenośnika taśmowego z uwzględnieniem losowo zmiennej strugi urobku. Oficyna Wydawnicza Politechniki Wrocławskiej 2013.
11. Król R. Ocena trwałości krążników dla rzeczywistych obciążeń przenośnika taśmowego. Przegląd Górniczy 2011; nr 11:82-90.
12. Król R., Gładysiewicz L. Kompleksowa ocena jakości krążników poliuretanowych stosowanych w górnictwie odkrywkowym. Prace Naukowe Instytutu Górnictwa Politechniki Wrocławskiej. Studia i Materiały 2009, 36:19-31.
13. Król R., Gładysiewicz L., Wajda A. Analiza rozkładu obciążeń krążników nośnych w kopalniach rud miedzi. Transport Przemysłowy i Maszyny Robocze 2010; 2(8):19-31.
14. Król R, Kisielewski W. Urządzenie do badania oporów obracania krążników pod obciążeniem. Zgłoszenie patentowe nr P406829 z dn. 13.01.2014.
15. Król R, Kisielewski W. Wpływ krążników na energochłonność przenośnika taśmowego. Mining Science 2014; 21(2):61-72.
16. Kulinowski P. - Simulation studies as the part of an integrated design process dealing with belt conveyor operation, Eksploatacja Niezawodnosc – Maintenance and Reliability 2013; 15 (1):83-88.
17. Lodewijks G. Strategies for AutomatedMaintenance of Belt Conveyor Systems. BulkSolids Handling 2004, 24 (1):16-22.
18. Łagoda T., Sonsino C.M. Comparison of different methods for presenting constant and variable amplitude loading fatigue results. Materialwissenschaft und Werkstofftechnik 2004; Vol.35, No.1:13-20, http://dx.doi.org/10.1002/mawe.200300692.
19. Mazurkiewicz D. Computer-aided maintenance and reliability management systems for conveyor belts. Eksploatacja i Niezawodnosc - Maintenance and Reliability 2014; 16 (3): 377-382.
20. Pang Y., Lodewijks, G. The application of RFID technology in large-scale dry bulk material transport system monitoring. Environmental Energy and Structural Monitoring Systems (EESMS), IEEE, 2011: 1-5.
21. Qing H., Daqian D. Zirui H., Dongmei D. Analytical Model between Power and Idler Spacing of Belt Conveyor. Second International Conference on Computer Modeling and Simulation 2010: 8-10.
22. Stefaniak P., Zimroz R., Król R., Górniak-Zimroz J., Bartelmus W., Hardygóra M. Some Remarks on Using Condition Monitoring for Spatially Distributed Mechanical System Belt Conveyor Network in Underground Mine - A Case Study. Condition Monitoring of Machinery in Non-Stationary Operations. Springer 2012:497-507.

Lech GŁADYSIEWICZ
Witold KAWALEC
Robert KRÓL

Faculty of Geoengineering, Mining and Geology
Wroclaw University of Technology
Wybrzeze Wyspianskiego 27, 50-370 Wroclaw, Poland

E-mail: lech.gladysiewicz@pwr.edu.pl,
witold.kawalec@pwr.edu.pl, robert.krol@pwr.edu.pl

Marek BABEŁ
Maciej SZKODA

DIESEL LOCOMOTIVE EFFICIENCY AND RELIABILITY IMPROVEMENT AS A RESULT OF POWER UNIT LOAD CONTROL SYSTEM MODERNISATION

POPRAWA EFEKTYWNOŚCI I NIEZAWODNOŚCI LOKOMOTYW SPALINOWYCH W WYNIKU MODERNIZACJI UKŁADU STEROWANIA OBCIĄŻENIEM ZESPOŁU NAPĘDOWEGO*

The article presents an idea of modernisation of a diesel locomotive power unit load control using SM31 locomotive. In the proposed solution an electronic rotations and power governor of a8C22W diesel engine is applied, developed in cooperation with Lokel (the Czech Republic) and Newag S.A. (Poland), in which a new optimal operational characteristic is realized in the locomotive. This characteristic was selected following optimization calculations using a mathematical model mapping the real conditions of the motor-generator work in a diesel engine. Test stand experimental investigations together with an over three-year supervised observation of the locomotive equipped with the electronic governor have proved its correct and reliable operation. Based on the data collected in supervised observation the efficiency of the proposed solution has been assessed, supported by an LCC (Life Cycle Cost) analysis.

Keywords: *reliability, operation, modernisation of locomotives, LCC analysis.*

W artykule przedstawiono koncepcję modernizacji układu sterowania obciążeniem zespołu napędowego lokomotywy spalinowej na przykładzie lokomotywy serii SM31. Proponowane rozwiązanie polega na zastosowaniu elektronicznego regulatora obrotów i mocy silnika wysokoprężnego a8C22W, opracowanego w wyniku wspólnych prac autorów z firmą Lokel (Czechy) i Newag S.A. (Polska), realizującego na lokomotywie nową, optymalną charakterystykę eksploatacyjną. Charakterystyka ta została wybrana w wyniku obliczeń optymalizacyjnych z wykorzystaniem opracowanego modelu matematycznego odwzorowującego rzeczywiste warunki pracy zespołu silnik-prądnica na lokomotywie spalinowej. Badania stanowiskowe oraz ponad trzyletnia eksploatacja obserwowana lokomotywy z zamontowanym regulatorem elektronicznym wykazały poprawne i niezawodne jego działanie. Bazując na danych zgromadzonych podczas eksploatacji obserwowanej, przeprowadzono ocenę efektywności proponowanego rozwiązania w oparciu o analizę LCC (Life Cycle Cost).

Słowa kluczowe: *niezawodność, eksploatacja, modernizacja lokomotyw, analiza LCC.*

1. Introduction

In the projects targeted at enhancing the efficiency of rail transport an important role is occupied by activities aimed at reduction of traction vehicles operation and maintenance costs. One of the ways to reach this aim is to modernise diesel locomotives, including additionally exhaust emissions control. The basic objectives of diesel locomotives modernisation include:

– reduction of fuel and operational materials consumption costs,
– availability of new sub-assemblies and spare parts,
– increase of technical availability,
– increase of mileage between downtimes,
– improvement of driver's work conditions,
– reduction of negative effect on the natural environment.

In recent years rail transport agencies have shown interest in the modernisation of diesel locomotives. In the years 2006 – 2014, as a result of the cooperation between the Institute of Rail Vehicles of the Cracow University of Technology and rail transport agencies various projects have been developed, including the modernisation of both railway line locomotives e.g.: ST44, SU45, SU46, SP32 and shunting locomotives: SM48, SM42 and SM31 [54, 55]. The majority of these projects have been fully implemented in practice.

The present paper presents an idea of SM31 locomotive power unit load control system modernisation by the implementation of a new operational characteristic of a8C22W diesel engine, executed by a modern electronic rotational speed and power governor. The new operational characteristic was selected on the basis of optimisation calculations using a mathematical model mapping the real working conditions of the locomotive in operation. To assess the efficiency of the proposed solution an LCC (Life Cycle Cost) analysis has been carried out including the reliability properties of the vehicle.

2. Characteristics of the study object

Diesel locomotives SM31 have been used in Poland for over thirty-five years. As of the end of 2014, in the operative use there were about 150 locomotives of this series. SM31 locomotive was designed mainly for the heavy job of shunting at stations and humps, but also for tractive work. The vehicle is equipped with a supercharged a8C22W engine (produced by HCP Poznań plant) built on the basis of the a8C22 engine. The basic technical parameters of the two engines are shown in Table 1b.

SM31 locomotives were manufactured based on the technology and technical solutions dating back to the early 1970s. Since their pro-

Table 1. *SM31 diesel locomotive and technical data of a8C22 and a8C22W engines*

Engine parameter	a8C22 (loc. SM42)	a8C22W (loc. SM31)
Piston stroke [mm]	220/270	220/270
Number od cylinders in system V	8	8
Effective (rated) power [kW]	590	885
Rated/idle running rotation [rpm]	1000/500	1000/500
Mean effective pressure [MPa]	0,88	1,32
Compression ratio	13,5	12
Supercharging pressure (absolute) [MPa]	0,15	0,20
Peak firing pressure [MPa]	10	11,5
Unitary fuel consumption [g/kW h]	235	225
Temperature of exhaust gases in front of turbine [K]	780	850
Supercharger revolutions [rpm]	14500	17700
Supercharging air cooling	none	cooler

[Photo: http://woziarze.cal.pl]

duction the design of the locomotives has practically not changed. No modernisation works have been done. The analysis of operation indices together with an assessment of the reliability of SM31 engines, performed at the Institute of Rail Vehicles, Cracow University of Technology, has proved the necessity of their modernisation with the focus on the most unreliable units and systems of the locomotive [7].

3. Analysis of SM31 locomotive failures

The reliability of SM31 diesel locomotives in operation is chiefly limited by the reliability of a8C22W supercharched diesel engines. For the analysis of the operation data obtained from PKP Cargo S.A.,
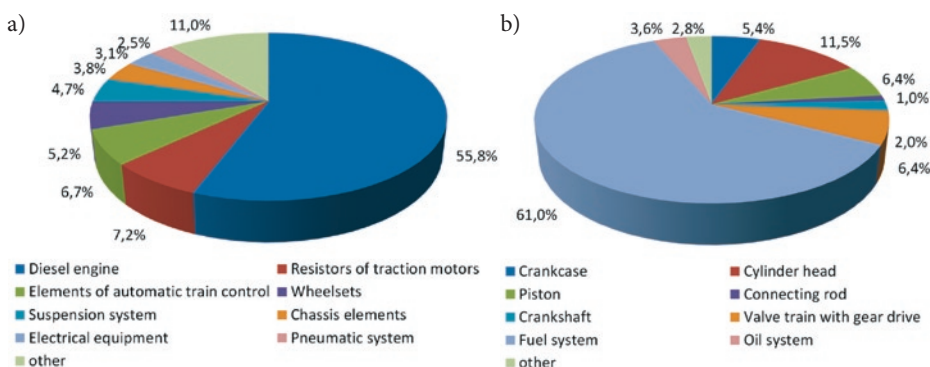
a sample of 36 SM31 locomotives, collected in the years 2010-14, it follows that about 56% of all the failures found in SM31 locomotives are related to the diesel engine (Fig. 1a). The reliability of a8C22W diesel engine is determined to the highest extent by the piston-cylinder system, and the majority of failures occurs in the fuel system (Fig. 1b) [4, 7]. This results from the considerable increase of thermal stresses which for the piston-cylinder system of an a8C22W diesel engine are generally several times higher than mechanical stresses.

The results of investigations prove that in order to improve the reliability of railway diesel engines in operation it is necessary to improve the quality of their work in transient states which for shunting locomotives are 50% of the overall time of engine working under load. The quality can be improved by implementing an optimal operation characteristic of an engine, selected using a specified criterion.

4. Mathematical model of diesel locomotive engine

The improvement of the reliability of some systems and units of diesel locomotives in operation is an optimisation task which cannot be solved by experimental methods. It requires mathematical modeling of power unit work conditions, i.e. creating a model of an object: motor-generator together with a simulation model mapping the work conditions of a locomotive in operation.

Some components of a traction vehicle LCC analysis have a temporary character and depend on operation conditions. The author's proposal is to calculate these components using a mathematical model of work processes in the locomotive power unit during operation.

The essential requirements for the application of a mathematical model in optimisation calculations include: adequacy to the object of research, conciseness and universality of the processes description for various types of diesel engines and supercharging systems. The need for developing mathematical models of diesel engine work processes in the conditions of operation has been a live issue for years. Numerous studies on the subject have appeared. In the field of motor-car IC engines the majority of investigations are related to IC engine systems control including dynamic states [10, 14, 15, 25, 36, 61]. In [11] an interesting mathematical model of transient processes in locomotive diesel engines was proposed. The model is based on the solution of a system composed of "n" differentia equations for the piston part and six equations describing the processes in the exhaust manifold in the case of pulsatory supercharging system. The same principles were applied in the mathematical models of transient processes in diesel engines presented in [60, 62]. It should be noted, however, that the applicability of these models is rather limited in solving optimisation tasks. This is because a significant number of calculation operations and subprograms are necessary and the calculation precision depends on the selection of the mode of differential equations solutions, which makes the calculations time-consuming.

The mathematical model of the work processes in a8C22W diesel engines in steady and transient state conditions, developed by the authors of this article, takes into account the joint work of a piston engine with a turbine, compressor, induction and exhaust systems in the locomotive as well as the operation properties of engines in shunting diesel locomotives. The mathematic model imitates the functional connections used in the crankshaft rotational speed and engine power control systems. The details of assumptions, requirements and mathematical equations related to the model are given in [5, 6, 31, 33]. The most important ones are presented in what follows.

Fig. 1 a) Structure of failures of SM31 locomotive; b) Structure of a8C22W engine failures

1. The final control units of control systems work in such a way that at each moment the rate of change of controlled value A is proportional to the value of divergence and in inverse proportion to time constant:

$$\frac{dA}{dt} \cong \frac{A^* - A}{T_A},$$ (1)

where:

A*, A – assigned and actual values of controlled value,
TA – time constant of A control system.

2. At any moment power balance is maintained:

$$b_T \cdot H_u \cdot \eta_i = P_M + P_B + P_P + J_\Sigma \cdot \omega_g \cdot \frac{d\omega_g}{dt}$$ (2)

where:

P_P – power transmitted to tractive generator,
P_M, P_B – power of mechanical losses in engine and auxiliary devices in locomotive,
J_Σ – cumulative moments of inertia of diesel engine and locomotive units, reduced to diesel engine crankshaft,
$d\omega_g/dt$ – angular acceleration of diesel engine crankshaft.

In the calculations, to select the values db_T/dt, $d\omega_g/dt$ and dP_P/dt equation (2) is used in the differential form:

$$J_\Sigma \left(\omega_g \frac{d^2\omega_g}{dt^2} + \left(\frac{d\omega_g}{dt}\right)^2 \right) = \frac{db_T}{dt} H_u \left(\eta_i + \frac{\partial \eta_i}{\partial b_T} b_T \right) + b_T \frac{\partial \eta_i}{\partial \omega_g} \frac{d\omega_g}{dt} H_u - \left(\frac{dP_M}{dt} + \frac{dP_B}{dt} + \frac{dP_P}{dt} \right)$$ (3)

For the SM31 diesel locomotive motor-generator dP_P/dt component is a sum of two components:

$$\frac{dP_P}{dt} = \frac{dP_C}{d\omega_G} + \frac{d\omega_G}{dt} + \frac{dP_{RM}}{dt}$$ (4)

where:

$dP_C/d\omega_g$ – diesel engine power change in the function of crankshaft rotational speed at a constant travelling,
dP_{RM}/dt – assigned diesel engine power change, controlled by power regulator, in the function of field rheostat regulator position (servo-motor).

3. Initially, the fuel charge possible increase (db_T/dt) calculated from diesel engine thermal cycle parameters boundaries is substituted in equation (3) and crankshaft angular acceleration at constant power P_P transferred to the tractive generator is calculated. On reaching the allowable crankshaft angular acceleration ($d\omega_g/dt$), assigned on the basis of restrictions or other conditions, the possible rate of fuel charge increase (db_T/dt) and the assigned crankshaft angular acceleration) ($d\omega^*_g/dt$) are substituted in equation (3) and the value of the possible tractive generator power increase (dP_P/dt) is determined. If the value of power increase rate is lower than allowable (dP_P/dt), the variables (db_T/dt) and (dP_P/dt) are the control values searched. If (dP_P/dt) is higher than the allowable value, allowable ($d\omega_g/dt$) and (dP_P/dt) are substituted in equation (3), and next fuel charge change rate (db_T/dt) is calculated. The variables (db_T/dt) and (dP_P/dt) are the control values searched.

If ($d\omega_g/dt$) and (dPP/dt) are expressed as components functionally dependent on time, crankshaft rotational speed, supercharging compression etc., this method can be used for the imitation of logical functions in the existing control systems. This approach enables excluding the effect of the control systems operation quality on the transition processes indices and developing new control principles when the variable interrelations in equation (3) are changed.

Diesel engines of a8C22W type are characterised by the use of pulsatory supercharging system. In creating the model it was assumed that a change of exhaust pressure in the exhaust manifold in the function of time or crankshaft rotation angle ω_g is a time periodic function of the period:

$$T = \omega_g \cdot \phi^*$$ (5)

The phase of exhaust pressure change in the manifold φ* will be equal to the value of cylinders work phase shift. Let us assume that the cyclic process in the manifold can be presented a series of processes of time duration Δφ, restricted by boundary conditions. The number of such series processes can be relatively large, but, connected with the processes in the suction manifold, there are two characteristic periods: the phase of exhaust escape (angle φ_b, φ_s) and phase of scavenging (angle φ_s, φ_{be}), Fig. 2a.

In a diesel engine with pulsatory supercharging system the exhaust escape is completely separated from the processes in the suction manifold and can be calculated after commonly known methods if the parameters of the working medium in the cylinder are assigned. The scavenging process is directly connected with the processes in the suction manifold. The scavenging process is calculated together with the calculations of the processes in the induction pipes including elements of a diesel locomotive, i.e. air filter 1, compressor 2, supercharging air cooler 3, piston part 4, turbine 7 and elements of outlet system 8 (Fig. 2b). Pressure drops in the suction and compulsory escape were
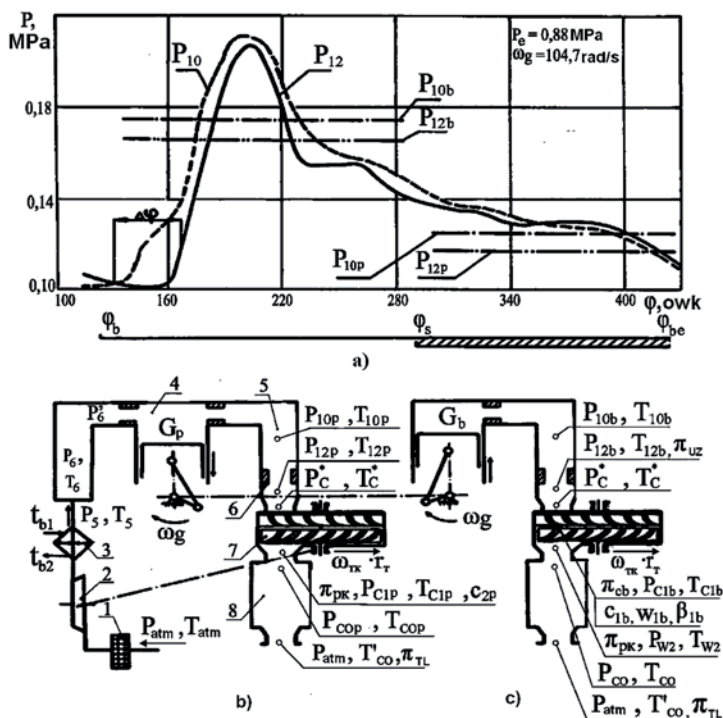
Fig. 2. Pressure modification in exhaust manifold [4]: a) calculation model of model a8C22W diesel engine with pulsatory supercharging system during scavenging b) and exhaust escape c)

calculated separately. Both processes are described with a system of nonlinear algebraic equations representing the quasi-steady flow of the working medium in the scavenging and escape phases were performed on the basis of mean values of pressure, temperature and rate of working medium flow in respective phases with an adopted duration time $\Delta\varphi$ (Fig. 2a). The initial parameters for the calculation of the processes in the exhaust manifold, in the case of compulsory escape, were the values of the parameters defined during the calculation of the processes in the exhaust manifold during scavenging. The gas dynamics calculations of the turbocharger turbine in the transition process included modifications of the angle of exhaust flow between the rotor vanes [3, 5, 31].

The working conditions of a diesel engine in steady states and in the transition processes are calculated with one program, whose block diagram is shown in Fig. 3. Using this diagram a program for calculating the indices of a8C22W engine performance in steady-state conditions and in the transition processes was developed [5].

Fig. 3. Block diagram of algorithm of diesel engine transition process calculation [3]

Fig. 4. Indices of a8C22W motor-generator operation: a) for operation characteristic, b) in transition process [3]

5. Optimal operation characteristic of SM31 locomotive power unit

A comparison of the calculation and experimental indices of a8C22W diesel engine performance for the operation characteristic – Fig 4a and transition process in the function of time – Fig. 4b, has shown a good convergence of results [3].

Notation in Figs 4a and 4b:

T_s, T_T – temperature of air in suction manifold and exhaust manifold in front of turbine; P_s, P_T – pressure of supercharging and exhaust in front of turbine (overpressure); ω_g, ω_{TK} – angular speed of diesel engine crankshaft and turbo-rotor; G_b – air; g_c – fuel charge per cycle; N_e – diesel engine effective power; _____ – result of experiments; - - - - – result of calculations.

The satisfactory compatibility of the mathematical models of working processes between a8C22W diesel engines and the actual curves makes it possible to formulate a strategy of selection of the motor-generator optimal full-load characteristic, including the diesel locomotive working conditions, on the basis of a selected criterion, which is proposed to be the product minimum:

$$W_\Sigma = \left(K_P + K_{NP} + K_{NN}\right)\cdot T_L \qquad (6)$$

where:

K_P – costs of fuel consumed over period T_L of assigned tractive work A_T performed by the locomotive,

K_{NP} – costs of predicted overhaul and repair works of a diesel engine in the period of one repair cycle,

K_{NN} – costs of unpredicted repair works (e.g.: piston-cylinder unit elements) resulting from emergency failures taking place in operation.

The calculations of engine and locomotive work indices over the period T_L of the tractive vehicle work are a result of modelling of the SM31 locomotive power unit in operation conditions. The costs of planned repairs K_{NP} are calculated according to the engine crankshaft mean operation angular velocity at a known cumulative cost of repairs and overhauls during one repair cycle. The value of costs K_{NN} is in linear dependence on the life of piston-cylinder unit elements, which in turn depends on the amount of failures. The quantitative assessment of the life of a8C22 engine piston-cylinder unit elements (cylinder heads) is done approximately using the grey cast iron fatigue curve and the linear hypothesis of fatigue failure summation according to the maximum calculated values of exhaust temperature in front of the turbine depending on [3].

Using the developed mathematical models optimisation calculations were performed, which resulted in, based on criterion (6), an optimal operation characteristic selection for a8C22W diesel engines of SM31 locomotives (Fig. 5).

Fig. 5. Characteristics of locomotive SM31 a8C22 engine [3]: 1 – boundary characteristic – exhaust allowable temperature in front of turbine [TT] = 850 K; 2, 3 – operation characteristics – present, compatible with the technical-motion of locomotive and proposed on the basis of cost minimum criteria; 4, 5 – selective characteristics – present and proposed for characteristic 3

The performed calculations indicate that the implementation of an optimal operation characteristic of the a8C22 engine may result in:
– significant reduction of thermal stresses in engine piston-cylinder unit elements, which leads to a threefold reduction of the rate of failures of cylinder heads and pistons, i.e. reduction of unplanned repairs costs,
– reduction of fuel consumption by about 3%.

6. Testing of modernised power unit load control system

The implementation of an optimal characteristic in SM31 locomotive requires modernisation works in load control and fuel charge systems. The power unit control system used in SM31at present is composed of the driver-operated controller, crankshaft rotations governor and main generator excitation system. The electrohydraulic controllers used in these locomotives have a very limited capacity for shaping the characteristic. They realise practically linear dependence between the assigned position of the fuel injection pump strip (of engine effective power Pe) on the crankshaft rotational velocity– curve 2 in figure 5. The selected optimal operation characteristic 3 is non-linear. The implementation of this characteristic in SM31 locomotive requires an advanced electronic rotation governor and the power of

the microprocessor technology-based a8C22W engine. In this type of control all the logic connections between the control system input and output state have the form of a control program. No alteration or correction introduced into the functions requires changes in the control system of the locomotive. To develop an electronic rotational velocity and power governor for a8C22 engines of SM31 diesel locomotives the following requirements had to be satisfied:
– to adapt the existing electromechanical equipment and apparatus of the main generator power control to the electronic controller;
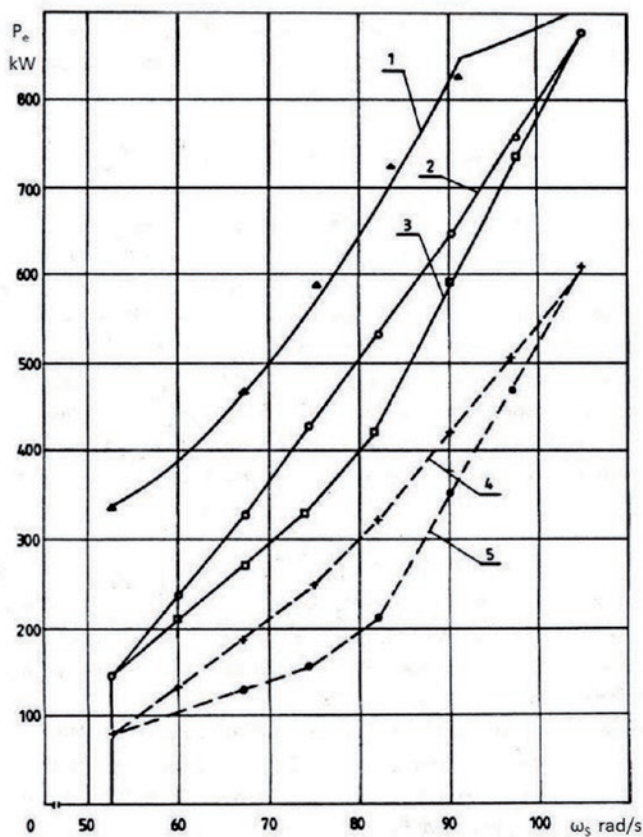– to ensure the interaction between the electronic governor actuator (servo motor) and the system of fuel charge control levers of injection pumps, existing in the diesel engine;
– in the construction of the electronic governor use Woodward or Heinzmann manufactured elements as tested and reliable in operation.

In cooperation of the authors of the article with Lokel firm (the Czech Republic) and Newag S.A. (Poland) a rotational speed and power electronic governor was built for a8C22 and a8C22W diesel engines. The governor consists of [7]:
– ProAct III Woodward electrical servo-motor;
– ProAct Driver Woodward servo-motor control module;
– INTELO 144 Lokel microprocessor controller;
– 110V/24V transducers, sensors of current and voltage of the main circuit, indicators of crankshaft rotations, oil pressure and cooling medium temperature.

The installation of the electronic governor in the a8C22W diesel engine (Fig. 6) enables the realisation of a selected operation characteristic in the power control system (capacity) of the SM31 locomotive. The complete assembly of the governor in the locomotive can be performed during preventive maintenance service: extended periodical inspection (level P3) or preventive repair (level P4).

The test stand examinations and over three-year supervised operation of the locomotive with the fixed electronic governor showed its failure free and reliable operation. The performance of the rotations and power control system in the locomotive is stable in both steady states and in the transient processes. The results of a trial operation indicated the major benefits of the modernisation of the locomotive power control system in the aspects of [3, 32]:
– reduction of locomotive ownership costs connected with the repair of electro-hydraulic governors worn in over the 35-year operation;
– reduction of locomotive servicing costs owing to eliminating the necessity of time-consuming regulation and setting of the operation characteristic in the resistor over the total operation period of the locomotive;
– improvement of accuracy and stability of power control, which reduces fuel consumption by about 5%.

7. Evaluation of efficiency of power control system modernisation using LCC analysis

To evaluate the efficiency of the proposed solution in the cost aspect an LCC (Life Cycle Cost) analysis has been performed. The idea of LCC analysis dates back to the 1960s. Information on its applications can be found in several projects run by U.S. Department of Defense which introduced calculations in various areas of activity of the American military [39-41]. LCC was used for, for instance, the evaluation of handling and maintenance of military equipment, armament and defense systems. The analyses indicated that in many cases the costs of handling and maintenance are at least 75% of the total costs, and in the period of 10 – 15 years of handling the costs exceed many times the initial acquisition costs [1, 8, 34, 42]. After that the application of LCC analysis was widely used in other branches of industry, e.g. aircraft industry [2], power industry [17, 49], oil and
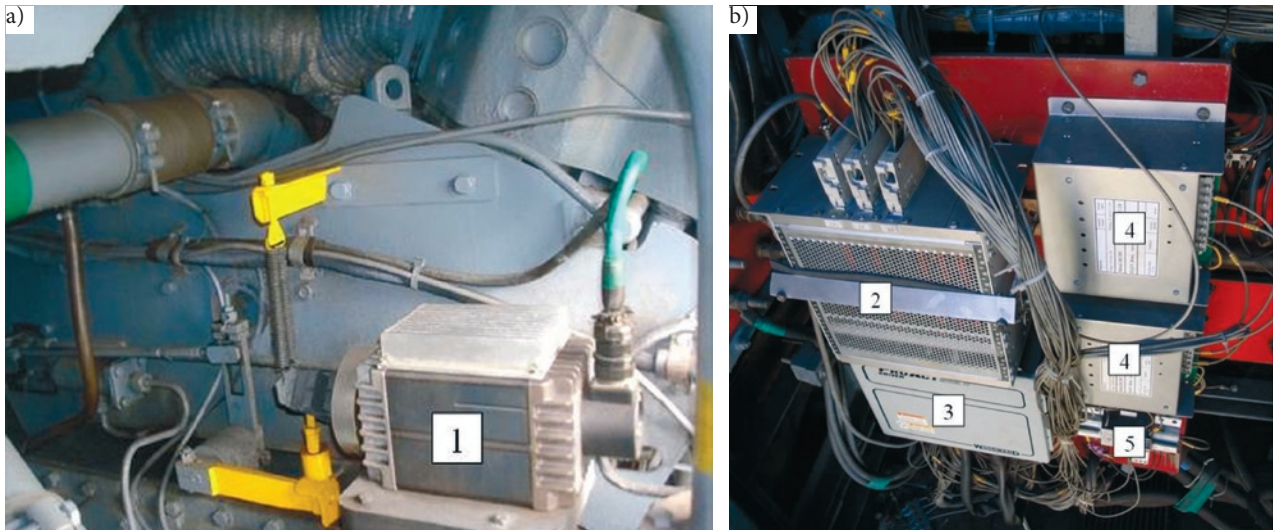
Fig. 6. Electronic governor of a8C22, a8C22W diesel engines rotations and power [7]: a) 1 – electrical servo-motor; b) 2 – microprocessor controller; 3 – electrical servo-motor control module; 4 – Voltage transducer; 5 – current and Voltage sensors

chemical industries [30, 46], building industry [16, 18] and transport [12, 43, 52].

In the literature and norms many methods of LCC calculations are proposed [9, 21, 23, 24, 28, 30, 35, 47, 49, 53, 56, 63]. For instance, in [15] the author compares nine models of LCC costing. The selection of an adequate model depends on available resources, input data, time horizon covering the analysis and the object itself of the analysis. In the case of modernisation of SM31 locomotive, which is the subject matter of the present considerations, LCC costing based on PN-EN 60300-3-3 (Reliability Management. Application Guide – Life Cycle Cost Estimation) *Dependability management. Application guide – Life cycle costing* was proposed. The method consists of six stages [58]:

1. Assumptions and aim of analysis;
2. RAM analysis;
3. LCC model development;
4. LCC model analysis;
5. Reporting the results;
6. Verification of analysis.

As a measure of efficiency LCC over a 25-year operation of the locomotive was adopted.

7.1. Assumptions and aim of analysis

It was assumed that the analysis is comparative. The aim of the analysis is to compare the economic effects reached in modernised operation of the locomotive with those before the modernisation. Two variants therefore were adopted:

1. **SM31 variant 0**: non-modernised SM31 locomotive with a8C22W engine,
2. **SM31 variant 1**: modernised locomotive SM31 with a8C22W engine, equipped with an electronic governor realising a selected optimal operation characteristic of the power unit.

In the first stage of the analysis a set of output data was developed for both variants. The data of the non-modernised locomotive included:

– determination of locomotive load distribution for actual operation conditions,
– measurement of actual fuel and engine oil consumption,
– calculation of mean service time, mileage, transport work per year,
– determination of periodicity, time consumption and cost of preventive maintenance resulting from the maintenance cycle,

– preparation of operation data connected with the periods of failure-free work, recovery time, necessary for reliability analysis.

The data of modernised locomotive covered:

– scope, periodicity of technical servicing for new systems and sub-assemblies,
– new maintenance schedule for an electronic governor equipped locomotive.

The output data for the evaluation of modernisation efficiency concern the locomotive work conditions. For the non-modernised SM31 locomotive they were obtained based on the operation of a series of locomotives in the PKP Cargo S.A. In the analysis the following operation indices were adopted:

– locomotive's mean work time in a calendar year: TZ = 5771,7 [hours/year],
– mean mileage: P = 50000,0 [km/year],
– mean transport work: PP = 9564,5 [thousand btkm/year].

7.1.1. Project execution period

For the LCC analysis the period of twenty-five year operation of the locomotive January 2015 – December 2039 was adopted, which corresponds to 144292,0 hours of power unit work.

7.2. RAM analysis

The reliability of SM31 locomotive is treated as a complex property covering the vehicle's features such as reliability, availability and maintainability. The general guidelines of RAM analysis are given in PN-EN 50126 *Railway applications. The specification and demonstration of Reliability, Availability, Maintainability and Safety* (RAMS) [22]. The literature on the subject provides detailed description, definitions and calculation formulae of various evaluation indices [29, 44, 53]. Many study projects on RAM analysis have been done in the recent decades. At present it is applied in many industrial sectors, e.g. aircraft, armament, power, processing and transportation industries [14, 19, 29, 38, 50, 55, 59].

7.2.1. Reliability data

The evaluation of non-modernised locomotive reliability was based on the operation data collected on thirty-six vehicles. These data were collected in cooperation with PKP Cargo S.A. in actual operation conditions in the years 2013 – 2014. The operation in various conditions was observed, which provided reliable and extensive information necessary for reliability analysis. For the modernised lo-

comotive the data were collected during three-year supervised observation.

7.2.2. Reliability, availability and maintainability indices

Locomotive SM31 can be analysed on various levels of complexity with respective RAM indices assigned to each. As the scope of the presented reliability analysis was very broad, in what follows the calculations of only some RAM indices the most important for effectiveness evaluation are discussed:

– Mean time between failures *MTBF*,
– Operation availability A_o,
– Mean time to repair *MTTR*.

The definitions and notation of the indices have been adopted according to PN-EN 50126 and PN-EN 61703 norms [22, 48], in the calculations Statistica, MiniTab and BlockSim packages have been used.

The failures of SM31 locomotive can be divided into minor, for which repair time does not exceed three hours and downtime is not necessary, and major failures which make the vehicle unavailable for operation and it needs to be sent to a rolling stock maintenance plant. In the performed analysis only major failures have been considered significant. Based on the collected operation data reliability models for failure-free work time have been made. In the analysis two parameters Weibull distribution was applied for which the probability density function of failure-free work time is expressed by the formula:

$$f(t) = \frac{a}{b}\left(\frac{t}{b}\right)^{a-1} \exp\left(-\frac{t}{b}\right)^{a}, \quad for \ t \geq 0 \qquad (7)$$

where:
   a – parameter of shape,
   b – parameter of scale.

The parameters of the distributions are presented in Table 2.

Table 2. Weibull distribution parameters for the study cases

No	Variant	Parameter of shape A	Parameter of scale B
1	SM31 variant 0	1,2313	348,788
2	SM31 variant 1	1,2025	847,734

Taking into account the collected operation data, mean times between failures MTBF were computed for the analysed variants [26, 37]. The results are given in table 3.

$$MTBF = \frac{\sum_{i=1}^{N(0)} TTF_i}{N(0)} \qquad (8)$$

where:
   TTFi – locomotive's total work time "i" during supervised operation in [hour],
   N(0) – total number of locomotives.

In the evaluation of maintainability of the analysed variants distribution functions of corrective maintenance time and mean time to repair MTTR were determined. In the calculations lognormal distribution was used for which the probability density function of recovery time is expressed by the formula [37]:

$$g(t) = \frac{1}{t \cdot \delta \sqrt{2\Pi}} \cdot \exp\left[-\frac{(\ln t - a)^2}{2\delta^2}\right], for \ t > 0 \qquad (9)$$

where:
   a – parameter of shape,
   δ – parameter of scale.

The statistic assessment of MTTR was determined from dependence [26, 37]:

Table 3. Lognormal distribution parameters for the study cases

No	Variant	Parameter of shape a	Parameter of scale Δ
1	SM31 variant 0	4,0392	0,9688
2	SM31 variant 1	4,0428	0,9261

$$MTTR = \frac{\sum_{i=1}^{N(0)} TTR_i}{N(0)} \qquad (10)$$

where:
   TTR_i – total time to repair of the locomotive "i" during supervised operation,
   N(0) – total number of locomotives.

The determination of mean times to recovery was based on the data collected from 503 corrective maintenance performed in the years 2013 – 2014 in the rolling stock maintenance plants of PKP Cargo S.A. The results are shown in Table 3.

To compare the technical availability the operation availability index was used, defined as a mean time share over the period of one year during of the locomotive's up time. For one vehicle this index was expressed by the formula [56]:

$$A_O = \frac{\sum_{i=1}^{N(0)} TZ_i}{\sum_{i=1}^{N(0)} TZ_i + \sum_{i=1}^{N(0)} TN_i} \qquad (11)$$

where:
   TZ_i – locomotive's up time "i" in [hours],
   TN_i – locomotive's non up time "i" in [hours]:

$$TN_i = MNF_i \cdot MTTR \qquad (12)$$

where:
   MNF_i – mean number of locomotive's failures "i" in the year of operation,
   N(0), MTTR – as above.

Table 4 presents the calculation results for some RAM indices of the variants considered.

Table 4. Calculation results from RAM analysis for analysed variants

No	Variant	MNF [failure/year]	MTBF [hour]	MTTR [hour]	A_o
1	SM31 variant 0	13,9	416,5	90,8	0,8223
2	SM31 variant 1	6,6	874,5	87,5	0,9097

7.3. LCC model

LCC model was expressed as a sum of acquisition costs and ownership costs:

$$LCC = KN + KE \qquad (13)$$

where:

LCC – life cycle cost,
KN – acquisition costs,
KE – operation costs.

Acquisition costs Koszty nabycia (KN) are a sum of investment outlays connected with in locomotive's modernisation and are paid only in the variant of locomotive's modernisation. Operation costs (KE) are costs connected with use and maintenance of the locomotive. Since the analysis is comparative, the costing covers only those cost categories that are different for each evaluated variant. The costs breakdown structure of in the adopted model is:

1. Acquisition costs (KN)
   • Modernisation costs (KM)
2. Operation costs (KE)
   • Maintenance costs (KUT):
      – Preventive maintenance costs (KUP),
      – Corrective maintenance costs (KUB),
      – Unavailability costs (KBG).
   • Costs of use (KUZ):
      – Diesel fuel consumption costs (KZP),
      – Engine oil consumption costs (KZO),
      – Environmental charges costs (KOS).

The elements of costs were evaluated using an engineering method of cost assessment and was based on constant prices (net price) as valid in 2015. The LCC analysis was performed on non-negotiated cost values. The assumptions adopted for calculations are discussed in sections 7.3.1 – 7.3.5.

7.3.1. Modernisation costs (KM)

The modernisation costs are cumulative expenditure for locomotive modernisation. They include costs of documentation, purchase of indispensable sub-assemblies and elements, costs of obtaining operation licence and labour costs. It was assumed that the modernisation of SM31 locomotive would be executed in the framework of preventive maintenance: periodical overhaul (level P3) or preventive repair (level P4). The modernisation costs are: KM = 75000,0 [PLN].

7.3.2. Preventive maintenance costs (KUP)

The costs of preventive maintenance (KUP) constitute the expenditure for repairs and periodical overhaul of the locomotive resulting from the maintenance schedule defined in the maintenance system documentation (table 5).

Table 5. Levels of SM31 locomotive maintenance [20]

No.	Maintenance level	Time interval
1	P1	max. 1300 km / max.102 h labour / max. 14 calendar days
2	P2/1	23 days ±3 days
3	P2/2	46 days ±6 days
4	P2/3	138 days ±18 days
5	P3	2 years ± 2 months
6	P4	200 000 km or 4 years
7	P5	1 200 000 km or 24 years

The preventive maintenance costs include labour costs (KUPR) as well as costs of materials and spare parts (KUPM). KUP per year is expressed by dependence:

$$KUP = \sum_{i=1}^{n} KUP_i \qquad (14)$$

where:

KUP_i – preventive maintenance costs for maintenance level "i"

$$KUP_i = KUPR_i + KUPM_i = NPMA_i(\text{t}) \cdot \left[(MMH_i \cdot CPH_P) + ACM_i \right] \quad \boldsymbol{[PLN / year]} \qquad (15)$$

where:

$NPMA_i(\text{t})$ – number of preventive services of level "i" over the given operation year,
MMH_i – mean time consumption of preventive maintenance service level "i",
CPH_P – cost of man-hour in preventive service: $CPH_P = 53,8$ [PLN/man-hr],
ACM_i – mean material consumption in preventive service maintenance level "i".

The calculations have proved that owing to the use of new sub-assemblies and elimination of the necessity of time-consuming regulation and setting operation characteristic of the resistor the modernisation of SM31 locomotive gives savings in preventive maintenance costs of about 9,6 [thousand PLN/year] compared with the non-modernised locomotive.

7.3.3. Corrective maintenance costs (KUB)

The corrective maintenance costs (KUB) are connected with running repairs of the locomotive. They include both labour costs (KUBR) and the expenditure for materials and spare parts (KUBM). The costs of corrective maintenance over a year for one vehicle are expressed as:

$$KUB = KUBP + KUBM = MNF \left[(MMH_B \cdot CPH_B) + ACM_B \right] \quad \boldsymbol{[PLN / year]} \qquad (16)$$

where:

MMH_B – mean labour consumption of corrective repair: $MMH_B = 10,9$ [man-hour/repair],
CPH_B – cost of man-hour in corrective repair: $CPH_B = 53,8$ [PLN/man-hour],
ACM_B – cost of material consumption in corrective repair: $ACM_B = 2324,3$ [PLN/repair],
MNF – mean failure rate over a year of operation:

$$MNF = \frac{TZ}{MTBF} \quad \left[\text{failures} \big/ \text{year} \right] \qquad (17)$$

where:

TZ – locomotive's mean work time over a calendar year in [hour/year],
$MTBF$ – mean time between failures in [hours].

The calculations performed using the mathematical model of a diesel engine have proved that the modernisation of the power unit load control system of SM31 locomotive reduces the cost of correc-

Table 6. Costs of corrective maintenance for the analysed variants

No.	Variant	Mean work time TZ [hours/year]	Mean time between repairs MTBF [hours]	Costs of corrective maintenance [PLN/year]
1	SM31 variant 0	5771,7	416,5	40 353,5
2	SM31 variant 1		874,5	19 210,8

tive maintenance of about 21,1 [thousand PLN/year] compared with non-modernised locomotive.

7.3.4. Costs of fuel consumption (KZP)

The costs of fuel consumption (KZP) for a non-modernised locomotive was calculated based on the actual operation data collected in the years 2013 - 2014 by PKP Cargo S.A. For a locomotive modernised as a result of modelling the vehicle tractive work and processes in the power unit realising a selected optimal operation characteristic we obtain instantaneous fuel consumption bPi in the period τj of a single regime of locomotive diesel engine. For the period of the assigned tractive work performance by a modernised SM31 locomotive the fuel consumption cost KZP was expressed as:

$$KZP = \int_{\tau_0}^{\tau_j} c_P b_{P_i} dt \quad [\textbf{PLN / hour}]] \qquad (18)$$

where:

b_{P_i} – instantaneous fuel consumption in the period τ_j [kg/s],

c_P – diesel oil cost: 4,43 [PLN/kg].

On the basis of the collected data and performed calculations mean fuel consumption was determined:
– SM31 variant 0: 17,74 [kg/hour];
– SM31 variant 1: 16,85 [kg/hour].

Table 7 presents the yearly fuel consumption costs for the analysed variants. The calculations indicate that the modernisation of SM31 locomotive in the proposed variant reduces fuel consumption by 5,0%, i.e. 22,7 [thousand PLN/year].

Table 7. *Fuel consumption costs for analysed variants*

No.	Variant	Work time [hours/year]	Diesel oil consumption [kg/year]	Diesel oil consumption cost [PLN/year]
1	SM31 variant 0	5 771,7	10 2360,8	453 458,3
2	SM31 variant 1		97 242,7	430 785,3

7.3.5. Costs of engine oil consumption (KZO)

For a non-modernised SM31 locomotive the mean consumption of engine oil, according to operation data, is 0,92% of fuel consumption. For a modernised locomotive owing to the implementation of a selected optimal operation characteristic of the power unit this consumption is 0,60%. Table 8 presents the yearly costs of engine oil consumption for both variants. For the costing the price of engine oil used in a8C22W engine was adopted as 10,88 [PLN/kg].

Table 8. *Engine oil consumption costs for analysed variants.*

No.	Variant	Engine oil consumption [kg/year]	Engine oil consumption [kg/year]	Engine oil consumption cost [PLN/year]
1	SM31 variant 0	102 360,8	941,7	10 245,9
2	SM31 variant 1	97 242,7	583,5	6 348,0

In the qualitative approach the savings of engine oil consumption for a modernised locomotive are 38,1% i.e. 3,9 [thousand PLN/year].

7.3.6. Costs of unavailability (KBG)

The costs of unavailability (KBG) are a sum of costs resulting from the locomotive's not being in a state to perform required tasks. They include: liability costs, warranty costs, lost opportunity costs,

costs of providing alternative vehicles and others. Unavailability costs are expressed by the formula:

$$KBG = \left[8760 \cdot (1 - A_O) \right] \cdot KPS \qquad (19)$$

where:

KBG – unavailability costs in [PLN/year],

A_O – operation availability index calculated within RAM analysis (section 7.2.2),

KPS – locomotive's downtime costs in [PLN/hour].

Assuming the yearly costs of locomotive downtime KPS = 35,5 [PLN/hour], the yearly unavailability costs are listed in Table 9.

Table 9. *Unavailability costs for analysed variants*

No	Variant	Locomotive downtime costs KPS [PLN/hour]	Operation availability A_o	Lack of operation availability [PLN/year]
1	SM31 variant 0	35,5	0,8223	55 261,2
2	SM31 variant 1		0,9097	28 081,5

It follows from the analysis that the proposed modernisation variant reduces the unavailability costs by 49,2%, i.e. 27,2 [thousand PLN/year] compared with the non-modernised locomotive.

7.3.7. Costs of environmental charges (KOS)

Costs of environmental charges (KOS) are connected with the charges fixed by the Ministry for the Environment imposed for emissions of hazardous substances in exhaust gases. The amount of charge depends on the indices issued by the Ministry and is proportional do fuel consumption by the locomotive. Table 10 lists charge rates per unit obligatory in 2015.

Considering the fuel consumed, following the calculations in section 7.3.4, the costs of environmental charges have been listed in table 11 for the analysed variants.

It follows from the analysis that the proposed modernisation variant reduces the environmental costs by 5,0% compared with the non-modernised locomotive.

7.4. Analysis of LCC model and presentation of results

The analysis performed using CATLOC software has proved that SM31 locomotive modernisation in the proposed version is fully economically effective. From the calculations it follows that the use of the new electronic programmer and implementation of the new operation characteristic ensures reduction of overall costs of over 2,0 [m PLN] over 25-year operation period, which equal to 10,97% less compared with the non-modernised locomotive. The comparison of overall LCC for the analysed variants over 25-year operation period is illustrated in figure 7.
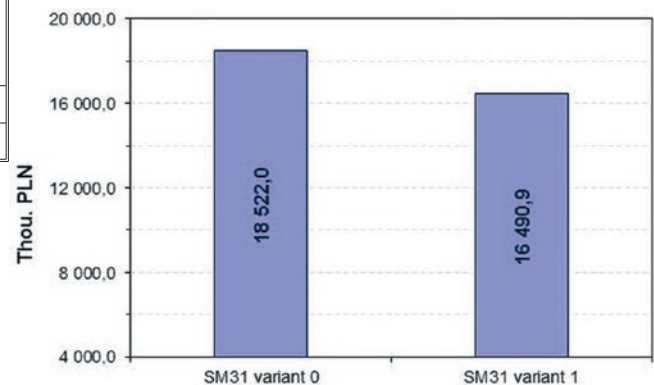

Fig. 7. *Comparison of overall costs (LCC) over 25-year operation period*

Table 10. Charge rates per unit for gases and flue gases emitted to air [45]

No	Emission component	Charge rate per unit [PLN/kg]	Calculation index [g/kg]
1	Sulphur dioxide	0,53	0,028
2	Nitric oxides (recalculated to NO2)	0,53	50
3	Carbon monoxide	0,11	20
4	Aliphatic hydrocarbons	0,11	2,5
5	Aromatic hydrocarbons	1,44	5,5
6	Flue gases	0,35	4,0

Table 11. Costs of environmental charges for analysed variants

No	Variant	Diesel oil consumption [kg/year]	Cost of environmental charges [PLN/year]
1	SM31 variant 0	102 360,8	3 391,1
2	SM31 variant 1	97 242,7	3 221,6

For the non-modernised SM31 locomotive the predominant costs in LCC are those of fuel consumption KZP – 61,2% and preventive maintenance costs KUP – 24,1%. The corrective repairs costs KUB and unavailabilityy costs KBG constitute over 12,9% of the overall costs (Fig. 8a).

For the modernised SM31 locomotive acquisition costs (KN) connected with the expenditure for modernisation are less than 0,5% of overall LCC (Fig. 8b). The major share in LCC is taken by fuel consumption costs (KZP) – 65,3%. The preventive maintenance costs (KUP) are about 25,6% of overall costs, while corrective maintenance costs (KUB) slightly over 2,9%. The most significant savings compared with the non-modernised vehicle are those in fuel consumption costs – 566,8 [thousand PLN]. The considerable cost reduction was achieved owing to the increased reliability and availability of the vehicle. This, in turn, led to the reduction of the corrective maintenance costs, lower costs of preventive servicing and lower costs of unavailability of the vehicle. The overall savings for these categories of costs are 1437,6 [thousand PLN] over the 25-year operation period (table 12).

8. Conclusions

The improvement of efficiency and reliability of SM31 diesel locomotive by the implementation of an optimal operation characteristic with the existing control system requires the use of an electronic regulator. As a result of joint project of the authors of the present article and Lokel and Newag S.A. firms a new electronic regulator of a8C22W engine rotations and power was developed and implemented. The efficiency of the proposed solution as applied in a SM31 locomotive was evaluated on the basis of actual operation data.

To carry out the evaluation a LCC costing method developed at the Institute of Rail Vehicles, Cracow University of Technology, was used. The calculations for a 25-year operation period have proved that the power control system modernisation in SM31 locomotives is cost effective and enable reaching measurable effects at minor financial expenditure. The research and analysis performed are a basis for the undertaking the decision of the locomotive modernization.
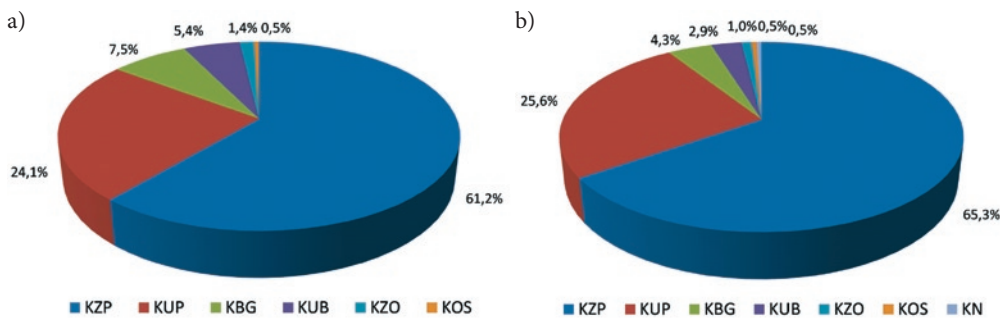

Fig. 8. LCC of analysed study cases: a) variant 0, b) variant 1. KZP – fuel consumption costs, KUP – preventive maintenance costs, KUB – corrective maintenance costs, KBG – unavailability costs, KOS – environmental charges costs, KZO – engine oil consumption costs, KN – acquisition costs

Table 12. Comparison of predominant costs for analysed variants

No	Variant	Fuel consumption costs [thousand PLN]	Preventive maintenance costs [PLN]	Corrective maintenance costs [PLN]	Unavailability costs [PLN]
1	SM31variant 0	11336,5	4454,7	1008,4	1381,5
2	SM31 variant 1	10769,6	4224,7	480,3	702,0

References

1. Augustine N R. Is Life Cycle Cost Costing Lives? Armed Forces Journal International 1978: 110-115.
2. Bååthe O. Life Cycle Management for the A/C JAS 39 Gripen. 11-th Logistics Congress Society of Logistics Engineers, Stockholm 1995.
3. Babeł M. Podstawy teoretyczne i metodologia wyboru zakresów oraz technologii modernizacji lokomotyw spalinowych w oparciu o kryterium kosztów cyklu istnienia. Rozprawa habilitacyjna. Instytut Naukowo-Badawczy Transportu Kolejowego, Moskwa, 2015.
4. Babeł M. Warunki pracy, charakterystyka eksploatacyjna a niezawodność doładowanych trakcyjnych silników spalinowych. Trakcja i wagony 1990; 9: 163-165.
5. Babeł M. Zwiększenie efektywności pracy trakcyjnych silników wysokoprężnych a8C22 na drodze dopasowania charakterystyk obciążenia do warunków eksploatacji. Rozprawa doktorska. Moskiewski Instytut Inżynierów Transportu (MIIT), Moskwa, 1989.
6. Babeł M, Kossov E E. Zwiększenie efektywności pracy lokomotyw spalinowych w eksploatacji na drodze optymalizacji warunków pracy silnika wysokoprężnego z wykorzystaniem elektronicznego regulatora obrotów i mocy. Materiały I Sympozjum Naukowego: Automatyzacja pracy silników wysokoprężnych, Poznań 1992: 69-78.
7. Babeł M, Szkoda M. Poprawa efektywności i niezawodności lokomotyw serii SM31 w wyniku modernizacji układu regulacji mocy. XXI Konferencja Naukowa POJAZDY SZYNOWE 2014, Wojanów, 26-28 maja 2014.

8. Barringer H P, Weber D P. Life Cycle Cost Tutorial. 5-th International Conference on Process Plant Reliability, TX: Gulf Publishing Company, 1996.
9. Barringer H P. A Life Cycle Cost Summary. International Conference of Maintenance Societies, Perth, Australia 2003: 20-23
10. Bianchi G M, Falfari S, Parotto M, Osbat G. Advanced modeling of common rail injector dynamics and comparison with experiments. SAE paper 2003-01-0006.
11. Володин А И. Моделирование на ЭВМ работы тепловозных дизелей. Транспорт, Москва, 1985.
12. Borghagen L, Brinkhagen L. LCC-procurement at the Swedish State Railways. Reliability and Maintainability Symposium 1984. Proceedings Annual IEEE, 1984: 349-358.
13. Chłopek Z. Badania zużycia energii przez samochód elektryczny w warunkach symulujących jazdę w mieście. Eksploatacja i Niezawodnosc – Maintenance and Reliability 2013; 15(1): 75-82.
14. Chłopek Z, Piaseczny L. Uwagi o modelowaniu w badaniach naukowych. Eksploatacja i Niezawodnosc - Maintenance and Reliability 2001; 4(11): 47-57.
15. Chłopek Z. Modelowanie procesów emisji spalin w warunkach eksploatacji trakcyjnej silników spalinowych. Prace Naukowe Seria Mechanika" z. 173. Warszawa: Oficyna Wydawnicza Politechniki Warszawskiej, 1999.
16. CILECCTA: Sustainability within the Construction Sector, Life Cycle Costing and Assessment. CILECCTA project EU 7-th Framework Programme FP7/2007-2013, grant no. 229061, 2013. (www.cileccta.com)
17. Coe C K. Life Cycle Costing by State Governments. Public Administration Review 1981; 41: 564-69, http://dx.doi.org/10.2307/976268.
18. Department of Sport and Recreation, Government of Western Australia: Life Cycle Cost Guidelines Sport and Recreation Facilities, 2005.
19. DoD Guide for Achieving Reliability, Availability and Maintainability. USA Department of Defense, Washington, 2005.
20. Dokumentacja Systemu Utrzymania lokomotywy spalinowej serii SM31 typu 411D. PKP Cargo S.A., 2011.
21. Durairaj S K, Ong S K, Nee A Y C, Tan R B H. Evaluation of Life Cycle Cost Analysis Methodologies. Corporate Environmental Strategy 2002; 9(1): 30-39, http://dx.doi.org/10.1016/S1066-7938(01)00141-5.
22. EN 50126 Railway applications. The specification and demonstration of Reliability, Availability, Maintainability and Safety (RAMS).
23. Fabrycky Wolter J, Blanchard B S. Life-Cycle Cost and Economic Analysis. Prentice Hall, Englewood Cliffs NJ, 1991.
24. Garcıa Marquez F P, Lewis R W, Tobias A M, Roberts C. Life cycle costs for railway condition monitoring. Transportation Research Part E: Logistics and Transportation Review 2008; 44(6): 1175-1187, http://dx.doi.org/10.1016/j.tre.2007.12.003.
25. Guzzella L, Onder Ch. Introduction to modeling and control of internal combustion engine systems. Springer Verlag. 2nd ed., 2010.
26. Hebda M, Janicki D. Trwałość i niezawodność samochodów w eksploatacji. Warszawa: WKiŁ, 1977.
27. Herder P M, van Luijk J A, Bruijnooge J. Industrial application of RAM modeling development and implementation of a RAM simulation model for the Lexan plant at GE Industrial, Plastics. Reliability Engineering & System Safety 2008; 93(4): 501-508.
28. Hokstad P. Life Cycle Cost Analysis in Railway Systems. SINTEF Safety and Reliability, 1998.
29. Jackson Y, Tabbagh P, Gibson P, Seglie E. The new Department of Defense (DoD) guide for achieving and assessing RAM. Reliability and Maintainability Symposium 2005. Proceedings Annual IEEE, 2005: 1-7.
30. Kawauchi Y, Rausand M. Life Cycle Cost (LCC) analysis in oil and chemical process industries. Norwegian University of Science and Technology 1999.
31. Kossov E E, Babeł M. Zagadnienia modelowania eksploatacyjnych warunków pracy trakcyjnych silników spalinowych. Silniki spalinowe 1988; 2: 27-31.
32. Коссов Е Е, Нестрахов А С, Аникиев И П, Бычков Д А. Микропроцессорная система регулирования дизель - генератора. Локомотив 2002; 12: 14-15.
33. Коссов Е Е, Сухопаров С И. Оптимизация режимов работы тепловозных дизель-генераторов. Труды ВНИИЖТ. Интекст. Москва 1999.
34. Lamar W E. Review and Assessment of System Cost Reduction Activities. Proceedings NATO AGARD Conference on Design to Cost and Life Cycle Cost, 12-22 May, 1980.
35. Lynch J P, Karlaftis M G, Sinha K C, Fricker J D. The Indiana Public Transportation Management System. Report No. CE-TRA-95-1, Purdue University, 1995.
36. Ma H, Xu H M, Wang J H. Real-time control oriented HCCI engine cycle-to-cycle dynamic modelling. International Journal of Automation and Computing 2011; 8(3): 317-325, http://dx.doi.org/10.1007/s11633-011-0587-z.
37. Manzini R, Regattieri A, Pham H, Ferrari E. Maintenance for Industrial Systems. Springer, 2010.
38. Martorell S, Villanueva J F, Carlos S, Nebot Y, Sanchez A, Pitarch J L, Serradell V. RAMS+C informed decision-making with application to multi-objective optimization of technical specifications and maintenance using genetic algorithms. Reliability Engineering & System Safety 2005; 87(1): 65-75, http://dx.doi.org/10.1016/j.ress.2004.04.009.
39. MIL-HDBK-259 Military Handbook, Life Cycle Cost in Navy Acquisitions. Global Engineering Documents 1983.
40. MIL-HDBK-276-1 Military Handbook, Life Cycle Cost Model for Defense Material Systems, Data Collection Workbook. Global Engineering Documents 1984.
41. MIL-HDBK-276-2 Military Handbook, Life Cycle cost Model for Defense Material Systems Operating Instructions. Global Engineering Documents 1984.
42. Navarro-Galera A, Ortúzar-Maturana R I, Mu-oz-Leiva F. The application of life cycle costing in evaluating military investments: An empirical study at an international scale. Defence and Peace Economics 2011; 22(5): 509-543, http://dx.doi.org/10.1080/10242694.2010.508573.
43. NCHRP: Bridge Life-Cycle Cost Analysis. Report No 483. Washington DC: Transportation Research Board of the National Academies, 2003.
44. O'Connor P. Practical Reliability Engineering. John Wiley & Sons Ltd., 2010.
45. Obwieszczenie Ministra Środowiska z dnia 11 sierpnia 2014 r. w sprawie wysokości stawek opłat za korzystanie ze środowiska na rok 2015. Monitor Polski, 18.09.2014 r., poz. 790.
46. Parra C, Crespo A, Kristjanpoller F, Viveros P. Stochastic model of reliability for use in the evaluation of the economic impact of a failure using life cycle cost analysis. Case studies on the rail freight and oil industries. Proceedings of the Institution of Mechanical Engineers, Part O: Journal of Risk and Reliability 2012; 226(4): 392-405.

47. PN-EN 60300-3-3 Zarządzanie niezawodnością. Przewodnik zastosowań - Szacowanie kosztu cyklu życia.
48. PN-EN 61703 Wyrażenia matematyczne dotyczące nieuszkadzalności, gotowości, obsługiwalności i zapewnienia środków obsługi.
49. Reiger A J. Solar Energy: The Market Realities. Real Estate Review 1979; 8: 49-52.
50. Senthil Kumaran D, Ong S K. Environmental life cycle cost analysis of products. Environmental Management and Health 2001; 12(3): 260-267, http://dx.doi.org/10.1108/09566160110392335.
51. Sharma R K, Kumar D, Kumar P. Performance modeling in critical engineering systems using RAM analysis. Reliability Engineering & System Safety 2008; 93(6): 891-897, http://dx.doi.org/10.1016/j.ress.2007.03.039.
52. Sherif Y S, Kolarik W J. Life cycle costing: concept and practice. Omega 1981; 9(3): 287-296, http://dx.doi.org/10.1016/0305-0483(81)90035-9.
53. Smith D J. Reliability, Maintainability and Risk: Practical Methods for Engineers. Butterworth-Heinemann, 2011.
54. Strategia odnowy parku lokomotyw w przedsiębiorstwie PKP LHS Sp. z o. o. Projekt nr M8/599/2007. Politechnika Krakowska Instytut Pojazdów Szynowych, Kraków, 2007.
55. Studium techniczno-ekonomiczne odnowy parku pojazdów trakcyjnych eksploatowanych przez PKP CARGO S.A. Projekt nr M8/631/2006. Politechnika Krakowska Instytut Pojazdów Szynowych, Kraków, 2006.
56. Szkoda M, Babeł M, Kossov E E. Анализ стоимости жизненного цикла (LCC) при оценке эффективности подвижного состава. Вестник ВНИИЖТ 2013; 6: 55-59.
57. Szkoda M. Assessment of Reliability, Availability and Maintainability of Rail Gauge Change Systems. Eksploatacja i Niezawodnosc - Maintenance and Reliability 2014; 16(3): 422-432.
58. Szkoda M. Ocena efektywności ekonomicznej środków transportu szynowego z zastosowaniem analizy LCC. TTS Technika Transportu Szynowego 2012; 11-12: 64-69.
59. ten Wolde M, Ghobbar A A. Optimizing inspection intervals - Reliability and availability in terms of a cost model: A case study on railway carriers. Reliability Engineering & System Safety 2013; 114: 137-147, http://dx.doi.org/10.1016/j.ress.2012.12.013.
60. Watson N. Transient performance simulation and analysis of turbocharged diesel engines. No 810338. SAE Technical Paper 1981: 1-19.
61. Wendeker M, Godula A. Research on variability in control parameters for spark ignition engines in real-life operation. Eksploatacja i Niezawodnosc – Maintenance and Reliability 2002; 16(4): 12-23.
62. Zellbeck H, Woschni G. Rechnerische Untersuchung des dynamischen Betriebs-verhaltens aufgeladener Dieselmotor. MTZ 1983; 3: 81-86.
63. Zoeteman A. Asset maintenance management: state of the art in the European railways. International Journal of Critical Infrastructures 2006; 2(2/3): 171-186.

Marek BABEŁ
Maciej SZKODA
Cracow University of Technology
Faculty of Mechanical Engineering
Institute of Rail Vehicles
ul. Jana Pawla II 37, 31-864 Krakow, Poland
E-mail: babel@mech.pk.edu.pl; maciej.szkoda@mech.pk.edu.pl

Zofia M. ŁABĘDA-GRUDZIAK

DIAGNOSTIC TECHNIQUE BASED ON ADDITIVE MODELS IN THE TASKS OF THE ONGOING EXPLOITATION OF GAS NETWORK

TECHNIKA DIAGNOSTYKI OPARTA NA ADDYTYWNYCH MODELACH REGRESYJNYCH W ZADANIACH BIEŻĄCEJ EKSPLOATACJI SIECI GAZOWEJ*

The article presents a method of estimating the pressure value at given nodes of natural gas transmission network for the purposes of predicting changes of the process state during its exploitation. For this purpose additive regression model was applied together with non-parametric estimation techniques, which was used for monitoring the operation of gas networks, as well as designing the system of fault detection, and then – the assessment of sensitivity for particular faults. Research was conducted on the basis of data from the analytical model of network simulator, which is adjusted to the actual gas transmission network.

Keywords: *fault detection, additive model, identification, exploitation, gas transmission network.*

W artykule przedstawiono metodę oszacowania wartości ciśnienia w określonych punktach węzłowych sieci przesyłowej gazu ziemnego dla potrzeb przewidywania zmiany stanu procesu w trakcie jego eksploatacji. W tym celu wykorzystano addytywny model regresji wraz z nieparametrycznymi technikami estymacji, który posłużył zarówno do monitorowania pracy sieci gazowej, jak i do konstrukcji układu detekcji uszkodzeń, a następnie do oceny wrażliwości na występowanie poszczególnych uszkodzeń. Badania przeprowadzono na podstawie danych z modelu analitycznego symulatora sieci, który dostrojony jest do rzeczywistej sieci przesyłowej gazu.

Słowa kluczowe: *detekcja uszkodzeń, addytywny model regresji, identyfikacja, eksploatacja, sieci przesyłowe gazu.*

1. Introduction

In extensive fittings used for transporting large quantities of gas under high pressure for long distances, monitoring of the fittings condition becomes a significant problem, in respect of correct functioning of the measuring devices, as well as the occurrence of possible leakage. Exploitation of gas network requires periodic tightness controls and elimination of faults and leaks. When a leak is discovered in the gas pipeline, it undergoes repair work, which is conducted after shutting down a certain section of the network by shut-off valves or temporary closure. Works on active gas pipelines are considered hazardous and must be performed by qualified teams.

Difficult conditions of exploitation are placing increasingly high demands on long duration and high degree of reliability of control systems. Due to flammability, any breakdowns causing unsealing of the fittings and gas effusion pose a risk of explosion and environmental contamination. These risks may be eliminated by current detection which enables prediction of the possible necessity of switching off pumping or excluding the leaky section of the pipeline.

In the current exploitation of gas networks a number of solutions can be used allowing for monitoring and diagnostics, with particular consideration of leakage detection. The methods of detection of transmission networks can be divided into two general categories [2, 11, 21]: direct (external), when the detection is conducted from the outside of the pipe by applying specialized devices and visual observation, and indirect (internal), when the detection is based on the measurements and analysis of parameters of flow process, such as pressure, flow, temperature. Among the direct methods we can differentiate acoustic methods [12], which are based on the detection of noise generated by a leak and require installing acoustic sensors along

the pipeline. Indirect methods are divided into methods based on detecting sound waves caused by effusion, methods based on balancing the medium inflowing to- and outflowing from the pipeline and analytical methods based on mathematical model and measuring data of the object, obtained from telemetric system [7, 8, 17, 22].

Natural gas is a viscous and compressible gas, the physicochemical parameters of which are strongly dependent on pressure and temperature conditions. For description of such a medium, application of complicated equations of state is necessary, such as virial or cubic equations of state of the gas [5, 23]. The dynamics of elementary section of the gas pipeline can also be described by partial differential equations system [7, 17], which can be derived from mass and momentum conservation principles and solved by explicit or implicit methods.

Optimization algorithms based on neural networks or swarm intelligence [1, 9, 16] can also be applied for the analysis of work of certain sections of transmission network. It is a technique of artificial intelligence based on the observation of social behavior in organized populations. To identify whether there is a leakage or not, a support vector machine (SVM) can be used, i.e. the algorithm identifying the relationship between the elements (measurement results, in this case) on the basis of the examples – sets of training data, comprising cases with and without a leakage [3].

Direct methods require vast experience from the operator of the device, thus fault detection services are each time contracted to specialized companies. On the other hand, indirect methods, in which the expert (company employee) observes network parameters and detect anomalies, have a number of disadvantages, significantly decreasing their value. First of all, the system doesn't indicate faults automatically what demands continuous attention of an expert. On the other hand,

the most technologically advanced solutions are based on a simulation model of gas transmission network and are the most complex at the same time.

2. Research methodology

It is extremely difficult to formulate a model on the basis of physical equation for such object as gas network, and identification of its parameters provides additional complications. It is not always possible to reconstruct geometric dimensions or roughness for old pipelines, which are hard to identify and locate. Moreover, gas pipelines are very diverse objects, in terms of daily and annual values of volume flow, what makes application of the above mentioned methods highly difficult. On the other hand, increasing the number of the process entries violently increases calculating inputs in neural modeling.

The paper presents alternative technique, which overcomes the limitations connected with non-linear multidimensional modeling. These are additive models [4]. The method of identification based on additive model is a new approach in the diagnostics of industrial processes and was presented in the Author's works published, among others, in [13, 15, 20] positions of Bibliography.

The aim of this paper is to develop effective methods of signal pressure modeling at certain nodes of gas transmission network for the purposes of fault detection. The model is intended to provide reproduction of measuring signals and to be used to calculate the residuals. The main assumption is a possibility to develop fault detection algorithms with the use of additive model, estimated on the basis of archive process data.

In the course of research the following research problems were formulated, related to the chosen process of fault detection:

- **Uncertainty and incompleteness of knowledge on the diagnosed object.** Detection methods based on object models require the possession of archive or simulation sets of measuring signals, related to the operation of the diagnosed object. Such sets are often subject to inaccuracies, errors, shortages and interferences. In order to create the correct model on the basis of uncertain measuring data, data mining methods were used as preliminary data processing in the form of cleaning/converting data.
- **High complexity of the diagnosed object.** Due to the dynamic nature of the phenomena occurring in the gas pipelines, the choice of the appropriate structure of the model of object diagnosis has significant impact on the accuracy of identification. Adopting oversimplified or excessively complicated model may influence the reliability of diagnostic system in an unfavorable way. It is necessary to compare models with different structure and complexity. In general, a model with a higher number of predictors gives more accurate prediction, however it is also more prone to over-training. In order to compare the quality of two or more models, expert knowledge was used, as well as final prediction error (FPE) test and Akaike information criterion (AIC), which measure of goodness of fit of the model to measuring data, considering the number of parameters.
- **Accuracy and generalization properties of the model.** Implementation of fault detection system requires correct model of diagnosed object. Such model has to be accurate so as to allow for proper estimation of the process outlet, and on the other hand – allowing for prediction resistant to interferences and measurement noises. The paper investigates the use of non-parametric estimation techniques – locally polynomial smoothers and natural cubic spline. These methods have single smoothing parameters controlling the "smoothness" of the estimator of regression function and their values are usually selected by generalized cross-validation (GCV) criterion, de-

grees of freedom (*df*), which is equal to the number of basic functions of a smoothing function, or by determining bandwidth (*span*), which is the proportion of data used in each local fit. Choosing the right technique and smoothing parameter allows for reducing the problem of over-fitting of the model to the learning data, thus increasing its generalization properties for the test data.

- **Uncertainty connected with the inaccuracy of the model, the influence of non-measurable interferences and noises.** Regardless of the applied identification technique, there is always the problem of model uncertainty, i.e. the difference between the behavior of the model and the system. This leads to the necessity of constructing the fault detection systems, which are robust to model inaccuracy, the influence of non-measurable interferences and noises. The quality of the detection system depends, to a great degree, on its decision-making part. In the research we used fixed thresholds imposed on the residual signal. Robustness was performed with the use of statistical characteristics of residuals.
- Below, the essence of the proposed method is presented in respect to the conducted research.

3. Additive regression model

Considering the MISO (Multiple Input, Single Output) system with $p > 1$ input signals $X_1, X_2, ..., X_p$, and one output signal Y, the additive model is defined by:

$$Y = \alpha + \sum_{j=1}^{p} \phi_j(X_j) + \varepsilon, \tag{1}$$

where α is some constant, error ε is a sequence of independent of $(X_1, X_2, ..., X_p)$ and identically distributed random variables with the mean $\mathrm{E}(\varepsilon) = 0$ and the finite variance $\mathrm{Var}(\varepsilon) = \sigma^2$. The ϕ_j s are arbitrary univariate functions one for each predictor X_j and not necessarily linear. We do not assume monotonic properties nor analytical forms of the functions ϕ_j. The additive model can be nonlinear in relation to X_j but still is linear with respect to $\phi_j(X_j)$. Let us point that we do not assume that the variables X_j are independent [6]. Hence, the use of lines delaying X_j signals ensures dynamic properties of the model (1) and leads to the increase of the robustness of the model (thus the increase of robustness of the fault detection system) to the influence of impulse interferences affecting measuring signals.

For a pair $\{(x_i, y_i)\}_{i=1}^{n}$ of a random sample, where $x_i = \{x_{ij}\}_{j=1}^{p}$, the additive model can be estimated by minimization of the residual sum of squares:

$$\arg\min_{\{\alpha, \phi_j\}} \sum_{i=1}^{n} (y_i - \alpha - \sum_{j=1}^{p} \phi_j(x_{ij}))^2, \tag{2}$$

which finds the value of parameter α, equals $\hat{\alpha}$ and the set of one dimensional functions $\hat{\phi}_j(\cdot)$. Thus, we avoid the necessity of estimation in the multidimensional space.

For higher flexibility, relations ϕ_j between output signal and input signals are fitted with the use of nonparametric smoothing techniques such as: locally linear smoothers or natural cubic splines [6, 13]. In

order to estimate additive model, we applied backfitting algorithm, which, when fulfilling certain assumptions, converges to the unique solution, independent of the starting functions [6].

3.1. Evaluation of process model and verification rules

Verification of the model is a procedure aiming at verifying the quality of the evaluated model, in fact it is specifying the type of error performed by the model while imitating the behavior of true process. The use of the specified model for simulation of output signal for the test data set is an objective evaluation of the process model.

Application of additive model of pressure distribution in the gas network requires its calibration, which takes place off-line on the basis of archive data, with the assumption that data have been recorded in the period when no faults occurred. A properly calibrated model has predictive properties allowing for achieving sufficiently close representation of the actual system under diverse conditions. In order to verify the quality of the estimated model, the mean squared error (MSE), mean absolute deviation error ($MADE$), mean absolute percentage error in relation to range of measured output signal ($MAPE$) and variance of errors (VAR) were obtained.

4. Fault diagnosis

A significant problem encountered by each pipeline operator is safe exploitation. With time, processes occurring in different parts of the construction with different intensity, change exploitation parameters of the pipeline. A lot of information can be provided by periodic inspections, regardless of the actual technical condition of the pipeline. On this basis operator may decide on possible repair or renovation of the pipeline, and in extreme case – on the replacement of a section or a whole pipeline. In the majority of cases, the service is not necessary as technical condition of the pipeline is good.

Present-day control and monitoring systems of industrial processes more and more often implement highly advanced functions related to diagnostics of process and automatic control devices. Such supervision over the object consists in making use of the model as the source of information on standard course of the processes, which enables noticing early symptoms of unfavorable changes in the object, as well as support the operators of the process in securing the object.

Diagnostics of technical object consists in carrying out a series of operations, which result in detecting, localizing and identifying possible faults. This article undertakes the issues of the first stage of diagnostic proceeding, i.e. fault detection – identifying prohibited deviations from the normal behaviour in the plant or its instrumentation like sensors and actuators [10]. The continuation of this research will be designing algorithms of fault localization.

4.1. Fault detection system

Fault detection aims at noticing faults in the object and specifying the moment of detection through the realization of diagnostic tests. A set of tests is automatically performed by the computer and should be suited in such a way to enable detecting all faults that may occur during exploitation of the industrial object. A negative test result is a symptom of abnormal state, e.g. a fault.

On the basis of additive model we are able to calculate pressure distribution in the network according to known values of accessible measurement variables, measured in actual network, and then to monitor the differences (the so-called residuals r) between the values of pressure measured in the actual network and those estimated with the use of additive model. The general scheme of generating the residuals with the use of additive model is presented in Figure 1.

For the majority of normal states of gas network operation, acknowledging veracity of the model, the residuals should be close to 0, and after the occurrence of fault their values should start to differ
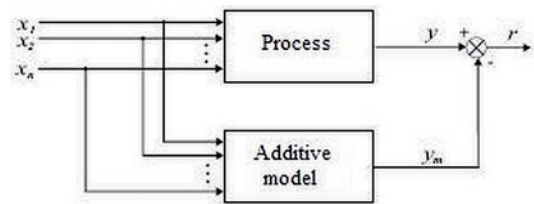

Fig. 1. The scheme of generating the residuals with the use of additive model.

from 0. Having residuals generated by the additive model, there is a need to design decision algorithm, on the basis of which the evaluation of residuals value will take place, and the decision on detecting the symptom of fault will be made.

In the research we applied the simplest decision algorithm, which compares the values of residuals with the threshold values. Fault symptom is detected in t time if the diagnostic signal takes on value equal to 1, i.e. when the threshold value has been crossed by the residual. The threshold values are calculated with the use of statistical data describing the residuals values in normal operating conditions. It has to be emphasized that a possibility of generating false symptoms depends on the selected thresholds size as the acceptance region of the residual values and time interval, on the basis of which a decision is made. When the limits are too low, the algorithms generate a lot of false alarms, and when the limits are too high – detection is significantly delayed.

4.2. Indicators of detection quality

The above scheme of fault detection is based on idealized assumptions that the model is a faithful copy of the system and perfectly represents its dynamics, as well as that noises and interferences in the system are known. These assumptions obviously cannot be fulfilled in practice. In terms of fault detection robustness can be defined as maximizing fault detection with simultaneous minimization of undesirable effects such as interferences, measurement noises, changes in input signals and system states.

In order to verify the quality of the proposed detection algorithm the following indicators of diagnosis quality were applied in the research:

- t_{dt} – detection time, which is measured from the beginning of simulation of the fault to the moment of its symptom occurrence
- θ_{fd} – the degree of false detection, the value of which provides information on the number of false alarms
- θ_{td} – the degree of correct detection, the value of which provides information on the effectiveness of fault detection.

It has to be taken into account that the values of indicators of detection quality are strictly dependent on the set of process variables fully reflecting functioning of the object and the choice of threshold values of the algorithm.

5. The object of diagnosis – a part of gas pipeline Warsaw-Białystok

Due to the inability to realize actual faults, research was conducted on the basis of data from gas network simulator adjusted to actual gas network located at the vast area of Poland. The simulator was designed on the basis of analytical models in the system of advanced monitoring and diagnostics (AMandD) [18, 19] in the Institute of Automatic Control and Robotics, Warsaw University of Technology.

This work was partially realized within a framework of a research and development project entitled "Research on the systems of detection and localization of gas pipelines leak", no OR00 0013 06 [14, 20, 22]. Verification tests were conducted with the use of R-project program, intended for advanced statistical calculations [4].

5.1. Description of the analyzed part of gas pipeline

The fragment of the gas network used for the research comprises a part of actual gas pipeline Warsaw-Białystok, from Wólka Radzymińska entrance station to all points of consumption supplied from this station, i.e. none of the sections conducts gas outside the monitored area (Figure 2). This gas pipeline is relatively well metered and is very typical for national network, as it contains numerous branches and collection points equipped with reduction-measurement stations.

Within research, parts of network were selected, for which additive partial models were prepared. Further, we specified the standard faults later used for testing detection algorithms, created the sets of learning and testing data, acknowledging simulation of the chosen faults.

5.2. The use of additive models

Diagnostics of the process with the use of additive partial models requires preparing models of small parts of the network, locally reacting for faults and covering the whole modeled object with it range. In the conducted research, we analyzed the possibility of application of additive models $ADD_{Name\_of\_the\_node}$ with different structure, rendering pressure values in particular nodes of the industrial gas network. Due to the lack of flow measurement (measurements of consumption flow in particular nodes are available only) we decided to use the value of pressure in the surrounding points of consumption and estimated flow of gas. The estimated flow is calculated on the basis of accumulated sum of consumptions from points located behind the analyzed fragment, taking into account the dynamics of the change of volume of gas accumulated in the pipeline [18]. In order to assess usability of additive models in fault detection of a gas pipeline, faults were simulated, such as leakage and malfunction of pressure measurement sensor in 2 chosen locations of the pipeline (Figure 2).

In order to achieve greater flexibility in estimating additive models, we conducted comparative analysis of the 2 alternative smoothing methods – natural cubic spline and locally polynomial smoother. Research showed that the most favorable results of identification were obtained by the former with *df*=4 parameter, or alternatively by local linear smoother with *span*=0.55 parameter. It has to be stressed that the choice of technique and smoothing parameter also influences the quality of fault detec-
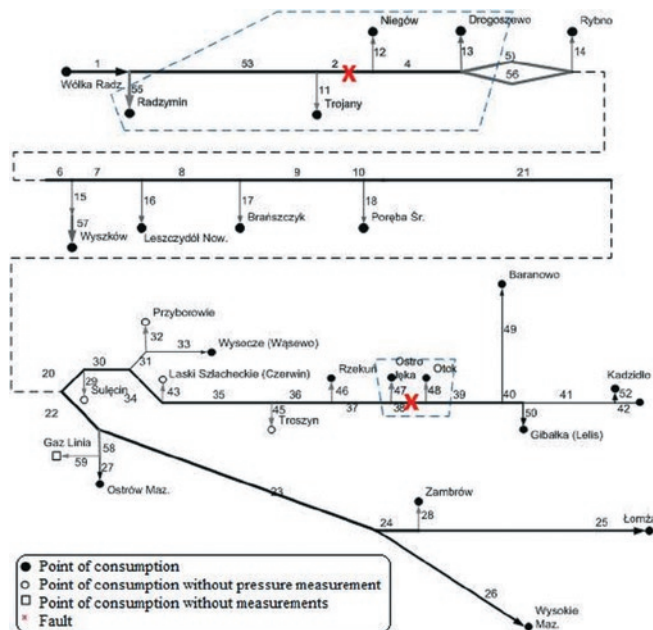
tion. In this paper, the results were presented for natural cubic spline with a parameter specifying the number of degrees of freedom of the smoothing function.

By applying backfitting algorithm, the models of particular nodes were able to be estimated. On the basis of learning data from the up state of the process, we achieved estimated values of gas pressure (Pwe prediction) together with actual values of gas pressure with process data (Pwe), as well as corresponding residuals. Below, exemplary results of modeling for Ostrołęka node are presented. Figures 3 and 4 show signal rendering, as well as residuals and histogram of residuals normalized to the range [−1, 1].
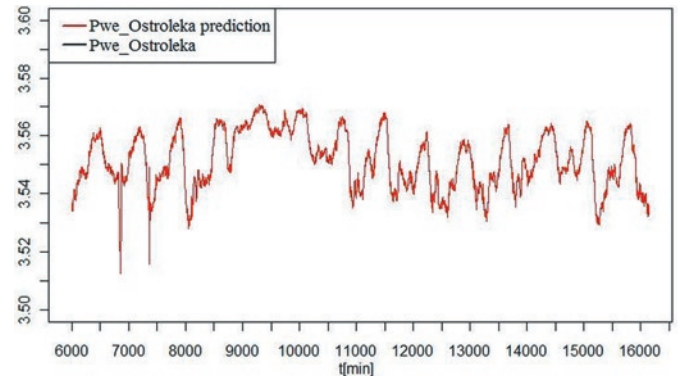

Fig. 3. Pwe_Ostroleka signal rendering on the basis of learning sample for ADD_{Ostr} model.
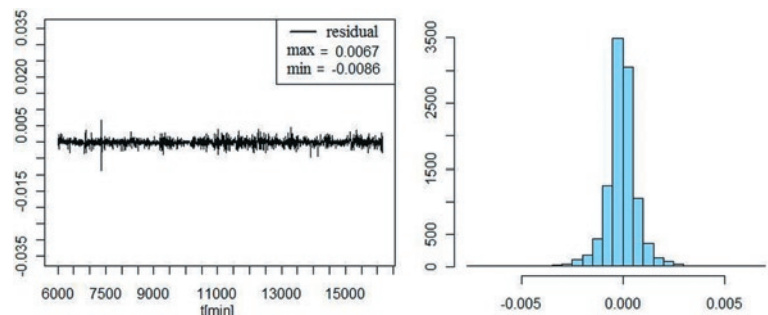
Fig. 4. Course and histogram of residuals on the basis of learning sample for ADD_{Ostr} model.

In order to check the quality of the estimated models, the values of different goodness-of-fit measures were calculated. Results for exemplary additive models ADD_{Troj}, ADD_{Nieg} and ADD_{Ostr} are presented in Table 1.

Table 1. The goodness-of-fit of additive models.

Model	MSE	MADE	MAPE	VAR
ADD_{Troj}	3e−06	2e−05	0.0423%	2e−06
ADD_{Nieg}	2e−06	1.4e−05	0.0254%	1e−06
ADD_{Ostr}	2e−06	3e−05	0.0513%	1e−06

The obtained results are satisfactory. Partial models accurately reflect the dynamics of the process, due to the use of inputs delayed by 1 and 2 sampling steps. The results of modeling almost perfectly follow the simulated process, what confirms the lack of significant deviation from null value, except for a single outliers. *MADE* and *MAPE* errors for particular models don't exceed the value of 3e-05 and 0.06% of the variability range of the process output, respectively.

For verification of detection algorithms 2 leaks and 2 malfunctions of pressure sensors were used, while different levels of fault extension were introduced in order to check general change of models sensitivity. Description of faults is presented in Table 2.

Fig. 2. Gas pipeline scheme. Crosses indicate the places of simulated leakage.

Table 2. *Chosen scenarios of fault simulation*

Name of the fault	Description of the fault	Symbol	Value
Leakage 1	Halfway through Trojany and Niegów stations (nominal flow of about 6000 m^3/h)	f_1	500 m^3/h
		f_2	1000 m^3/h
Leakage 2	Halfway through Ostrołęka and Otok stations (nominal flow of about 600 m^3/h)	f_3	150 m^3/h
		f_4	300 m^3/h
Pressure 1	Niegów station (current value)	f_5	-2%
		f_6	-5%
		f_7	-10%
Pressure 2	Otok station (current value)	f_8	+2%
		f_9	+5%
		f_{10}	+10%

Detailed plots of the chosen scenarios simulating appropriately nominal f_0 working conditions and particular faults and the corre-

absolute values of residuals were achieved for faults such as pressure jump in the pipeline station. All local models detect faults very well in all tested localizations. In the case of leakage simulation the reaction of residual (at such a high level of leakage) is noticeable, but significantly smaller. As an example, sensitivity of ADD$_{Troj}$ model for f_1 leakage is 0.96% of variability range of the measured value, and ADD$_{Nieg}$ model – 0.37%, actually at the level of about 25% of calculating errors of the model for testing sample.
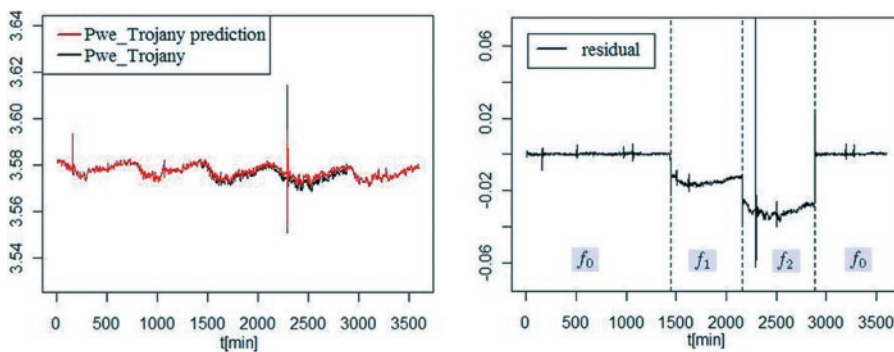
The values of indicator of θ_{td} true detection for decision algorithm based on particular additive models are compiled in Tables 3–4.

Table 3. θ_{td} *indicator of the quality of f_1 - f_4 faults detection*

Model	Faults			
	f_1	f_2	f_3	f_4
ADD$_{Troj}$	0.9972	1	0.0112	0.7878
ADD$_{Nieg}$	1e-05	0.0083	0.0153	0.8641
ADD$_{Ostr}$	1e-05	0.0069	0.0014	0.0194

In the above tables the values of indicators of true detection, which were the highest among particular models are marked in red. The values of θ_{td} indicator were very high, and the rate of t_{dt} detection time – about 1-2 minutes. Moreover, the highest values of θ_{td} false detection factor in particular test samples were 0.5%. It results mostly from some defects of thresholding methods. When analyzing residual signal recorded during the operation of gas pipeline in nominal conditions (Figure 5 and 6) we can observe that in some time intervals there are significant deviations of residual signal from null value (momentary fault symptoms). Such deviations, caused by interferences or modeling errors may result in false alarms.

Fig. 5. *Pressure distribution in the network (Pwe_Trojany), residuals under nominal conditions and the occurrence of f_1 and f_2 faults*

6. Conclusions

The paper presents an effective solution allowing for modeling and prediction of pressure distribution in precisely determined nodes of gas network with the use of additive model for the purposes of fault detection. This is a new approach in industrial processes diagnostics, which expands the possibilities in the field of dynamic approximation and multidimensional non-linear objects. Basic objective of the prepared fault detection algorithms was fulfilling requirements resulting from the specificity of process diagnostics, presented in section 2.

The proposed additive models are a favorable approach to process identification issues. They avoid problems of dimensionality, because the regression function is modeled by the sum of the functions of particular input signals. They allow for constructing non-linear process models on the basis of expert knowledge and with the use of measuring data, available from

Fig. 6. *Pressure distribution in the network (Pwe_Niegow), residuals in nominal conditions and the occurrence of f_1 and f_2 faults*

sponding plots of the residual values are presented in Figures 5–9.

It can be stated on the basis of the above residuals that we obtained very good detection of measuring circuits faults – the highest

contemporary automatic control systems. At the same time, it needs to be stated that the accuracy of the model describing gas pressure distribution in the network and the quality of the introduced data (learn-
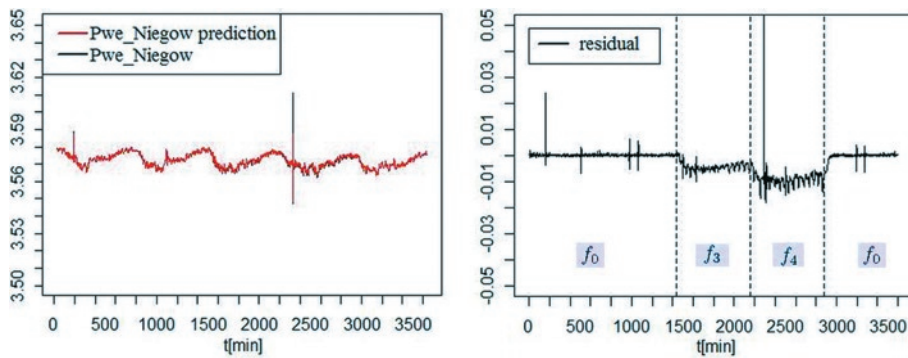
Fig. 7. Pressure distribution in the network (Pwe_Niegow), residuals in nominal conditions and the occurrence of f_3 and f_4 faults
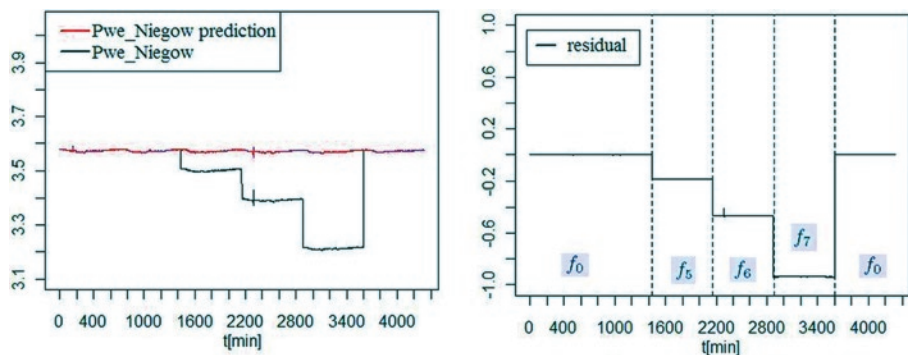

Fig. 8. Pressure distribution in the network (Pwe_Niegow), residuals in nominal conditions and the occurrence of f_5, f_6 and f_7 faults

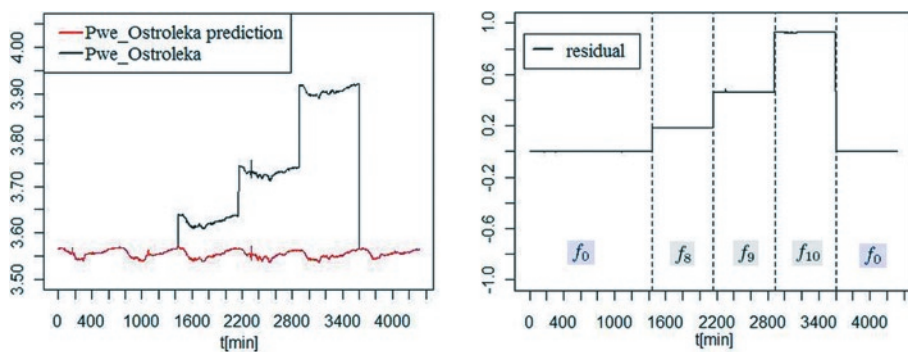*Fig. 9. Pressure distribution in the network (Pwe_Ostroleka), residuals in nominal conditions and the occurrence of f_8, f_9 and f_{10} faults*

Table 4. θ_{td} indicator of the quality of f_5 – f_{10} faults detection

Model	Faults					
	f_5	f_6	f_7	f_8	f_9	f_{10}
ADD$_{Troj}$	1e-04	0.0083	0.0014	0.0014	0.0111	0.028
ADD$_{Nieg}$	1	1	0.9958	1e-05	0.0027	1e-05
ADD$_{Ostr}$	1e-05	0.0083	1e-05	1	1	0.9958

ing data, comprising a whole range of signals variability) were significant factors influencing the quality of process identification and thus the quality of fault detection. Moreover, additive models possess simple structure and low grade, what considerably shorten the time of their learning. They don't demand adapting assumptions on the form of functions linking input and output signals, hence the use of non-parametric methods of estimation enabling identification of non-linear processes in a situation where initial information is so sparse that parametric methods cannot be effectively applied.

The accuracy of additive models obtained in the phase of identification was high and sufficient to be used in detection algorithms. The majority of verified models are of high sensitivity towards pressure measuring circuits faults. Faults of 2% of the measured value can be effectively detected. The usability of partial models for leakage detection is much lower than towards the faults of pressure measuring circuits. Leak detection of quite large size is possible behind the modeled section. At the same time, constructed models are hardly sensitive for faults in the form of small leakages. Generally, sensitivity of residuals for gas leakage is much higher with the use of those nodes of network, which are located near the leakage (just in front of).

Due to high compressibility of gas, which makes the pressures in the pipeline much less sensitive for gas leakage (variation of pressures in the situation of leak is inconsiderable) and variable gas flow, which is a function of gas demand, which the supplier doesn't have impact on, the values of residuals differentiated from the models of pressure distribution in the network will change. Hence, the diagnostics of gas transmission network is much more complicated than diagnostics of liquid conducting pipelines.

To sum up, we can state that additive models are a more favorable approach to fault detection issues. They avoid the problems of non-linear dynamic modeling and don't require large calculating inputs, what create good prospects for future applications of these models in the issues of fault location. However, it needs to be emphasized that additive model is almost always an approximation of the true regression surface, but nevertheless it retains high prognostic usability.

References

1. Ahmad A, Abd. Hamid M. K. Pipeline Leak Detection System in a Palm Oil Fractionation Plant Using Artificial Neural Network. Proceedings of the International Conference on Chemical and Bioprocess Engineering 2003, Kota Kanibalu.
2. Bilman L, Isermann R. Leak detection methods for pipelines. Automatica 1987; 23(3): 381-385, http://dx.doi.org/10.1016/0005-1098(87)90011-2.

3. Chen H, Ye H, Su H. Application of support vector machine learning to leak detection and location in pipelines. Proceedings of the 21st IEEE Instrumentation and Measurement Technology Conference 2004; 3.

4. Good P I. Introduction to statistics through reasampling methods and R/S-PLUS. Wiley, 2005, http://dx.doi.org/10.1002/9780471722502.

5. Gregorowicz J, Warowny W. Równania stanu w przemyśle naftowym i gazowniczym. Nafta - Gaz 1998; 54: 15-23.

6. Hastie T, Tibshirani R. Generalized additive models. Chapman and Hall, 1990.

7. Hauge E, Aamo O M, Godhavn J M (2009): Model based pipeline monitoring with leak detection, SPE Projects, Facilities & Construction 2009; 4(3): 53-60, http://dx.doi.org/10.2118/114218-PA.

8. Jin H, Hang L, Liang W, Ding Q. Integrated leakage detection and localization model for gas pipelines based on the acoustic wave method. Journal of Loss Prevention in the Process Industries 2014; 27(1): 74-88, http://dx.doi.org/10.1016/j.jlp.2013.11.006.

9. Kogut K. Możliwości wykorzystania sztucznych sieci neuronowych w analizie pracy sieci przesyłowej gazu ziemnego. Nowoczesne Gazownictwo 2004; 3: 1-4.

10. Kościelny J M. Diagnostyka zautomatyzowanych procesów przemysłowych. Warszawa: Akadem. Oficyna Wyd. EXIT, 2001.

11. Kowalczuk Z, Gunawickrama K. Detekcja i lokalizacja wycieków w rurociągach Przemysłowych; rozdział 21 pracy zbiorowej pod red. J. Korbicza i J. Kościelnego. Warszawa: WNT, 2002.

12. Liang W, Hang L, Xu Q, Yan C. Gas pipeline leakage detection based on acoustic technology. Engineering Failure Analysis 2013; 31: 1-7, http://dx.doi.org/10.1016/j.engfailanal.2012.10.020.

13. Łabęda-Grudziak Z M. Identification of dynamic system additive models by KDD methods. Pomiary Automatyka Kontrola 2010; 57(3): 249-252.

14. Łabęda-Grudziak Z M. Identyfikacja i symulacja rozkładu ciśnienia w sieciach gazowych z wykorzystaniem addytywnego modelu regresji. Pomiary Automatyka Robotyka 2010; 11: 60-64.

15. Łabęda-Grudziak Z M. Smoothing parameters selection in the additive regression models approach for the fault detection scheme. Pomiary Automatyka Kontrola 2010; 57(2): 197-200.

16. Neuroth M, MacConnell P, Stronach F, Vampllew P. Improved modeling and control of oil and gas transport facility operations using artificial intelligence. Knowledge-Based Systems 2000; 13: 81-92, http://dx.doi.org/10.1016/S0950-7051(00)00049-6.

17. Osiadacz A J. Simulation and Analysis of Gas Networks. Gulf Publishing Company, 1987.

18. Stachura M, Syfert M. Model sieci gazowej w systemie monitorowania i diagnostyki AMandD. Pomiary Automatyka Robotyka 2010; 11: 110-115.

19. Syfert M, Wnuk P, Kościelny J M. System zaawansowanego monitorowania i diagnostyki AMandD. Pomiary Automatyka Kontrola 2005; 9: 157-159.

20. Syfert M, Jankowska A, Łabęda-Grudziak Z, Tabor Ł. Porównanie cząstkowych modeli parametrycznych w zadaniu detekcji uszkodzeń sieci gazowej Pomiary Automatyka Kontrola 2012; 58(1): 3-9.

21. Turkowski M, Bratek A, Słowikowski M. Methods and system of leak detection in long range pipelines. Journal of Automation, Mobile Robotics & Intelligent Systems 2007; 1(3): 39-46.

22. Turkowski M, Bratek A, Słowikowski M, Bogucki A. Postępy i problemy realizacji systemów detekcji i lokalizacji nieszczelności rurociągów. Pomiary Automatyka Robotyka 2009; 1: 5-9.

23. Warowny W. Kubiczne równania stanu i ich wykorzystanie w gazownictwie ziemnym. Nafta - Gaz 2007; 10: 613-623.

Zofia M. ŁABĘDA-GRUDZIAK
Institute of Automatic Control and Robotics
Faculty of Mechatronics
Warsaw University of Technology
ul. św. A. Boboli, 02-525 Warsaw, Poland
E-mail: z.labeda@mchtr.pw.edu.pl

Mariusz ZIEJA
Mariusz WAŻNY
Sławomir STĘPIEŃ

DISTRIBUTION DETERMINATION OF TIME OF EXCEEDING PERMISSIBLE CONDITION AS USED TO DETERMINE LIFETIMES OF SELECTED AERONAUTICAL DEVICES/SYSTEMS

WYZNACZENIE ROZKŁADU CZASU PRZEKRACZANIA STANU GRANICZNEGO I JEGO ZASTOSOWANIE DO OKREŚLANIA TRWAŁOŚCI WYBRANYCH URZĄDZEŃ LOTNICZYCH*

The paper refers to the modelling of changes in ever-growing deviations from diagnostic parameters that describe health/maintenance status of one from among numerous aircraft systems, i.e. of a sighting system. Any sighting system has been intended, first and foremost, to find a sighting angle and a lead angle, both of them essential and indispensable to fight hostile targets. Destructive factors such as, e.g. ageing processes, that keep affecting the aircraft as a whole throughout its operation, make these angles change: actual values thereof differ from the calculated ones. Such being the case, a considerable error may be introduced in the process of aiming the weapons to, in turn, result in the reduction of values that describe the quality of the sighting process. That is why any sighting system requires specific checks possibly (if need be) followed with some adjustments (based on the findings of these checks) to remove negative effects of any ageing processes that might have affected this system. Determination of the density function of the deviation using difference equations and the Fokker-Planck equation is a basic element of the presented method, which enables next analyses. Innovative elements of the paper are as follows:
– determination of distributions of time of exceeding the permissible (boundary) condition using the density function of the deviation,
– application of distributions of time of exceeding the permissible (boundary) condition for modification of operation/maintenance systems of selected aeronautical devices. The paper has been concluded with a numerical example that proves the application-oriented nature of the issues in question, represented by the earlier conducted assessment of lifetimes of the systems intended to find the sighting and lead angles (ε and β). The in the paper discussed method to assess the lifetime may as well be applied to another systems/devices. It shows a versatile nature and makes a valuable contribution to the methods of maintaining any engineered systems in good condition (i.e. of providing maintenance to any engineered systems).

Keywords: reliability, life, permissible condition, lead angle, sighting angle, airborne sighting system.

Praca dotyczy modelowania zmian narastających odchyłek parametrów diagnostycznych charakteryzujących stan techniczny jednego z systemów statku powietrznego, tj. systemu celowniczego. Jednym z głównych zadań systemu celowniczego jest wyznaczenie kątów celowania i wyprzedzenia niezbędnych do zwalczania celów przeciwnika. Oddziaływanie w czasie eksploatacji statku powietrznego czynników destrukcyjnych m.in. procesów starzeniowych, powoduje, że kąty te ulegają zmianie i ich rzeczywiste wartości różnią się od wartości kątów obliczeniowych. Wystąpienie takiej sytuacji powoduje wprowadzenie dość istotnego błędu do procesu celowania i obniża wartość wskaźników charakteryzujących jakość jego przebiegu. Z tego też względu system celowniczy wymaga określonej kontroli i w oparciu o uzyskane wyniki, potencjalnej regulacji mającej na celu usunięcie ujemnych skutków procesów starzeniowych celownika. Podstawowym elementem pracy umożliwiającym dalsze analizy było wyznaczenie funkcji gęstości odchyłki z wykorzystaniem równań różnicowych oraz równania Fokkera-Plancka. Do nowatorskich elementów pracy należy zaliczyć:
– wyznaczenie rozkładu czasu przekroczenia stanu dopuszczalnego (granicznego) z wykorzystaniem funkcji gęstości odchyłki,
– zastosowanie rozkładu czasu osiągania stanu granicznego do modyfikacji systemów eksploatacji urządzeń lotniczych. Praca podsumowana jest przykładem obliczeniowym przedstawiającym aplikacyjny charakter poruszanej tematyki, odwzorowanej na przykładzie oceny trwałości układów określających kąt celowania i wyprzedzenia (ε i β). Przedstawiona metoda oceny trwałości w niniejszym artykule może być zastosowania do innych urządzeń. Ma ona ogólny charakter i stanowi wkład do metod utrzymania systemów technicznych.

Słowa kluczowe: niezawodność, trwałość, stan dopuszczalny, kąt wyprzedzenia, kąt celowania, celownik lotniczy.

1. Introduction

The issues of providing maintenance to any engineered systems require to be approached from many aspects. The reasons are: many and various areas they are functioning in, and many and various factors that considerably affect processes of providing maintenance to the engineered systems [1, 21, 32, 35, 36, 42]. The available literature

---

on the designing of strategies of how to provide maintenance to engineered objects delivers numerous classifications of models in question [2, 4, 5, 19, 26, 29]. Among them, there are some of extremely great significance, i.e. ones where the system's renewal is based on checking some specific diagnostic parameters. These are models of the so-called condition-based maintenance [7, 8, 12, 17, 22]. Furthermore, there are many studies where authors have assumed that a failure to a system is a rapidly occurring event. In the 1970s an idea of the Delay-Time Analysis (DTA) was developed. A good deal of publications on the modelling and implementation of the DTA concept have been issued up to the present [20, 25, 40]. The maintenance-dedicated literature proves both the significance of keeping devices/systems operational and the ever growing costs of maintaining this serviceability. At the same time, it should be emphasized here that there is a good many works in the available literature that deal with the problems of the environment/ambient conditions, ageing and wear-and-tear processes, etc. that affect the functioning of any engineered system [14, 31, 33, 37].

Devices/systems used in military aircraft are usually highly technologically advanced. This is the reason why formulation/generation of optimum operational models of these systems proves a complicated task. Methods based on changes in diagnostic parameters prove then extremely useful for the assessment of reliability and life of aeronautical devices/systems [24, 38, 39, 41, 43, 44]. The primary objective of a military aircraft is to perform a specified mission, in the course of which it quite often happens that air warfare agents have to be used. Effectiveness of applying them depends on many and various factors, just to mention:

1) health/maintenance status of an aircraft weapon system,
2) conditions for performing the combat mission in question,
3) the kind of a target to be attacked,
4) pilot's skill, etc.

Since the range of topics in this area is really wide, the main focus of attention is analysis of health/maintenance status of a selected subsystem of an air weapon system, in the case given consideration, a sighting system which remained under examination throughout its operation.

The sighting system is considered serviceable (fit for use), if check parameters remain within the tolerance limits (interval). If not, the system should be subjected to maintenance to restore nominal values of its functional qualities/parameters. Therefore, the essence of the whole process of the sighting system's operation resolves itself into that diagnostic parameters are not permitted to exceed the specified level of error, which makes the system fully and successfully used. Destructive processes affecting the sighting system are unavoidable. What results is the loss of nominal values by the diagnostic parameters. Hence, it is essential to determine the moment values of the diagnostic parameters reach the permissible (boundary) level. Such being the situation, it is necessary to interfere in the system's structure to remove negative effects of destructive factors affecting it.

The sighting marker displayed on the reflector of a sight head is probably the most essential functional parameter of a sighting system. While aiming at a target, the pilot/operator is expected to make the sighting marker stay in alignment with the target. Its position is defined with two angles, i.e. a sighting angle and a lead angle. Hence, final effects of the aiming process are conditioned by the accuracy of values found for these angles.

Let us assume that deviation from the analytical value can be found in the following way:

$$\Delta x_0 = \left| X - W_0 \right| = \left| \left[X - \bar{X} \right] + \left[\bar{X} - \bar{X}_1 \right] + \left[\bar{X}_1 - W_0 \right] \right|, \quad (1)$$

where:

X – analytical value of the lead angle at the final instant of the aiming process;

W_0 – a real-time value of the sighting angle or the lead angle found at the final instant of the aiming process;

$\left[X - \bar{X} \right]$ – an error of the model of calculating the sighting angle or the lead angle;

$\left[\bar{X} - \bar{X}_1 \right]$ – a transferred error of data for calculating the angle of interest;

$\left[\bar{X}_1 - W_0 \right]$ – an error generated by the algorithm for calculating the $\bar{X}_1$ function.

Destructive processes result, among other things, in some change in W_0. Hence, deviation effected by these processes can be determined in the following way:

$$Z_{(t)} = \left| W_{(t)} - W_0 \right|, \quad (2)$$

where:

$W_{(t)}$ – destructive-processes-affected value of an angle;

$Z_{(t)}$ – deviations described as an increasing stochastic process.

Increments in the value of deviation result from the deterioration in the health/ maintenance status of assemblies and units of a system/device due to destructive processes of the ageing, wear-and-tear, and fatigue nature that affect the system's/device's components, assemblies, etc. Deterioration in health of the system's assemblies/units is not always directly indicated and warned of, which makes any evaluation thereof rather difficult; hence the idea of applying the ever growing deviations in diagnostic parameters or operating characteristics of the system/device in question to estimate probability that a failure occurs within the interval (0, t) by means of a reliability function determined on the basis of the distribution of time of exceeding the permissible (boundary) condition.

The sight to be used on an aircraft has to be set up in some correct position (aligned to its axis), so that the optical line of the sight points to the null position. Destructive effect of ageing processes results in the deviation of the optical line of the sight from the null position. Therefore, relationship (2) can be written down in the following form:

$$z = \left| Z - Z_0 \right|, \quad (3)$$

where:

z – deviation from the null position of the line of sighting, treated as a diagnostic parameter;

Z – position of the line of sighting as evaluated with account taken of effects of destructive processes;

Z_0 – required value of the null position of the line of sighting.

2. How to find the density function of the null position of the line of sighting

The following assumptions have been made in the model proposed to evaluate stability of the null position of directions of sighting and allowance:

1) the system's health/maintenance status is determined with one diagnostic parameter "z" in the form of deviation from the initial (zero) value:

$$z = |Z - Z_{nom}|, \qquad (4)$$

where: Z_{nom} – nominal value (null position) of the diagnostic parameter;

2) deviation of the diagnostic parameter changes throughout the whole operational phase of the aircraft, i.e. while in the air and during parking;
3) the "z" parameter is non-decreasing;
4) the rate of changes in the diagnostic parameter can be described with the following relationship:

$$\frac{dz}{dt} = c, \qquad (5)$$

where:

c – random variable that describes changes affected by features of the system's components;
t – calendar-based time.

The dynamics of the rate of changes in the deviation of "z" can be described, when approached stochastically, with the following difference equation:

$$U_{z, t+\Delta t} = (1 - P)U_{z, t} + PU_{z-\Delta z, t}, \qquad (6)$$

where:

$U_{z, t}$ – probability that the diagnostic parameter takes value z at time instant t;
P – probability that value of the deviation increases throughout time interval Δt by the amount of Δz;
Δz – increment in the deviation.

For probability equal to $P = 1$, eq (6) can be written down - with the functional notation applied - in the following form:

$$u(z, t+\Delta t) = u(z - \Delta z, t), \qquad (7)$$

where: $u(z,t)$ – density function of values of deviations of the diagnostic parameter as affected by time.

Eq (7) should be read in the following way: probability that at time instant t value of the deviation was $z - \Delta z$ and throughout time interval Δt increased by Δz. Eq (7) is now to be rearranged into a partial differential equation. Therefore, the following approximations are to be introduced now [10, 13, 28, 30]:

$$u(z, t+\Delta t) = u(z,t) + \frac{\partial u(z,t)}{\partial t}\Delta t,$$
$$u(z - \Delta z, t) = u(z,t) - \frac{\partial u(z,t)}{\partial z}\Delta z + \frac{1}{2}\frac{\partial^2 u(z,t)}{\partial z^2}(\Delta z)^2. \qquad (8)$$

Now, if we apply eq (8) to eq (7), the latter takes the form:

$$\frac{\partial u(z,t)}{\partial t} = -b\frac{\partial u(z,t)}{\partial z} + \frac{1}{2}a\frac{\partial^2 u(z,t)}{\partial z^2}, \qquad (9)$$

where:

$b = E[c]$ – an average increment in the diagnostic parameter's deviation per time unit;

$b = E[c^2]$ – a mean square of the increment in the diagnostic parameter's deviation per time unit.

Let us find a particular solution to eq (9), such that for $t \to 0$ is convergent to the so-called Dirac function, i.e. $u(z, t) \to 0$ for $z \neq 0$ and $u(0, t) \to +\infty$ but in such a way that the integral of function u equals '1' for all $t > 0$.

Solution to eq (9) for the above-formulated condition takes the form [10, 13, 28, 30]:

$$u(z,t) = \frac{1}{\sqrt{2\pi A(t)}}e^{-\frac{(z-B(t))^2}{2A(t)}}, \qquad (10)$$

where:

$$B(t) = \int_0^t bdt = bt = \overline{c}t,$$
$$A(t) = \int_0^t adt = at = \overline{c}^2 t. \qquad (11)$$

The density function of the increase in value of the diagnostic parameter's deviation can be directly applied to evaluate reliability of the system/device in question.

3. How to find distribution of time of exceeding the permissible (boundary) condition

Probability that the diagnostic parameter exceeds the permissible (boundary) value can be presented – using the density function of changes in the diagnostic parameter's deviation (10) – in the following form [3]:

$$Q(t; z_g) = \int_{z_g}^{\infty} \frac{1}{\sqrt{2\pi at}}e^{-\frac{(z-bt)^2}{2at}}dz, \qquad (12)$$

The density function of the distribution of time the permissible value z_g has been exceeded for the first time takes the following form:

$$f(t) = \frac{\partial}{\partial t}Q(t; z_g). \qquad (13)$$

With account taken of eq (10), the following is arrived at:

$$f(t) = \frac{\partial}{\partial t}\int_{z_g}^{\infty} \frac{1}{\sqrt{2\pi at}}e^{-\frac{(z-bt)^2}{2at}}dz. \qquad (14)$$

Therefore,

$$f(t) = \int_{z_g}^{\infty}\left\{\frac{\partial}{\partial t}\left[\frac{1}{\sqrt{2\pi at}}e^{-\frac{(z-bt)^2}{2at}}\right]\right\}dz. \qquad (15)$$

Having accepted definition (10), we get:

$$f(t) = \int_{z_g}^{\infty}\left\{\frac{\partial}{\partial t}u(z,t)\right\}dz. \qquad (16)$$

Furthermore, the time derivative of function (10) takes the following form:

$$\frac{\partial}{\partial t}\left[u(z,t)\right] = u(z,t)\left(\frac{z^2 - b^2 t^2 - at}{2at^2}\right). \qquad (17)$$

Eq (17) has been substituted into eq (16):

$$f(t)_{z_g} = \int_{z_g}^{\infty}\left[u(z,t)\left(\frac{z^2 - b^2 t^2 - at}{2at^2}\right)\right]dz. \qquad (18)$$

Now, we are looking for the antiderivative of the function for the integrand in eq (18). We predict that function of the following form:

$$w(z,t) = u(z,t)\left(-\frac{z+bt}{2t}\right),$$

is the antiderivative of the function for the integrand in eq (14). Let us make a check:

$$\frac{\partial}{\partial z}\left[u(z,t)\left(-\frac{z+bt}{2t}\right)\right] = -u(z,t)\left(-\frac{z-bt}{at}\right)\left(-\frac{z+bt}{2t}\right) + u(z,t)\left(-\frac{1}{2t}\right) =$$
$$= u(z,t)\left[\frac{(z-bt)(z+bt)}{2at^2} - \frac{1}{2t}\right] = u(z,t)\left[\frac{z^2 - b^2 t^2 - at}{2at^2}\right]. \qquad (19)$$

Hence the inference that the antiderivative of the function against the integrand in eq (18) takes the form:

$$w(z,t) = u(z,t)\left(-\frac{(z+bt)}{2t}\right) \qquad (20)$$

Therefore, if the integral (18) is calculated, we arrive at what follows:

$$f(t)_{z_g} = u(z,t)\left(-\frac{z+bt}{2t}\right)\Bigg|_{z_g}^{\infty} = \frac{z_g + bt}{2t}\frac{1}{\sqrt{2\pi at}}e^{-\frac{(z_g-bt)^2}{2at}}. \qquad (21)$$

Relationship (21) determines the density function of time the boundary (permissible) condition has been exceeded for the first time by the diagnostic parameter's deviation.

4. Evaluation of lifetimes of some selected structural units of the sight

A formula for the reliability of the aircraft system's/device's unit takes the form [11]:

$$R(t) = 1 - \int_0^t f(t)_{z_g} dt, \qquad (22)$$

where the density function $f(t)_{z_g}$ is defined with eq (21).

On the other hand, the unreliability of the aircraft system's/device's unit can be found from the following relationship:

$$Q(t) = \int_0^t \frac{z_g + bt}{2t}\cdot\frac{1}{\sqrt{2\pi at}}e^{-\frac{(z_g-bt)^2}{2at}}dt. \qquad (23)$$

The integral (23) should be reduced to some simpler form. It can be noticed that the integrand can be written down in the following form:

$$\frac{z_g + bt}{2t}\cdot\frac{1}{\sqrt{2\pi at}}e^{-\frac{(z_g-bt)^2}{2at}} = \frac{z_g + bt}{2t}\cdot\frac{1}{\sqrt{2\pi at}}e^{-\frac{(bt-z_g)^2}{2at}}, \qquad (24)$$

the problem can then be reduced to solving the indefinite integral:

$$\int \frac{(z_g + bt)}{2t}\cdot\frac{1}{\sqrt{2\pi at}}e^{-\frac{(bt-z_g)^2}{2at}}dt. \qquad (25)$$

After substitution

$$\frac{(bt-z_g)^2}{2at} = u,$$

the integral (25) takes the form:

$$\int \frac{z_g + bt}{2t}\frac{1}{\sqrt{2\pi at}}e^{-u}\cdot\frac{2at^2}{(bt+z_g)(bt-z_g)}du = \frac{1}{2\sqrt{\pi}}\int \frac{1}{\sqrt{u}}e^{-u}du. \qquad (26)$$

Then, another substitution should be made:

$$\sqrt{u} = w,$$
$$du = 2wdw.$$

Taking account of the above written relationships the integral (23) can be written in the following form:

$$\frac{1}{2\sqrt{\pi}}\int \frac{1}{w}e^{-w^2}2wdw = \frac{1}{\sqrt{\pi}}\int e^{-w^2}dw. \qquad (27)$$

After substitution:

$$w^2 = \frac{y^2}{2},$$

$$dw = \frac{y}{\sqrt{2}},$$

the integral of the form:

$$\frac{1}{\sqrt{2\pi}}\int e^{-\frac{y^2}{2}}dy. \qquad (28)$$

has been arrived at, where:

$$y = \frac{bt - z_g}{\sqrt{at}} \ .$$

If the results found are introduced into eq (22), the following formula for reliability is arrived at, providing that the limits of integration are properly written down:

$$R(t) = 1 - \frac{1}{\sqrt{2\pi}} \int_{-\infty}^{\frac{bt - z_g}{\sqrt{at}}} e^{-\frac{y^2}{2}} \, dy \ . \qquad (29)$$

Cumulative distribution function for the standard normal distribution takes the form [27]:

$$\Phi(x) = \frac{1}{\sqrt{2\pi}} \int_{-\infty}^{x} e^{-\frac{y^2}{2}} \, dy . \qquad (30)$$

With eq (29) taken into account, the final form of the formula for reliability of the aircraft's structural component can be expressed with the following relationship:

$$R^*(t) = 1 - \Phi\left(\frac{b^* t - z_g}{\sqrt{a^* t}} \right), \qquad (31)$$

where:

b^* and a^* – coefficients estimated on the basis of data received from the aircraft operation-and-maintenance processes.

Therefore, the probability that an aircraft's system/device suffers a failure can be found from the following relationship:

$$Q^* = 1 - R^*(t) = \Phi(\gamma), \qquad (32)$$

where:

$$-\gamma = \frac{b^* t - z_g}{\sqrt{a^* t}} \ . \qquad (33)$$

Eq (33) is multiplied by '−1'. This is the way to pass from the negative semi-axis to the positive one; now, the 'reliability' can be referred to instead of the 'unreliability'.

$$\gamma^* = \frac{z_g - b^* t}{\sqrt{a^* t}} \ . \qquad (34)$$

To settle the reliability level, one has to find the γ* value from the normal distribution tables. Then, with the γ*value known, stability of the null system can be determined:

$$T = \frac{\left(2b^* z_g + (\gamma^*)^2 a^*\right) - \sqrt{\left(2b^* z_g + (\gamma^*)^2 a^*\right)^2 - 4b^{*2} z_g^2}}{2b^{*2}} \ . \qquad (35)$$

To make use of eq (35), one needs to find (estimate) values of constants in this formula. Therefore, it is assumed that observation of the system/device in question throughout the whole operational phase (i.e. operation and maintenance) thereof has delivered data on the growth of the diagnostic parameter's deviation, in the following form:

$$\left[(z_0, t_0), (z_1, t_1), (z_2, t_2), \ldots, (z_n, t_n)\right]. \qquad (36)$$

The best way to find values of 'a' and 'b' for the data at hand is a method that uses the likelihood function. The general-case form of this function can be presented as the following relationship [6, 27]:

$$L = \prod_{k=0}^{n-1} g\left(t_k, z_k, \theta_1, \theta_2, \ldots, \theta_m\right), \qquad (37)$$

where:

$g\left(t_k, z_k, \theta_1, \theta_2, \ldots, \theta_m\right)$ – density function of the total probability of variable z;

$(\theta_1, \theta_2, \ldots, \theta_m)$ – parameters of the density function;

z_k – measured values of the parameter z consumption at time instants $(t_1, t_2, \ldots, t_k)$, respectively.

Finding estimates $\theta_1^*, \theta_2^*, \ldots, \theta_m^*$ of unknown parameters $\theta_1, \theta_2, \ldots, \theta_m$ with the maximum likelihood method means nothing but having solved equations of the following form:

$$\frac{\partial \ln L}{\partial \theta_j} = 0 \ , \qquad (38)$$

where:

$j = 1, 2, \ldots, m$;
m – the number of parameters that describe a given engineered object.

Such being the case, finding estimates b^* and a^* of unknown parameters b and a with the maximum likelihood method means having solved the following system of equations [6,27]:

$$\begin{cases} \dfrac{\partial \ln L}{\partial b} = 0 \\[2mm] \dfrac{\partial \ln L}{\partial a} = 0 \end{cases} . \qquad (39)$$

Having solved the system of equations (39) the b^* and a^* are found:

$$b^* = \frac{z_n}{t_n}, \qquad (40)$$

$$a^* = \frac{1}{n} \sum_{k=0}^{n-1} \frac{\left[(z_{k+1} - z_k) - b^* (t_{k+1} - t_k) \right]^2}{(t_{k+1} - t_k)} . \quad (41)$$

5. A numerical case and final remarks

A sighting head is one of the major components of an airborne sighting system. A sighting marker is displayed thereon. At the stage of the manufacture all the components are adjusted to have them furnished with nominal values to, in turn, perform a combat mission with the smallest error possible.

In the course of operation a check of the system's components being adjusted against each other is performed, i.e. two parameters ε and β are analysed. These are parameters that describe co-ordinates of the sighting marker's position for some pre-set conditions of the system's operation. With the operation-delivered data on these co-ordinates it has been confirmed that values of these parameters change with time of the system's operation (*Fig. 1*).
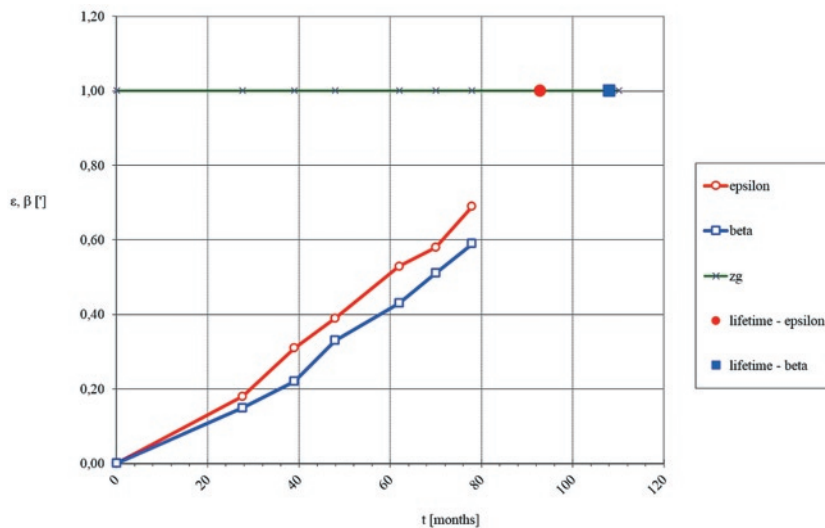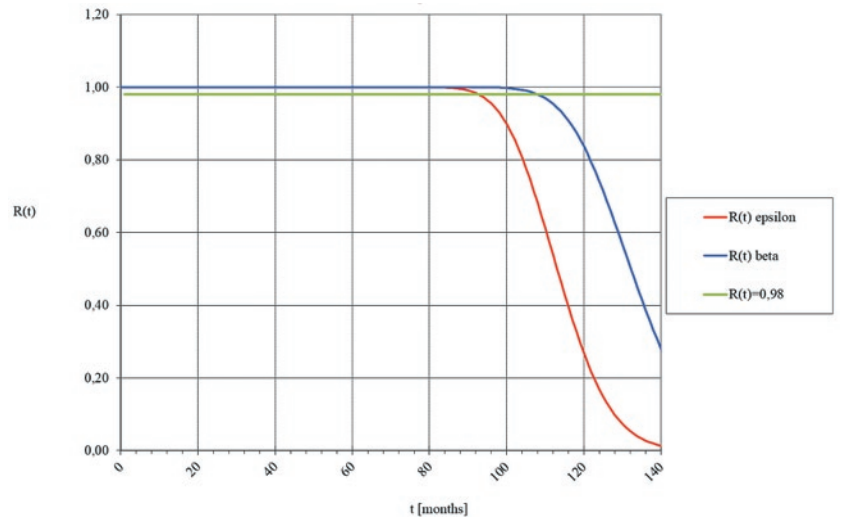

Fig. 3. *A graphically presented form of function of sighting head's reliability with account taken of the diagnostics parameters under consideration*

Numerical verification of the method in question, based on the data shown in Fig. 1, consisted in finding values of the density function coefficients '*a*' and '*b*' for both the diagnostic parameters; respectively, these values were as follows:

$$a_\varepsilon^* = 0.009, \qquad b_\varepsilon^* = 0.0076, \qquad a_\beta^* = 0.0001, \qquad b_\beta^* = 0.0001. \quad (42)$$

With the reliability level assumed to be $R^*(t) = 0.98$, value of the diagnostic parameter has been found from the normal distribution tables: $\gamma^* = 2.32$. Then, the z_g parameter has been found using technical documentation dedicated to maintenance services (e.g. Maintenance Hanbdbook/Manual); what is to be found there is information on permissible values of deviations of the above-mentioned diagnostic parameters.

With the relationships derived above and values found, time after which values of deviations of the diagnostic parameters in question exceed the boundary condition has been calculated. For the case given consideration, the time in question is as follows, respectively:

$$t_\varepsilon^* = 93 \text{ [months]}, \qquad t_\beta^* = 108 \text{ [months]}. \quad (43)$$

Furthermore, using the above presented data, graphical forms of: the density function of the time the deviation keeps growing up to finally reach the boundary value (Fig. 2), and the reliability function $R(t)$ for the analysed parameters (Fig. 3) have been found.

The discussed method of estimating effects of destructive processes upon the availability of airborne sighting systems seems correct and proper. The presented numerical case has both enabled verification of the formulated model and emphasised application-oriented advantages of the developed method. The in this way obtained results enable:

1) The assessment of residual life of the sighting system with the required reliability level maintained;

Fig. 1. *Graphically presented changes in values of diagnostic parameters of the sighting head against time of its operation*

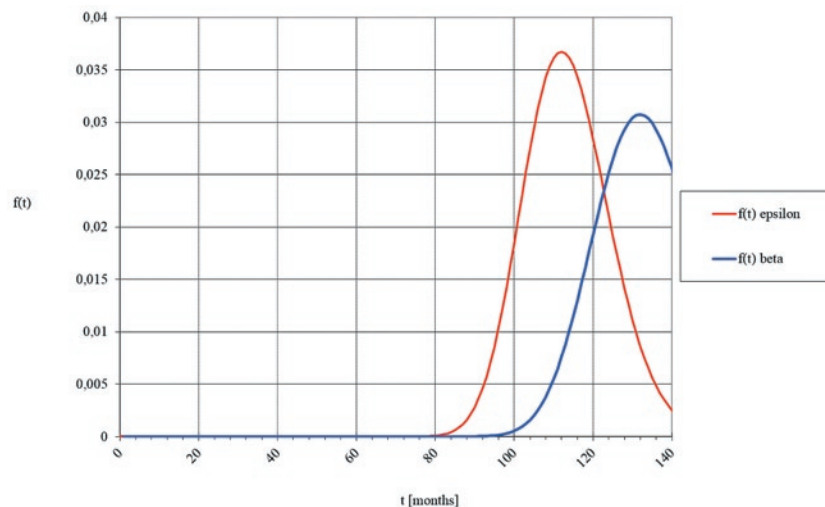Fig. 2. *A graphical form of the density function of time the deviation increases up to the boundary value*

2) Estimation of the system's reliability on the basis of a group of parameters recorded in the course of the system's operation:

3) Estimation of the system's reliability on the basis of a selected diagnostic parameter;

4) Verification of the process of operating the sighting system (making correction) to maintain the suitable level of reliability between particular checks.

The above-presented method may prove useful in further efforts to make the process of operating and maintaining the aircraft furnished with sighting systems more efficient.

Considering the fact the method proves extremely versatile, it may be successfully applied to determine residual life of any engineered object, the health/maintenance status of which is found using values of diagnostic parameters.

References

1. Augustynowicz J, Dudek D, Dudek K, Figiel A. Prognozowanie okresu bezpiecznej eksploatacji maszyn górniczych. Rozważania o degradacji obiektu. Górnictwo i Geoinżynieria 2007; 31(2): 55-66.
2. Birolini A. Quality and Reliability of Technical Systems. Theory – Practice – Management. Berlin: Springer Verlag, 1984.
3. Bobrowski D. Modele i metody matematyczne teorii niezawodności. Warszawa: WNT, 1985.
4. Casciati F, Roberts B. Mathematical Models for Structural Reliability Analysis. Boca Raton/New York/London/Tokyo: CRC Press, 1996.
5. Cho I D, Parlar M. A survey of maintenance models for multi-unit systems. European Journal of Operational Research 1991; 51, http://dx.doi.org/10.1016/0377-2217(91)90141-h.
6. DeLurgio SA. Forecasting principles and applications. University of Missouri-Kansas City: Irwin/McGraw-Hill, 1998.
7. Dhillon BS. Design Reliability. Fundamentals and Applications. Boca Raton/New York/London/Washington: CRC Press, 1999, http://dx.doi.org/10.1201/9781420050141.
8. Dhillon BS. Mechanical Reliability: Theory, Models and Applications. Washington: AIAA Education Series, 1988.
9. Dinesh Kumar U, Knezevic J, Crocker J, El-Haram, M. Reliability, Maintenance and Logistic Support - A Life Cycle Approach. Boston: Kluwer Academic Publishers, 2000, http://dx.doi.org/10.1007/978-1-4615-4655-9.
10. Franck TD. Nonlinear Fokker-Planck Equations. Fundamentals and Applications. Berlin Heildenberg: Springer-Verlag, 2005.
11. Gercbach IB, Kordoński CB. Modele niezawodnościowe obiektów technicznych. Warszawa: WNT, 1968.
12. Girtler J. Zastosowanie diagnostyki do decyzyjnego sterowania procesem eksploatacji urządzeń. Diagnostyka 2006; 2(38):151-158.
13. Grasman J, Herwaarden OA. Asymptotic Methods for the Fokker-Planck Equation and the Exit Problem in Applications. Berlin Heildenberg: Springer-Verlag, 1999, http://dx.doi.org/10.1007/978-3-662-03857-4.
14. Idziaszek Z, Grzesik N. Object characteristics deterioration effect on task reliability - outline method of estimation and prognosis. Eksploatacja i Niezawodnosc – Maintenance and Reliability 2014; 16 (3): 433-440.
15. Kececioglu DB. Maintainability, Availability & Operational Readiness Engineering Handbook. Lancaster: DEStech Publications, 2003.
16. Kececioglu DB. Reliability Engineering Handbook. Lancaster: DEStech Publications, 2002.
17. Kinnison H, Siddiqui T. Aviation Maintenance Management. New York: The McGraw-Hill Companies, Inc. 2013.
18. Knezevic J. Systems Maintainability. London: Chapman & Hall, 1997.
19. Kołowrocki K, Soszyńska Budny J. Reliability and Safety of Complex Technical Systems and Processes. London: Springer-Verlag, 2011, http://dx.doi.org/10.1007/978-0-85729-694-8.
20. Kovalenko IN, Kuznetsov NY, Pegg PA. Mathematical Theory of Reliability Of Time Dependent Systems with practical Applications. Chichester: John Wiley & Sons, 1997.
21. Legutko S. Development trends in machines operation maintenance. Eksploatacja i Niezawodnosc - Maintenance and Reliability 2009; 2(42): 8-16.
22. Moubray J. Reliability-centered Maintenance II. New York: Industrial Press Inc., 1997.
23. Narayan V. Effective Maintenance Management, New York: Industrial Press Inc., 2012.
24. Nechval KN, Nechval NA, Berzins G, Purgailis M. Planning inspections in service of fatigue-sensitive aircraft structure components under crack propagation. Eksploatacja i Niezawodnosc – Maintenance and Reliability 2007; 4: 3-8.
25. Nowakowski T. Niezawodność systemów logistycznych. Wrocław: Oficyna Wydawnicza Politechniki Wrocławskiej, 2011.
26. Pham H, Wang H. Imperfect maintenance. European Journal of Operational Research 1996; 94, http://dx.doi.org/10.1016/s0377-2217(96)00099-9.
27. Pham H. Handbook of Engineering Statistics. London: Springer-Verlag 2006, http://dx.doi.org/10.1007/978-1-84628-288-1.
28. Risken H. The Fokker-Planck Equation. Methods of Solution and Applications. London: Springer-Verlag, 1984, http://dx.doi.org/10.1007/978-3-642-96807-5.
29. Scarf PA. On the application of mathematical models in maintenance. European Journal of Operational Research 1997; 99, http://dx.doi.org/10.1016/s0377-2217(96)00316-5.
30. Soize C. The Fokker-Planck Equation for Stochastic Dynamical Systems and Its Explicit Steady State Solutions. World Scientific Publishing, 1994.
31. Sugier J, Anders GJ. Modelling and evaluation of deterioration process with maintenance activities. Eksploatacja i Niezawodnosc - Maintenance and Reliability 2013; 15 (4): 305-311.
32. Szpytko J. Integrated Decision Making supporting the exploitation and control of transport devices. Kraków: Uczelniane Wydawnictwa Naukowo-Dydaktyczne 2004.
33. Tomaszek H, Ważny M. Zarys metody oceny trwałości na zużycie powierzchniowe elementu konstrukcji z wykorzystaniem rozkładu czasu przekroczenia stanu granicznego (dopuszczalnego). Radom: Zagadnienia Eksploatacji Maszyn 2008; 155(3).
34. Tomaszek H, Wróblewski H. Podstawy oceny efektywności eksploatacji systemów uzbrojenia lotniczego. Warszawa: Dom Wydawniczy Bellona, 2001.
35. Tomaszek H, Żurek J, Jasztal M. Prognozowanie uszkodzeń zagrażających bezpieczeństwu lotów statku powietrznego. Radom: Wydawnictwo Naukowe JTE, 2008.

36. Tomczyk W. Uwarunkowania racjonalnego procesu użytkowania maszyn i urządzeń rolniczych. Inżynieria Rolnicza 2005; 7: 359-366.
37. Wang H. A survey of maintenance policies of deteriorating systems. European Journal of Operational Research 2002; 139, http://dx.doi.org/10.1016/s0377-2217(01)00197-7.
38. Ważny M. The method of determining the time concerning the operation of a chosen navigation and aiming device in the operation system. Eksploatacja i Niezawodnosc - Maintenance and Reliability 2008; 38(2): 4-11.
39. Ważny M. The metod for assessing residual durability of selected of devices in avionics system. Eksploatacja i Niezawodnosc - Maintenance and Reliability 2009; 43(3): 55-64.
40. Werbińska-Wojciechowska S. Time resource problem in logistics systems dependability modelling. Eksploatacja i Niezawodnosc - Maintenance and Reliability 2013; 15(4): 427-433.
41. Zieja M. Metoda oceny trwałości wybranych urządzeń lotniczych wojskowych statków powietrznych. Problemy utrzymania systemów technicznych. Warszawa: Oficyna Wydawnicza Politechniki Warszawskiej, 2014: 151-160.
42. Zio E. Computational Methods For Reliability and Risk Analysis. Singapore: World Scientific Publishing, 2009, http://dx.doi.org/10.1142/7190.
43. Żurek J, Tomaszek H, Zieja M.: The reliability estimation of structural components with some selected failure model. 11th International Probabilistic safety Assessment and management Conference and the Annual European Safety and Reliability Conference 2012, Curran Associates, Inc., 2012:1741-1750.
44. Żurek J.; Tomaszek H.; Zieja M.: Analysis of structural component's lifetime distribution considered from the of wearing with the characteristic function applied. Safety, Reliability and Risk Analysis: Beyond the Horizon – Steenbergenet al. London: Taylor & Francis Group, 2014: 2597-2602.

Mariusz ZIEJA
Air Force Institute of Technology
ul. Księcia Bolesława 6, 01-949 Warszawa 96, Poland

Mariusz WAŻNY
Sławomir STĘPIEŃ
Military University of Technology
ul. Kaliskiego 2, 00-908 Warszawa 49, Poland

E-mail: mariusz.zieja@itwl.pl,
mwazny@wat.edu.pl, sstepien@wat.edu.pl

Żaneta Anna MIERZEJEWSKA
Paulina KUPTEL
Jarosław SIDUN

ANALYSIS OF THE SURFACE CONDITION OF REMOVED BONE IMPLANTS

ANALIZA STANU POWIERZCHNI USUNIĘTYCH IMPLANTÓW KOSTNYCH*

The requirements that must be met by implant materials are rigorous and diverse. These materials are tasked with supporting or replacing sick or damaged parts of the musculoskeletal system, where loads and a heterogeneous stress state frequently occur. Thus, they must have the appropriate strength properties and resistance to many types of corrosion, which is related to biotolerance, or neutrality of the material to the human body during use. This article presents the results of studies of three implant groups: set for stabilization of long bones made of 316L austenitic steel, set for intramedullary nail insertion in grafts of femur bones made of Ti6Al4V titanium alloy, and a straighty reconstruction plate made of Ti6Al4V titanium alloy coated with an oxide layer. These implants were implanted into the human body and then removed at the end of the treatment process or due to implant failure during its operation. Next, implants were studied in order to determine the level of wear. Investigations were carried out using an Hitachi S-3000N scanning microscope. Their results indicate a series of changes that took place on implant surfaces and confirm the existence of typical implant wear mechanisms presented in reports in the literature. Traces of corrosion, fatigue cracks, tribological wear, and traces of fretting were found on examined implant surfaces. The study of implant wear cases, determination of their character, and evaluation of the intensity of destructive processes may contribute to the improvement of both the mechanical properties of these implants and their shape, so that modern bone implants perform their roles without the risk of failure during their operation.

***Keywords**: implant, surface analysis, operating wear, tribological wear.*

Wymagania stawiane materiałom na implanty są wysokie i bardzo zróżnicowane. Mają one wspomagać lub zastępować chore lub uszkodzone części układu kostno-mięśniowego, gdzie często pojawiają się obciążenia i różnorodny stan naprężeń. Muszą zatem charakteryzować się odpowiednimi własnościami wytrzymałościowymi i odpornością na różne rodzaje korozji, powiązaną z biotolerancją oznaczającą neutralność materiału wobec organizmu podczas użytkowania. W pracy przedstawiono wyniki badań trzech grup implantów: zestawu do stabilizacji kości długich, wykonanego ze stali austenitycznej 316L, zestawu do gwoździowania śródszpikowego do zespoleń złamań kości udowej, wykonanego ze stopu tytanu Ti6Al4V oraz płytki rekonstrukcyjnej prostej, wykonanej ze stopu tytanu Ti6Al4V pokrytego warstwą tlenków. Implanty te wszczepione były do organizmu ludzkiego, a następnie usunięte, wraz z zakończeniem procesu leczenia lub wskutek uszkodzenia implantu podczas jego eksploatacji. Następnie poddano je badaniom w celu określenia stopnia zużycia. Badania realizowano z wykorzystaniem mikroskopu skaningowego Hitachi S-3000N. Wyniki badań wskazują na szereg zmian, które zaszły na powierzchni implantów i potwierdziły istnienie typowych mechanizmów zużycia implantów prezentowanych w doniesieniach literaturowych. Na powierzchni badanych implantów zauważono ślady korozji, pęknięcia zmęczeniowe, zużycie tribologiczne oraz ślady frettingu. Badania zużycia implantów, określenie ich charakteru oraz ocena intensywności zachodzenia procesów niszczenia mogą w przyszłości znacznie wpłynąć na poprawę zarówno właściwości mechanicznych tych implantów, jak również na próbę zmiany ich kształtu tak, by nowoczesne implanty kostne spełniały swoją rolę bez ryzyka zniszczenia w trakcie ich eksploatacji.

***Słowa kluczowe**: implant, analiza powierzchni, zużycie eksploatacyjne, zużycie tribologiczne.*

1. Introduction

The development of technology, mainly motorization, and active lifestyle of modern man that are currently being observed make a significant contribution to the growth of various types of injuries of the musculoskeletal system [1]. This is a challenge for reconstructive surgery of the skeletal system, and an effective search for solutions regarding selection of materials for implants and surgical instruments requires the direct cooperation of doctors and engineers [14].

Thanks to such cooperation, significant progress has taken place in the field of implantology over the last decade or so. The development of diverse techniques in the field of materials engineering for medical applications, particularly including materials and surface engineering, has expanded our ability to restore complete or partial functionality of parts of the musculoskeletal system [7, 10-11]. Bone implants make it possible to restore destroyed systems and improve a patient's health condition and functionality [15-17].

Implant is the name given to a foreign body made of one or more biomaterials that may be placed inside of the human body as well as partially or completely under the epithelium, which may remain in the human body for an extended period of time [1, 21]. Such long-term contact of an implant with the tissue environment necessitates many properties of implant materials. They must have specific physicochemical and functional properties, which will determine their suitability for application in the context of a bone-implant interface [12, 13].

These materials must have the appropriate mechanical properties and lifetime in the biological environment appropriately to the functions that they are to perform in the body [5]. This particularly applies to materials used to manufacture joint endoprostheses and bone stabilizers, which are subjected to large loads, both static and dynamic, during operation [4, 22, 23]. Biomaterials work under a variable state of stresses and displacements as well as in the reactive environment of tissues and bodily fluids. This fact may lead to irreversible changes in such materials, and in consequence, to a loss of their functionality [2, 3 ,18-20].

During use of engineering materials applied in bone implants, significant changes take place in their structure due to operating conditions and the fact of operation itself [2, 3, 19]. The properties of materials change as their operating time increases, often leading to significant degradation [6, 24]. These processes of bone implant destruction, occurring during use under clinical conditions, are very interesting and important.

Investigations of how metal bone implants are worn or destroyed during their operation in a living organism are an interesting area of materials research [8, 9, 18]. By analyzing changes on implant surfaces, the factors having a decisive impact on the occurrence of a given type of damage can be identified. This type of analysis is the principal component of the presented article. The research problem that serves as the basis of the article is determination of what processes of surface destruction occur in metallic implants in the environment of the human body.

2. Materials and methods

Three groups of metallic orthopedic implants for bone grafts (Fig. 1), which were present in the human body for a period of approx. 6 months, were studied. Investigations of surface changes were carried out on the following elements:

- set for stabilization of long bones used for osseosynthesis of the femur shaft, consisting of a load-bearing plate, clamping plate, as well as joining screws and cortical screws (316L austenitic steel),
- set for intramedullary nail insertion for grafts of femur bone fractures (Ti6Al4V titanium alloy),
- straight reconstruction plate used to graft bones of the forearm (anodized Ti6Al4V titanium alloy).
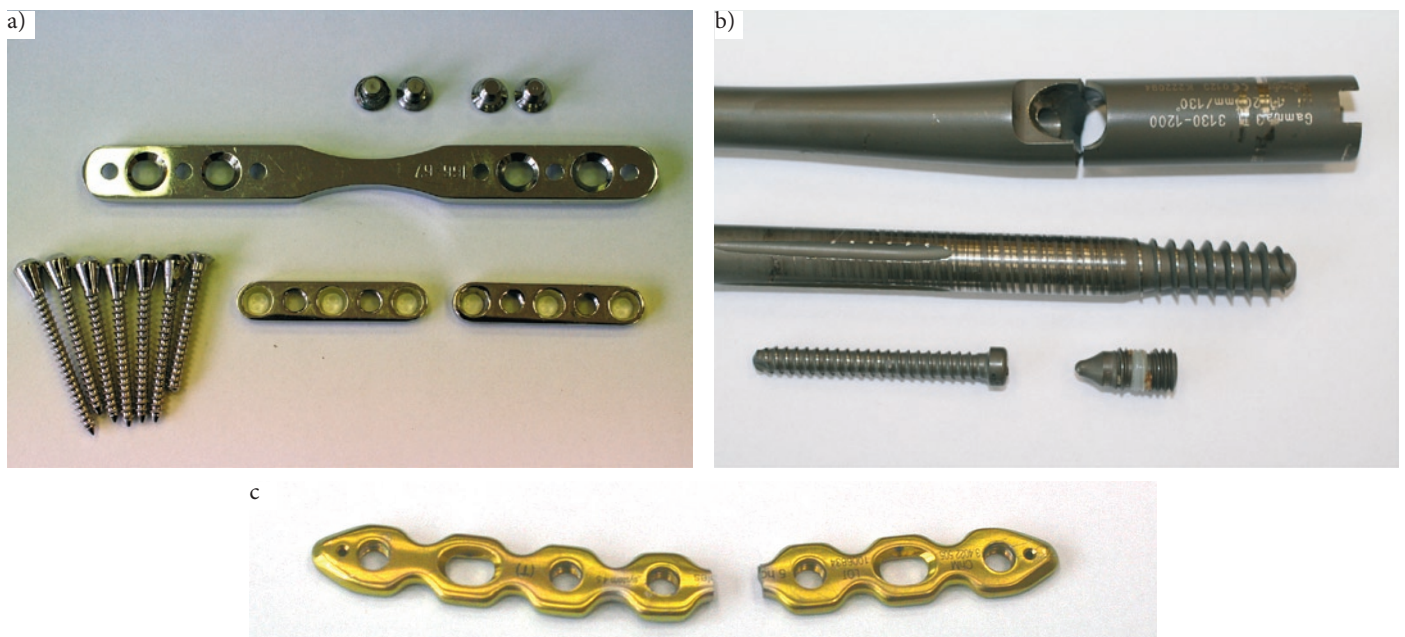
The investigative part of the study was based on assessment of changes on the surfaces of bone implants that had been removed at the end of treatment or as a result of implant failure during its operation in the body. For this purpose, preliminary macroscopic assessment was conducted, followed by detailed examinations under the microscope.

Microscope observations were conducted at the Department of Materials Science and Biomedical Engineering of the Faculty of Mechanical Engineering at Bialystok University of Technology using an Hitachi S-3000N scanning electron microscope (with an attachment for X-ray microanalysis – EDS type NSS from the THERMO NORAN company, and an attachment for examination of biological specimens), located in the Laboratory for Structural Testing of Materials.

3. Research results and discussion

3.1. POLFIX stabilizer

Observation of the plate's surface under a microscope revealed visible corrosion pits formed due to the interaction of bodily fluids with the material of the implant. Furthermore, the presence of degradation products was observed on the plate's surface. These products were formed as a result of the reciprocal interaction of the surface of the plate's seat with the screw head during the implant's presence in the body. Adhesion of wear products to the implant's surface is the result of adhesive interactions (Fig. 2).

In implants used to stabilize bone fractures, such as plates, openings serving to fasten screws are particularly exposed to damage. In the case of the investigated plate, these are both threaded and tapered seats. Fretting was observed on the thread, as shown in the photographs below (Fig. 3). Characteristic pits and areas where fine microcracks are present are indicative of this.

Corrosion has developed near openings as a result of the impact of the body's aggressive environment on the implanted metal. Numerous corrosion pits are visible on the surface (Fig. 4a) along with discolorations indicating the initial stage of corrosion development (Fig. 4b). Traces of abrasive wear can also be found near openings. In addition, slight deformation of the shape of openings also took place. Both processes usually occur as a result of mechanical wear occurring when the screws are being fastened and during further exploitation of the implant.

Fig. 1. Research materials: a) set for stabilization of long bones, b) set for intraosseous stabilization, c) straight reconstruction plate
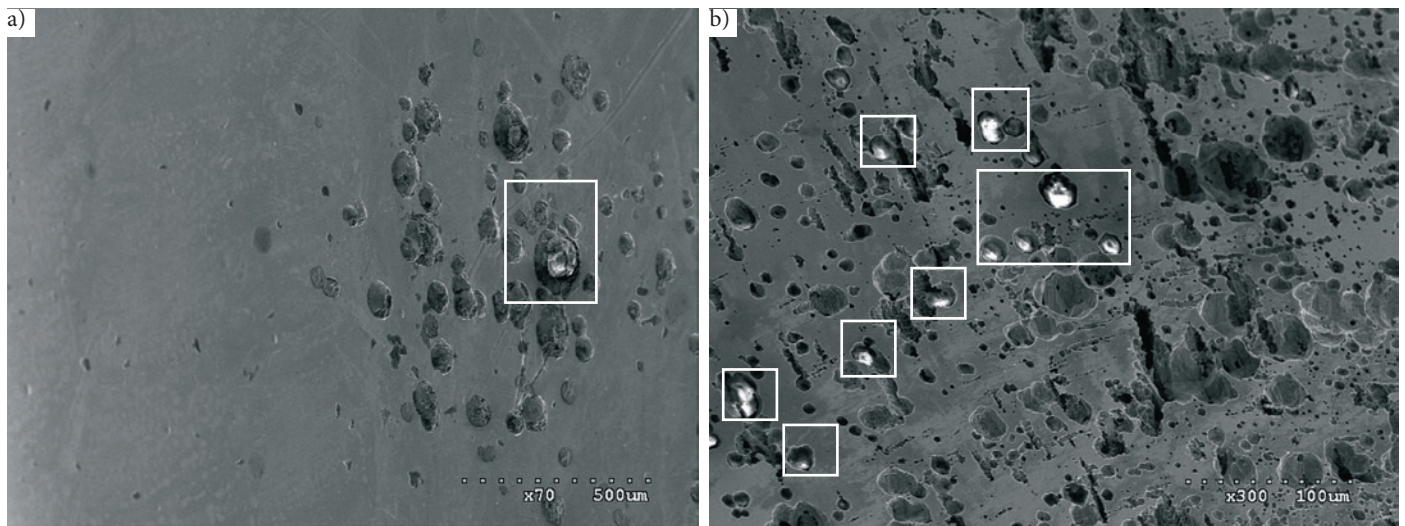
Fig. 2. Photograph of POLFIX plate surface, a) mag. x70, b) x300. Areas where metal particles formed during the wear process, adhere to the implant surface are marked on photographs
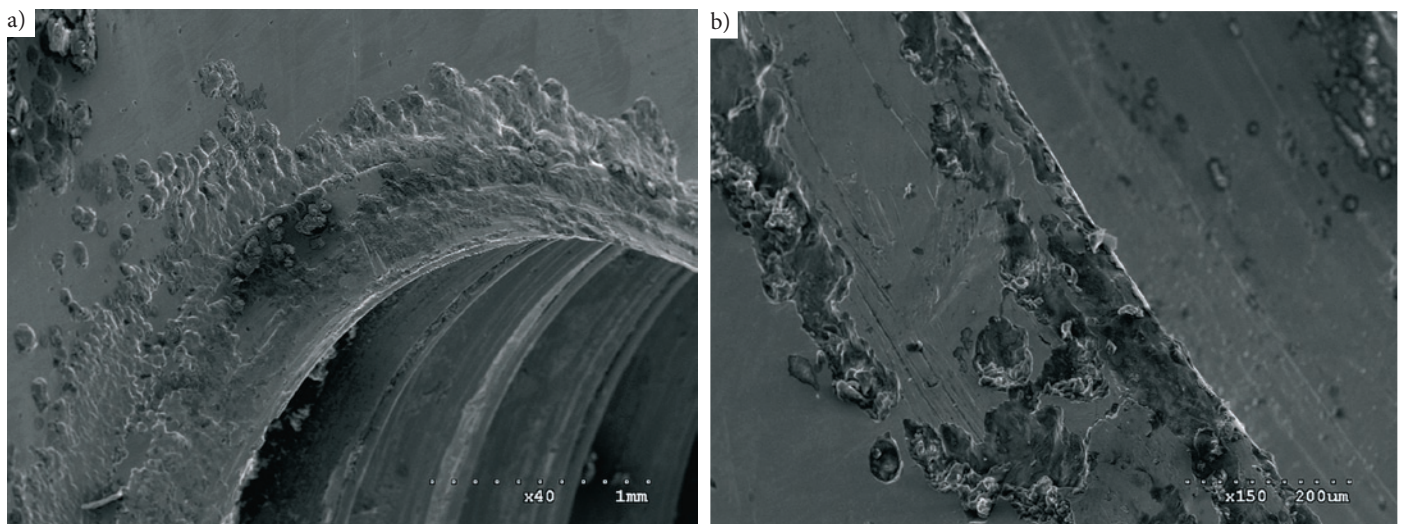
Fig. 3. Photograph of the surface of a threaded seat on the plate, mag. x40, mag. x150
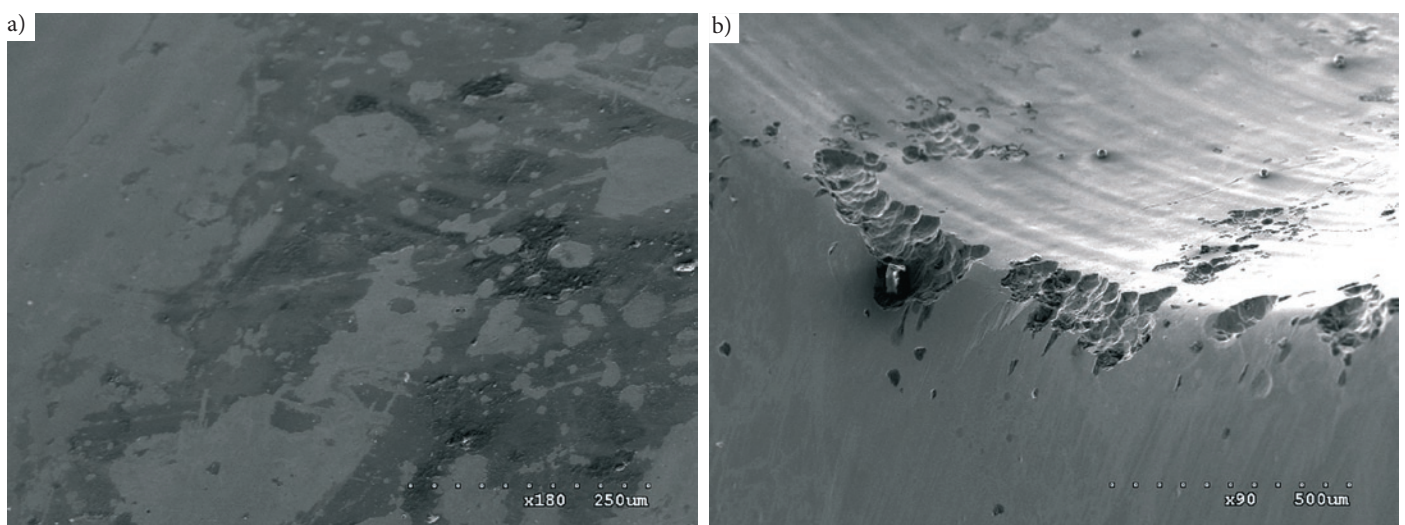
Fig. 4. View of the surface of the plate's tapered seat: a) corrosion pits (mag. x90), b) discolorations (mag. x180)

In the set for stabilization of long bones, the cortical screw is the element that fixes the plate's position after it is screwed into the bone. For this reason, this screw is subjected to large loads. The point of contact between the screw and the plate is the point where the greatest forces act on the screw.

Wear processes occurring near the screw head are already initiated during the surgical procedure, when the stabilizer is implanted. As the screw is fastened, its head is pressed down to the tapered seat, and because actual unit pressures are large, galling may occur when the screw is rotated. After initial installation of the stabilizer, final tightening of bone screws is performed. A diagram of the distribution of forces in the tapered joint: bone screw head – plate has been presented in figure 5.
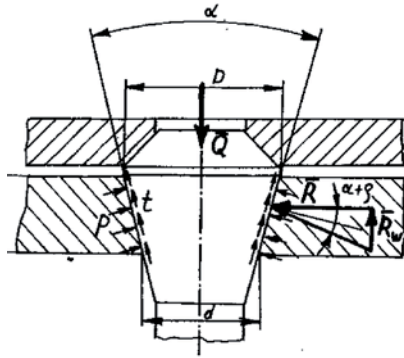

Fig. 5. *Distribution of forces in the tapered joint: bone screw head – plate: Q – force of tapered joint assembly, R – radial pressure on contact surface, p – unit pressure on contact surface, t – infinitesimal friction force, R_w – push-in force: $R_w = Rtg(\rho+\alpha)$ [16]*
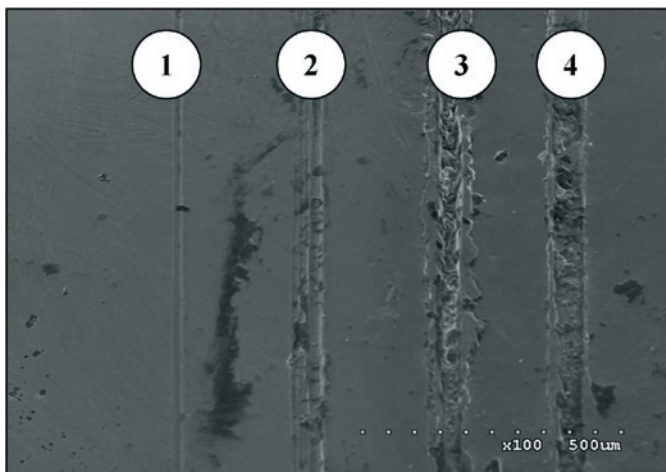

Fig. 6. *View of the surface of a cortical screw with the development of successive stages of crevice corrosion, mag. x100*

Microscope observations of a cortical screw revealed traces of crevice corrosion on its surface. It developed in areas where the implant was scratched as it was fastened in the plate. Scratches occurred as a result of intensified friction between these components. The passive layer of the screw's material was damaged during installation
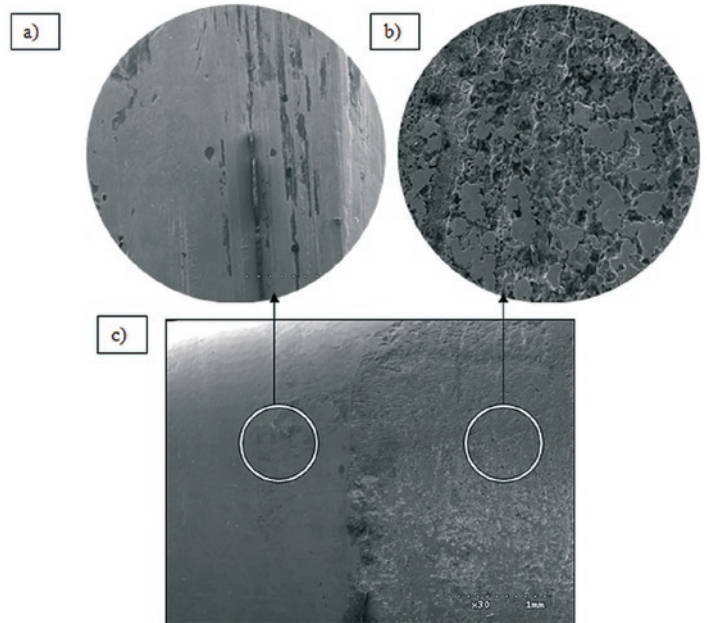

Fig. 7. *View of the surface of a long POLFIX screw, a) mag. x100, b) mag. x200, c) mag. x30*

of the implant, which initiated the development of crevice corrosion. The progression of expansion of this type of damage has been presented on the microscope photograph below (Fig. 6).

Fretting is another type of wear that was observed on screws. Due to micromovements with the involvement of elastic deformations occurring between the stabilizer's components, losses of material have developed on the screw's surface. These are chracteristic pits. This damage of the material is visible in figure 7b.

In addition, discolorations have formed and the pitting corrosion process has been initiated in areas on the screw's surface where there was intensive contact of the metal implant with bone tissue. The factor initiating pit development was the action of the surrounding environment with reduced pH relative to the proper acid-base equilibrium in the human body.

Microscope photographs of the investigated screws display the extent of destruction of their surface layer. Traces of abrasive wear were formed as a result of the mechanical interaction of the cortical screw head with the plate, initially at points of contact. As operating time increased and micromovements caused by variable loads took place, an increase in surface coarseness occurred. In the later period of fretting wear, recesses were formed in the material of screws. These changes, typical for fretting, are presented in figure 8.

Changes in areas where there was less interaction with the plate were also observed during investigations (Fig. 9). Discolorations and breaches of the continuity of the implant's surface layer were observed in the form of small corrosion pits. These pits were most likely

Fig. 8. *View of the surface of the POLFIX fastening screw head: a) mag. x30, b) mag. x50*
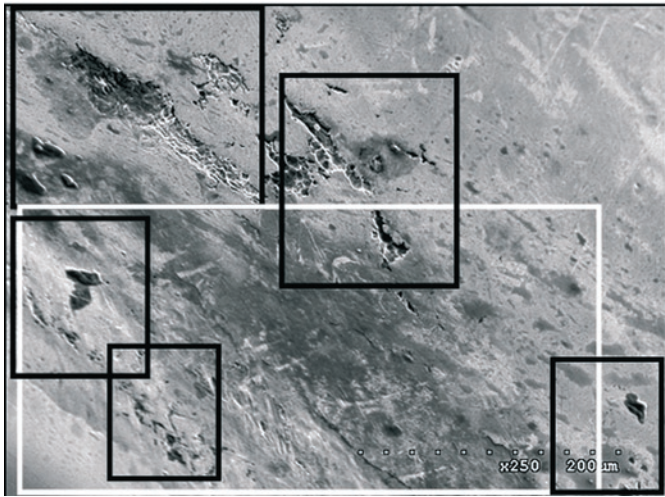
Fig. 9. View of the surface of the joining screw, mag. x250 (areas of visible corrosion pits marked in black frames and discolorations in white frames)

Fig. 10. Blocking screw, a) fracture, microscope photographs showing characteristic damage: b) mag. x30, c) mag. x300

formed as a result of a breach of the metal's passive layer, maybe even during implantation. The corrosion process was initiated as a result of the action of the tissue environment, with a pH lower than 6.8, on the metal. The surroundings of the pit are a cathode, and oxygen reduction takes place there. During the first stage, discolorations are formed, and then an increase in the concentration of aggressive ions and significant pH reduction occur inside the pit. A layer of corrosion products is formed at the bottom of the pit. Exchange of electrolyte between the pit and surroundings takes place through openings and pores in the passive layer. The composition, thickness, and porosity of this layer have an impact on the quantity and size of pits and on the rate of their development.

Two primary types of damage were distinguished as a result of macro- and microscopic observations:

- damage of the first type – has a form typical of tribological wear; in macroscopic terms, these are traces of friction (Fig. 6) that are present on both the surfaces of tapered openings in clamping plates and on the seats of connectors and the bone screw heads inter-operating with them;
- damage of the second type – has a form typical of corrosion wear (Fig. 4); in macroscopic terms, these are matte areas where occasional pits are visible with the naked eye on the surfaces of tapered seats in clamping plates and seats of connectors as well as the bone screw heads cooperating with them.

3.2. Intramedullary nail

The set for intramedullary nailing of femur bone fractures consists of: the intramedullary nail and three types of screws – blocking, reconstruction, and plugging. Two components of the set were subjected to detailed microscope examinations: intramedullary nail and reconstruction screw.

An intramedullary nail is an implant that is subjected to the enormous loads resulting from human locomotion as it performs its stabilizing role. The examined nail was damaged during exploitation – it was broken due to material fatigue.

Macroscopic observation was already sufficient to observe some changes that occurred in the implant during its time in the tissue environment. Traces of abrasive wear and the development of corrosion processes can be observed at the fracture point of the intramedullary nail (Fig. 10a).

Scratches on the interior surface of the nail, visible on the microscope photograph (Fig. 10b), were formed during fastening of the reconstruction screw. These scratches were created
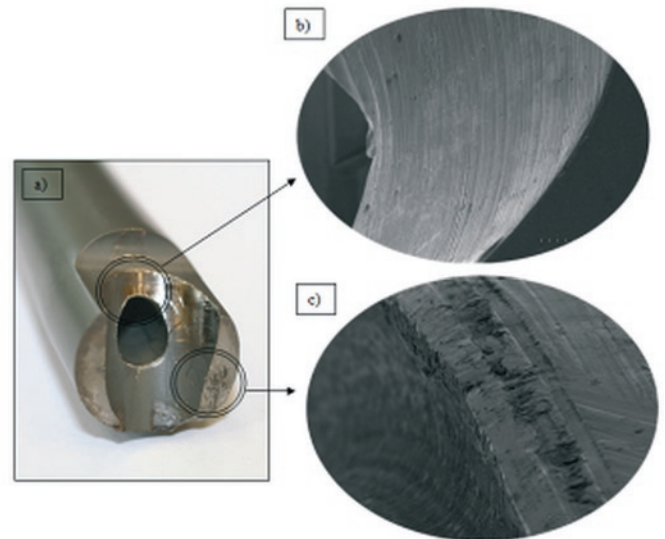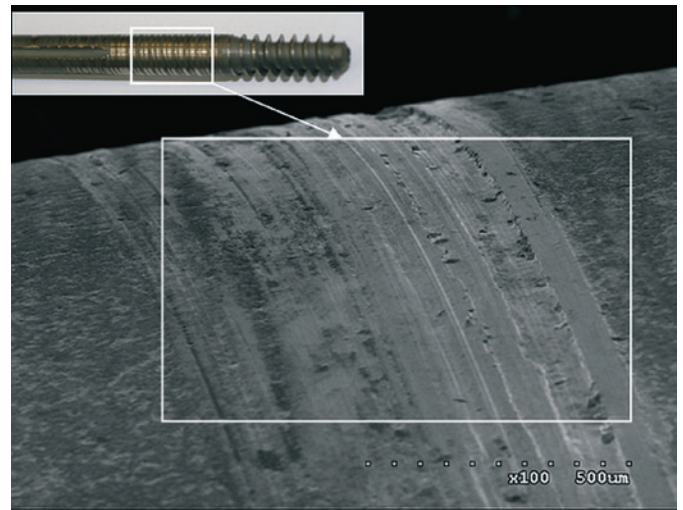
Fig. 11. Photograph of the reconstruction screw surface, showing scratches on the surface, mag. x100

as a result of friction between the screw surface and the nail surface. Moreover, plastic deformation of the seat resulting from cyclically variable loads occurring between these components is also visible. This deformation was caused by clearance between the screw and the nail, leading to micromovements.
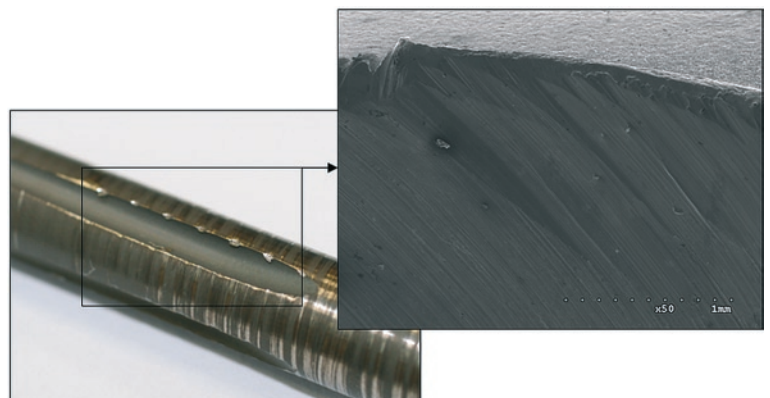
Fig. 12. View of damaged reconstruction screw surface, mag. x50.

The destruction of the fracture surface by corrosion is visible in figure 10c. This surface has increased coarseness and bears visible traces of corrosion pits. Damage of the reconstruction screw has the nature of abrasive wear. Scratches formed on its surface can be observed macroscopically (Fig. 11). The grooves visible on the surface were formed as a result of screw rotation while it was pressed to the surface of the nail seat. A slight loss of material is also visible (Fig. 11). The reconstruction screw was also mechanically damaged. Its surface was deformed during installation, and this deformation progressed over the course of further installation, as shown in the figure below (Fig. 12).

3.3. Straight reconstruction plate

The straight reconstruction plate (Fig. 1c) is made of Ti6Al4V titanium implant alloy. In addition, its surface was anodized to provide corrosion protection of the surface. The implant was damaged as a result of the action of variable loads and of the organic environment on the implant The plate cracked as a result of material fatigue. The surface of the plate and of its openings, as well as the plate's fracture, were observed under a microscope.

The results of microscope observations showed that the plate's surface underwent significant changes despite the application of additional protection against destruction. The presence of discolorations over a significant area and the initiation of corrosion pitting in the largest areas of discoloration were observed (Fig. 13). The aforemen-

tioned processes most likely took place as a result of elevated concentration of Cl^- ions on the surface layer of the implant material, which was in contact with electrolytes found in the bodily fluids surrounding it. The concentration of Cl^- ions has an impact on the incubation time of pitting corrosion. The greater the concentration and the higher the critical potential of pit nucleation, the shorter the incubation time.

Moreover, at greater magnification, increased coarseness of the plate's surface layer was also observed. Despite cleaning in an ultrasonic cleaner, the plate's surface bore contaminants in the form of irregular particles. Clear contamination sometimes remains on certain surfaces of implants implanted into a living organism. This contamination is sometimes difficult or even impossible to remove due to the presence of strong adhesive interactions. In this case, the adhering particles may be residue of peri-implant tissue (Fig. 14).

Observation of the plate's seat revealed damage of its surface layer in the form of abrasive wear. The scratches and grooves visible in the photograph (Fig. 15) are indicative of this. The plastic deformation that was observed most likely took place during the installation procedure, where a screw was inserted into the seat in order to fasten the plate.

Traces of fatigue wear of the reconstruction plate's seat are visible in the following figure (Fig. 16). Visible grooves were formed as a result of cyclically variable loads acting on components of the stabilizer and reciprocal interactions between the screw head and the surface of the seat in the plate. The cause of such deformation may have been clearance between the screw and the plate, which leads to micromovements of both components.

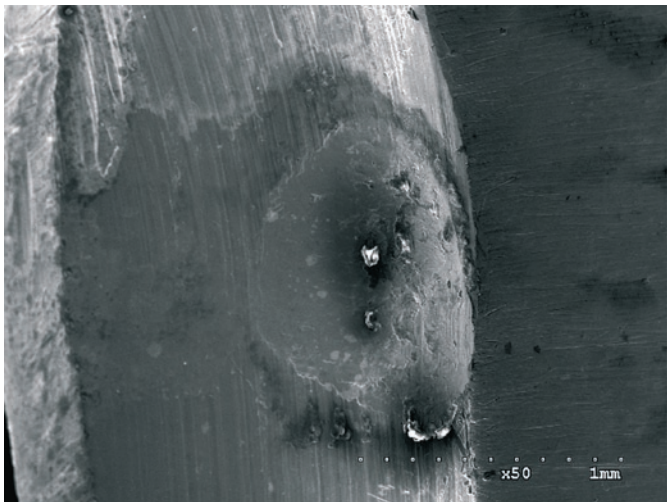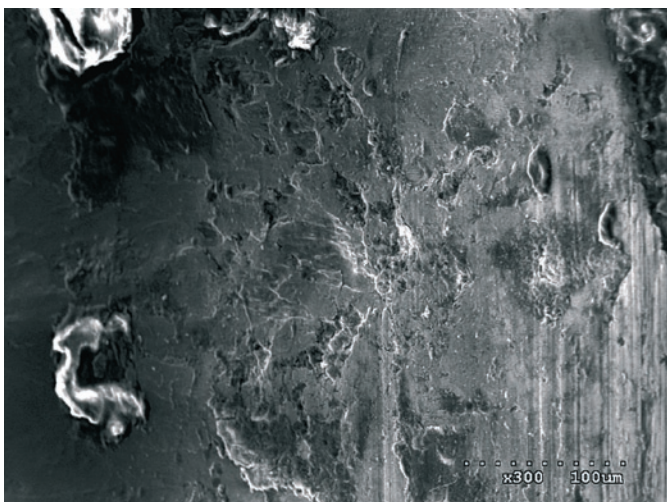Fig. 13. Corrosion damage on the surface of the reconstruction plate

Fig. 14. View of the plate surface with visible irregular particles, mag. x300

Fig. 15. Photograph of the surface of the seat in the anodized plate, mag. x70. Scratches formed during implantation of the component are marked in the photograph
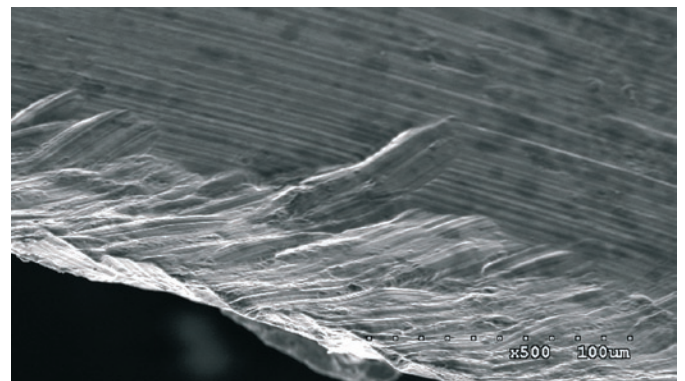

Fig. 16. Photograph of the surface of the seat in the anodized plate, mag. x500.

Because high loads are carried, this clearance may increase, making the entire system more susceptible to damage.

Both of the types of damage on seat surfaces in the anodized plate described above lead to a change of seat shape. Deformations of a plate's seats take place as a result of reciprocal interaction between the screw head and the plate. Deformation of an opening may occur as early as at first contact of the plate with the body, or during its installation, due to rotation of screws while their heads are pressed into seats in plates. Moreover, improper positioning of a screw may also cause deformations. In such a case, the micromovements taking place during exploitation are intensified as a result of the action of variable loads. This, in turn, exacerbates deformations of openings. It should be emphasized that deformation of plate seats is an undesirable process because it may lead to instability of the entire implanted stabilizer system.

4. Conclusions

Conducted macro- and microscopic investigations have revealed a series of changes occurring on implant surfaces and have confirmed the existence of typical mechanisms of implant wear presented in reports in the literature.

The largest areas of wear are visible on the inter-operating surfaces of plate seats and bone screw heads. Many types of damage typical of corrosion processes and tribological wear, mainly abrasive and fretting wear, are observed here. Traces of abrasive wear are present at points of contact between inter-operating parts. Wear processes are initiated during the surgical procedure - during installation, and develop with particular intensity in areas of microcontact between joining elements.

The following conclusions can be drawn based on conducted studies and analyses:
- typical implant surface wear mechanisms are: pitting corrosion, local material loss due to fretting, tribological wear, mechanical damage caused during the surgical procedure, and cracks due to material fatigue,
- wear processes are most commonly initiated during the surgical procedure - when the implant is introduced into the body, and develop with particular intensity in areas of microcontact between joining elements,
- tribological processes and their wear products initiate tissue reactions as a result of disruption of the acid-base equilibrium that threatens the organism (pH lower than 6.8), leading to an increase in the concentration of Cl^- ions, which are incubators of pitting corrosion.
- a technological change of the surface condition of components should decidedly limit damage during implantation as well as tribological and corrosive wear.

References

1. Ackrermann K.: Implantologia, Urban&Partner, Wrocław 2004.
2. Albert K., Schledjewski R, Harbaugh M, Bleser S, Jamison R, Friedrich K.: Characterization of wear in composite material orthopaedic implants, Part 2. The implant/bone interface. Biomedical Materials Eng. 1994: 199-211.
3. Benea L., Mardare-Danaila E., Celis J-P.: Increasing the tribological performances of Ti–6Al–4V alloy by forming a thin nanoporous TiO layer and hydroxyapatite electrodeposition under lubricated conditions. Tribology International, 2014; 78: 168–175, http://dx.doi.org/10.1016/j.triboint.2014.05.013.
4. Ciupik L. F., Krasicka-Cydzik E., Mstowski J., Zarzycki D.: Metalowe implanty kręgosłupowe. Cz. I: Techniczne aspekty biotolerancji. W: System DERO: rozwój technik operacyjnego leczenia kręgosłupa. (red.) Zarzycki D., Ciupik L. F., Wyd. Grupa DERO LfC, Zielona Góra 1997: 93-104.
5. Dąbrowski J.R., Klekotka M., Sidun J.: Fretting and fretting corrosion of 316L implantation steel in the oral cavity environment. Eksploatacja i Niezawodnosc – Maintenance and Reliability, 2014; 16(3): 441–446.
6. Diomidis N., Mischler S., More N.S., Manish Roy: Tribo-electrochemical characterization of metallic biomaterials for total joint replacement. Acta Biomaterialia, 2012; 8: 852–859, http://dx.doi.org/10.1016/j.actbio.2011.09.034.
7. Dobrzański L. A.: Kształtowanie struktury i własności powierzchni materiałów inżynierskich i biomedycznych. Wyd. International OC&CO World Press, Gliwice 2009.
8. Geringer J., Mathew M.T., Wimmer M.A.: Synergism effects during friction and fretting corrosion experiments – focusing on biomaterials used as orthopedic implants. Biomaterials and Medical Tribology 2013: 133–180, http://dx.doi.org/10.1533/9780857092205.133.
9. Guo F., Dong G., Dong L.: High temperature passive film on the surface of Co–Cr–Mo alloy and its tribological properties. Applied Surface Science, 2014; 314: 777–785, http://dx.doi.org/10.1016/j.apsusc.2014.07.086.
10. Kakubo T., Kim H.-M., Kawashita M, Nakamura T.: Bioactiwe metals: preparation and properties. Journal of Materials Science: Materials in Medicine 2004; 15: 99-107, http://dx.doi.org/10.1023/B:JMSM.0000011809.36275.0c.
11. Kasemo B.: Biological surface science. Surface Science 2002; 500): 656-677, http://dx.doi.org/10.1016/S0039-6028(01)01809-X.
12. Krasicka-Cydzik E., Mstowski J., Ciupik L.F.: Materiały implantowe: stal a stopy tytanu. System DERO: rozwój technik operacyjnego leczenia kręgosłupa. Zielona Góra 1997.
13. Long M., Rack H. J.: Titanium alloys in total joint replacement – a materials science perspective. Biomaterials, 1998; 19: 1621–1639, http://dx.doi.org/10.1016/S0142-9612(97)00146-4.
14. Łaskawiec J., Michalik R.: Zagadnienia teoretyczne i aplikacyjne w implantach. Wyd. Politechniki Śląskiej, Gliwice 2002.
15. Marciniak J.: Biomateriały w chirurgii kostnej. Wyd. Politechniki Śląskiej, Gliwice 2002.
16. Marciniak J.: Biomateriały metaliczne. Biomateriały tom 4, Biocybernetyka i inżynieria biomedyczna. Akademicka Oficyna Wydawnicza Exit, W-wa 2003.
17. Marciniak J.: Perspektywy stosowania biomateriałów metalicznych w chirurgii rekonstrukcyjnej. Inżynieria Biomateriałów 1997; 1: 12-19.
18. Skrzypiec P., Sajewicz E., Koronkiewicz T.: Analiza zużycia wybranych implantów. W: Wybrane zagadnienia z inżynierii biomedycznej. (red.) Dąbrowski J. R., Sajewicz E., Sidun J., Wyd. Politechniki Białostockiej, Białystok 2005: 95-106.

19. Sidun J., Dąbrowski J.R.: Aspekty biomechaniczne uszkodzeń miniplytek zespalających kości twarzoczaszki. Motrol 2009; T.11C: 176-181.
20. Sidun J.: Evaluation of wear processes of titanium plates used for internal maxilofacial fixation. Scientific Journals Martime University of Szczecin, 2010; 24 (96): 88-92.
21. Szymański K., Olszewski W., Satła D., Rećko K., Waliszewski J., Kalska-Szostko B., Dąbrowski J.R., Sidun J., Kulesza E.: Characterization of fretting products between austenitic and martensitic stainless steels using Mossbauer and X-ray techniques. Wear 2013; 300: 90–95, http://dx.doi.org/10.1016/j.wear.2013.01.116.
22. Toshikazu Akahori, Mitsuo Ninomi, Kei-Ichi Fukunaga,: An Investigation of the Effect of Fatigue Deformation on the Residual Mechanical Properties of Ti-6Al-4V ELI. Metallurgical and Materials Transaction, 2000, 31A(8): 1937-1948, http://dx.doi.org/10.1007/s11661-000-0221-0.
23. Wagner W., Nawas B. A.: Materiały stosowane w implantologii oraz zasady konstrukcyjne śródkostnych części wszczepów – z chirurgicznego punktu widzenia. W: Implantologia. (red.) Koeck B., Wagner W., Wyd. Medyczne Urban & Partner, Wrocław 2004: 62-73
24. Wang S., Liao Z., Liu Y., Liu W.: Influence of thermal oxidation temperature on the microstructural and tribological behavior of Ti6Al4V alloy. Surface & Coatings Technology, 2014; 240: 470–477, http://dx.doi.org/10.1016/j.surfcoat.2014.01.004.

Żaneta Anna MIERZEJEWSKA
Paulina KUPTEL
Jarosław SIDUN
Department of Materials Science and Biomedical Engineering
Bialystok University of Technology
ul. Wiejska 45 C, 15-351 Białystok, Poland
E-mail: a.mierzejewska@doktoranci.pb.edu.pl,
paulinakuptel@wp.pl, j.sidun@pb.edu.pl

Olga GZIUT
Józef KUCZMASZEWSKI
Ireneusz ZAGÓRSKI

ANALYSIS OF CHIP FRAGMENTATION IN AZ91HP ALLOY MILLING WITH RESPECT TO REDUCING THE RISK OF CHIP IGNITION

ANALIZA FRAGMENTACJI WIÓRÓW PODCZAS FREZOWANIA STOPU AZ91HP W ASPEKCIE ZMNIEJSZENIA RYZYKA ZAPŁONU*

Magnesium alloys are used as advanced structural materials for producing machine components for the aircraft or automotive industry. The machining of these components involves the risk of uncontrolled ignition during machining operations and production of fine-grained chip fractions causing the wear of kinematic pairs in technological machines. Given the operation of machine tools, the determination of a method for assessing risk based on determining a safe milling range and suitable operational parameters seems justified. The paper presents the results of investigations on chip fragmentation, chip mass and dimensions. Based on these parameters, we determine effective and safe regions with respect to operation of machine tools. The experiments are performed on magnesium alloy AZ91HP, one of the most widely used casting alloys.

***Keywords**: high-speed dry milling, magnesium alloys, safety, reliability, maintenance of machines.*

Stopy magnezu są wykorzystywane jako nowoczesne materiały konstrukcyjne na elementy maszyn wytwarzane m.in. na potrzeby przemysłu lotniczego czy motoryzacyjnego. Obróbka skrawaniem tych elementów wiąże się z ryzykiem niekontrolowanego zapłonu podczas wykonywania operacji obróbkowych oraz powstawaniem drobnoziarnistych frakcji wiórów powodujących przyspieszone zużycie węzłów kinematycznych maszyn technologicznych. Zaproponowanie oceny ryzyka związanego z wyborem zakresu, uznawanego za bezpieczny, parametrów technologicznych frezowania, wydaje się celowe ze względów eksploatacyjnych maszyn obróbkowych. W artykule przedstawiono wyniki badań fragmentacji wiórów, ich masy oraz wymiarów charakterystycznych wiórów. Istotnym wydaje się określenie (na podstawie wymienionych wskaźników) obszarów uznawanych ze efektywne a zarazem bezpieczne z punktu widzenia eksploatacji maszyn obróbkowych. Do badań wytypowano często stosowany stop magnezu, z grupy odlewniczych, AZ91HP.

***Słowa kluczowe**: frezowanie na sucho, stopy magnezu, bezpieczeństwo, niezawodność, eksploatacja maszyn.*

1. Introduction

The growing demand for tools, vehicles or devices with their weight reduced as much as possible has led to the popularity of magnesium alloys which can be an alternative to other structural materials. From the point of view of machining, magnesium alloys have very good machining properties. They have low specific cutting resistance, low cutting loads and low temperatures in the cutting zone, among others. Magnesium alloys are also characterized by high strength and casting properties, high vibration damping capacity and good electromagnetic radiation shielding [23]. Owing to these properties, magnesium alloys are widely used in such spheres as the automotive industry as well as aircraft and machine design. The growing interest in applications of magnesium alloys in various spheres of life was also generated by advancements in alloy technology and production methods for magnesium products which include, among others, extensive research on special machine tools.

Assuming that maintenance is the whole of events and phenomena that occur in a given technical object (from manufacturing to disposal), it is possible to determine safe regions regarding the criterion of reliable and failure-free operation. Given the complexity of machining devices, the assessment of their operational reliability should rather be made in terms of synthesis and analysis of utility, machine reliability and life regarding optimum machining effect and the use

ensuring their longest maintenance possible. When it comes to describing state-of-art technological machines (complex cases), it seems advisable to use models with a serial structure, as every machine component must remain usable [13]. The maintenance of certain devices and machines also depends on their structural parameters and their role in a production process. The operational strategy should therefore be tailored to specific devices and machines (Fig. 1) as well as their operational conditions [12].

Fig. 1. *Example of a reliable structure of a technical object (technological machine) in a series-based system (R1÷Rn – reliability of all elements in the series) [13]*

In technical sciences, the concept of safety refers only to people (their health or life hazard), while all economic aspects pertain to reliability. The notion of reliability should be extended to cover operational safety of machine tools. Operational safety can be defined as operation which does not pose the risk of machine tool component damage. Safety is measured by the so-called "risk", which means assessing the probability of given losses in the system at a specific time
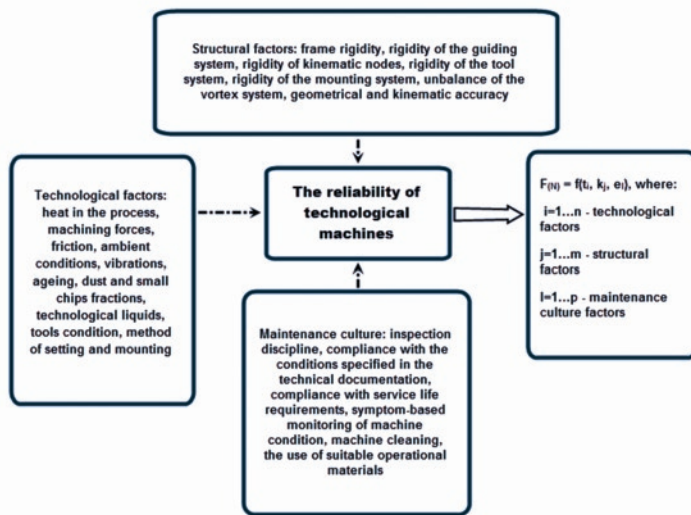

Fig. 2. Factors affecting operational reliability of a technological machine as a complex technical object

interval. There are many methods for risk assessment. Safety can be measured in terms of hazards or failure intensity [18].

A technological machine is a complex technical object. Its operational reliability depends on a number of factors, the most significant of which are given in Fig. 2. As can be observed, the "output function" is described by three main groups of factors characterizing operational reliability of technological machines. They are technological, structural and maintenance culture-related factors.

In recent years, optimization of the machining process has become the object of detailed research. Particular attention is paid to the problem of machined surface quality [6, 20] and surface layer analysis of machine components [3, 4].

The selection of tool geometry and machining parameters is a key problem in face milling. The results demonstrate that both efficiency and workpiece surface roughness in the face milling process were higher than those in the classical milling process with shank cutters. Machining times in machining by plunge milling can be reduced by even 60% compared to other machining strategies, particularly if the HSM technique is applied. This will bring substantial benefits for the technological process, leading to more effective operation of the machine as well as a longer life and higher reliability of cutting tools. One of the key criteria of technological process effectiveness is machining time. Taking this criterion into account, the best tool is one that can be operated at the highest cutting speed and feed per tooth in the assumed tool life under cut. The application of such tools requires the use of a suitable machine which can be operated at the required cutting parameters [19]. As the practice shows, tool life is also significant in the machining of high-silicon aluminium alloys (the so-called "silumins"), particularly in automated machining performed on numerically controlled machining centres. In these cases, frequent replacement of tools due to wear can cause problems connected with machine control and machined product quality. Increased tool wear in the machining of these alloys generates higher cutting loads, which has a negative effect on operational conditions of machine tools [9].

One of the most serious threats in magnesium alloy machining is self-ignition which can occur due to a sudden increase in temperature caused by e.g. tooth wear or built up edge. The temperature of magnesium ignition ranges from 480÷645ºC [16, 17]; at higher temperatures, chips and dust ignite and burn with a light flame which is difficult to extinguish. The built up edge resulting from higher adhesion is another problematic issue which can be reduced by selecting suitable machining parameters and coatings for cutting tools. On the one hand, the low mass density of magnesium (1.74g/cm^3) is one of its greatest

advantages; on the other, it leads to formation of magnesium dust. This dust generated during machining can have a negative effect on the health of a machine-operating staff. In addition to this, fine chips and dust seriously impair the machine's operational efficiency. They can damage the machine tool if they get into its work space (guides, bearings), thereby leading to faster machine wear. Moreover, they pollute the work space of the machine as they are difficult to remove. Finally, their storage generates additional costs.
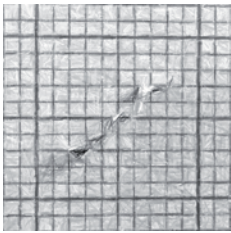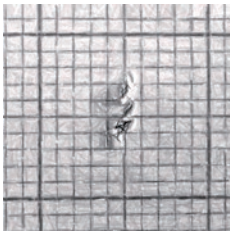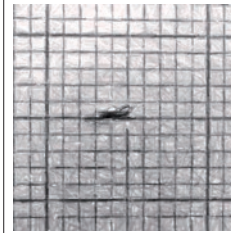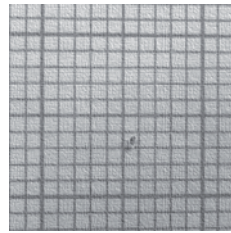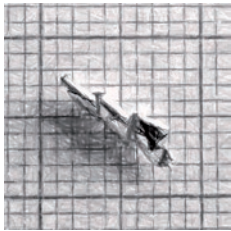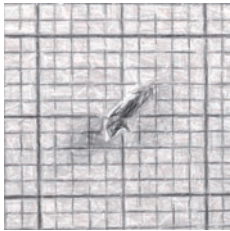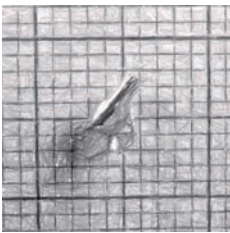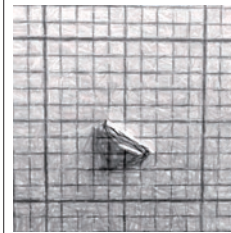
Despite these shortcomings, the interest in magnesium alloys continues unabated; there are more and more studies on optimization of magnesium alloy products in terms of machining safety and stability. Magnesium alloys are advanced innovative structural materials which are applied, among others, in the aircraft industry due to reduced operational costs. Structural components made of Mg alloys provide an interesting alternative to components made of polymer materials (polymers are more difficult to recycle) and Al alloys (higher density) [4, 17]. In various treatment processes, attempts are made at developing methods for chip control so as to obtain inflammable chips [2]. Partial meltings or burns on chip flanks can occur when the melting point is exceeded (for Mg it is about 650°C) during machining. Partial meltings are often observed by scanning electron microscopy (SEM) [3] or optical microscopy [10]. Magnesium alloy chips have a characteristic structure. One side has a lamellar structure, while the other is characterized by a glossy and smooth surface. Lamellas are regular laminar structures, usually in parallel arrangement. The glossy and smooth surface is created due to contact between the chip and the tool's rake face [4].

Chip shapes can be classified according to the standard PN-ISO 3685:1996 developed with respect to turning operations. However, this classification should be considered exemplary in light of the great number of chip types that can be formed. It is therefore recommended that a classification system describing every real machining process be developed. The shape of chips also greatly depends on cutting tool geometry, states of strain and stress, or so-called "material decohesion" (separation) in the zone of chip formation [22].

The results of investigations into magnesium alloys machining reveal that with conventional machining and the application of higher cutting speeds (using popular milling machines manufactured by different producers), fragmentation of chips and increase in their average unit mass are affected to the highest degree by the feed per tooth f_z and the depth of cut a_p. An increase in f_z and a decrease in a_p led to increasing the number of intermediate chip fractions, which is not desired in terms of machining safety. An excessive increase in the cutting speed v_c in high-speed machining (HSM) can lead to a higher number of intermediate chip fractions [10].

The research on the machining of magnesium alloys also involved analysis of the effect of heat generated in the cutting zone. To this end, we measured chip temperature in the cutting zone, the mean temperature of tool application surface and the temperature on the tool-workpiece contact [3, 11]. It was equally important to examine the problem of chip ignition for machining processes run at small depths of cut and the so-called ignition point of a given type of Mg alloy [5, 21]. The investigation into chip ignition during machining is connected with determination of the so-called "undeformed chip thickness." For theoretical reasons, attempts are made at assessing undeformed chip thickness [14, 15]. An increase in the cutting loads leads to an increase in the so-call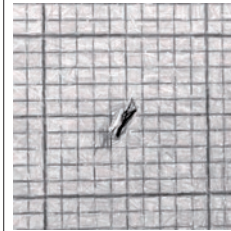ed "deformed chip thickness." When the undeformed chip thickness decreases, the shearing angle decreases, too, which makes the temperature in the shearing plane increase [3]. The type of produced chips (hence, the type of ignition) depends on such factors as cutting speed, depth of cut and the type (chemical composition) of a magnesium alloy. Chip ignition is hindered with increasing Al content, among others [1].

Table 1. *Examples of AZ91HP alloy chip fractions on varying the depth of cut a_p: a) a_p=0.5mm, b) a_p=1.5mm, c) a_p=3mm at v_c=800m/min, f_z=0.05mm/tooth and γ=5°*

Fractions / Parameter	Leading fraction A	Intermediate fraction B	Intermediate fraction C	Intermediate fraction D
a) a_p=0.5 [mm]				
b) a_p= 1.5 [mm]				no fraction detected
c) a_p= 3 [mm]				no fraction detected

2. Programme and experimental details

Fig. 3 presents the plan of investigations plan followed in analysis of the investigated parameters. The first stage of analysis involved defining chip geometry, the results of which were then used to divide the chips into individual fractions (degree of fragmentation) depending on changes in the examined parameters. Next, we analyzed the unit mass of chips and their overall dimensions. The changeable parameters included: a depth of cut a_p (0,5; 1,5; 3[mm]), a feed per tooth f_z (0,05; 0,15; 0,3[mm/tooth]), a cutting speed v_c (400; 800; 1200[m/min]) and a rake angle γ (5° and 30°). The constant parameters included a milling width a_e=14mm and a type of material, i.e. magnesium alloy AZ91HP.

The experiments were performed using an AVIA VMC 800HS milling centre. We used two three-tooth carbide milling cutters with different tooth geometry (Fig. 4), dedicated to the machining of magnesium alloys.

The measurements of length, width and field of chips produced in the milling process were made using a Nikon SMZ1500 optical microscope. The unit mass of chips was measured by a **DV215CD laboratory scales with an accuracy of** 0.00001g. The analyzed process was continuous; for every variant, the geometrical characteristics, mass and dimensions of chips were determined based on 5÷10 measurement repetitions.

The objective of the investigations was to examine the shape of

Fig. 4. *Three-tooth carbide milling cutter described by an angle of: a) $\gamma = 5°$, b) $\gamma = 30°$*

chips produced in AZ91HP alloy milling, to determine the degree of fragmentation and unit mass of chips. As for magnesium alloys, the determination of chip shape and regions of dust fraction occurrence is a key problem in the context of selecting operational parameters aimed at minimizing the risk involved in the machining of these alloys.

3. Results and discussion

The experiments were performed for specific operational parameters, with chips being collected after each pass of the tool. For the depth of cut set to a_p=0.5mm, a_p=1.5mm and a_p=3mm, we used five passes of the tool. Next, for each variable, the chips were divided into fractions depending on their shape and size. Hence, Fraction A comprises the biggest chips, while Fraction D contains the smallest chips.

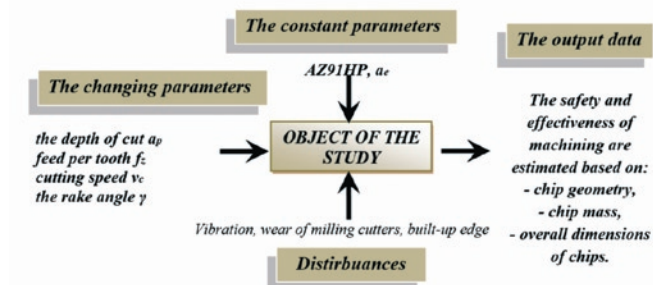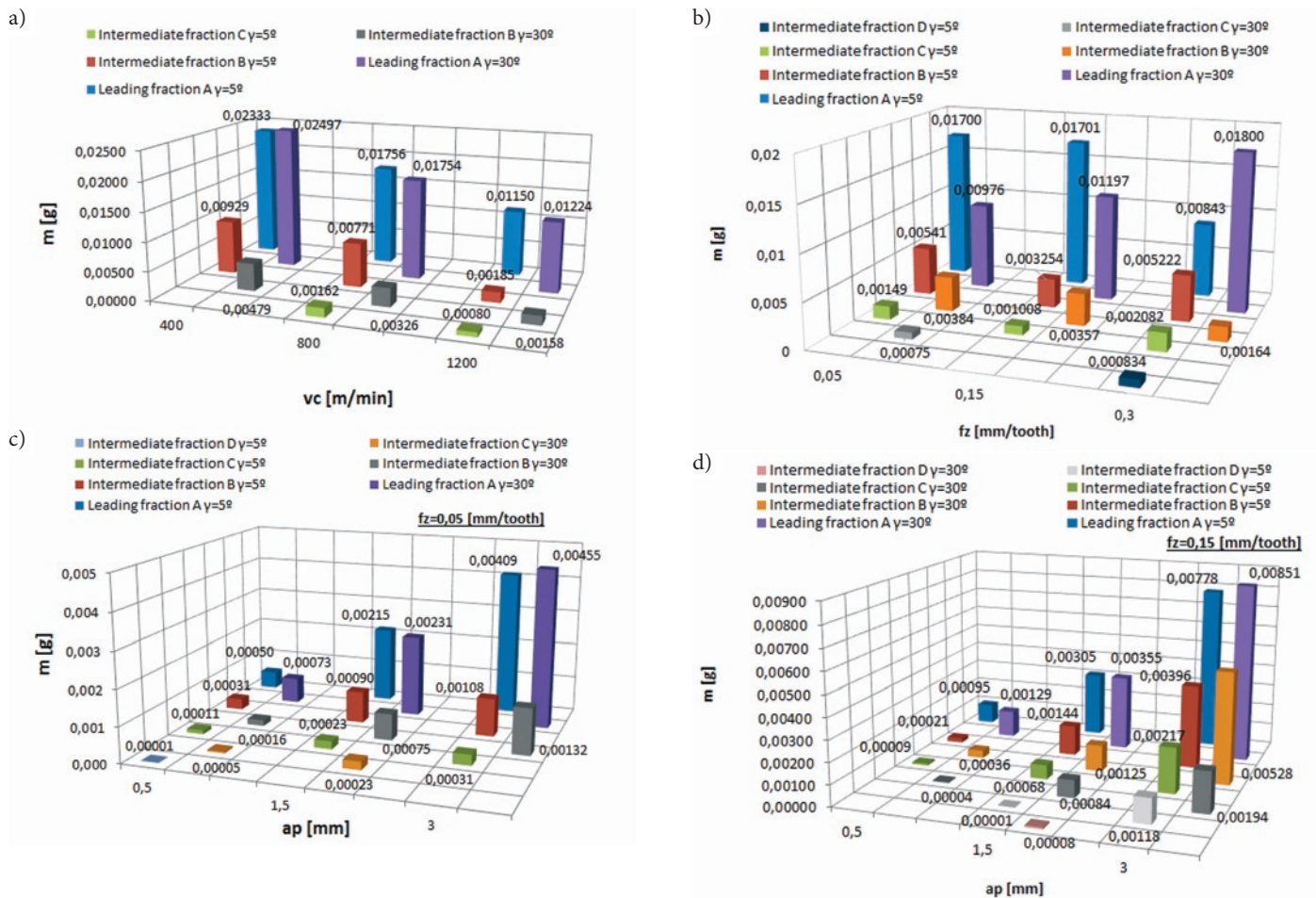Fig. 3. *Plan of investigations into chip geometry, mass and characteristic dimensions depending on changes in variable factors*

Fig. 5. Effect of changing the operational parameters and tooth geometry on the mass of chips in individual fractions for magnesium alloy AZ91HP: a) v_c, b) f_z, c), d) a_p (f_z=0.05mm/tooth, f_z=0.15mm/tooth)

Fraction A was described as the "leading fraction," while fractions of smaller chips were denoted as "intermediate fractions." We also measured the dimensions of chips assigned to individual fractions and determined the width-to-length ratio for selected chip fractions. Below we give examples of the results of fraction determination.

Table 1 illustrates the effect of the depth of cut a_p on both the number of isolated chip fractions and their shape. The greatest number of fractions was isolated at the smallest depth of cut; what is more, Fraction D isolated the smallest depth of cut was described as dust.

To describe phenomena in chip milling, we introduced the following terms:
– *fraction,* i.e. a population of particles of a specific size or specific dimensions,
– *fragmentation,* i.e. formation of fractions with different chip shapes and masses, apart from the leading fraction (the biggest and most characteristic one).

The intermediate fraction was defined in two stages: as a fraction with a different shape (compared to that of the leading chip fraction) and as a fraction with a lower mass (in most cases) than approx. 50% mass of the leading or preceding fraction.

Fig. 5 shows the effect of changing the milling parameters on chip mass and formation of intermediate fractions. The changes in mass of the leading and intermediate chip fractions are presented. The diagrams are given to visualize the effect of selected operational parameters on the examined characteristics of chips.

The data given in Fig. 5a reveal that chips produced at a cutting speed of 400m/min have the highest mass. All isolated fractions reveal a constant relationship involving a decrease in their mass with increasing the cutting speed. Regarding the leading fractions, it can

be observed that chip masses for individual values of v_c were similar despite the application of other tools. According to the data given in Fig. 5b, the masses of the leading fractions for the feed per tooth f_z=0.05mm/tooth and f_z=0.15mm/tooth are similar. Differences between the leading fractions can be observed for f_z=0.3mm/tooth. This is directly related to the differences in chip width: the leading fraction chips produced by the tool described by the angle γ=30° are much narrower than those created at γ=5°, which has a direct effect on their mass. Figs. 5c and 5d, where the cutting speed is changeable, show a gradual increase in mass with increasing depth of cut and feed per tooth, a phenomenon which seems to be obvious given the increase in the section of the machined layer. It is worth drawing attention to intermediate fractions D (a_p=0.5mm, γ=5°) and C (a_p=0.5mm, γ=30°) shown in Fig. 5c and to intermediate fractions C (a_p=0.5mm and γ=5°), C (a_p=0.5mm and γ=30°) and D (a_p=1.5mm and γ=5°), D (a_p=1.5mm and γ=30°) shown in Fig. 5d. The above fractions were described as dust. Their mass did not exceed 0.0001g; in the case of Fraction D (a_p=0.5mm, γ=5°, Fig. 5c) and D (a_p=1.5mm and γ=5°, Fig. 5d) the mass was too low (0.00001g) to measure even with the aforementioned precise scales.

Fig. 6 illustrates the ratio of chip width to their length for the changeable values of operational parameters v_c, f_z and a_p. The figure shows the biggest fraction (leading fraction A) and the smallest fraction for the applied parameters. Fig. 6 presenting the quantitative assessment of chips based on their width-to-length ratio reveals some interesting relationships. Analyzing the diagram (Fig. 6a) illustrating the effect of changing the cutting speed, it can be observed that the chips in the leading fractions at γ=30° were narrower than those at γ=5°. A constant trend can be observed in the case of the smallest
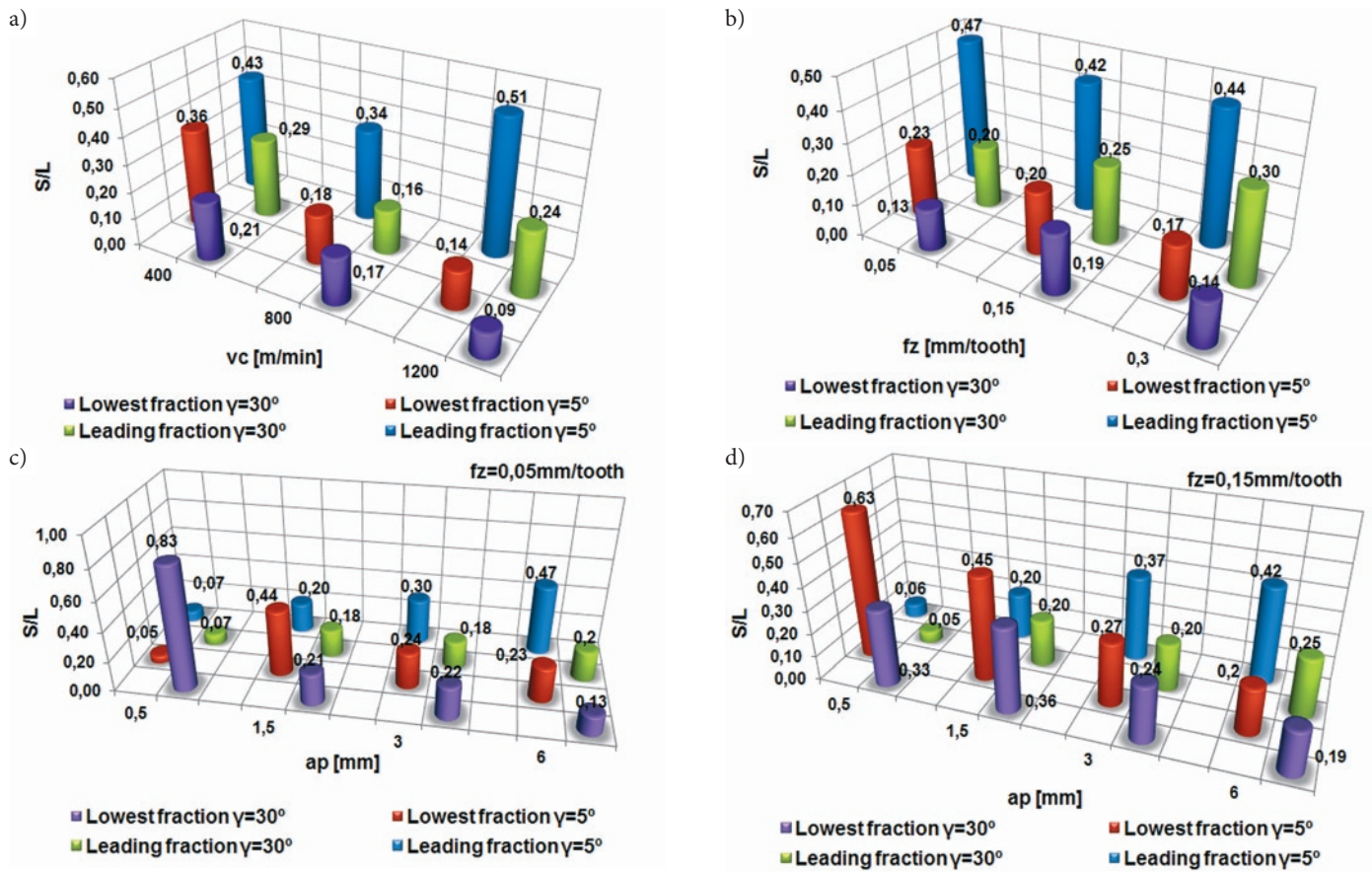
Fig. 6. Ratio of chip width S to length L depending on changes in: a) cutting speed v_c, b) feed per tooth f_z, c) depth of cut a_p (f_z=0.05mm/tooth), d) depth of cut a_p (f_z=0.15mm/tooth)
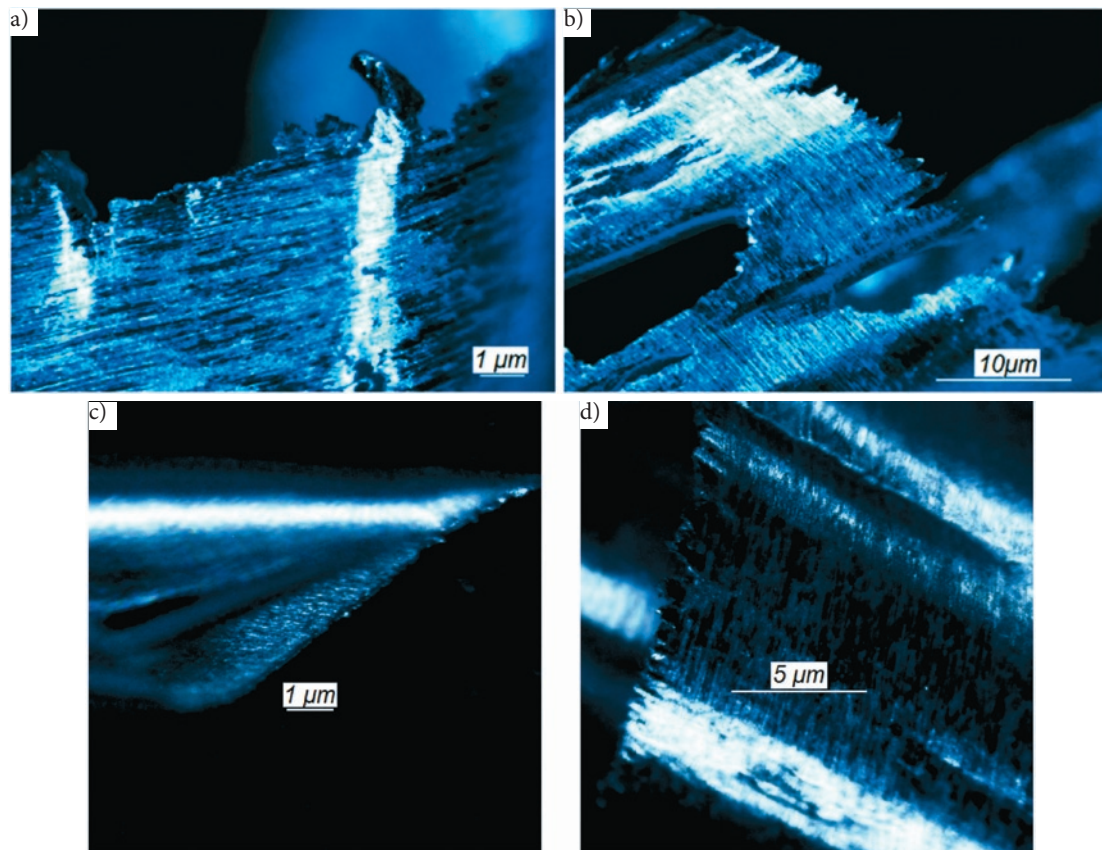
Fig. 7. Analysis of chip partial melting produced in the milling of magnesium alloy AZ91HP using a milling cutter with an angle set to: a) γ=5° (v_c=1200m/min, Fraction B), b) γ=5° (f_z=0.3mm/tooth, Fraction C), c) γ=30° (v_c=1200m/min, Fraction A), d) γ=30° (f_z=0.3mm/tooth, Fraction B)

fractions which become more and more coiled with increasing the cutting speed. Given the variable feed per tooth, it can be observed that the width-to-length ratio of the leading fraction chips produced at γ=5° remains at the same level, while at γ=30° - it gradually increases. This ratio decreases for the lowest fractions at γ=5°. The chips of the smallest fraction (for γ=30°) produced at f_z=0.15mm/tooth are only slightly wider than the chips of the smallest fractions produced at other feed per tooth values (f_z=0.05mm/tooth and f_z=0.3mm/tooth). Another diagram (Fig. 6c) illustrates variations in the depth of cut a_p at f_z=0.05mm/tooth.At the depth of cut a_p=0.5mm, the smallest fractions produced two extreme results: 0.05 for γ=5° and 0.83 for γ=30°. The above two fractions were marked as dust; this significant difference between the results is connected with the form of chips in these fractions. The chips produced with the tool described by the angle γ=5° has a high length-to-thickness/width ratio, whereas the chips for γ=30° were fine elements of similar width and length. When f_z=0.15mm/tooth (Fig. 6d), the width-to-length ratio for the biggest fractions increased with increasing the depth of cut, while for the smallest fractions – it decreased. The small values of the leading fractions obtained at a_p=0.5mm (0.06 for γ=5° and 0.05 for γ=30°) can be attributed to the width of the measured chips – compared to their length, the width was very small. With increasing the depth of cut, the chip width was increasing, too, thereby reducing this dimensional difference.

Fig. 7 shows the analysis of chip partial melting produced in the milling of magnesium alloy AZ91HP. Fig. 7 shows the photographs of chips isolated for the highest cutting speeds and feeds per tooth. The edges of chips produced by milling with an end mill described by γ=30° are less fuzzy than those produced by an and mill described by γ=5°. However, none of the above photographs reveals the presence of partial meltings which occur at a temperature that is close to the temperature of ignition. For this reason, it can be concluded that the temperature in the chip formation zone was much lower than ignition temperature. This means that machines can be safely operated under dry machining conditions even in HSC.

Figs. 8 and 9 summarize the results of research on chip fragmentation in the machining of magnesium alloy AZ91HP. The regions prone to the formation of a dust fraction are marked in red.

Both Fig. 8 and Fig. 9 demonstrate that dust fractions are most likely to occur at the smallest depths of cut a_p=0.5mm and a_p=1.5mm. The application of these parameters generated the highest number of dust fractions. The smallest degree of fragmentation was affected by cutting speed and feed per tooth, while the use of the tool described by the rake angle γ=30° led to the production of fewer numbers of fractions.

4. Summary and conclusions

The results of chip fragmentation demonstrate that a lower number of isolated fractions, hence a smaller degree of chip fragmentation are produced by the tool described by the rake angle γ=30°. Moreover, the largest number of chip fractions are isolated when the depth of cut a_p is changed, while the smallest number of fractions are isolated when the cutting speed v_c is changed. In terms of chip size, the lengths of all leading fractions are similar on changing the above parameters; more significant differences can be observed with respect to chip width. The width of leading chip fractions produced with the tool described by the rake angle γ=5° is higher than those of the chips produced at γ=30° for all variables (v_c, f_z, a_p).

The main objective of the investigation was to determine regions in the space of independent variables that are undesired due to the highest concentration of dust fraction. These regions include the lowest depths of cut (a_p=0.5mm and a_p=1.5mm). Examining the shape of the obtained chips, it can be observed that the chips produced at the depth of cut a_p=6mm, feed per tooth f_z=0.15mm/tooth and two cutting speeds v_c: 400m/min and 800m/min, are the most desired in terms of ease of their storage and removal from the machine's working space.

The results have led to the formulation of the following general conclusions with respect to AZ91HP alloy milling:
– from the point of view of milling machine operation, effective (reliable) and safe (failure-free) dry milling treatment of magnesium alloys is a viable process,
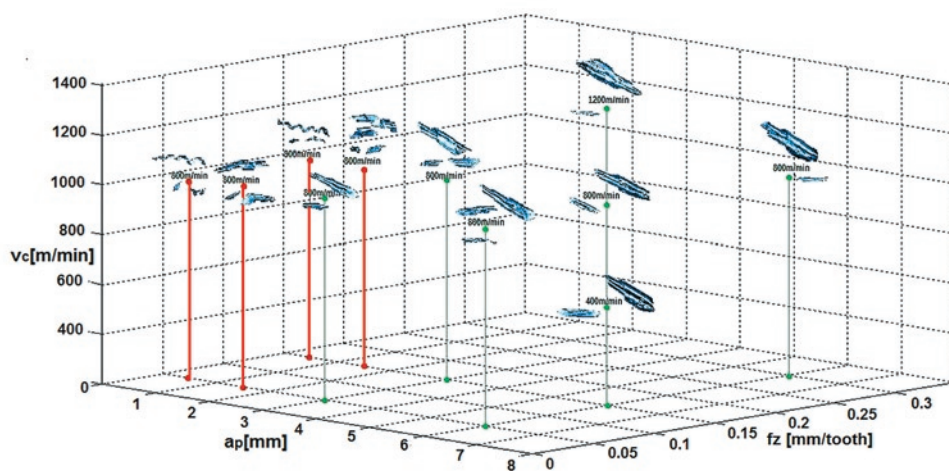

Fig. 8. Degree of chip fragmentation depending on changes in operational parameters v_c, f_z, a_p for the milling cutter with an angle γ=5°
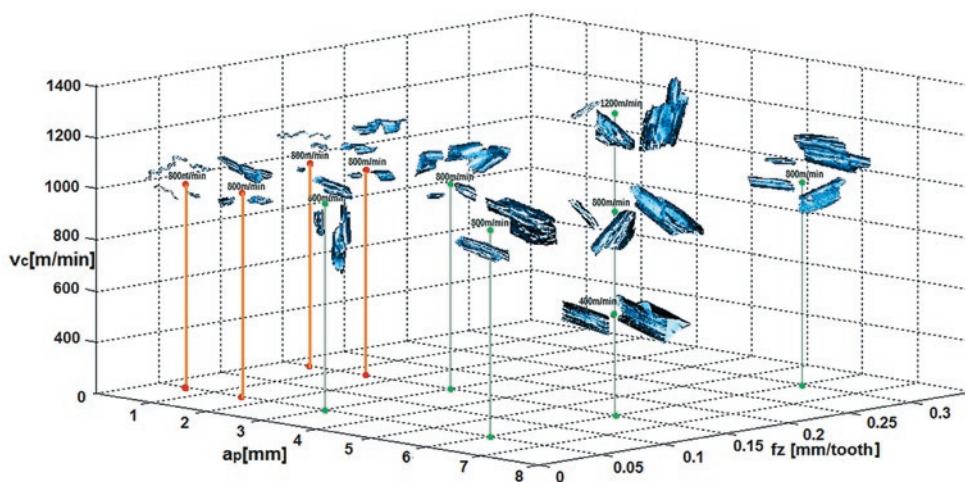

Fig. 9. Degree of chip fragmentation depending on changes in operational parameters v_c, f_z, a_p for the milling cutter with an angle γ=30°

- the desired machining regions are those where magnesium dust does not occur,
- for operational reasons, it is recommended to avoid both small values of a_p and of γ,
- operational parameters which do not lead to damage of the technological machines are contained in the following range: $v_c = 400 \div 800$ m/min, $f_z = 0.15 \div 0.3$ mm/tooth and $a_p \geq 1.5$mm.

The operational parameters of the machining process run under specific conditions can be changed within a certain range of techno-logical variables. It should also be underlined that safe and reliable operation of technological machines in the machining of magnesium alloys is also strongly related to a general culture of machine tool maintenance.

References

1. Akyuz B. Machinability of magnesium and its alloys. TOJSAT: The Online Journal of Science and Technology 2011; 1(3): 31-38.
2. Arai M, Sato S, Ogawa M, Shikata H I. Chip Control in Finish Cutting of Magnesium Alloy. Journal of Materials Processing Technology 1996; 62: 341-344, http://dx.doi.org/10.1016/S0924-0136(96)02432-6.
3. Fang F Z, Lee L C, Liu X D. Mean Flank Temperature Measurement in High Speed Dry Cutting. Journal of Materials Processing Technology 2005; 167: 119-123, http://dx.doi.org/10.1016/j.jmatprotec.2004.10.002.
4. Guo Y B, Salahshoor M. Process mechanics and surface integrity by high-speed dry milling of biodegradable magnesium-calcium implant alloys. CIRP Annals - Manufacturing Technology 2010; 59: 151-154, http://dx.doi.org/10.1016/j.cirp.2010.03.051.
5. Hou J Z, Zhou W, Zhao N. Methods for Prevention of Ignition during Machining of Magnesium Alloys. Key Engineering Materials 2010; 447-448: 150-154, http://dx.doi.org/10.4028/www.scientific.net/KEM.447-448.150.
6. Krolczyk G., Legutko S. Investigations Into Surface Integrity in the Turning Process of Duplex Stainless Steel. Transactions of FAMENA 2014; 38: 77-82.
7. Krolczyk G., Legutko S., Nieslony P., Gajek M. Study of the surface integrity microhardness of austenitic stainless steel after turning. Tehnički Vjesnik – Technical Gazette 2014; 21: 1307-1311.
8. Krolczyk G., Nieslony P., Legutko S., Stoic A. Microhardness changes gradient of the Duplex Stainless Steel (DSS) surface layer after dry turning. Metalurgija 2014; 53: 529-532.
9. Kuczmaszewski J, Pieśko P. Wear of milling cutters resulting from high silicon aluminium alloy cast AlSi21CuNi machining. Eksploatacja i Niezawodnosc – Maintenance and Reliability 2012; 16(1): 37-41.
10. Kuczmaszewski J, Zagórski I. Badania fragmentowania wiórów w procesie frezowania stopów magnezu. Mechanik 2014; 8-9: 321-328.
11. Le Coz G, Marinescu M, Devillez A, Dudzinski D, Velnom L. Measuring temperature of rotating cutting tools: Application to MQL drilling and dry milling of aerospace alloys. Applied Thermal Engineering 2012; 36: 434-441, http://dx.doi.org/10.1016/j.applthermaleng.2011.10.060.
12. Legutko S. Development trends in machines operation maintenance. Eksploatacja i Niezawodnosc – Maintenance and Reliability 2009; 2: 8-16.
13. Legutko S. Podstawy eksploatacji maszyn i urządzeń. Warszawa: Wyd. Szkolne i Pedagogiczne, 2007.
14. Li H Z, Liu K, Li X P. A new method for determining the undeformed chip thickness in milling. Journal of Materials Processing Technology 2001; 113(1-3): 378-384, http://dx.doi.org/10.1016/S0924-0136(01)00586-6.
15. Lotfi Sai, Bouzid W, Zghal A. Chip thickness analysis for different tool motions for adaptive feed rate. Journal of Materials Processing Technology 2008; 204(1-3): 213-220, http://dx.doi.org/10.1016/j.jmatprotec.2007.11.094.
16. Oczoś K E. Extension of the magnesium alloys application range. Mechanik 2009; 5-6: 386-400.
17. Oczoś K E, Kawalec A. Kształtowanie metali lekkich. Warszawa: PWN, 2012.
18. Oziemski S. Efektywność eksploatacji maszyn, Podstawy techniczno-ekonomiczne. Radom: Wyd. Instytutu Technologii Eksploatacji, 1999.
19. Semotiuk L. An analysis of the operational characteristics of innovative tool structures used in high speed rough milling processes. Eksploatacja i Niezawodnosc – Maintenance and Reliability 2009; 1: 46-53.
20. Wojciechowski S., Twardowski P., Wieczorowski M. Surface texture analysis after ball end milling with various surface inclination of hardened steel. Metrology and Measurement Systems 2014; 21(1): 145-56, http://dx.doi.org/10.2478/mms-2014-0014.
21. Zhao N, Hou J, Zhu S. Chip ignition in research on high-speed face milling AM50A magnesium alloy. Second International Conference on Mechanic Automation and Control Engineering 15-17 July 2011; Inner Mongolia, China, http://dx.doi.org/10.1109/MACE.2011.5987127.
22. POLSKA NORMA Badanie trwałości noży tokarskich punktowych. PN–ISO 3685:1996.
23. http://www.polmag.pl/, z dnia 20.03.2015r.

Olga GZIUT
Józef KUCZMASZEWSKI
Ireneusz ZAGÓRSKI
Lublin University of Technology
Mechanical Engineering Faculty
Department of Production Engineering
ul. Nadbystrzycka 36, 20-618 Lublin, Poland
E-mail: j.kuczmaszewski@pollub.pl, i.zagorski@pollub.pl

Jinlei QIN
Yuguang NIU
Zheng LI

A COMBINED METHOD FOR RELIABILITY ANALYSIS OF MULTI-STATE SYSTEM OF MINOR-REPAIRABLE COMPONENTS

ŁĄCZONA METODA ANALIZY NIEZAWODNOŚCI SYSTEMU WIELOSTANOWEGO SKŁADAJĄCEGO SIĘ Z ELEMENTÓW PODLEGAJĄCYCH DROBNEJ NAPRAWIE

This paper discusses the multi-state system (MSS) consisted of multi-state components with minor failure and minor repair. In order to obtain the reliability indices of MSS, a new combined method is suggested. This method is based on the Markov stochastic process and the universal generating function (UGF) technology. The traditional idea of modeling the MSS is to use straightforward Markov process. That is not effective enough for the MSS because the model of the system is complicated usually and the state space often arouses "dimension curse" - huge numbers of the states. We suggest it should model the multi-state components and the UGF of multi-state components can be obtained firstly. Then the MSS can be decomposed into several subsystems which only contain simple series-parallel structure. According to the physical nature of the subsystems, the UGF of those subsystems can be employed recursively. Furthermore the UGF of the entire MSS will be obtained. Therefore, the reliability indices of the MSS can be evaluated easily. The suggested method simplifies greatly the complexity of calculation and is well formulized. Two numerical examples illustrate this method.

***Keywords**: multi-state system, reliability index, Markov stochastic process, universal generating function, minor repair.*

W artykule omówiono system wielostanowy (multi-state system, MSS) składający się z elementów wielostanowych, które mogą ulegać drobnym uszkodzeniom i podlegają drobnym naprawom. Zaproponowano nową metodę łączoną, która pozwala wyznaczać wskaźniki niezawodności MSS. Metoda ta opiera się na procesie stochastycznym Markowa oraz technologii uniwersalnej funkcji tworzącej (universal generating function, UGF). Tradycyjnie do modelowania MSS wykorzystuje się sam proces Markowa. Metoda ta nie jest jednak wystarczająco skuteczna w przypadku MSS, ponieważ modele tego typu systemów są zazwyczaj skomplikowane, a przestrzeń stanów często prowadzi do tzw. "przekleństwa wielowymiarowości" – konieczności uwzględnienia ogromnej liczby stanów. Nasza metoda polega na modelowaniu elementów wielostanowych, dla których, w pierwszej kolejności wyznacza się UGF. Następnie MSS można rozłożyć na kilka podsystemów, które mają prostą strukturę szeregowo-równoległą. Charakter fizyczny tych podsystemów, pozwala na rekurencyjne stosowanie UGF dla tych podsystemów. Ponadto metoda umożliwia wyznaczenie UGF dla całego MSS, co pozwala na łatwą ocenę wskaźników niezawodności MSS. Proponowana metoda znacznie upraszcza obliczenia i jest dobrze sformalizowana. W pracy przedstawiono dwa przykłady numeryczne, które ilustrują omawianą metodę.

***Słowa kluczowe**: system wielostanowy, wskaźnik niezawodności, proces stochastyczny Markowa, uniwersalna funkcja tworząca, drobne naprawy.*

1. Introduction

The classical reliability principles allow that a system and/or a component can only have two functional states, perfect functionality and complete failure. Numerous research efforts have been devoted to binary-state reliability theory, modeling, indices analysis and calculation etc [6, 5, 35, 4, 33]. However, those theories and assumptions are oversimplified for the realistic situations. In addition to the two states mentioned above, many complicated systems and/or their constitutive components have several intermediate states typically in real world. For example, the manufacturing, production, power generation and oil and/or gas transportation systems, whose overall performance can be settled on different levels (e.g. 100%, 80%, 50% of the nominal capacity), depending on their operating conditions of their constitutive multi-state elements [12, 31, 24, 34, 44, 9]. These phenomena make it cumbersome to suffice increasingly stringent requirements for accurate reliability assessment using traditional binary reliabil-ity methods. Therefore, the reliability theories for multi-state system (MSS) have been impelled strongly.

The early research in MSS had been focused on the extensions of binary-state components and coherent systems. The generalization of binary coherent systems had been developed early for multi-state components by Barlow and Wu [7]. The widespread recognition of MSS is that it has been defined as having different performance levels and/or some failure modes with corresponding effects on the system's entire performance. Many researchers have made various contributions for the MSS reliability evaluation and modeling theory recently [13, 23, 8, 9, 27, 40]. The commonly adopted methods have five basic approaches, such as, an extension of binary theory to MSS cases, the stochastic process approach, the universal generating function (UGF), the Monte-Carlo simulation and recursive algorithm etc [14, 45, 22, 19, 2, 20, 37]. The recent advances in MSS reliability theory have been collected in [1].

The modern stochastic process theory provides an advanced probabilistic framework which allows one to do many thing, just to name a few, to formulate the general failure models for the real systems, to obtain explicit formulas of various reliability indices for calculation, and to determine the optimal maintenance plans in complex situation etc. [3, 29, 24, 34, 2]. Especially the random process methods are often suggested to evaluate its reliability for a MSS with repairable components. Based on these methods, the state-space diagram of an MSS should be constructed firstly and then the transitions between all the states should be also determined subsequently. Usually the evolution process of a system can be represented by a continuous-time discrete state random process.

Usually, when the number of the system state is not too large, the mentioned above can be adopted directly. However, for the realistic engineering system, the straightforward using of random process for MSS reliability assessment is very difficult due to the "dimension explosion" - herds of system states. In order to formalize the analysis of MSS, considering a system made up of n different repairable components. Each component i has $m_i + 1$ different performance levels, $i = 1, 2, \ldots, n$, such that the system is characterized by a state set of $M_{sys} = \prod_{i=1}^{n}(m_i + 1)$. The value of M_{sys} may be very huge even for a relative small MSS. For example, the maintenance strategies optimization of series-parallel systems often is involved in the combination of the component-level maintenance strategies. As the MSS described in [42], there are more than six millionaire possible combinations for multi-state component replacement strategy even though the system has only 4 subsystems and 14 components with less than 5 degradation states for each component. According to the maintenance strategy structure considered in [43], the size of the system-level strategy space will be also able to reach more than 100 million which is too large to be processed by the general enumeration method, where the system contains only 6 subsystems and 21 components with not more than 6 states. This "combinatorial explosion" situation can be also encountered in [41, 11, 38] etc.

In addition, for a MSS the drawing of state-space diagram or modeling of construction is also a trivial work because non-formularized process may bring numerous mistakes even for a moderate scale MSS. The correct identification for all of the states and the transitions between states are also not a simple assignment. At the same time the current available computer resources may limit the feasibility of solving a model of hundreds of state equations.

In order to reduce the computational complexity of MSS, the UGF method, which had been proven to be very effective for high-dimension combinational problems, was introduced primarily by Ushakov [36]. A comprehensive up-to-date representation of UGF with many technical applications and its mathematical foundations can be found in [16]. A novel algorithm based on this technology had been developed for the reliability evaluation of an acyclic multi-state-node network system in [39]. It has also been extended in various fields such as the applications of fuzzy set theory, reliability redundancy optimal problem, maintenance decision-making etc resorting to its straightforward properties [10, 26, 28, 21]. The MSS performance distribution can be determined by the using of UGF method. The output performance levels of an MSS with series, parallel, series-parallel and bridge structure were evaluated in [18, 17, 25, 30, 32, 38] by the defined different composition operators.

Our contributions are as follows. We focus on the problem of evaluating the reliability and performance level of MSS consisted of repairable elements with statistically independent and with given failure probabilities. Considering the complexity of state and computation, the method's development may be extremely appealed to reliability engineers. The suggested approach is based on the stochastic process and UGF with the combination of block diagram method.[15].

2. Stochastic process for MSS

2.1. Model for the MSS

For the purpose of modeling an MSS, the characteristics of its elements need to be first defined. Generally speaking, any elements i in MSS can have $m_i + 1$ different states corresponding to the performance levels which can be represented by the set:

$$\mathbf{g}_i = \left\{ g_{i0}, g_{i1}, \cdots, g_{im_i} \right\}, \tag{1}$$

where: g_{is} is the performance level of element i in the state s, $s \in \{0, 1, \cdots, m_i\}$. The current performance level G_i of element i at any instant time is a discrete random variable that takes value from $\mathbf{g}_i$: $G_i \in \mathbf{g}_i$. The probabilities of each different state or performance level for element i can be denoted by the set:

$$\mathbf{p}_i = \left\{ p_{i0}, p_{i1}, \cdots, p_{im_i} \right\}, \tag{2}$$

where:

$$p_{is} = \Pr\{G_i = g_{is}\}. \tag{3}$$

Furthermore, one element's entire states composed a complete group are mutually exclusive event. That is to say, the element i will be always in one and only one of $m_i + 1$ states, such that:

$$\sum_{s=0}^{m_i} p_{is} = 1. \tag{4}$$

Actually, eq. (3) defines the probability mass function (pmf) of the random variable G_i. The performance level distribution of element i will be determined completely by the collection of pairs:

$$CP_i = (g_{is}, p_{is}), s = 0, 1, \cdots, m_i. \tag{5}$$

The system elements have certain performance levels corresponding to their respective states at one instant time. The modeling of an MSS performance level is totally determined by the $CP_i, i = 1, 2, \cdots n$ when some external factors such as human incorrect operation, environmental effect etc, are out of consideration. Therefore, the states of an MSS are determined totally by the states of its components. Suppose the MSS has $k + 1$ different states and the performance level corresponding to one state of the MSS at certain moment can be represented by $v_j, j = 0, 1, \cdots, k$. The MSS performance level is a random variable denoted by V that takes values from the set:

$$V = \{v_0, v_1, \cdots, v_k\}. \tag{6}$$

The pmf of the MSS performance levels can be obtained in the following form:

$$q_j = \Pr\{V = v_j\}, j = 0, 1, \cdots, k. \tag{7}$$

Using Cartesian product, we can define the space of all possible combinations of performance levels for all of system components as:

$$C^n = \prod_{i=1}^{n} \left\{ g_{i0}, g_{i1}, \cdots, g_{im_i} \right\}. \qquad (8)$$

The MSS system structure function is naturally introduced as:

$$\Phi(G_1, G_2, \cdots, G_n) : C^n \rightarrow V, \qquad (9)$$

whose function is to map the space of the component's performance levels into the space of performance levels of MSS.

From the analysis mentioned above, the model of MSS includes two parts: one is the pmf of performance levels for all of the components, and the other is the structure function of the system. They can be rewritten as the following:

$$\begin{cases} \mathbf{g}_i, \mathbf{p}_i, 0 \le i \le n \\ V = \Phi(G_1, \cdots G_n) \end{cases}. \qquad (10)$$

2.2. Repairable model for multi-state component

One pervasive situation for a multi-state component is that it has a degradation (wear-out) and opposite (repairing) process. Without the loss of generality, the two processes can be defined as minor failures and minor repairs. For the multi-state component i there is a performance level g_{is} corresponding to every state s. Those states will be ordered by performance level so that $g_{is} \le g_{is+1}$ for any state s. The minor failures cause state transition only from s to an adjacent state $s-1$ where $1 \le s \le m_i$. Conversely the minor repairs can only lead to the state transition from s to an adjacent state $s+1$ where $0 \le s \le m_i - 1$. That is to say, the component in the state s will be in transition to $s-1$ if failure occurs and if repair has been accomplished the component in the state s will transit to $s+1$. The special case is that in the state 0 it can only be repaired and transit to the state 1 and in the state m_i it can only degrade to state $m_i - 1$. The state transition diagram of component i with minor failure and minor repair has been presented in Fig.1.
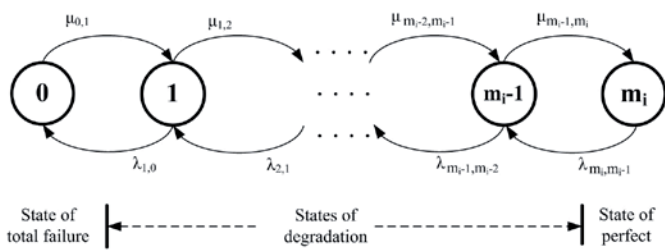
Fig. 1. State transition diagram of multi-state component i with minor failure and minor repair

For a multi-state component its performance transition process will have Markov property and can be modeled as a Markov stochastic process if all its failure and repair times are exponential distribution. For a Markov stochastic process, each state transition has its own transition probability density. As represented in Fig.1, the failure rate $\lambda_{1,0}$ denotes the transition probability density from state 1 to state 0 because of minor failure and the repair rate $\mu_{0,1}$ indicates the corresponding transition intensity from state 0 to state 1 after the minor repair had been implemented. The other transition intensities have the mimic meanings. The corresponding performance level g_{is} is associated with each component's state s.

Because the probability distribution of multi-state component i associated to one state s is a function of time t, the index i of one multi-state component has been omitted for the straightforward expression. Such that eq. (3) can be rewritten as:

$$p_s(t) = \Pr\{G(t) = g_s\}, 0 \le t. \qquad (11)$$

Probabilities $p_s(t), s = 0, 1, \cdots, m$ can be figured out from the solution in the following system of differential equations for the Markov stochastic process of multi-state component:

$$\frac{dp_s(t)}{dt} = \sum_{\substack{i=0 \\ i \ne s}}^{m} p_i(t) \alpha_{is} - p_s(t) \sum_{\substack{i=0 \\ i \ne s}}^{m} \alpha_{si}, \qquad (12)$$

where α_{is} is the transition intensities from state i to state s. In this paper all transitions are triggered by the component's minor failures and repairs and so the α_{is} and α_{si} is corresponded to the repair rates and failure rates for the state s respectively. Therefore, the corresponding system of differential equations may be unfolded as:

$$\begin{cases} \dfrac{dp_0(t)}{dt} = \lambda_{10} p_1(t) - u_{01} p_0(t) \\ \dfrac{dp_1(t)}{dt} = \mu_{01} p_0(t) + \lambda_{21} p_2(t) - (u_{12} + \lambda_{10}) p_1(t) \\ \cdots = \cdots \\ \dfrac{dp_m(t)}{dt} = \mu_{m-1,m} p_{m-1}(t) - \lambda_{m,m-1} p_m(t) \end{cases}. \qquad (13)$$

In terms of the reliability meaning, the component's initial state should be in the best performance level, scilicet in the state m at the time $t = 0$. So we can reasonably assume that:

$$\begin{cases} p_0(0) = p_1(0) = \cdots = p_{m-1}(0) = 0 \\ p_m(0) = 1 \end{cases}. \qquad (14)$$

Wherefore, the multi-state component probabilities distribution $p_s(t), s = 0, 1, \cdots, m$ can be obtained by solving eq. (13) and eq. (14).

3. Universal generating function technology

Universal generating function, which is proven to be a very effective method for high-dimension combinatorial problem, is also named as u-function or universal z-transform [16]. Its mathematical fundamental is the extension of the widely known ordinary moment generating function and z-transformation.

The UGF of a multi-state component i with performance level associated with the pmf is defined as a polynomial:

$$u_i(z) = \sum_{h_i=0}^{m_i} p_{ih_i} z^{g_{ih_i}}, i = 1, 2, \cdots, n. \qquad (15)$$

The essential property of UGF enables the entire UGF for a MSS, whose components were connected in series or parallel, to be obtained using simple algebraic operations on individual UGF of multi-state component. To represent the pmf of the stochastic variable $V = \Phi(G_1, \cdots G_n)$, the composition operator $\underset{\phi}{\otimes}$ is defined by:

$$U(z) = \underset{\phi}{\otimes}(u_1(z), u_2(z), \cdots, u_n(z)) = \underset{\phi}{\otimes}(\sum_{h_1=0}^{m_1} p_{1h_1} z^{g_{1h_1}}, \sum_{h_2=0}^{m_2} p_{2h_2} z^{g_{2h_2}}, \cdots, \sum_{h_n=0}^{m_n} p_{nh_n} z^{g_{nh_n}})$$

$$= \sum_{h_1=0}^{m_1} \sum_{h_2=0}^{m_2} \cdots \sum_{h_n=0}^{m_n} \left(\prod_{i=1}^{n} p_{ih_i} z^{\phi(g_{1h_1}, g_{2h_2}, \cdots, g_{nh_n})} \right)$$

(16)

Note that the polynomial $U(z)$ represents all possible mutually exclusive combinations of individual independent component's UGF. The function $\phi(g_{1h_1}, g_{2h_2}, \cdots, g_{nh_n})$ is determined according to the physical nature of the interaction between component's performances.

Indeed, the derivation of $U(z)$ for various types of systems is a troublesome task usually. As shown in [16], from the computation simplicity and derivation clarity viewpoints representing the $U(z)$ in a recursive form is beneficial. Especially when an MSS has a complex configuration, the entire system can be represented as the composition of some subsystems corresponding to some subsets of multi-state components. This property can be defined by:

$$\underset{\phi}{\otimes}(u_1(z), \cdots, u_k(z), u_{k+1}(z), \cdots, u_n(z)) = \underset{\phi}{\otimes}(\underset{\phi}{\otimes}(u_1(z), \cdots, u_k(z)), \underset{\phi}{\otimes}(u_{k+1}(z), \cdots, u_n(z)))$$

(17)

The configuration of any MSS can always be represented as a composition of independent subsystems containing only components connected in parallel or series. For any components connected in the parallel or in series in the MSS, the composition operator can be applied recursively for obtaining UGF of the intermediate pure parallel or pure series structures.

Considering one type of MSS system, for example power system, energy or materials continuous transmission system, and manufacturing system with its performance level defined as productivity. For components in parallel, the system total productivity is the sum of productivities of all its components. If two independent components (i and j) work in parallel, the total productivity is the sum of their individual productivity. The function ϕ_p should get the sum of corresponding parameters. The performance of the pair of components in this case is defined as:

$$U_{ij}(z) = u_i(z) \underset{\phi_p}{\otimes} u_j(z) = \sum_{h_i=0}^{m_i} \sum_{h_j=0}^{m_j} p_{ih_i} p_{jh_j} z^{sum(g_{ih_i}, g_{jh_j})}. \quad (18)$$

For components in series, the component with the minimal productivity becomes the system bottleneck. The function ϕ_s should get the minimum of all parameters. Therefore, the UGF for this case should take this form:

$$U_{ij}(z) = u_i(z) \underset{\phi_s}{\otimes} u_j(z) = \sum_{h_i=0}^{m_i} \sum_{h_j=0}^{m_j} p_{ih_i} p_{jh_j} z^{min(g_{ih_i}, g_{jh_j})}. \quad (19)$$

4. MSS reliability evaluation method

Based on the considerations presented above, the method consisted of Markov stochastic process and UGF can be applied using the following algorithm:

1) Drawing the state-space diagram for the multi-state components of the MSS.
2) Based on the reliability data (failure and repair data, state space) for all the multi-state components in MSS, individual

pmf of each component can be obtained by solving the corresponding systems of differential eq. (13) and eq. (14).

3) Having the performance level and corresponding probabilities for each component, the UGF for one component can be written in the form of eq. (15).
4) According to the configuration of system structure, the UGF of the entire MSS can be obtained by applying eq. (17), (18) and (19) recursively:

$$U(z,t) = \sum_{j=0}^{M_{sys}} p_j^{(sys)}(t) z^{g_j^{(sys)}}, \quad (20)$$

where M_{sys} is the state where system has the highest performance level and $g_j^{(sys)}$ is the system performance level in the corresponding state j, $j = 0, 1, \cdots, M_{sys}$.

5) Calculating reliability indices by the UGF of the entire MSS.

5. Reliability indices for entire MSS

When the UGF of the entire MSS has been obtained, the following reliability indices can be evaluated easily.

The entire MSS availability $A(t)$ at instant $t > 0$ cab be evaluated as:

$$A(t) = \delta(U(z,t)) = \sum_{j=0}^{M_{sys}} p_j^{(sys)}(t) \delta(g_j^{(sys)} > 0), \quad (21)$$

where $\delta(True) \equiv 1, \delta(False) \equiv 0$.

For a arbitrary constant demand w, the MSS availability $A(t,w)$ at instant $t > 0$ has the like form:

$$A(t,w) = \delta(U(z,t),w) = \sum_{j=0}^{M_{sys}} p_j^{(sys)}(t) \delta(g_j^{(sys)} \geq w). \quad (22)$$

The MSS expected output performance level $E(t)$ at instant $t > 0$ is defined as:

$$E(t) = \delta_E(U(z,t)) = \delta_E(\sum_{j=0}^{M_{sys}} p_j^{(sys)}(t) z^{g_j^{(sys)}}) = \sum_{j=0}^{M_{sys}} p_j^{(sys)}(t) g_j^{(sys)}. \quad (23)$$

The MSS expected performance deficiency $D(t,w)$ at instant $t > 0$ for arbitrary constant demand w is of the form:

$$D(t,w) = \delta_D(U(z,t),w) = \delta_D(\sum_{j=0}^{M_{sys}} p_j^{(sys)}(t) z^{g_j^{(sys)}}, w) = \sum_{j=0}^{M_{sys}} p_j^{(sys)}(t) \max(w - g_j^{(sys)}, 0). \quad (24)$$

6. Illustrative examples

Example 1. A numerical example illustrates the algorithm presented above. Series-parallel structure is often used for the configuration of system as shown in Fig. 2.

This configuration can be seen for example in a flow transmission system whose components are transmission pipe. The steam/oil flow is transmitted from left (A) to right (B) by three pipes denoted
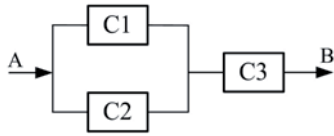
Fig. 2. Series-parallel structure reliability block diagram

as C1, C2 and C3. The component's performance is measured by its transmission capacity (t/m: tons per minute). Assuming for all the components the times to failure and times to repair are distributed exponentially. C1 and C2 are repairable and each has two states: total failure (0) and perfect function (1). C3 is a multi-state component with minor failures and minor repairs. It has three states: total failure (0), partial failure (1) and perfect function (2).

Applying the evaluation method described above, component's state-space transition diagrams are shown firstly in Fig. 3.
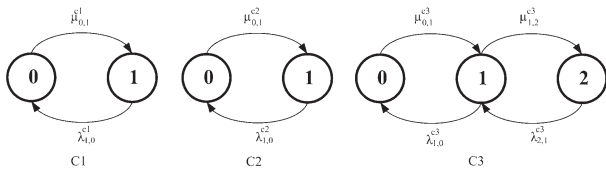
Fig. 3. Component's state-space transmission diagrams

Second, according to the Markov stochastic process, the following systems of differential equations of individual component can be built separately using the corresponding state-space transmission diagram.

The basic reliability data are presented in Table 1 which gives the $\mathbf{g}$, λ and μ of each component.

Table 1.   Reliability data for multi-state components

Component	States	Performance (t/m)	Failure rate (year^{-1})	Repair Rate (year^{-1})
i	j	g_j^i	$\lambda_{j,j-1}^i$	$\mu_{j,j+1}^i$
C1	0	0	-	100
	1	1.5	7	-
C2	0	0	-	80
	1	2	10	-
C3	0	0	-	120
	1	1.8	7	110
	2	4	10	-

For C1, one can obtain:

$$\begin{cases} \dfrac{dp_0^{c1}(t)}{dt} = \lambda_{10}^{c1} p_1^{c1}(t) - u_{01}^{c1} p_0^{c1}(t) \\ \dfrac{dp_1^{c1}(t)}{dt} = -\lambda_{10}^{c1} p_1^{c1}(t) + u_{01}^{c1} p_0^{c1}(t) \end{cases}, \qquad (25)$$

where the initial parameters are $p_0^{c1}(0) = 0, p_1^{c1}(0) = 1$.

For C2, its differential equations are:

$$\begin{cases} \dfrac{dp_0^{c2}(t)}{dt} = \lambda_{10}^{c2} p_1^{c2}(t) - u_{01}^{c2} p_0^{c2}(t) \\ \dfrac{dp_1^{c2}(t)}{dt} = -\lambda_{10}^{c2} p_1^{c2}(t) + u_{01}^{c2} p_0^{c2}(t) \end{cases}, \qquad (26)$$

likewise the initial conditions are $p_0^{c2}(0) = 0$, $p_1^{c2}(0) = 1$.

For C3, we can also get its state differential equations

$$\begin{cases} \dfrac{dp_0^{c3}(t)}{dt} = \lambda_{10}^{c3} p_1^{c3}(t) - u_{01}^{c3} p_0^{c3}(t) \\ \dfrac{dp_1^{c3}(t)}{dt} = \lambda_{21}^{c3} p_2^{c3}(t) + u_{01}^{c3} p_0^{c3}(t) - (\lambda_{10}^{c3} + u_{12}^{c3}) p_1^{c3}(t), \\ \dfrac{dp_2^{c3}(t)}{dt} = -\lambda_{21}^{c3} p_2^{c3}(t) + u_{12}^{c3} p_1^{c3}(t) \end{cases} \qquad (27)$$

where the initial conditions are $p_0^{c3}(0) = p_1^{c3}(0) = 0$, $p_2^{c3}(0) = 1$.

According to the property of Laplace transform, the closed form solutions of $\mathbf{p}^{c1}(t), \mathbf{p}^{c2}(t), \mathbf{p}^{c3}(t)$ can be obtained from eq. (25), (26) and (27).

Third, the UGF of the individual component can be obtained combining the performance level and corresponding probability distribution:

$$\begin{cases} u_1(z) = p_0^{c1}(t) z^{g_0^{c1}} + p_1^{c1}(t) z^{g_1^{c1}} = p_0^{c1}(t) z^0 + p_1^{c1}(t) z^{1.5} \\ u_2(z) = p_0^{c2}(t) z^{g_0^{c2}} + p_1^{c2}(t) z^{g_1^{c2}} = p_0^{c2}(t) z^0 + p_1^{c2}(t) z^2 \\ u_3(z) = p_0^{c3}(t) z^{g_0^{c3}} + p_1^{c3}(t) z^{g_1^{c3}} + p_2^{c3}(t) z^{g_2^{c3}} = p_0^{c3}(t) z^0 + p_1^{c3}(t) z^{1.8} + p_2^{c3}(t) z^4 \end{cases} \qquad (28)$$

Fourth, according to the configuration of components, the UGF of subsystem $sub12$ consisted of C1 and C2 connected in parallel can be obtained using eq. (18):

$$\begin{aligned} U_{sub12}(z) &= u_1(z) \underset{\phi_p}{\otimes} u_2(z) = (p_0^{c1}(t) z^0 + p_1^{c1}(t) z^{1.5}) \underset{\phi_p}{\otimes} (p_0^{c2}(t) z^0 + p_1^{c2}(t) z^2) \\ &= p_0^{c1}(t) p_0^{c2}(t) z^0 + p_1^{c1}(t) p_0^{c2}(t) z^{1.5} + p_0^{c1}(t) p_1^{c2}(t) z^2 + p_1^{c1}(t) p_1^{c2}(t) z^{3.5} \end{aligned} \qquad (29)$$

As can be found the resulting of U_{sub12} is actually the algebraic product of $u_1(z)$ and $u_2(z)$. Then the entire MSS can be seen as a series connected $sub12$ and C3, the eq. (19) should be espoused to solve the UGF of the system:

$$U(z) = U_{sub12}(z) \underset{\phi_s}{\otimes} u_3(z). \qquad (30)$$

In addition to the same point that the resulting UGF $U(z)$ is also a product of polynomials, what is in difference with function ϕ_p is that function ϕ_s deals with the powers of z as the minimum of powers of the corresponding terms. Taking into account that:

$$\begin{cases} p_0^{c1}(t) + p_1^{c1}(t) = 1 \\ p_0^{c2}(t) + p_1^{c2}(t) = 1 \\ p_0^{c3}(t) + p_1^{c3}(t) + p_2^{c3}(t) = 1 \end{cases}, \qquad (31)$$

The UGF of the total MSS can be obtained in the following form:

$$U(z) = \sum_{i=0}^{4} p_i(t) z^{g_i} . \qquad (32)$$

where:

$$\mathbf{g} = (g_0, g_1, g_2, g_3, g_4) = (0, 1.5, 1.8, 2.0, 3.5) , \qquad (33)$$

$$\mathbf{p} = \begin{pmatrix} p_0(t) \\ p_1(t) \\ p_2(t) \\ p_3(t) \\ p_4(t) \end{pmatrix} = \begin{pmatrix} p_0^{c1}(t) p_0^{c2}(t) + p_0^{c1}(t) p_1^{c2}(t) p_0^{c3}(t) + p_1^{c1}(t) p_0^{c3}(t) \\ p_1^{c1}(t) p_0^{c2}(t) (p_1^{c3}(t) + p_2^{c3}(t)) \\ p_1^{c2}(t) p_1^{c3}(t) \\ p_0^{c1}(t) p_1^{c2}(t) p_2^{c3}(t) \\ p_1^{c1}(t) p_1^{c2}(t) p_2^{c3}(t) \end{pmatrix} . \qquad (34)$$

Finally, the MSS reliability indices can be calculated respectively by using eq. (21), (22), (23) and (24) based on the UGF of the entire MSS.

The instantaneous MSS availability $A(t)$ at $t > 0$:

$$A(t) = \delta(U(z,t)) = \sum_{j=0}^{4} p_j(t) \delta(g_j > 0) = \sum_{j=1}^{4} p_j(t) = 1 - p_0(t) . \quad (35)$$

For a arbitrary constant demand $w = 2.0 t / m$, the MSS availability $A(t, w)$ at instant $t > 0$:

$$A(t, w) = \sum_{j=0}^{4} p_j(t) \delta(g_j \geq 2) = p_3(t) + p_4(t) . \qquad (36)$$

The MSS expected output performance level $E(t)$ at instant $t > 0$:

$$E(t) = \delta_E(U(z,t)) = \sum_{j=0}^{4} p_j(t) g_j . \qquad (37)$$

The MSS expected performance deficiency $D(t, w)$ at instant $t > 0$ for arbitrary constant demand $w = 2.0 t / m$:

$$D(t, w) = \sum_{j=0}^{4} p_j(t) \max(2 - g_j, 0) = 2 p_0(t) + 0.5 p_1(t) + 0.2 p_2(t). \quad (38)$$

From the above we can find that the MSS mentioned will be of 2*2*3=12 differential equations if the straightforward Markov stochastic method were performed. Consequently the computational efforts will be consumed numerously. However the presented combined approach needs only to solve three differential equations of component: two of second-order and one of third-order. The further derivation of the MSS state probabilities and reliability indices is based on the UGF which can be implemented by simple mathematical calculation.

Example 2. A more realistic system can be adopted to validate its applicability and effectiveness of the new approach. The system is a power station coal feeding system supplying a boiler with coal. It consists of five basic subsystems as shown in Fig. 4 [43].

The function of each subsystem can be described as following. The subsystem 1 is the primary feeder which loads the coal from the bin to the primary conveyor. The primary conveyor can be seen as the subsystem 2 which transports the coal to the stacker-reclaimer. The subsystem 3 is the stacker-reclaimer which lifts the coal up to the burner level. The secondary feeder is the subsystem 4 which loads
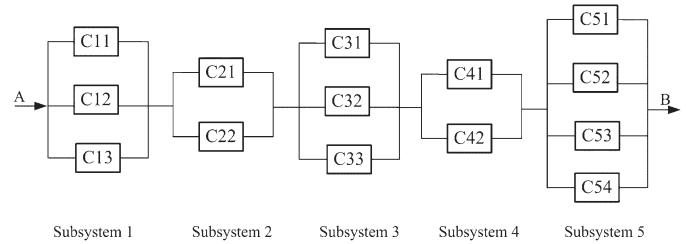
Fig. 4. Reliability block diagram of the coal feeding system with five subsystems

the secondary conveyor. The subsystem 5 is the secondary conveyor which supplies the burner feeding system of the boiler [29]. The elements in subsystem 1, 3 and 4 have four states corresponding to their performance level. The subsystem 2 consists of two three-state elements while the subsystem 5 consists of four elements with five states. Generally speaking, we can assume that each subsystem consists of the same type of component respectively. The state transition intensities and state performance rate of each component extracted from [42] are tabulated in Table 2. For the purpose of terseness, the first component of subsystem 1 and subsystem 2 are only listed and we will only discuss the series of subsystem 1 and subsystem 2.

Table 2. The basic data of each type component

Component	States	Performance (ton/day)	Failure rate (year^{-1})	Repair Rate (year^{-1})
i	j	g_j^i	$\lambda_{j,j-1}^i$	$\mu_{j,j+1}^i$
C11	0	0	-	2
	1	40	0.5	2
	2	60	0.3	2
	3	80	0.2	-
C21	0	0	-	3
	1	70	0.5	3
	2	120	0.2	-

Here, we omit the steps, which are similar to the first example, to solve the state probability distribution of each multistate component. The state probability of each component can be written as $\mathbf{P}^{C11}(t) = (p_0^{C11}(t), p_1^{C11}(t), p_2^{C11}(t), p_3^{C11}(t))$ and $\mathbf{P}^{C21}(t) = (p_0^{C21}(t), p_1^{C21}(t), p_2^{C21}(t))$. The UGF of component C11 and C21 will be obtained as:

$$\begin{cases} U_{C11} = p_0^{C11}(t) * z^0 + p_1^{C11}(t) * z^{40} + p_2^{C11}(t) * z^{60} + p_3^{C11}(t) * z^{80} \\ U_{C21} = p_0^{C21}(t) * z^0 + p_1^{C21}(t) * z^{70} + p_2^{C21}(t) * z^{120} \end{cases} .$$

$$(39)$$

Because the type of component within subsystem1 is same, such that $U_{C11} = U_{C12} = U_{C13} = U_{C14}$. According to eq. (18), the UGF of the subsystem 1 will be rewritten as:

$$U_{subs1} = U_{C11} \underset{\phi_p}{\otimes} U_{C12} \underset{\phi_p}{\otimes} U_{C13} \underset{\phi_p}{\otimes} U_{C14} . \qquad (40)$$

When $t = 0.5$ year, the probability distribution of each state for each component of subsystem 1 will be same as $\mathbf{P}^{C11}(0.5) = (0.0004, 0.0055, 0.0894, 0.9407)$. Substituting the $\mathbf{P}^{C11}(0.5)$ into the above equation, the eq. (40) can be expressed as:

$$U_{subs1} = 0.2560e\text{-}13*z^0 + 0.1408e\text{-}11*z^{40} + 0.2289e\text{-}10*z^{60} + 0.2606e\text{-}9*z^{80} + 0.9441e\text{-}9*z^{100} +$$
$$0.1749e\text{-}7*z^{120} + 0.1683e\text{-}6*z^{140} + 0.1129e\text{-}5*z^{160} + 0.5473e\text{-}5*z^{180} + 0.5837e\text{-}4*z^{200} +$$
$$0.3963e\text{-}3*z^{220} + 0.1874e\text{-}2*z^{240} + 0.7415e\text{-}2*z^{260} + 0.5554e\text{-}1*z^{280} + 0.2648*z^{300} + 0.6699*z^{320}$$

.

(41)

From the above formula, it can be found that the probability transporting performance less 200 ton/day for subsystem 1 at the time 0.5 year is less 0.0001 and almost can be neglected.

In the same way, the probability for each component of subsystem 2 can be figured out as $\mathbf{P}^{C21}(0.5) = \mathbf{P}^{C22}(0.5) = (0.0047, 0.0477, 0.9476)$.

Combining the probability with the operator $\otimes_{\phi_p}$, the UGF of the subsystem 2 will be written as:

$$U_{subs2} = 0.2209e\text{-}4*z^0 + 0.4484e\text{-}3*z^{70} + 0.8907e\text{-}2*z^{120}$$
$$+ 0.2275e\text{-}2*z^{140} + 0.9040e\text{-}1*z^{190} + 0.8979*z^{240} \quad .(42)$$

In order to calculate the probability distribution of the series structure of subsystem 1 and subsystem 2 at $t = 0.5$ year, we tabulate their state/performance probability distribution in the Table 3. Among all the states, those states whose probability is very little are ignored.

Denoted the series structure of subsystem1 and subsystem 2 by $S_{sub1,sub2}$, according to the operator $\otimes_{\phi_s}$, the state/performance and corresponding probability can be shown in the last two columns of the above table. Furthermore, we can calculate the relevant reliability indices. For example, given a constant demand $w = 200$, we have $A_{S_{sub1,sub2}}(0.5, 200) = 0.897864$ and the expect of output performance $E_{S_{sub1,sub2}}(0.5) = 234.043$. In this way, we can obtain state/performance probability distribution of the whole system and calculate other reliability indices.

When the combination method is adopted directly, the state space of the series of subsystem 1 and subsystem 2 can reach $4^4 * 3^3 = 6912$. However, the realistic result based on the analyzing mentioned above will be reduced to only six because many duplicated or little probability states can be cut or omitted by using the UGF technology. These justify the combined method put forward in this paper.

7. Conclusoin

In this paper an important type of repairable MSS that does not existed in traditional binary-state systems has been considered. Mathematical models based on straightforward Markov process are usually not effective enough for engineering application because of huge number of system states. A new combined method to evaluate the reliability indices of MSS with minor failure and minor repair is suggested. The method is based on the combination of the Markov stochastic process and the UGF technology. Furthermore, multi-state models for system components have been taken into account.

The method is highly suitable for engineering applications because the procedure is well formalized and based on the natural decomposition of the entire MSS. By using this method, the process for modeling of the MSS and solving of system differential equations has been greatly simplified. The performance levels and reliability indices of MSS can be calculated accurately.

Table 3. state/performance probability distribution of subsystem 1, subsystem 2 and their series at $t = 0.5$ year

Subsystem 1		Subsystem 2		$S_{sub1,sub2}$	
State/Performance (ton/day)	Probability	State/Performance (ton/day)	Probability	State/Performance (ton/day)	Probability
320	0.6699	-	-	-	-
300	0.2648	-	-	-	-
280	0.0555	-	-	240	0.897451
260	0.0074	240	0.8979	220	0.000359
240	0.0019	190	0.0904	200	0.000054
220	0.0004	140	0.0023	190	0.090396
200	0.00006	120	0.0089	140	0.002299
<200	0.00004	≤70	0.0005	120	0.008899

References

1. Anatoly, L. and F. Ilia. Recent Advances in System Reliability. London, Springer-Verlag, 2012.
2. Anatoly Lisnianski, D. E., David Laredo, Hanoch Ben Haim. A multi-state Markov model for a short-term reliability analysis of a power generating unit. Reliability Engineering and System Safety 2012; 98(1): 1-6, http://dx.doi.org/10.1016/j.ress.2011.10.008.
3. Aven, T. and U. Jensen. Stochastic Models in Reliability. New York, Springer-Verlag, 1999. http://dx.doi.org/10.1007/b97596
4. Barlow, R. E. Mathematical reliability theory: from the beginning to the present time 2002; World Scientific.

5.   Barlow, R. E. Mathematical theory of reliability: A historical perspective. Reliability, IEEE Transactions on 1984; R-33(1): 16-20, http://dx.doi.org/10.1109/tr.1984.6448269.

6.   Barlow, R. E. and F. Proschan. Mathematical theory of reliability. New York, Wiley, 1965.

7.   Barlow, R. E. and A. S. Wu. Coherent Systems with Multi-State Components. Mathematics of Operations Research 1978; 3(4): 275-281. http://dx.doi.org/10.1287/moor.3.4.275

8.   Chang, P. C. and Y. K. Lin. Fuzzy-based system reliability of a labour-intensive manufacturing network with repair. International Journal of Production Research 2015; 53(7): 1980-1995, http://dx.doi.org/10.1080/00207543.2014.944279.

9.   Di Maio, F., D. Colli, E. Zio, L. Tao and J. Tong. A Multi-State Physics Modeling approach for the reliability assessment of Nuclear Power Plants piping systems. Annals of Nuclear Energy 2015; 80: 151-165, http://dx.doi.org/10.1016/j.anucene.2015.02.007.

10. Ding, Y. and A. Lisnianski. Fuzzy universal generating functions for multi-state system reliability assessment. Fuzzy Sets and Systems 2008; 159(3): 307-324, http://dx.doi.org/10.1016/j.fss.2007.06.004.

11. Doostparast, M., F. Kolahan and M. Doostparast. A reliability-based approach to optimize preventive maintenance scheduling for coherent systems. Reliability Engineering & System Safety 2014; 126(0): 98-106, http://dx.doi.org/10.1016/j.ress.2014.01.010.

12. Gandini, A. Importance and sensitivity analysis in assessing system reliability. Reliability, IEEE Transactions on 1990; 39(1): 61-70, http://dx.doi.org/10.1109/24.52613.

13. Guilani, P. P., M. Sharifi, S. T. A. Niaki and A. Zaretalab. Reliability evaluation of non-reparable three-state systems using Markov model and its comparison with the UGF and the recursive methods. Reliability Engineering & System Safety 2014; 129: 29-35, http://dx.doi.org/10.1016/j.ress.2014.04.019.

14. Janan, X. On Multistate System Analysis. Reliability, IEEE Transactions on 1985; R-34(4): 329-337.

15. Levitin, G. Block diagram method for analyzing multi-state systems with uncovered failures. Reliability Engineering & System Safety 2007; 92(6): 727-734, http://dx.doi.org/10.1016/j.ress.2006.02.009.

16. Levitin, G. The universal generating function in reliability analysis and optimization. London, Springer-Verlag, 2005.

17. Levitin, G. and A. Lisnianski. Joint redundancy and maintenance optimization for multistate series-parallel systems. Reliability Engineering & System Safety 1999; 64(1): 33-42, http://dx.doi.org/10.1016/S0951-8320(98)00052-0.

18. Levitin, G., A. Lisnianski, H. Ben-Haim and D. Elmakis. Redundancy optimization for series-parallel multi-state systems. Reliability, IEEE Transactions on 1998; 47(2): 165-172, http://dx.doi.org/10.1109/24.722283.

19. Levitin, G., L. Xing, H. Ben-Haim and Y. Dai. Multi-state systems with selective propagated failures and imperfect individual and group protections. Reliability Engineering & System Safety 2011; 96(12): 1657-1666, http://dx.doi.org/10.1016/j.ress.2011.08.002.

20. Levitin, G., L. Xing, H. Ben-Haim and Y. Dai. Reliability of Series-Parallel Systems With Random Failure Propagation Time. Ieee Transactions on Reliability 2013; 62(3): 637-647, http://dx.doi.org/10.1109/TR.2013.2270415.

21. Li, C.-y., X. Chen, X.-s. Yi and J.-y. Tao. Heterogeneous redundancy optimization for multi-state series-parallel systems subject to common cause failures. Reliability Engineering & System Safety 2010; 95(3): 202-207, http://dx.doi.org/10.1016/j.ress.2009.09.011.

22. Li, W. and M. J. Zuo. Reliability evaluation of multi-state weighted k-out-of-n systems. Reliability Engineering & System Safety 2008; 93(1): 160-167, http://dx.doi.org/10.1016/j.ress.2006.11.009.

23. Lin, Y.-K. and C.-F. Huang. Reliability Evaluation of a Multi-state Network with Multiple Sinks under Individual Accuracy Rate Constraint. Communications in Statistics-Theory and Methods 2014; 43(21): 4519-4533, http://dx.doi.org/10.1080/03610926.2012.716137.

24. Lisnianski, A. and Y. Ding. Redundancy analysis for repairable multi-state system by using combined stochastic processes methods and universal generating function technique. Reliability Engineering & System Safety 2009; 94(11): 1788-1795, http://dx.doi.org/10.1016/j.ress.2009.05.006.

25. Lisnianski, A., G. Levitin and H. Ben-Haim. Structure optimization of multi-state system with time redundancy. Reliability Engineering & System Safety 2000; 67(2): 103-112, http://dx.doi.org/10.1016/S0951-8320(99)00049-6.

26. Ming Tan, C. and N. Raghavan. A framework to practical predictive maintenance modeling for multi-state systems. Reliability Engineering & System Safety 2008; 93(8): 1138-1150, http://dx.doi.org/10.1016/j.ress.2007.09.003.

27. Mo, Y. C., L. D. Xing, S. V. Amari and J. B. Dugan. Efficient analysis of multi-state k-out-of-n systems. Reliability Engineering & System Safety 2015; 133: 95-105, http://dx.doi.org/10.1016/j.ress.2014.09.006.

28. Nahas, N., A. Khatab, D. Ait-Kadi and M. Nourelfath. Extended great deluge algorithm for the imperfect preventive maintenance optimization of multi-state systems. Reliability Engineering & System Safety 2008; 93(11): 1658-1672, http://dx.doi.org/10.1016/j.ress.2008.01.006.

29. Nourelfath, M. and D. Ait-Kadi. Optimization of series-parallel multi-state systems under maintenance policies. Reliability Engineering & System Safety 2007; 92(12): 1620-1626, http://dx.doi.org/10.1016/j.ress.2006.09.016.

30. Pandey, M., M. J. Zuo and R. Moghaddass. Selective maintenance modeling for a multistate system with multistate components under imperfect maintenance. IIE Transactions 2013; 45(11): 1221-1234, http://dx.doi.org/10.1080/0740817X.2012.761371.

31. Parikh, C. R., M. J. Pont and N. Barrie Jones. Application of Dempster¨CShafer theory in condition monitoring applications: a case study. Pattern Recognition Letters 2001; 22(6): 777-785, http://dx.doi.org/10.1016/S0167-8655(01)00014-9.

32. Rami, A., H. Hamdaoui, H. Sayah and A. Zeblah. Efficient harmony search optimization for preventive-maintenance-planning for nuclear power systems. International Journal for Simulation and Multidisciplinary Design Optimization 2014; 5: A17, http://dx.doi.org/10.1051/smdo/2013011.

33. Rueda, A. and M. Pawlak. Pioneers of the reliability theories of the past 50 years. Reliability and Maintainability, 2004 Annual Symposium - RAMS 2004; 102-109, http://dx.doi.org/10.1109/rams.2004.1285431.

34. Tian, Z., G. Levitin and M. J. Zuo. A joint reliability-redundancy optimization approach for multi-state series-parallel systems. Reliability Engineering & System Safety 2009; 94(10): 1568-1576, http://dx.doi.org/10.1016/j.ress.2009.02.021.

35. Ushakov. "Reliability: past, present, future," Recent Advances in Reliability Theory: Methodology, Practice, and Interface,. Boston, Birkhäuser, 2000.

36. Ushakov, I. Optimal standby problems and a universal generating function. Soviet journal of computer and systems sciences 1987; 25(4): 79-82.

37. Wang, L., X. Jia and J. Zhang. Reliability Evaluation for Multi-State Markov Repairable Systems with Redundant Dependencies. Quality Technology and Quantitative Management 2013; 10(3): 277-289.

38. Xiao, H. and R. Peng. Optimal allocation and maintenance of multi-state elements in series-parallel systems with common bus performance sharing. Computers & Industrial Engineering 2014; 72(0): 143-151, http://dx.doi.org/10.1016/j.cie.2014.03.014.
39. Yeh, W.-C. Evaluation of all one-to-many reliabilities for acyclic multistate-node distributed computing system under cost and capacity constraints. Computer Communications 2007; 30(18): 3796-3806, http://dx.doi.org/10.1016/j.comcom.2007.09.005.
40. Yeh, W. C. A novel node-based sequential implicit enumeration method for finding all d-MPs in a multistate flow network. Information Sciences 2015; 297: 283-292, http://dx.doi.org/10.1016/j.ins.2014.11.007.
41. Yu, L. and H. Hong-Zhong. Optimal Selective Maintenance Strategy for Multi-State Systems Under Imperfect Maintenance. Reliability, IEEE Transactions on 2010; 59(2): 356-367, http://dx.doi.org/10.1109/TR.2010.2046798.
42. Yu, L. and H. Hong-Zhong. Optimization of multi-state elements replacement policy for multi-state systems. Reliability and Maintainability Symposium (RAMS), 2010 Proceedings - Annual 2010; 1-7.
43. Zhou, Y., T. R. Lin, Y. Sun, Y. Bian and L. Ma. An effective approach to reducing strategy space for maintenance optimisation of multistate series-parallel systems. Reliability Engineering & System Safety 2015; 138(0): 40-53, http://dx.doi.org/10.1016/j.ress.2015.01.018.
44. Zio, E. Reliability engineering: Old problems and new challenges. Reliability Engineering & System Safety 2009; 94(2): 125-141, http://dx.doi.org/10.1016/j.ress.2008.06.002.
45. Zio, E., M. Marella and L. Podofillini. A Monte Carlo simulation approach to the availability assessment of multi-state systems with operational dependencies. Reliability Engineering & System Safety 2007; 92(7): 871-882, http://dx.doi.org/10.1016/j.ress.2006.04.024.

Jinlei QIN
Information and Network Management Center
North China Electric Power University
Baoding, 071003, China

Yuguang NIU
State Key Laboratory of Alternate Electric Power System
with Renewable Energy Sources
North China Electric Power University
Beijing, 102206, China

Zheng LI
Department of Computer Science and Technology
North China Electric Power University
Baoding, 071003, China

Email: jlqin717@163.com, nyg@ncepu.edu.cn,
yeziperfect@163.com

Mirosław WENDEKER
Zbigniew CZYŻ

ANALYSIS OF THE BEARING NODES LOADS OF TURBINE ENGINE AT AN UNMANNED HELICOPTER DURING A JUMP UP AND JUMP DOWN MANEUVER

ANALIZA OBCIĄŻEŃ WĘZŁÓW ŁOŻYSKOWYCH SILNIKA TURBINOWEGO W BEZZAŁOGOWYM ŚMIGŁOWCU PODCZAS MANEWRU SKOK W GÓRĘ I SKOK W DÓŁ*

The article is part of the work, which was made to systematize the operating conditions of bearing loads in the rotor assembly of FSTC-1 turbine engine, which is designed in the Department of Thermodynamics, Fluid Mechanics and Aviation Propulsion Systems at Lublin University of Technology. This engine assumes the use of the gas bearing in compressor drive unit to improve the operating characteristics. This is justified by difficult working conditions associated with high speeds, high temperatures and difficult access, as in the case of gas bearings is not a major problem. A mathematical model of possible states of load bearing nodes in compressor drive unit was also presented. Load analysis was carried out for maneuver jump up and jump down based on the time course of geometric altitude from the radio altimeter based on real tests of a manned PZL W3-Sokol helicopter. The dependence of the altitude changing during the time was approximated by the least squares method and then the velocity and acceleration changes were determined. On this basis, the forces acting on the bearing in compressor drive unit under static and dynamic conditions were calculated. These values will be confronted with the values obtained during other maneuvers, and will be used as input assumptions to project of the gas bearings.

Keywords: gas bearings, helicopters, turbine engines.

Artykuł stanowi część prac, w których dokonano usystematyzowania eksploatacyjnych stanów obciążeń łożysk zespołu wirnikowego silnika turbinowego FSTC-1, który projektowany jest w Katedrze Termodynamiki, Mechaniki Płynów i Napędów Lotniczych na Politechnice Lubelskiej. Silnik ten zakłada zastosowanie w zespole wytwornicowym łożysk gazowych w celu poprawy właściwości eksploatacyjnych. Jest to uzasadnione trudnymi warunkami pracy związanymi z dużymi prędkościami obrotowymi, wysokimi temperaturami oraz trudnym dostępem, co w przypadku łożysk gazowych nie stanowi większego problemu. Przedstawiono również matematyczny model możliwych do wystąpienia stanów obciążeń węzłów łożyskowych zespołu wytwornicowego. Analizę obciążeń przeprowadzono dla manewru skok w górę i skok w dół na podstawie przebiegu czasowego wysokości geometrycznej z radiowysokościomierza w oparciu o rzeczywiste badania załogowego śmigłowca PZL W3-Sokół. Zależność zmiany wysokości w czasie aproksymowano metodą najmniejszych kwadratów a następnie wyznaczono dla niej zmiany prędkości oraz przyspieszeń. Na tej podstawie wyznaczono wartości sił działające na łożyska zespołu wytwornicowego w warunkach statycznych jak i dynamicznych. Wartości te zostaną skonfrontowane z wartościami uzyskanymi podczas innych manewrów oraz posłużą, jako założenia wejściowe do projektu łożysk gazowych.

Słowa kluczowe: łożyska gazowe, śmigłowce, silniki turbinowe.

1. Introduction

Gas bearings are used in many types of rotating machines such as turbochargers, turbine engines or high-speed electro tools e.g. grinding machines. Such a bearings have many advantages as compared to conventional bearings, which include mainly resistance to thermal loads, high speeds, very small friction value, high durability, susceptibility, the ability to damp vibrations, impact resistance (foil gas bearing) and stable operation at high speeds. Gas bearings are currently mostly used in the temperature range up to 300°C and cryogenic applications. However, the highest operating temperature that was observed by [5], amounts to 815°C. Operating temperature of foil gas bearings depends directly on the used materials and sliding coatings. The most common coatings are formed with polymer materials which protect the sliding foil surface against wear [5]. However, load capacity of gas bearing, is even worse, so it's important to use rotating assembly with normal overloads. Properties of gas bearings including a foil gas bearings are described in several studies based on the

experimental works [7, 8, 12]. There are many mathematical models and studies describing the operation of the bearings, including the thermal-hydrodynamic analysis like [14], where the established mathematical models can be used to design more advanced foil bearings, in particular foil bearings with variable axial stiffness. Interest of gas bearing is very high, but it should be remembered that the bearing assembly design process requires knowledge of the applications of your device and especially the knowledge of the dynamic conditions during the operation. The article describes the state of the bearing node in turbine engine to power an unmanned helicopter with the take-off mass up to 100 kg.

Turbine engines are still a competition with piston engines in aerospace applications. By Dudziak [1], mass of the turbine engine assembly, including fuel, is significantly less than the mass of the assembly with a piston engine in the case of one hour flight and the difference of the mass decreases with increasing operation time. This is due to the fact that the turbine engines have a specific fuel consumption of 0.4-0.7 kg/kWh while piston engines has 0.35 kg/kWh. However, to

power the unmanned aerial vehicles, including light helicopters that perform missions lasting about 1-2 hours, more profitable it becomes to use a turbine engine. Cost-effectiveness of the use of turbine engines is increasing even more due to differences in fuel prices. In the case of Lublin Airport EPLB, price per liter of Avgas 100LL aviation gasoline without excise duty, currently is an average of 7.18 PLN, while a liter of Jet A-1 aviation kerosene costs 2.69 PLN. But on other hand the piston engines are much more eco-friendly in comparison with the turbine engines [17], especially according to the diesel engines [13].

In Poland and all over the world people are working on unmanned aircraft including the unmanned helicopters. An example of two helicopters, of which one is a construction based on SW-4 helicopter from PZL Swidnik S.A., while the second is ILX-27 developed by the Institute of Aviation, Air Force Institute of Technology and Military Aviation Company No. 1 in Lodz [4, 6]. In the ILX-27 helicopter, a piston engine Lycoming 0-540-F1B5 is used with a power of 191kW (260hp), which gives the mass/power ratio with a maximum mass a helicopter equal to 4.23 kg/hp. In addition to the higher value of mass to power ratio, another disadvantage of piston engines are also the vibrations, but in the 6-cylinder F1B5 drive unit, vibration level is relatively low. In the case of the RUAV Solo helicopter by PZL-Swidnik construction, drive unit represents a turbine engine, Rolls-Royce 250-C20R/2 with a power of 457 hp (336 kW).

Helicopters completing missions are often in such flight conditions, in which the rotor, tail rotor, the hull structure and drive components (including the drive engines), and also bearing nodes of rotor assembly of engines are exposed to considerable loads. These states are the result of extreme flight maneuvers from flight scenario or either from the changing environmental conditions of flight. In addition, rapidly changing flight parameters in such maneuvers cause an intense change in the parameters, accordingly to engines actions to achieve the engine limit states [2].

During the operation of the helicopter, on the bearings of rotor assembly of turbine engine, in addition to high speeds of several tens of thousands rpm, the forces resulting from the kinematic motion of the helicopter and flow processes occurring in the engine are also acting. These forces create state changes, which are characterized by difficult to establish design values. This article attempts to systematize states and causes of operational loads and shows how to simulate such work conditions depending on operating conditions. Causes of bearing loads of rotor assembly, according to [3] can be divided into two main groups

shown in Figure1. The first are the causes of structural nature, resulting from the design features of the engine rotor assembly and its mounting on the aircraft, while the second reasons stems from the course and nature of the operation (operating conditions).

From the analysis of the operating conditions of helicopters, including military helicopters operating conditions, and helicopters form the [3], it can be deduced that some insights allows to systematize the causes of the load in the compressor drive unit of the rotor assembly of turbine engine as follows:
– states of load resulting from the profile operation of the aircraft that was established by the manufacturer,
– states resulting from the failure or air accident without engine destroying - these conditions can be considered like extreme for failure-free operation of bearing in rotor assembly,
– states resulting from extreme helicopter flights while performing different maneuvers (acrobatic maneuvers, combat flying).

These observations allow to create simulation model of rotor assembly with bearing nodes.

2. Research object

One turbine engines designed in the Department of Thermodynamics, Fluid Mechanics and Aviation Propulsion Systems in the Lublin University of Technology requires the use the gas bearings in bearing nodes in compressor drive unit. This engine is shown in Figure 2, together with the basic parameters in the Table 1.

The use of gas bearings in illustrated engine is necessary to improve performance characteristics. However, this only applies to the bearing nodes in compressor drive unit shaft. This is justified by difficult working conditions (high speed, high temperatures and difficult
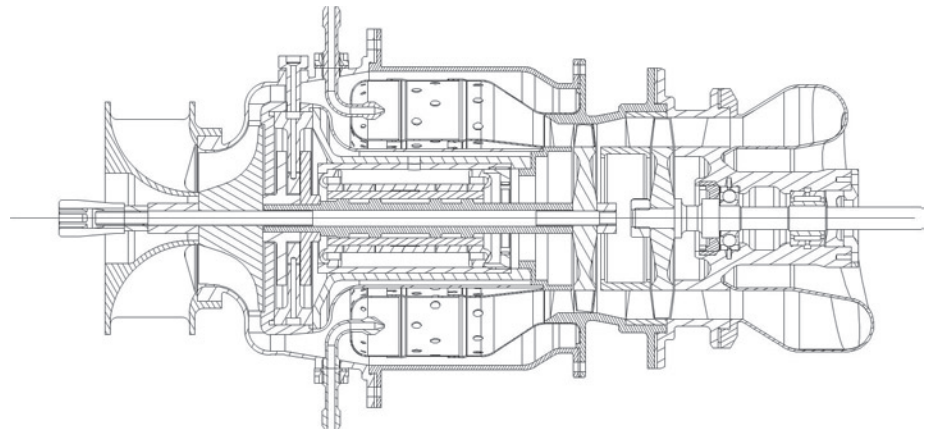
Fig. 2. FSTC-1turbine engine with a power takeoff on shaft, own study

Table 1. Basic parameters of FSTC-1 engine

FSTC-1 engine parameters	
Calculated effective power Ne [kW]	18
Rotation frequency of compressor drive unit turbine nTW [rmp]	96000
Rotation frequency of drive turbine nTN [rpm]	60000
Compressor compression ratio	3
Air mass flow rate mp [kg/s]	0.256
Fuel consumption per seconds Bs [kg/s]	0.003

access), which in the case of gas bearing is permissible [9, 11, 15, 16]. Compressor drive unit, which was analyzed, is schematically shown in Figure3. It consists of a shaft on which the axial radial compressor rotor and turbine axis rotor were positioned. All of the structure is mounted on two radial and one axial gas bearings. Gas bearings
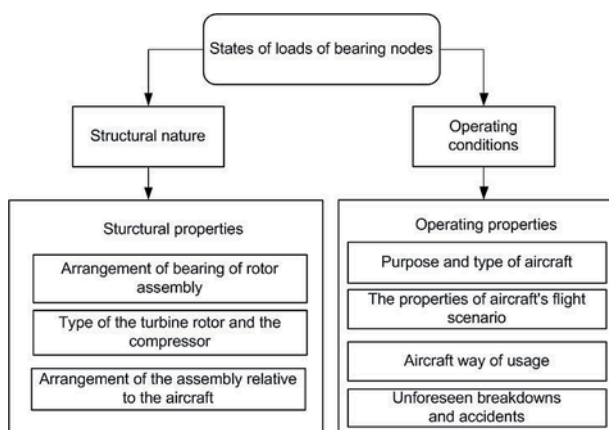
Fig. 1. Scheme to systematize the causes of the load in the compressor drive unit in the rotor assembly of turbine engine [7]

are mounted inside (between the compressor and the turbine), but the radial bearing trunnions are the fragments of the shaft and the thrust disc of axial bearings is connected with the shaft. The analysis assumed that the engine is arranged longitudinally in a helicopter and states of bearing loads depend on the flight scenario and the way of flight, where several cases of operation of the helicopter were distinguished.
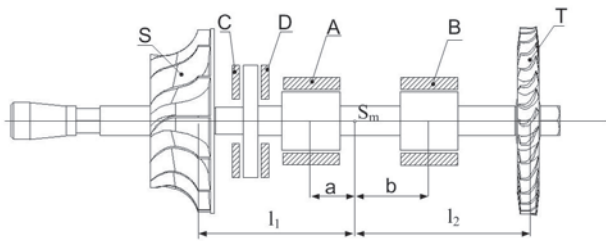
Fig. 3. Schematic model of a compressor drive unit rotor assembly, including a system of sliding bearings. A, B- radical bearing bush, C, D- axial bearing thrust disc, S- compressor, T- turbine, own study based on [7]

3. Analysis of the load states of drive assembly during a jump up and jump down maneuver

State model of bearing loads based on actual values obtained from the analysis of flight data from helicopter PZL W-3 Sokol. Despite the size difference it was assumed that the unmanned helicopter equipped with a designed engine will be able to perform missions with such flight scenario like bigger helicopter. The analysis of acceleration, which the rotor assembly of designed engine is subjected, was carried out based on the results of experimental studies of the behavior of the helicopter W-3 Sokol in flight NOE [10]. Helicopters, especially unmanned versions must perform certain combat tasks such as, observation of the enemy, the discharge of the explosive materials or taking a shot at his maneuverability in the sufficient way to avoid possible shootout. These maneuvers enable to achieve it targets sufficiently. It is assumed that the helicopter does not take air combat. This analysis is sufficient due to the lack of experimental data relating to the behavior of unmanned helicopters in extreme flying.

The most common maneuvers that occur during the execution of the flight mission by unmanned helicopters may include the following: jump up and jump down, acceleration and deceleration, braking before the attack, tight curve and return to the target. From the five maneuvers listed in this article, it was decided to analyze the maneuver jump up and jump down, which is shown in Figure4.

Jump up and jump down allows, among other things, checking the vertical damping, i.e. the ability to accurate vertical acceleration and deceleration, and at the same time for the actual time estimation of this maneuvers, and with the given speeds, for the calculation of acceleration acting on the tested system. It is a maneuver often used by

combat helicopters on the battlefield and normally used in an attack using such covers like vertical deflection behind the wall (which can be a forest, building etc.) and then lunching a missile and hide behind the cover. It requires a high precision (it determines the accuracy of shots etc.), but also a relatively short period of time for maneuver implementation to avoid shouting down by the lurking enemy.

The analyzed maneuver begins by hovers at a height of 3.05 m, and then the helicopter rises to the desired height in the range of 12.2−15.2 m (fig. 4). For a fixed altitude, the helicopter hovers for at least 2 seconds for lunching the missile at the target, and then drops to a predetermined altitude 3.05 m [10].

The analysis was carried out taking into account the time course of geometric height from a radio altimeter. The maneuver was divided into two parts: the ascent and descent. From publication [10], the coordinates put in the table 2 was imported. Coordinates were approximated by the least squares method, what gives the following five-degree polynomial function. The degree of the polynomial is conditional on receiving the best quality data.

Polynomial function describing the change in altitude during time

Table 2. Coordinates of the altitude changes depending on the time for maneuver jump up during the rising

No.	Time [s]	Registered altitude [m]	No.	Time [s]	Registered altitude [m]
1	3.68	3.00	10	5.22	9.00
2	4.05	4.05	11	5.36	9.90
3	4.38	5.00	12	5.53	10.89
4	4.63	6.00	13	5.77	12.00
5	4.75	6.58	14	6.03	13.05
6	4.82	6.95	15	6.17	13.57
7	4.92	7.47	16	6.30	14.10
8	5.03	8.00	17	6.60	15.00
9	5.18	8.89	18	7.20	18.00

H= f(t) for the raising during the maneuver jump up is described by equation (1), while (2) and (3) are respectively from first degree derivative (speed) and second degree derivative (acceleration):

$$H = f(t) = 0.0720438301538917\, x^5 + 0.072043830153892\, x^4$$
$$+ 20.9743333138697\, x^3 - 106.48692542687\, x^2 \qquad (1)$$
$$+ 262.855196462725\, x^1 - 252.639998086681\, x^0$$

$$V = \frac{\partial H}{\partial t} = 5 \cdot 0.07204383015389\, x^4 + 4 \cdot 0.07204383015389\, x^3$$
$$+ 3 \cdot 20.974333313869\, x^2 + 2 \cdot (-106.486925427)\, x^1 \qquad (2)$$
$$+ 262.855196462725\, x^0$$

$$a = \frac{\partial V}{\partial t} = 20 \cdot 0.07204383015389\, x^3 + 12 \cdot 0.0720438301539\, x^2$$
$$+ 6 \cdot 20.97433331387\, x^1 + 2 \cdot (-106.48692542687)\, x^0$$
$$\qquad (3)$$

Figure 5 shows the function created with measuring points and function approximating form the altitude of the helicopter PZL W-3 Sokol flight depending on the time during a maneuver jump up. Figures 6 and 7 show a change in climbing speed and acceleration of the helicopter.
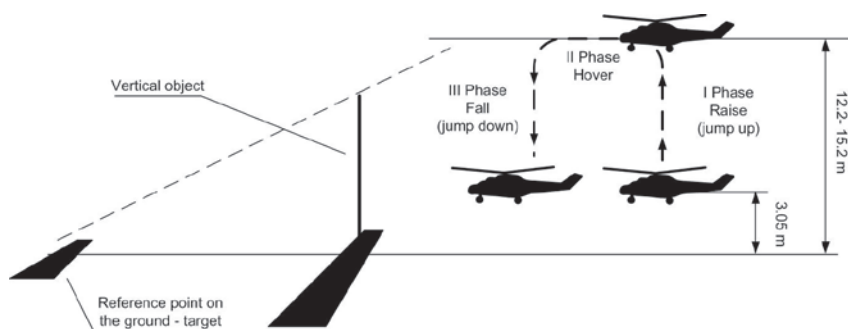
Fig. 4. Scheme of maneuver jump up and jump down, own study based on [10]
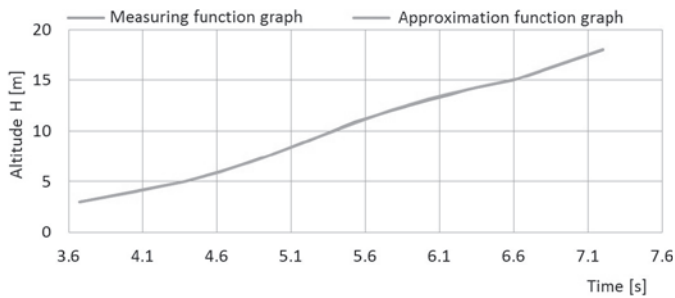
Fig. 5. Measurement and approximating functions form the altitude of the helicopter PZL W-3 Sokol flight depending on the time during a maneuver jump up
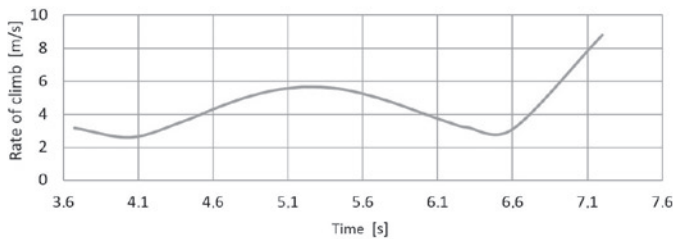
Fig. 6. Change in climbing speed of helicopter W-3 Sokol for maneuver jump up
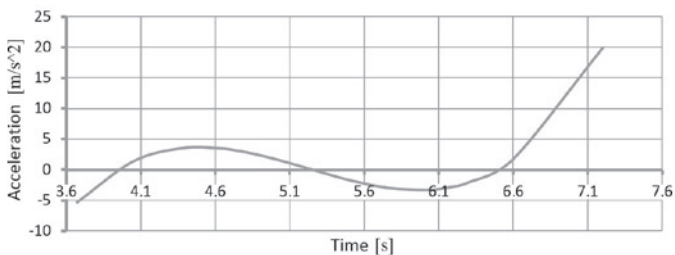
Fig. 7. Change in climbing acceleration of helicopter W-3 Sokol for maneuver jump up

Table 2. Coordinates of the altitude changes depending on the time for maneuver jump up during the rising

No.	Time [s]	Registered altitude [m]	No.	Time [s]	Registered altitude [m]
1	3.68	3.00	10	5.22	9.00
2	4.05	4.05	11	5.36	9.90
3	4.38	5.00	12	5.53	10.89
4	4.63	6.00	13	5.77	12.00
5	4.75	6.58	14	6.03	13.05
6	4.82	6.95	15	6.17	13.57
7	4.92	7.47	16	6.30	14.10
8	5.03	8.00	17	6.60	15.00
9	5.18	8.89	18	7.20	18.00

The coordinates given in table 3 were approximated by the least squares function described below, what gives the following five-degree polynomial function. The degree of the polynomial is conditional on receiving the best quality data.

Polynomial function describing the change in altitude during time H= f(t) for the falling during the maneuver jump down:

$$H = f(t) = -0.0625269149733026 \; x^5 + 3.72504261903523 \; x^4 - 88.0177032174416 x^3$$
$$+ 1030.67671304047 \; x^2 - 5982.84455547936 \; x^1 + 13798.715321263 \; x^0$$

(4)

$$V = \frac{\partial H}{\partial t} = 5 \cdot (-0.06252691497330) \; x^4 + 4 \cdot 3.725042619035 \; x^3$$
$$+ 3 \cdot (-8.0177032174416) \; x^2 + 2 \cdot 1030.676713040 \; x^1 - 5982.84455547936 \; x^0$$

(5)

$$a = \frac{\partial V}{\partial t} = 20 \cdot (-0.0625269149733) \; x^3 + 12 \cdot 3.72504261903 \; x^2$$
$$+ 6 \cdot (-88.017703217441) \; x^1 + 2 \cdot 1030.676713040 \; x^0$$

(6)

Figure 8 shows the function created with measuring points and function approximating form the altitude of the helicopter PZL W-3 Sokol flight depending on the time during a maneuver jump down. Figures 9 and 10 show a change in climbing speed and acceleration of the helicopter.
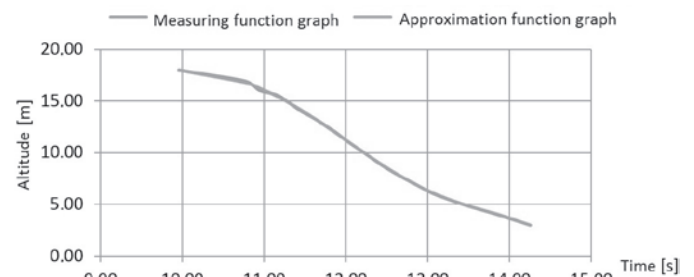
Fig. 8. Measurement and approximating functions form the altitude of the helicopter PZL W-3 Sokol flight depending on the time during a maneuver jump down
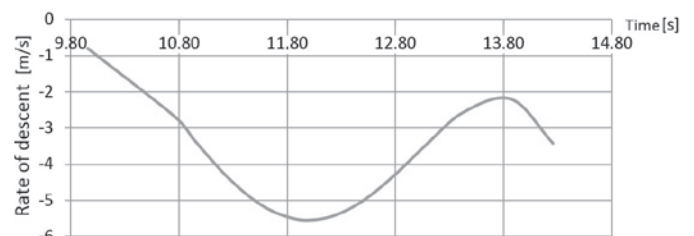
Fig. 9. Change in climbing speed of helicopter W-3 Sokol for maneuver jump down
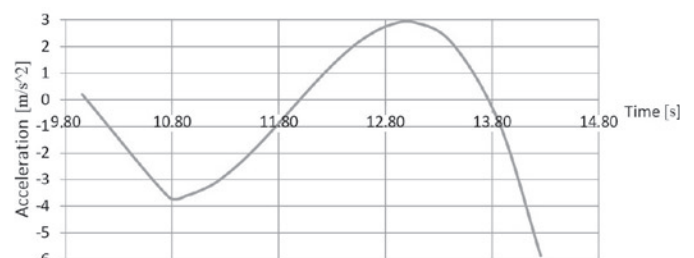
Fig. 10. Change in climbing acceleration of helicopter W-3 Sokol for maneuver jump down

4. The states model of loads of the gas bearing

The functioning of the nodes loads of the gas bearing was described in accordance with [7] equations for different types of forces in Cartesian system (fig. 11). In order to generalize the discussion, dimen-
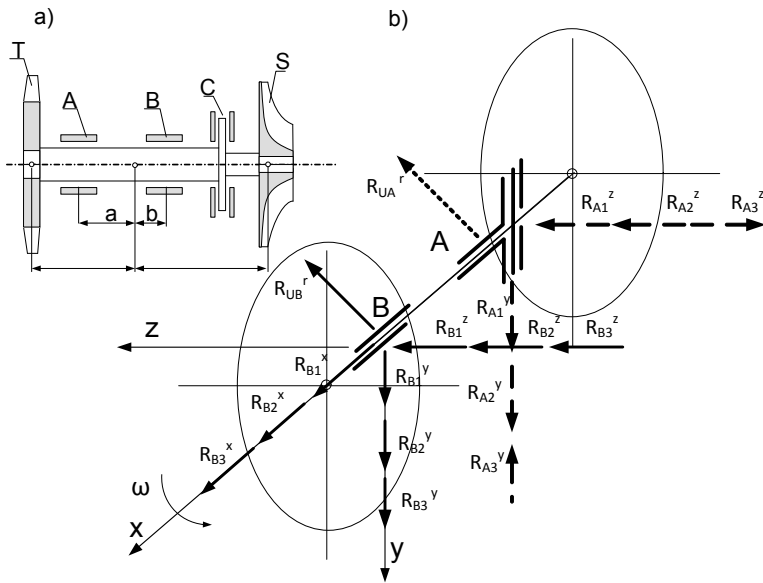
Fig. 11. Schematic model of rotor assembly with bearing nodes, a- geometric model of assembly, b- state diagram of bearing loads of assembly, own study based on [3]

sionless forces forms were used (with respect to gravity of the system). A list of equations that describe the forces of loads of bearing nodes in rotor assembly are contained in table 4.

5. Loads of bearing nodes of rotor assembly under static conditions.

Radial bearings are subjected to static forces of gravity derived from each of the components of rotor assembly which are connected to the shaft. All these elements of compressor drive
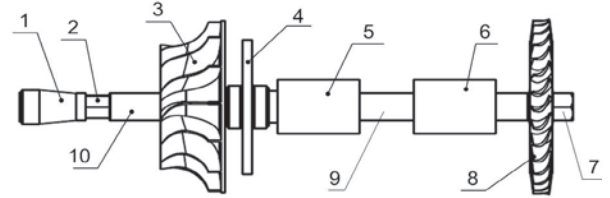
Fig. 12. Diagram showing the components of compressor drive unit rotor assembly of the turbine engine, 1- clamping sleeve with the internal splines, 2- clamping nut from rotor compressor, 3- compressor rotor, 4- thrust disc of axial bearing, 5, 6- radical bearing sleeve, 7- clamping nut from rotor of compressor drive unit turbine, 8- rotor of compressor drive unit turbine, 9- compressor drive unit shaft, 10- compressor rotor sleeve, own study.

Table 4. A list of equations that describe the forces of loads of bearing nodes in rotor assembly [3].

No.	Force name	Radial bearing					
		Bearing A			Bearing B		
		Force symbol	Equation	No.	Force symbol	Equation	No.
1	The gravity force of rotor assembly	R_{A1}^y	$\dfrac{m_z \cdot g \cdot b}{a+b}$	(7)	R_{B1}^y	$\dfrac{m_z \cdot g \cdot a}{a+b}$	(14)
2	The force caused by maneuver jump up/down	R_{A2}^y	$n_W \cdot Q \cdot \dfrac{b}{a+b}$	(8)	R_{B2}^y	$n_W \cdot Q \cdot \dfrac{a}{a+b}$	(15)
3	The force caused by gyroscopic torque	R_{A3}^y	$\dfrac{I_z \cdot V \cdot \omega}{\rho(a+b)}$	(9)	R_{B3}^y	$\dfrac{I_z \cdot V \cdot \omega}{\rho(a+b)}$	(16)
4	Centrifugal force caused by the tight curve maneuver	R_{A1}^z	$m_z \cdot \dfrac{V^2 \cdot b}{\rho \cdot (a+b)}$	(10)	R_{B1}^z	$m_z \dfrac{V^2 \cdot a}{\rho \cdot (a+b)}$	(17)
5	The force caused by maneuver called return on target	R_{A2}^z	$n_W \cdot Q \cdot \dfrac{b}{a+b}$	(11)	R_{B2}^z	$n_W \cdot Q \cdot \dfrac{a}{a+b}$	(18)
6	The force caused by gyroscopic torque	R_{A3}^z	$\dfrac{I_z \cdot V \cdot \omega}{\rho(a+b)}$	(12)	R_{B3}^z	$\dfrac{I_z \cdot V \cdot \omega}{\rho(a+b)}$	(19)
7	Residual unbalance force	R_{UB}^r	$\dfrac{V_d \cdot m_z \cdot \omega}{\dfrac{2 \cdot l_1 \cdot l_2 + b \cdot (l_2 - l_1)}{(l_1 + l_2) \cdot (a+b)}}$	(13)	R_{UB}^r	$\dfrac{V_d \cdot m_z \cdot \omega}{\dfrac{2 \cdot l_1 \cdot l_2 + b \cdot (l_2 - l_1)}{(l_1 + l_2) \cdot (a+b)}}$	(20)

No.	Force name	Axial bearing		
		Force symbol	Equation	No.
1	Aerodynamics gas force	R_{B1}^x	$F_{TP}^W - F_{SP}^W + F_{TC}^W - F_{SC}^W$	(21)
2	The axial force caused by the acceleration and deceleration maneuver	R_{B2}^x	$n_W \cdot Q$	(22)
3	The centrifugal force caused by the maneuver jump over an obstacle	R_{B3}^x	$m_z \cdot \dfrac{V^2}{\rho}$	(23)

Table 5. Basic parameters of the components of compressor drive unit rotor assembly

No.	Element name	Material	Volume [m³]	Mass [kg]	Weight [N]
1	Clamping sleeve with the internal splines	Titanium	2.644e-6	0.012	0.118
2	Clamping nut from rotor compressor	Steel	6.761e-7	0.005	0.049
3	Compressor rotor	Titanium	3.413e-5	0.152	1.491
4	Thrust disc of axial bearing	Steel	1.325e-5	0.104	1.020
5, 6	Radical bearing sleeve	Steel	0.843e-5	0.067	0.657
7	Clamping nut from rotor of compressor drive unit	Steel	8.284e-7	0.007	0.069
8	Rotor of compressor drive unit turbine	Steel	2.091e-5	0.164	1.609
9	Compressor drive unit shaft	Steel	1.824e-5	0.143	1.400
10	Compressor rotor sleeve	Titanium	1.763e-6	0.008	0.079

Density of used materials: steel, density= 7860 kg/m³; titanium, density= 4460 kg/m³

unit rotor assembly are determined and parameterized in Figure12 and in table 5.

The components weight as indicated in table 5 determines the formation of the forces acting on the radical bearing. The method of calculation is shown below.
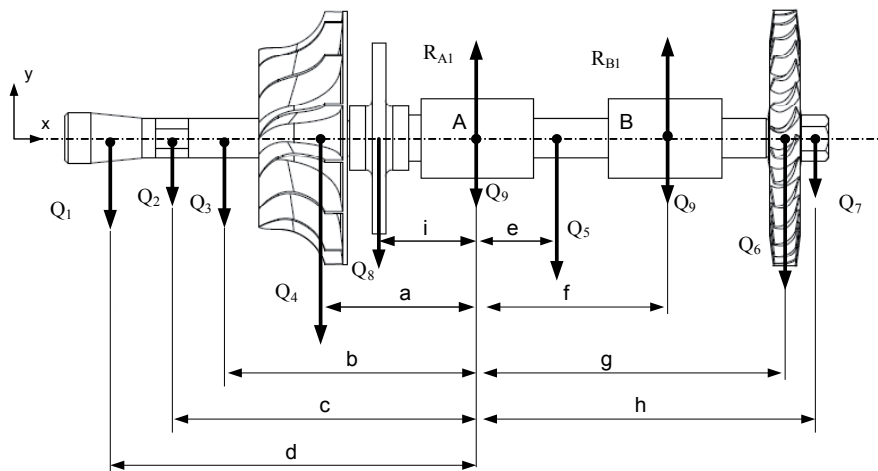
Fig. 13. Forces acting on radial bearings. Forces names as given in the tables 5 and 6, own study

Table 6. Distance between the gravity center of individual elements from the rotor assembly and the bearing node A (see Fig. 13)

Distance name	Length [mm]	Distance name	Length [mm]	Distance name	Length [mm]
a	46.29	d	110.07	g	91.42
b	75.38	e	16.42	h	100.51
c	90.21	f	56.00	i	29.50

The values of the reaction forces acting on the bearing nodes has been determined from the equation of forces sum on the y axis and the equations of torque sum with respect to A point, what is presented below:

$$\sum P_{iy} = R_{A1} + R_{B1} - Q_1 - Q_2 - Q_3 - Q_4 - Q_5 - Q_6 - Q_7 - Q_8 - Q_9 - Q_9 = 0 \quad (24)$$

$$\sum M_{iA} = Q_8 \cdot i + Q_4 \cdot a + Q_3 \cdot b + Q_2 \cdot c + Q_1 \cdot d - Q_5 \cdot e + R_{B1} \cdot f - Q_6 \cdot g - Q_7 \cdot h - Q_9 \cdot f = 0 \quad (25)$$

$$R_{B1} = (-Q_8 \cdot i - Q_4 \cdot a - Q_3 \cdot b - Q_2 \cdot c - Q_1 \cdot d + Q_5 \cdot e + Q_6 \cdot g + Q_7 \cdot h + Q_9 \cdot f) / f \quad (26)$$

$$R_{A1} = (-(-Q_8 \cdot i - Q_4 \cdot a - Q_3 \cdot b - Q_2 \cdot c - Q_1 \cdot d + Q_5 \cdot e + Q_6 \cdot g + Q_7 \cdot h + Q_9 \cdot f) / f) + \quad (27)$$

$$Q_1 + Q_2 + Q_3 + Q_4 + Q_5 + Q_6 + Q_7 + Q_8 + Q_9 \quad (28)$$

$$P_{A1}^{st} = R_{A1} = 5.638 N$$

$$P_{B1}^{st} = R_{B1} = 1.631 N$$

According to Newton's third law of motion, if the bearing pan acts on the shaft with the force P_{A1} (acting force), the shaft is acting on the pan with the reacting force R_{A1}, with the same magnitude but opposite direction (fig. 14).
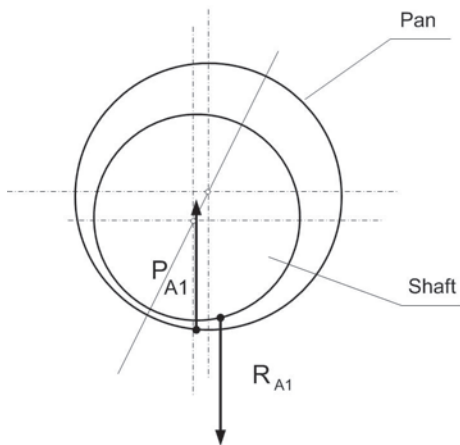
Fig. 14. Scheme of each other interaction between pan and shaft. P_{A1} – force that pan is acting the shaft, R_{A1} – reaction force from P_{A1} force, own study

Reaction values indicate greater load in A bearing, which is a consequence of the position of the mass center closer to that node. Already at this stage we can assume, that the calculations will be carried out taking into account the A bearing, because it is more exposed to possible damage.

6. Loads of bearing nodes of rotor assembly under dynamic conditions.

On the rotor assembly in addition to static forces (non time-varying values) also dynamic loads operates. While in the first case, there are only fixed values, directions and points of forces application, in dynamic loading there is the situation in which external and inertia forces due to accelerations arising from the mass of the body are acting on the body. The overload magnitude is dependent mainly on the acceleration and in extreme states it can load and unload the tested bearings.

The purpose of the analysis of dynamic loads of bearing in rotor assembly is to determine such k coefficient, depending on the maximum acceleration values, that guarantee correct operation of the bearings in the tested range of loads:

$$P_{A1}^{dyn} = k \cdot P_{A1}^{st} = k \cdot g \cdot \sum m_i \quad (28)$$

where:

P_{A1}^{dyn} – dynamic force acting on bearing,
g – gravity acceleration (9,81 value was chosen for the calculation),
k – the overload value, the ratio of acceleration experienced during the flight g_{zast} and gravity acceleration.

$$g_{zast} = k \cdot g$$

$$g_{zast} = a_{\sum} = k \cdot g$$

$a_{\sum}$ – the sum of the acceleration components acting in the same direction.
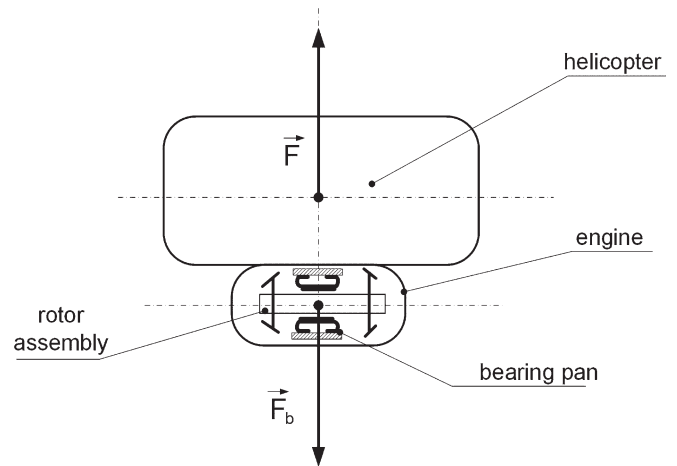
Fig. 15. Scheme of the helicopter accelerations impact on the rotor assembly in the drive system, own study

If the helicopter acts with F force with a certain acceleration, then a shaft (rotor assembly), depending on the size of the mass, will act on the bearing pan with inertial force F_b that has an opposite direction to the acceleration, as shown in Figure15:

$$\vec{F} - m\,\vec{a} = 0 \quad (30)$$

$$\vec{F}_b = -m\,\vec{a} \quad (31)$$

$$\vec{F} + \vec{F}_b = 0 \quad (32)$$

To determine the value of overloading, the individual maneuvers should be analyzed in terms of acceleration values and the direction of their actions, and also the kind of loaded bearings (axial, radial). During the jump up maneuver from all of the forces shown in Figure11 and table 4, only forces shown below occurs:

R_{A1}^y / R_{B1}^y – gravity force of the rotor assembly,

R^y_{A2} / R^y_{B2} – force caused by acceleration during the jump up maneuver,

R^x_{B1} – aerodynamic gas force.
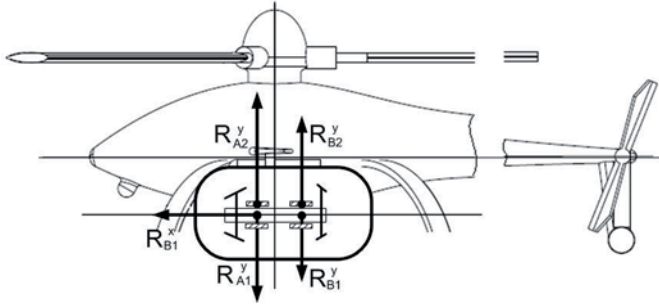
Fig. 16. Scheme of load of bearing nodes during a maneuver jump up, own study

It is assumed that the elements of the compressor drive unit assembly are structured in such way that they make an axial aerodynamic forces to equilibrate. This fact causes force equal zero, but the gravity forces are equal (based on static calculations):

$$R^y_{A1} = P^{st}_{A1} = 5.638N$$
$$R^y_{B1} = P^{st}_{B1} = 1.631N$$

The forces of inertia R^y_{A2} / R^y_{B2} caused by acceleration during the maneuver are multiplication of the respective gravity forces, where the multiplication coefficient is the value of the overload. Based on the performed analysis, the maximum acceleration value was equal a_{max}=19.92 m/s², what gives as follow:

$$a_\Sigma = a_{max} + g$$
$$a_\Sigma = 29.73m / s^2$$

According to equation (28) and (29), the *k* coefficient is:

$$k = \frac{a_\Sigma}{g} = 3.03$$
$$P^{ydyn}_{A1} = k \cdot P^{st}_{A1} = 17.1N$$

During the jump down maneuver, such a forces occurs:

R^y_{A1} / R^y_{B1} – gravity force of rotor assembly,

R^y_{A2} / R^y_{B2} – force caused by acceleration during the jump down maneuver,

R^x_{B1} – aerodynamic gas force.

It is assumed that the elements of the compressor drive unit are structured in such way that they make an axial aerodynamic forces to equilibrate. This fact causes R^x_{B1}. force equal zero, but the gravity forces are equal (based on static calculations):
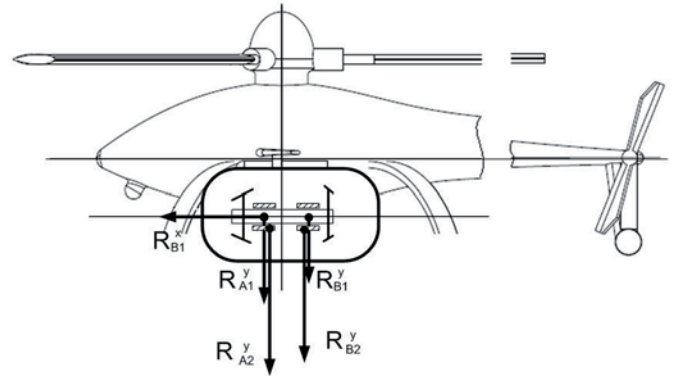
Fig. 17. Scheme of load of bearing nodes during a maneuver jump down, own study

$$R^y_{A1} = P^{st}_{A1} = 5.638N$$
$$R^y_{B1} = P^{st}_{B1} = 1.631N$$

The forces of inertia R^y_{A2} / R^y_{B2} caused by acceleration during the maneuver are multiplication of the respective gravity forces, where the multiplication coefficient is the value of the overload. Based on the performed analysis, the maximum acceleration value was equal a_{max}=5, 85 m/s², what gives as follow:

$$a_\Sigma = a_{max} - g$$
$$a_\Sigma = -3.96m / s^2$$

According to equation (28) and (29), the *k* coefficient is:

$$k = \frac{a_\Sigma}{g} = -0.4$$
$$P^{ydyn}_{A1} = k \cdot P^{st}_{A1} = -2.26N$$

5. Conclusion

The performed analysis of maximum load states of the bearing nodes in the rotor assembly shows, that during a maneuver jump up and jump down radial bearing A is more loaded than bearing B. The maximum value of the load force acting on radial bearings node A is P_p = 17.1 N and in the case of axial bearings, acting force is always equal zero, in the case that the working components of the compressor drive unit are structured such that they create an axial aerodynamic forces to equilibrate. It is important to note, that the resulting values refer only to one maneuver jump up and jump down. Therefore, these values will be confronted with the values obtained during other maneuvers such as acceleration and deceleration, deceleration before the attack, tight curve and return to the target. However, they will be the subject of the future work. Statement of comprehensive analysis of possible loads will allow the use of the compressor drive unit of turbine engine in normal conditions, while extending the service life.

References

1. Dudziak J. Mass analysis of profitability of use piston and turbine engines for driving light helicopters. Transactions of the Institute of Aviation 2013; 232: 15-23, http://dx.doi.org/10.5604/05096669.1106587.
2. Dudziak J. Analiza numeryczna dynamiki współdziałania schładzacza spalin z silnikiem napędowym w ekstremalnych lotach śmigłowca. Lublin University of Technology, diploma thesis, 2011.

3. Fijałkowski S. Materiały naukowe na zebranie środowiskowe Sekcji Podstaw Eksploatacji PAN. Lublin: Lublin University of technology Publishing, 1988.
4. Guła P, Gorecki T. Design and development of a Polish unmanned rotorcraft ilx-27. Transactions of the Institute of Aviation 2013; 232: 39-49, http://dx.doi.org/10.5604/05096669.1106664.
5. Giemza B, Nowiński E, Domański M. Gas-dynamic foil bearings application in high-speed turbines. Journal of KONBiN 2013; 3,4 (27,28): 100-101.
6. Hajduk J, Sabak R. Flight of the unmanned helicopter ilx-27 - some selected issues. Journal of KONBiN 2013; 1(25): 45-58.
7. Heshmat H, Shapiro W, and Gray S. Development of Foil Journal Bearings for High Load Capacity and High Speed Whirl Stability. ASME Journal of Lubrication Technology 1982; 104(2): 149-156, http://dx.doi.org/10.1115/1.3253173.
8. Heshmat H. Operation of Foil Bearings Beyond the Bending Critical Mode. ASME Journal of Lubrication Technology 1999; 122(1): 192-198.
9. Kazimierski Z., Krysiński J. Łożyskowanie gazowe i napędy mikroturbinowe. Warszawa: WNT, 1981.
10. Kazulo Z., Bereżański J. Sprawozdanie z prób w locie śmigłowca PZL Sokół dla określenia granicznych warunków eksploatacji w kontekście wymogów zastosowań specjalnych. WSK-Świdnik S.A. in cooperation with Aviation Institute 1999; 1LSP-36/367/2.
11. Konstantinesku W. N. Gazowaja smazka. Moscow: Maszinostrojenie, 1968.
12. Lee Y. B., Kim T. H., et al. Dynamic Characteristics of a Flexible Rotor System Supported by a Viscoelastic Foil Bearing. Journal of Lubrication Technology 2004; 37: 679-687, http://dx.doi.org/10.1016/s0301-679x(03)00013-6.
13. Magryta P., Majczak A. Diesel engine applicability in a light helicoter. Autobusy 2012; 4: 98-103.
14. Peng Z, Khonsari M. M. A Thermo-hydrodynamic Analysis of Foil Journal Bearings. ASME 2006; 128: 534.
15. Szejnberg S. A. et al. Opory skolrzenija s gazowoj smaskoj. Moscow: Maszinostrojenie, 1979.
16. Śmiech A. Analiza możliwości zastosowania łożysk gazowych w sprężarce doładowującej typu Comprex. Lublin University of Technology, diploma thesis, 2002.
17. Wendeker M., Siadkowska K., Magryta P., Czyz Z., Skiba K. Optimal Diesel Engine Technology Analysis Matching the Platform of the Helicopter. International Journal of Mechanical, Industrial Science and Engineering 2014; 8(5): 790-794.

Mirosław WENDEKER
Zbigniew CZYŻ
Department of Thermodynamics, Fluid Mechanics and
Aviation Propulsion Systems
Lublin University of technology
Nadbystrzycka 36, 20-618 Lublin, Poland
E-mail: m.wendeker@pollub.pl, z.czyz@pollub.pl

Junxing LI
Yongbo ZHANG
Zhihua WANG
Huimin FU
Lei XIAO

RELIABILITY ANALYSIS OF THE PRODUCTS SUBJECT TO COMPETING FAILURE PROCESSES WITH UNBALANCED DATA

OPARTA NA NIEZBILANSOWANYCH DANYCH ANALIZA NIEZAWODNOŚCI PRODUKTÓW PODLEGAJĄCYCH PROCESOM POWSTAWANIA USZKODZEŃ KONKURUJĄCYCH

Considering the degradation and catastrophic failure modes simultaneously, a general reliability analysis model was presented for the competing failure processes with unbalanced data. For the degradation process with highly unbalanced data, we developed a linear random-effects degradation model. The model parameters can be estimated based on a simple least square method. Furthermore, to fully utilize the degradation information, we considered the last measured times of the degradation units that had only one or two measured time points as zero-failure data or right-censored data of the catastrophic failure mode. Then the incomplete data set was composed of zero-failure data and catastrophic failure data. To analyze the incomplete data, the definition of the interval statistics was firstly given. The best linear unbiased parameter estimators of catastrophic failure were obtained based on the Gauss-Markov theorem. Then, the reliability function of the competing failure processes was given. The corresponding two-sided confidence intervals of the reliability were obtained based on a bootstrap procedure. Finally, a practical application case was examined by applying the proposed method and the results demonstrated its validity and reasonability.

Keywords: reliability evaluation, competing failure model, unbalanced data, interval statistics.

W pracy przedstawiono ogólny model analizy niezawodności procesów związanych z powstawaniem uszkodzeń konkurujących, który pozwala na wykorzystanie danych niezbilansowanych oraz umożliwia jednoczesne uwzględnienie uszkodzeń wynikających z obniżenia charakterystyk i uszkodzeń katastroficznych. Opracowano liniowy model efektów losowych dla procesu degradacji o wysoce niezbilansowanych danych. Parametry tego modelu można określić na podstawie prostej metody najmniejszych kwadratów. Ponadto, aby w pełni wykorzystać informacje dotyczące obniżenia charakterystyk, dane pochodzące z ostatniego pomiaru jednostek podlegających degradacji, dla których przeprowadzono tylko jeden lub dwa pomiary, rozpatrywano jako dane o zerowym uszkodzeniu lub jako ucięte prawostronnie dane dotyczące uszkodzenia katastroficznego. W ten sposób otrzymano zbiór niepełnych danych składający się z danych o uszkodzeniach zerowych oraz danych o uszkodzeniach katastroficznych. Aby móc przeanalizować uzyskane niepełne dane, podano definicję statystyki przedziałowej. Najefektywniejszy nieobciążony estymator liniowy (BLUE) parametrów uszkodzeń katastroficznych uzyskano na podstawie twierdzenia Gaussa-Markowa. Następnie, podano wzór funkcji niezawodności procesów związanych z powstawaniem uszkodzeń konkurujących. Odpowiednie dwustronne przedziały ufności dla oszacowanej niezawodności uzyskano metodą bootstrapową. Na koniec, przedstawiono przypadek praktycznego zastosowania proponowanej metody, którego wyniki wykazały jej trafność i zasadność.

Słowa kluczowe: ocena niezawodności, model uszkodzeń konkurujących, dane niezbilansowane, statystyki przedziałowe.

1. Introduction

Competing failure involving performance degradation and catastrophic failure can be found in many products [8, 22]. During the working span, if any one of the failure modes occurs first, the product fails. The performance degradation failure, which is also termed soft failure, is due to aging degradation which makes the performance value reach an unacceptable level. Compared with the degradation failure, the catastrophic failure is more severe because the product may not function once it occurs [15]. For example, a semiconductor device's failure may be due to electrical malfunctions or mechanical fatigue of I/O connectors (e.g., solder joints, etc.). The failure of the insulation system of a DC motor can be attributed to turn failure, phase failure, or ground failure. Failures of ball bearing assemblies are attributed to either race or ball failures [23]. Competing failure is

an important failure concept for products, so it is significant to study the reliability of products with competing failure modes.

Reliability analysis for products that experience only degradation has been extensively studied in the literature. Lu et al. [20] presented a general mixed-effects path model and used a two-stage approach to estimate the parameters of normally distribution. Subsequently, Lu and Meeker [21] used a simple degradation model to compare degradation analysis and traditional failure-time analysis in terms of asymptotic efficiency, and the results showed that degradation analysis provided more precision estimations. Bae and Kvam [2] developed a nonlinear random-effect model to describe the degradation of vacuum fluorescent displays. Furthermore, Bae et al. [3] investigated the link between a choosing mixed-effects model and the resulting lifetime model and pointed out that the degradation implied the lifetime distribution. In addition, stochastic process formulations have

attracted considerable attention from researchers in the degradation analysis, such as Markov chain, Wiener process and Gamma process, etc. Among them, Wiener process is one of the most prominent degradation models and has been studied rather extensively. Tseng et al. [29] used a Wiener process to describe the degradation o f the light intensity of LED lamps. Whitmore and Schenkelberg [31] presented a time-scale transformation Wiener process to analyze the reliability of self-regulating heating cables, and so on.

A variety of reliability models for competing failure modes have been developed. Zuo et al. [37] presented a mixture model which can be used to model both catastrophic failures and degradation failures. This mixture model also shows engineers how to design experiments to collect both hard failure data and soft failure data. Huang et al. [11, 12] developed an extension of reliability analysis of electronic devices with multiple competing failure modes and derived the probability of a product with a specific failure mode, then predicted the probability of the dominant failure mode on the product. Li et al. [18] proposed a reliability evaluation model of multi-state degraded systems subject to multiple competing failure processes and assumed that these processes were independent. Jiang et al. [13] presented a reliability and maintenance model for systems subject to competing failure processes, which included a soft failure caused by continuous degradation due to a shock process and a hard failure caused by the instantaneous stress. Song et al. [25] developed a multi-component system reliability model for the complex multi-component systems, which would experience multiple competing failure processes of each component due to simultaneous exposure to degradation and shock loads. Wang et al. [30] established a competing failure model for aircraft engines based on the data fusion method. Wu et al. [32] investigated the reliability and quality problems when the competing risks data are progressive type-I interval censored with binomial removals. Tang et al. [28] studied a replacement problem for a continuously system subject to the competing risk of soft and sudden failures.

Before statistical analysis, the competing failures are usually assumed that the failure modes are independent or dependent. Recently, reliability modeling for products with multiple independent competing failure modes has been investigated by several researchers. Huang et al. [12] presented an extended method of reliability analysis for an electronic device, which has two failure modes—solder/Cu pad interface fracture (a catastrophic failure) and light intensity degradation (a degradation failure). They assumed that the two failure modes were mutually independent due to the failure modes caused by different stresses. Recently, Cha et al. [6] used an improved method to analyze the reliability of this electronic device and the competing failure modes also were considered independent. Li et al. [18] developed models for evaluating the reliability of multi-state degraded systems with multiple competing failure modes, which were assumed independent. Applications of such systems can also be found in the Space Shuttle computer complex, electric generator power systems, and so on. Bocchetti et al. [5] proposed a competing risk model to access the reliability of the cylinder liners of a marine Diesel engine, and the two failure modes (wear and thermal crack) of cylinder liners were considered independent. Furthermore, in the practical engineering, the competing failure modes that each may have a different root cause can be considered independent. For example [9, 16], a semiconductor device failure may be due to electrical malfunctions or mechanical fatigue of I/O connectors (e.g., solder joints, etc.). Therefore, we assume that the competing failure modes are independent of each other in this paper.

In practice, the observed degradation data are often highly unbalanced. Here unbalanced means that the number and time of measurements are not identical for degradation units in a given population of products. Due to the unbalanced nature, the degradation data cannot be rationally analyzed by using the traditional models. Many researchers have studied this problem. Zhou et al. [35] presented a

nonparametric degradation modeling framework for making inference on the evolution of degradation signals that are observed sparsely or over short time intervals. Rao [24] and Swamy [27] have analyzed the linear random-effects regression model and given the parameter estimation approaches. Zhuang et al. [36] proposed a linear mixed-effects model and estimated the parameters with the repeated measurements data and the unbalanced data respectively. Yuan et al. [33] presents an advanced nonlinear mixed-effects model for modeling and predicting degradation in nuclear piping system. The model offers considerable improvement by reducing the variance associated with degradation of a specific unit, which leads to more realistic estimates of risk. It has been widely believed that the regression method is the most convenient and important tool for analyzing the unbalanced data of performance degradation.
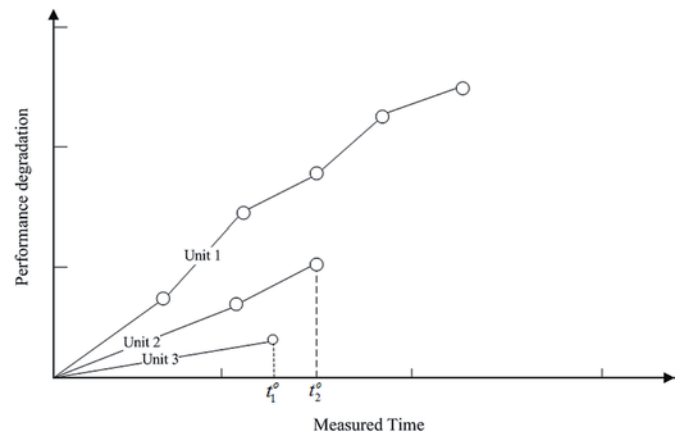
Fig. 1. Zero-failure data from degradation units
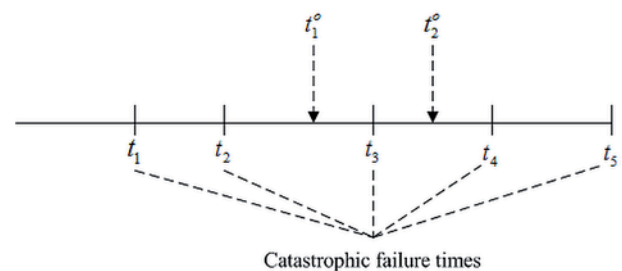
Fig. 2. Incomplete data

Furthermore, some degradation units may only be inspected at one or two time point, such as unit 2 and unit 3 in Fig.1. These degradation units make the analysis more challenging due to the sparse measured data. And this degradation data may be abandoned due to being unable to fit the degradation path. Therefore, in order to fully utilize the degradation information, we consider the last observation time points

of these degradation units, such as t_1^o and t_2^o shown in Fig.1, as the zero-failure data or right-censored data of the catastrophic failure mode. Then, the incomplete data consists of the zero-failure data from the degradation units and the failure data from the catastrophic failure, as shown in Fig.2. Kaplan et al. [14] proposed Kaplan-Meier estimation method to analyze the reliability for the incomplete data. Amster [1] developed an average rank method to estimate the parameters of the life distribution. Lawless [17] used the maximum likelihood method to analyze the incomplete data. Lin [19] used the Expectation Maximization algorithm to compute the non-parametric maximum likelihood estimation. In this paper, we define the interval statistic and propose a non-parametric estimation method to analyze the incomplete data, and then the best linear unbiased estimates of the distribution parameters can be obtained. In addition, to the best of our

knowledge, most of the studies in the competing failure analysis have not considered the two-sided confidence intervals of the reliability, which is an important index in the reliability evaluation, such as Zuo et al. [37], Li et al. [18], and Bocchetti et al. [5], etc. To remedy this deficiency, we develop a bootstrap (simulation) procedure to derive the two-sided confidence intervals for the reliability of the competing failure.

In this paper, we propose a generalized reliability analysis model for the competing failure mode under the hypotheses that i) the product fails when a first of the competing failure mechanisms reaches a failure state; ii) each failure mode has a known life distribution model; iii) the competing between degradation failure and catastrophic failure results in products failure. A linear random-effect model is presented for analyzing the highly unbalanced measurement data from performance degradation failure, and a least square method for parameter estimation has been developed in the situation where the degradation and catastrophic failures are independent. For the catastrophic failure mode, the concept of interval statistics is introduced, by combining the catastrophic failure data and the last measured time points of the degradation units that have one or two measured time points, a reliability model based on Weibull distribution is proposed. Moreover, the two-sided confidence intervals of the reliability for competing failure mode are given based on the bootstrap method.

The rest of this paper is organized as follows. Section 2 introduces the reliability models for the performance degradation model, catastrophic failure model and competing failure model. Section 3 and Section 4 present the estimation theory of the parameters of performance degradation model and catastrophic failure model, respectively. Section 5 gives the steps for reliability confidence interval estimation of competing failure mode. Section 6 contains an engineering example to demonstrate the proposed method. Section 7 includes the summary and conclusions.

2. Model assumptions

2.1. The performance degradation model

For product performance degradation, it can be considered as failure when the degradation reaches to the failure level D_f. Among several existing modeling approaches, a widely used one is the linear random-effect model. Its modeling procedure is as follows.

1. Assuming n units are put into test, n_q units occur catastrophic failure and m units occur performance degradation failure, where $n_q + m = n$. For each degradation unit, the measured

times are random. For example, the performance of unit i is measured at n_i^* times $t_{i1} < t_{i2} < \cdots < t_{in_i^*}$ with corresponding measurements $z_{i1}, z_{i2}, \cdots, z_{in_i^*}$, $i = 1, 2, \cdots, m$ (see Table.1). In Table 1, $\delta = 0$ means that the performance degradation occurs only, $\delta = 1$ means that the catastrophic failure occurs only.

2. Based on the properties of the linear random-effect degradation model, we have:

$$z_{ij} = \beta_{i1} + \beta_{i2}t_{ij} + \varepsilon_{ij}, \quad i = 1, 2 \cdots m; j = 1, 2, \cdots n_i^* \quad (1)$$

For convenient calculation, let:

$$\mathbf{z}_i = \begin{bmatrix} z_{i1} \\ z_{i2} \\ \vdots \\ z_{in_i} \end{bmatrix} \quad \mathbf{X}_i = \begin{bmatrix} 1 & t_{i1} \\ 1 & t_{i2} \\ \vdots & \vdots \\ 1 & t_{in_i^*} \end{bmatrix} \quad \beta_i = \begin{bmatrix} \beta_{i1} \\ \beta_{i2} \end{bmatrix} \quad \varepsilon_i = \begin{bmatrix} \varepsilon_{i1} \\ \varepsilon_{i2} \\ \vdots \\ \varepsilon_{in_i^*} \end{bmatrix}$$

Thus the linear random-effect degradation model can be expressed by:

$$\begin{cases} \mathbf{z}_i = \mathbf{X}_i \beta_i + \varepsilon_i \\ \beta_i \sim N(\mathbf{b}, \Sigma), \varepsilon_i \sim N(0, \sigma^2) \\ i = 1, 2 \cdots m; j = 1, 2, \cdots n_i^* \end{cases} \quad (2)$$

where $\beta_{i1} \sim N(b_1, \sigma_1^2)$ and $\beta_{i2} \sim N(b_2, \sigma_2^2)$, so $\mathbf{b} = (b_1, b_2)'$ and

$\Sigma = \begin{bmatrix} \sigma_1^2 & \rho\sigma_1\sigma_2 \\ \rho\sigma_1\sigma_2 & \sigma_2^2 \end{bmatrix}$. ρ denotes the correlation of β_{i1} and β_{i2}.

β_i is the random-effect parameter vector of the i th unit. ε_i denotes the measurement error. The β_i and ε_{ij} are assumed to be mutually independent of each other.

3) Let $\Theta = (b_1, b_2, \sigma_1^2, \sigma_2^2, \rho, \sigma^2)$ denote the vector of the unknown parameters. Then, a simple least square method can be developed to estimate the unknown parameters Θ in the proposed degradation model.

4) Let $D(t) = \beta_{i1} + \beta_{i2}t$ denote the actual degradation path for unit i. Then, $D(t) \sim N(b_1 + b_2 t, \sigma_1^2 + 2\rho\sigma_1\sigma_2 t + \sigma_2^2 t^2)$. Without loss of generality, we assume that the degradation measurements increase over time. Thus, the distribution of time-to-failure T can be defined as:

$$F_T(t \mid D_f, \Theta) = P\{T \le t \mid D_f, \Theta\} = P\{\eta(t) \ge D_f\}$$

$$= 1 - P\{\eta(t) \le D_f\} = 1 - \Phi\left(\frac{D_f - (b_1 + b_2 t)}{\sqrt{\sigma_1^2 + 2\rho\sigma_1\sigma_2 t + \sigma_2^2 t^2}}\right)$$

$$= \Phi\left(\frac{t - (D_f - b_1)/b_2}{\sqrt{(\sigma_1^2 + 2\rho\sigma_1\sigma_2 t + \sigma_2^2 t^2)/b_2^2}}\right) \quad (3)$$

Table 1. Product competing failure data

					Test units				
1		2	3		4	5		⋯ ⋯	n
t_{11} z_{11}		t_3	t_{31} z_{31}		t_4	t_{51} z_{51}		⋯ ⋯	t_{n1} z_{n1}
t_{12} z_{12}			t_{32} z_{32}					⋯ ⋯	t_{n2} z_{n2}
t_{13} z_{13}								⋯ ⋯	⋮ ⋮
⋮ ⋮								⋮ ⋮	$t_{n(n_1-1)}$ $z_{n(n_1-1)}$
t_{1n_1} z_{1n_1}								⋯ ⋯	
$\delta = 0$		$\delta = 1$	$\delta = 0$		$\delta = 1$	$\delta = 0$		⋯ ⋯	$\delta = 0$

5) Finally, the reliability function at a given time t can be defined as:

$$R_d(t) = 1 - \Phi\left(\frac{t - (D_f - b_1)/b_2}{\sqrt{(\sigma_1^2 + 2\rho\sigma_1\sigma_2 t + \sigma_2^2 t^2)/b_2^2}}\right) \quad (4)$$

2.2. The catastrophic failure model

For the degradation unit that only has one or two measurement time point and the catastrophic failure does not occur, the last measured time points can be regarded as zero-failure data, such as t_{32} and t_{51} in Table 1. Then, the incomplete catastrophic failure data consists of zero-failure data and catastrophic failure data. This is true. First, it is assumed that the competing failure modes are independent due to different root causes. Second, the catastrophic failure has not occurred until the last test time point for an individual degradation unit. Moreover, the corresponding performance degradation value is far enough from the predefined failure level.

For n_q units of the catastrophic failures, the corresponding failure times are $t_1 \le t_2 \le \cdots \le t_{n_q}$. Let $t_1^o \le t_2^o \le \cdots \le t_{n_p}^o$ denote the zero-failure data set. So the incomplete data set can be defined as

$t_1 <, \ldots, t_1^o <, \ldots, < t_i, \ldots < t_{n_p}^o <, \ldots, < t_{n_q}$.

We assume that the catastrophic failure time follows a Weibull distribution. Thus, the probability distribution function can be defined as:

$$F_{TC}(t) = 1 - \exp\left\{-\left(\frac{t}{\eta}\right)^\alpha\right\} \quad (5)$$

And the reliability function of the catastrophic failure can be represented by:

$$R_{TC}\left(t \,\middle|\, \left(t_1, t_2, t_1^o, t_2^o, t_3, t_3^o, \cdots, t_{n_q-1}, t_{n_p}^o, t_{n_q}\right)\right) = \exp\left\{-\left(\frac{t}{\eta}\right)^\alpha\right\} \quad (6)$$

2.3. The competing failure model

The reliability analysis presented in this paper is based on the assumption that the degradation failure mode and the catastrophic failure mode are independent of each other. Thus the reliability function of the competing failure for an operating time t is expressed as:

$$R(t) = P\{\min\{t_{TC}, t_d\} > t\} = P(t_{TC} > t) \cdot P(t_d > t) = R_{TC}(t) R_d(t) \quad (7)$$

where t_{TC} and t_d denote the catastrophic time-to-failure and degradation time-to-failure, respectively.

3. Parameter estimation of performance degradation model

In this section, we discuss a simple least square method for estimating the unknown parameters in degradation model. First, let

$$e_i = \mathbf{X}_i(\beta_i - \boldsymbol{b}) + \varepsilon_i \quad (8)$$

Therefore, the linear model of performance degradation can be rewritten as:

$$\begin{cases} \mathbf{z}_i = \mathbf{X}_i \boldsymbol{b} + \boldsymbol{e}_i \\ \boldsymbol{e}_i \sim N\left(0, \mathbf{X}_i \Sigma \mathbf{X}_i^{'} + \sigma^2 \mathbf{I}_{n_i^*}\right) \end{cases} \quad i = 1, 2, \cdots, m \quad (9)$$

where $\mathbf{I}_{n_i^*}$ is an identity matrix.

Based on the least square theory, the sum of squared error of performance degradation model can be expressed as:

$$Q = \sum_{i=1}^{m}(\mathbf{z}_i - \mathbf{X}_i \boldsymbol{b})^{'}(\mathbf{z}_i - \mathbf{X}_i \boldsymbol{b}) \quad (10)$$

Let:

$$\frac{\partial Q(\boldsymbol{b})}{\partial \boldsymbol{b}} = -2\sum_{i=1}^{m}\mathbf{X}_i^{'}\mathbf{z}_i + 2\sum_{i=1}^{m}\mathbf{X}_i^{'}\mathbf{X}_i \boldsymbol{b} = 0 \quad (11)$$

So the unbiased estimation of the random coefficient's mean is:

$$\hat{\boldsymbol{b}} = (\hat{b}_1, \hat{b}_2)^{'} = \left(\sum_{i=1}^{m}\mathbf{X}_i^{'}\mathbf{X}_i\right)^{-1}\sum_{i=1}^{m}\mathbf{X}_i^{'}\mathbf{z}_i \quad (12)$$

An estimator of the error variance $\hat{\sigma}_i^2$ for degradation unit i is

$$\hat{\sigma}_i^2 = \frac{1}{(n_i^* - p)}(\mathbf{z}_i - \mathbf{X}_i\hat{\boldsymbol{b}}_i)^{'}(\mathbf{z}_i - \mathbf{X}_i\hat{\boldsymbol{b}}_i) \quad (13)$$

where p is the dimension of β_i.

$$\hat{\boldsymbol{b}}_i = (\mathbf{X}_i^{'}\mathbf{X}_i)^{-1}\mathbf{X}_i^{'}\mathbf{z}_i \quad (14)$$

It can be proved that the unbiased estimation of error variance σ^2 is:

$$\hat{\sigma}^2 = \frac{1}{m}\sum_{i=1}^{m}\hat{\sigma}_i^2 \quad (15)$$

In [36], the author discussed the unbiased estimation of variance-covariance matrix Σ for the linear mixed-effect model. So we derive the unbiased estimation of the random coefficient's variance-covariance matrix based on [36].

$$\hat{\Sigma} = \sum_{i=1}^{m}\frac{(\hat{\boldsymbol{b}}_i - \bar{\boldsymbol{b}})(\hat{\boldsymbol{b}}_i - \bar{\boldsymbol{b}})^{'}}{m-1} - \frac{\hat{\sigma}^2}{m}\sum_{i=1}^{m}(\mathbf{X}_i^{'}\mathbf{X}_i)^{-1} \quad (16)$$

where

$$\bar{\boldsymbol{b}} = \frac{1}{m}\sum_{i=1}^{m}\hat{\boldsymbol{b}}_i, i = 1, 2, \cdots, m \quad (17)$$

4. Parameter estimation of catastrophic model

4.1. Definition of interval statistics

Definition 1. Suppose $X_1 < X_2 < \cdots < X_N$ are order statistics, where X_i illustrates a distribution function $F(x)$ and a density function $f(x)$. Then, X_i^o is defined as the i th interval statistics, if X_i^o satisfies:

$$X_i < X_i^o < X_{i+1} \qquad i = 0, 1, 2, \cdots, N \qquad (18)$$

where $X_0 = -\infty, X_{N+1} = +\infty$.

Theorem 1. For the interval statistics $X_1^o < X_2^o < \cdots < X_N^o$, the probability density function of X_i^o is:

$$g(x_i^o) = \frac{(N+1)!}{i!(N-i)!} \left[F(x_i^o) \right]^i \times \left[1 - F(x_i^o) \right]^{N-i} f(x_i^o), i = 0, 1, 2, \cdots, N \quad (19)$$

Theorem 2. For the interval statistics $X_1^o < X_2^o < \cdots < X_N^o$, the joint probability density function of X_i^o and X_j^o is:

$$g(x_i^o, x_j^o) = \frac{(N+2)!}{i!(j-i)!(N-j)!} f(x_i^o) f(x_j^o) \left[F(x_i^o) \right]^i \left[F(x_j^o) - F(x_i^o) \right]^{j-i} \left[1 - F(x_j^o) \right]^{N-j}$$

$$(20)$$

where $i = 0, 1, 2, \cdots, N-1$, $j = 0, 1, 2, \cdots, N$ and $i < j$.

Theorem 3. For the statistics $X_1 < X_1^o < X_2 < X_2^o < \cdots < X_N^o < X_N$, the joint probability density function of the i th interval statistics X_i^o and the j th order statistics X_j is:

$$g(x_i^o, x_j) = \frac{(N+1)!}{i!(j-i-1)!(N-j)!} f(x_i^o) f(x_j) \left[F(x_i^o) \right]^i \left[F(x_j) - F(x_i^o) \right]^{j-i-1} \left[1 - F(x_j) \right]^{N-j}$$

$$(21)$$

if $i < j$, and $i = 0, 1, 2, \cdots, N-1; j = 0, 1, 2, \cdots, N$, or as:

$$g(x_i^o, x_j) = \frac{(N+1)!}{(j-1)!(i-j)!(N-i)!} f(x_i^o) f(x_j) \left[F(x_j) \right]^{j-1} \left[F(x_i^o) - F(x_j) \right]^{i-j} \left[1 - F(x_i^o) \right]^{N-i}$$

$$(22)$$

if $i \geq j$, and $i, j = 0, 1, 2, \cdots, N$. The proof of Theorem 1-3 are detailed in Appendix A.

4.2. Parameter estimation of catastrophic failure model

According to the above discussions, the incomplete data t follows a Weibull distribution. Let $t^* = \ln t$, $n_p + n_q = n'$, $\sigma = \frac{1}{\alpha}$ and $\mu = \ln \eta$, so t^* follows the Extreme value distribution:

$$F(t^*) = 1 - \exp\left\{ -\exp\left(\frac{t^* - \mu}{\sigma} \right) \right\} \qquad (23)$$

The transformed catastrophic failure times $t_1^* \leq t_2^*, \cdots, \leq t_{n_q}^*$ can be considered as the realizations of the order statistics $X_1 \leq X_2, \cdots, \leq X_{n_q}$, and the transformed zero-failure times $t_1^{o*} \leq t_2^{o*}, \cdots, \leq t_{n_p}^{o*}$ from degradation units can be regarded as the realizations of the interval statistics $X_1^o \leq X_2^o, \cdots, \leq X_{n_p}^o$.

Letting $t' = (t^* - \mu)/\sigma$, the transformed time t' follows the standard Extreme value distribution

$$F(t') = 1 - \exp\left\{ -\exp(t') \right\} \qquad (24)$$

For clarity, let t_i' denote the i th transformed catastrophic failure time, and $t_j^{o'}$ denote the j th transformed zero-failure time for degradation unit, $i, j = 1, 2, \ldots, n'$. Thus, the incomplete data set $t_1 <, \ldots, t_1^o <, \ldots, < t_i, \ldots < t_{n_p}^o <, \ldots, < t_{n_q}$ can be transformed as $t_1' \leq t_2' < t_3^{o'}, \ldots, t_{n_p-1}' < t_{n_p}^{o}{}' < t_{n_p+1}' <, \ldots, < t_n'$.

The transformed catastrophic failure time t_j' can be considered as the realization of the $(j-i)$ th order statistic, if there are i transformed zero-failure times before t_j', $i < j$. Similarly, the transformed zero-failure time $t_i^{o'}$ can be considered as the realization of the j th interval statistic, when there are j transformed catastrophic failure times before $t_i^{o'}$, $i > j$.

For convenient calculation, we use t^* and t' to represent t^{o*} and $t_i^{o'}$, respectively. According to $t' = (t^* - \mu)/\sigma$, we know

$$\begin{cases} t_i^* = \mu + \sigma t_i' \\ E(t_i^*) = \mu + \sigma \mu_i \\ Cov(t_i^*, t_j^*) = \sigma^2 v_{ij} \\ i, j = 1, 2, \cdots, n' \end{cases} \qquad (25)$$

where

$$\mu_i = E(t_i') = \int_{-\infty}^{+\infty} t_i' g(t_i') dt_i' \qquad (26)$$

if t_i' denotes the interval statistic; i.e., $t_i' = t_i^{o'}$. Otherwise, μ_i can be calculated based on the method proposed in [4] if t_i' denotes the order statistic. v_{ij} can be obtained by:

$$v_{ij} = Cov(t_i', t_j') = E(t_i' t_j') - E(t_i') E(t_j')$$
$$= \int_{-\infty}^{+\infty} \int_{-\infty}^{+\infty} t_i' t_j' g(t_i', t_j') dt_i' dt_j' - \mu_i \mu_j \qquad (27)$$

and ν_{ij} can be calculated based on Equation (19), (25), and (26), if both $t_i^{'}$ and $t_j^{'}$ are interval statistics. Otherwise, ν_{ij} can be calculated based on Equation (20) or (21), (25), and (26), if either $t_i^{'}$ or $t_j^{'}$ is interval statistic. In addition, ν_{ij} can be estimated based on the method proposed in [4], when both $t_i^{'}$ and $t_j^{'}$ are order statistics.

Thus, the residual sum of squares Q can be obtained

$$Q = \sum_{i,j=1}^{n_q+n_p} \left(t_i^* - \mu - \sigma\mu_i \right) \nu_{ij}^{-1} \left(t_j^* - \mu - \sigma\mu_j \right) \tag{28}$$

Let $\dfrac{\partial Q}{\partial \mu} = \dfrac{\partial Q}{\partial \sigma} = 0$, so the best linear unbiased of the parameters μ and σ of Extreme value distribution can be estimated by the Gauss-Markov theorem.

$$\hat{\mu} = \frac{1}{\varphi}\left[\left(\sum_{i,j=1}^{n_q+n_p} \nu_{ij}^{-1}\mu_i\mu_j \right)\left(\sum_{i,j=1}^{n_q+n_p} \nu_{ij}^{-1}t_i^* \right) - \left(\sum_{i,j=1}^{n_q+n_p} \nu_{ij}^{-1}\mu_i \right)\left(\sum_{i,j=1}^{n_q+n_p} \nu_{ij}^{-1}\mu_i t_i^* \right) \right] \tag{29}$$

$$\hat{\sigma} = \frac{1}{\varphi}\left[\left(\sum_{i,j=1}^{n_q+n_p} \nu_{ij}^{-1} \right)\left(\sum_{i,j=1}^{n_q+n_p} \nu_{ij}^{-1}\mu_j t_i^* \right) - \left(\sum_{i,j=1}^{n_q+n_p} \nu_{ij}^{-1}\mu_i \right)\left(\sum_{i,j=1}^{n_q+n_p} \nu_{ij}^{-1}t_i^* \right) \right] \tag{30}$$

$$\varphi = \left(\sum_{i,j=1}^{n_q+n_p} \nu_{ij}^{-1} \right)\left(\sum_{i,j=1}^{n_q+n_p} \nu_{ij}^{-1}\mu_i\mu_j \right) - \left(\sum_{i,j=1}^{n_q+n_p} \nu_{ij}^{-1}\mu_i \right)^2 \tag{31}$$

$$\nu_{ij}^{-1} = \left[\nu_{ij} \right]^{-1}_{(n_q+n_p)\times(n_q+n_p)} \tag{32}$$

Then, the parameters α and η of Weibull distribution can be estimated by:

$$\begin{cases} \hat{\alpha} = \dfrac{1}{\hat{\sigma}} \\ \hat{\eta} = \exp\left(\hat{\mu}\right) \end{cases} \tag{33}$$

5. Estimation of confidence intervals for $R(t)$

Based on the methods given in Sections 3 and 4, we can obtain the estimates of the competing failure model parameters $\hat{\mathbf{b}}$, $\hat{\Sigma}$, $\widehat{\sigma^2}$, $\hat{\alpha}$, $\hat{\eta}$. The reliability $R(t)$ of competing failure can be calculated by substituting the estimates into $R(t; \hat{\mathbf{b}}, \hat{\Sigma}, \hat{\alpha}, \hat{\eta}, D_f)$; that is, point estimation $\hat{R}(t) = R(t; \hat{\mathbf{b}}, \hat{\Sigma}, \hat{\alpha}, \hat{\eta}, D_f)$. There are many methods to construct confidence intervals for a point on a distribution function.

One should note that it is nearly impossible to estimate the standard error of $R(t)$ directly, and we cannot select an appropriate distribution for the reliability function. Therefore it is a difficult problem to construct confidence intervals for $R(t)$. The bootstrap method is often used to construct confidence intervals or assess standard errors when there is no appropriate approach that is both tractable and sufficiently accurate. Accordingly, we develop the following bootstrap procedure to construct pointwise confidence intervals for $R(t)$.

1. Estimate the degradation model parameters $\mathbf{b}$, Σ, and the catastrophic model parameters α, η by using the method in Section 3 and 4 respectively, giving $\hat{\mathbf{b}}$, $\hat{\Sigma}$, $\widehat{\sigma^2}$, $\hat{\alpha}$, $\hat{\eta}$.

2. The Weibull distribution is transformed into

$$t = \hat{\eta}\left[-\ln\left(1-U\right) \right]^{1/\hat{\alpha}}$$

   where $U \sim U(0,1)$.

3. Generate $m - n_p$ simulated realizations $\tilde{\beta}_i = \left(\tilde{\beta}_{i1}, \tilde{\beta}_{i2} \right)'$ $i = 1,2,\cdots,m-n_p$ from $N\left(\hat{\mathbf{b}}, \hat{\Sigma}\right)$ and n_q simulated realizations $\tilde{t}_j$ $j = 1,2,\cdots,n_q$ of catastrophic failure time from Eq. (34). Then the incomplete data consist of n_q simulated realizations $\tilde{t}_j$ and n_p zero-failure data from degradation units.

4. Compute $m - n_p$ simulated degradation paths from $\tilde{z}_{ij} = \tilde{\beta}_{i1} + \tilde{\beta}_{i2}t_{ij} + \tilde{\varepsilon}_{ij}$, where $\tilde{\varepsilon}_{ij}$ are pseudo measuring errors generated from $N\left(0, \widehat{\sigma^2} \right)$ and t_{ij} are the same measurement times used in the original test.

5. Use the $m - n_p$ simulated degradation paths and the incomplete data to estimate parameters of the competing model, giving the bootstrap estimates $\hat{\hat{\mathbf{b}}}$, $\hat{\hat{\Sigma}}$, $\hat{\hat{\alpha}}$, $\hat{\hat{\eta}}$.

6. Generate N_B simulated realizations $\hat{\tilde{\beta}}_i = \left(\hat{\tilde{\beta}}_{i1}, \hat{\tilde{\beta}}_{i2} \right)'$ from $N\left(\hat{\hat{\mathbf{b}}}, \hat{\hat{\Sigma}}\right)$ and compute the corresponding degradation failure times $\tilde{t} = \left(D_f - \hat{\tilde{\beta}}_{i1} \right)\Big/ \hat{\tilde{\beta}}_{i2}$.

7. Compute the estimate $\hat{\tilde{R}}_d(t)$ from the simulated empirical distribution:

$$\hat{\tilde{R}}_d(t) = \text{number of } \tilde{t} > t \Big/ N_B \tag{35}$$

8. Compute the estimate $\hat{\tilde{R}}_{TC}(t)$ by substituting $\hat{\hat{\alpha}}$, $\hat{\hat{\eta}}$ into Eq.(6)

9. Compute the estimate $\hat{\tilde{R}}(t)$ of the competing reliability by substituting the bootstrap estimates $\hat{\tilde{R}}_d(t)$, $\hat{\tilde{R}}_{TC}(t)$ into Eq. (7) for any desired value t.

10. Do step 2-9 B times to obtain the bootstrap estimates $\widehat{\widehat{R}}(t)_1$, $\widehat{\widehat{R}}(t)_2, \ldots, \widehat{\widehat{R}}(t)_B$.

11. Sort the estimates $\widehat{\widehat{R}}(t)_1$, $\widehat{\widehat{R}}(t)_2, \ldots, \widehat{\widehat{R}}(t)_B$ in increasing order for each desired time t to give $\widehat{\widehat{R}}(t)_{[1]}$, $\widehat{\widehat{R}}(t)_{[2]}, \ldots, \widehat{\widehat{R}}(t)_{[B]}$.

12. Following [10], determine the lower and upper bounds of pointwise $1-\alpha$ confidence intervals for $R(t)$ as $\left[\widehat{\widehat{R}}(t)_{[l]}, \widehat{\widehat{R}}(t)_{[u]}\right]$, where $l = B\Phi\left[2\Phi^{-1}(q) + \Phi^{-1}(\alpha/2)\right]$, $u = B\Phi\left[2\Phi^{-1}(q) + \Phi^{-1}(1-\alpha/2)\right]$, and Φ is the standard normal distribution function, q =number of $\widehat{\widehat{R}}(t)_b \leq \widehat{R}(t)/B$, $b = 1, 2, \ldots, B$.

6. Case study

The reliability evaluation method presented in this paper for products with competing failure can be illustrated by an engineering example based on a well-known data set given in [26]. The data (Table 2) contains information about 33 cylinder liners of 8 cylinder SULZER RTA58 engines which were tested. A liner's failure is the competing result of wear failure and thermal crack failure. The wear failure mode can be treated as a performance degradation process and the thermal crack failure mode can be treated as a catastrophic failure. In this paper, we assume the two failure modes are independent. In Table 2, δ=1 and δ=0 represent the catastrophic failure and performance degrada-

Table 2. Performance degradation and catastrophic failure data of cylinder liners

unit/ i	t_{ij} (h) / z_{ij} (mm)				unit/ i	t_{ij} (h) / z_{ij} (mm)			
1 δ=1	36370h				18 δ=1	16870h			
2 δ=1	28930h				19 δ=1	11600h			
3 δ=1	27970h				20 δ=1	14300h			
4 δ=1	21830h				21 δ=1	14596h			
5 δ=0	14810 1.90	18700 2.25	28000 2.75		22 δ=1	31900h			
6 δ=1	39500h				23 δ=1	25300h			
7 δ=0	10000 1.20	30450 2.75	37310 3.05		24 δ=0	12100 1.00			
8 δ=1	25200h				25 δ=0	12000 1.95	27300 2.70	49500 3.15	56120 4.05
9 δ=1	27750h				26 δ=0	8800 1.40			
10 δ=1	25680h				27 δ=1	16738h			
11 δ=1	29900h				28 δ=0	33000 2.90	38500 3.25	55460 4.10	
12 δ=0	18320 2.20	25310 3.00	37310 3.70	45000 3.95	29 δ=1	28100h			
13 δ=0	10000 2.1	16620 2.75	30000 3.60		30 δ=0	8250 0.70			
14 δ=0	9350 0.85	15970 1.20			31 δ=1	31330h			
15 δ=1	18270h				32 δ=1	5430h			
16 δ=1	18650h				33 δ=1	16790h			
17 δ=0	7700 1.60								

tion failure, respectively. The measured time points and time intervals of degradation units are listed in Table 2.

6.1. Reliability of the performance degradation failure mode

From Table 2, we observe that the data from 11 units (i = 5, 7, 12, 13, 14, 17, 24, 25, 26, 28 and 30) can be considered as the degradation failure mode. The cylinder liner is defined to have failed, if the wear exceeds a degradation threshold value D_f =4 mm. However, it is obvious that the 14th, 17th, 24th, 26th and 30th degradation units only have one or two performance degradation measurement. Then we can consider the last measured times of these degradation units as the zero-failure data or right-censored data of the catastrophic failure mode. Therefore, the degradation data consist of the remaining 6 units (i = 5, 7, 12, 13, 25, and 28).

To test the normality assumption, we give the quantile-quantile (Q-Q) plot for the degradation data, as shown in Fig. 3, which shows that the plot of the quantiles of degradation data versus theoretical quantiles from a normal distribution is close to linear. In addition, we perform the Shapiro-Wilk (S-W) goodness-of-fit tests. The S-W test also verifies the normality assumption of the random-effects model for the degradation data with p-values of 0. 73.

For each degradation unit, the estimates of the degradation parameters $\widehat{\beta}_{i1}$ and $\widehat{\beta}_{i2}$ can be obtained based on the least

Fig. 3. Q-Q plot of the degradation data

Fig. 4. P-P plot of the model parameter $\widehat{\beta}_{i1}$

square method given in Section 3. Then we use these estimated results to test the assumptions required for the degradation model. For the random-effects degradation model, we assume that $\beta_{i1} \sim N\left(b_1, \sigma_1^2\right)$ and $\beta_{i2} \sim N\left(b_2, \sigma_2^2\right)$. In order to demonstrate the normality, we first give the P-P plots of $\widehat{\beta}_{i1}$ and $\widehat{\beta}_{i2}$, as shown in Fig. 4 and Fig. 5.
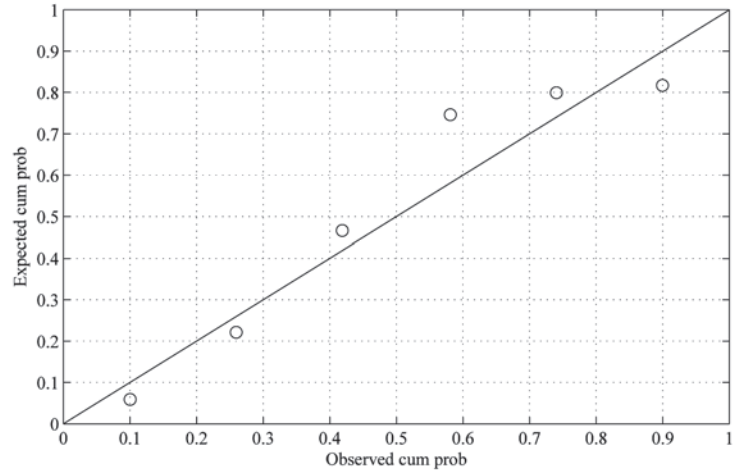

Fig. 5. P-P plot of the model parameter $\widehat{\beta}_{i2}$

The sample points will be approximately linear if they are normal. From Fig. 4 and Fig. 5, it can be observed that both the estimated values of $\widehat{\beta}_{i1}$ and $\widehat{\beta}_{i2}$ perform quite well. To further test the normality of the degradation model parameters, the S-W goodness-of-fit tests are performed. For the random-effects model, the S-W test failed to reject the null hypothesis that $\widehat{\beta}_{i1}$ and $\widehat{\beta}_{i2}$ are normally distributed with p-values of 0.57 and 0.29, respectively.

Then, we apply the proposed random-effects degradation model to fit the data. Based on the simple least square method mentioned in Section 3, the parameters in the degradation model can be estimated as:

$$\hat{b}_1 = 1.43, \hat{b}_2 = 0.48, \widehat{\sigma}_1^2 = 0.35, \widehat{\sigma}_2^2 = 0.05, \widehat{\rho} = -0.77, \widehat{\sigma}^2 = 0.03$$

To demonstrate the goodness of fit, the estimated mean degradation path is used to compare with the degradation sample. The results are depicted in Fig. 6, which shows the goodness-of-fit of the degradation model.

For further illustration, the 100pth percentile of performance degradation at a given time t can be expressed as:

$$z_p(t) = \phi(t) + \Phi^{-1}(p)\varphi(t) \tag{36}$$

where $\Phi(\cdot)$ is the distribution function of the standard normal distribution,

$$\begin{cases} \phi(t) = E(z) = b_1 + b_2 t \\ \varphi(t) = Var(z) = \sqrt{\sigma_1^2 + 2\rho\sigma_1\sigma_2 t + \sigma_2^2 t^2 + \sigma^2} \end{cases} \tag{37}$$
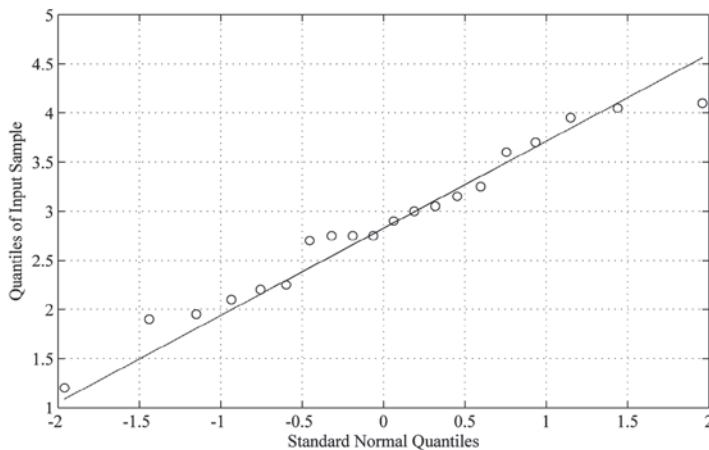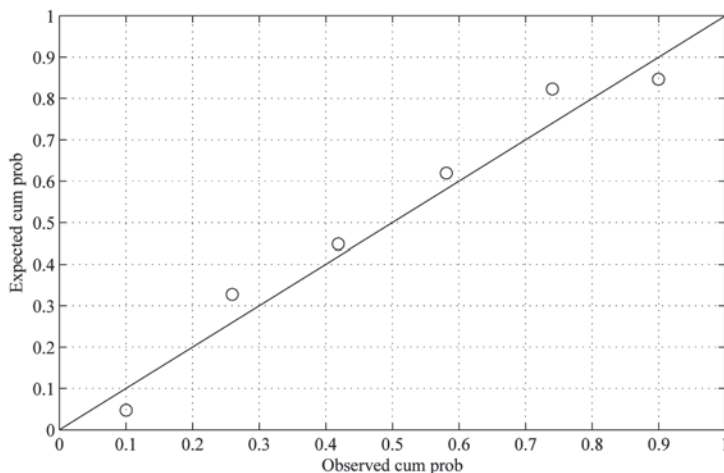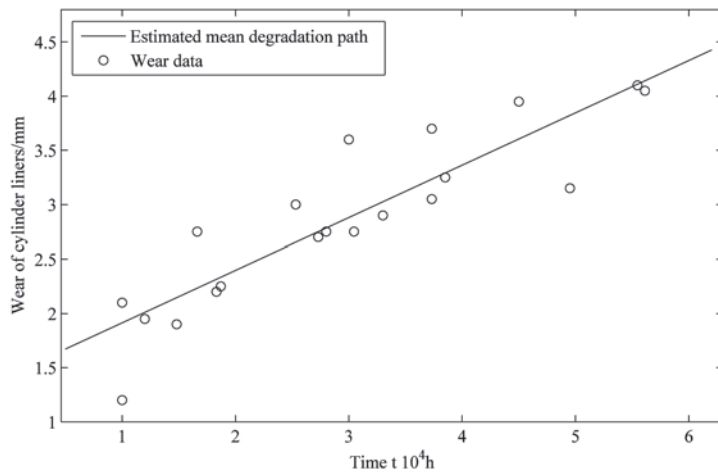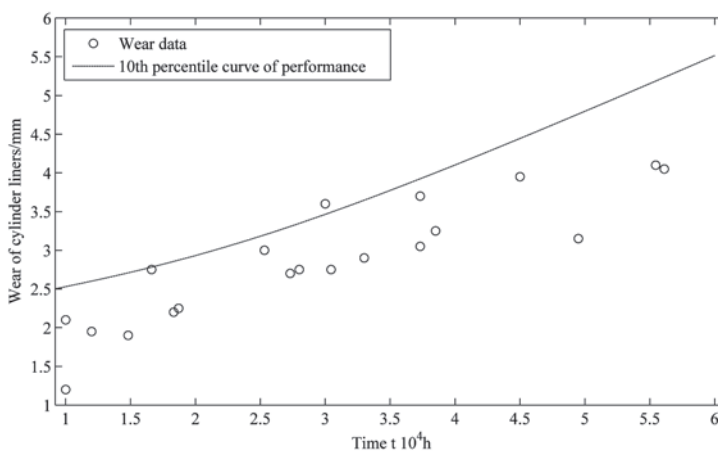
Fig. 6. Estimated mean degradation path

Fig. 7. 10th percentile curve of wear data

Then, the 10th percentile curve $\hat{z}_{0.1}(t)$ of performance degradation is given, as shown in Fig. 7. From the concept of percentiles, $\hat{z}_{0.1}(t)$ means an average of 90% of the population of the wear of cylinder liners $z(t)$ will be smaller than $\hat{z}_{0.1}(t)$. From Fig. 7, it can be observed that most wear data is under the 10th percentile curve obtained from the proposed model. The standard residuals plot over time is further given in Fig. 8, which shows that the proposed degradation model is appropriate to describe the degradation data.

Thus, we can obtain the reliability function $\hat{R}_d(t)$ of the performance degradation failure by substituting the estimated parameters into Eq. (4).

6.2. Reliability of the catastrophic failure mode

The incomplete data set consists of 22 catastrophic failure units and 5($i = 14, 17, 24, 26, 30$) performance degradation units. According to the lifetime of the two failure mode, the incomplete data is listed in Table 3. The last measured time points of the 30*th*, 26*th* and 17*th* degradation

units can be considered as the values of the 1st, 9th and 13th interval statistics, and the last measured time points of the 24th and 14th degradation units both can be considered as the values of the 10th interval statistic.

Assuming the catastrophic failure times follow a Weibull distribution, this assumption can be justified based on theoretical considerations that fatigue life data is often shown to be adequately analyzed using the Weibull distribution and is supported by a graphical analysis. In particular, the graphical analysis is performed by plotting on Weibull paper as Fig.9. Fig.9 shows that the points roughly follow a straight line and gives no obvious evidence that the catastrophic failure data do not fit a Weibull distribution.

The calculated catastrophic failure model parameters of incomplete data are listed in Table 4. In comparison with the conventional approach, the estimates of Weibull distribution parameters have significantly increased. The estimated shape parameter $\hat{\alpha}$ increases from 3.1914 to 10.4123, and the reason is that the current incomplete data estimation theory combines the catastrophic failure data with the last test time points of the degradation units that only have one or two inspection time points so that the sample size is enlarged, which means that the population properties can be depicted more properly. Meanwhile, with the increasing of life information content, the estimated scale parameter $\hat{\eta}$ also increases. In addition, the MTTF $\bar{t}$ is improved twice due to full use of the test information.

According to the results listed in Table 4, the reliability of the catastrophic failure at given time t can be obtained as:

Table 4. Comparison between the estimated results from traditional method and this paper

The parameters of Weibull distribution	Estimated by traditional method[7]	Estimated by the method in this paper
The shape parameter	3.19	10.41
The scale parameter	19322.12	32602.90
Mean time to failure	17302.96	31070.57

Table 3. Incomplete data consisting of catastrophic failures and degradation data

| Order number k	Lifetime t_k /h	Unit i	δi	Order number k	Lifetime t_k /h	Unit i	δi
1	5430	32	1	15	25200	8	1
2	8250	30	0	16	25300	23	1
3	11600	19	1	17	25680	10	1
4	14300	20	1	18	26770	17	0
5	14596	21	1	19	27750	9	1
6	16738	27	1	20	27970	3	1
7	16790	33	1	21	28100	29	1
8	16870	18	1	22	28930	2	1
9	18270	15	1	23	29900	11	1
10	18650	16	1	24	31330	31	1
11	20950	26	0	25	31900	22	1
12	21830	4	1	26	36370	1	1
13	23720	24	0	27	39500	6	1
14	25100	14	0				
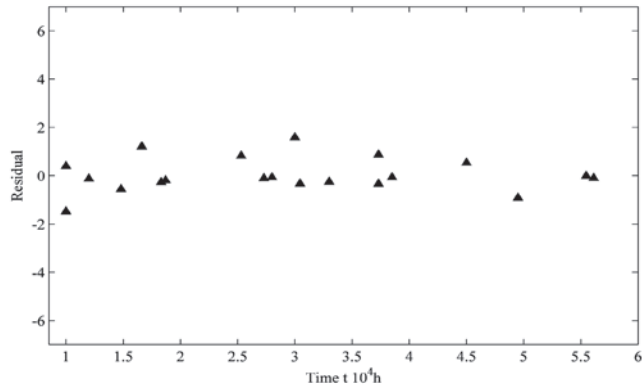
Fig. 8. Residual plot
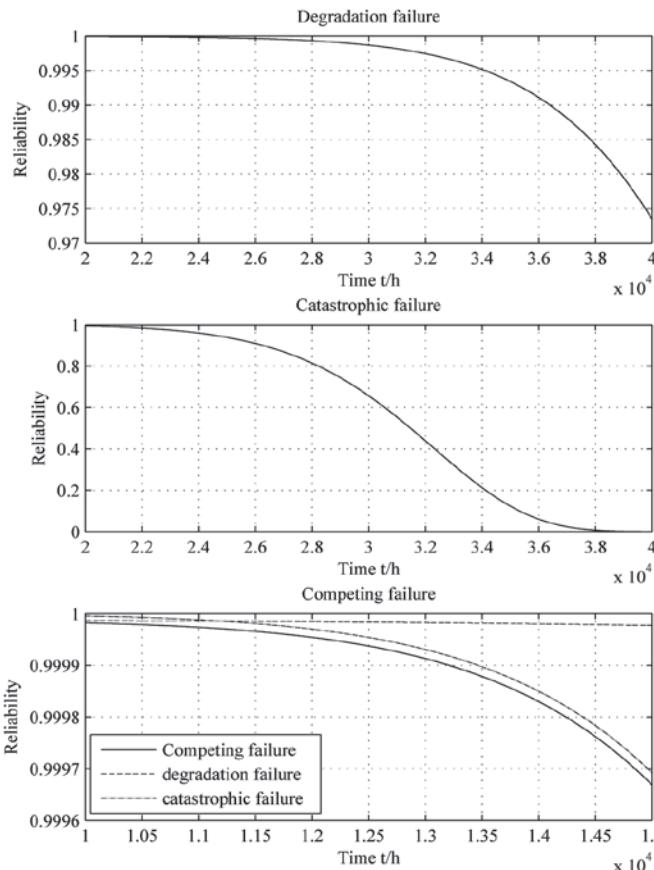
Fig. 10. Reliability of the competing failure, performance degradation and catastrophic failure
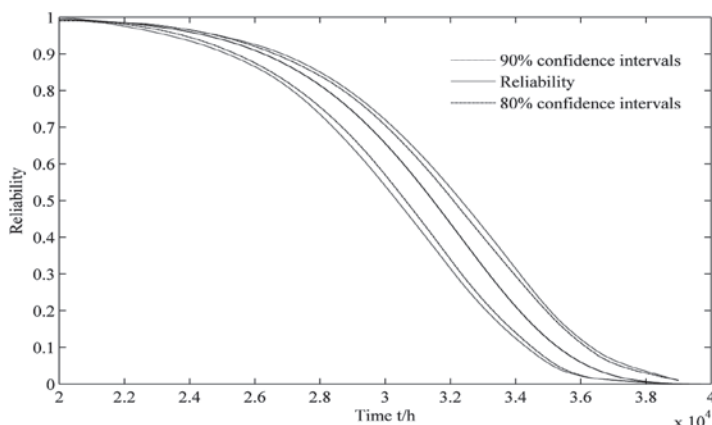

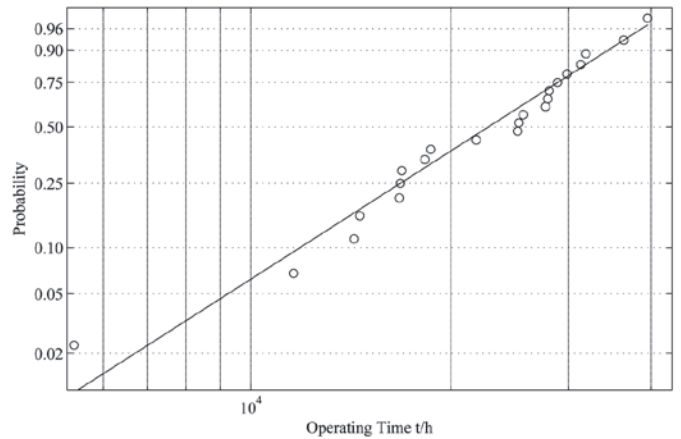*Fig. 11. Reliability estimate of the competing model with two-sided 90% and 80% confidence intervals*

Fig. 9. Graphical analysis of incomplete data on the Weibull plot

$$R_{TC}(t) = \exp\left\{-\left(\frac{t}{\eta}\right)^{\alpha}\right\} = \exp\left\{-\left(\frac{t}{32602.90}\right)^{10.41}\right\}$$

6.3. Reliability of the competing failure

Following Eq. (7), we can obtain the estimates of the reliability $\widehat{R}(t)$, $\widehat{R}_d(t)$ and $\widehat{R}_{TC}(t)$ by substituting the estimates $\hat{\mathbf{b}}$, $\widehat{\Sigma}$ and $\hat{\alpha}$, $\hat{\eta}$. Fig.10 depicts the product's reliability $\widehat{R}(t)$ under the competing failure model together with the reliability $\widehat{R}_d(t)$ and $\widehat{R}_{TC}(t)$ versus t respectively. It can be observed that the catastrophic failure of cylinder liner is the dominant failure mode. After operating the first 12000h, the reliability of the catastrophic failure mode begins to significantly decrease. This result can be explained by the fact that the probability that the thermal crack occurs will be enlarged with the increase of the wear loss.

Following Section 5, we obtain the competing failure model estimate of $\widehat{R}(t)$ with pointwise two-sided 90% and 80% confidence intervals as shown in Fig.11. The confidence intervals are obtained by the bootstrap simulation with B=5000 and N_B =10000.

7. Conclusions

The conclusions drawn from this research are as follows:
1. Considering degradation and catastrophic failures, a general reliability analysis model for the competing failure mode has been presented.
2. Unlike the previous studies assuming that the degradation data are repeated measurements, this paper presents a linear random-effect model for the highly unbalanced measurement data, and has developed a least square method for parameter estimation in the situation where the degradation and catastrophic failures are independent.
3. For the catastrophic failure mode, we propose a reliability model based on Weibull distribution. By combining the catastrophic failure data and the last measured time points of the degradation units that have only one or two measured time points, we obtain the estimates of the catastrophic failure model based on interval statistics theory. This method makes full use of the test information and improves the accuracy of estimation.
4. Based on the bootstrap method, we obtain the two-sided confidence intervals of the competing failure model for reliability assessment.

5. A practical application case was examined by applying the proposed methods to analyzing the competing failure data of cylinder liners. The results show that the degradation and catastrophic failure models presented in this paper are feasible and reasonable in practical applications.

However, the performance degradation failure and the catastrophic failure in some products are dependent of each other. In addition, more than two failure modes have been found in some products. Therefore, future study would also focus on the competing failure model of product which takes more than two dependent failure modes.

Appendix A

Proof of Theorem 1:

For N order statistics $X_1 < X_2 < \cdots < X_N$, the distribution function and density function of X_i are $F(x)$ and $f(x)$, respectively. And the corresponding interval statistics are $X_1^o < X_2^o < \cdots < X_N^o$, which also can be represented by $X_0^o < X_1 < X_1^o < X_2 < \cdots < X_{N-1}^o < X_N < X_N^o$. Define a interval $(x, x + \triangle x)$, then we have the probability:

$$\begin{cases} P\{X_i^o \le x\} = F(x) \\ P\{x < X_i^o < x + \triangle x\} = f(x)\triangle x \\ P\{x + \triangle x \le X_i^o\} = 1 - F(x + \triangle x) \end{cases} \tag{38}$$

For N order statistics, there are the corresponding $N+1$ interval statistics. We assume that one interval statistic X_i^o is in the interval $(x, x + \triangle x)$, and i interval statistics are in the interval $(-\infty, x)$. Thus, there are $N - i$ interval statistics in the interval $(x + \triangle x, +\infty)$. Therefore,

$$P\{x < x_i^o < x + \triangle x\} = C_{N+1}^1 C_N^i \left[F(x) \right]^i f(x)\triangle x \left[F(x + \triangle x) \right]^{N-i} \tag{39}$$

Then, the probability density function of X_i^o can be obtained by:

$$g(x_i^o) = \lim_{\triangle x \to 0} \frac{P\{x < x_i^o < x + \triangle x\}}{\triangle x} = \frac{(N+1)!}{i!(N-i)!} \left[F(x_i^o) \right]^i \times \left[1 - F(x_i^o) \right]^{N-i} f(x_i^o), \ i = 0,1,2,\cdots,N \tag{40}$$

Similarly, Theorem 2 and 3 can be proved.

References

1. Amster S J. The statistical treatment of fatigue experiments. Technometrics 1965; 7: 455, http://dx.doi.org/ 10.1080/00401706.1965.10490284.
2. Bae S J, Kvam P H. A nonlinear random-coefficients model for degradation testing. Technometrics 2004; 46: 460-469, http://dx.doi.org/10.1198/004017004000000464.
3. Bae S J, Kuo W, Kvam P H. Degradation models and implied lifetime distributions. Reliab Eng Syst Safe 2007; 92: 601-608, http://dx.doi.org/10. 1016/j.ress.2006.02.002.
4. Balakrishnan N, Chan PS. Order statistics from extreme value distribution, I: Table of means, variances and covariances. Commun. Statist. -Simula 1992; 21(4): 1199-1217.
5. Bocchetti D, Giorgio M, Guida M, Pulcini G. A competing risk model for the reliability of cylinder liners in marine diesel engines. Reliab Eng Syst Safe 2009; 94: 1299-1307, http://dx.doi.org/10.1016/j.ress.2009.01.010.
6. Cha J H, Gui M, Pulcini G. A competing risks model with degradation phenomena and catastrophic failures. International Journal of Performability Engineering 2014; 10: 63.
7. Chen K, Li S, Li F. Reliability mathematics and its application. JiLin: Jilin education press, 1987.
8. David H A, Moeschberger M L. The theory of competing risks. London: Griffin Publishers, 1978.
9. Di Giacomo G. Reliability of electronic packages and semiconductor devices. New York: McGraw-Hill Publishers, 1997.
10. Efron B. Bootstrap confidence intervals for a class of parametric problems, Biometrika, 1985; 72, 45-58, http://dx.doi.org/10.1093/ biomet/72.1.45.
11. Huang W. Reliability analysis considering product performance degradation. Tucson: University of Arizona; 2002.

12. Huang W, Askin R G. Reliability analysis of electronic devices with multiple competing failure modes involving performance aging degradation. Quality and Reliability Engineering International 2003; 19(3): 241-254, http://dx.doi.org/10.1002/qre.524.
13. Jiang L, Feng Q, Coit D W. Reliability and maintenance modeling for dependent competing failure processes with shifting failure thresholds. Reliability, IEEE Transactions on 2012; 61: 932-948, http://dx.doi.org/10.1109/TR.2012.2221016.
14. Kaplan E L, Meier P. Nonparametric estimation from incomplete observations. J Am Stat Assoc 1958; 53: 457-481, http://dx.doi.org/10.1080/01621459.1958.10501452.
15. Kececioglu D. Reliability engineering handbook. DEStech Publications Inc, 2002.
16. Lau J H. Solder joint reliability: theory and applications. Springer, 1991, http://dx.doi.org/10.1007/978-1-4615-3910-0.
17. Lawless JF. Statistical models and methods for lifetime data. John Wiley & Sons, 2011.
18. Li W, Pham H. Reliability modeling of multi-State degraded systems with multi-competing failures and random shocks. IEEE Trans 2005; 54(2): 297-303, http://dx.doi.org/10.1109/tr.2005.847278.
19. Lin Y. Parametric estimation in competing risks and multi-state models. University of Kentucky, 2011.
20. Lu C J, Meeker W Q. Using degradation measures to estimate a Time-to-Failure distribution. Technometrics 1993; 161-174. http://dx.doi.org/10.1080/00401706.1993.10485038
21. Lu C J, Meeker W Q, Escobar L A. A comparison of degradation and failure-time analysis methods for estimating a time-to-failure distribution. Stat Sinica 1996; 6: 531-546.
22. Misra K B. Reliability analysis and prediction: A methodology oriented treatment. Elsevier, 1992.
23. Nelson W B. Accelerated testing: Statistical models, test plans, and data analysis. John Wiley & Sons, 2009.
24. Rao C R. Linear statistical inference and its applications. John Wiley & Sons, 2009.
25. Song S, Coit D W, Feng Q, Peng H. Reliability analysis for multi-component systems subject to multiple dependent competing failure processes. Reliability, IEEE Transactions on 2014; 63: 331-345, http://dx.doi.org/10.1109/TR.2014.2299693.
26. Sulzer. Service instructions for diesel engine G.M.-Sulzer RT58-Type: 8 RTA 58. Sulzer; 1986.
27. Swamy P. Statistical inference in random coefficient regression models. Berlin: Springer, 1971, http://dx.doi.org/10.1007/978-3-642-80653-7.
28. Tang D, Yu J. Optimal replacement policy for a periodically inspected system subject to the competing soft and sudden failures. Eksploatacja i Niezawodnosc - Maintenance and Reliability, 2015, 17(2): 228-235, http://dx.doi.org/10.17531/ein.2015.2.9.
29. Tseng S T, Tang J, Ku I H. Determination of burn in parameters and residual life for highly reliable products. Naval Research Logistics (NRL) 2003; 50: 1-14, http://dx.doi.org/10.1002/nav.10042.
30. Wang H, Gao J. A reliability evaluation study based on competing failures for aircraft engines. Eksploatacja i Niezawodnosc - Maintenance and Reliability, 2014; 16 (2): 171-178.
31. Whitmore G A, Schenkelberg F. Modelling accelerated degradation data using Wiener diffusion with a time scale transformation. Lifetime Data Analysis 1997; 3: 27-45, http://dx.doi.org/10.1023/A:1009664101413.
32. Wu S J, Huang S R. Planning progressive Type-I interval censoring life tests with competing risks. Reliability, IEEE Transactions on 2014; 63: 511-522, http://dx.doi.org/10.1109/TR.2014.2313708.
33. Yuan X, Pandey M D. A nonlinear mixed-effects model for degradation data obtained from in-service inspections. Reliability Engineering & System Safety, 2009, 94(2): 509-519, http://dx.doi.org/10.1016/j.ress.2008.06.013.
34. Zhao W, Elsayed E A. An accelerated life testing model involving performance degradation. Reliability and Maintainability Annual Symposium-RAMS IEEE, 2004.
35. Zhou R R, Serban N, Gebraeel N. Degradation modeling applied to residual lifetime prediction using functional data analysis. The Annals of Applied Statistics 2011; 1586-1610, http://dx.doi.org/10.1214/10-AOAS448.
36. Zhuang D, Mao S. Statistical analysis of degradation data. Beijing: China Statistics Press, 2013.
37. Zuo M J, Jiang R, Yam R. Approaches for reliability modeling of continuous-state devices. Reliability, IEEE Transactions on, 1999; 48(1): 9-18, http://dx.doi.org/10.1109/24.765922.

Junxing LI
Yongbo ZHANG
Zhihua WANG
Huimin FU
School of Aeronautic Science and Engineering
New Main Building C-928, Beihang University
37 Xueyuan Street, Haidian District, Beijing 100191, China

Lei XIAO
The State Key Lab of Mechanical Transmission
Chongqing University
174 Shazheng Street, Shapingba District
Chongqing 400030, China

E-mail: lijun-xing2008@163.com, zhangyongbo@buaa.edu.cn, wangzhihua@buaa.edu.cn, fuhuimin@263.net, leixiao211@163.com

Ľubomír AMBRIŠKO
Daniela MARASOVÁ
Peter GRENDEL

DETERMINATION THE EFFECT OF FACTORS AFFECTING THE TENSILE STRENGTH OF FABRIC CONVEYOR BELTS

OCENA WPŁYWU CZYNNIKÓW NA WYTRZYMAŁOŚĆ NA ROZCIĄGANIE TAŚM PRZENOŚNIKOWYCH TKANINOWO – GUMOWYCH

The Design of experiment (DOE) method was used in this paper to rubber conveyor belt tension testing. Using DOE method were from experimentally obtained data established effects of factors and interactions that affect the value of the measured strength and also were determined regression models, which apply input and output variables to the relation. The regression model presents the complete multifactor experiment that contains main factors and interactions.

Keywords: *mechanical testing, tension, conveyor belt, DOE method (Design of Experiments).*

Metoda planowania eksperymentu (DOE) w artykule użyta do testowania napięcia taśm przenośnikowych tkaninowo – gumo-wych. Korzystanie z metody DOE były ustalonych poszczególnych czynników oraz ich interakcji ze danych uzyskanych w sposób doświadczalny. Czynniki i interakcje wpływające na wartość zmierzonej wytrzymałości, a także określono modele regresji, wy-kazującego związki pomiędzy zmiennymi wejściowymi i wyjściowymi. Model regresyjny przedstawia kompletny wieloczynnikowy eksperyment obejmujący podstawowe zmienne oraz ich interakcje.

Słowa kluczowe: *testy mechaniczne, napięcie, taśma przenośnikowa, metoda DOE.*

1. Introduction

Belt conveyor system is a high-power conveyance system broadly applied in practice [16]. The main reason of such broad application is its structural and economic adaptability [26]. According to [14, 25], a belt conveyor represents the most cost-effective solution in the loose material transportation. It can be broadly used in the fields, such as coal mining, ports, chemical industry, electric energy, metallurgy, ar-chitecture, and food supplies [13]. Requirements demanded by pro-duction plants regarding minerals are currently rising, which results in the increasing traffic intensity of material flows in mining companies within the transportation of bulk solid materials. Bulk materials are currently transported mainly by trucks. Therefore, an alternative to this kind of transport must be searched [21, 23]. Transportation solu-tion is offered by the continuous belt conveyor system with the crush-ing carried out directly in the quarry, using portable crushers [6].

Large scale belt conveyor is a key (one of the most important) de-vice to transport bulk-solid material for long distance at high rates [5]. Belt conveyors are complex systems with drive groups as functional-ly very important components [15]. For belt conveyors, the trans-port task can be defined as a process whose purpose is to transport the set quantity of handled material within a defined time between the set loading and offloading locations [12].

Due to the fact that a conveyor belt, as a carrying and tractive element, represents the most important part of a belt conveyor, it is essential to reduce the costs of manufacture and maintenance thereof. Maintenance cost reduction can be achieved by improvements in util-ity properties of conveyor belts [16]. Conveyor belt properties sig-nificantly affect the reliability of the entire belt conveyor system. Insufficient strength of a conveyor belt can cause its rupture and sub-sequent downtime due to repair and replacement thereof. Rupture of a conveyor belt represents unacceptable risk in the operation of a belt

conveyor system and [3] classify it as unsystematic risk in an under-ground mine plant.

During the operation, a conveyor belt is affected by various stress-es that cause its damage and wear-out [8]. Awareness of mechanical properties of conveyor belts is very important for a smooth opera-tion of belt conveyors [24]. Requirements regarding conveyor belts depend on the method of their use; therefore, entire belt conveyor, as well as its individual components, is subject to compulsory tests. Re-quired properties of conveyor belts are identified by tests determined by standards and technical or technological regulations.

According to Hardygora [10] and Taraba [22] tests of conveyor belts can be divided into three groups: standard tests, certification tests and non-standard tests. The first group includes tests of physi-comechanical properties for their compliance with the standards in force. The second group comprises certification tests on belts required for permitting the latter to be operated in underground mines. The third group embraces non-standard tests – specialist tests performed on special test stands, usually not covered by standards but concern-ing parameters important for the operation of belts.

Non-standard tests include, for example, determination of the im-pact resistance of a conveyor belt. The methodology of testing the impact resistance using a special testing equipment is described by authors [7] and determination of impact resistance on the basis of ex-perimental measurements, with the results evaluation using the regres-sion analysis, is described by authors [1, 4]. By using DOE methods in the examining stress conveyor belts in relation to their resistance to breakdown deal works [2, 9].

Conveyor belt tests carried out within the experimental research and the results presented in this article can be classified as the group 1st tests, according to [10]. In addition to the results obtained by standard testing, the article presents a new approach to the evalua-

tion thereof, with the determination of the impact of the selected factors on the tensile strength of a conveyor belt.

2. Materials and experimental procedure

2.1. Experimental material

A belt conveyor as a composite consists of several materials. Fabric conveyor belts usually consist of a wear resistant top layer ('top cover'), a fabric carcass providing tensile strength, skim layers for adhesion between rubber and carcass, and a bottom layer ('bottom cover') to cover the carcass and provide sufficient friction to the drive pulley [18].

Experiments were carried out using conveyor belts (CB) of TRANSBELT type intended for general use. They are textile conveyor belts intended for the transportation of loose and piece materials in common operating conditions. They are typically used in the mining and processing industries, as well as in operations, such as gravel sand works, lime works, cement works, thermal power plants, dumps and docks. Their cover layers (CL) are made of rubber in five categories, depending on the type of transported material. The conveyor belt carcass (Fig. 1) consists of one to five fabric plies. The plies are made in two versions. In the first version, individual layers of fabric reinforcement are made of polyamide fibres in the lengthwise and transversal direction. In case of polyamide reinforcement material, the mark of a conveyor belt type contains letter P. In the second version, individual plies are made of the combination of polyamide and polyester fibres.

Table 2. Required mechanical properties of the examined conveyor belts

Property	Unit	Conveyor belt type		
		800	1000	1250
Tensile strength				
• along the warp, min.	N/mm	800	1000	1250
• in woof, min.		160	200	250
Permitted tensile stress (reference load), max.	N/mm	80	100	125
Elongation at break along the warp, min.	%	10	10	10
Proportional elongation with permitted stress, max.	%	3	3	3

In such case, polyester fibres are used in the lengthwise direction of the fabric (in warp). Transverse direction of a ply, also called woof, consists of polyamide fibres. In such version of the fabric reinforcement, a conveyor belt type is marked with letters EP. Experiments were carried out using CBs (Table 1) with cover layers of AA category – for the transportation of very abrasive, grainy, and loose material. Required mechanic properties of the examined CBs are listed in Table 2.
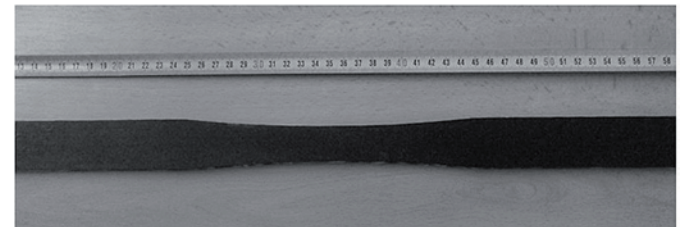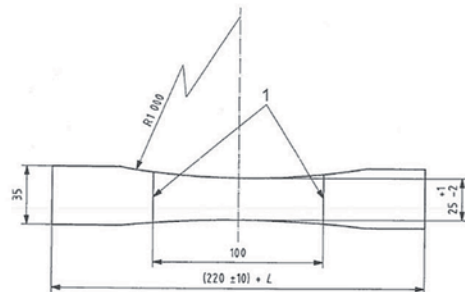
Fig. 2. Type A testing specimen, L – Testing specimen length [mm], 1 – reference lines
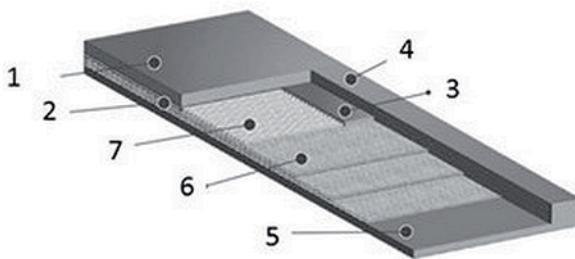

Fig. 1. Structure of a conveyor belt with a textile carcass 1 – top cover layer, 2 – carcass, 3 – adhesive mixture, 4 – protective rubber selvage, 5 – bottom cover layer, 6 – fabric plies, 7 – bumper

2.2. Testing specimens

Type A testing specimens were prepared using a cutting die by cutting them out from each type of a conveyor belt in the quantity of three pieces, in the lengthwise direction, as specified in [11]. None of the ply objects contained joints. Shapes and dimensions of testing specimens are documented in Fig. 2. Two reference lines were drawn on the testing specimens across their lengthwise axes in their working sections, in the distance of 100 mm. Subsequently, these objects were conditioned pursuant to [11]. Tensile tests were carried out immediately after the conditioning period terminated.

Table 1. Used types of conveyor belts

Ord. no.	Carcass material		Nominal tensile strength [N/mm]	Number of layers	CL category	CB mark
	Warp	Woof				
1.	P	P	800	3	AA	P 800/3 AA
2.	P	P	800	4	AA	P 800/4 AA
3.	E	P	800	3	AA	EP 800/3 AA
4.	E	P	800	4	AA	EP 800/4 AA
5.	P	P	1000	3	AA	P 1000/3 AA
6.	P	P	1000	4	AA	P 1000/4 AA
7.	E	P	1000	3	AA	EP 1000/3 AA
8.	E	P	1000	4	AA	EP 1000/4 AA
9.	P	P	1250	3	AA	P 1250/3 AA
10.	P	P	1250	4	AA	P 1250/4 AA
11.	E	P	1250	3	AA	EP 1250/3 AA
12.	E	P	1250	4	AA	EP 1250/4 AA

2.3. Test fundamentals and procedure

Test fundamentals – a testing specimen, cut out from the whole thickness of a conveyor belt, is loaded, under the prescribed conditions, on the tensile testing equipment, applying the tension, until the testing object disturbance is observed. Experimental tests of mechanical properties of conveyor belts were carried out using a testing machine of the Zwick Roell Z 100 type. Due to the need to measure the elongation of the testing specimen during the test, the testing machine was equipped with the videoXtens extensometer, which applies the contactless deformation measurement principle. The main advantage of this extensometer is that it can be used until the sample's rupture without any damage. A full-area camera scans a digitalized image of a tested specimen and processes it in the real time. The system automatically identifies reference marks, while calculating their displacement as the specimen is loaded [27].

Test procedure – Testing specimens were symmetrically fixed between grips of the testing machine so that the lengthwise axes of a testing object, the central line of the grip, and the direction of tensile force were aligned. Testing specimens were loaded with the constant loading rate of 100 mm/min. During the test, elongation was recorded at the instance of reaching the reference load, corresponding to one tenth of the nominal tensile strength in the lengthwise direction (Table 2), multiplied by the width of the testing specimen in mm. The testing continued, until the specimen's rupture, first signs of carcass disturbance, or reaching the maximum value on the force measuring device. This maximum force and the elongation at such force were recorded. The same procedure was carried out with all testing objects. Recorded values are invalid, if a testing specimen is not disturbed between the reference lines, or if during the test the specimen is skidding between the grips [20], which, however, did not happen.

2.4. Determination of mechanical properties

Experimental research determined the following mechanical properties of the examined CBs, determined pursuant to [19]:

- **Full thickness tensile strength** – the most intensive force measured during the tensile test, divided by the testing specimen's width:

$$f_s = \frac{F_r}{b_t} \qquad (1)$$

Table 3. Maximum measured values of mechanical properties of the examined CBs

Type CB	f_s [N/mm]				ε_r [%]				ε_t [%]			
	x_1	x_2	x_3	$\bar{a}(x_i)$	x_1	x_2	x_3	$\bar{a}(x_i)$	x_1	x_2	x_3	$\bar{a}(x_i)$
P 800/3	893	979	939	937	19	20	20	19.7	1.1	1.2	1.2	1.2
P 800/4	1004	1009	987	1000	22	22	22	22.0	1.3	1.4	1.5	1.4
EP 800/3	943	885	942	923	18	18	18	18.0	1.0	1.1	1.1	1.1
EP 800/4	1050	1069	1059	1059	19	19	19	19.0	0.9	0.9	0.9	0.9
P 1000/3	1250	1255	1275	1260	25	24	25	24.7	1.5	1.6	1.6	1.6
P 1000/4	1240	1167	1209	1205	24	22	23	23.0	2.4	2.6	2.5	2.5
EP 1000/3	1270	1239	1219	1243	19	18	18	18.3	1.1	1.2	1.4	1.2
EP 1000/4	1240	1250	1290	1260	18	19	19	18.7	0.9	1.0	0.8	0.9
P 1250/3	1460	1500	1471	1477	22	22	22	22.0	1.6	1.7	1.7	1.7
P 1250/4	1583	1569	1660	1604	24	25	25	24.7	1.5	1.6	1.5	1.5
EP 1250/3	1575	1580	1581	1579	20	20	20	20.0	0.8	0.7	0.7	0.7
EP 1250/4	1830	1667	1791	1763	18	18	18	18.0	1.1	1.3	1.2	1.2

Table 4. Minimum measured values of mechanical properties of the examined CBs

Type CB	f_s [N/mm]				ε_r [%]				ε_t [%]			
	x_1	x_2	x_3	$\bar{a}(x_i)$	x_1	x_2	x_3	$\bar{a}(x_i)$	x_1	x_2	x_3	$\bar{a}(x_i)$
P 800/3	862	848	870	860	23	22	22	22.3	1.8	1.6	1.7	1.7
P 800/4	950	968	970	963	21	21	21	21.0	1.4	1.3	1.3	1.3
EP 800/3	884	835	894	871	18	19	18	18.3	1.3	1.2	1.1	1.2
EP 800/4	880	856	861	866	20	20	20	20.0	1.2	1.0	0.9	1.0
P 1000/3	1167	1180	1220	1189	27	26	25	26.0	1.8	1.7	2.1	1.9
P 1000/4	1102	1074	1100	1092	20	20	20	20.0	1.5	1.6	1.6	1.6
EP 1000/3	1159	1138	1156	1151	17	16	17	16.7	0.9	0.9	1.0	0.9
EP 1000/4	1127	1122	1126	1125	17	18	18	17.7	1.0	1.1	1.1	1.1
P 1250/3	1361	1367	1364	1364	24	25	24	24.3	2.5	2.5	2.3	2.4
P 1250/4	1580	1494	1529	1534	24	25	25	24.7	1.5	1.7	1.6	1.6
EP 1250/3	1333	1342	1340	1338	18	18	18	18.0	1.1	1.1	1.1	1.1
EP 1250/4	1291	1295	1315	1300	21	21	20	20.7	0.8	0.8	0.7	0.8

where f_s – tensile strength [N/mm],

F_r – sample load force at rupture [N],

b_t – specimen width [mm].

The resulting value of the tensile strength is the arithmetic average of the values for three testing objects in the lengthwise direction.

- **Elongation at break** – elongation at the maximum force expressed as the percentage gain in the distance between two reference lines

$$\varepsilon_r = \frac{(L_2 - L_1)}{L_1} \cdot 100 \qquad (2)$$

where ε_r – elongation at break [%],

L_1 – distance between reference lines prior to loading [mm],

L_2 – distance between reference lines at specimen's disturbance [mm].

- **Elongation at the reference load** – is expressed as the percentage gain in the distance between two reference lines with the reference force:

$$\varepsilon_t = \frac{(L_R - L_1)}{L_1} \cdot 100 \qquad (3)$$

where ε_t – elongation at the reference load [%],

L_R – distance between reference lines with the reference load of the testing specimen [mm],

L_1 – distance between reference lines prior to loading [mm].

The resulting value of the elongation at break and the elongation at the reference load is the arithmetic average of values for three testing objects in the lengthwise direction.

For each examined type of a conveyor belt, we tested the testing objects marked as x_i, where i = 1, 2, 3. Results of the measurements are listed in Tables 3 and 4.

3. Design and evaluation of experiment

In this work, we monitored the impact of three main factors (Table 5): nominal strength, i.e. specified minimum value of the tensile strength (factor A), type of carcass (factor B), and number of plies (factor C). Our task was to determine which of the factors, or which of their interactions, have a significant impact on the response, i.e. the tensile strength of a conveyor belt.

We have developed a plan of the complete three-factor experiment with two levels without repetition together with two-factor interactions (first-order interactions), whereas the number of all steps is 2^3 – the square root represents the number of levels and the exponent represents the number of factors. For one experiment design, it was necessary to enter 8 values of the response on the upper and lower levels of each factor, which are listed in Tables 3 and 4. For the DOE method, maximum and minimum values of measured tensile strength of CBs were applied separately for 3 strength intervals: a) 800 and 1,250 N/mm, b) 800 and 1,000 N/mm, c) 1,000 and 1,250 N/mm; i.e. totally 6 designs of experiment. Each experiment design can be

Table 5. List of input factors and their levels

	Factors	Low level (−1)	High level (+1)
A	Nominal strength [N/mm]	X_i	X_j
B	Carcass type [-]	P	EP
C	Number of plies [-]	3	4

Where: $X_i X_j$: a) $X_1 X_3$ 800 and 1,250 N/mm, b) $X_1 X_2$ 800 and 1,000 N/mm, c) $X_2 X_3$ 1,000 and 1,250 N/mm

graphically represented using a cube (Fig. 3), whereas cube corners contain the entered response values.
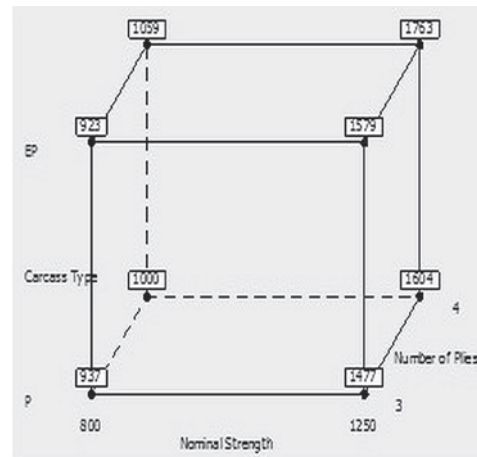

Fig. 3. Graphical representation using cube

3.1. Designs of experiments for maximum response values

In the assessment of the significance of effects and their interactions, the DOE method facilitates the use of several graphical outputs, such as:

- Graphical representation of main effects;
- Normal probability plot of the significance of factors and interactions;
- Interaction plot of main effects.

As several individual experiments designs were carried out, the most frequently used Pareto chart was selected (Fig. 4), which defines factors and interactions with the statistically significant impact on the monitored response. Significance of individual impacts of factors or interactions was tested using the t-test and by the determination of the p-value on the significance level of $\alpha=0.05$. In all the monitored intervals for the maximum values of the measured tensile strength of CBs, statistically significant impact of three main factors was confirmed. Insignificant impact on the measured tensile strength value was observed only in certain first-order interactions.
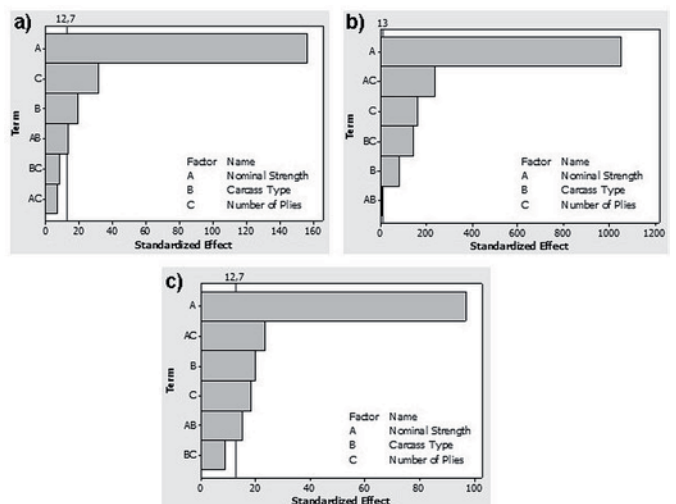

Fig. 4. The Pareto chart of the significance of factors and interactions; a) 800 and 1,250 N/mm, b) 800 and 1,000 N/mm, c) 1,000 and 1,250 N/mm

Table 6 shows the average values of the response on the upper and lower level of each factor, as well as effects of individual factors.

Table 6. The main effects of factors

800 & 1250	A	B	C
$\bar{y}.-$ (low level)	979.75	1254.5	1229
$\bar{y}.+$ (high level)	1605.75	1331	1356.5
Effect of factors	626	76.5	127.5
800 & 1000			
$\bar{y}.-$ (low level)	979.75	1121.25	1131
$\bar{y}.+$ (high level)	1242	1100.5	1090.75
Effect of factors	262.25	20.75	40.25
1000 & 1250			
$\bar{y}.-$ (low level)	1242	1386.5	1389.75
$\bar{y}.+$ (high level)	1605.75	1461.25	1458
Effect of factors	363.75	74.75	68.25

The strongest significance on the monitored response in all strength intervals was observed in factor A (nominal strength).

The model of a full three-factors experiment containing the main factors and all two-factors interactions is determined by the relation:

$$y = \beta_0 + \beta_1 x_1 + \beta_2 x_2 + \beta_3 x_3 + \beta_{12} x_1 x_2 + \beta_{13} x_1 x_3 + \beta_{23} x_2 x_3 + \varepsilon \quad (4)$$

where y is the response, x_1, x_2, x_3, $x_1 x_2$ up to $x_2 x_3$ represent values of factors A, B, C and interactions between the respective two factors (e.g. $x_1 x_2$ represents the AB interaction).
The point estimate of the regression model is:

$$y = \hat{\beta}_0 + \hat{\beta}_1 x_1 + \hat{\beta}_2 x_2 + \hat{\beta}_3 x_3 + \hat{\beta}_{12} x_1 x_2 + \hat{\beta}_{13} x_1 x_3 + \hat{\beta}_{23} x_2 x_3 \quad (5)$$

Table 7. The coefficients point estimate of the regression model

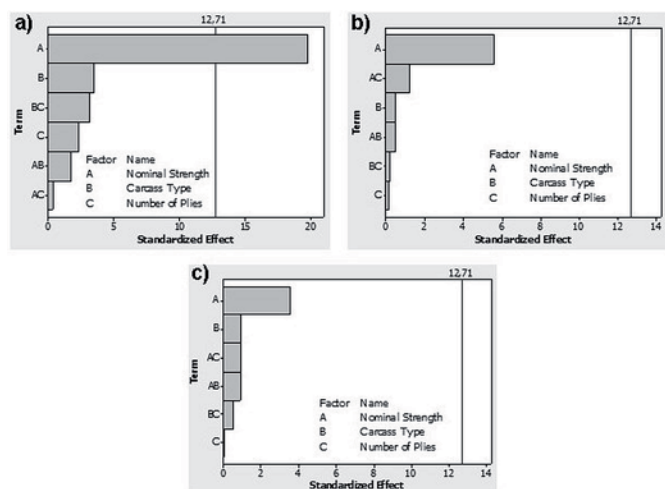|	coefficient	$\hat{\beta}_0$	$\hat{\beta}_1$	$\hat{\beta}_2$	$\hat{\beta}_3$	$\hat{\beta}_{12}$	$\hat{\beta}_{13}$	$\hat{\beta}_{23}$
800 & 1000	value	1110.88	131.12	10.37	20.13	−0.87	−29.63	18.12
100%	p−value	0.000	0.001	0.008	0.004	0.090	0.003	0.004
800 & 1250	value	1292.75	313	38.25	63.75	27.00	14.00	16.25
99.97%	p−value	0.001	0.004	0.033	0.020	0.047	0.090	0.078
1000 & 1250	value	1423.88	181.88	37.38	34.12	27.87	43.62	16.13
99.94%	p−value	0.001	0.007	0.032	0.035	0.043	0.027	0.074

Fig. 5. The Pareto chart of the significance of factors and interactions; a) 800 and 1250 N/mm, b) 800 and 1000 N/mm, c) 1000 and 1250 N/mm

where $\hat{\beta}_0$, $\hat{\beta}_1$, up to $\hat{\beta}_{23}$ are estimates of the regression model coefficients that can also be calculated using the effects [17]. Values of all model coefficients and the value of **the determination coefficient** in % are shown in Table 7.

3.2. Designs of experiment for minimum response values

Almost in all the monitored intervals for the minimum values of measured tensile strength of CBs, statistical significance of main factors and first-order interactions was not confirmed, with the exception of the 800 and 1250 N/mm interval, where the significance of factor A was manifested (nominal strength), Fig. 5.
Table 8 shows the average values of the response on the upper

Table 8. The main effects of factors

800 & 1250	A	B	C
$\bar{y}.-$ (low level)	890	1180.25	1108.25
$\bar{y}.+$ (high level)	1384	1093.75	1165.75
Effect of factors	494	−86.5	57.5
800 & 1000			
$\bar{y}.-$ (low level)	890	1026	1017.75
$\bar{y}.+$ (high level)	1139.25	1003.25	1011.5
Effect of factors	249.25	−22.75	−6.25
1000 & 1250			
$\bar{y}.-$ (low level)	1139.25	1294.75	1260.5
$\bar{y}.+$ (high level)	1384	1228.5	1262.75
Effect of factors	244.75	−66.25	2.25

and lower level of each factor, as well as effects of individual factors. Again, the strongest impact on the monitored response in all strength intervals was observed in factor A (nominal strength), even though it is not significant in all intervals. The values of all model coefficients and the value of **the determination coefficient** in % are shown in Table 9.

4. Discussion

This paper is focused on the experimental research of the tensile strength of fabric conveyor belts. The research was carried out applying the Design of Experiment method (DOE), whereas the relation between the strength properties of conveyor belts was monitored in the selected factors. Six experiments were designed, in which 12 conveyor belts types were used with the nominal strength of 800, 1000 and 1250 N/mm. Conveyor belts of the same nominal strength were also differing in the number of plies and the material of the textile carcass. In all experiments, the setting of factors B and C values (type of carcass and number of plies) was identical. Only the upper and lower levels of factor A were changing (nominal tensile strength).

In all the monitored intervals for the maximum values of the measured tensile strength of CBs, significant impact of all examined factors – the nominal tensile strength (factor A), a type of carcass (factor B), and the number of plies (factor C) on the response (tensile strength of a conveyor belt) was confirmed. Also the impact of some interactions on the given dependent variable was manifested. The scope of the experimental program did not allow supplementation of one more factor. The setting of the strength interval has thus a decisive impact on

Table 9. The coefficients point estimate of the regression model

	coefficient	$\hat{\beta}_0$	$\hat{\beta}_1$	$\hat{\beta}_2$	$\hat{\beta}_3$	$\hat{\beta}_{12}$	$\hat{\beta}_{13}$	$\hat{\beta}_{23}$
800 & 1000	value	1014.63	124.63	−11.38	−3.13	10.13	−27.63	−4.62
100%	p-value	0.014	0.113	0.701	0.912	0.729	0.433	0.870
800 & 1250	value	1137	247	−43.25	28.75	−21.75	4.25	−39.50
98.34%	p-value	0.007	0.032	0.179	0.261	0.332	0.791	0.195
1000 & 1250	value	1261.63	122.38	−33.13	1.12	−31.88	31.88	−17.12
56.60%	p-value	0.018	0.177	0.516	0.979	0.529	0. 529	0.709

Table 10. Significant factors and interactions in the monitored intervals for the minimum and maximum values of the measured tensile strength of CBs

Strength interval	Factors and interactions	
	MIN	MAX
800 and 1250	A	A, C, B, AB
800 and 1000	–	A, AC, C, BC, B
1000 and 1250	–	A, AC, B, C, AB

Table 11. Interval range for the maximum measured values

Strength interval	[%]		
	MIN	MAX	Interval range
800 and 1250	15.4	41	25.7
800 and 1000	15.4	26	10.6
1000 and 1250	20.5	41	20.5

Table 12. Interval range for the minimum measured values

Strength interval	[%]		
	MIN	MAX	Interval range
800 and 1250	7.5	22.7	15.2
800 and 1000	7.5	18.9	11.4
1000 and 1250	9.2	22.7	13.5

the determination of the impact of factors. In the monitored intervals for the minimum values of the measured tensile strength of CBs, only the statistically significant impact of factor A was confirmed (nominal strength) in the interval of 800 and 1250 N/mm. The list of all significant factors and interactions is presented in Table 10.

The differences between the measured tensile strength and the nominal strength of conveyor belts were used to determine the range of individual strength intervals. On the basis of the maximum (MAX) and the minimum (MIN) values, separately for the maximum (Table 11) and minimum (Table 12) measured values, the strength interval range was determined. With the falling interval range in the maximum measured values, the number of more significant interactions is rising. However, in the minimum measured values, particularly in the broadest strength interval of 800 and 1250 N/mm, significance of factor A was confirmed.

5. Conclusions

During the operation, a conveyor belt is exposed mainly to the uniaxial quasi-static tensile stress in the lengthwise direction, due to its required initial tension for the transfer of tensile forces and the dynamic stress in the transverse direction induced by its troughability. Improper dimensioning of conveyor belt mechanical properties and selection of inappropriate cover layers or a conveyor belt carcass can result in the belt rupture. Therefore, the experimental research was focused on the testing of tensile strength of fabric conveyor belts, while monitoring the relation between the mechanical properties of conveyor belts and the selected factors. To achieve improved strength parameters of conveyor belts, it is important to identify possible impact of input factors. Using the DOE method, factors and their interactions affecting the response – tensile strength of a conveyor belt were identified. The impact of three monitored factors was confirmed, i.e. the nominal strength (factor A), the number of plies (factor C), and the type of carcass (factor B), as well as certain mutual interactions, for the maximum values of the measured strength. In certain two-factor interactions, however, statistically significant impact was not confirmed.

The results indicate that the nominal strength has the strongest impact on the tensile strength of a conveyor belt, i.e. on the monitored response in all experiment designs, although it is not significant in each case. In the examined responses, the relation between the DOE method and the range of the input experimental data was not manifested.

Regression models were also determined to describe the functional relation of the output characteristics and the input factors. Each obtained regression model represents a complete three-factor experiment containing factors and first-order interactions.

References

1. Andrejiová M, Pavlisková A. Analysis of regression model of functional dependency in impact force from height and weight of ram for conveyor belt. Annals of Faculty Engineering Hunedoara 2010; 8 (3): 267-270.
2. Andrejiová M, Pavlisková A, Marasová ml. D, Husáková N. The design an experiment the stress of the conveyer belts. Transport and Logistics 2012; Mimoriadneč. 10: 242-248.
3. Beljič Č, Lazovič M. Risk assesment in underground mine plant. Transport and Logistics 2001; 1: 123-127.
4. Berežný Š, Grinčová A. Regresná analýza špecifických matematických modelov získaných pri skúškach dopravných pásov proti prierazu. Transport and Logistics 2010; Mimoriadneč. 7: 296-308.
5. Du D M, Li H, Zhu C S, He Q. Virtual prototype modeling and starting method of belt conveyor. Applied Mechanics and Materials 2011; 148-149: 879-882, http://dx.doi.org/10.4028/www.scientific.net/AMM.148-149.879.
6. Drottboom M. A rising global trend. New technological developments increase range of IPCC applications. Bulk Solids Handl. 2013; 33 (5): 22-26.

7.   Grinčová A, Hlúbiková A, Krešák J. Metodika skúšania dopravných pásov pri prieraze. Transport and Logistics 2008; Mimoriadneč. 5: 209-213.
8.   Grinčová A, Marasová D. Experimental research and mathematical modelling as an effective tool of assessing failure of conveyor belts. Eksploatacja i Niezawodnosc - Maintenance and Reliability 2014; 16 (2): 229-235.
9.   Grujic M, Andrejiova M, Marasova D, Grendel P. Using the DOE method by experimental research of conveyor belts quality. TTEM Journal: Technics Technologies Education Management 2013; 8 (2): 558-564.
10. Hardygora M. Trends in conveyor belt research. Transport and Logistics 2002; 3: 1-12.
11. ISO 18573: 2013, Coveyor belts - Test atmospheres and conditioning periods.
12. Kulinowski P. Simulation studies as the part of an integrated design process dealing with belt conveyor operation. Eksplotacja i Niezawodnosc – Maintenance and Reliability 2013; 15 (1): 83-88.
13. Leng Y F, Liu J, Zu F. Parametric design on belt conveyor drums based on VBA. Adv Mater Res 2010; 156-157: 1243-1246, http://dx.doi.org/10.4028/www.scientific.net/AMR.156-157.1243.
14. Luo X, Li T, Hu B, Zheng M, Peng Q J. The modeling and simulating of conveyor belt based on ADAMS. Adv Mater Res 2012; 562-564: 1451-1455, http://dx.doi.org/10.4028/www.scientific.net/AMR.562-564.1451.
15. Maneski T, Jovančič P, Ignjatović D, Milošević-Mitić V, Maneski M. Condition and behaviour diagnostics of drive groups on belt conveyors. Eng. Failure Anal. 2012; 22: 28-37, http://dx.doi.org/10.1016/j.engfailanal.2012.01.001.
16. Marasová D. Mathematical and experimental support for belt conveyors. Ostrava: VŠB-TU, 2013.
17. Montgomery D C. Design and Analysis of Experiments. New York: J. Wiley, 2002.
18. Röthemeyer F, Sommer F. Kautschuk Technologie, München Wien: Carl Hanser Verlag, 2006.
19. STN 26 0370: 1987, Dopravné pásy s textilnou kostrou - Metódy skúšania základných vlastnosti.
20. STN EN ISO 283: 2007, Textilné dopravné pásy - Pevnosť v ťahu v celej hrúbke dopravného pása, predĺženie pri pretrhnutí (ťažnosť) a predĺženie pri referenčnom zaťažení - Skúšobná metóda.
21. Šaderová J, Rosová A, Bindzár P, Kačmáry P. Multi-Criteria evaluation - A tool for the selection of steel wire rope. Applied Mechanics and Materials 2014; 683: 33-38, http://dx.doi.org/10.4028/www.scientific.net/AMM.683.33.
22. Vladimír T. The methods of conveyor belt basic characteristics testing and special tests. Transport and Logistics 2004; 4 (6): 59-68.
23. Turnbull D. A game changer in Mining. IPCC and continuous mining solution are set to gain more Ground. Bulk Solids Handl. 2013; 33 (5): 16-18.
24. Valentova H, Skrbek B, Neubert M, Hana P, Nedbal J. Mechanical and ultrasound properties of conveyor belt rubbers. in: SGEM2011 Conference Proceedings, Bulgaria, 2011: 839-844, http://dx.doi.org/10.5593/sgem2011/s03.125.
25. Wang F S. Indentation rolling resistance of conveyor belts based on Maxwell model. Adv Mater Res 2012; 479-481: 1526-1529, http://dx.doi.org/10.4028/www.scientific.net/AMR.479-481.1526.
26. Westphal H. Optimierung von Fördergurten mit Textil-Einlagen. Hebezeuge Fördermittel 1985; 25 (3): 81-85.
27. Zwick Materials Testing Machines [online]. [cit. 2015-03-30]. <http://www.zwick.com/en/products/static-materials-testing-machines.html>

Ľubomír AMBRIŠKO
Daniela MARASOVÁ
Institute of Logistics
Faculty of Mining, Ecology, Process Control and Geotechnologies
Technical University of Košice
Letná 9, 040 01 Košice, Slovakia

Peter GRENDEL
Driving School Grendel
Secondary School Automobile
Moldavská 2, 040 11 Košice, Slovakia

E-mail: lubomir.ambrisko@tuke.sk, daniela.marasova@tuke.sk, grendel@grendel.sk

Gyan Ranjan BISWAL

SYSTEM RELIABILITY OPTIMISATION OF COOLING-CUM-CONDENSATE-EXTRACTION SYSTEM

OPTYMALIZACJA NIEZAWODNOŚCI UKŁADU CHŁODZENIA Z SYSTEMEM ODPROWADZANIA SKROPLIN

A novel methodology is presented for condensation in power generation plants; this section is the main intersection of heat loss, typically 40% thermal efficiency of a plant. Condensate section is interfaced with the generating section to enhance the active contribution of the system. Both the cooling section and the condensate section are integrated and interfaced through the low-pressure and high-pressure cycles to attain the improved electrical efficiency, which affects the heat transfer capability of the power generation plants. This paper proposess a Cooling-cum-Condensate-Extraction System (CCES), to dedicate a 36-MW- captive power plant. The paper is dedicated for the design and development of an effective CCES, analyzing its impact over the systems in terms of system reliability optimization, and the role of real-time optimization. The designed model also contributes in discharging lesser amount of flu gases as against existing technologies with its improved active operation hours.

Keywords: *Cooling-cum-Condensate-Extraction System, Fault Tree Analysis, System Reliability, System Safety, Machine Health Monitoring.*

W artykule przedstawiono nowatorską metodologię procesu skraplania do zastosowania w części kondensacyjnej elektrowni, gdzie dochodzi do największych strat ciepła – przeważnie aż 40% wydajności termicznej elektrowni. W proponowanym rozwiązaniu instalację kondensacyjną sprzężono z częścią prądotwórczą aby zwiększyć aktywny wkład systemu. Część chłodzącą zintegrowano i sprzężono z częścią kondensacyjną poprzez cykle nisko- i wysokociśnieniowe, uzyskując w ten sposób lepszą wydajność elektryczną, co ma wpływ na zdolność wymiany ciepła w elektrowni. W artykule przedstawiono układ chłodzenia z systemem odprowadzania skroplin (CCES) przeznaczony dla elektrowni potrzeb własnych o mocy 36 MW. Pracę poświęcono projektowaniu i konstrukcji efektywnego CCES, analizując jego wpływ na systemy elektrowni w zakresie optymalizacji niezawodności systemów oraz roli optymalizacji w czasie rzeczywistym. Zaprojektowany przez nas model, w porównaniu z istniejącymi technologiami, przyczynia się również do zmniejszenia emisji gazów odlotowych dzięki zoptymalizowanemu czasowi pracy.

Słowa kluczowe: *układ chłodzenia z odprowadzeniem skroplin, analiza drzewa błędów, niezawodność systemu, bezpieczeństwo systemu, monitorowanie stanu maszyn.*

1. Introduction

1.1. Overview

In case of 100 MW and above size generators, air cooling system (ACS) is found ineffective because of the amount of power cannibalized by the ACS. It also becomes more inefficient when the condensation section of the power plants appears at Heat Recovery Steam Generator (HRSG) section. It is vital to incorporate such a complex process with some supervisory system. In recent past, Biswal et al. presented schemes for the optimal cooling of electrical generators, that is, Level – II (control level) only by improving the reliability at systems' level [3], [4] [8], [15], [16]. However, they did not consider the condensate section in their work, which attains the maximum heat loss around 40% of the total generation capacity of the plant. Biswal et al. done a considerable amount of work on cooling of electrical generators through hydrogen. However, they did not count the condensate section in their introduced schemes [3], [4].

To study the effectiveness of Cooling-cum-Condensate-Extraction System (CCES), the cooling section, the portion of feed-water control section and the condensation sections are clubbed together. The presented model meets the requirements of Level – II (Control level) and the Level – III (that is Supervisory level) of the Supervisory Control And Data Acquisition (SCADA) system. Condensate section is the most inefficient section of any combined cycle power plants.

In recent time, role of integration is also increasingly critical to deal with the complexity involved in power systems after entertaining both conventional and sustainable sources of energy [7].

1.2. State-of-the-art

Unlike the office environment, power generation and energy management components are expected to handle ruthless situations come across because of surrounding atmosphere and the complexity involved in the process. Even chances of 0.1% failure cause a serious loss, irrespective of significant improvement noticed in component reliability. Emphasis on uninterrupted operation is equally applicable both at system level and considering component(s) of plant as an individual unit. Thus, redundancy is always taken into account as far as any industry applications are concerned [5], [11], [14– 16]. As, there is considerable amount of stress on power stations for generating electricity with unity power factor, and also, its uninterrupted and cost-effective supply to the end-users. System safety is a vital factor in process design and modeling. In the same line, a controller area network based an adaptive fault diagnosis algorithm was discussed by Kelkar and Kamal [12]. Fault Tree Analysis (FTA) is a widely used reliability assessment tool for large and complex engineering systems [13].

Surface condensers followed by the large size electrical generators are the vital components of an Integrated Gasification Combined Cycle (IGCC) power plant. This portion of the closed-loop cycle has experienced the maximum heat to work loss of the Rankine Cycle,

which is almost 40% of the total thermal efficiency [6]. Biswal et al. proposed a complete analysis over the reliability aspect of system design for industry applications (power generation area). In their paper, the application area was considered for the cooling of large electrical generators through hydrogen cum water [2], [5]. A condensate heat exchanger is provided for recovering heat from condensate draining from a condensate boiler [9]. Condensate generated from latent water vapor must be collected and discarded to avoid any damage to the heating /cooling unit, and to prevent this contaminant from surrounding environment [6]. Fujita and Machii proposed a condenser design, which includes a plurality of cooling pipes and supporting plates to take care the downstream of condenser [10]. For many years, process C&I was considered as an art rather than science. In recent years, some integrated solutions have been evolved dedicated for optimal operations of the various components power systems using real-time platforms [1]. Objectives of this manuscript are:

To propose a model to improve the efficiency of CCES by enhancing the gain of the model.

To enhance the design of discussed model from system reliability point of view.

2. System specifications of the CCES

This section highlights the role of critical sub-sections of the generating section and the condensate section of the IGCC plants, and their parameters, viz., the C&I; process / physical parameters, WCT (water cooling tower), Cooling Section, and the Condensate Section. Here, both the sections are interfaced through a novel designed close-loop cycle. Suitable transducers, control valves, switches, communication links, a master PLC and the HMI are the integral part of the presented design for the different measurements.

The Control and Instrumentation (C&I) take care of supplying low pressure (LP) and high pressure (HP) water channelized through water cooling tower (WCT); pressurized hydrogen to generating sections of the plant, and actuations of different valves at both the cooling section and condensation section. Further, each input-output (I/O) signal is assigned a unique card and slot number to identify its job by PLC. The database is a must for on-line control, virtual monitoring, and prediction of the system. Descriptions of some of the tags which are governed by PLC of the CCES are summarized in Fig. 1. Performance of the overall power generation can be optimized by ensuring levels and pressures of hydrogen at cooling section, the level of vacuum and pressure inside the condensate section, and the water concentration at WCT.
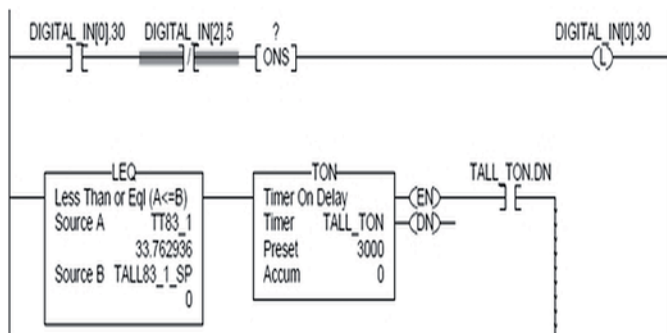

Fig. 1. A segment of ladder-logic program of the CCES

Number of indicators and transmitters are mounted in the design at different location of the CCES for the local monitoring and / or pre-processing of data and further communicating to master controller unit through a balance type communication link. As depicted in Fig. 1, different sub-groups are T, P, F (Temperature, Pressure, and Flow) and L, T (Level, Temperature) across the surface condenser

and at both inlet and outlet respectively. Similarly, other set of indicators and transmitters namely, F, T (Flow and Temperature) and only T (Temperature) are mounted at WCT site.

- Process Parameters: The differential pressure method, which is used to measure the parameters pressure, level and flow rate through vessels are governed by $\Delta P = \rho g h \ (\because \Delta P = P_b - P_a)$. Where, ΔP is the differential pressure in *pascal* (Pa); ρ is the density of fluid / gas (in kg / m^3) at the respective section; g is the gravitational force in N / m^2, and h is the vertical height of the chamber in *meters*. Thus, the same scheme can be used for the measurement of two physical quantities viz. inside chamber pressure and the volume of fluid at WCT, hydrogen at cooling section, and vacuum at condensate section respectively, which resultant to be simple and cost-effective. Fluid storage limits such as volume limits, starting and stop volumes are governed as per industry standard and practices. Where, the temperature of the module is directed by $\Delta T_{range} = \{Q_{out} / w_{cool} - C_{Pcool}\} = T_{in} - T_{out}$ [1], [3], [5].

- Cooling and Condensate Sections: With the increasing size of generating plants, more attention is given on the design of the exhaust of the machine / section. Proper safety measures are taken in account to avoid the chances of explosion because of hydrogen leakage as per industry standards. The standard sensors are used for the measurement of respective physical parameter are as follows:

i   Temperature: $\pm 1^o C$ .Pressure: $\pm 5\%$ in mercury (Hg) manometer tube.

ii   Relative humidity: 5% and 0% at the maximum and the minimum threshold.

iii   Vibration tolerance band: $\pm 30\%$ to any random input.

3. Methodology of the CCES

Two decision making points and three other check points are assigned for the execution of the control philosophy of the presented model. The entire integrated system is handled by two lever positions viz., the cooling section and the condensate section. Loops are strategically directed to meet the requirements of HRSG (heat recovery steam generator) section of the captive plant. The line of actions is well depicted in Fig. 2. Further, need and effectiveness of all the check points / assessment points are selected, and assigned their roles. Role of all the decision making and the check points are as follows:

- *Mixer*: injection of hydrogen in cooling section at desired pressure, circulation of fluid to maintain the temperatures of cooling, generator, and condensate sections are taken care.
- *WCT*: (water cooling tower) is responsible for using waste heat, and recycle it through the close-loop cycle (HRSG section) of the power station.
- *CWP*: (cooling water pump) has a major role in injecting treated water to both the cooling section and the condensate section using 3-way plug valve.
- *Plug* valve: this valve bifurcate the low pressure (LP) and the high pressure (HP) line of circulating fluid flow at cooling section and condensate extraction section, respectively.
- *Condensate*: at this stage, the fluid is circulated inside the matrix of shell through the pipes to retain the optimal temperature, flow and desired pressure inside the chamber.
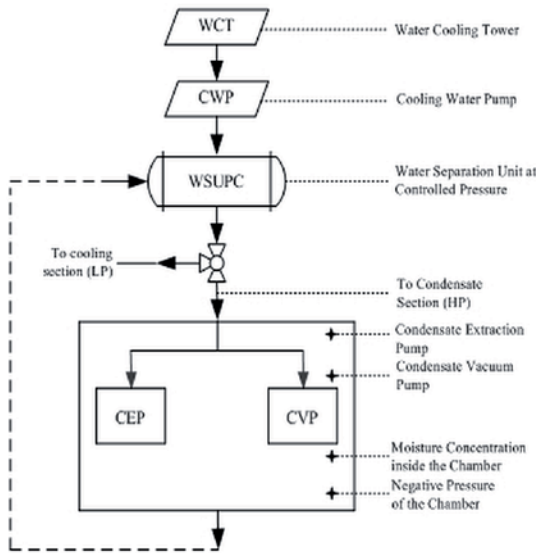
Fig. 2. The control philosophy of the proposed CCES

4. System reliability and failure modeling

Prediction of system's reliability is very much essential as the system (in this paper, CCES) is a collection of different components, assembly lines, and married of close-loop control in a specific pattern in order to identify the desired mathematical model with utmost efficiency and reliability. It is observed from industry standard and practices, fault avoidance methods [5], [13] are overall expansive because of increasing costs (both commissioning and operation costs) versus the linear improvement in reliable life of the system. For the first time, the three parameter Weibull distribution function is used for evaluating the effectiveness of the C&I model at the supervisory level of the SCADA system. This mathematical model is also considered the location of the fault if it occurs. All the symbols referred in Eq. (1) and (2) have standard nomenclatures:

$$\Re(T) = e^{-(T-\gamma/\eta)^{\beta}} \ for \ \lambda(t) \geq 0, T \geq 0, and \ T \geq \gamma \\ or \ \gamma, \beta, > 0, \eta > 0, -\infty < \gamma < \infty. \tag{1}$$

$$\Re_s(t) = \sum_{i=0}^{k} \{\int_0^t \lambda(t)dt\}^i e^{-\int_0^t \lambda(t)dt} (i!)^{-1} = \sum_{i=0}^{k} \frac{(\lambda \cdot t)^i e^{-\lambda t}}{i!} \tag{2}$$

For CCES (Cooling-cum-Condensate Extraction System), Water Separation Unit at Controlled Pressure (WSUPC), 3-way Valve, WCT, CWP, CEP, CVP, the cumulative distribution function for the removal of random variable selected is the three-parameter Weibull distribution, given by:

$$\lambda(t) = (\beta/\eta) \cdot (T - \gamma/\eta)^{\beta-1} \ for \ T \geq \gamma \\ and \ \lambda(t, \beta, \gamma, \lambda) = 0 \ for \ T < \gamma \tag{3}$$

$$\therefore f(t) = 1 - e^{-(T-\gamma/\eta)^{\beta}} \tag{4}$$

It is also noted that after burn-in period T_o, considering $\gamma = 0, T_o = 200$ days, if $t = 100$ days that is, taking the double of the operation duration. For, fixed β, η changes as the mean (MTTF/MTBF), the median, and the mode (modal life), and standard devia-

tion, all models / systems are different as is different for all. η, considers a maximum operation hour is equal to 365 days.

$$\Re\left(\frac{t}{T_o}\right) = e^{-(t+T_o/\eta)^{\beta} + (T_o/\eta)^{\beta}} \ for \ \lambda(t) \geq 0, T \geq 0, and \ T \geq \gamma. \tag{5}$$

The reliability factors of the different components are categorized into following sections: (i) reliability factors of converters, reservoirs R_{TX}, R_{TY}, R_{iv}, R_v, and R_{ov} (ii) reliability factors of all the heat exchangers $R_{HEx/z/1A...5B}$, (iii) reliability factor of insulated chamber and vacuum lines R_C or R_S. In terms of system reliability, equivalent models of all the methods discussed in section 4.1– 4.4 are worked out as per specifications of IEEE 1413-2010. From Section 3 and onwards, the method anticipated in this paper (Active CCES) is represented by $S4$, while $S1$ represents Farrell and Billett scheme [9], $S2$ represents Currier system [6], and $S3$ represented Fujita and Machii model [10].

4.1. Scheme of Farrell and Billett

Authors introduced a scheme of utilizing heat flow between condensate section and boiler section. It has a typical matrix (2x6) of the devices inside the heat exchanger which may be placed in the boiler flue gas flow bath. The system model is given by (6):

$$S1 = \Re_{FB}(t) = R_{iv} * R_{TX} * R_{TY} * R_{ov} \\ \because R_{TX} = R_{HEx} \| R_{ov}, 1 \leq x \tag{6}$$

4.2. System of Currier

Currier introduced a condensate pump that provides an efficient expel system for the exit of warm air from the surrounding of a pump-motor. The pump has married of a motor-driven fan, an enclose (cover), and an opening which allow air flow. The system is expressed by (7):

$$S2 = \Re_C(t) = R_{HEx} * R_v * R_{HEz} \ for \ 1 \leq x, z \leq 1 \tag{7}$$

4.3. Fujita and Machii model

Fujita and Machii proposed a condenser which includes plurality of cooling pipes, and further cooling water used for exchange of heat with steam flows. Overall, the model is dedicated to improve the condensate performance. The reliability model is expressed as:

$$S3 = \Re_{FM}(t) = R_{TX} * R_{HEx} * R_\gamma * R_v * R_{HEz} \\ \because R_\gamma = R_{HEx} \| R_{HEy}, 1 \leq x, y \leq 2 \\ \Rightarrow S3 = \Re_{FM}(t) = R_{HEx} * R_{SI} * R_v * R_{HEz} \tag{8}$$

4.4. Proposed method: Active-CCES

The proposed model presents an Active – CCES, which is reliable and cost-effective for the plant capacity of 36-MW generation units. Here, typical hazard rate of $s - out - of - t$ is considered for designing the CCES based on steps shown in (9) and (10):

$$R_Y = R_{HE1A} \| R_{HE1B}, \; R_Z = R_{HE2A} \| R_{HE2B}, \therefore R_Y = R_Z$$
$$\Rightarrow R_S = R_{TB} * R_Y = R_Z = R_O, \because R_O = R_{HE3A} \| R_{HE3B};$$
$$R_\beta = R_{HE4A} \| R_{HE4B} = R_\gamma; \; \Re_{S^3RS}(t) = R_X * R_\alpha * R_\beta * R_\gamma \quad (9)$$

$$\therefore S4 = \Re_{S^3RS} * (R_m \| R_{SC'}), \because R_{SC'} = R_{SC} * (R_a \| R_b) \quad (10)$$

$R_{SC'}$, R_{S^3RS}, and R_m are connected serially in forward direction. Fig. 3a-3b and Table 1, shows proportion perfection of $S4$ versus the system reliability of $S1$, $S2$, and $S3$. Respective data are also highlighted in Table 1, which shows performance of presented system, $S4$ as against the existing models.
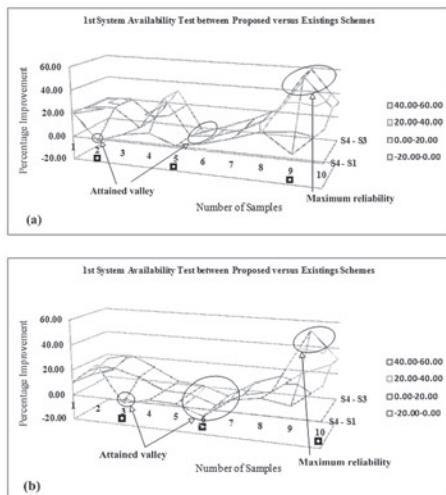

Fig. 3. System availability analysis between of proposed model, S4 as against existing schemes S1, S2, and S3

Table 1. System Availability: Proposed Method (S4) as against systems S1, S2, and S3

System's Availability in Run–mode					
$R_S(t)$ of Test I (Proposed – Existing)			$R_S(t)$ of Test II (Proposed – Existing)		
S4–S1	S4–S2	S4–S3	S4–S1	S4–S2	S4–S3
21.65	18.99	19.00	9.92	8.68	16.00
−1.17	19.41	21.28	25.89	16.32	21.29
6.44	3.97	3.97	−2.14	10.71	12.27
9.85	31.85	31.85	2.45	1.99	1.79
1.33	1.06	−3.52	1.56	1.51	0.79
5.80	3.78	3.78	−5.80	−5.58	−6.18
12.48	11.74	12.37	9.32	4.87	6.59
20.43	23.72	24.05	12.70	9.62	14.17
4.55	59.05	59.05	9.17	25.05	52.60
26.92	34.93	32.33	26.12	34.13	31.53

4.5. System Failure Mode: Active-CCES

The system failure mode is presented the reverse philosophy of the analysis addressed in sub-section IV A–D that is, called the 'chances of survival' of active-CCES (sub-section 4.4) than that of all the schemes (sub-section 4.1 – 4.3):

$$\therefore F(t) = F_{CS} + F_{SHXE} + F_{3-wV} = F4$$
$$= F_{S^3RS} + (F_m * F_{SC'}) - (F_{S^3RS} * F_m * F_{SC'})$$
$$\because F_{SC'} = F_{SC} + (F_a * F_b) - (F_{SC} * F_a * F_b)$$
$$F_{SHXE} = F_q + F_{CEP} - (F_r * F_{CEP}) = F_r \quad (11)$$

$$\because F_q = F_p + F_{CVP} - (F_p * F_{CVP})$$
$$\because F_p = F_{BV} + F_{OOV} - (F_{BV} * F_{OOV})$$
$$F_s(t)_{OR} = F_s(t)_+ = F_1 + F_2 - (F_1 * F_2)$$
$$F_s(t)_{AND} = F_s(t)_* = F_1 * F_2 \quad (12)$$

Eqs. (11) – (12) have formulated the mathematical statements of the 'chances of survival of $F4 = 1 - S4$ as compared to $F1, F2$, and $F3$. As shown in Fig. 4, the proposed CCES only fails if the cooling section, surface condenser, and 3-way valve section fail collectively which is the combination of ten source points.

Thus, the chances of survival of active – CCES, that is of $S4$ is very high as compared to existing schemes as the statistics framed in Table 1 and Table 2. Further analysis and discussions of this section is done in Section 5.2 based on Fig. 3, Fig. 4, Table 1, and Table 2.

Table 2. System Failure: (S4) as against systems S1, S2, and S3

| System's Failure in Run-mode (= 1– Availability)					
$F_S(t)$ of Test III (Proposed – Existing)			$F_S(t)$ of Test IV (Proposed – Existing)		
F1–F4	F2–F4	F3–F4	F1–F4	F2–F4	F3–F4
78.35	81.01	81.00	87.01	89.36	84.29
71.17	80.59	78.72	98.98	102.90	101.07
93.56	96.03	96.03	101.46	85.18	78.62
90.15	68.15	68.15	76.96	76.00	74.82
98.67	94.94	83.52	88.97	92.39	88.75
94.20	96.22	96.22	96.28	93.80	93.80
87.52	88.26	87.63	95.49	97.38	97.38
79.57	76.28	75.95	95.83	96.17	96.14
125.45	70.95	70.95	81.62	86.29	85.89
73.98	65.97	65.97	73.98	65.97	67.68
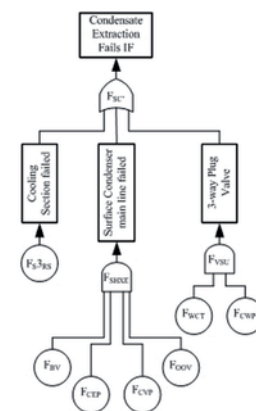
Fig. 4. Static fault tree analysis of the proposed CCES model.

5. Results and Discussions

5.1. Virtual platform of the CCES

Fig. 5 (a)-and-(b) depicts PLC based the project tree of the proposed CCES, and the network view which is used to link the PLC with the HMI of the system. The HMI is the virtual base from where the performance and operation of the entire system (CCES) is continuously observed in real-time. It acts as a virtual plant. Real-time observations of the different parameters of the plant/ process are vital to implement an efficient and reliable system.
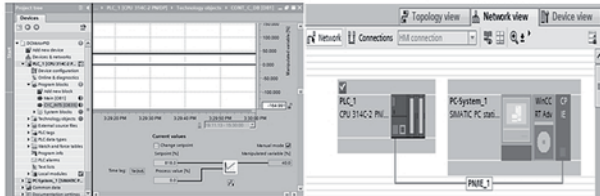

Fig. 5. (a) PLC project tree module of the CCES. (b) Communication interface of the PLC with the HMI

As shown in Fig. 5(b), the network view of the CCES is implemented using wireless HART (IEEE 802.15.4) based protocol which is highly reliable for industrial / robust environment applications. At the same time, cost-effective network/ communication interface is established because of multi-drop configuration. All the sensors/ actuators are mounted over the filed are treated as slaves (RTUs) while the controller is hold the master position. Since there are multiple buses are lying on the same line, only digital communication mode (Bell – 202, FSK standard) is referred for increased reliability. Bell – 202 is referred to interface all the RTUs with controller, and enabling the bidirectional flow of data.

The presented system is also facilitated the trend and the diagnosis modules. These modules are easy the jobs of 'operation and health monitoring of section(s) in real-time', and the diagnosis of any unhealthy signature of a component in auto mode. Thus, the CCES is endowed with the facility of 'bump-less restart', which enable to switch the system (CCES) from manual-to-auto mode and vice –versa without any delay. The model presented in Fig. 5 satisfies the specifications discussed in Section 2.

Fig. 6(a)-and-(b) shows the elements of the programming of the controller (PLC) of the system. Snaps depicted in Fig. 6(a) are in edit-mode, which is ultimately the brain of the system. Further, the activation of the PID (one of the sub-controller of the PLC) followed by the threshold limit of the process variables are depicted in Fig. 6(b). Algorithm is developed to interface the field sensors, the controller (PLC), and the HMI through a balanced type communication link. Aforementioned features of the designed
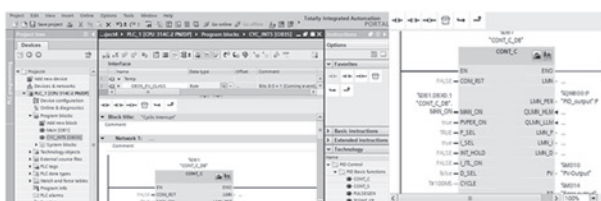

Fig. 6. (a) PLC's Ladder Logic Rungs in Edit Mode. (b) Snap-shot of the Ladder Logic design of the CCES

platform helps to realize an integrated automation platform which improves the availability of the CCES (the last sections of CCPPs and the first close-loop component of the HRSG) in operation mode as against the existing schemes. Further sub-sections 5.2 is demonstrated the performance of the CCES (S4) in terms of performance supervision and the system reliability / availability of the process.

5.2. System availability and failure of the S4

As shown in Fig. 3(a)-(b) and Table 1, two different tests have been conducted viz., Test I and Test II. Observations are segregated into three domains in terms of the worst case, healthy case/ status, and the optimal availability. Different test events are used to analyze the performances of all the schemes, existing and the proposed one in terms of the worst case (the minimum reliability), healthy state (the average reliability), and the best-fit case (that is optimal availability). Respective data of both the test are fetched in Table 1. The abscissa represents different events / samples collected at different instant of time, varies from the minimum to the verge of the reliability of the individual components. Here, first row of Table 1 indicates the numbers of samples are collected. The second column of the second row shows Test 1, which indicates the performance of S4 versus the existing systems, S1, S2, and S3 in terms of system reliability $R_s(t)$. Similarly, data of Test II is referred from the fourth, fifth and the sixth lines of the row respectively. It is recognized clearly that for the most of the events S4 is performed superior than that of S1, S2, and S3.

As depicted in Fig. 3 and Table 1, at the best fit conditions, S4 has performed 64.6%, 62.12%, and 61.83% enhancement in availability in operation/ active mode as against of S1, S2, and S3 respectively. On the other hand, at the worst –fit conditions S4 has attained negative growth from 0.4% to 25.45%. This is experienced by S4 because of the level of complexity and the higher level of integration involved with the system. Therefore, at the healthy state (average performance), it is observed that S4 has shown 22.51% and 26.02% improvement as compared to S1, while S4 has reflected 34.03% average improvement than that of S2 and S3. Generally, it occurs due to same type of components shared in the P&I (Piping and Instrumentation) diagram of the model. It is also
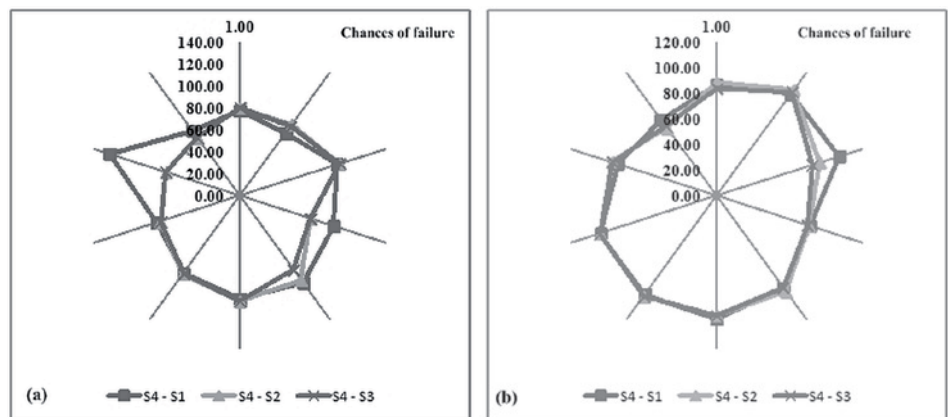

Fig. 7. (a)- (b). System safety analysis of CCES as against the available schemes.

analyzed that the S4 has the least chances of failures versus the existing systems because of increased amount of availability.

A quantitative analysis is conducted based on Fig. 2 to identify the strength of the proposed design in terms of fault tree analysis (FTA). FTA is considered to be a top-down approach by which each level of fault is expanded to its input from the down. In order to guarantee the reliability of the proposed design (CCES), probability of safety is also evaluated, and the results are depicted in Table 2 and Fig. 7(a)-and-(b).

At this stage, two different sample tests, Test III and Test IV are conducted to judge the effectiveness of CCES. It is noticed that the chances of failure of F4 (1 − S4) has been drop-down from 65.97% to 98.98% as compared to F1 (1 − S1), F2 (1 − S2), and F3 (1 − S3). Data are having more than 100% values are the indices of complexity of the CCES (S4) in contrast to the design of S1, S2, and S3. In some odd cases as reflected from Table 2 and Fig. 7, S4 is reported inferior by more than 1% to 25% than the counterparts. In contrast, the overall availability of S4 is measured in between 26% to 32%. Therefore, it can be recapitulated that the CCES model proves advantage over all others in terms of system reliability.

6. Conclusion

The model CCES is designed and analyzed for the optimal performance of the sizes of 36-MW generation capacity, particularly for the married of cooling cum condensate extraction sections of the power stations. The CCES has publicized (25.89% to 59.05%) significant enhancement not only in terms of the availability but also in terms of system safety (that is, the least chance of failure) of the system in active mode. Active mode is the reflection of the increased electrical gain of the system. S4 has been attained the maximum amount of availability, and framed the highest degree of the safety module. Thus, from the bidirectional analysis, it can be establish that proposed CCES model is on upper hand side than that of all the counterparts. This improved model (CCES) is finally implemented by injecting a methodology for the optimization of a dedicated size process (surface condensation). Process supervision model is designed for the captive power plant to meet the requirement of specific environment in real-time.

References

1. Alvarez E G, Stothert A, Antoine M, Morton S. Optimal operation of a power plant. US Patent 7,426,456 B2 2008.
2. Arnold J J, Capener J R. Modern power station practice. Pergamon Press, Elsevier, 3rd e. incur. Modern Power System Practice, Turbine, Generators and Associated Plant, British Elect. Int., London 2008; (3).
3. Biswal G R, Dewal M L, Maheshwari R P. A novel scheme for cooling of large generators using hydrogen cooling systems. IEEE 8th Int. Colloquium on Signal Processing & Its Applications, Malacca, Malaysia, 2012; 105 - 109.
4. Biswal G R, Dewal M L, Maheshwari R P. Process control and instrumentation of SeSWRS based hydrogen cooling system of a thermal power station: a 2x660 MW unit. Int. Conf. on Energy, Automation and Signal, Bhubaneswar, India, 2011.
5. Biswal G R, Maheshwari R P, Dewal M L. System reliability and fault tree analysis of SeSHRS based augmentation of hydrogen: dedicated for combined cycle power plants. IEEE Systems Journal 2012; 6(4), 647-656, http://dx.doi.org/10.1109/JSYST.2012.2192065.
6. Currier J. Condensate pump. US Patent 2009/0226329 A1 2009.
7. Erdener B C, Pambour K A, Lavin R B, Dengiz B. An integrated simulation model for analyzing electricity and gas systems. Electrical Power and Energy Systems 2014; 61, 410- 420, http://dx.doi.org/10.1016/j.ijepes.2014.03.052.
8. Fan J, Zhang Y, Zheng Z. Observer-based reliable stabilization of uncertain linear systems subject to actuator faults, saturation, and bounded system disturbances. ISA Transactions 2013; 52, 730- 737, http://dx.doi.org/10.1016/j.isatra.2013.06.007.
9. Farrell C C, Billett R A. Condensate heat exchanger. US Patent 2009/0226329 A1 2009.
10. Fujita, Machii K. Condenser. US Patent 2010/0065253 A1 2010.
11. Grigg et al. The IEEE reliability test system – 1996: A report prepared by the reliability test system task force for the application of probability methods subcommittee. IEEE Trans. Power Syst. 1999; 14(3), 1010- 1015, http://dx.doi.org/10.1109/59.780914.
12. Kelkar S, Kamal R. Adaptive fault diagnosis algorithm for controller area network. IEEE Trans. Indus. Elect. 2014; 61(10), 5527- 5537, http://dx.doi.org/10.1109/TIE.2013.2297296.
13. Li Y, Huang H, Liu Y, Xiao N, Li H. A new fault tree analysis method: fuzzy dynamic fault tree analysis. Eksploatacja i Niezawodnosc - Maintenance and Reliability 2012; 14(3), 208- 214.
14. Michlin Y H, Grabarnik G Y, Leshchenko E. Comparison of the mean time between failures for two systems under short tests. IEEE Trans. Relia. 2009; 58(4), 589- 596, http://dx.doi.org/10.1109/TR.2009.2020102.
15. Peng W, Huang H, Zhang X, Liu Y, Li Y. Reliability based optimal preventive maintenance of series-parallel systems. Eksploatacja i Niezawodnosc - Maintenance and Reliability 2009; 59(1), 04-07.
16. van Gemund J C, Reijns G L. Systems with single cold standby using pearson distributions. IEEE Trans. Relia. 2012; 61(2), 526- 532, http://dx.doi.org/10.1109/TR.2012.2192587.

Gyan Ranjan BISWAL
Department of Electrical and Instrumentation Engineering
Thapar University,
Patiala - 147004, India
E-mail: gyan.biswal@thapar.edu; gyanbiswal@gmail.com

Wojciech STACHURSKI
Stanisław MIDERA
Bogdan KRUSZYŃSKI

MATHEMATICAL MODEL DESCRIBING THE COURSE OF THE PROCESS OF WEAR OF A HOB CUTTER FOR VARIOUS METHODS OF CUTTING FLUID SUPPLY

MODEL MATEMATYCZNY OPISUJĄCY PRZEBIEG ZUŻYCIA FREZU ŚLIMAKOWEGO DLA RÓŻNYCH METOD PODAWANIA CIECZY OBRÓBKOWEJ*

In the paper the method of determining the mathematical relationship for calculating the flank wear VB_c of the most worn hob tooth is discussed. The relationship, in the form of a multiple regression function, was determined based on the acceptance and rejection method. The data for the calculations was obtained from experiments carried out for hobbing of carbon steel C45 with the use of a cutting fluid supplied in flood mode (WM) and with a minimum quantity lubrication mode (MQL). Based on the developed equations the impact of the selected machining parameters the course of the hob wear was assessed. In the final part of the paper, the obtained mathematical relationships were analysed and verified.

Keywords: *hobbing, hob, wear, cutting fluid, MQL.*

W artykule omówiono metodę wyznaczania zależności matematycznej do obliczania wielkości starcia VB_c najbardziej zużytego ostrza frezu ślimakowego. Zależność w postaci funkcji regresji wielorakiej wyznaczono metodą dołączania i odrzucania. Dane do obliczeń uzyskano przeprowadzając badania eksperymentalne frezowania stali węglowej C45 z udziałem cieczy obróbkowej podawanej w trybie obfitym oraz z minimalnym wydatkiem (MQL). W oparciu o wyznaczone równania dokonano oceny wpływu wybranych warunków obróbki na przebieg zużycia frezów ślimakowych. W końcowej części artykułu dokonano analizy uzyskanych zależności matematycznych oraz przeprowadzono ich weryfikację.

Słowa kluczowe: *frezowanie obwiedniowe, frez ślimakowy, zużycie, ciecz obróbkowa, MQL.*

1. Introduction

The gears machining, with the application of a cutting fluid supplied with a minimum flow rates (MQL - Minimum Quantity Lubrication) is a technology still under development. However, in industrial applications, it is still a novelty. This concerns, among other manufacturing processes, hobbing which is the most popular method of machining gears. In this method, the allowance is removed by many cutting teeth distributed on the hob circumference. In the gear hobbing, cutting teeth are unevenly loaded and this results in uneven wear distribution on particular hob teeth. Out of the total number of hob teeth, only a part of them remove work material, and only few of them present maximum wear land [3]. In practice, when tool wear reach critical values even at one hob tooth the hob is regarded as dull.

The available literature concerned the hobbing process shows that the impact of the application of the MQL method on the effectiveness of this process has not been investigated yet or it concerns a limited scope only [5]. In the research described in the literature [16, 17] it was shown that the use of this method in some circumstances enables to obtain the results comparable to the conventional method of the cutting fluid supply and much better than those obtained for "dry machining". However, the results and conclusions drawn from those studies could be misleading because research was carried out for a single-tooth tool (the so-called "fly tool") instead hobbing.

The basis for assessing the effectiveness of various methods of the cutting fluid supply are the courses of the tool wear in the entire hob tool life. Therefore, the effectiveness of lubrication and/or cooling in the MQL method can be determined by comparing the courses of hob wear with those obtained for hobbing with flood supply of cutting fluid (WM - Wet Machining).

It should be taken into consideration, that the tool being worn is the weakest item in machining systems. Therefore, the possibility to predict the tool wear rates in various cutting conditions is of particular importance, especially to minimize the cost- and time-consuming durability investigations. In order to predict tool wear, appropriate mathematical procedures can be used, e.g. the method of trend analysis [8], artificial neural networks [9], fuzzy logic modelling based on the TSK structure [10], or the model of a second degree equation that predicts the durability of the hob by using the surface response method [13].

In various research centres, investigations on the hob teeth wear process were undertaken. In the study [6] a method to determine the variable load of the active cutting edges was proposed, by application of a tool in the form of a rack (flute hobbing), which is the progress in relation to the method of using a single-tooth tool [3]. In [7] it was indicated that for tools with TiN coating, application of the MQL method causes less intensive tool wear rates when compared with those obtained for uncoated tools. Another problem undertaken in the study [18] is to determine the cutting edge condition's impact on the wear rate during hobbing without any cutting fluid (DM - Dry Machining). As part of the research studies [2, 4] the mathematical description of the hob wear changes was also proposed. In those studies the mathematical description is based mainly on the analysis of the load variations on the active cutting edges during machining, resulting from the

variable chip cross-section areas in different angular positions of the hob in relation to the gear being machined.

In the paper, the method to determine the mathematical relationship for the calculation of the flank wear land width *VB* of the most worn hob tooth is discussed. The data necessary to evaluate equation parameters was obtained from experimental investigations. The relationship, in the form of the multiple regression function, were determined by means of the acceptance and rejection method algorithm. Then, based on power polynomial equations, the impact of the selected machining conditions (cutting speed, feed, the cutting fluid supply method) on the courses of the hob wear rates as well as on cutting forces was assessed.

2. Experiments

The aim of the experimental investigations was to collect data concerning the hob wear rates and the cutting forces in gear hobbing:

– with the supply of cutting fluid in a flood mode (WM)
– with the minimum quantity lubrication mode (MQL).

In the investigations, various machining parameters were applied (cutting speed, feed), and the values VB_c were measured (no vital wear was observed on the rake face) as well as the corresponding cutting forces F_c. Those data were selected just because they have a considerable impact on the tool wear process. The previous investigations of the gear hobbing, e.g. [11], proved that among all the cutting parameters the cutting speed v_c has the greatest impact on tool wear. The main reason for that is that cutting speed determines, to the greatest extent, the cutting temperature. This was confirmed by other researchers, e.g. [1]. On the other hand, the cutting force can be used as an indirect measure of hob wear magnitude. This is because the wear of hob leads, during the machining process, to the change of the cutting conditions, which in turn leads to an increase of cutting forces. Also deterioration of the quality of the workpiece being machined can be observed.

2.1. Durability tests

Durability tests were carried out for hobbing of spur gears made of carbon steel C45 (20±2 HRC). The blanks to machine gears had an outer diameter of d=72 mm and a width of b=15 mm. Using the ZFC-20 hobbing machine involute teeth of module m=3 mm, pressure angle $α$=20°, and tooth inclination angle $β$=0°, were cut. The NMFc-3/20°/B gear-cutting hobs made of high-speed steel HS6-5-2 without any coatings were used. The cutting fluid Ferokol EP machine oil was applied for wet machining with a flow rate of about 10 l/h. For MQL the MKS-G100 device was applied with an external single-channel generation of oil mist with flow rate of 15 ml/h. The investigations were carried out for different cutting parameters (Table 1) with a constant hobbing path L=400 mm.

The gears being machined were fastened on a specially designed mandrel intended for fixing a single-component piezoelectric dynamometer KISTLER, type 9321B, enabling the cutting force F_c to be measured. The measuring signal from the dynamometer was directed to the single-channel laboratory amplifier KISTLER, type 5011B, and converted into a voltage signal. Next, the signal from the amplifier

Table 1. Cutting parameters.

Cutting parameters		
cutting speed v_c [m/min]	feed f [mm/rev]	depth of cut a_p [mm]
34,4 44,2 54,0 69,9	0,50 1,25	6,6

was sent to the measuring card KEITHLEY, type KPCMCIA–12AI–C installed in the computer. The software for the recording the measurement data was developed in the Institute of Machine Tools and Production Engineering of the Lodz University of Technology and described in details in [20].

In Fig. 1 an example of the graph of the cutting force course obtained during the gear hobbing was presented. It can be seen that due to the variable number of the hob teeth cutting simultaneously during one hob revolution the total chip cross-section varies. This affects, in turn, the cutting force magnitude.
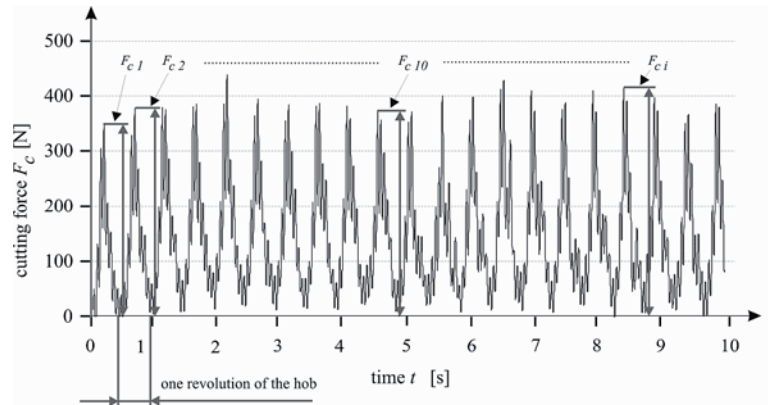

Fig. 1. Example of cutting force vs. time relationship.

The 10 seconds duration of the measurement cutting forces was set. At that time the hob was running at about 20 revolutions. As the result of particular test as a cutting force measurement result, the average value of the maximum cutting forces peaks $F_{c“i”}$ (where "i" is the successive number of the hob cutter revolution) observed for each revolution of the hob was taken.

An optical microscope was used to measure the hob teeth wear lands. The wear of the hob teeth was observed on the flank surfaces as a wear lands unevenly distributed along cutting edges. The highest value of the wear land width VB_{c-in} was observed in the vicinity of the tooth corner area on the side entering tooth space. This value, for the most worn tooth, was taken as a measure of hob wear during the analysis of the investigation results.

2.2. Determination of mathematical relationship

To determine the mathematical relationships for the calculation of tool wear, the original SKZ software was developed in the Institute of Machine Tools and Production Engineering of the Lodz University of Technology [14]. The SKZ software makes it possible to determine the coefficients of a multiple regression equation. The procedure for regression analysis was developed on the basis of the algorithm of the acceptance and rejection method described in the paper [15].

The procedure of the software application began with entering input data (v_c, f, F_c) from a text file prepared earlier, and selecting the form of the regression function (Y1 = B0 + Sum (Bi * Xi)). Since the durability tests were carried out for a constant depth of cut a_p, this parameter was not taken into consideration.

The selection of the critical statistics values (F_{kr}) is made on the significance level $α$=0,4, and after having the regression function determined it is changed into the value of $α$=0,1. The calculations began with the simplest regression function, and new elements are attached (accepted) successively. If a newly attached element lowers the significance of an element that has already been introduced, the irrelevant element is removed from the regression function. After having introduced all the relevant elements a preview panel with the calculation results is displayed. Finally, the function of the object investigated took on the form shown below:

$$VB_{c-in} = VB_0 \cdot v_c^{f_v} \cdot f^{f_f} F_c^{f_F} \text{ [mm]} \qquad (1)$$

where: v_c – [m/min]; f – [mm/rev]; F_c – [N].

The values of the coefficients and constants of this function determined on the basis of calculations are listed in Table 2.

Table 2. Values of constants and coefficients for experimental function

Constants and coefficients	
WM	MQL
$VB_0 = 9,98 \cdot 10^{-21}$ $f_v = -2,194$ $f_f = -0,633$ $f_F = 8,962$	$VB_0 = 2,15 \cdot 10^{-12}$ $f_v = -1,569$ $f_f = -0,604$ $f_F = 5,282$
Coefficient of multiple correlation R	
0,7502	0,7418

After entering the numerical values from Table 2 into the function of the object of investigation (1) the following equations were obtained:

– for the supply of cutting fluid in the flood mode (WM):

$$VB_{c-in} = 9,98 \cdot 10^{-21} \cdot v_c^{-2,194} \cdot f^{-0,633} \cdot F_c^{8,962} \text{ [N]} \qquad (2)$$

– the MQL method:

$$VB_{c-in} = 2,15 \cdot 10^{-12} \cdot v_c^{-1,569} \cdot f^{-0,604} \cdot F_c^{5,282} \text{ [N]}. \qquad (3)$$

3. Analysis of the relationships obtained

The significance of the coefficients obtained for the multiple correlation R were determined by means of the Fisher-Snedecor F test through the calculation of the F coefficient test values and comparing them with the critical values F_{kr}. Because the calculations showed the relation $F > F_{kr}$, the correlation coefficients should be regarded as relevant, and this means the conformity (at the significance level of $\alpha=0,1$) of the regression equation with the investigation's results [12].

The analysis of the constants and the exponents presented in Table 2 indicates that those values differ, depending on the cutting fluid supply method applied. This concerns both the VB_0 constants which generally define the wear rate level, and the exponents determining the impact of the individual machining conditions on the changes of the wear rate.

The highest differences were observed when comparing the f_F and f_v exponents for the MQL method with the exponents obtained for the WM mode. The values of the f_v exponents differ by almost 40 %, whereas the f_F exponents differs by 70 %. This indicates that with the cutting fluid supply in the flood mode (WM) the VB_{c-in} wear sensitivity for the v_c changes of cutting speed is much higher when compared to MQL. The same relationship concerns the cutting forces F_c that changes according to the hob wear magnitude.

For the f_f coefficients no significant differences in their values were observed (−0,633 and −0,604 respectively). This shows that the impact of the feed f on the wear rate is similar, regardless of the cutting fluid supply method. It is worth to point out that this situation could be caused by the fact that the longitudinal feed is a relevant parameter influencing the maximum value F_c of cutting force [19] and as such it is already considered in the f_F coefficient.

The illustration that presents the impact of the v_c and F parameters, dependent mostly on the cutting fluid supply method, on the hob wear VB_{c-in} is shown in Fig.3. The graphs are presented for the feed f=0,5 mm/rev. The graphs for the feed f=1,25 mm/rev are of a similar nature. The surfaces on the graph present the hob wear rate levels to be expected depending on variable cutting conditions.

As it results from Fig. 3 and the relationships (2) and (3) the application of higher cutting speed v_c leads to the conclusion that in any case when the assumed criterial wear VB_{c-kr} is achieved higher F_c cutting forces were observed. This is confirmed by the values listed in Table 3.

It should be noted that for the flood cutting fluid supply mode (WM) the increase in cutting speed (in particular to v_c=54 m/min and v_c=69,9 m/min) results in lower forces F_c occured in relation to that observed in the case of the MQL application. For the hob wear equal to 0,3 mm the difference between the cutting forces for lowest and highest cutting speeds is 64 N, whereas for the MQL method amounts to 80 N. Similarly, for the hob wear of 0,5 mm the difference between the cutting forces for the lowest and highest cutting speeds is 68 N, whereas for the MQL method amounts to 88 N. This confirms the previous observations concerning the higher wear sensitivity VB_{c-in} to the changes of the cutting speed v_c and the cutting force F_c for "wet cutting" (WM) when compared to the MQL method.

a)

b)

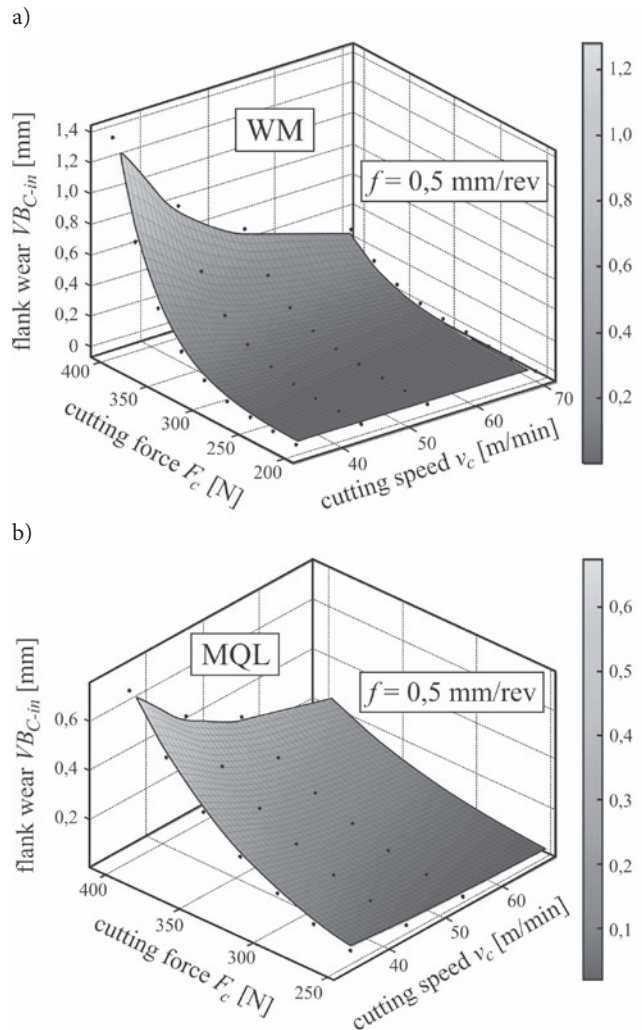Fig. 2. Influence of cutting force and cutting speed on hob's flank wear: a) WM, b) MQL; f=0,5 mm/rev

Table 3. *Cutting force values for the critical flank wear*

f [mm/rev]	VB_{c-kr} [mm]	v_c [m/min]	WM	MQL
			F_c [N]	
0,5	0,3	34,4	338	340
		44,4	359	367
		54,0	377	389
		69,9	402	420
	0,5	34,4	357	375
		44,4	380	404
		54,0	399	429
		69,9	425	463

4. Verification of the mathematical model

In spite of the satisfactory values of the multiple correlation co-efficients for the developed mathematical model its verification was also carried out consisting of a comparison of the measured wear values VB_{c-in} with the values calculated on the basis of this model.

In Fig. 4 the comparison of the calculated and measured wear values VB_{c-in} while hobbing gears with the cutting fluid supply in the flood mode (Fig. 4a) and the minimum quantity lubrication mode (Fig. 4b) is presented. The graphs were made for constant cutting parameters: v_c=69,9 m/min, f=0.5 mm/rev, a_p=6,6 mm.
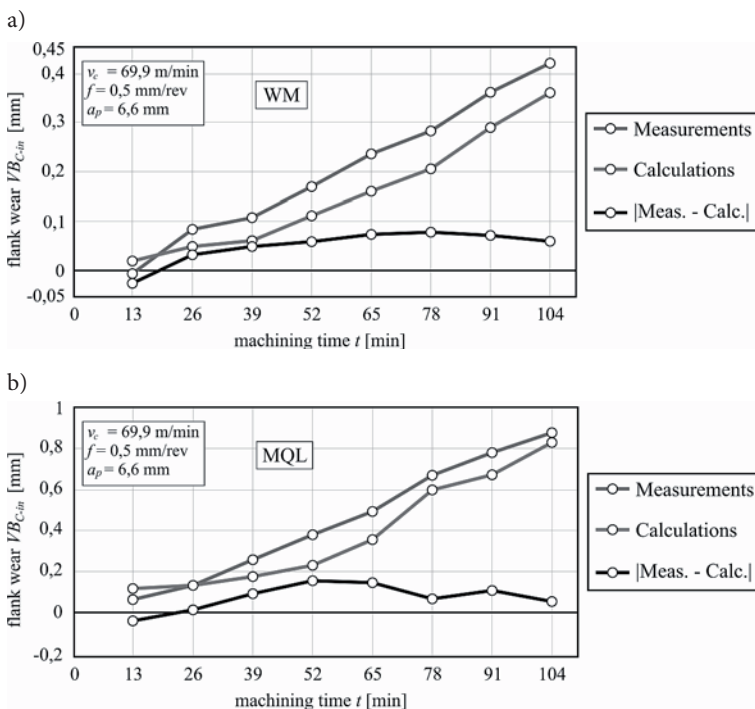
a)

b)

Fig. 3. *Comparison of calculated results to measured values of flank wear VB_{c-in}: a) WM, b) MQL; v_c=69,9 m/min, f=0,5 mm/rev, a_p=6,6 mm.*

The differences between the calculated and measured wear rates vary within the range from 0,03 mm up to 0,08 mm for the hobbing with the flood cutting fluid supply method (WM) and in the range from 0,02 up to 0,12 mm for the hobbing with the MQL method. It should be noted that for both methods the differences decrease as the machining time increases. For the WM method in the final stage of the diagram the difference amounts to 14 %, and for the MQL method it drops to 6 %. In both cases, the hob wear vs. time diagrams drawn on the basis of calculations run below the experimental ones.

Similar hob wear diagrams for both the measured as well as the calculated values were also obtained in other tests. This proves the correctness of the developed model.

5. Conclusions

The aim of this study was to evaluate the mathematical relationships enabling a prediction of the flank wear VB_c of the most worn out hobbing tooth. The possibility to predict tool wear is a relevant factor affecting the correct planning of the gear machining process when using the hobbing method. Based on an analysis of the obtained results the following conclusions have been drawn:

1. A mathematical model has been developed in the form of a multiple regression function which enabled a calculation of the VB_{c-in} wear rate for the most worn tooth.
2. The acceptance and rejection method used for working out the model is relatively easy to apply with the use of appropriate software.
3. With a continuous measurement of cutting forces, it is possible to monitor the state of hob wear during machining.
4. Experimental verification of the obtained relationships have proved their correctness for both cutting fluid supply methods (WM and MQL).
5. The model developed creates a good basis for the analysis of the hobbing gear process. Thanks to the determined mathematical relationships it is possible to avoid labor-, and time-consuming experimental studies.

Based on the work performed and the obtained results it should otherwise be noted that:

1. The analysis of the exponents determining the impact of machining conditions on the wear rate has shown that the cutting speed v_c and the cutting force F_c are the parameters most sensitive to the cutting fluid supply method (WM, MQL).
2. For the cutting fluid supply in the flood mode (WM) higher wear sensitivity to the cutting speed changes v_c occurs when compared with the MQL method. The same relationship concerns the cutting forces F accompanying the hob wear process.
3. The impact of the feed f on the wear rate does not depend on the cutting fluid supply method.
4. The application of the MQL method in in presented experiments was only possible as an external supply of cutting fluid to the cutting zone. It seems that the supply of oil mist directly to the cutting zone through the tool would improve cutting conditions and slow down the process of tool wear. This should be the objective of further works and experimental studies.

References

1. Azizpour Jalali M., Majd Mohammadi H. Wear mechanisms in high speed steel gear cutting tools. World Academy of Science, Engineering and Technology 2010; 4: 739-741.
2. Belis T., Antoniadis A. Hobbing wear prediction model based on 3D chips determination. Bulletin of the Polytechnic Institute of Iasi 2010; LXI(LX) 2: 9-20.

3.   Bouzakis K.-D., Kombogiannis S., Antoniadis A., Vidakis N. Gear hobbing cutting process simulation and tool wear prediction models. Journal of Manufacturing Science and Engineering 2001; 124(1): 42-51, http://dx.doi.org/10.1115/1.1430236.

4.   Bouzakis K.-D., Lili E., Michalidis N., Friderikos O. Manufacturing of cylindrical gears by generating cutting processes: A critical synthesis of analysis methods. CIRP Annals - Manufacturing Technology 2008; 57: 676-696, http://dx.doi.org/10.1016/j.cirp.2008.09.001.

5.   Byrne G., Dornfeld D., Denkena B. Advancing cutting technology. CIRP Annals - Manufacturing Technology 2003; 52/2: 483-507.

6.   Claudin C., Rech J. Development of a new rapid characterization method of hob's wear resistance in gear manufacturing-Application to the evaluation of various cutting edge preparations in high speed dry gear hobbing. Journal of Materials Processing Technology 2009; 209: 5152-5160, http://dx.doi.org/10.1016/j.jmatprotec.2009.02.014.

7.   Fratila D. Evaluation of near-dry machining effects on gear milling process efficiency. Journal of Cleaner Production 2009; 17: 839-845, http://dx.doi.org/10.1016/j.jclepro.2008.12.010.

8.   Gawlik J., Karbowski K. Matematyczne modelowanie procesu zużycia narzędzi skrawających-Nadzorowanie stanu narzędzi. Kraków: Politechnika Krakowska, Monografia 231, seria Mechanika, 1998.

9.   Grzesik W. Podstawy skrawania materiałów konstrukcyjnych. Warszawa: WNT, 2010.

10.   Ren Q., Balazinski M., Baron L., Jemielniak K. TSK fuzzy modeling for tool wear condition in turning processes: An experimental study. Engineering Applications of Artificial Intelligence 2011; 24/2: 260-265, http://dx.doi.org/10.1016/j.engappai.2010.10.016.

11.   Kiepuszewski B., Legutko S., Wieczorowski K. Skrawanie metali. Poznań: Wydawnictwo Politechniki Poznańskiej, 1980.

12.   Korzyński M. Metodyka eksperymentu-Planowanie, realizacja i statystyczne opracowanie wyników eksperymentów technologicznych. Warszawa: WNT, 2013.

13.   Królczyk G., Gajek M., Legutko S. Predicting the tool life in the dry machining of duplex stainless steel. Eksploatacja i Niezawodnosc -– Maintenance and Reliability 2013; 15 (1): 62-65.

14.   Kruszyński B., Midera S., Kaczmarek J. Forces in generating gear grinding-theoretical and experimental approach. CIRP Annals - Manufacturing Technology 1998; 47: 287-290, http://dx.doi.org/10.1016/S0007-8506(07)62835-2.

15.   Mańczak K. Technika planowania eksperymentu. Warszawa: WNT, 1976.

16.   Matsuoka H., Tsuda Y., Suda S., Yokota H. Fundamental research on hobbing with minimal quantity lubrication of cutting oil (effect of quantity of oil supply). JSME International Journal 2006; C 49/2: 590-599.

17.   Matsuoka H., Tsuda Y., Suda S., Yokota H. Fundamental research on hobbing with minimal quantity lubrication of cutting oil (effect of cutting speed). JSME International Journal 2006; C 49/4: 1140-1150.

18.   Rech J. Influence of cutting edge preparation on the wear resistance in high speed dry gear hobbing. Wear 2006; 261: 505-512, http://dx.doi.org/10.1016/j.wear.2005.12.007.

19.   Stachurski W. Wpływ warunków podawania cieczy obróbkowej w strefę skrawania z minimalnym wydatkiem na zużycie frezu ślimakowego. Łódź: Praca doktorska, 2008.

20.   Stachurski W. Application of minimal quantity lubrication in gear hobbing. Mechanics and Mechanical Engineering 2012; 16/2: 133-140.

Wojciech STACHURSKI
Stanisław MIDERA
Bogdan KRUSZYŃSKI
Institute of Machine Tools and Production Engineering
Lodz University of Technology
ul. Stefanowskiego 1/15, 90-924 Łódź, Poland

E-mail: wojciech.stachurski@p.lodz.pl,
stanislaw.midera@p.lodz.pl, bogdan.kruszynski@p.lodz.pl

Ratnesh KUMAR
Somnath CHATTOPADHYAYA
Sergej HLOCH
Grzegorz KROLCZYK
Stanislaw LEGUTKO

WEAR CHARACTERISTICS AND DEFECTS ANALYSIS OF FRICTION STIR WELDED JOINT OF ALUMINIUM ALLOY 6061-T6

CHARAKTERYSTYKA ZUŻYCIA I ANALIZA USZKODZEŃ ZŁĄCZA ZE STOPU ALUMINIUM 6061-T6 ZGRZEWANEGO TARCIOWO Z PRZEMIESZANIEM

This paper deals with the wear characteristics and defects developed during friction stir welding at different process parameter of aluminium alloy (AA) 6061-T6 having thickness 6 mm. Four welded samples are prepared with rotational speed 500 rpm, 710 rpm, 1000 rpm and with welding speed of 25 mm/min & 40 mm/min. Welded samples and base material are put in wear condition under grinding machine for 120 s. Material removal is measure by taking the difference of weight before and after wear. Different types of defects and fracture are observed on the wear surface. These defects and fractures are analysed under field emission scanning electron microscope (FESEM). It is concluded that material removal from welded sample is less compared to base metal, hence wear resistance increases after friction stir welding.

Keywords: *Friction stir welding (FSW), Wear, Defect, Grinding Machine, Field Emission Scanning Electron Microscope (FESEM).*

Praca dotyczy charakterystyki zużycia i uszkodzeń podczas zgrzewania tarciowego z przemieszaniem stopu aluminium (AA) 6061-T6 o grubości 6 mm dla zmiennych parametrów. Cztery zgrzewane próbki były wykonane z prędkością obrotową 500 obr/min, 710 obr/min, 1000 obr/min dla prędkości zgrzewania 25 mm/min i 40 mm/min. Zgrzewane próbki i materiał bazowy były poddawane zużywaniu za pomocą szlifierki w czasie 120 s. Ubytek materiału mierzono jako różnicę wagi przed i po zużywaniu. Różne rodzaje wad i pęknięć zaobserwowano na zużytej powierzchni. Wady i pęknięcia analizowano za pomocą mikroskopu polowego (FESEM). Stwierdzono, że ubytek materiału ze zgrzewanych próbek jest mniejszy w porównaniu z ubytkiem dotyczącym materiału bazowego. Zwiększa się więc odporność na zużycie po zgrzewaniu tarciowym z przemieszaniem.

Słowa kluczowe: *Zgrzewanie tarciowe z przemieszaniem, zużycie, uszkodzenie, szlifierka, mikroskop polowy.*

1. Introduction

Friction stir welding (FSW) is developed and patented by Mr. Wayne Thomas at The Welding Institute (UK) in the year 1991 [28]. It is a solid state joining technique at which materials are joined below their melting point. Hence compared to other traditional techniques it is energy efficient, versatile and environment friendly. Aluminium alloys especially 2XXX and 7XXX series are difficult to weld by conventional fusion welding process because of poor solidification and porosity in fusion zone. Hence aluminium alloys are easily welded by FSW process [23]. Friction stir welding quality is determined and controlled by the process parameters like rotational speed, welding speed, plunge depth etc. Figure 1 shows the schematic diagram of friction stir welding process. In this process material that is going to be joined is fixed on bed with the help of fixtures and a non consumable rotational tool plunges through the material. There is generation of friction heat due to contact between tool and work piece, which brings the material in semi solid state. Due to stirring action and consolidated pressure by the tool the semi solid material gets joined [7].

Won-Bae Lee et al. studied the microstructures and wear property of friction stir welded AZ91 Mg alloy/SiC particles reinforced composite (AZ91/SiC/10p). They found an improvement in the wear property of the weld zone as compared to base metal. They concluded
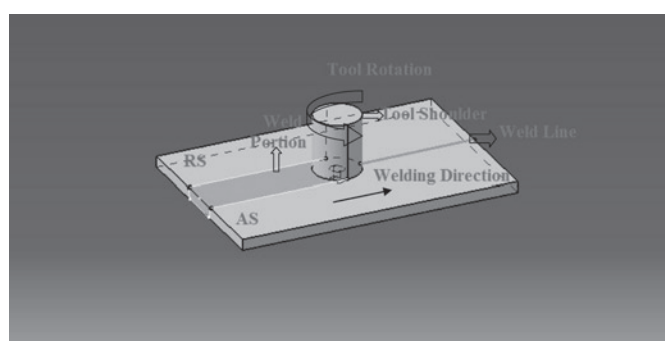

Fig. 1. Schematic drawing of friction stir welding

the wear resistance within the weld zone, as evaluated by the specific wear loss, was superior, as compared to the base metal [19]. R. Palanivel et al. developed an empirical relationship between FSW process parameter and wear resistance of friction stir welded joint of two dissimilar aluminium alloy AA5083H111-AA6351T6. It was found that wear resistance increases as tool rotational speed, welding speed and axial force increases up to certain level then it starts decreasing. It was also observed that joints fabricated using straight pin profiles yielded highest wear resistance due to intense plastic flow and mixing of dis-

similar alloys as compared to tapered pin profile tool [24]. Dinaharan I. et al. developed an empirical relationship to predict the effect of process parameter on sliding wear behaviour of butt joints of friction stir weld AA6061/ 0-10 wt.% ZrB_2 composites. They concluded that wear rate decreases as tool rotational speed, welding speed and axial force increases. After that further increase in these process parameter increases the wear rate. They also studied the scanning electron microscopy (SEM) micrographs of wear surface [6]. Prakash et al. studied the tribological behaviour i.e. dry sliding wear characteristics using a computer aided pin on disc wear testing machine of friction stir processed Al 6061 sheet with metal reinforced. They concluded that wear rate decreased as weight percentage of Al_2O_3 increased. Through SEM they studied the wear surfaces and observed wear tracks that are covered with the compact debris and delamination [26]. Jankauskas V. et al. analysed the influence of welded layers composition on the abrasive wear mechanism of friction couples "hard layer-steel". They investigated the arc welded layer's strength, surface morphology; chemical and structural composition and abrasive wear resistance. Wear was determined by weighing the samples before and after the test. The microstructure was analysed with the optical metallographic microscope and morphology of friction surfaces were analysed with SEM [12]. As per literature it can be found that researchers studied the wear characteristics of different friction stir welded joints. Some have compared the wear resistance property of weld zone compared to base material and concluded that wear resistance property is better at weld zone compared to base material.

Karam et al. study the possibility of joining two dissimilar alloy i.e. A319 and A413 using friction stir welding. They examined the weld bead visually in which they found flash formation on upper surface. They found formation of tunnel defect through X-ray radiograph and defects at macrostructure analysis on sample prepared at high welding speed [15]. Joulo T. Le et al. have investigated the fatigue strength and failure mechanism of defect free and flaw bearing friction stir butt-weld of 3.1 mm thick AA2198-T8 Al-Li-Cu alloy via S-N curve. Under this study detailed fractography was carried out to link fatigue crack initiation sites and propagation paths to the presence of defects on monotonic loading. They used scanning electron microscope for the fracture surface examination and also for the defect observation. They observed the intergranular cracks and concluded that fracture occurs always from inter granular cracks [13]. Dehghani M. et al. has joined the Al 5186 to mild steel using friction stir welding technique. They investigated the effect of process parameters on defects like tunnel formation, cavity and porosity. At higher pin diameter and with lower welding speed tunnel formation was observed but as pin diameter decreases and welding speed increases such defects could be avoided. Also the threaded pin profile can minimise the formation of cavity [3]. Kadlec Martin et al. studied the effects of kissing bond defect on the tensile and fatigue properties of 7475-T7351 friction stir welds with respect to a reference weld without any flaws and a base material. They determined the defects size by investigating various kissing bond defects. Using SEM they investigated a new process of crack initiation and propagation from the kissing bond surface rather than from its end [14]. Ramulu P. Janaki et al. analyzed the effect of process parameter on the formation of internal defects of friction stir welded joint of AA 6061 T6 having thickness 6.1 mm. They have discussed the defect due to less tool plunge, insufficient heat generation and plastic deformation. They concluded that higher welding speed, higher rotation speed and higher plunge depth are preferred for producing a defect free weld. They also optimized the welding parameter for producing the internal defect free welds [27]. Li J. Q. et al. has studied the defects developed at different rotational speed for the external non-rotational shoulder assisted friction stir welding on 2219-T6 aluminium alloy. They investigated the morphology of the cavity defect with high magnification. They observed the cavity defect close to the top surface of the weld [20]. Chen Hua Bin et al. made an at-

tempt to investigate the formation of defect like void on friction stir welded joint of 5456 aluminium alloy. They used optical microscopy and scanning electron microscope to analyse these defects [2]. Zhang Huijie et al. has characterized and proposed mechanism for formation of welding defects in underwater friction stir welded 7.5 mm thick 2219-T6 aluminium alloy. They analysed the defects such as voids and grooves through the material flow patterns. They concluded that welding defects can occur at both low as well as high rotational speed. They studied the high magnification images of welding defects formed under different process parameters [32]. Janjic M. et al. investigated the tunnel defect on the advancing side of friction stir welded joint of AA 6082-T6. They put it in the category of density error caused due to insufficient transport of material around the pin [11]. Podrzaj P. et al. studied different types of defects at friction stir welding. They discussed defects like tunnels, voids, surface grooves, excessive flash, surface galling, nugget collapse and kissing bond. They have given the energy input as main reason for these defects [25]. Dimic Ivana et al. has conducted three dimensional finite element analysis to quantify the influence the weld defects on integrity of pipe elbows subjected to internal pressure. They concluded that local defects reduce the load carrying capacity and deformation ability of a piping system. They discovered the defect through ultrasonic measurement [5]. From the literature it can be observed that researchers have examined the defects in friction stir welded joints. Some have found the defects like voids, cavity and tunnel defects.

Wear characteristics and defects analysis is important in technical diagnostics which includes assessment of the technical condition of machines parts by studying the properties of its work processes. Failure of machine parts can be avoided by proper welded joints. Through root cause analysis of defects maintenance of machine parts reduces. The diagnostics is important for mining, metallurgy, processing industry and materials science [16, 9, 8, 30, 17, 4, 10, and 31]. Mazurkiewicz described the most popular diagnostic systems used in the maintenance of internal transport conveyors system and also presented a new method of computer-aided maintenance of such systems. He found that with the help of described monitoring system maintenance diagnosis of a single belt conveyor or an entire transport system enables effective assessment of the current state of bonded joints [22]. Wang explained that demands of spare parts are usually generated by the need of maintenance either preventively or at failures. He suggested that proper planned maintenance intervention can reduce the number of failures [29].

Hence from above findings of all researchers it can be summarized that wear of any welded component causes defect. Defects in any welded part can arise due to improper selection of process parameter or due to wear of the welded part. These wear and defects causes the failure of any welded part. Therefore there is need of maintenance either post failure or to prevent this failure.

This paper deals with the study of wear characterization and investigation of different weld defects generated in friction stir welded joint of aluminium alloy 6061-T6. The aim of this paper is to study the effect of process parameter with the material removal during wear condition and comparing it with base material under same condition. FSW samples are put in wear condition in grinding machine to create the extreme real harsh wear condition. These welded samples will face such type of harsh wear condition at automobile or shovel teeth. Under this paper different types of defects are studied under FESEM. These defects may arise in friction stir welded joints when welded joints are put in wear condition. AA 6061-T6 is a light weight aluminium alloy used in rail coaches, truck frames, ship building, civil bridges, for aerospace applications including helicopter rotor skin etc.

2. Experimental procedure

The friction stir welding set-up is developed on HMT 1U-make milling machine. SS 410 stainless steel was selected as FSW tool material and 6 mm thick AA 6061 T6 is chosen as working material. The welding samples are prepared at four process parameters as given in Table 2. Friction stir welded sample and base metal sample of dimension 30 mm X 25 mm are put in wear condition with the help of grinding machine for 120 s as shown in Figure 2. Specification of grinding wheel is shown in below Table 1.

Fig. 2. Experimental setup

Table 1. Specification of grinding wheel

Rotational Speed (N)	1600 rpm
Diameter of grinding wheel (D)	130 mm
Width of grinding wheel	40 mm
Time duration of test	120 sec

With the help of precision weighing machine initial weight of all samples i.e. weight before wear and final weight of all sample i.e. weight after wear is measured. With the difference in final weight and initial weight material removal from each sample is find out to study the abrasive wear phenomena of welded sample.
Table 2 shows the detail of welded sample prepared at their corresponding process parameter.

During the friction stir welding experiment, temperature is observed with the help of Infrared camera of CHAUVIN ARNOX C.A. 1888.

Table 2. Process parameter of specimen

Sl. No.	Sample no.	Type	Rotational Speed (rpm)	Welding Speed (mm/min)
1.	1	Welded Sample	500	25
2.	2	Welded Sample	710	25
3.	3	Welded Sample	1000	25
4.	4	Welded Sample	710	40
5.	5	Base Material		

3. Result & Discussion

3.1. Maximum temperature

Maximum temperature during the process can be measured with the help of thermal images taken from infrared camera. Figure 3 shows the maximum temperature generated during the experiment for sample no 2. Table 3 gives the maximum temperature generated at all the four process parameters.

From Table 3 it can be concluded that maximum temperature achieved during the process is maximum for sample 3. Hence it can be derived that temperature obtained during the process increases as rotational speed increases.

3.2. Theoretical formulation of material removal during grinding operation

Theoretically material removal rate (MRR) in case of grinding operation can depend upon width of cut, depth of cut and feed rate of work piece:

Hence,
$$MRR\left(\frac{mm^3}{s}\right) = d * w * v, \qquad (1)$$

where: d = depth of cut,
w = width of cut, in this case it is 25 mm,
v = feed rate of work piece.

Since rotational speed of grinding wheel (N) = 1600 rpm.

where:
$$\left(\frac{m}{s}\right) = (*D * N) / 60 , \qquad (2)$$

Now, by inserting value of v from eq (2) to eq (1),

therefore,
$$MRR(\frac{m^3}{s}) = 0.27 * d . \qquad (3)$$

Fig. 3. Infrared image of FSW

Table 3. Maximum temperature attained at different welding condition

Sl. No.	Sample no.	Maximum Temperature
1.	1	482.00
2.	2	518.57
3.	3	539.07
4.	4	515.4

Material removal in, $120s(m^3) = 32.67 * d$⌊   (4)

Hence, $removed(Kg) = 88.21 * d$,   (5)

Since density of aluminium is taken as $(\rho_{al}) = 2.7$ Kg/m^3.

So, $mass\ removed(mg) = 88.21 * 10^6 * d$ (6)

Hence from equation (6) material removal depends on depth of cut. In this experiment depth of cut is not known. Since, there is only surface contact between grinding wheel and work piece.

3.3.   Experimental analysis of wear

Material removal is obtained by measuring the weight of all five specimens before and after wear. Material wear from all five samples are plotted in Figure 4.
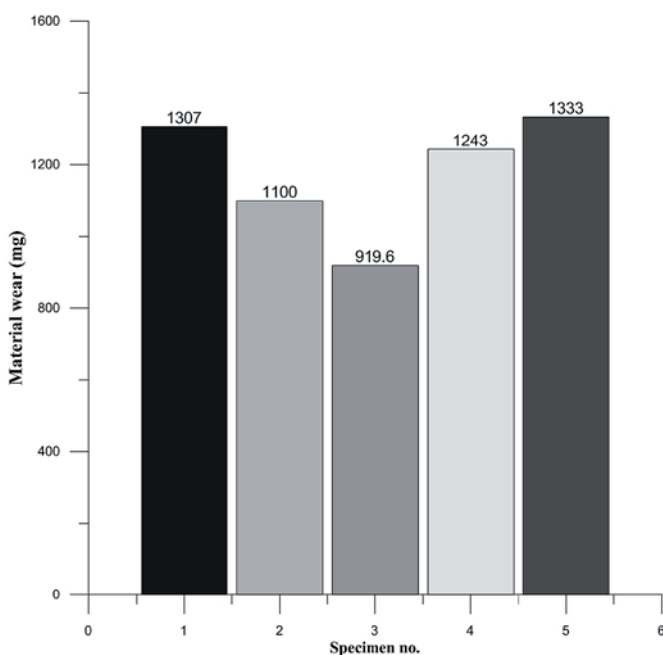
Fig. 4. Comparison of material removal of different welded sample with base metal

From the Figure 4 maximum material removals can be observed for sample no 5 i.e. base metals as compared to welded samples. Hence it can be concluded that wear resistant of welded material is more than that of base material. The reason for such variation is that friction stir welding occurs at a temperature below the melting point of material, so there is no chance of second phase formation. Hence material gets heat treated, so wear resistance property increases. From the above graph it can be observed that material removal is lowest in case of sample no 3 i.e. at 1000 rpm and 25 mm/min. It implies that best welding has occurred in this case. Since for higher rotational speed and lower welding speed, heat generated is maximum; as clear from Table 2, so material easily stirs and mixed. It is clear that material removal in case of sample no 4 is more than that of sample no 2. Hence it can be concluded that for same rotational speed as welding speed increases quality of weld decreases, since temperature developed reduces as given in Table 3.

3.4.   Defects found in welded sample

After welding the samples through visual inspection defects are observed on the welded plates. These defects caused the rejection of welded plates through visual inspection only.

3.4.1. Exit hole and Flash

Friction stir welding process can be sub divided in three phase i.e. plunging in, welding and plunging out. In the plunging out step tool is taken out of the work piece. When tool is taken out of the work piece an exit hole is left at that place. This phenomenon is shown in the Figure 5 of sample 3.
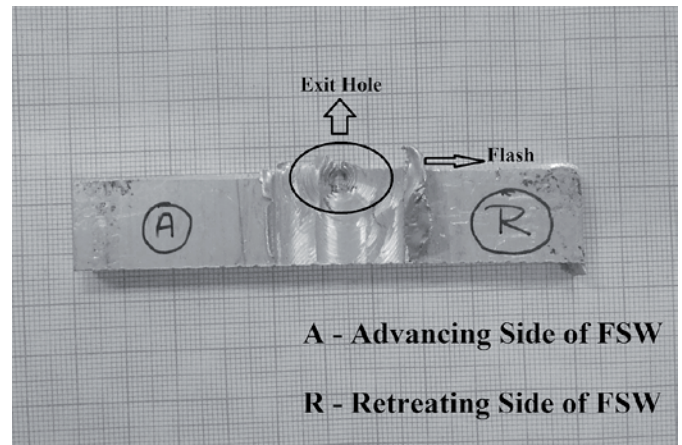

Fig. 5. Exit hole and flash

Exit hole phenomena is observed during all the process parameters. So that amount of material is wasted every time. It is observed that size of exit hole is equal to that of pin size. In Figure 3 at the weld joint area extra material is observed known as flash. The reason for the flash formation is the excessive heat generation. Excessive heat generation leads to the thermal softening of the work piece beyond the boundary of tool shoulder. Hence upper layer of the material come out forming an excessive surface known as flash. Consequently this leads to the thinning of the material in the weld area. Hence at the weld root area, pin starts making contact with the backing bar which causes rupture of material. Ultimately it will damage both the pin and backing bar.

Due to low heat generation, material doesn't get soft. Hence tool is not able to stir and mix the material. So, improper weld result. In the Figure 6, which is the weld joint at tool rotational speed 500 rpm and
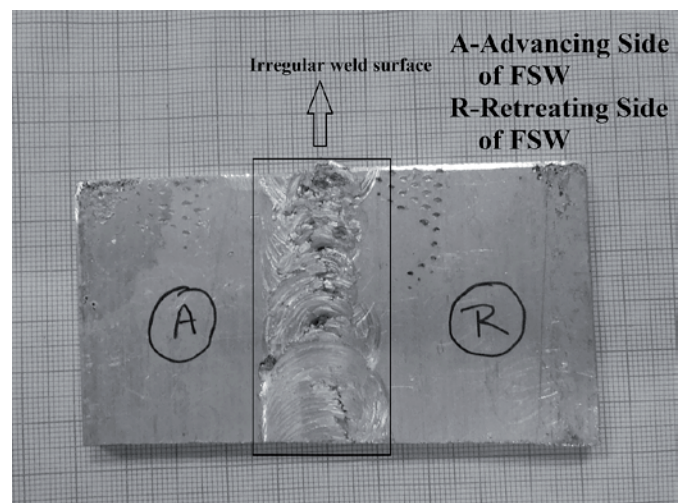

Fig. 6. Irregular weld surface

weld speed 40 mm/min, irregular weld surface can be observed from the visual inspection. The reason for such surface is less heat generation due to lower rotational speed and high welding speed [18]. Hence this sample is rejected.

3.5. Defects generated during wear

After putting the welded sample in wear condition, several defects are observed. These defects are one of the major causes behind the failure of any friction stir welded structure. So, for the efficient performance of any welded joints these defects must be minimised.

3.5.1. Fracture along the welding direction on back side of plate

It is observed that when welded samples are put in the wear condition defects are noticed. A fracture is observed on the back side of plate along the welding direction for sample 1. It shows that at low
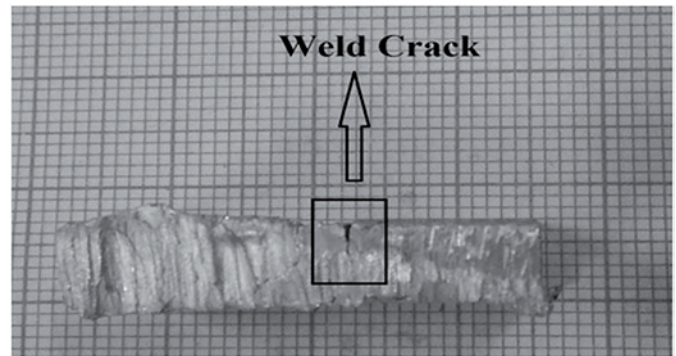

Fig. 9. Weld crack

terized with a lot of dimples, which clearly shows the ductile failure mechanism and ductile fracture morphology reveals that the metallic bonding is performed in this region [33].

3.5.2. Crack propagates along the thickness as seen from the thickness

Welded sample 4 put in wear condition, abrasive wear phenomena was observed. After the process when its cross-section was observed there is a propagation of crack along the thickness as shown in Figure 9. FESEM image of the crack is taken and it is shown in Figure 10.

From Figure 10 it is clear that crack propagates along the thickness after wear. It is one of the major causes for the failure of any welded joint [1]. Rectangular part is further magnified and it is seen in the FESEM in the right figure. It can be observed that surface has broken into small particles and hence propagating the crack.

3.5.3. Porosity

In sample 2, porosity is observed near the surface as shown in Figure 11.

Porosity is being observed under FESEM as shown in Figure 12.

Figure 12 shows the porosity on the wear surface. It can be observed from the Figure that due to grinding wear surfaces are overlapped to one another. Here also it can be observed that surfaces are broken into segments to form the pores.
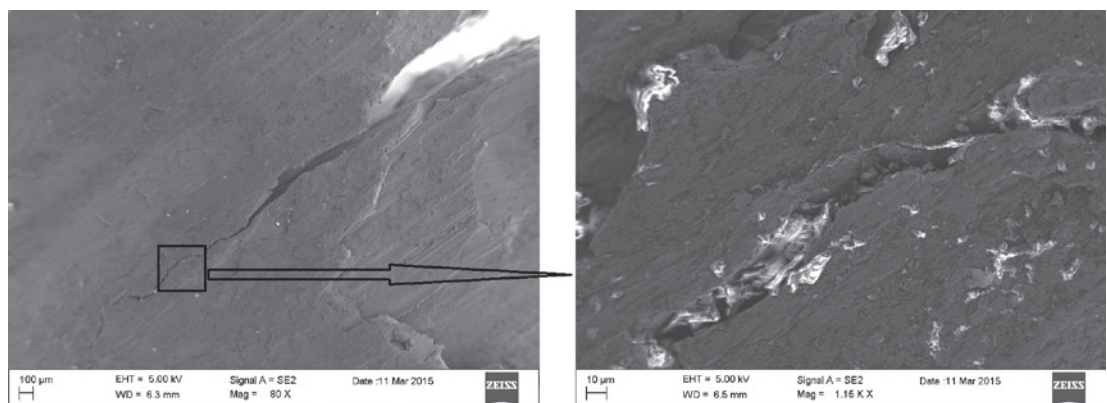

Fig. 7. Weld fracture

Fig. 8. FESEM image of fracture surface

welding speed due to inadequate amount of heat generated, welded part may fail when put in severe working condition. Figure 7 shows the fracture in sample 1.

Figure 8 shows the FESEM image of fracture surface shown in Figure 7. This clearly shows the failure of the welded part.

Circular part is further magnified and seen on the FESEM. It is clear that the fracture surface is charac-

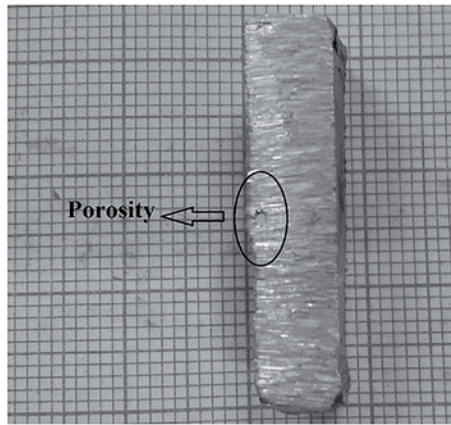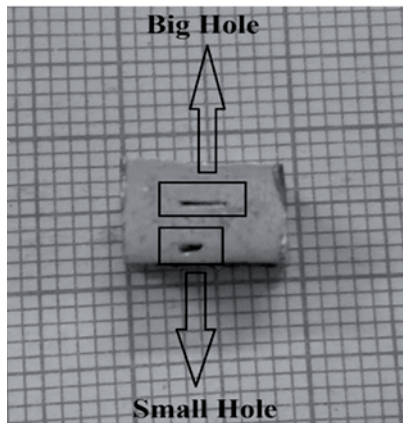Fig. 10. FESEM image of weld crack

Fig. 11. Porosity

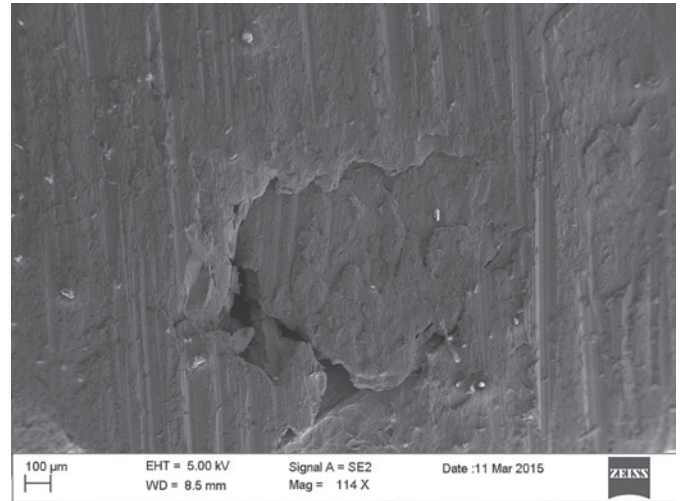*Fig. 13. Holes on weld surface*

Fig. 12. FESEM image of porosity

3.5.4. Discontinuity

When welded sample 2 is cut to see their cross section there is no defect like hole is observed. But when the surface is further polished to prepare samples for microstructure evaluation, two holes are observed i.e. one is small hole and another is big hole as shown in Figure 13. These are also known as tunnel defect in friction stir welding process [21].

FESEM image of small hole is shown in Figure 14.

Left image of Figure 14 shows the FESEM image of small hole. It can be observed from the image that it is a through hole. Hence the reason for such dole is that no proper heating of welding material, so that tool is not able to stir the work piece properly. Right image of Figure 14 shows the magnified view of the circular part as shown in left image. Here irregular cracks are observed on the surface.

While observing bigger hole through FESEM a crack is spontaneously observed as shown in Figure 15.

On the left image of Figure 15 big hole along with the horizontal crack can be observed. Big hole is also a through hole like small hole. Right image of Figure 15 is the magnified view of the circular part at crack shown in the left image. Further vertical cracks are observed in the horizontal crack. These type of cracks are the main reason for the hole generation and failure of welded parts under wear condition.
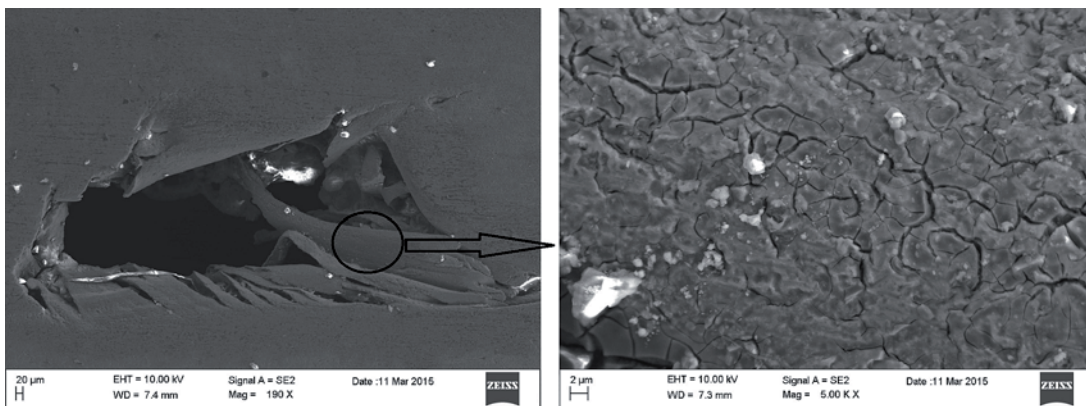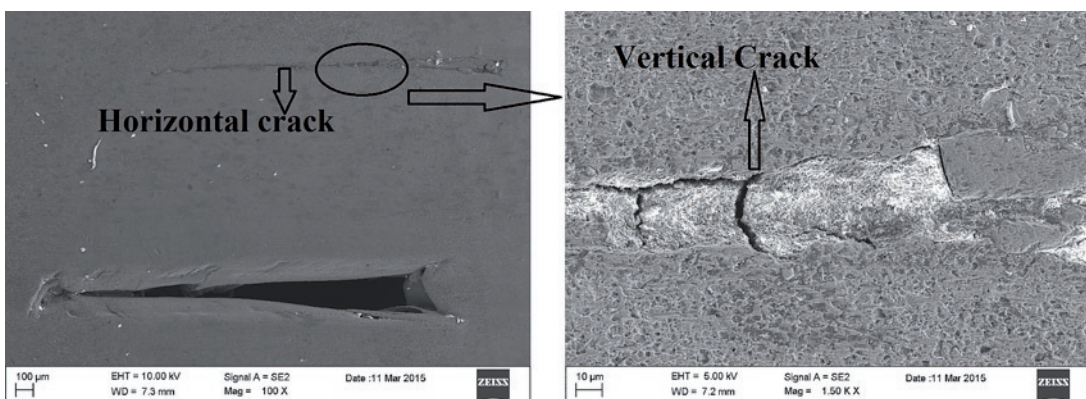

Fig. 14. FESEM image of small hole

Fig. 15. FESEM image of big hole & crack

4. Conclusion and future scope

From the above study on wear characterization and weld defects of friction stir welding of AA 6061-T6 following conclusions are made.

1. Wear resistance of friction stir welded joint is increased compared to base material. Since material is joined below melting point of material, hence material does not melt during the welding therefore there is no chance of second phase formation.
2. Fracture surfaces of welded joint shows the ductile failure mechanism.
3. At high tool rotational speed (i.e. 1000 rpm), defect free welds are obtained. Since, at higher rotational speed more heat is generated compared to lower rotational speed (i.e. 500 rpm and 710 rpm). So material can easily stir and good weld will be obtained at high temperature.

In future wear characteristics and formation of defects at friction stir welded joints; can be studied by the variation of different process parameters like tool tilt angle. Formation of defects during friction stir welding of different materials especially steel can also be analyzed. Remedies of these defects should also be found out.

References

1. Bernasovsky Peter, Failure analysis of welded components-Importance for technical practice, IIW International congress in central and east European region Slovakia, High Tatras, 14-16 October 2009.
2. Chen Hua-Bin, Yan Keng, Lin Tao, Chen Shan-Ben, Jiang Cheng-Yu, Zhao Yong, The investigation of typical welding defects for 5456 aluminium alloy friction stir welds, Materials Science and Engineering A 2006; 433: 64-69, http://dx.doi.org/10.1016/j.msea.2006.06.056.
3. Dehghani M., Amadeh A., Mousavi S.A.A. Akbari, Investigations on the effects of friction stir welding parameters on intermetallic and defect formation in joining aluminium alloy to mild steel, Materials and Design 2013; 49:433-441, http://dx.doi.org/10.1016/j.matdes.2013.01.013.
4. Dewangan Saurabh, Chattopadhyaya Somnath, Hloch Sergej, Wear assessment of conical pick used in coal cutting operation, Rock Mech Rock Eng 2014; DOI 10.1007/s00603-014-0680-z, http://dx.doi.org/10.1007/s00603-014-0680-z.
5. Dimic Ivana, Arsic Miodrag, Medo Bojan, Stefanovic Ana, Grabulov Vencislav, Rakin Marko, Effect of welded joint imperfection on the integrity of pipe elbows subjected to internal pressure, Technical Gazette 2013; 20: 285-290.
6. Dinaharan I., Murugan N., Influence of friction stir welding parameters on sliding wear behaviour of AA6061/0-10 wt.% ZrB2 in-situ composite butt joints, Journal of Minerals & Materials Characterization & Engineering 2011; 10(14):1359-1377, http://dx.doi.org/10.4236/jmmce.2011.1014107.
7. Gibson B. T., Lammlein D. H., Prater T. J., Longhurst W. R., Cox C. X.,Ballun M. C., Dharmaraj K. J., Cook G. E., Strauss A. M., Friction stir welding: process, automation and control, Journal of Manufacturing Processes 2004;16: 56-73, http://dx.doi.org/10.1016/j.jmapro.2013.04.002.
8. Glowacz, A., Recognition of Acoustic Signals of Loaded Synchronous Motor Using FFT, MSAF-5 and LSVM, Archives of Acoustics 2015; 40 (2):197-203, http://dx.doi.org/10.1515/aoa-2015-0022.
9. Glowacz A., Glowacz A., Korohoda P., Recognition of monochrome thermal images of synchronous motor with the application of binarization and nearest mean classifier, Archives of Metallurgy and Materials 2014; 59 (1):31-34, http://dx.doi.org/10.2478/amm-2014-0005.
10. Hreha P., Radvanska A., Knapcikova L., Krolczyk G.M., Legutko S., Krolczyk J., Hloch S., Monka P., Roughness parameters calculation by means on-line vibration monitoring emerging from AWJ interaction with material, Metrology and Measurement Systems 2015; Vol. XXII (2):315-326, http://dx.doi.org/10.1515/mms-2015-0024.
11. Janjic M., Vukecevic M., Mandic V., Pavletic D., Sibalic N., Microstructural evolution during friction stir welding of AlSi Mg Mn alloy, Metalurgija 2012;51(1):29-33.
12. Jankauskas V., Kreivaitis R., Milcius D., Baltusnikas A., Analysis of abrasive wear performance of arc welded hard layers, Wear 2008; 265:1626-1632, http://dx.doi.org/10.1016/j.wear.2008.03.022.
13. Jolu T. Le, Morgeneyer T. F., Denquin A., Gourgues-Lorenzon A. F., Fatigue lifetime and tearing resistance of AA2198 Al-Cu-Li alloy friction stir welds: effects of defects, International journal of fatigue 2015; 70:463-472, http://dx.doi.org/10.1016/j.ijfatigue.2014.07.001.
14. Kadlec Martin, Ruzek Roman, Novakova Lucie, Mechanical behaviour of AA 7475 friction stir welds with the kissing bond defects, International Journal of Fatigue 2015;74:7-19, http://dx.doi.org/10.1016/j.ijfatigue.2014.12.011.
15. Karam A., Mahmoud T. S., Zakaria H. M., Khalifa T. A., Friction stir welding of Dissimilar A319 and A413 cast aluminium alloys, Arabian Journal for Science and Engineering 2014; 39:6363-6373, http://dx.doi.org/10.1007/s13369-014-1220-6.
16. Krolczyk G.M., Nieslony P., Krolczyk J.B., Samardzic I., Legutko S., Hloch S., Barrans S., Maruda R.W. Influence of argon pollution on the weld Surface Morphology, Measurement 2015; 70:203-213, http://dx.doi.org/10.1016/j.measurement.2015.04.001.
17. Kuczmaszewski J., Piesko P., Wear of milling cutters resulting from high silicon aluminium alloy cast AlSi21CuNi machining, Eksploatacja i Niezawodnosc - Maintenance and Reliability 2014; 16(1): 37-41.
18. Lakshminarayanan A. K., Malarvizhi S., Balasubramanian V., Developing friction stir welding window for AA2219 aluminium alloy, Transactions of Nonferrous Metals Society of China 2011; 21:2339-2347, http://dx.doi.org/10.1016/S1003-6326(11)61018-2.
19. Lee Won-Bae, Lee Chang-Yong, Kim Myoung-Kyun, Yoon Jung-I1, Kim Young-Jig, Yoen Yun-Mo, Jung Seung-Boo, Microstructures and wear property of friction stir welded AZ91Mg/SiC particle reinforced composite, Composites Science and Technology 2006; 66:1513-1520.
20. Li. J. Q., Liu H. J., Design of tool system for the external nonrotational shoulder assisted friction stir welding and its experimental validations on 2219-T6 aluminium alloy, International Journal of Advanced Manufacturing Technology 2013;66: 623-634, http://dx.doi.org/10.1007/s00170-012-4353-3.
21. Lofti Amir Hossein, Nourouzi Salman, Effect of welding parameters on microstructure, thermal and mechanical properties of friction stir welded joints of AA7075-T6 aluminium alloy, Metallurgical and Materials Transactions A 2014; 45A: 2792-2807.
22. Mazurkiewicz D., Computer-aided maintenance and reliability management systems for conveyor belts, Eksploatacja I Niezawodnosc- Maintenance and reliability 2014; 16 (3): 377-382.

23. Mishra R. S., Ma Z. Y., Friction stir welding and processing, Materials science and Engineering R 2005; 50:1-78.
24. Palanivel R., Mathews P. Koshy, Murugan N., Dinaharan I., Prediction and optimization of wear resistance of friction stir welded dissimilar aluminium alloy, Procedia Engineering 2012; 38: 578-584, http://dx.doi.org/10.1016/j.proeng.2012.06.072.
25. Podrzaj P., Jerman B., Klobcar D., Welding defects at friction stir welding, Metalurgija 2015; 54 (2): 387-389.
26. Prakash T., Sivasankaran S., Sasikumar P., Mechanical and tribological behaviour of friction-stir-processed Al 6061 aluminium sheets metal reinforced with Al2O3/0.5 Gr hybrid surface nanocomposits, Arabian Journal for Science and Engineering 2015; 40: 559-569, http://dx.doi.org/10.1007/s13369-014-1518-4.
27. Ramulu P. Janaki, Narayanan R. Ganesh, Kailash Satish V., Reddy Jayachandra, Internal defect and process parameter analysis during friction stir welding of Al 6061 sheets, International Journal of Advanced Manufacturing technology 2013; 65: 1515-1528, http://dx.doi.org/10.1007/s00170-012-4276-z.
28. Thomas WM, Nicholas ED, Needhan JC, Murch MG, Templesmith P, Dawes CJ (1991) International patent application PCT/GB92/02203 and GB patent application no. 9125978.9.
29. Wang Wenbin, A stochastic model for joint spare parts inventory and planned maintenance optimisation, European Journal of Operational Research 2012; 216:127-139, http://dx.doi.org/10.1016/j.ejor.2011.07.031.
30. Wojciechowski S., Chwalczuk T., Twardowski P., Krolczyk G.M. Modeling of cutter displacements during ball end milling of inclined surfaces, Archives of Civil and Mechanical Engineering, 2015: 15 (4): 798 – 805 http://dx.doi.org/10.1016/j.acme.2015.06.008.
31. Wojciechowski S., Twardowski P., Wieczorowski M., Surface texture analysis after ball end milling with various surface inclination of hardened steel. Metrology and Measurement Systems 2014; 21(1):145-56, http://dx.doi.org/10.2478/mms-2014-0014.
32. Zhang Huijie, Liu Huijie, Characteristics and formation mechanisms of welding defects in underwater friction stir welded aluminium alloy, Metallography, microstructure and analysis 2012; 1:269-281.
33. ZhaoYong, Zhou Lilong, Wang Quingzhao, Yan Keng, Zou Jiasheng, Defects and tensile properties of 6013 aluminium alloy T-joints by friction stir welding, Materials and design 2014; 57:146-155, http://dx.doi.org/10.1016/j.matdes.2013.12.021.

Ratnesh KUMAR
Somnath CHATTOPADHYAYA
Department of Mechanical Engineering
Indian School of Mines
Dhanbad-826004, India

Sergej HLOCH
Faculty of Manufacturing Technologies,
Technical University of Kosice,
1 Bayerova St., 080 01 Presov, Slovak Republic

Institute of Geonics AS CR, v. v. i.,
Studentska 1768, Ostrava-Poruba, 708 00, Czech Republic

Grzegorz KROLCZYK
Opole University of Technology
76 Proszkowska St., 45-758 Opole, Poland

Stanislaw LEGUTKO
Faculty of Mechanical Engineering and Management
Poznan University of Technology
ul. Piotrowo 3, 60-965 Poznan, Poland

E-mail: ratan_876@yahoo.co.in, somuismu@gmail.com,
hloch.sergej@gmail.com, grzegorz.krolczyk@wp.pl,
Stanislaw.legutko@put.poznan.pl

Grzegorz BARTNIK
Daniel PIENIAK
Agata M. NIEWCZAS
Andrzej MARCINIAK

PROBABILISTIC MODEL FOR FLEXURAL STRENGTH OF DENTAL COMPOSITES USED IN MODELING RELIABILITY OF THE "TOOTH-DENTAL COMPOSITE" SYSTEM

PROBABILISTYCZNY MODEL WYTRZYMAŁOŚCI NA ZGINANIE KOMPOZYTÓW STOMATOLOGICZNYCH W ZASTOSOWANIU DO MODELOWANIA NIEZAWODNOŚCI UKŁADÓW „ZĄB – KOMPOZYT STOMATOLOGICZNY"*

In the article the application of Bayesian probabilistic modeling was presented as a way to standardize analytics of measurement results, which completes the operational and procedural standardization of determining the strength of dental composites. The traditional way of conducting studies of strength performed as services and calculations, and which do not refer to previous studies, was changed into an adaptation process of knowledge accumulation in a form of an increasing precise models. Probabilistic flexural strength models were used to create a reliability ranking of studied dental composites. Conceptualization of reliability of a biotechnological system, such as a "tooth-dental composite" required the expansion of the notion of "failure" with random events involving the occurrence of compatibility failure.

***Keywords:** probabilistic modeling, reliability of the "tooth-dental composite" system, dental composites, flexural strength.*

W pracy przedstawiono zastosowanie bayesowskiego modelowania probabilistycznego jako sposobu standaryzacji opracowania wyników pomiarów, uzupełniającego standaryzację operatorowo – proceduralną wyznaczania wytrzymałości kompozytów stomatologicznych. Tradycyjny sposób prowadzenia badań wytrzymałościowych, wykonywanych usługowo i obliczeniowo nienawiązujących do badań poprzednich, zmieniono w adaptacyjny proces kumulacji wiedzy w postaci coraz dokładniejszych modeli. Probabilistyczne modele wytrzymałości na zginanie wykorzystano do utworzenia rankingu niezawodnościowego badanych kompozytów stomatologicznych. Konceptualizacja niezawodności układów biotechnologicznych takich jak „ząb – wypełnienie stomatologiczne" wymagała rozszerzenia zakresu pojęcia uszkodzenie o losowe zdarzenia polegające na zaistnieniu niezgodności pomiędzy komponentami układu biotechnologicznego (compability failure).

***Słowa kluczowe:** modelowanie probabilistyczne, niezawodność układów ząb-kompozyt stomatologiczny, kompozyty stomatologiczne, wytrzymałość na zginanie.*

1. Introduction

Obtaining information and knowledge included in the production processes is a fundamental paradigm of production systems based on knowledge and information. It means that knowledge and information constitute one of the most important products – main or side – of each production process. The knowledge remains in the process as a wear-free production resource [3].

Flexural strength is one of the fundamental parameters characterizing dental composites. Flexural strength is measured using a 3-point flexural test (TFS) which is considered by the International Organization for Standardization as applicable in strength studies of polymer-based dental composites and described in standard PN-EN ISO 4049:2010E „Dentistry – Reconstructive polymer-based materials" introducing standard EN **ISO 4049-2009 „Dentistry - Polymer-based restorative materials"[14] in Poland.**

Flexural strength is a complex characteristic, sensitive to even insignificant structure heterogeneity and chemical composition, as well as the shape of the tested samples both at micro and macro scales. The result of the above includes scattered measurement results of samples made of the same material. In other words, the measurement result is burdened with uncertainty regarding the value of flexural strength. Probability is assumed as the measurement of uncertainty. It means that after a series of measurements the flexural strength of the studied material is known with the accuracy of the probability distribution. In literature [10, 15] it is assumed that the distribution is Weibull distribution, the cumulative distribution function of which is presented in formula 1:

$$F(\sigma \mid m, \sigma_0, \sigma_u) = 1 - exp\left[-\left(\frac{\sigma - \sigma_u}{\sigma_0}\right)^m\right]$$ (1)

where:

σ – *breaking stress,*
σ_0 – *scale parameter of Weibull distribution,*
m – *shape parameter,*
σ_u – *location parameter (in the considered case σ_u=0)*

F(σ/m, σₒ, σᵤ)– probability of destruction of the sample with breaking stress σ, for σ≥σᵤ.

Application of Weibull distribution as a flexural strength model for dental materials was considered in this article [10]. In order to estimate Weibull distribution parameters a method of double logarithmic grids was used [10]. It is a method based on classical mathematical statistics, in which distribution probability parameters are treated as fixed values for established conditions of the experiment, even though they are unknown. While the measurement results area random variable with values generated by probability distribution with specific, but unknown parameters. From an engineering point of view, it is the measurement resultsthat area stated fact, and therefore the uncertainty is related to the distribution parameters and not the measurement results. If we consider the distribution parameters to be random variables we deal with Bayesian statistics [5, 6]. Such an approach is meaningful in case of strength measurements in material engineering, anexample of which can be Bayesian Inference for NASA Probabilistic Risk and Reliability Analysis NASA/SP-2009-569, June 2009[2].

The purpose of this article is among others to present the application of Bayesian probabilistic modeling as the proposed method to determine and compare strength characteristics of dental materials. The authors believe that in order to increase the predictability and comparability of strength tests not only the method and measuring devices should be normalized, but also the method of developing measurement results and their formal interpretation. Application of Bayesian statistics has a significant advantage here over classical statistics because it is possible to combine knowledge with measurement results in a way which is compliant with engineering practices.

Another purpose of the article is to signal the problem of reliability of biotechnological systems. Conceptualization of reliability of biotechnological systems, such as the "tooth-dental filling" system requires the introduction of a new subcategory of failure[1], which is *compatibility failure*. An event involving the occurrence of compatibility failure between a biological object and a dental component is treated as a new category of failure-like random events and to them we refer the notion of reliability of biotechnological systems. In accordance with standard PN-EN ISO 4049:2010 three types of non-compatibility should be considered: biological, aesthetical and compatibility related to strength. Each of these categories has more detailed sub-categories, specified in separate standards. In the above mentioned standard there are sub-categories of compatibility related to strength and anti-radiation.

2. Bayesian probabilistic model for flexural strength of dental materials

Bayesian probabilistic models (Bayesian networks) have graph representation [8, 11, 12]. Graph nodes represent values describing the modeled discipline in question. Each of these values has a determined set of values and measure of uncertainty regarding the values, set in the form of *a priori* probability distribution over the set of its values. Graph nodes are connected with arches representing a causal relationship.

Probability distributions related to child nodes of the other nodes are *a priori* conditional distributions. The Bayesian model should be structured in such a way so that the graph representing it does not contain cycles. Using the conditional independence principle a complete probabilistic characteristic is obtained in the form of factorised cumulative probability distribution [4].

Probabilistic models can be generative or discriminative. The essence of Bayesian statistics involves creation of generative models. A question regarding the total probability distribution of random variables is asked provided that their specific implementations are ob-

served taking into account the knowledge of the cause and effect relationship between the variables. The hypothesis concern distribution parameters regarding which it is assumed that they are known with the accuracy of *a priori* probability distribution. Each inflow of new data (implementation of observed random variables) results in updating the conditional probability distributions of all variables in the model, including distribution parameters. Then *a posteriori* distributions of particular random variables are obtained, as well as total *a posteriori* probability distribution [5, 6, 7, 8, 9].

Assuming that Weibull distribution is a probabilistic model for flexural strength of dental composites, the model in the form of Bayesian network is presented in Fig. 1. The graph has as many nodes as there are parameters in formula 1 (when building the network, the scale parameter was marked η "eta", and the shape parameter - β "beta")and nodes representing factors of the experiment. In this case they are: type of the material, type of light used in the hardening process and time of radiation.
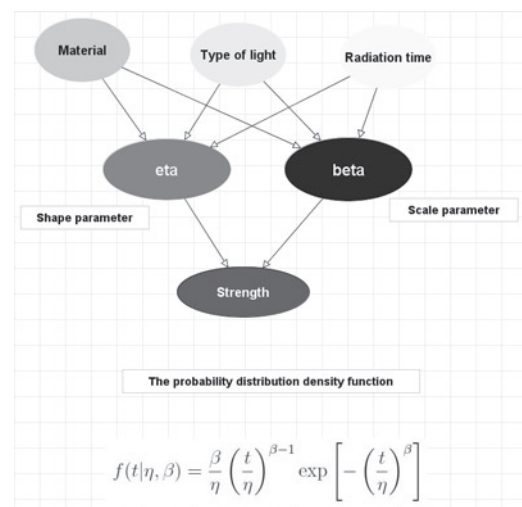

$$f(t|\eta,\beta) = \frac{\beta}{\eta}\left(\frac{t}{\eta}\right)^{\beta-1}\exp\left[-\left(\frac{t}{\eta}\right)^{\beta}\right]$$

Fig. 1. Probabilistic model for flexural strength of dental materials

3. "Learning the models" on examples of measurement results

Results of measurements conducted and published in the article [11] were used. The data concerns dental composites based on siloranes and methacrylate compounds. They were: FiltekSiloran (FSi), Gradia Direct Anterior (GDA), Gradia Direct Posterior (GDP), Herculite XRV (H). Photopolymerization with two types of light: a diode lamp and a halogen lamp were applied. The assumed radiation time was 40 sec. and 60 sec. For flexural strength tests the three-point flexural strength test was used in accordance with the requirements of standard ISO 4049. Tested samples in an amount of N=20 of each material had a form of cuboid beams [1, 4, 10, 13]. Probabilistic modeling was conducted using the AgenaRisk[2] program.

The purpose of learning the probabilistic network is to estimate parameters β and η for various materials and various conditions of the experiment. Learning the network involves backward propagation of results of the measurements of flexural strength (Fig. 2). At the initial stage of learning, the values of parameters β and η are uncertain, therefore the *a priori* probability distribution over the values of these parameters was assumed as steady in the range between 0 and 200 for parameter η and between 1 and 20 for parameter β. Results of learning the network were presented in Fig. 3 and 4.

---

1 Failure is not semantically equivalent to the concept of failure used in reliability theory

2 The AgenaRisk program was used: http://www.agenarisk.com
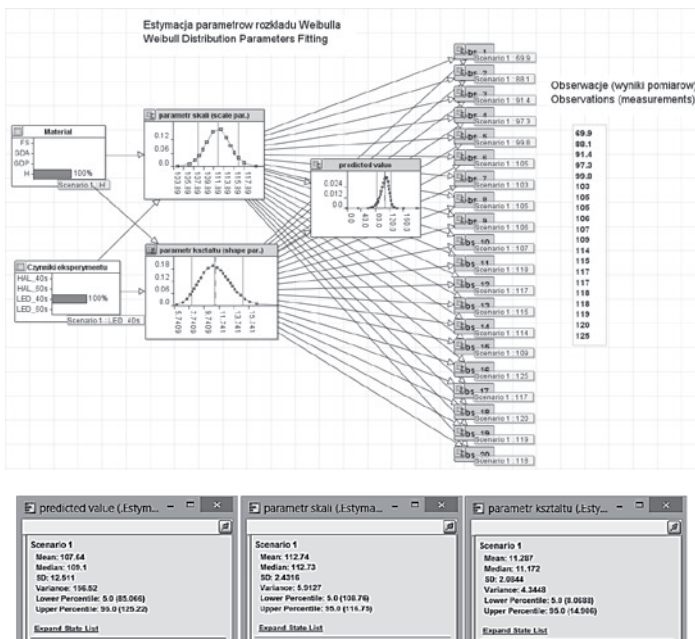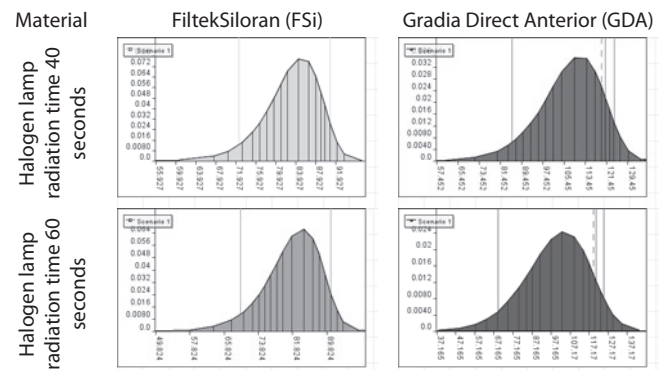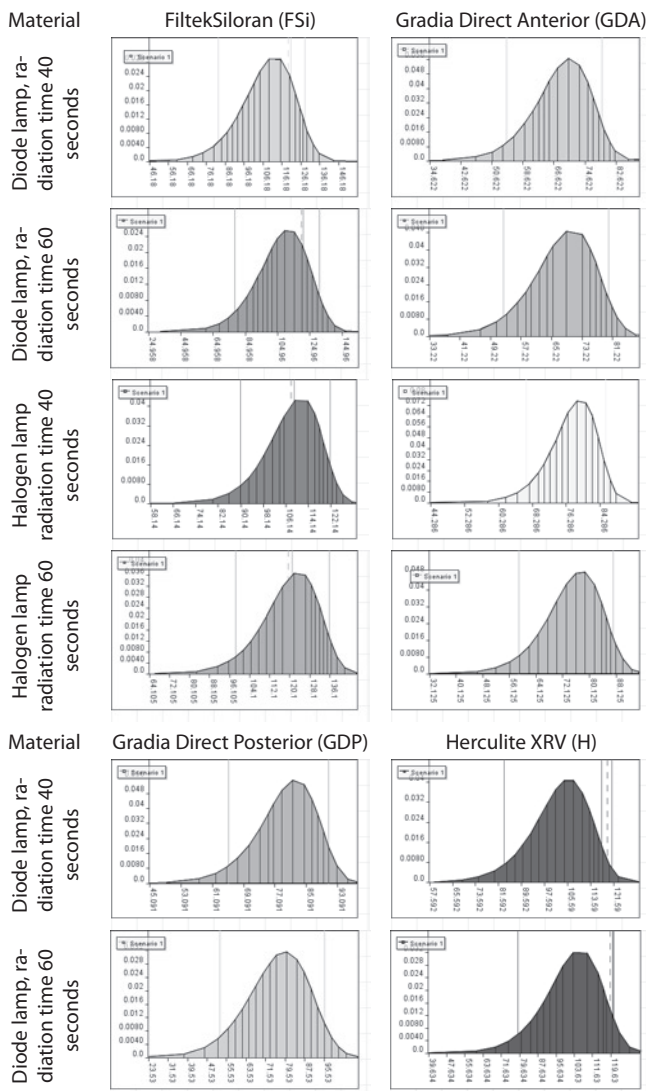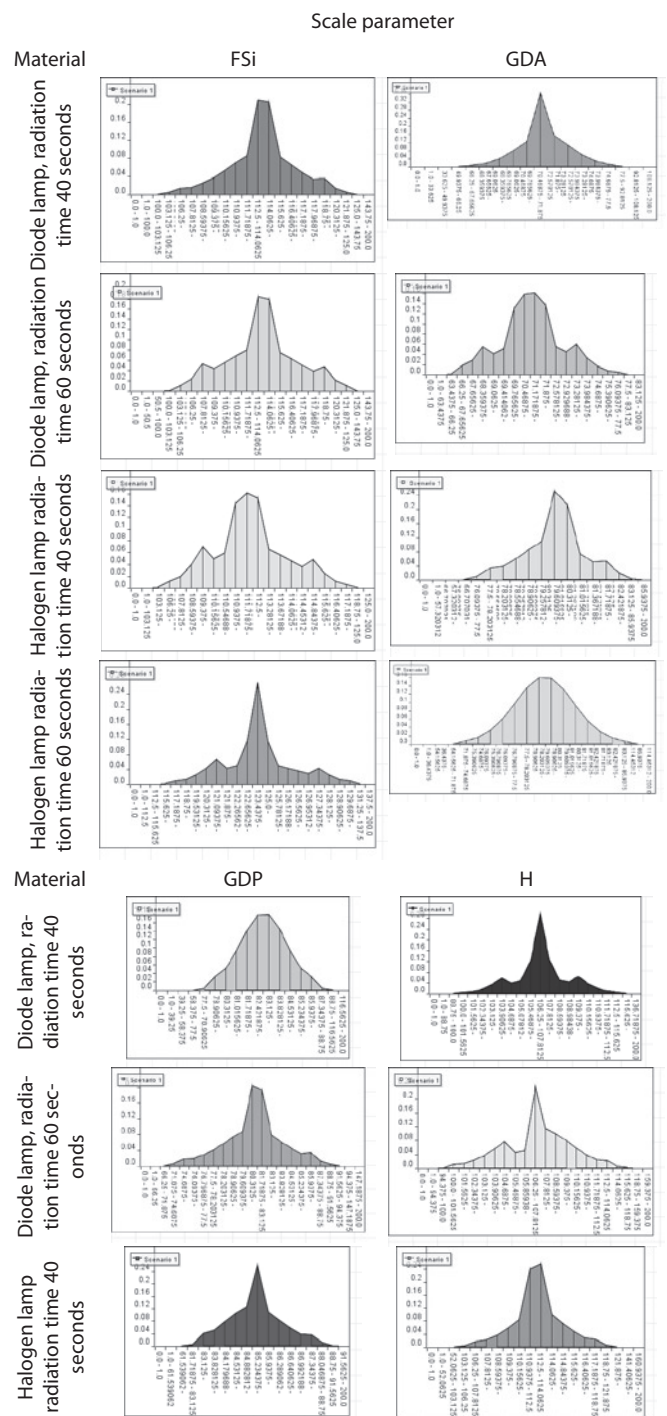
Fig. 2. Learning the network on the basis of measurement results

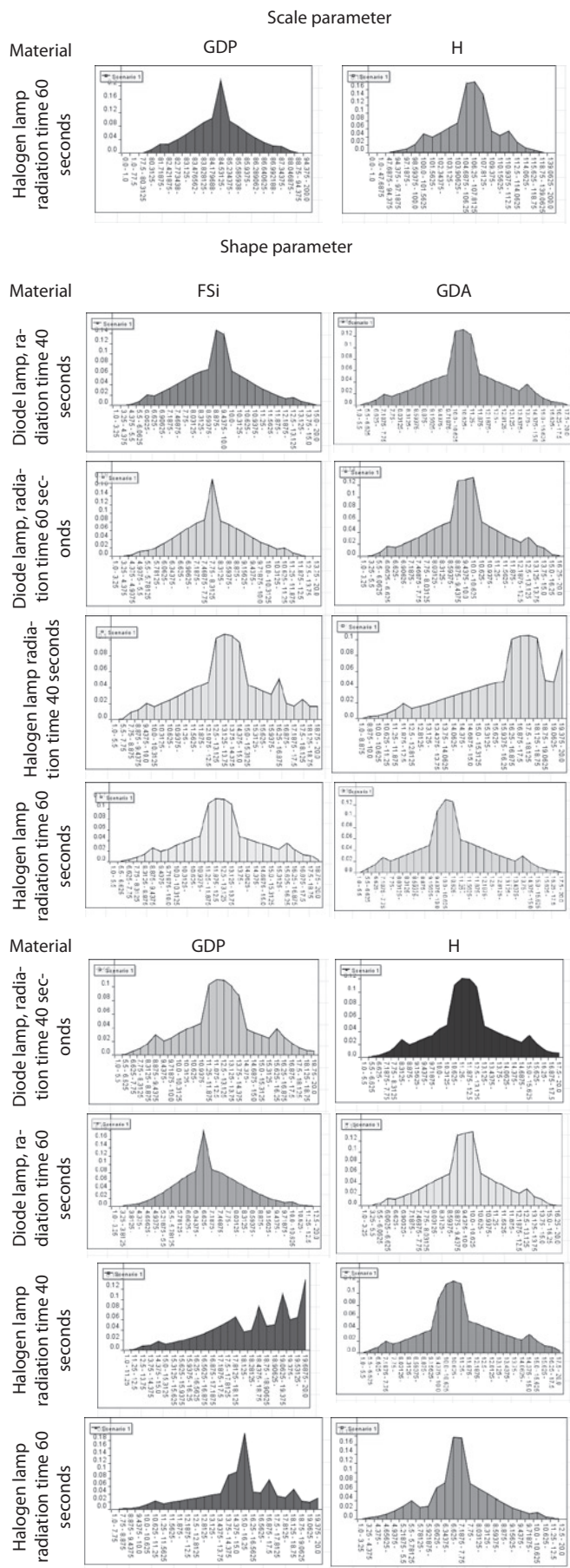Fig. 3. Conditional probability distributions of flexural strength σ

Fig. 4. A posteriori conditional probability distributions of Weibull distribution parameters

4. Using the model to compare the studied materials regarding their flexural strength.

The problem of comparing objects with properties known with the accuracy to probability distribution in classical statistics involves comparing average values, taking into account their confidence intervals. In the case of Bayesian statistics we have total probability distributions. It allows us to obtain answers with an accuracy up to probability distribution for numerous conclusive or comparative questions, e.g.:

– Isn't flexural strength of material A subject to radiation in accordance with procedure W1 lower than the flexural strength of the same material subject to radiation in accordance with procedure W2?
– Which of the studied materials with the same kind of treatment has the highest strength regarding the probability that the selected material will not be worse than other materials in further comparisons?
– Can the material which in the same conditions of treatment is worse than others be improved by the application of the same kind of treatment?

In Bayesian networks the comparison involves the activation of inferential procedures. The purpose of inference is in this case an answer to a question regarding the ratio (how many times?) or difference (by how much?) between the compared values with determined probability distributions. For this purpose to Bayesian network we add deterministic nodes representing the difference or the ratio of the compared values [3]. Exemplary results of the comparisons were presented in Figure 5.

Markings on Fig. 5:Material: FSI - FiltekSiloran, GDA - Gradia Direct Anterior , GDP - Gradia Direct Posterior, H - Herculite XRV.Radiation: HAL_40s – a halogen lamp, radiation time 40 sec., HAL_60s –a halogen lamp, radiation time 60 sec., LED_40s –a diode lamp, radiation time 40 sec., LED_60s –a diode lamp, radiation time 60 sec.

An example interpretation of comparisons included in figure 5 is as follows:

– in case of Fig. 5, a) flexural strength of the FSI material radiated with a halogen lamp for 40 sec. is compared with flexural strength of the FSI material radiated with a diode lamp for 40 sec. From the figure it can be concluded that the null hypothesis, stating that application of photopolymerization with a diode lamp results in lower flexural strength than photopolymerization with a halogen lamp, is real with a probability of 50,839%. Such a result means that the difference of strength in these two cases is insignificant.
– in case of fig. 5, b) flexural strength of the GDA material is compared with the flexural strength of the GDP material both radiated using a halogen lamp for 40 sec. From the figure it can be concluded that the null hypothesis, stating that application of the GDP material results in lower flexural strength than GDS, is real with a probability of 25,067%. Such a result means that the difference of strength in these two cases is significant for the benefit of the GDP material.

Other comparisons are interpreted analogically.

5. Reliability model of the tooth-dental filling system

To model this type of system Bayesian networks constitute a comfortable tool, and especially their sub-category – probabilistic Boolean networks. Nodes in these networks are in this case predicates representing particular types of non-compatibility of the biotechnological system (Fig. 6).

In the article we limited ourselves to consider reliability regarding strength compatibility failure. We treat an event involving the occurrence of strength incompatibility as a random event involving the
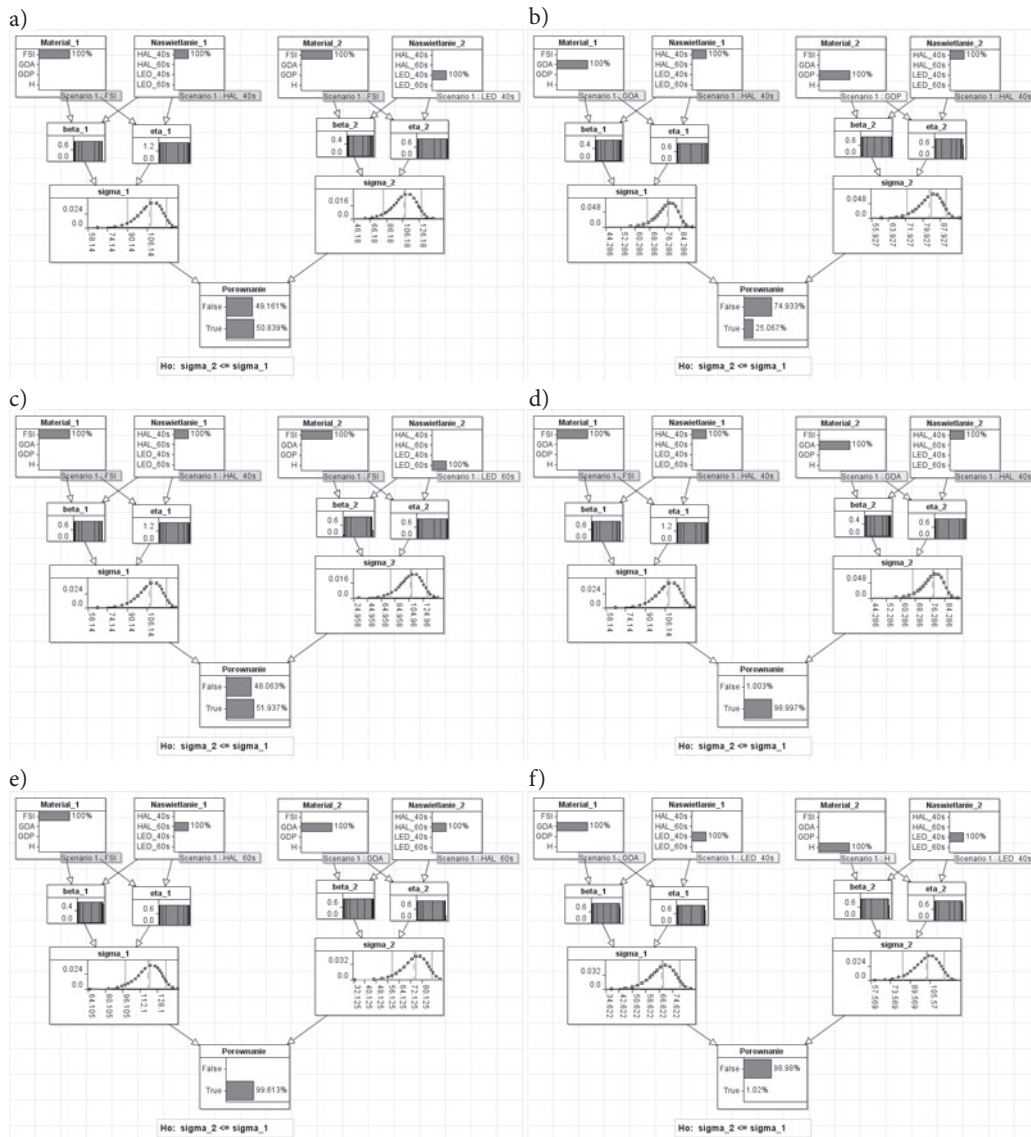
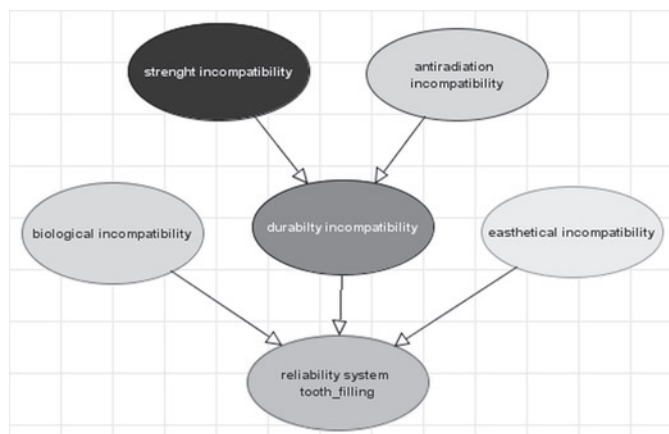*Fig. 5. Comparison of flexural strength of samples subject to radiation according to various procedures*

Flexural strength of the studied materials required by standard PN-EN ISO 4049:2010E (Type 1, class 2, group 1) is 80 MPa. Figure 7 presents a fragment of the network which allows compatibility failure for Filtek Siloran radiated with a diode lamp for 40 seconds to be determined. In this case the hypothesis stating that a material prepared in such as was is not compatible regarding strength is true; in other words its flexural strength is lower than 80 MPa.

Applying the measure of reliability of the "tooth-dental filling" system defined as probability of non-occurrence of compatibility failure for other dental materials and various conditions of their polymerization we obtained the results presented in Fig. 8. Most of the studied materials do not ensure strength compatibility within acceptable probability.

6. Summary

In the first part of the paper, an application of Bayesian probabilistic modeling was presented as a method to standardize analytics of measurement results, complementing the standardization determining strength of dental composites. The technology of Bayesian probabilistic modeling imposes a uniform and sufficiently expressive interpretation of obtained results. The product of this technology is a formal and executable model (knowledge representation sys-

Fig. 6. Diagram of the network representing the reliability model of the tooth-dental filling system.

Fig. 7. Reliability of the "tooth-dental filling" system as probability of the occurrence of strength compatibility failure

tem). It is a change to the traditional manner of interpreting strength studies conducted upon request – studies which refer to previous studies regarding calculations, into an adaptation process of accumulating knowledge in the form of increasingly precise models.

In the second part of the article we proposed conceptualization and a method of reliability modeling of biotechnological systems re-

occurrence of a dental composite with lower flexural strength than required by the standard (at the moment of planting the dental material its strength is known with the accuracy up to the probability distribution). Probability of the occurrence of such an event constitutes the measure of failure (Fig. 7).
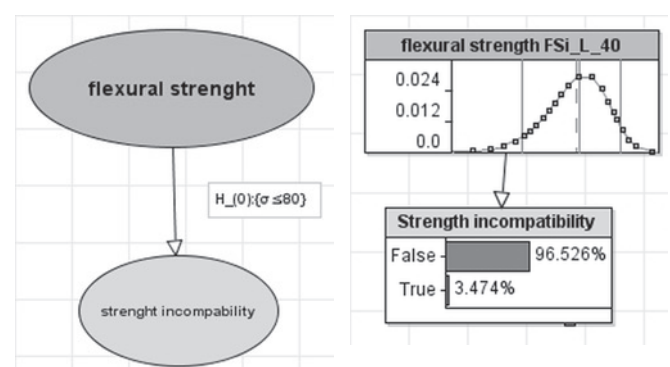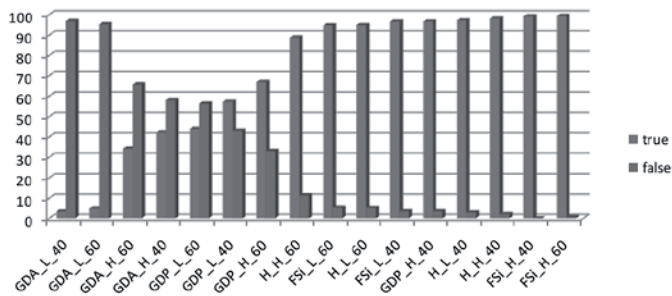
Fig.8. Ranking of dental materials regarding their strength compatibility

garding failures involving the occurrence of a specific type of compatibility failure between the components of the biotechnological system. In this case the appropriate method of reliability modeling involves Bayesian networks the nodes of which represent events of compatibility failure known with an accuracy up to probability distribution.

References

1. Asmussen E., Peutzfeldt A. Influence of UEDMA, BisGMA and TEGDMA on selected mechanical properties of experimental resin composites. Dental Materials, 1998 Jan;14(1): 51-6, http://dx.doi.org/10.1016/S0109-5641(98)00009-8.
2. Bayesian Inference for NASA Probabilistic Risk and Reliability Analysis NASA/SP-2009-569, June 2009.
3. Ben-Gal I., Bayesian Networks, in Ruggeri F., Faltin F. & Kenett R., Encyclopedia of Statistics in Quality & Reliability, Wiley & Sons (2007).
4. Della Bona A. Characterizing ceramics and the interfacial adhesion to resin: I – The relationship of microstructure composition, properties and fractography. Journal Applied Oral Science 2005; 13: 1-9, http://dx.doi.org/10.1590/S1678-77572005000100002.
5. Fenton NE and Neil M. VisualisingRisk, www.agenarisk.com, 2006.
6. Fenton NE and Neil M. Combining Evidence in Risk Analysis Rising Bayesian Networks, Agena White Paper, Agena White Paper W0704/01, www.agena.co.uk, 2004.
7. Halpern J. Y. Reasoning about uncertainty. The MIT Press Cambridge, Massachusetts, London, 2005.
8. Jansen F. V. An introduction to Bayesian Networks. Taylor & Francis, London 1996.
9. Neil M, Fenton NE, Nielsen L. Building large-scale Bayesian Networks. The Knowledge Engineering Review, 2000,(3)15: 257-284, http://dx.doi.org/10.1017/S0269888900003039.
10. Niewczas A., Pieniak D., Ogrodnik P. Analiza niezawodnościowa wytrzymałości kompozytów stomatologicznych poddanych zróżnicowanym procedurom fotopolimeryzacji. Eksploatacja i Niezawodnosc - Maintenance and Reliability2012; 3(14): 249-255.
11. Pearl J. (1986). Fusion, Propagation, and Structuring in Belief Networks. Artificial Intelligence 29(3): 241-288, http://dx.doi.org/10.1016/0004-3702(86)90072-X.
12. Pearl J. Probabilistic reasoning in intelligent systems: networks of plausible reasoning. Morgan-Kaufman Publ. Inc. 1988.
13. Pieniak D., Niewczas A.M., Niewczas A., Bieniaś J. Analysis of Survival Probability and Reliability of the Tooth-composite Filling System. Eksploatacja i Niezawodnosc - Maintenance and Reliability 2011; 2(50): 25-34,
14. PN-EN ISO 4049:2010E.Stomatologia - Materiały polimerowe do odbudowy.
15. Rodriguez S. A. Jr., Ferracane J.L., Della Bona A. Flexural strength and Weibull analysis of a microhybrid and a nanofill composite evaluated by 3- and 4- point bending tests. Dent Mater 2008; 24(3): 426-431, http://dx.doi.org/10.1016/j.dental.2007.05.013.

Grzegorz BARTNIK
Department of Mechanical Engineering and Automation,
University of Life Sciences Lublin,
ul. Doświadczalna 50 A, 20-280 Lublin, Poland

Daniel PIENIAK
Department of Applied Mechanic,
Main School of Fire Service, Warsaw
ul. J. Słowackiego 52/54, 01-629 Warsaw , Poland

Agata M. NIEWCZAS
Department of Conservative Dentistry
Medical University of Lublin,
ul. Karmelicka 7, 20-081 Lublin, Poland

Andrzej MARCINIAK
University of Economics and innovation in Lublin
ul.Projektowa 4, 20-209 Lublin, Poland

E-mail: agata.niewczas@umlub.pl, dpieniak@sgsp.edu.pl
grzegorz.bartnik@up.lublin.pl, andrzej.marciniak@wsei.lublin.pl

Radiša DJURIĆ
Vladimir MILISAVLJEVIĆ

INVESTIGATION OF THE RELATIONSHIP BETWEEN RELIABILITY OF TRACK MECHANISM AND MINERAL DUST CONTENT IN ROCKS OF LIGNITE OPEN PITS

BADANIE ZWIĄZKU MIĘDZY NIEZAWODNOŚCIĄ PODWOZIA GĄSIENICOWEGO A ZAWARTOŚCIĄ PYŁÓW MINERALNYCH W SKAŁACH KOPALNI ODKRYWKOWYCH WĘGLA BRUNATNEGO

This paper describes a mathematical relation which is developed to estimate the occurrence of track mechanism failure in function on the mineral dust (SiO$_2$) content, i.e. wear intensity. This relation is based on actual data of track-type machine (bulldozers) failures, the properties of rocks and measurements of wear intensity on the upper rollers of track mechanism. Failures of bulldozers were recorded during the period of 12 months on six open pits in Serbia, together with their location which is correlated rock type and SiO$_2$ content. This enabled establishment of the reliability indicators using two-parameter Weibull distribution. Further on, correlation is interpreted based on the linearization model using the method of least square. This research has impact on proper management of track-type machines operating on lignite open pits, in the sense of predicting time to failures and cost of maintenance of these machines. This approach provided guidelines for the establishment of reliability centered maintenance model.

Keywords: maintenance engineering, reliability function, abrasive wear, mineral dust, bulldozer, track mechanism.

Artykuł opisuje relację matematyczną, która pozwala oszacować czas do wystąpienia uszkodzenia podwozia gąsienicowego w funkcji zawartości pyłu mineralnego (SiO2), czyli intensywności zużycia. Relacja ta została oparta na rzeczywistych danych o uszkodzeniach maszyn gąsienicowych (spycharek) i właściwościach skał oraz na pomiarach intensywności zużycia rolek podtrzymujących (górnych) podwozia gąsienicowego. Uszkodzenia koparek rejestrowano przez okres 12 miesięcy w sześciu kopalniach odkrywkowych w Serbii. Obserwacje prowadzono w kopalniach o lokalizacji podobnej pod względem występujących typów skał i zawartości SiO2. Pozwoliło to na wyznaczenie wskaźników niezawodności przy pomocy dwuparametrycznego rozkładu Weibulla. Omawianą korelację interpretowano na podstawie modelu liniowego z zastosowaniem metody najmniejszych kwadratów. Przedstawione badania mają znaczenie dla właściwego zarządzania maszynami gąsienicowymi pracującymi w kopalniach odkrywkowych węgla brunatnego, jako że pozwalają na przewidywanie czasu do uszkodzenia oraz kosztów utrzymania tych maszyn. Prezentowana metoda zawiera wytyczne do opracowania niezawodnościowego modelu utrzymania ruchu.

Słowa kluczowe: inżynieria utrzymania ruchu, funkcja niezawodności, ścieranie, pył mineralny, spychacz, podwozie gąsienicowe.

1. Introduction

Reliability is a concept that is the most written in the systems sciences for the maintenance engineering and development of quality of service in industry in general. With the beginning of systems' sciences development, practically after the World War II, reliability engineering as a concept of technical systems' assessment had the most progressive development. Development of reliability theory paralleled with development of soft computing and theory of probability. Scientific investigations are moving in several directions. Some of them will be mentioned bellow. In many articles is written about correlation between reliability and maintenance policy [5, 25], in terms of determining optimal maintenance action intervals in dependence of reliability [17], i.e. in terms of Reliability Centered Maintenance (RCM) [9, 30], in terms of reducing the maintenance costs and improve the effectiveness of the maintenance activities [3, 9], in terms of investigation of dependence between reliability and phenomena such as fatigue [21, 23], corrosion [5] and so on, or in terms of reliability based design of machine [1]. RCM is a systematic analysis method for planning the preventive maintenance of technical systems. RCM is used to develop scheduled maintenance plans that will provide an acceptable level of

availability and dependability, considering to acceptable level of risk, in an efficient and cost-effective manner [15]. This approach was also introduced into SAE JA1012 standard. RCM is most commonly used for prediction of preventive action and spare parts stocks, depending on the cost [9]. There is no general recommendation in the level of reliability to perform preventive replacement. Every engineering system is a special case.

Mining equipment is a key element of mining production. Mining equipment complexity and dimension are continually increasing. Unplanned failures of mining equipment cause higher repair and replacement costs. On the other side, lost production costs are even more important. Risk for environmental and workers are also high. Those facts emphasize the importance of a reliability analysis into the operation of mining equipment [2, 3, 21, 24]. In [24] says that reliability function is the basis of reliability investigations and he goes to perform a comparative analysis of twenty studies dealing with the mining equipment reliability, which highlight the importance of reliability research especially in the mining industry.

Track-type machines are very often used in mines. Undercarriage expense can be a major portion of the operation costs for track-type machines. The upper structure of the machine can be in great position

and the undercarriage is completely wasted, in the same time. Because of that, reliability of undercarriage is most important for systematic analyze, among the parts of track-type machines. Major equipment manufacturers identified five primary conditions affecting probable life-expectancy of track-type undercarriage: impact, abrasiveness i.e. wear, terrain structure, operation and maintenance, as mentioned in Caterpillar's Performance Handbook Ed. 43. It is evident that all of these effects can be monitored and even avoided, except abrasiveness.

One of the important process which is causing reduced reliability of machines in mining industry is wear. Reason is contact of cutting elements and the working environment [13] or contact of transport mechanisms and the soil [8] that contains abrasive elements (sand with quartz – SiO_2). Issue of abrasion, SiO_2 content and wear was a research topic by several authors in the past. Cerchar test [4] and Cerchar Abrasiveness Index (CAI) are commonly used for assessment of rock abrasivity worldwide [18]. This test and derived index are used to estimate wear of cutting picks and associated replacement cost during rock excavation. Another research suggested that quartz content is most important rock property influencing the wear of cutting tools [27]. Research performed for coal measures rocks confirmed correlation, i.e. linear relationship between abrasiveness and average quartz grain size [28].

However, relation between wear caused by SiO_2 content in the rocks and remaining capabilities of mechanical equipment was not examined-researched in detail.

In any case, it is important that determining parameters of reliability are accompanied with defining the precise engineering conclusions which will contribute to advance quality of service of technical systems. The idea of this article is to find explicit correlation between reliability parameters and wear intensity parameters, in order to predict timeline of replacement of upper roller on bulldozer track mechanism and avoid unplanned down-time. Bulldozers are one of the most important machines of auxiliary machinery at lignite open pit mines. In terms of quality management of the mine, it is very important to be able to predict the moment when the machines should undergo the repair. Therefore, this article provides mathematical model and procedure which can be used to improve maintenance policy design and to reduce operational costs, according to principle of RCM.

2. Wear and problems with track mechanism and upper roller

Maximum effects of mining mechanization operating at open pit mines are obtained through timely and quality performing of the auxiliary works. For these operations to be performed, open pit must have a sufficient number of respective auxiliary machines, primarily bulldozers. They operate in extremely difficult conditions on spoil levels of open pits, within extremely variable operation conditions, from maximum drive to the transportation conditions. For these reasons, life time of these machines at open pits is relatively short and usually lasts for several years. Their reliability declines rapidly while exploitation and maintenance costs grow rapidly. For these reasons it is necessary to continuously monitor the indicators of dependability of these machines [22]. In the first place this refers to weak points on bulldozers. One of these weak points is upper roller assembly at track mechanism (Figure 1). Upper roller is exposed to the process of wear from the soil on which bulldozer moves. As the percentage of abrasive components in material is higher, so is the roller wear more intense.

Moderate wear of material on the surface is considered to be normal occurrence. However, in many cases wear is increased or abnormally high with significant surface damage of softer material in contact [10]. Such wear in relatively short period of time leads to cancellation and cracking of elements, and thus breakage of machines. This is the case with the upper rolls on bulldozers analyzed in this pa-

per. Abrasive wear of the upper rolls on bulldozer is a distinctive type of wear. Working conditions of bulldozers in lignite open pit mines in Serbia are different depending on the input of abrasive contaminants. These contaminants, depending on the type of exploited mineral resource, can have very different composition. The main ingredient is typically sand with quartz.

Wear monitoring techniques [6] are based on noise detection during regular operation, increased vibrations, detection of infrared radiation caused by friction, visualization of contact surface with high resolution cameras. In general, these techniques are supported by tribology system which contains greasing system or other cooling system. There is no greasing system of the upper roller assembly of the bulldozer. However, above mentioned techniques are relevant in numerous situations, especially in laboratory conditions. On-site measurement of such tribo-mechanical system, as described in this paper, is hindered by few circumstances. First, it is very difficult to detect noise emitted by this tribo-mechanical system during regular operation of the bulldozer due to significant background noise emitted in its vicinity by noisier components (such as engine, as well as technological process). Secondly, vibration measurement requires accurate positioning of probes, which is impossible in case of upper roller due to large dynamic loading and impacts. Thirdly, heat sensing with infra-red camera can't be applied because of dust and dirt deposits on the surface of this tribo-mechanical system (acquired data would not be accurate since heat emission varies depending from the amount of dirt and dust deposits). Finally, visualization of contact surface with high resolution camera is mainly used in controlled conditions, such as laboratory, i.e. without dust, and in case of upper roller this can't be achieved. It is obvious that these techniques are providing more reliable determination of condition and behavior of a tribo-mechanical system. However, in case of upper roller on bulldozer these techniques are not applicable, and application of measuring tools is still an optimal method for measurement of wearing. Therefore, it makes sense to monitor the statistical data, and processing based on reliability theory.

Layout of machine TD25M bulldozer with details of upper roller is presented on Figure 1, as provided by the Dressta, manufacturer of bulldozer. Figure 1.a presents the position of the upper roller of track mechanism. Figure 1.b presents photo of the new upper roller, and Figure 1.c presents the cross-section and dimensions of the upper roller with the wear area. Figure 1.c presents photo of the upper roller on the spot, namely in operation. During the operation it has been observed that the wear (figure1.c) is more intense when the machine is running on the soils that have higher percentage of sand, in the surface layer.

Abrasive wearing is most frequently deterioration-removal of metal due to presence of SiO_2 particles between mating surfaces. In this case these surfaces are track wearing plate and upper roller. Size of particles is between 150 and 200 μm. There is no lubricant between two metal surfaces, while the concentration of abrasive material (sand - SiO_2) is high. Therefore, this mechanism has no adhesive wearing, but solely abrasive wearing. Basic abrasive process is shown on Figure 2. Figure 2 shows detail of the upper roller with theoretical interpretation of abrasion occurring between wheel and tracked plat. This process is showed for two situations: beginning of wearing and wear after 700 operating hours. A reduced thickness of hardened zone is evident, as well as increased roughness.

Wearing diagram i.e. relation between wearing intensity and time in operation, for Drmno, Tamnava Zapad and Veliki Crljeni open pits is shown on Figure 3, as well as quartz content (SiO_2) in rocks of these open pits. Multiple measurements were performed by Vernier gauge on several locations of roller diameter and average value was used for wearing diagram. It is obvious that wearing intensifies after 1205, 1880 and 2242 operating hours for respective open pits. Increase is caused by hardness zone wearing off. Therefore, these times could

be considered as times for upper roller replacement as a preventive measure.
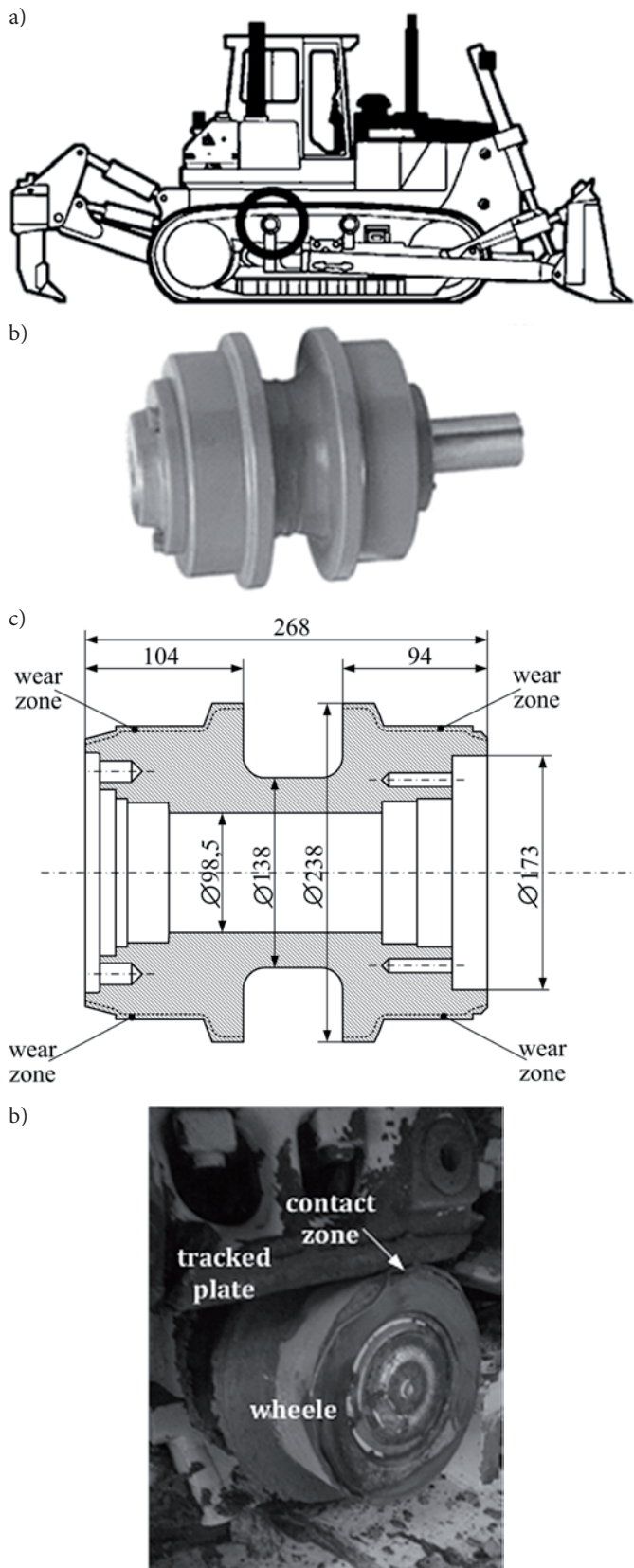
a)

b)

c)

b)

Fig. 1. a. Layout of bulldozer, position of upper roller at track mechanism of bulldozers b. Photo of new upper roll c. Dimension of upper roll d. Photo of upper roll in operation
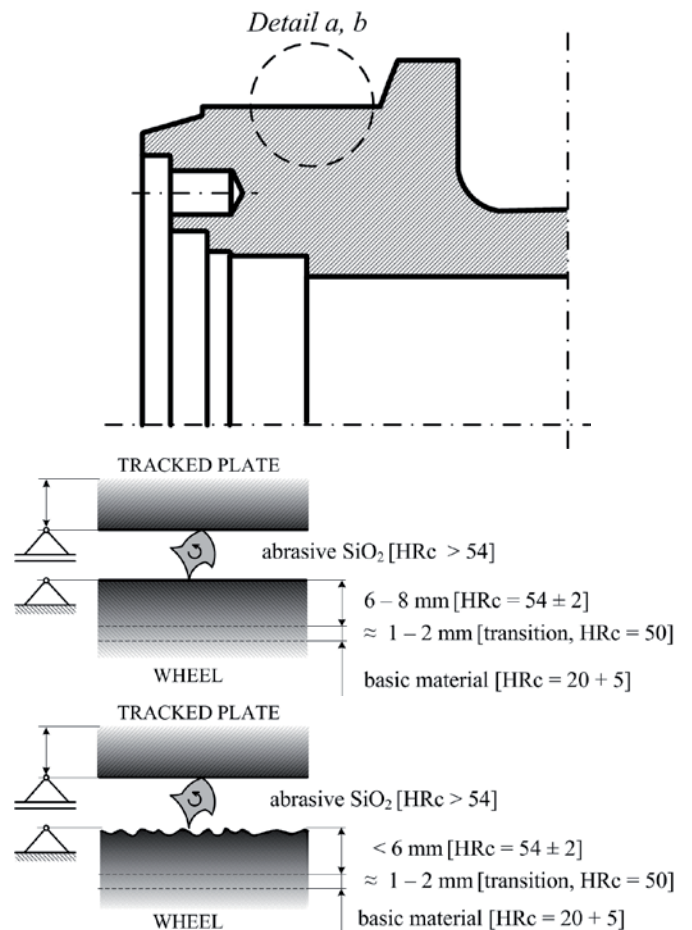

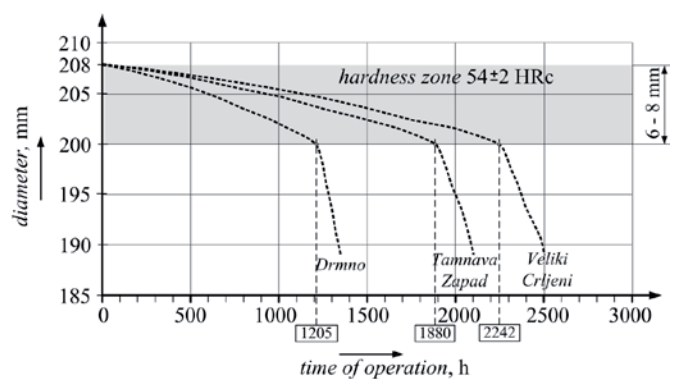*Fig. 2. The process of abrasive wear of the dozer upper roller TD25M*

Fig. 3. Diagram of wear of dozer upper roller TD25M

Fig. 4. [Part 1]

Fig. 4. Upper rollers of bulldozer TD-25M on the open pits Drmno, Tamnava Zapad and Veliki Crljeni after 1205, 1880 and 2242 hours in operation respectively

3. Analysis of two-parameter Weibull distribution and application in reliability engineering

Reliability characteristics of observed technical systems are determined on the basis of empirical data about Time To Failure (TTF). This data is collected during observing of systems during operation or experiment. One of the tasks for reliability analysis is to determine what theoretical distribution might be suitable for the best interpretation of the collected empirical data. In probability theory and statistic, it is developed dozens of distribution laws. Swedish engineer, scientist, and mathematician Ernst Hjalmar Waloddi Weibull (1877-1979), in 1939 published an article in which he described the Weibull distribution. Due to its parametric nature, this distribution was proved to be suitable for presenting large number of phenomena. It can also successfully interpret phenomena which can be presented trough some other distribution (Exponential, Rayleigh, Normal) [26]. The Weibull distribution is an important distribution especially for reliability and maintainability analysis. In article [21] on the base of the two-parameter Weibull distribution, authors were calculate mathematical correlation between conveyor rubber belt failures rate function and belt length. Authors proved trough reliability monitoring, that larger number of bending per unit length, i.e. increased fatigue loading, reduces operational life of the rubber belt. It should be noted that number of belt's bending is larger with shorter belts-conveyors. Dependence between mean time to failure and belt length is linear character. In [24] Exponential, Lognormal, Normal and Weibull distribution law, were used for analyze of draglines' mechanical failures. According to Kolmogorov-Smirnov statistical test, shows that empirical data to be best modeling with Weibull distribution. In articles [7, 29] authors suggests that the Weibull distribution is commonly used to model and analyze the failure data and lifetime data in general.

3.1. Definition of reliability function

Reliability function, on the base of two parameters Weibull distribution is written as [14, 16]:

$$R(t) = e^{-\left(\frac{t}{\eta}\right)^{\beta}} \tag{1}$$

where β is shape and η is scale parameter.

Dependence between parameter β and $R(t)$ is quite evident (Figure 5). For the cases when $0.5 \leq \beta \leq 1.5$ Weibull distribution is inclined to Exponential distribution, while when $2.5 \leq \beta \leq 5$ Weibull distribution is inclined to Normal distribution [14, 16].
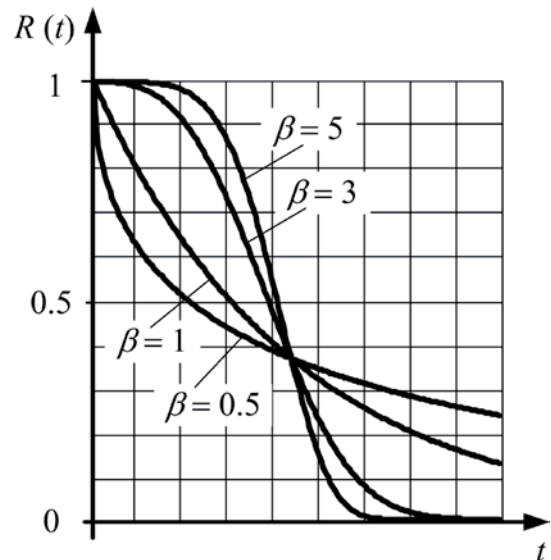

Fig. 5. Reliability function R(t) and shape parameter β

The two parameter Weibull cumulative distribution function [14, 16], i.e. probability of failure at time is defined as:

$$R(t) + F(t) = 1 \Rightarrow F(t) = 1 - R(t) = 1 - e^{-\left(\frac{t}{\eta}\right)^{\beta}} \tag{2}$$

The mean time could be calculated as:

$$\bar{T} = \eta \cdot \Gamma\left(1 + \frac{1}{\beta}\right) \tag{3}$$

where Γ is gamma function: $\Gamma(p) = \int_0^{\infty} t^{p-1} e^{-t} dt$ and $p = 1 + \frac{1}{\beta}$.

Gamma function is not easy for calculate and usually is given in appropriate tables [16].

3.2. Procedure for determination of reliability function

Procedure for determination of reliability function on the base of the two-parameter Weibull distribution, consist of next steps: data collection and ranking, data entry in Weibull Plotting Paper (WPP) [14], assessment of distribution parameters and testing of hypothesis for distribution law. Data for the analysis are periods until the failures - up times, apropos the times that the system correctly operates. In real conditions this step is very complicated because there is no existing quality system for detection of failures and their correct recording. Usually, small number of data is available. In cases where the number of data is $n30$, median rank (MR) also known as Bernard's approximation, is used instead of empirical cumulative distribution function $F(t)$ [16]:

$$MR = \frac{i - 0.3}{n + 0.4} \qquad (4)$$

where $i = 1 \ldots n$ is rank number of the data.

Mean rank and Symmetrical cumulative distribution function did not find a significant place in reliability engineering.

WPP (Figure 5) [14], has axes that transform the cumulative probability distribution function into straight line. If the data that is plotted on this type of paper forming straight line, it means that hypothesis is proper. WPP can simply be created. The Weibull distribution is defined as (1) and (2). This can be written as:

$$\frac{1}{1 - F(t)} = e^{-\left(\frac{t}{\eta}\right)^{\beta}} \qquad (5)$$

Taking two times the natural logarithms (lnln) of both sides gives an equation of a straight line:

$$\ln\ln\left(\frac{1}{1 - F(t)}\right) = \beta \cdot \ln(t) - \beta \cdot \ln(\eta) \qquad (6)$$

This equation is a straight line $y = a \cdot x + b$ on coordinate system with ordinate axis: $y = \ln\ln\left(\frac{1}{1 - F(t)}\right)$ versus abscissa axis: $\underline{x} = \ln(t)$. If at WPP entered points with coordinates $F(t)$ and t, they should be approximated with straight line. The slope of the straight line in this plot is the shape parameter β. Values of t for point on line with coordinate $F(t) = 0.63212$, is scale parameter η. It is known that: $\ln\ln\left(\frac{1}{1 - 0.63212}\right) = 0$.

There are several analytical methods used in estimating Weibull parameters [12]. Least Squares Method (LSM) is commonly applied in engineering and mathematics problems. According to this method, can be written:

$$a \cdot \sum_{i=1}^{n} x_i^2 + b \cdot \sum_{i=1}^{n} x_i = \sum_{i=1}^{n} x_i \cdot y_i; \quad a \cdot \sum_{i=1}^{n} x_i + n \cdot b = \sum_{i=1}^{n} y_i \quad (7)$$

Solving the system of equations is obtained:

$$a = \beta; \quad b = -\beta \cdot \ln(\eta) \Rightarrow \eta = e^{-\left(\frac{b}{a}\right)} \qquad (8)$$

The Kolmogorov–Smirnov test (K–S test) is the most common method for testing of hypothesis of established distribution law. K-S test has been used to decide if the failure data comes from a population with a specific distribution. K–S test compare empirical cumulative distribution function and theoretical function $F(t)$, on the base of their distance D_n. Necessity is that the distance is less than the critical value $D_{n\alpha}$, and we can conclude that the data is a good fit with the specified distribution law. Critical value can be found in the Kolmogorov-Smirnov Table [14, 16].

Probability that the observed data would follow by specified theoretical law, can be defined in dependence of significance level (α):

$$P(D_n \leq D_{n\alpha}) = 1 - \alpha \qquad (9)$$

4. Implementation of two-parameter Weibull distribution for determination of reliability of track-type mechanism of bulldozers and relationship between reliability parameters and share of mineral dust

Kostolac and Kolubara are major surface mines in Serbia, producing lignite in following open pits: Drmno and Ćirikovac (Kostolac) and Tamnava Zapad, Polje D, Polje B, Veliki Crljeni (Kolubara). Kostolac and Kolubara mines are operating as a part of the Electric Power Industry of Serbia (EPS) [11]. As reported in EPS internal documents, more than 700 auxiliary machines are operating in these open pits. These machines are very important for the unhampered execution of core operation, and any unplanned absence of machines can cause enormous costs. Among the auxiliary machinery, bulldozers are certainly the most important and it is therefore necessary to monitor the reliability and maintainability of these machines [6]. There are more than 120 bulldozers within Electric Power Industry of Serbia.

Mineralogy analyses of rocks in mentioned open pits were performed for each pit separately and provided in respective mining iand geological documents – Elaborate on reserves [19, 20]. Elaborate on reserves are in fact Governmental records on the amount and properties of mineral resources, and as such are available on each individual mine. After reviewing these documents it was possible to identify rocks with significant content of mineral dust-sand, for each open pit:

1. Kostolac „Drmno" – sandy sediment – 85%
2. Kostolac "Ćirikovac" – sandy clayey sediment – 54%
3. Kolubara "Tamnava zapad" – clayey sandy sediment (siltstone) – 41%
4. Kolubara "Polje D" – clayey sandy sediment (siltstone) – 40%
5. Kolubara "Veliki Crljeni" – clay type sediment – 14%
6. Kolubara "Polje B" – clayey sandy sediment (siltstone) – 38%

On the mentioned open pit mines were noted time to failures (TTF) in relation to failures of upper roller (Table 1). The first mentioned open pit Drmno is being observed. Number of data is $n = 10$, namely $n < 30$, therefore the median rank method (equation 4) is used for determining the cumulative distribution function $F(t)$. Points that represent given times in Table 1 and corresponding MR are then drawn into WPP (Figure 3), and the straight line is drawn so that it best approximates the given points. According to the plotting paper it can be seen that the assumption about the Weibull distribution is correct. Coordinates of specified points (Table 2, column 1) in accordance with WPP are given in Table 2 (column 2 and 3).

It should be mentioned that main goal of this research was to analyze failures of identical components (upper roller of Dressta TD-25M bulldozer) in different operating conditions (SiO_2 content), and consequence of this approach is a small sample, which is a common situation in mining engineering. Uzgoren et al. are stating „The primary problem with the data was the lack of information" in their effort of promoting the reliability theory in real conditions of mining industry [24]. It is simply impossible to stop the production system in order to analyze individual machines for experimental research. Therefore, data on TTF, collected at lignite open cast mines of Electric Power Industry of Serbia, in presented case study must be processed by MR method, i.e. approximated with Bernard's approximation (equation 4). Furthermore, only realistic approach was to collect the data for identical machines operating in different conditions-open cast mines during the period of one year (Table 1).

Using the LSM (equation 7) the equation of the straight line from WPP is obtained (Table 2, column 4-7), namely the values of shape parameter (β) and scale parameter (η) of the two-parameter Weibull distribution (equation 8):

Table 1. Time to failures (TTF)

i	Drmno	Ćirikovac	Tamnava Zapad	Polje D	Polje B	Veliki Crljeni
			TTF, hours			
1	812	1172	1522	1530	1606	1986
2	1082	1621	1898	1892	1958	2297
3	1102	1783	2000	2063	2077	2464
4	1297	1848	2053	2088	2202	2601
5	1356	2012	2086	2118	2401	2903
6	1382	2425	2182	2251	2763	
7	1437		2307	2392		
8	1521		2588	2689		
9	1688					
10	1820					

$$F(1297)_{teor.} = 1 - e^{-\left(\frac{1297}{1474.06}\right)^{4.67}} = 0.42311$$

$$D_{n(i=4)} = \left| F(1297) - F(1297)_{teor.} \right| = \left| 0.35577 - 0.42311 \right| = 0.06734$$

For the given example that contains $n = 10$ data, according to K-S test for goodness of fit (equation 9), the acceptable difference between empirical and theoretical value is:

$$D_{n;\alpha} = D_{10;0,05} = 0.410$$

Usually calculated with level of significance $\alpha = 0.05$; i.e. confidence 95% (equation 9).

Since $D_n = 0.067 < 0.410 = D_{10,0.05}$, we conclude that the data is a good fit with the Weibull distribution.

At the same way, count $R(t)$ and *MTTF* for others mines. This paper will present only the results – Table 3. On the

Table 2.Procedure for obtaining of reliability function for "Drmno Open Pit Mine"

1	2	3	4	5	6	7	8	9
i	TTF = t	MR = F(t)	ln(t) = x	$y = \ln\ln\left(\frac{1}{1-F(t)}\right) = y$	x^2	$x \cdot y$	$F(t)_{teor.}$	D
1	812	0.06731	6.69950	−2.66384	44.88330	−17.84642	0.05987	0.00743
2	1082	0.16346	6.98657	−1.72326	48.81211	−12.03969	0.21018	0.04672
3	1102	0.25962	7.00488	−1.20202	49.06837	−8.42003	0.22665	0.03296
4	1297	0.35577	7.16781	−0.82167	51.37749	−5.88955	0.42311	0.06734
5	1356	0.45192	7.21229	−0.50860	52.01719	−3.66814	0.49193	0.04001
6	1382	0.54808	7.23129	−0.23037	52.29151	−1.66584	0.52286	0.02522
7	1437	0.64423	7.27031	0.03292	52.85745	0.23937	0.58848	0.05576
8	1521	0.74038	7.32712	0.29903	53.68674	2.19105	0.68578	0.05460
9	1688	0.83654	7.43130	0.59398	55.22421	4.41402	0.84789	0.01135
10	1820	0.93269	7.50659	0.99269	56.34892	7.45171	0.93121	0.00148
			Σ = 71.83767	−5.23113	516.56730	−35.23351		

$a \cdot x^2 + b \cdot x = x \cdot y$
$a \cdot 516.56730 + b \cdot 71.83767 = -35.23351$

$a \cdot x + b \cdot n = y$
$a \cdot 71.83767 + b \cdot 10 = -5.23113$

$a = 4.67 = \beta$
$b = -34,07392 = -\beta \cdot \ln(\eta) \Rightarrow \eta = 1474,06$ hours.

Finally, we get reliability function $R(t)$ (equation 1) and mean time between failures MTTF (equation 3), for the presented case:

$$R(t) = e^{-\left(\frac{t}{\eta}\right)^{\beta}} = e^{-\left(\frac{t}{1474,06}\right)^{4,67}}$$

$$MTTF = \eta \cdot \Gamma\left(1 + \frac{1}{\beta}\right) = 1474.06 \cdot \Gamma\left(1 + \frac{1}{4,67}\right) = 1474.06 \cdot \Gamma(1,21412) = 1348.13 \text{ hours.}$$

Maximum difference between empirical (Table 2 - column 3) and theoretical (Table 2 - column 8) value of function $F(t)$, is for data $i=4$:

$MR(i=4) = 0,35577$

Figure 7, it can be seen that reliability function $R(t)$ is in dependence of sand percentage. In the case of „Veliki Crljeni" for the data $i = 5$, the difference between empirical and theoretical value of cumulative distribution of failure has value $D = 0.09414$, which is acceptable from the point of K-S test for goodness of fit.

It can be noted that value of shape parameter (β) for all cases is between 4.28 and 7.29. This means that the analyzed cases have small data dispersion about mean time (Figure 2).

As it can be seen on Figure 7, most rapid decline of reliability is at Drmno open pit, which has highest content of SiO_2. Best reliability is at Veliki Crljeni open pit, where SiO_2 content is the lowest. Measurements for individual open pits (Figure 3) are used to form upper roller replacement recommendation (Chapter 2). In mentioned cases, reliability was:

$$R_{Drmno} = e^{-\left(\frac{1205}{1474.06}\right)^{4.67}} = 68\%$$

$$R_{T.Zapad} = e^{-\left(\frac{1880}{2218.10}\right)^{6.88}} = 73\%$$

$$R_{V.Crljeni} = \mathrm{e}^{-\left(\frac{2242}{2600.09}\right)^{7.29}} = 71\%$$

Fig. 5. Weibull plotting paper

There is an obvious correlation between measurements and calculated reliability function. At the time of increased wearing occurrence, reliability is approximately 70%. This conclusion can be used for selection of upper roller replacement moment, in order to avoid unexpected failures.

In this article RCM model of bulldozer is set on the base of wear of the undercarriage of the machine. It is necessary to find right moment for maintenance actions, in this case replacement of worn parts with new spare parts.

On the Figure 8, it can see dependence between mean time to failure MTTF and sand percent. From Figure 8 it is evident linear dependence between MTTF and sand percent. Using the LSM (equation 7) for $n = 6$ (Table 4), can be obtained and the mathematical relationship between these values in the form:

$a \cdot x^2 + b \cdot x = x \cdot y$
$a \cdot 24487958.38 + b \cdot 11947.41 = 498263.10$

$a \cdot x + b \cdot n = y$
$a \cdot 11947.41 + b \cdot 6 = 272$

$a = -0.06212$
$b = 169.03227$

$$MTTF = \frac{S - b}{a} = \frac{S - 169.03227}{-0.06212}$$
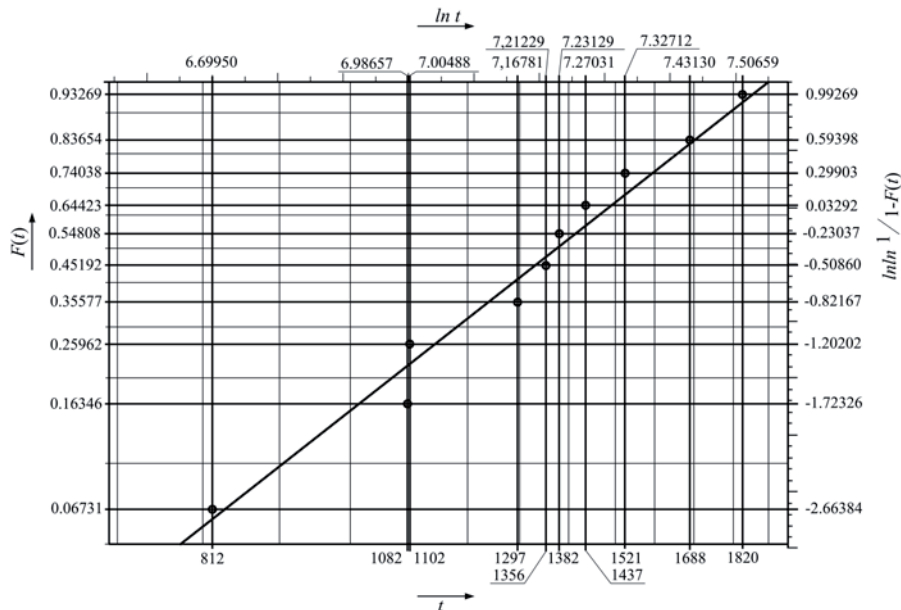$$MTTF = 2720.98 - 16.10 \cdot S \qquad (10)$$

Table 3. Reliability function and Mean time to failure for analyzed mines

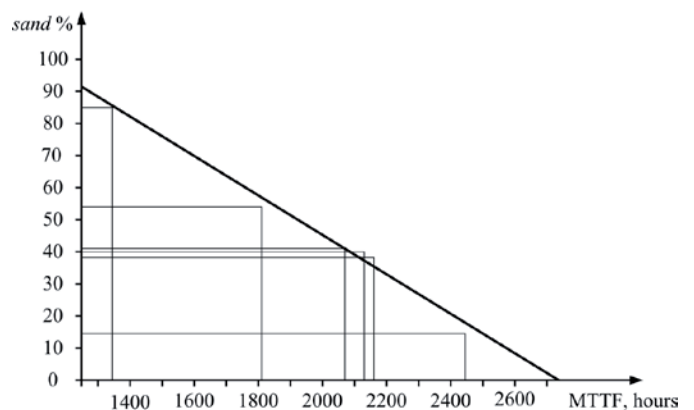|	Drmno	Ćirikovac	Tamnava Zapad
	$e^{-\left(\frac{t}{1474.06}\right)^{4.67}}$	$e^{-\left(\frac{t}{1987.21}\right)^{4.28}}$	$e^{-\left(\frac{t}{2218.10}\right)^{6.88}}$
MTTF=	1348.13	1808,36	2073.02
	Polje D	Polje B	Veliki Crljeni
	$e^{-\left(\frac{t}{2278.39}\right)^{6.41}}$	$e^{-\left(\frac{t}{2334.46}\right)^{5.68}}$	$e^{-\left(\frac{t}{2600.09}\right)^{7.29}}$
MTTF=	2121.40	2159.16	2437.37

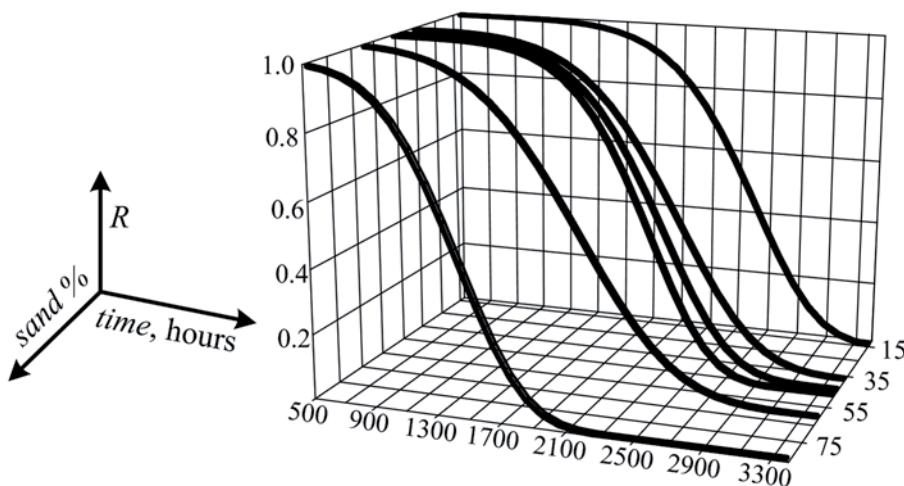*Fig. 7. Dependence between mean time to failure and sand percentage in soil*

where $S = sand\ \%$

The largest difference between the empirical and theoretical dependence function MTTF i sand% is for data $i = 6$ (Table 4 – column 7), where it is around 2.5%. It can be considered that the high accuracy of the assumption.

Presented research was performed on six different open pits on same machine-bulldozer, and it was related to reliability and wear process. Main result is ability to identify the moment (MTTF – Eq. 10) of bulldozer failure, depending on the content of sand (SiO_2) in the soil.

Fig. 6. Reliability function R in dependence of time and sand percent

Table 4.   *Procedure for obtaining of correlation between MTTF and sand percent*

1	2	3	4	5	6	7
i	MTTF $= x$	sand $\% = y$	x^2	$x \cdot y$	MTTF$_{teor.}$	D
1 – Drmno	1348.13	85	1817453.58	114591.02	1352.70	4.57
2 – Ćirikovac	1808.36	54	3270151.35	97651.22	1851.72	43.37
3 – TamnavaZapad	2073.02	41	4297415.28	84993.85	2060.99	12.03
4 – Polje D	2121.40	40	4500345.22	84856.07	2077.09	44.31
5 – Polje B	2159.16	38	4661989.73	82048.24	2109.28	49.88
6 – VelikiCrljeni	2437.34	14	5940603.22	34122.69	2495.62	58.29
$\Sigma =$	11947.41	272	24487958.38	498263.10		

5. Conclusion

In this paper on the base of theory of reliability and contents of abrasive components in composition of soil, i.e. based on analysis of data on time to failure and the percent of quartz in soil on which bulldozers move, set the model of reliability centered maintenance. It is calculated the mathematical dependency between mean time to failure and percent of quartz (equation 10). This relationship has a linear character (Figure 7), and can serve as a simple and easily applicable criterion for making decisions about the way bulldozers are utilized for the efficient work in the pit. In that sense it is recommended that preventive changes upper roller when reliability is reduced to about 70 %, when the expected increase in the intensity of wear.

Equation 10 can serve to predict the mean time in the work of the bulldozers which are analyzed in relation to sand percentage in the soil. Equation covers larger scope of types of soils. Equation also proves the hypothesis of chapter 2 of this article, a large amount of hard components in one of the contact areas contributes to intensive wear and shorter life time of contact elements. Dependence is linear, between life time and content of contact materials. Equation 10 can be used as a base for the implementation of maintenance policy (RCM) regarding the spare parts replacement.

References

1. Abo-Alkheer AK, El-Hami A, Kharmanda MG, Mouazen AM. Reliability-based design for soil tillage machines. Journal of Terramechanics 2011;48(1): 57–64, http://dx.doi.org/10.1016/j.jterra.2010.06.001.
2. Barabady J, Kumar U. Reliability analysis of mining equipment: A case study of a crushing plant at Jajarm Bauxite Mine in Iran. Reliability Engineering and System Safety 2008; 93(4): 647-653, http://dx.doi.org/10.1016/j.ress.2007.10.006.
3. Bugaric U, Tanasijevic M, Polovina D, Ignjatovic D, Jovancic P. Lost production costs of the overburden excavation system caused by rubber belt failure. Eksploatacja i Niezawodnosc – Maintenance and Reliability 2012; 14(4): 333-341
4. Cerchar - Centre d´ Etudes et Recherches de Charbonnages de France, The Cerchar Abrasiveness Index.- 12 S., 1986. Verneuil
5. Chateauneuf A, Cocheteux F, Deffarges F, Sourget F. Reliability analysis of screwed connections in high-speed trains, considering fatigue, corrosion, and imperfect maintenance operations. Proceedings of the Institution of Mechanical Engineers, Part O: Journal of Risk and Reliability September 2011; 225: 293-306, http://dx.doi.org/10.1177/1748006x11402738.
6. Chen SL, Wood RJK, Wang L, Callan R, Powrie HEG. Wear detection of rolling element bearings using multiple-sensing technologies and mixture-model-based clustering method. Proceedings of the Institution of Mechanical Engineers, Part O: Journal of Risk and Reliability June 1, 2008; 222: 207-218, http://dx.doi.org/10.1243/1748006xjrr89.
7. Freeman LJ, Vining GG. Reliability data analysis for life test designed experiments with sub-sampling. Quality and Reliability Engineering International 2013; 29(4): 509-519, http://dx.doi.org/10.1002/qre.1398.
8. Ivanov V, Shyrokau B, Augsburg K, Algin V. Fuzzy evaluation of tyre–surface interaction parameters. Journal of Terramechanics 2010; 47(2): 113–130, http://dx.doi.org/10.1016/j.jterra.2009.08.003.
9. Jaarsveld WV, Dekker R. Spare parts stock control for redundant systems using reliability centered maintenance data. Reliability Engineering and System Safety 2011; 96(11): 1576–1586, http://dx.doi.org/10.1016/j.ress.2011.06.015.
10. Jakobsen PD, Bruland A, Dahl F. Review and assessment of the NTNU/SINTEF Soil Abrasion Test (SAT™) for determination of abrasiveness of soil and soft ground. Tunnelling and Underground Space Technology 2013; 37: 107-114, http://dx.doi.org/10.1016/j.tust.2013.04.003.
11. Jovancic P, Tanasijevic M, Ivezić D. Serbian energy development based on lignite production. Energy Policy 2011; 39(3): 1191-1199, http://dx.doi.org/10.1016/j.enpol.2010.11.041.
12. Lei Y. Evaluation of three methods for estimating the Weibull distribution parameters of Chinese pine. Journal of Forest Science 2008; 54(12): 566–571.
13. Muro T. Abrasive wear resistance of surface coatings on an excavating tip against a rock mass. Journal of Terramechanics 1985; 22(2): 87–109, http://dx.doi.org/10.1016/0022-4898(85)90145-4.
14. Murthy D.N.P, Xie M, Jiang R. Weibull Models, John Wiley & Sons, Inc., 2004.
15. NASA Reliability Centered Maintenance Guide for Facilities and Collateral Equipment, February 2000.
16. O'Connor PDT, Kleyner A. Practical Reliability Engineering – Fifth edition. John Wiley & Sons Ltd., 2012.
17. Peng W, Huang H, Zhang X, Liu Y, Li Y. Reliability based optimal preventive maintenance policy of series-parallel systems. Eksploatacja i Niezawodnosc – Maintenance and Reliability 2009; 42(2): 4-7.
18. Plinninger R., Kasling H, Thuro K, Wear Prediction in Hardrock Excavation Using the Cerchar Abrasiveness Index (CAI); EUROCK 2004 & 53rd Geomechanics Colloquium. Schubert (ed.), VGE, 2004. Germany, Esse; 599–604.
19. Project "Actualized investment program of construction of surface mine Tamnava West Field" University of Belgrade - Faculty of Mining and Geology, October 2007. Belgrade, Serbia. (In Serbian)
20. Study "The revised long-term program of development of coal mining in Kostolac", University of Belgrade - Faculty of Mining and Geology, December 2006. Belgrade, Serbia. (In Serbian)

21. Tanasijevic M, Bugaric U, Jovancic P, Ignjatovic D, Polovina D. Relationship between the reliability and the length of conveyor rubber belt. Proceedings of the 29th Danubia-Adria Symposium on Advances in Experimental Mechanics, 26th-29th September 2012. Beograd; 274-277. ISBN 978-86-7083-762-1

22. Tanasijevic M, Ivezic D, Jovancic P, Ignjatovic D, Bugaric U. Dependability assessment of open-pit mines equipment – study on the bases of fuzzy algebra rules. Eksploatacja i Niezawodnosc – Maintenance and Reliability 2013; 15(1): 66–74.

23. Thies PR, Johanning L, Smith GH. Assessing mechanical loading regimes and fatigue life of marine power cables in marine energy applications. Proceedings of the Institution of Mechanical Engineers, Part O: Journal of Risk and Reliability February 2012; 226: 18-32, http://dx.doi.org/10.1177/1748006x11413533.

24. Uzgoren N, Elevli S, Elevli B, Uysal O. Reliability analysis of draglines' mechanical failures. Eksploatacja i Niezawodnosc– Maintenance and Reliability 2010; 4(48): 23-28.

25. Wang Z, Huang HZ, Du X. Reliability - based design incorporating several maintenance policies. Eksploatacja i Niezawodnosc – Maintenance and Reliability 2009; 44(4): 37-44.

26. Weibull W. A statistical distribution functions of wide applicability. Journal of Applied Mechanics - Transaction ASME 1951; 18(3): 293–297.

27. West G. Technical Note - Rock Abrasiveness Testing for Tunnelling. International Journal of Rock Mechanics and Mining Science & Geomechanics 1989. 26(2): 151-160, http://dx.doi.org/10.1016/0148-9062(89)90003-X.

28. Yaralı O, Yasar E, Bacak G, Ranjith PG. A study of rock abrasivity and tool wear in Coal Measures Rocks, International Journal of Coal Geology 2008; 74: 53–66, http://dx.doi.org/10.1016/j.coal.2007.09.007.

29. Zhang T, Dwight R. Choosing an optimal model for failure data analysis by graphical approach, Reliability Engineering and System Safety 2013; 115: 111-123, http://dx.doi.org/10.1016/j.ress.2013.02.004.

30. Zhou X, Xi L, Lee J. Reliability-centered predictive maintenance scheduling for a continuously monitored system subject to degradation. Reliability Engineering and System Safety 2007; 92(4): 530-534, http://dx.doi.org/10.1016/j.ress.2006.01.006.

Radiša DJURIĆ
Electric Power Industry of Serbia
Nikole Tesle 5-7
12208 Kostolac, Serbia

Vladimir MILISAVLJEVIĆ
University of Belgrade Faculty of Mining and Geology
Djusina 7, 11000 Belgrde, Serbia

E-mail: djuraisa@gmail.com
vladimir.milisavljevic@rgf.bg.ac.rs

Tomas SKRUCANY
Branislav SARKAN
Jozef GNAP

INFLUENCE OF AERODYNAMIC TRAILER DEVICES ON DRAG REDUCTION MEASURED IN A WIND TUNNEL

WPŁYW WYPOSAŻENIA AERODYNAMICZNEGO NACZEP NA ZMNIEJSZENIE OPORU POWIETRZA MIERZONEGO W TUNELU AERODYNAMICZNYM

The value of aerodynamic drag is the largest, when a vehicle is moving with higher velocity. It seems that drag reduction is the most important step for reducing the fuel consumption of haulage trailer sets. Using aerodynamic trailer devices is one of many ways for reduction of fuel consumption. This paper deals with experimental measuring of the truck set model in a wind tunnel. The scale of the model was 1/24. Resultant values of the drag reduction for chosen aerodynamic devices are discussed at the end of the paper.

Keywords: *aerodynamic trailer device, drag counts, truck trailer, wind tunnel.*

Wartość oporu aerodynamicznego jest największa gdy pojazd porusza się z większą prędkością. Wydaje się, że redukcja oporu jest najważniejszym krokiem do zmniejszenia zużycia paliwa zestawów transportowych zawierających naczepy. Zastosowanie wyposażenia aerodynamicznego naczep jest jednym z wielu sposobów na zmniejszenie zużycia paliwa. Niniejszy artykuł poświęcony jest eksperymentalnym pomiarom modelu zestawu ciągnika z naczepą w tunelu aerodynamicznym. Skala modelu wynosiła 1:24. Uzyskane wartości zmniejszenia oporu powietrza dla wybranych elementów wyposażenia aerodynamicznego omówiono w końcowej części pracy.

Słowa kluczowe: *wyposażenie aerodynamiczne naczep, pomiary oporu, naczepa, tunel aerodynamiczny.*

1. Introduction

The moving of road vehicles is the biggest consumer of energy in the transport duty. So in this area it is still possible to reach some rising effectiveness despite the significant progress of the last years. In Europe the highest speed limit for HGVs is 90 km×h⁻¹. The biggest share of driving performance is done on motorways and highways at the velocity of over 80 km×h⁻¹. At this velocity the biggest resistance of all driving resistances acting on moving vehicle is the aerodynamic drag, which anticipates the rolling resistance at the velocity of 80 km×h⁻¹. If we consider a tractor-trailer set (30 000 kg gross mass) with all operational characteristics of common values, so at the velocity of 90 km×h⁻¹ the representation of each resistance power is: aerodynamic drag power 68 kW (47.5%), rolling resistance power 58 kW (40.5%), powertrain losses power 17 kW (12%).

This proportion points at the importance of raising the effectiveness of moving vehicle by reducing the aerodynamic drag [1, 3, 5, 9].

2. Boundary Layer Wind Tunnel (BLWT)

The measurement was done in the wind tunnel (Fig. 1), which belongs to the Slovak Technical University in Bratislava (The Faculty of Civil Engineering).

Universal BLWT tunnel contains two operating spaces – the front space (FOS) and the rear space (ROS). It is a vacuum tunnel with an opened circuit of air flow. The air is induced in its front part. Then is comes into the FOS where the uniform non-gradient wind flow with fluctuation less than 5% is created. The FOS is suitable for the analysis of uniform non-gradient wind flow with the velocity up to 32 m×s⁻¹, [4, 10].
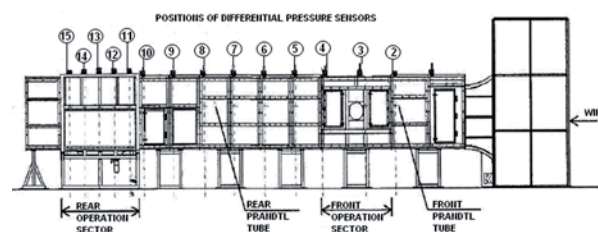

Fig. 1. Scheme of BLWT tunnel with positions of measuring devices [4]

3. Measuring Devices

Differential Pressure Sensors were placed at the cover along the tunnel in height of 1150 mm from tunnel floor. They were used for permanent monitoring of pressures inside the tunnel. Each sensor had two measuring points. Resultant value of pressure was calculated as the average from both values.

Prandtl tubes were placed in the tunnel (1st in FOS, 2nd in ROS). It determined the value of wind velocity by method of different between values of pressure in two places located on the cover of probe.

Almeo Type MA25902 with Thermo-Anemometer Probe Type FVAA935TH5K2 was used for the measurement of wind velocity [4, 10].

4. Measurement and Evaluation

Aerodynamic drag or air drag – these expressions are common as direct wind resistance, too. This is the force, which causes the resistance acting during a vehicle is moving. For the equation this resistance the Eq. 1 is used.

$$F_W = \frac{1}{2} \cdot \rho_a \cdot C_d \cdot S \cdot v^2 \qquad (1)$$

Where: F_W – aerodynamic drag; wind resistance [N],
ρ_a – air density [kg×m^{-3}],
C_d – drag coefficient [-],
S – frontal vehicle area [m^2],
v – velocity of wrapping air [m×s^{-2}].

The principle is the direct measuring of the wind force (aerodynamic drag) which is acting on a vehicle model through blowing wind (Fig. 2, Fig. 3). Its value is influenced by current air conditions (air pressure and air temperature). The vehicle shape and size and the most important element is the velocity of the wrapping wind [5, 12, 19].

This drag is directly proportional to the multiple of mentioned elements (Eq. 1). It is possible to change the only one element from the Eq. 1. It is the drag coefficient C_d. Air density is a dynamical changing natural dimension that cannot be influenced by a human being. The vehicle size is limited by legislation and it is using on the edge. Downsizing is not acceptable because of the vehicle volume effectiveness. The vehicle velocity is an important element in the transport duties since it depends on the delivery time. It is possible to change only the vehicle shapes and they relate to the C_d. The coefficient expresses fluency of the wind wrapping [6, 8, 20].

A number of physical data was read by detection devices during the measurement for precise determination of results. Especially the atmospheric pressure and air temperature were measured. From these values the instantaneous air density ρ_V were calculated. The speed of the airflow was measured by Prandtl tubes in several places in the tunnel and anemometer was used directly at the site wrapping around the model with four levels within the height of the model. Therefore it was possible to determine the mean velocity of the air, which was used in the calculations below.
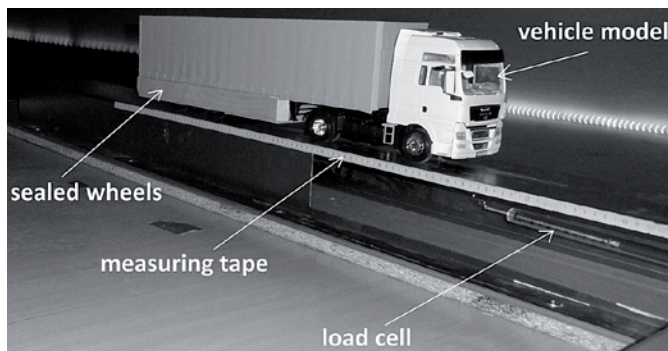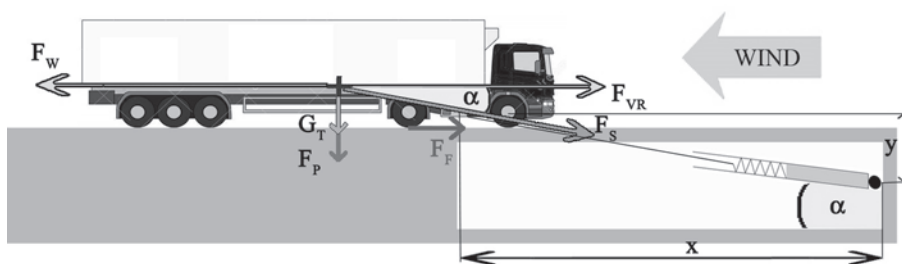

Fig. 2. Measuring apparatus

Fig. 3. Measuring scheme (F_W – wind force, F_{WR} – wind force reaction, F_S – load cell force. F_f – rolling resistance force. F_P – additional downforce caused by F_S, G_T – vehicle gravity force, T – gravity centre, x - horizontal distance between two anchor points of loading cell , y – vertical distance between two anchor points of loading cell, α – angle between load cell axle and horizontal plane)

Face of the model represents the area bounded by its maximum height and width due to the scale model of the 1/24 the size of both dimensions. Thus the area represents 1/576 of the real vehicle surface.

The wind resistance was measured by a load cell placed in the model preparation (Fig. 3). Mechanical load cell was equipped with a spring of linear characteristic and reached a measurement range of 0 N to 5 N with accuracy of 0.05N.
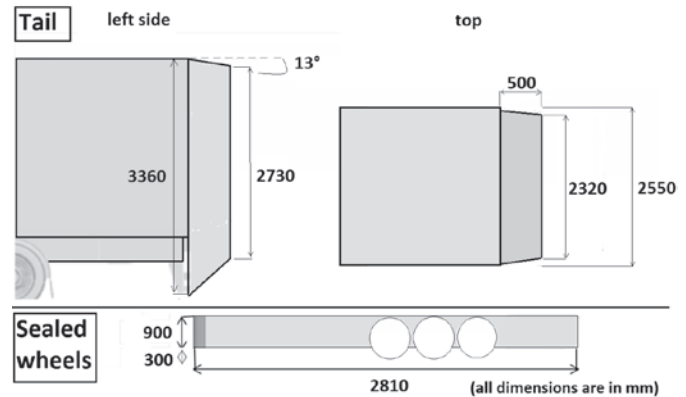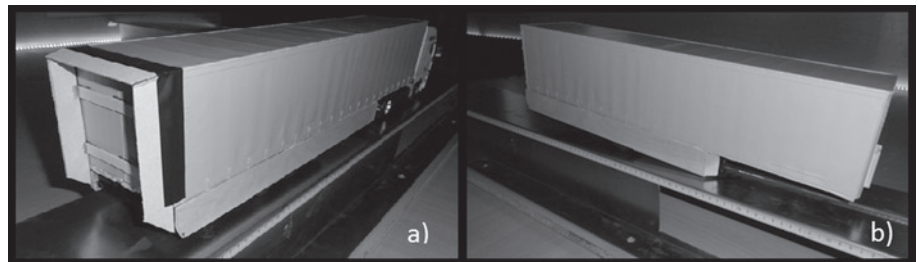

Fig. 4. Dimensions of aerodynamic devices

Fig. 5. Aerodynamic devices: a) combination of sealed wheels and tail, b) sealed wheels

5. Aerodynamic Devices

The scopes of this measurement were two types of devices (Fig. 4). They were chosen because of the present trend of using these devices. The following devices have been chosen: sealed wheels, tail and combination of them.

Nowadays many measurements are done to describe the influence of these devices on the truck fuel consumption. Some transport companies already use sealed wheels on a part of the trailers and the trailer producers offer them as the optional trailer trim. But using the tail is not possible because of current legislation (length of truck sets). The new European legislation is in preparation, which allows this aerodynamic tail. The actual truck length will be about 500 mm longer.

The dimensions pointed on the Fig. 4 represent the devices of the real size in millimetres. Such devices were used on the model as well as their dimensions are scaled in 1/24. Devices were made personally from soft wood (spruce) and attached to the model by a double – sided tape (Fig. 5).

6. Conclusion

During the measurement air pressure reached the values 99360 – 99460 Pa and air temperature was (24 ÷ 24.4)°C. Thanks to the steady conditions approximate value of air density was 1.196 kg×m^{-3}.

Each examined state (2 aerodynamic devices, their combination and reference "mass-produced" vehicle model) was measured for two cases of wind yaw angle – 0° and 5°.

The velocity of wind flow was regulated by the frequency of two electric motors in the tunnel. All measurements were repeated for three frequencies (velocities) – 28 Hz, 32 Hz and 34 Hz. These values correspond to following wind velocities – 15.48 m×s^{-1}, 17.28 m×s^{-1} and 18.08 m×s^{-1}.

The model is resting on its wheels which are rotatable mounted. This fact was used and the model was pushed on the wheels by blowing wind in its direction. The model is equipped with rubber wheels. They cause rolling resistance. Also friction losses of wheel shafts represent resistance to movement of the vehicle. These resistive forces were measured after the measurement by hydraulic cylinder (laboratory equipment of the Department of Road and Urban Transport) and load cell. Using the cylinder, the model was driven by a very slow rate evenly over the measuring mat, so the rolling resistance value was given. This was done with multiple burdens placed on the model. Since cosine force component FS (Fig. 3) also creates additional downforce on the model surface.

The exact value of the angle α was determined by the distance between clamping load cell for measuring surface and clamping the model and the height difference of the two points. This distance was measured by using the measuring tape mounted on the substrate under the measurement model (Fig. 2).

During the measurement load cell senses the force F_S which is not identical with the force of the wind, but must be recalculated due to the diversion load cell angle from the horizontal plane and the rolling resistance of tires.

$$F_W = F_{VR} + F_f$$
$$F_W = F_S \cdot \cos\alpha + (G_T + F_P) \cdot f \qquad (2)$$
$$F_W = F_S \cdot \cos\alpha + (G_T + F_S \cdot \sin\alpha) \cdot f$$

where: f – rolling resistance coefficient related for each experiment; other signs are described in Fig. 3.

After substituting Eq. 2 into the Eq. 1 we will obtain the resultant equation (Eq. 3). According to it the drag coefficient C_d was calculated by inserting measured individual values.

$$C_d = 2 \cdot \frac{\left[F_S \cdot \cos\alpha + (G_T + F_S \cdot \sin\alpha) \cdot f \right]}{\rho_a \cdot S \cdot v^2} \qquad (3)$$

The measurement was performed in two cases namely the yaw angle of 0° and of 5°. Several angles used to be examined in similar measurements. Their impact is expressed in the weighted average. However, the most relevant of which are right angles 0° and 5°. The yaw angle is affected mainly by the strength and direction of the blowing wind while driving vehicle. In still air or direct headwind shall take this angle to 0°. Resulting yaw angle increases with increasing angle and speed of blowing wind [2, 15, 16],
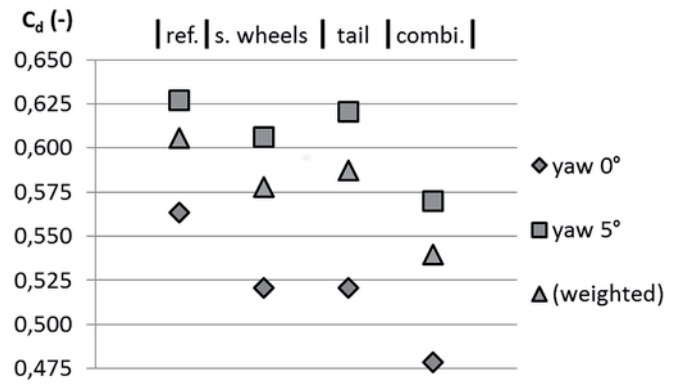

Fig. 6. Drag coefficient

$$C_{dw} = \tfrac{1}{3} C_{d0} + \tfrac{2}{3} C_{d5} \qquad (4)$$

where: C_{dw} – weighted drag coefficient [-],
  C_{d0} – drag coefficient at yaw 0° [-],
  C_{d5} – drag coefficient at yaw 5° [-].

The column values (Fig. 7) represent the reducing of aerodynamic drag in units designated as DC (Drag counts – unit air resistance). They represent thousands of times the difference of the coefficients Cd for reference vehicle and vehicle with devices. This is a simplified labelling of drag coefficients difference.
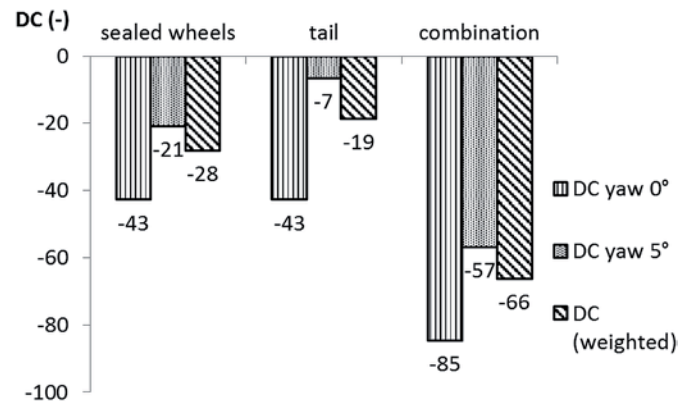

Fig. 7. Drag values in DC

$$DC = 1000 \cdot \Delta C_d \qquad (5)$$

where ΔC_d is the difference of C_d for reference vehicle and vehicle equipped with devices [-].

Fig. 6 and Fig. 7 express the influence of aerodynamic devices on the drag coefficient. From this graphic evaluation the influence rate of each device in the absolute expression as C_d or in the difference as DC is clear. The lower rates of coefficient are better because they are directly proportional to the aerodynamic drag. With decreasing of the drag also truck fuel consumption decreases and that is the main reason of testing and using aerodynamic devices. As the main result value we consider the weighted C_d or DC. Theoretically it reflects light crosswind wind influence which acts during a vehicle is moving. The best result reaches combination of both devices at the value of −66 DC.

Table 1. Evaluation of measured values

Device	C_d yaw 0°	C_d yaw 5°	C_d (weighted)	DC yaw 0°	DC yaw 5°	DC (weighted)
Reference model	0.563	0.627	0.606	-	-	-
Sealed wheels	0.521	0.606	0.578	-43	-21	-28
Tail	0.521	0.620	0.587	-43	-7	-19
Combination	0.479	0.570	0.540	-85	-57	-66

Higher influence reflects at the yaw of 0° what is probably due to the bigger surface where the crosswind at the yaw of 5° can act. Sealed wheels reach higher decreasing of C_d than tail without enlarging the truck length and side surface and without decreasing manoeuvrability (tail does it) [11, 13, 14].

5. Summary

During measuring and its evaluation we took the view that using a model vehicle of higher scale would probably get results with accuracy. But the measured values present common rates of C_d used in the scientific area of the ground vehicles. Next measurement on the real sized vehicle on real road would be more appropriate. According to the comparison of real condition and this measuring the differences are: static wheels on the model and a static road (mat) in a wind tunnel. These two facts should have influence on smaller differences to C_d values of the real truck set [15, 17, 18].

The results provide values which reflect negligible effect on the aerodynamic drag of truck sets. They show that using these devices consumed fuel can be spared and so the effectiveness of the transport duty and of a vehicle can be increased.

References

1. Barnard R H. Road vehicle aerodynamic design - an introduction. St. Albans: Mechaero Publishing, 2001.
2. Choi H, Lee J, Park H. Aerodynamics of Heavy Vehicles. Annual Review of Fluid Mechanics 2014; 46: 441–468, http://dx.doi.org/10.1146/annurev-fluid-011212-140616.
3. Davila A. Report on Fuel Consumption. Project 233683 SARTRE, ECE, 2013.
4. Ghoreyshi M, Kim A D H, Jirasek A, Lofthouse A J, Cummings R M. Validation of CFD simulations for X-31 wind-tunnel models. Aeronautical Journal 2015; 119 (1214): 479–500.
5. Gunes D. On the similarity of wind tunnel experiments and numerical simulation of heavy-duty trailer flow. Progress in Computational Fluid Dynamics 2010; 10 (3): 168–176, http://dx.doi.org/10.1504/PCFD.2010.033328.
6. Hakansson Ch, Lenngren M J. CFD Analysis of Aerodynamic Trailer Devices for Drag Reduction of Heavy Duty Trucks. Goteborg: Chalmers University of Technology, 2010.
7. Hausberger S, Rexeis M, Blassnegger J, Silberholz G. Evaluation of fuel efficiency improvements in the Heavy-Duty Vehicle (HDV) sector from improved trailer and tire designs by application of a new test procedure. Graz: TU Graz, 2011.
8   Holt J, Garry K, Velikov S. A wind tunnel investigation into the effects of roof curvature on the aerodynamic drag experienced by a light goods vehicle. International Journal of Vehicle Design 2015; 67 (1): 45–62, http://dx.doi.org/10.1504/IJVD.2015.066478.
9. Hromadko J, Miller P, Honig V. Use of the vehicle movement model to determine economic and environmental impact caused by separate vehicles. Eskploatacja I Niezawodnosc - Maintanence and Reliability 2009; 1: 70–73.
10. Hubova O, Konecna L, Lobotka P. Influence of Walls and Ceiling on a Wind Flow in BLWT Tunnel. Applied Mechanics and Materials 2014; 617: 257 – 262, http://dx.doi.org/10.4028/www.scientific.net/AMM.617.257.
11. Jazar R. Vehicle Dynamics, Theory and applications. Springer Science + Bussines Media, 2009.
12. Kendra M, Babin M, Barta D. Changes of the infrastructure and operation parameters of a railway line and their impact to the track capacity and the volume of transported goods. Procedia - social and behavioral sciences 2012; 48: 743–752, http://dx.doi.org/10.1016/j.sbspro.2012.06.1052.
13. Liscak S, Matejka R, Rievaj V, Sulgan M. Operational characteristics of vehicles. Zilina: Edis publisher, 2004.
14. Levulyte L, Zuraulis V, Sokolovskij E. The research of dynamic characteristics of a vehicle driving over road roughness. Eksploatacja i Niezawodnosc – Maintenance and reliability 2014; 16 (4): 518–525.
15. Parczewski K, Wnenk H. Using mobile scaled vehicle to investigate the truck lateral stability. Eskploatacja i Niezawodnosc – Maintanence and Reliability 2013; 4: 414–420.
16. Rajamani R. Vehicle dynamics and control. New York: Springer, 2012, http://dx.doi.org/10.1007/978-1-4614-1433-9.
17. Watkins S. Wind-Tunnel Modelling of Vehicle Aerodynamics: with emphasis on turbulent wind effects on commercial vehicle drag. Melbourne: Victorian University of Technology, 1990.
18. Wong J Y. Theory of ground vehicles. Ottawa: John Wiley & Sons. Inc., 2001.
19. Zvolensky P, Stuchly V, Grencik J, Poprocky R. Evolution of maintenance systems of passenger and freight wagons from the ECM certification point of view. Communications: scientific letters of the University of Zilina 2014; 16: 40–47.
20. Zuraulis V, Sokolovskij E, Matijosius J. The opportunities for establishing the critical speed of the vehicle on research in its lateral dynamics. Eksploatacja i Niezawodnosc – Maintenance and Reliability 2013; 15 (4): 312–318.

Tomas SKRUCANY
Branislav SARKAN
Jozef GNAP
Department of Road and Urban Transport
Faculty of Operations and Economic of Transport and Communications
University of Žilina
Univerzitná 1, 010 26 Žilina, Slovakia
E-mail: tomas.skrucany@fpedas.uniza.sk
branislav.sarkan@fpedas.uniza.sk, jozef.gnap@fpedas.uniza.sk

INFORMATION FOR AUTHORS

Eksploatacja i Niezawodnosc – Maintenance and Reliability – the journal of the Polish Maintenance Society, under the scientific supervision of the Polish Academy of Sciences (Branch in Lublin), published four times a year.

The scope of the Quarterly

The quarterly *Eksploatacja i Niezawodnosc – Maintenance and Reliability* publishes articles containing original results of experimental research on the durability and reliability of technical objects. We also accept papers presenting theoretical analyses supported by physical interpretation of causes or ones that have been verified empirically. *Eksploatacja i Niezawodność – Maintenance and Reliability* also publishes articles on innovative modeling approaches and research methods regarding the durability and reliability of objects.

The following research areas are particularly relevant to the journal:

1. degradation processes of mechanical and biomechanical systems,
2. diagnosis and prognosis of operational malfunctions and failures.
3. analysis of failure risk/wear,
4. reliability-and-environmental-safety engineering in the design, manufacturing and maintenance of objects,
5. management and rationalization of object maintenance,
6. risk management in the processes of operation and maintenance,
7. the human factor and human reliability in operation and maintenance systems.

Terms and Conditions of Publication

The quarterly *Eksploatacja i Niezawodnosc – Maintenance and Reliability* publishes only original papers written in English or in Polish with an English translation. Translation into English is done by the Authors after they have received information from the Editorial Office about the outcome of the review process and have introduced the necessary modifications in accordance with the suggestions of the referees! Acceptance of papers for publication is based on two independent reviews commissioned by the Editor.

The quarterly *Eksploatacja i Niezawodnosc – Maintenance and Reliability* proceeds entirely online at submission.ein.org.pl

Technical requirements

- After receiving positive reviews and after acceptance of the paper for publication, the text must be submitted in a Microsoft Word document format.
- Drawings and photos should be additionally submitted in the form of high resolution separate graphical files in the TIFF, SVG, AI or JPG formats.
- A manuscript should include: names of authors, title, abstract, and key words that should complement the title and abstract (in Polish and in English), the text in Polish and in English with a clear division into sections (please, do not divide words in the text); tables, drawings, graphs, and photos included in the text should have descriptive two-language captions, if this can be avoided, no formulae and symbols should be inserted into text paragraphs by means of a formula editor; references (written in accordance with the required reference format); author data – first names and surnames along with scientific titles, affiliation, address, phone number, fax, and e-mail address.

The Editor reserves the right to abridge and adjust the manuscripts. All submissions should be accompanied by a submission form.

Detailed instructions to Authors, including evaluation criteria can be found on the journal's website: www.ein.org.pl

Editor contact info

Editorial Office of „Eksploatacja i Niezawodnosc - Maintenance and Reliability"
Nadbystrzycka 36, 20-618 Lublin, Poland
e-mail: office@ein.org.pl

INFORMATION FOR SUBSCRIBERS

Fees

Yearly subscription fee (four issues) is 100 zloty and includes delivery costs. Subscribers receive any additional special issues published during their year of subscription free of charge.

Orders

Subscription orders along with authorization to issue a VAT invoice without receiver's signature should be sent to the Editor's address.

Note

In accordance with the requirements of citation databases, proper citation of publications appearing in our Quarterly should include the full name of the journal in Polish and English without Polish diacritical marks, i.e.,

Eksploatacja i Niezawodnosc – Maintenance and Reliability.